Design, Synthesis, and Structure-Activity Relationship Studies of Dual *Plasmodium falciparum* Phosphatidylinositol 4-kinase and cGMP-dependent Protein Kinase Inhibitors

BY

SAMUEL NJOROGE GACHUHI

Supervisor: **Prof Kelly Chibale**

Co. Supervisor: **Dr Lauren B. Arendse**

Thesis submitted for the Degree of **DOCTOR OF PHILOSOPHY** in the

Department of Chemistry, Faculty of Science, University of Cape Town,

Rondebosch, 7701, Cape Town

South Africa

May 2022

DECLARATION

I declare that the project titled "***Design, Synthesis, and Structure-Activity Relationship Studies of Dual Plasmodium falciparum Phosphatidylinositol 4-kinase and cGMP-dependent Protein Kinase Inhibitors***" is my original work and has not been submitted elsewhere for examination, award of a degree or publication. Where other people's work has been used, this has been acknowledged and referenced in accordance with the University of Cape Town requirements.

Signature: …….....

SAMUEL NJOROGE GACHUHI

(GCHSAM002)

Department of Chemistry

Faculty of Science

University of Cape Town

DEDICATION

This work is dedicated to my family, for their unconditional love, prayers, faith and patience to which I cherish everyday

ACKNOWLEDGMENTS

My academic journey has been influenced positively by many people who have played indispensable roles towards my academic endeavours.

My former lecturers and supervisors at Moi University and the University of Nairobi are warmly acknowledged for your guidance and encouragement in my studies. To be specific, Dr Peter Njogu and Dr Eric Guantai, both from the Department of Pharmacology and Pharmacognosy, and Dr Albert Jairo Ndakala of the Department of Chemistry, University of Nairobi deserve special mention for the trust you endowed in me and your eventual recommendation to my PhD supervisor.

With utmost humbleness, I wish to convey my gratitude, respect, and admiration to my supervisor Prof. Kelly Chibale (KC) and co-supervisor Dr Lauren B. Arendse, for believing in me and for their exemplary work as my supervisors and mentors during my entire PhD period. I am highly indebted to you for the opportunity to pursue my PhD studies in your labs and under your guidance and mentorship. Your financial and moral support, inspiration, and more so for the laboratory space, resources, and professional guidance during my entire research period is deeply appreciated. It was a noble and rare opportunity envied by many. Also, worth a mention are Dr Greg Basarab, Dr Leslie Street and Dr Sandeep Ghorpade from the Holistic Drug Discovery, and Development (H3D) Centre at UCT who despite working behind the scenes, have been immensely instrumental and resourceful towards the successful realization of this project.

Sincere gratitude goes to the H3D Centre for the invaluable technical expertise and infrastructure provided throughout my studentship. My heartfelt appreciation goes to the H3D team at the Department of Medicine, Division of Clinical Pharmacology for the assistance in anti-plasmodium assays, physicochemical profiling and DMPK studies. Special thanks to Dr Dale Taylor, Dr Mathew Njoroge, and Dr Liezl Gibhard, all of H3D. Also, worth my appreciation is Lynn Wambua and Dr Andani Mulelu who under the leadership of Dr Lauren B. Arendse have been very instrumental on enzymological aspects such as the laborious purification of proteins and standardization of assays employed in this work.

My special thanks to members of the H3D and KC ADME computational team led by Dr Joe Eyermann and Dr Stephen Fienberg, for development of the homology model and for your

generous assistance in docking experiments employed in this study. Also, worth my appreciation is my friend and Kenyan colleague, Ms Stephanie Kamunya with whom we have worked tirelessly on computational design aspects and laying ground for the understanding of *in silico*, enzymological, and medicinal chemistry profile of the chemotypes explored in this study. I am grateful to the Swiss Tropical and Public Health Institute (STPH), particularly Dr Sergio Wittlin's lab for anti-plasmodium tests of selected compounds against both the drug-sensitive and multidrug resistant strain. Prof. Lynn-marie Birkholtz and her team at University of Pretoria, Department of Biochemistry and Institute of Sustainable Malaria Control are highly acknowledged for the gametocytocidal assays, and selected cytotoxicity and anti-plasmodium assays.

Special thanks to Peter Roberts and Marwaan Rylands for acquisition of my NMR data. I am also grateful to former and current postgraduate students of the KC Medicinal Chemistry Group with whom I have worked tirelessly with for the realization of this work. Their generous assistance, constant encouragement, and at times much needed criticism, which acted as a catalyst to immense ideas, was more than I could ask for. Radwan Alnajjar is acknowledged for assistance in the generation of some Pymol images included in this work. Administrative input from the UCT Department of Chemistry and H3D staff, especially Elaine Rutherfoord-Jones, Saroja Naicker, Ayesha Bandeker, and Deidre van Rooyen, are deeply acknowledged.

Many thanks to H3D, Merck and Medicines for Malaria Venture (MMV) for provision of the much-needed funding for this project. The travel grant from the Bill and Melinda Gates Foundation (BMGF) through Keystone Symposia to facilitate my poster presentation at Addis Ababa, Ethiopia is also worth my appreciation. Special thanks to The UCT Postgraduate Centre and Funding Office (PGFO) for your financial support through the J. W. Jagger Scholarship for International Students and the Contingency Foundation Award. The GSK Cellzome facility and H3D are acknowledged for sharing the enzymatic and anti-plasmodium data used as the foundation of this study. Dr Lebu Taleli (H3D) is acknowledged for proof-reading sections of this document.

Finally, special thanks to my parents, Elizabeth Wanjiku, and the late David Gachuhi, for the moral support, patience, trust, and the sacrifices you have made for me throughout my academic career. Mum, you are a woman of wonders and may all your prayers never go unanswered. The journey and the waiting has been long, but the ship has finally come to dock. Thanks Mama.

PUBLICATIONS AND CONFERENCES

Publications

Dziwornu, G. A.; Attram, H.; **Gachuhi, S.**; Chibale, K. Chemotherapy for human schistosomiasis: how far have we come? What's new? Where do we go from here? *RSC Med. Chem.* **2020**, DOI: 10.1039/d0md00062k.

Conference Presentations: Poster

Gachuhi, S.; Arendse, L.; Wambua, L.; Fienberg, S.; Kamunya, S.; Eyermann, J.; Basarab, G.; Chibale, K. *Imidazopyridazines as dual Plasmodium PI4K/PKG inhibitors.* Keystone Symposia, 30th October - 2nd November 2019, The Malaria Endgame: Innovations in Therapeutics, Vector Control and Public Health Tools. Venue: Hilton Addis Ababa Hotel, Addis Ababa, Ethiopia.

ABSTRACT

Malaria is a life-threatening disease caused by protists in the genus *Plasmodium* and transmitted by the female *Anopheles* mosquito. Amongst five species which infect humans, *Plasmodium falciparum* (*Pf*) causes the severest form of the disease. Although significant efforts have been made to reduce the overall impact of malaria in endemic regions, the ever emergence and continuous spread of parasite resistance to available chemotherapeutics, threatens to undermine advances made thus far. In addition, the current portfolio of drugs is non-effective in addressing chemoprotection, transmission blockade and relapse in *P. vivax* and *P. ovale* species. Thus, drugs targeting multiple stages of the parasite life cycle and of low risk to resistance, are highly desirable to support malaria elimination and/or eradication efforts.

Considering the success of human kinase inhibitors as anti-cancer drugs and the identification of *Plasmodium* kinases as promising targets for malaria chemotherapy, this study aimed to optimize anti-plasmodium phosphatidylinositol 4-kinase (PI4K) and the cGMP-dependent protein kinase (PKG) inhibitors, based on two distinct chemotypes. *Plasmodium* PI4K and PKG are validated targets, each with the potential to deliver pan-stage active compounds with potentially moderate to low risk of resistance.

Part 1 of this study focused on the repositioning of the oncological clinical Phase-1 mammalian target of rapamycin (mTOR) inhibitor, **MLN0128,** as a dual *Plasmodium* PI4K/PKG inhibitor for malaria. **MLN0128** was identified by GlaxoSmithKline (GSK) Cellzome facility as a *Plasmodium* multi-kinase inhibitor with potent PI4K and PKG inhibitory activity. In this study, an *in silico*-guided structural modification strategy was undertaken towards optimizing dual *Plasmodium* kinase inhibition and anti-plasmodium activity while also mitigating potency against its oncological human target, mTOR and off-target PI4KIIIb (**Figure 1**). Arising from this work, analogues equipotent against both the chloroquine sensitive (*Pf*NF54) and multi-drug resistant (*Pf*K1) strains simultaneously

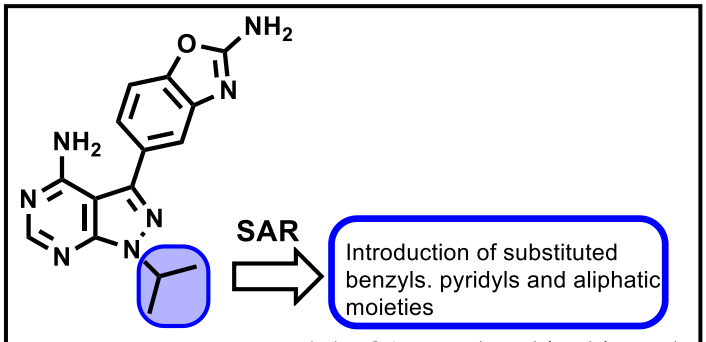

Figure 1: MLN0128 and the SAR explored in this study

targeting PI4K and PKG were identified. Docking studies using a *Pf*PI4K homology model and a *Pv*PKG crystal structure discerned the molecular features responsible for the high affinity of the inhibitors for these *Plasmodium* targets.

Benzyl analogues containing a fluoro or chloro group at the *meta* or *para* positions displayed high anti-plasmodium activity with potent *Pv*PI4K inhibition but weak *Pf*PKG inhibition. Notable analogues included **7** (*Pf*NF54 IC_{50} = 0.029 µM; *Pv*PI4K IC_{50} = 0.007 µM; *Pf*PKG IC_{50} > 2 µM) and **35** (*Pf*NF54 IC_{50} = 0.086 µM; *Pv*PI4K IC_{50} = 0.008 µM; *Pf*PKG IC_{50} > 10 µM). Introduction of basic or pyridyl substituents proved important for dual *Plasmodium* kinase activity as exemplified by the active anti-plasmodium pyridyl analogues **44** (*Pf*NF54 IC_{50} = 0.104 µM; *Pv*PI4K IC_{50} = 0.004 µM; *Pf*PKG IC_{50} = 0.834 µM) and **49** (*Pf*NF54 IC_{50} = 0.189 µM; *Pv*PI4K IC_{50} = 0.006 µM; *Pf*PKG IC_{50} = 0.384 µM). In addition, the two compounds displayed low cytotoxicity against the Chinese Hamster Ovarian cell line, with a favorable selectivity index (CHO; SI > 100), low human ether-*a-go-go*-related gene (hERG) activity (IC_{50} > 10 µM) and high metabolic stability against human, rat, and mouse (H/R/M) liver microsomes (> 75% remaining after 30-min incubation).

Selected compounds from the series also showed the potential for transmission blockade with specificity for stage IV/V gametocytes (IC_{50} < 1 µM). Furthermore, human off-target PI4KIIIb profiling displayed low activity (< 5% inhibition at 1 µM) for two representative compounds. However, the most promising compounds demonstrated sub-optimal solubility (< 50 µM) and high human mTOR inhibitory activity, issues that necessitate further optimization for progression of this scaffold as an antimalarial chemotype.

Part 2 of the study focused on the improvement of solubility, mitigating the hERG liability, and retaining dual *Plasmodium* PI4K/PKG activity of an established anti-malarial imidazopyridine scaffold. Medicinal chemistry optimization strategies largely revolved around the incorporation of water-solubilizing features (**Figure 2**). Thus, a series of phenyl carboxamides were appended on the left-hand side of the core

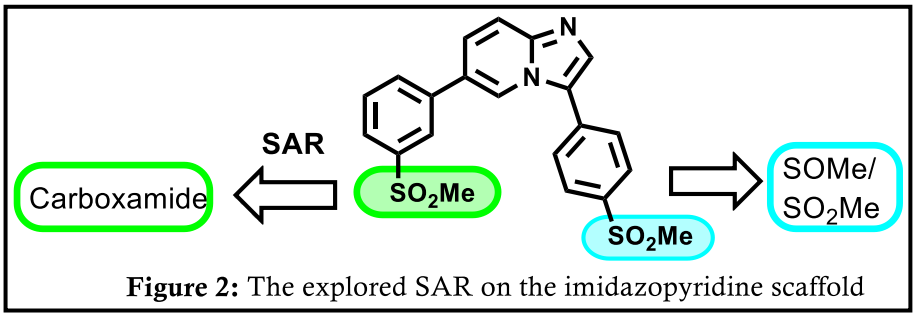

Figure 2: The explored SAR on the imidazopyridine scaffold

scaffold while phenyl sulfinyl and sulfonyl moieties were explored on the right-hand side. Incorporation of these features led to several active analogues (*Pf*NF54 IC_{50} < 1 μM) with high aqueous solubility (> 100 μM). Compounds displayed potent *Pv*PI4K inhibition but weak *Pf*PKG inhibition (IC_{50} > 1 μM) in enzyme assays. Four compounds, including one sulfoxide analogue, displayed high stability when incubated with H/R/M liver microsomes in microsomal metabolic stability assays. These features also mitigated hERG activity as five analogues tested displayed an IC_{50} > 10 μM. Ultimately, a front-runner lead compound (**86**; **GS1 16**) with high biological activity and a good safety profile (*Pf*NF54/*Pf*K1 = 0.063/0.100 μM; *Pv*PI4K IC_{50} = 0.003 μM; CHO SI > 793), optimal solubility (195 μM), favorable microsomal metabolic stability (H/R/M = 96/85/88%) and low affinity on the hERG-encoded potassium channel (IC_{50} = 44.80 μM), was identified for further progression.

LIST OF ABBREVIATIONS AND ACRONYMS

ACN: Acetonitrile
ACT: Artemisinin-combination therapy
ADME: Absorption, distribution, metabolism, and excretion
ADP: Adenosine diphosphate
APCI: Atmospheric pressure chemical ionization
AR: Analytical-grade reagent
ATP: Adenosine triphosphate
ATP4: Adenosine triphosphatase 4
AUC: Area under the curve
BMGF: Bill and Melinda Gates Foundation
BSA: Bovine serum albumin
CADD: Computer-aided drug design
CARL: Cyclic amine resistance locus
CC: Column chromatography
^{13}C-NMR: ^{13}Carbon nuclear magnetic resonance
CDC: Centre for Disease Control and Prevention
CDPK: Calcium-dependent protein kinase
cGMP: Cyclic guanosine monophosphate
CHO: Chinese hamster ovarian cell line
CK1: Casein kinase 1
CLK1: Cdc2-like-kinase 1
COVID-19: Coronavirus disease 2019
CQ: Chloroquine
CRKs: Cysteine-rich receptor-like protein kinase
CYP450: Cytochrome P450
DCM: Dichloromethane
DDQ: 2,3-Dichloro-5,6-dicyano-1,4-benzoquinone
DHA: Dihydroartemisinin
DHODH: Dihydroorotate Dehydrogenase
DHFR: Dihydrofolate reductase
DHPS: Dihydropteroate synthase
DIPEA: Di-isopropylethylamine
DMEM: Dulbecco's modified eagle's medium
DMF: *N*, *N*-Dimethylformamide
DMSO: Dimethyl sulfoxide
DMPK: Drug metabolism and pharmacokinetics
DNA: Deoxyribonucleic acid
DTT: Dithiothreitol
EC_{50}: Half-maximal effective concentration
ED_{90}: Effective dose for 90% inhibition
EG: Early-stage gametocytes
EGTA: Ethylene glycol-bis(β-aminoethyl ether)-*N*,*N*,*N*′,*N*′-tetraacetic acid

E_H:	Hepatic extraction ratio
ESI:	Electrospray ionization
EtOH:	Ethanol
FDA:	Food and Drug Administration of USA
FXR:	Farnesoid X receptor
G6PD:	Glucose-6-phosphate dehydrogenase
GSK:	GlaxoSmithKline
GTS:	Global Technical Strategy for Malaria
HATU:	Hexafluorophosphate azabenzotriazole tetramethyl uronium
HBA:	Hydrogen bond acceptor
HBD:	Hydrogen bond donor
H3D:	The Holistic Drug Discovery, and Development Centre at UCT
HepG2:	Human hepatocellular liver carcinoma cell line
HEPES:	4-(2-Hydroxyethyl)-1-piperazineethanesulfonic acid
hERG:	Human ether-*a-go-go*-related gene
HLM:	Human liver microsomes
^{1}**H-NMR**:	Proton nuclear magnetic resonance
HMBC:	Heteronuclear multiple bond correlation
HPLC:	High-performance liquid chromatography
HPMC:	Hydroxypropyl methylcellulose
HSQC:	Heteronuclear single quantum coherence
HTS:	High-throughput screening
IC_{20}:	20% Inhibitory concentration
IC_{50}:	50% Inhibitory concentration
ITNs:	Insecticide-treated nets
J:	NMR coupling constant
K_d^{app}:	Apparent dissociation constant
KDR:	Kinase detection reagent
LAH:	Lithium aluminium hydride
LC-MS:	Liquid chromatography-mass spectrometry
LG:	Late-stage gametocytes
LHS:	Left-hand side
LLE:	Lipophilic Ligand Efficiency
MDGs:	Millennium Development Goals
MeOH:	Methanol
MHz:	Megahertz
MLM:	Mouse liver microsomes
mLST8:	Mammalian lethal with sec13 protein 8
MMGBSA:	Molecular Mechanics/Generalized Born Surface Area

MMV: Medicines for Malaria Venture

MoA: Mechanistic mode of action

MP: Melting point

mTOR: Mammalian target of rapamycin

mTORC: Mammalian target of rapamycin complex

MS: Mass spectrometry

MTT: 3-(4,5-Dimethylthiazol-2-yl)-2,5-diphenyltetrazolium bromide

MW: Molecular weight

m*/*z: Mass to charge ratio

NADH: Nicotinamide Adenine Dinucleotide

NADPH: Nicotinamide adenine dinucleotide phosphate (reduced form)

NCA: Non-compartmental analysis

ND: Not determined

NIS: *N*-Iodosuccinimide

nM: Nanomolar

NMR: Nuclear magnetic resonance

NSG: Non-obese diabetic severe combined immunodeficiency gamma *Pf* mouse model

PBS: Phosphate buffered saline

PD: Pharmacodynamics

PDB: Protein Data Bank

***Pf*:** *Plasmodium falciparum*

***Pf*ATP4**: *Plasmodium falciparum* P-type ATPase

***Pf*CRT**: *Plasmodium falciparum* Chloroquine resistance transporter

***Pf*3D7**: Chloroquine-sensitive strain of *Plasmodium falciparum*

***Pf*NF54**: Drug-sensitive strain of *Plasmodium falciparum*

***Pf*K1**: Multidrug-resistant strain of *Plasmodium falciparum*

***Pf*PK7**: Protein kinase 7

PI: Phosphatidylinositol

PI3K: Phosphoinositide 3-kinase

PI4K: Phosphatidylinositol 4-kinase

PIKK: Phosphatidylinositol 3-kinase-related kinase

PK: Pharmacokinetics

PKG: c-GMP dependent protein kinase G

pLDH: Parasite lactate dehydrogenase

PMB: *para*-Methoxybenzyl group

ppm: Parts per million

PPQ: Piperaquine

PRR: Parasite reduction ratio

PTFE: Polytetrafluoroethylene

QSAR: Quantitative structure-activity relationship

RBCs: Red blood cells

R_f: Retardation factor

RHS: Right-hand side

RI: Resistance index

RIPK2: Receptor-interacting serine/threonine-protein kinase 2

RLM: Rat liver microsomes

RNA: Ribonucleic acid

Ro5: Lipinski's rule of five

SAR: Structure-activity relationship

SARS-CoV2: Severe acute respiratory syndrome coronavirus 2

SCID: Severe combined immunodeficiency gamma

SEM: 2-(Trimethylsilyl) ethoxymethyl group

SFK: SoftFocus Kinase library

SI: Selectivity index

S_N2: Bimolecular nucleophilic substitution

SREBP: Sterol regulatory element-binding protein

SPR: Structure-property relationship

STPH: Swiss Tropical and Public Health Institute

SUB1: Subtilisin-like serine protease 1

$t_{1/2}$: Half-life

TCPs: Target candidate profiles

TFA: Trifluoroacetic acid

TGF: Transforming growth factor

THF: Tetrahydrofuran

TLC: Thin layer chromatography

TPP: Target product profile

TPSA: Topological polar surface area

t_R: Retention time

UHPLC-MS: Ultra-high-performance liquid chromatography-mass spectrometry

UV: Ultraviolet

WHO: World Health Organization

TABLE OF CONTENTS

LIST OF FIGURES

LIST OF TABLES

LIST OF SCHEMES

CHAPTER 1

INTRODUCTION AND LITERATURE REVIEW

1.1 Malaria disease and epidemiology

Malaria is a deadly parasitic infectious disease caused by the protozoan genus *Plasmodium*, and transmitted by the female *Anopheles* mosquito. Initially, four species of *Plasmodium* were known to infect humans namely *Plasmodium vivax*, *P. malariae*, *P. ovale*, and *P. falciparum* with the latter being the deadliest.[1] *P. falciparum* is responsible for what is commonly referred to as malaria tropica, *P. vivax* and *P. malariae* cause malaria tertiana while *P. ovale* causes malaria quartan. In addition, recent studies have shown that some strains of *P. knowlesi*, a species known to infect primates, also infects humans.[2]

Over the last few decades, ground-breaking advances have been made to reduce malaria morbidity and mortality. According to the recent 2020 World Health Organization (WHO) report, 229 million cases occurred globally in 2019 resulting in 409,000 deaths, of which 94% occurred in Africa. Unequivocally, exceptional progress has been made over the last decade to reduce fatality from the 600,000 deaths that occurred in 2010.[3] Although this is encouraging, a more critical analysis of the overall progress reveals a worrying trend.

In 2000, 238 million cases of malaria were reported globally, thus indicating a slight decrease in 2019.[3,4] However, statistical analysis indicate that although the rate of decline was initially significant, this trend has since stalled or even reversed in some regions. For example, the global case reduction from 2016 to 2017 was only 10,000. Moreover, the WHO estimates that 229 million cases occurred globally in 2019 indicating an increase by 1 million cases compared to the previous year. This is only a slight decline from the 231 million cases that occurred in 2017, indicating a stalling annual global decline in the number of infections. In addition, there is a likelihood of underreporting of cases in some regions and existence of a significant number of asymptomatic carriers.[5]

Based on the more rational global incidence rate index, which considers population growth, the figure fell from 71 cases per 1000 people at risk in 2010 to 57 cases in 2014. However, the rate of decrease has worryingly stagnated since.[4] The African region continues to carry the largest burden of malaria cases and the trend in mortality has remained unchanged over several

years, with nineteen African countries accounting for 94% of the global malaria deaths.[5] Malaria endemic regions as at 2019 are shown in **Figure 1.1**.

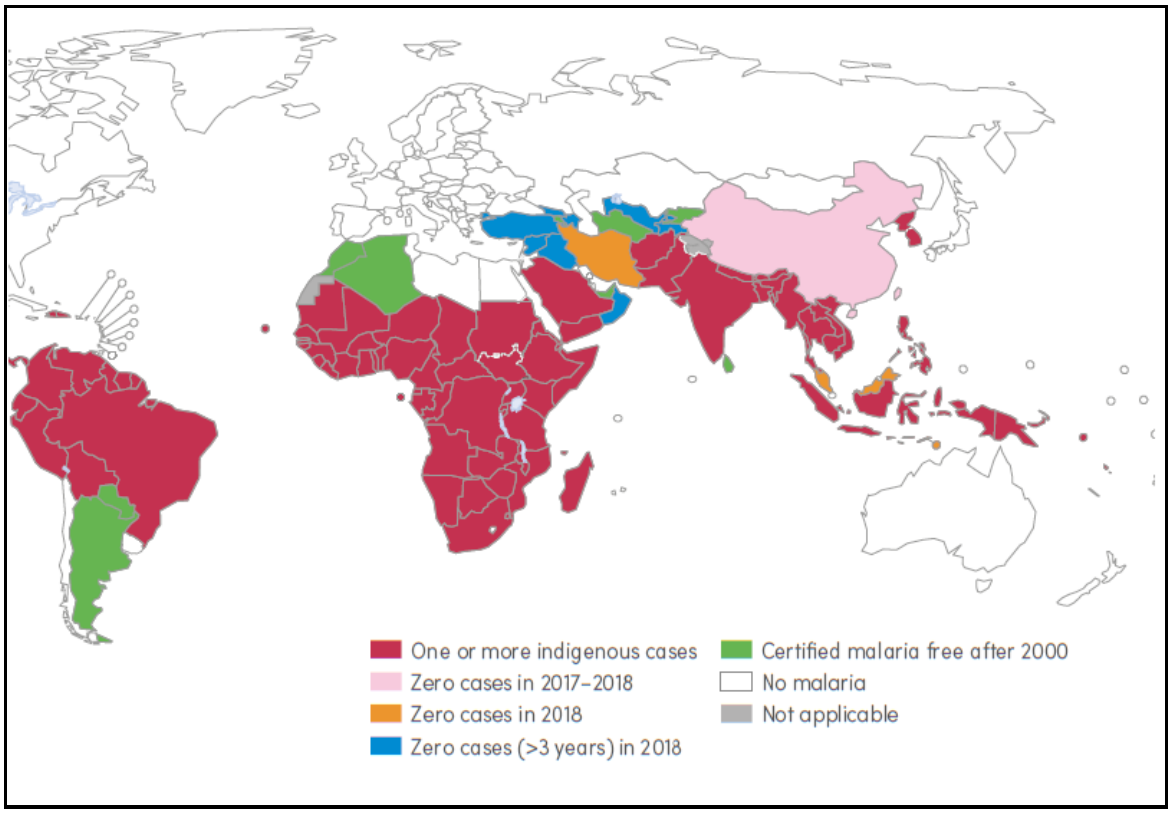

Figure 1.1: Global malaria endemic regions in 2019 as reported in the WHO World Malaria Report 2020[3]

Alarmingly, five sub-Saharan countries accounted for over half of the global malaria cases with Nigeria (27%), the DRC (12%), and Uganda (5%) experiencing the highest number of cases.[3] This trend is indeed worrying, considering that the 2016-2030 Global Technical Strategy (GTS) for malaria milestone striving for a 40% reduction in mortality and global incidence by 2020 has not been met.[6] This further exerts more pressure on the GTS milestone targets for 2025 (75% global reduction) and 2030 (90%), which are likely to remain unmet if strategies are not implemented urgently.[6] Finally, the effects of the recent and ongoing pandemic associated with the novel and severe acute respiratory syndrome coronavirus 2 (SARS-CoV2), which causes coronavirus disease 2019 (COVID-19), on global malaria intervention programs remain unclear.[3]

Malaria poses a devastating social and economic burden on countries most affected and remains one of the most serious infectious diseases in the world. In 2019, the mortality rate in children under the age of 5 years in the sub-Saharan region was greater than 67%.[7] Although

the number of deaths caused by malaria in children is reported to have decreased by approximately 37% since 2010, the disease remains a major risk to children and is responsible for over 274,000 deaths annually.[5,8] Furthermore, in 2019, an estimated 822,000 low-birth-weight deliveries in sub-Saharan Africa were associated with mothers suffering from malaria during pregnancy, indicating a strong correlation with other health complications such as anemia.[4] In addition, the emergence of COVID-19 has posed a formidable challenge to malaria responses with regard to essential services and funding, while its effects on patients with co-morbidities in the endemic population remain unclear.[3]

One of the main causes of mortality and morbidity in malaria is the increasing resistance of *Plasmodium* parasites to available antimalarial drugs.[9] Of particular concern is the parasite's tolerance to artemisinin, the core compound in current front-line artemisinin-combination therapies (ACTs), as reported in South East Asia and other parts of the world. Resistant strains dramatically reduce the efficacy of existing drugs and increase the risk of complications and death in patients with severe infections.[10] Alarmingly, resistance is spreading in *P. falciparum*, which is responsible for the most severe form of infection and the greatest number of malaria-associated deaths. In addition, there are few antimalarial drugs available to treat pregnant women and young children, the two most vulnerable populations.[11,12]

Also, the malaria problem is compounded by increasing mosquito resistance to pyrethroids, the only class of compounds used in insecticides-treated nets (ITNs). In addition, application of non-pyrethroids in ITNs is controlled because of environmental and human safety concerns. Global vector resistance to insecticides used for indoor and outdoor residual spraying such as carbamates and organochlorines has also been reported, although it is less prevalent.[3] Viable interventions including new medicines for malaria are therefore required to prevent vector-host interactions and eliminate this deadly human disease.

1.2 Malaria transmission and life cycle

The *Plasmodium* parasite has a complex life cycle involving female *Anopheles* mosquitoes as the vector and humans as the host. All *Plasmodium* parasites have similar life cycles progressing through both sexual and asexual stages of development as summarized in **Figure 1.2**.[13]

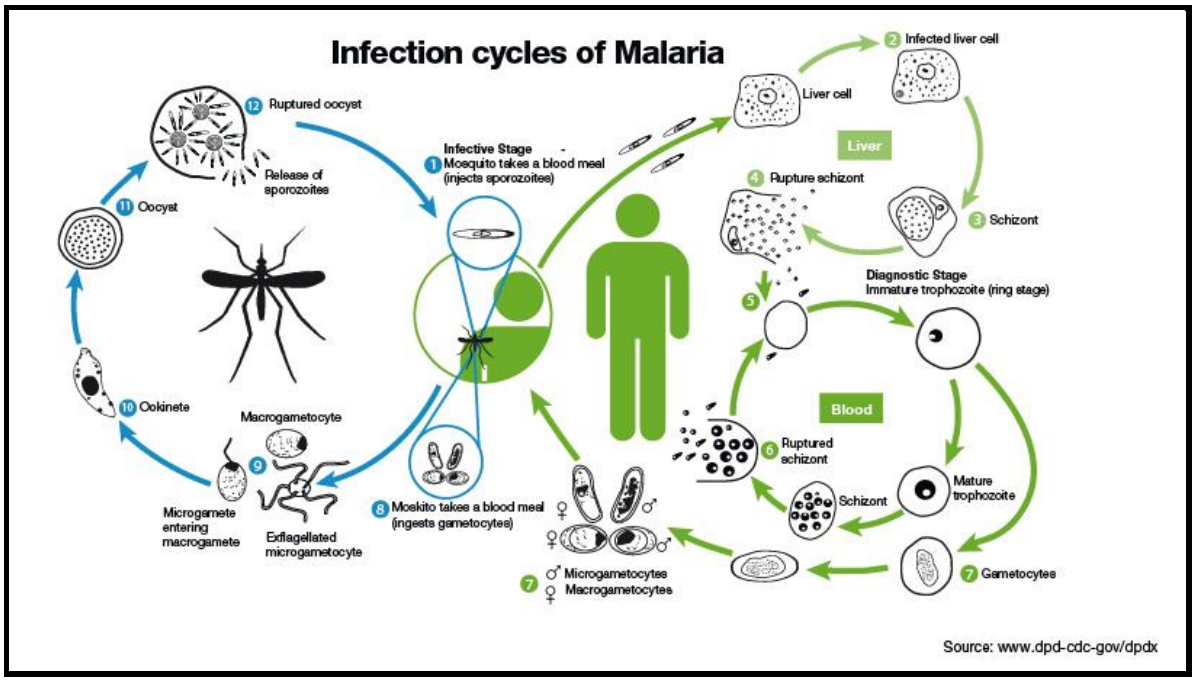

Figure 1.2: The life cycle of the malaria parasite in the human host and mosquito vector[1]

Human malaria infection begins when sporozoites are inoculated into the host's bloodstream by an infected mosquito during a blood meal.[14] Sporozoites then enter circulation before reaching the liver where they initiate the process of hepatocyte invasion. Here, the parasite undergoes an iterative asexual replication through a process known as exoerythrocytic schizogony. This eventually results in the production of thousands of merozoites that are released into the bloodstream.[15] During hepatic invasion, *P. vivax* and *P. ovale* species may enter a dormant period before asexual replication, which can then be responsible for later relapse.[13,16]

Upon release into the bloodstream, merozoites invade erythrocytes where they sub-divide and undergo asexual growth, a process involving active ingestion of the host cell cytoplasm and haemoglobin metabolism into amino acids needed for growth.[17] This asexual cycle proceeds via morphologically distinct stages of the parasite (rings, trophozoites and, schizonts) before eventual maturation and release of merozoites (8–25 from a single erythrocyte). This then reinitiates another round of the blood-stage replicative cycle.[18] At the same time, some merozoites undergo differentiation into sexual male and female gametocytes within the red blood cells (RBCs).[19,20] Therefore, due to the invasion of RBCs, malaria in humans is characterized by a sudden onset of fever, headache, chills, diarrhoea, and vomiting. The invasion and rupture of RBCs also result in breathing difficulties, low blood sugar, severe

anaemia and even coma in case of severe cerebral malaria. If untreated, the symptoms may lead to death.[21]

Mature male and female gametocytes formed in the sexual blood stage, may then be taken up and ingested by a mosquito. Upon reaching the midgut, female gametocytes shed the RBCs and remain free in the extracellular space as macrogametes. At the same time, the nuclei of male gametocytes divide into flagellated microgametes, which leave the erythrocyte, enter the midgut, and initiate fertilization.[19,20] This leads to the formation of a zygote, which progressively develops into an elongated, slowly motile ookinete. The ookinete actively penetrates the midgut and settles beneath the basal lamina of the outer gut wall where it develops into a non-motile oocyst.[22,23] Eventually, the oocyst nucleus divides repeatedly to form sporozoites that leave the gut wall for the salivary glands. There, they penetrate the basal membrane, pass through the secretory cell, and settle into the salivary duct to await infection of a healthy person.[16]

1.3 Malaria prevention and control

The spread of malaria may be controlled by various interventions including the use of ITNs, elimination of mosquitoes at the larval stage by routine indoor and outdoor spraying, and removal of stagnant pools of water that act as breeding sites for the vector.[19,11]Although vector control significantly reduces the number of new infections, preventive measures are not completely effective and infections eventually occur, necessitating diagnosis and treatment.[8,12]

In addition to traditional malaria eradication strategies, prevention of the disease amongst part of the vulnerable population has recently received a major boost with the development of malaria vaccines. For example, GlaxoSmithKline (GSK), with support from the Bill and Melinda Gates Foundation (BMGF), has been involved in the development of RTS,S/AS01, a malaria vaccine primarily targeting young infants and children which aims to provide 3–4-year immunity against the parasite. Like several other vaccines, RTS,S/AS01 works by triggering the immune system to develop immunity against the pre-erythrocytic stage of the parasite.[24]

Results from the ongoing phase-3 human clinical studies suggest that the vaccine may provide meaningful benefits by preventing malaria infection in infants and young children, particularly if used alongside other interventions such as spraying and use of pre-treated bed nets. This has necessitated WHO to recommend its widespread application for children under the age of 5, despite possessing moderate efficacy after administration of a single dose (39%).[25] If

successfully adopted, it will make a substantial contribution to malaria control and reduce mortality when used alongside chemoprophylaxis and chemotherapy.[11,16]

1.4 Malaria chemotherapy

1.4.1 Quinine and quinoline-based antimalarials

Quinine, and its closely related stereoisomer **quinidine** (**Figure 1.3**), are some of the oldest naturally derived antimalarials initially isolated from the Cinchona tree. Their antimalarial properties were recognized as early as the 1600s.[26] Unfortunately, after extensive use over subsequent centuries, quinine-resistant *Plasmodium* strains emerged. The first quinine-resistant *P. falciparum* case was reported in 1910, creating a need for alternative front-line therapeutic options.[27] This led to the development of synthetically derived 4- and 8-aminoquinolines and arylaminoalcohol derivatives such as **chloroquine** (CQ), **quinacrine**, **piperaquine**, **amodiaquine**, **primaquine**, and **mefloquine** (**Figure 1.3**). Their mechanism of action (MoA) is by primarily inhibition of hemozoin formation.[28,29]

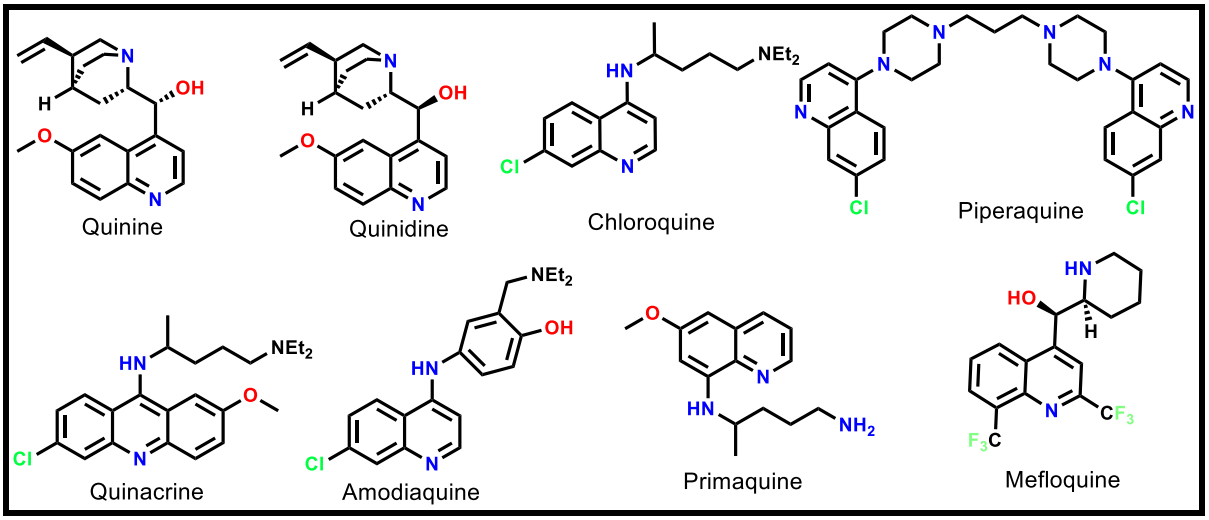

Figure 1.3: Chemical structures of quinine and selected key aminoquinoline drugs

Despite quinine remaining in the WHO's model list of essential medicines, its use is limited to treatment of *P. vivax* or *P. falciparum* in endemic areas where resistance has not emerged.[30] Drugs such as mefloquine are more efficacious against CQ-resistant *P. falciparum* but are often associated with a variety of neuro-psychiatric side effects. Moreover, mefloquine's MoA is similar to that of quinine and this along with its long half-life (14–21 days) contributes to the rapid development of parasite resistance. Consequently, it is recommended for use in combination with artesunate.[11]

1.4.2 Antifolate antimalarial drugs

These antimalarial compounds inhibit the biosynthesis of parasitic pyrimidines, required for the bio-polymerization of genetic material, deoxyribonucleic acid (DNA), and ribonucleic acid (RNA). Generally, there are two types of antifolates: dihydrofolate reductase (DHFR) and dihydropteroate synthase (DHPS) inhibitors.[31] Antifolate drugs inhibit enzymes required for the synthesis of the parasite's genetic material and thus suppress parasite growth and proliferation. Antifolate drugs include **pyrimethamine**, **proguanil**, **chlorproguanil**, and **sulfadoxine** (**Figure 1.4**).[16,32] Studies indicate that proguanil and chlorproguanil are prodrugs, metabolizing *in vivo* into their respective triazine forms, **cycloguanil** and **chlorcycloguanil**, which are active secondary metabolites.[33]

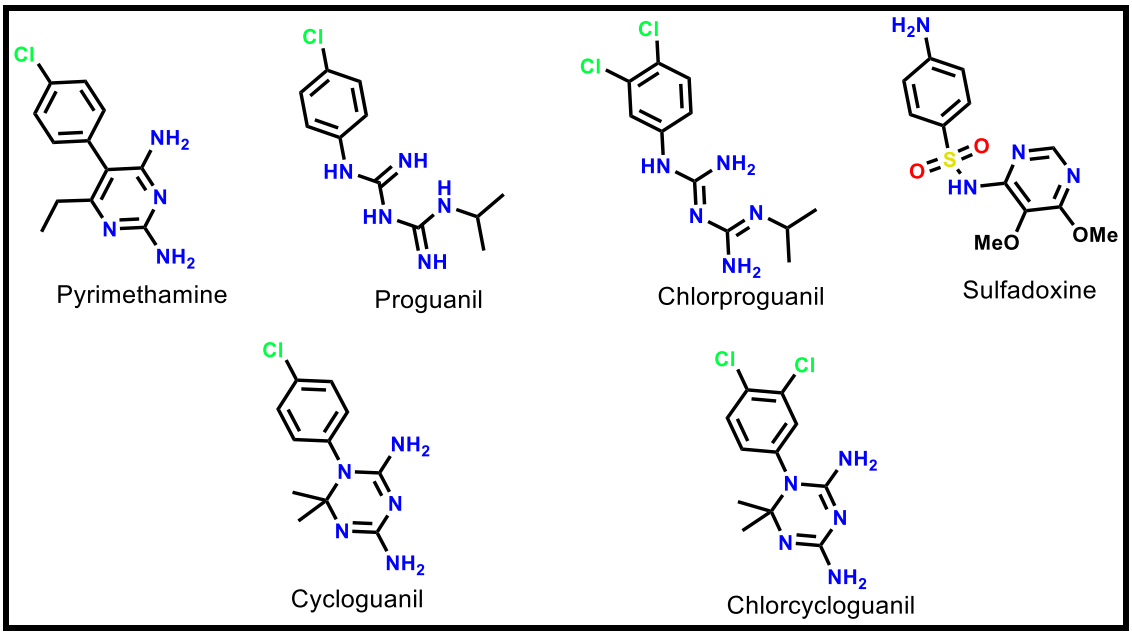

Figure 1.4: Chemical structures of established antifolate drugs for malaria

Pyrimethamine, chlorproguanil, and proguanil inhibit DHFR while the rest are DHPS inhibitors.[31] To improve synergy, DHFR inhibitors are often used in combination with DHPS inhibitors. A single-dose pyrimethamine-sulfadoxine combination is the most popular regimen recommended by the WHO, especially to expectant mothers who remain part of the most affected patient population.[16]

1.4.3 Antimalarial napthoquinones

Amongst the class of napthoquinones, **atovaquone** (**Figure 1.5**) remains the most notable antimalarial drug.[31] Structurally, it is a hydroxynaphthoquinone derivative, analogous to ubiquinone, a co-factor of the dihydroorotate dehydrogenase (DHODH) enzyme involved in

the parasite mitochondrial electron-carrier within the pyrimidine biosynthesis pathway. Atovaquone is a synthetic derivative of **lapachol** (**Figure 1.5**), a natural antimalarial compound isolated from the *Tabebuia* species.[28] The MoA of atovaquone is attributed to structural similarity and consequently competition with ubiquinone (**CoQ**), a co-enzyme involved in the cytochrome bc_1 complex associated with mitochondrial electron transport. This pathway is involved in the make-up of genetic materials and energy metabolism needed for the parasite's survival.[34]

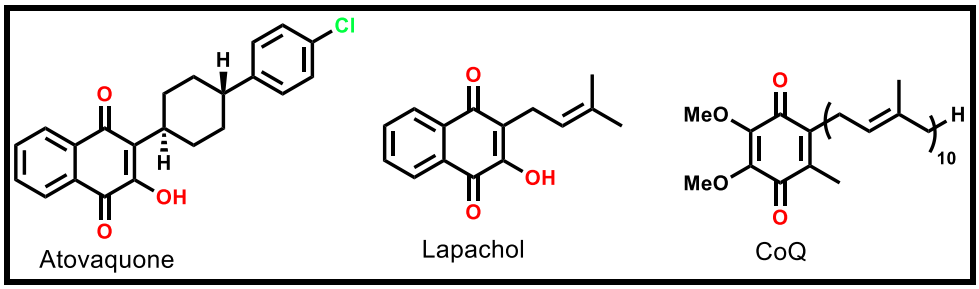

Figure 1.5: Chemical structures of atovaquone, lapachol, and ubiquinone

Atovaquone is usually administered in combination with proguanil under the trade name Malarone®. This combination is well tolerated in cases of uncomplicated multi-drug resistant *P. falciparum* infection with higher efficacy than CQ or mefloquine. However, widespread use of atovaquone is hampered by high costs, making it unaffordable across many endemic sub-Saharan countries.[35]

1.4.4 Artemisinin-based combination therapies

The current first-line recommended treatment of malaria includes artemisinin-combination therapy (ACT), which employs an artemisinin derivative in combination with other drugs as a strategy aimed to delay the onset of resistance.[36] Although artemisinin is highly efficacious, it is hampered by low solubility and bioavailability, and is therefore synthetically derived to obtain more soluble forms. The main artemisinin-derived drugs include artesunate (**Figure 1.6**), which is used in conjunction with mefloquine, amodiaquine, or **pyronaridine**, and **artemether** and **dihydroartemisinin**, which are used in combination with **lumefantrine** and piperaquine, respectively.[9,36] **Arteether** (Armotil; **Figure 1.6**) is an ethyl-containing semi-derivative often used as an alternative treatment for complicated cases. The current WHO-recommended ACTs and their target populations are listed in **Table 1.1**.[36]

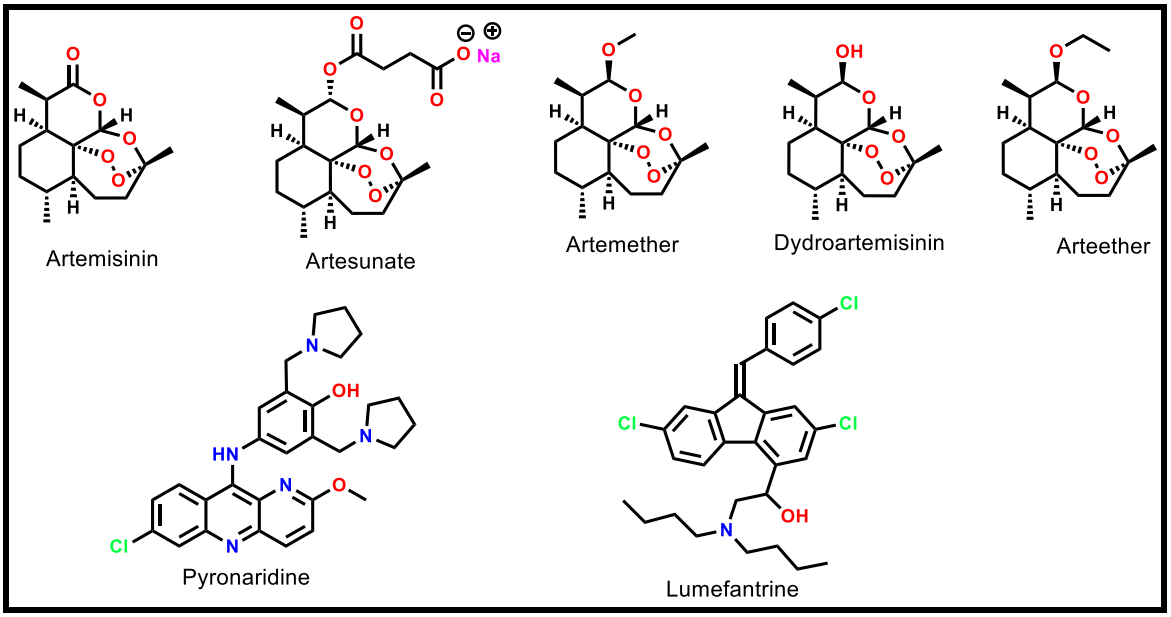

Figure 1.6: Chemical structure of artemisinin, derived drugs and selected partners

Table 1.1: Artemisinin derivatives available for treatment of malaria

Artemisinin derivative	Partner drug	Common trade names	Intended population
Artemether	Lumefantrine	Coartem, Artefan	Children and adults with uncomplicated *Pf* malaria
Artesunate	Amodiaquine	ASAQ Winthrop, Camoquine	
Artesunate	Mefloquine	ASMQ, Falcigo, Larinate MF	
Dihydroartemisinin	Piperaquine	Eurartesim, Artekin	
Artesunate	Sulfadoxine-pyrimethamine	Fansidar, Fanlar, SPAQ-CO	
Artesunate	Pyronaridine	Pyramax	
Arteether	-	Artemotil	Second line drug for CQ-resistant and severe malaria

Artemisinins are highly active clinically against asexual blood stage parasites. They are also fast-acting, safe, and well tolerated in patients.[37] Although the MoA remains contentious, certain authors incriminate the formation of active adducts that conjugate to parasite proteins and cause death.[38,39] Other research suggests that these compounds work by inhibiting *Pf* sarco/endoplasmic reticulum Ca^{2+}-ATPase (SERCA) orthologue (*Pf*ATP6), which has been incriminated as one of the primary MoAs of artemisinin and these derived drugs.[40–42]

1.5 The need for new antimalarials

Malaria remains one of the most severe life-threatening diseases to date. Nearly half of the world's population is at risk of infection and the disease continues to be particularly lethal in children under the age of 5 years.[19] As a result of increased parasite tolerance to artemisinin and combination partners, therapeutic options for malaria are dwindling and substitute drugs such as the atovaquone-proguanil combination would offer little protection against the total collapse of malaria chemotherapy.[9,35] The success of ACTs in replacing mono-therapeutic antimalarials such as CQ to overcome the evolution of drug-resistant strains is diminishing.[43] If urgent concerted efforts are not implemented, the risk of malaria chemotherapy becoming ineffective remains high, as experienced in Cambodia, Laos, and parts of Thailand where parasites have become resistant to almost all available antimalarial drugs.[10]

In addition, other challenges remain in the management of the disease in countries within sub-Saharan Africa that are heavily affected.[44] These issues include the high toxicity of alternative drugs such as primaquine, the high cost of optional drugs such as atovaquone, misdiagnosis, counterfeits, poor drug surveillance and under-dosing of patients due to lack of knowledge and poverty.[45–49] Furthermore, the discovery of new antimalarial drugs often focuses on already established MoAs and relies on the lengthy process of development, validation, and approval, further limiting the availability of ACT alternatives.[12]

There is a compelling need for urgent and accelerated efforts to discover novel classes of antimalarial drugs, if the Millennium Development Goals (MDG) for the eradication of malaria are to be achieved by 2025.[50] New drugs with novel mechanisms of action are needed to stop the spread of drug-resistant strains. In this regard drug rescue, repurposing, and repositioning of old drugs and clinical candidates for other indications remain viable strategies for accelerated drug discovery.[51–53]

1.6 Newly defined target candidate profiles (TCPs) for future antimalarials

Recent concerted efforts by stakeholders in antimalarial drug discovery have led to a dramatic increase in the number and diversity of molecules in pre-clinical and early clinical stages of development.[54] However, the need to expand the antimalarial arsenal has necessitated the development of strict guidelines to add value to future clinical candidates and avoid the emergence of resistance. Policies for the selection of compounds progressing to human trials must be strengthened, especially considering the pressures exerted by multiple seasonal infections in vulnerable populations.[55,56]

To this end, newly defined target candidate profiles (TCPs 1-6) have been developed for future drugs, focusing not only on the treatment of clinical symptoms associated with the asexual erythrocytic stages of the parasite, but also on blocking transmission, chemoprotection, and eliminating the parasite at the vector stage. Although not mandatory, these TCPs are strategic tools promoting the successful generation of safe, efficacious, resistance-proof, and broad-spectrum scaffolds with activity against multiple life-stages.[57,58]

1.6.1 TCP-1 (and -2): Potent asexual blood-stage activity

TCP-1 emphasizes the need to develop compounds achieving fast plasma parasite clearance comparable to that of artemisinin, while TCP-2 involved compounds with long half-lives and sustained antiparasitic activity comparable to that of aminoquinolines. Overall, both TCPs focused on the discovery of compounds resulting in potent asexual blood stage, and thus have been merged and TCP-2 retired.[57] Although artemisinin derivatives are highly efficacious, they are hampered by short half-lives and rapid hepatic clearance necessitating repeated administration with possible toxicity concerns. Consequently, they are partnered with drugs that have longer half-lives to mitigate this shortcoming. Such drugs include mefloquine, amodiaquine, and piperaquine.[59]

In essence, any antimalarial should solely achieve fast and complete or near-complete (10^{12}-fold) parasite clearance after multiple administration. Parasite clearance achieved by future compounds is assessed relative to that of *Pf*ATP4 inhibitors (very fast), endoperoxides (fast), and mefloquine (medium). Consequently, a suitable candidate should have low clearance and a high volume of distribution to sustain a sufficiently long half-life. Moreover, an ideal TCP1/2 drug should possess activity against all *Plasmodium* species infecting humans.[60]

1.6.2 TCP-3: Hypnozoiticidal activity

Human malaria is most commonly caused by *P. falciparum* and *P. vivax* species. Although both species are endemic in tropical areas, *P. falciparum* is responsible for the deadliest form of the disease and co-infections often occur. Treatment of the asexual blood stage of the parasite does not eradicate dormant liver hypnozoites associated with *P. vivax* and *P. ovale*, which often lead to relapse.[61] A radical anti-relapse cure is necessary to prevent re-activation and infection. Currently, primaquine and the recently FDA-approved tafenoquine are the only compounds active against these dormant forms of the parasite, despite their high propensity to cause acute hemolysis in individuals with glucose-6-phosphate dehydrogenase (G6PD) deficiency, a condition highly prevalent in malaria-endemic regions (3–30%).[62-63]

An ideal TCP-3 molecule should clear dormant hypnozoites either by direct kill or by facilitating re-activation, thus allowing eradication by an appropriate partner drug. Issues including the prolonged course for treatment (14 days), gastro-intestinal intolerability, and acute hemolysis associated with primaquine, the gold-standard drug, must be overcome.[57,60]

1.6.3 TCP-4: Hepatic schizonticidal activity

The protection of individuals entering malaria-endemic regions and the treatment of clinically asymptomatic malaria in local populations are needed for complete eradication. Commonly referred to as chemoprotection, this involves the elimination of hepatic schizonts in the blood and early liver stage before progression into blood schizonts, which are responsible for clinical symptoms. Chemo-protector agents should be fast-acting suppressants of the erythrocytic stage, thus preventing progression of the disease to the clinical stage.[64,65]

The atovaquone-proguanil combination is currently the recommended regimen for chemoprotection as it demonstrates dual TCP-1 and TCP-4 activity. To date, there are no antimalarial drugs exhibiting pure TCP-4 activity with most showing dual or exclusive TCP-1 activity, like mefloquine.[57,60] Thus, there is a need for proactive research towards the discovery of next-generation liver schizonticides.

1.6.4 TCP-5: Gametocytocidal activity

A key breakage point in the malaria life cycle is the human host-mosquito vector transmission stage. TCP-5 focuses on the need to eliminate gametocytes, the transmissible intra-erythrocytic sexual form of the parasite.[66] Malaria treatment should also clear these gametocytes to prevent transmission from the human host back to the vector and consequent onward transmission. However, the major challenge in the treatment of *Pf* gametocytes is their long lifespan: 10–12 days to reach maturation in comparison to 48 h for asexual-stage parasites. In contrast, the asexual stage maturation period of *Pv* gametocytes is only slightly longer than that of the asexual phase.[67,68]

Conventionally, gametocytes undergo five morphologically and biochemically recognizable stages of development before maturation (stages I-V). Immature stages I - III are biochemically rigorous, non-transmissible, and are sequestered in tissues and bone marrow.[19] The biochemical activities of immature gametocytes are more aligned to those of the asexual stage, (**Figure 1.7**) which explains their sensitivity to CQ, pyrimethamine, artemisinins, methylene blue, and primaquine.[20]

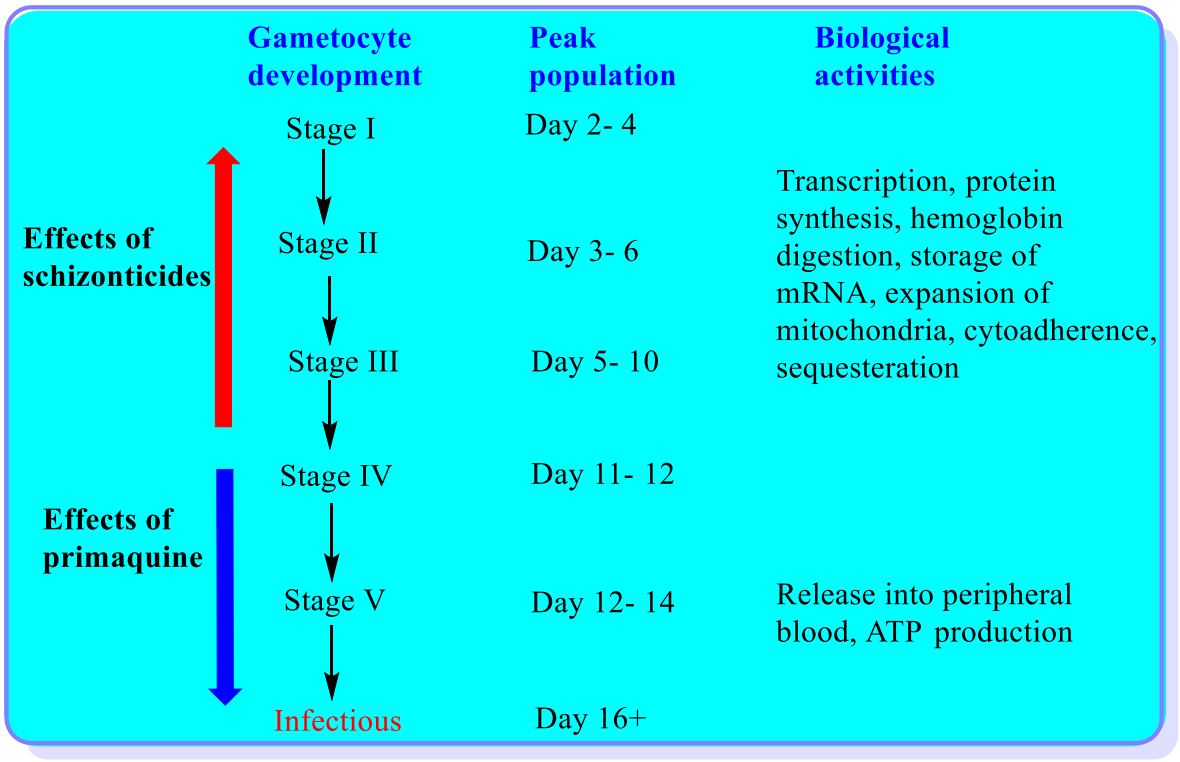

Figure 1.7: Gametocytocidal stage-specific activities of well-established antimalarials

In contrast, late stage-IV and mature stage-V gametocytes are infectious and circulate in the blood. Their metabolism is markedly decreased and only vital biochemical activities such as ATP generation are retained.[69] These are more resistant to currently used antimalarials, thus making it difficult to achieve TCP-5 clinically.[70] Low-dose administration of primaquine, and more recently its analogue tafenoquine, remain the only recommended gametocytocidal drugs for treatment in transmission areas.[71] Unlike other antimalarial drugs, these are effective against mature gametocytes and *Pv* hypnozoites, with a single dose of 15 $mg.kg^{-1}$ achieving complete clearance in 7 days. However, as earlier mentioned, safety concerns relating to blood toxicity in patients with G6PD deficiency limit their usage.[72]

1.6.5 TCP-6: Endectocidal activity

This TCP focuses on the discovery of molecules that would potentially block transmission at the vector stage by eliminating the *Plasmodium* parasite in mosquitoes feeding on patients under treatment.[73] To date, no antimalarial drug exhibits endectocidal activity. However, ivermectin, a drug used to treat river blindness, scabies, and lymphatic filariasis, has been employed in studies.[74] Oocyte maturation in the mosquito is slow, temperature-sensitive, and highly dependent on the vector. Widespread application of such endectocides to mass populations for oocyte elimination and the vector has been envisaged as a plausible way to

eradicate the parasite. Long-acting endectocidal activity, the safety of vulnerable patients, and cost must be considered in the design of viable molecules.[19,60]

1.7 Development pipeline for new chemotherapeutic regimens

Collaborative efforts between not-for-profit virtual R&D organizations such as Medicines for Malaria Venture (MMV), pharmaceutical industries, and academia have resulted in initiatives to curb the problem of drug resistance. Programs towards the identification of novel anti-plasmodium compounds preferably with non-classical MoAs are continually funded and implemented. Such undertakings have resulted in the development of novel candidates, backups, and lead compounds with diverse chemical scaffolds that are currently at different stages of clinical and pre-clinical development. The details of several of these and their MoAs are summarized in **Table 1.2**.[75]

Table 1.2: Selected key antimalarial drugs currently in various stages of development

Stage of development		Compound	Mode of action/ drug target	Developer
Product development	Regulatory review	Arterolane-PPQ	Multiple	Sun Pharma
	Patient confirmatory	Co-trimoxazole	DHFR/ DHPS	ITM Antwerp
		Artemisinin-napthoquinone	Multiple	Kunming Pharma
		Artemisinin-PPQ	Multiple	Artepharm
		DHA-PPQ	Multiple	Alfasigma
		Artemisone	Unknown	UHKST
		DSM 265	DHODH	Takeda
		Ferroquine/ artefenomel	Hemozoin/oxidative stress	Sanofi
		AQ13	Hemozoin formation	Immtech
		KAE609	*Pf*ATP4	Novartis
		KAF156	Unknown	Novartis
		Fosmidomycin	DXR	DMG Deutsche
Translational	Human volunteers	JPC-3210	Hemozoin formation	Jacobus
		SJ733	*Pf*ATP4	Kentucky/Eisai
		P218	DHFR-TS	Janssen
	Preclinical	MK4815	Unknown	Merck
		MMV253	*Pf*ATP4	Astrazeneca
	Lead compounds	ML10	*Pf*PKG	London SHTM

KAE609 (also known as NITD 609 or cipargamin; **Figure 1.8**), a potential P-type ATPase (*Pf*ATP4) inhibitor, shows potent *in vitro* activity against the artemisinin-resistant K13 strain of *P. falciparum* and recently passed Phase IIa clinical trials in humans.[76] *Pf*ATP4 is an ATP-

dependent cationic transporter involved in intraerythrocytic regulation of the Na^+/K^+ gradient by the parasite.[77,78] **KAF156** is another promising antimalarial compound active against uncomplicated malaria caused by *P. falciparum* and *P. vivax* infection. This compound recently passed Phase IIa trials and shows promising activity against parasites in the liver and transmissible stages.[75] However, its MoA remains unclear.[79]

Other promising compounds include **DSM265**, a DHODH inhibitor that is active against the liver stage (schizont formation), and **MMV390048**, which targets *P. falciparum* phosphatidylinositol 4-kinase (*Pf*PI4K) and reached Phase IIa human clinical trials. Unfortunately, further clinical advancement of **MMV390048** was recently discontinued while further studies are undertaken to investigate safety issues observed in advanced animal models.[80,75] Other notable candidates in clinical and preclinical development include the quinolone-based **ferroquine**, **artemisone**, **SJ557733**, **AQ13**, **methylene blue**, **P218**, **OZ277** (also called Rbx11160 or arterolene), and its related congener **OZ439** (artefenomel; **Figure 1.8**).[21,75,81]

Renewed interest in the previously neglected antimalarial aminomethylphenol **WR 194, 965** by implementation of discrete structural modifications have resulted in the successful development of **JPC-3210** and its progression to clinical studies. This compound shows favorable pharmacokinetic (PK) and safety profiles and is not associated with recrudescence, an issue previously observed with its original congener.[82,83] Its non-quinolone scaffold, low cytotoxicity against a panel of human and rodent cell lines, long plasma half-life (over 20 days in monkeys), and ability to achieve complete cure of *Pf* and *Pv* infections in non-immune *Aotus* monkeys are indicative of its potential as a long-acting blood schizonticide and prophylactic antimalarial.[84,85]

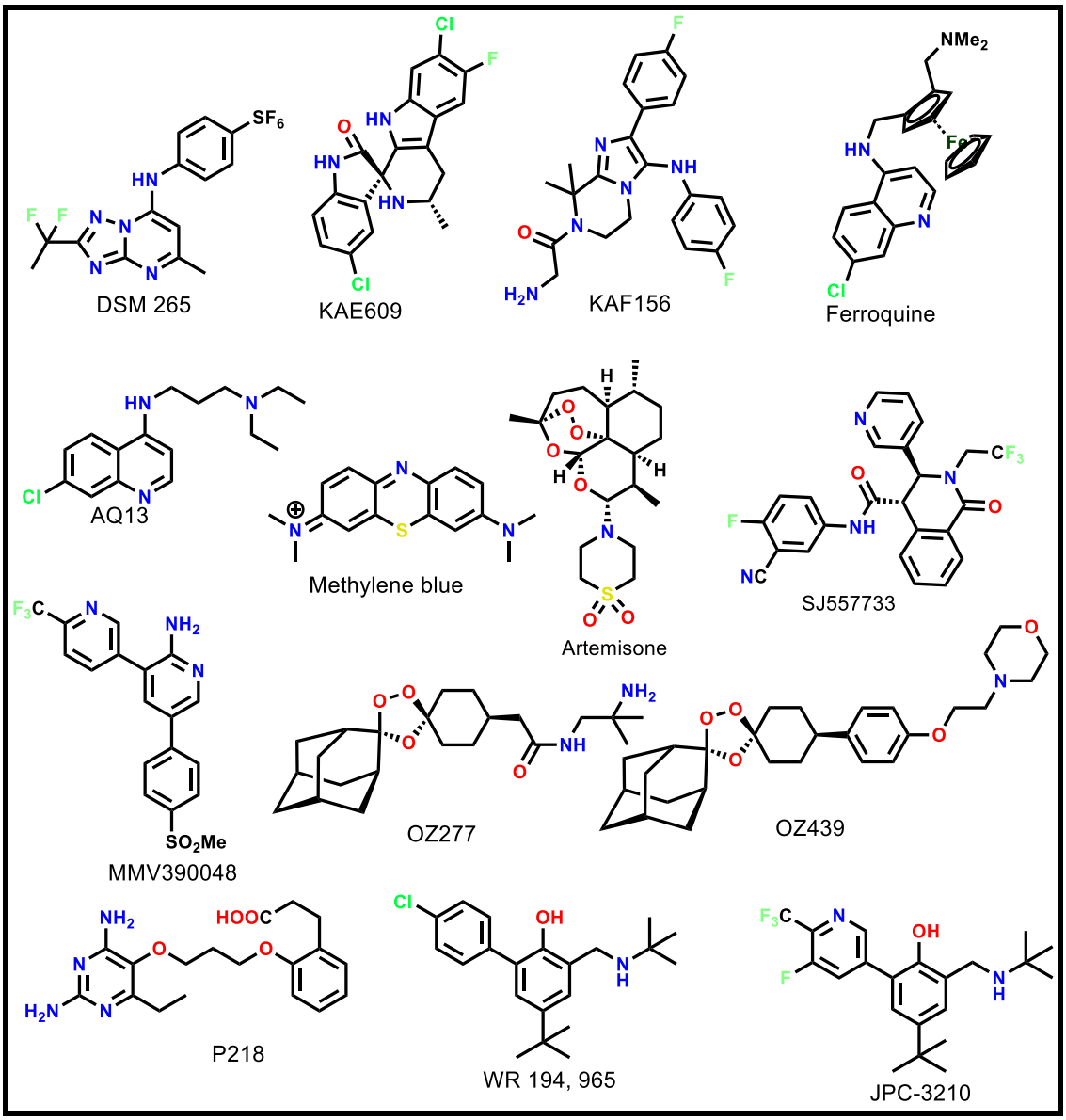

Figure 1.8: Chemical structures of selected candidates in clinical development

Priority for the approval of new drugs is based on superiority over classical antimalarials such as increased safety, low risk of resistance, blocking of transmission, decreased cost, and more favorable PK and pharmacodynamic (PD) properties, such as greater efficacy and a longer half-life. An ideal antimalarial should be fast-acting, highly efficacious, well tolerated in vulnerable population groups such as pregnant women and young children, and affordable for mass administration in poor localities.[86]

To date, the development of resistant-proof chemotypes remains a priority in the discovery of new drugs to combat the spread of parasite resistance against ACTs. Accordingly, renewed efforts are directed towards the discovery of clinical candidates that implicate new targets, to

combat existing resistance. However, as demonstrated by the *Pf*PI4K inhibitor **MMV390048**, the future of candidate compounds in development remains unknown.[81,87]

1.8 Approaches to antimalarial drug discovery

The first approach undertaken to address parasite resistance was to optimize therapy by using combinations of established antimalarial drugs and implementation of new dosing regimens and formulations. This strategy was generally driven by the need to deliver enhanced efficacy and avoid resistance by partnering two or more drugs with independent MoAs/molecular targets.[36] Other strategies continually explored for ultimate eradication of the disease include the development of novel drug entities, implementation of chemical modifications on existing drugs with well-defined targets, exploitation of natural products, and sourcing of new templates with or without prior knowledge of their biological targets.[33] Selected approaches employed in the discovery of new antimalarial chemical matter that are relevant to this study are discussed in subsequent sections of this document.

1.8.1 Phenotypic whole-cell screening

In this strategy, the focus is on the effect of a drug on the whole parasite cell, with little or no prior knowledge of its MoA. This traditional method has been the most commonly used and is credited with the successful discovery of multiple drugs and hit compounds. However, before automation, it was slow. The development of automated screening techniques has accelerated the number of compounds that can be tested, making it a common approach in numerous antimalarial drug discovery programs.[88,89] High-throughput screening facilitated by partnerships between pharmaceutical companies (such as GSK and Novartis), academic, and non-governmental organizations (such as St. Jude Children's Research Hospital) enables sharing of chemical matter and technological facilities. This has made possible the biological screening of thousands of compounds in a relatively short time-period.[90,91]

Phenotypic screening offers several intrinsic benefits in comparison to other approaches. First, impermeable drugs unable to reach the site of action are naturally eliminated. Moreover, potential leads with pan-lifecycle activity, multiple targets or new MoAs are captured.[92] Screening of multiple compounds without consideration of their MoAs enable identification of new scaffolds active through both known and previously unidentified mechanisms. Such compounds are particularly relevant in the search for new drugs able to curb drug resistance.[93,94]

This technique was used in the discovery of structurally and mechanistically novel antimalarials such as the novel *Pf*PI4K inhibitors **MMV390048** and **UCT943**, and **DSM265**, a DHODH inhibitor. This approach has also culminated in the identification of thousands of lead compounds such as those that led to the discovery of the imidazolopiperazine **KAF156** and the spiroindolone **KAE609**, which, as already indicated above, is currently undergoing human clinical trials.[95,96]

A prevailing downside of whole cell screening is that it traditionally focused on the discovery of antimalarials targeting the asexual stages of the parasite life cycle. Often, this also led to the identification of compounds with non-novel MoA's. To combat antimalarial resistance, the treatment arsenal must be expanded to target other stages of the *Plasmodium* lifecycle.[97] Target deconvolution is also necessary to avoid the colloquial "me too" resistance-prone drugs. More robust combinational approaches, such as target-based strategies, are required to elucidate the MoAs of potential candidates.[98]

1.8.2 Target-based approach

A target-based approach typically involves examination of the effects of a drug on an essential purified protein whose inhibition would result in interference with a critical biochemical pathway, resulting in parasite death. Parasitologists assist with the identification and validation of essential enzymes that are used as drug targets. Prior understanding of a compound's MoA provides a springboard for the discovery of next-generation drugs. In practice, several approaches are employed to identify a druggable target, including genomic, metabolomic, and proteomic techniques.[99,100]

Once a target is identified, the recombinant protein is purified, and an *in vitro* biochemical assay is developed to identify potential inhibitors. The process can be further improved if high-resolution inhibitor-bound structures of the target protein are elucidated. *In silico* tools can be used in the design of potential inhibitors to take advantage of the protein's putative binding site(s) and predict specific interactions between the amino acids within the binding site and a ligand. These tools also help to improve the potency and selectivity of ligands for the parasite protein(s) relative to those of the host.[101] Proponents of this approach argue that understanding the MoA of a compound early in the drug discovery process facilitates medicinal chemistry efforts, thus accelerating the identification of potential candidates. Furthermore, knowledge of the metabolic pathways or specific drug target can inform future combination therapies.[98,102]

However, employing a target-based approach in drug discovery has distinct pitfalls. For instance, *in vitro* potency rarely translates directly to *in vivo* efficacy if the PK properties of a compound are poor. Exposure of compounds in *in vitro* settings does not take into consideration permeability in the host and parasitic membranes and often discriminates compounds with high permeability as *in vitro* studies are based on drug-target interactions rather than drug-organism interactions.[103] Therefore, identified hits need to show proof-of-concept in the appropriate animal model of infection. Numerous compounds identified through this approach fail mid-stage when subjected to parasite strains or animal models of disease, confirming that drug permeation and target validation are paramount for success in drug discovery.[104]

Consequently, target-based drug discovery is often integrated with phenotypic strategies for hit optimization and target validation. Fortunately, a range of *in vitro* and *in vivo* disease models are available for the various stages of *Plasmodium* infection and are used in PK and efficacy studies. While phenotypic approaches have traditionally been used for antimalarial drug discovery, target-based approaches are credited with the successful delivery of many drugs to the market in other disease areas. Notably, the anticancer drugs **gefitinib**, **sorafenib**, and **sunitinib** are classical examples developed through this approach (**Figure 1.9**).[93]

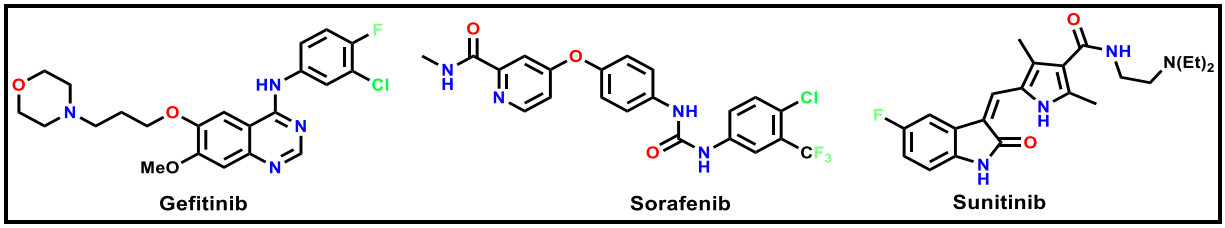

Figure 1.9: Examples of anticancer drugs developed through the target-based approach

1.8.3 *In silico* tools and computer aided drug design

In silico drug repositioning using libraries of established drugs and clinical candidates is currently viewed as one of the most viable and cost-effective methods of drug discovery. The identification of compounds with drug-like properties is an important component of a successful drug discovery program.[105] Quantitative structure-activity relationships (QSARs) are often developed using physicochemical descriptors such as molecular weight (MW), lipophilicity, number of rotatable bonds, topological polar surface area (TPSA), and numbers of hydrogen-bond donors and acceptors and validated to predict the absorption, distribution, metabolism, and excretion (ADME) properties of molecules.[106] Buoyed by advancements in molecular biology, genomics, and complex analytical tools such as X-ray crystallography and

nuclear magnetic resonance (NMR), computational approaches have gained significant popularity in recent drug discovery programs.[107]

Clinical candidates and approved drugs with well-established PK and toxicological profiles, offer an appealing starting points for the development of drugs for other indications.[108] This is also aided by the availability of freely accessible depositories containing thousands of small molecule hits from pharmaceutical companies, advancement in computer hardware and software, machine learning techniques and automation, tools which enable accurate predictions, and high-throughput phenotypic assays and target screening.[109]

Computational approaches such as structure-based virtual screening (also known as molecular docking) are progressively being incorporated in target-based drug discovery programs. Availability of validated, high-resolution protein structures in online platforms such as the RCSB and BMRB Protein Data Bank (PDB) give compelling insight into drug-target interactions useful in drug or target repositioning.[110] This is achieved by studying the 3-dimensional architecture between a ligand and the amino acid residues of a known biological target, at the putative binding site. Schrodinger's Glide, Norvatis QXP and GSK's GOLD are examples of software utilized in such experiments. In the absence of a high-resolution structures, homology models may be used as substitutes despite their likelihood of inaccurate predictions.[111] In addition, even with the availability of high resolution crystal structures, high throughput *in silico* docking methods are often prone to various short-comings which include low predictability of protein flexibility and ligand conformations, and inconsideration of the physiological context, factors likely to hinder accuracy and selectivity. Highly accurate predictive models are usually employed for advanced lead compounds due to their advanced computational requirement and low throughput nature.[112,113]

1.8.4 Drug repurposing, repositioning and rescue

Drug repurposing, repositioning, and rescue of marketed drugs, clinical candidates, and lead compounds are techniques that can be employed for time- and cost-efficient drug development. These approaches take advantage of a candidate whose PK and toxicology profiles are already validated to find a solution to the countless obstacles that researchers must overcome to optimize and discover new drugs for a particular indication.[114] Drug repurposing refers to the practice where an existing drug is re-directed towards the treatment of a completely different ailment, while drug repositioning describes a scenario where an active drug is employed as a template to generate analogues that are suitable for other indications.[115] Where the target for

one disease is known, similarities with the molecular and cellular biology of another disease-causing organism can be exploited for successful drug repurposing and repositioning.[116]

By screening existing drugs for new uses, the drug development timeframe may be shortened with low risks and reduced costs. Recently, this strategy was credited for the development of over 30% of newly FDA-approved drugs.[117] Successfully repurposed drugs include **miltefosine** (**Figure 1.10**), a breast cancer drug now used in the treatment of visceral leishmaniasis,[118] and **thalidomide**, serendipitously discovered for treatment of morning sickness then repositioned to **lenalidomide** (Revlimid), a drug with improved PK and clinical efficacy, for the treatment of multiple myeloma.[119,120]

Another notable success is the Pfizer's blockbuster "magic blue" pill, **sildenafil** (**Figure 1.10**), a compound initially developed for the treatment of pulmonary hypertension but due to retrospective clinical experience was successfully repositioned as a sex-drive enhancer for erectile dysfunction.[121] Employing a similar approach has led to near success of antimalarial drugs from **methotrexate**, an antifolate anticancer drug, **astemizole**, an antihistamine drug and **tinidazole**, an anti-amoebic compound.[122-124]

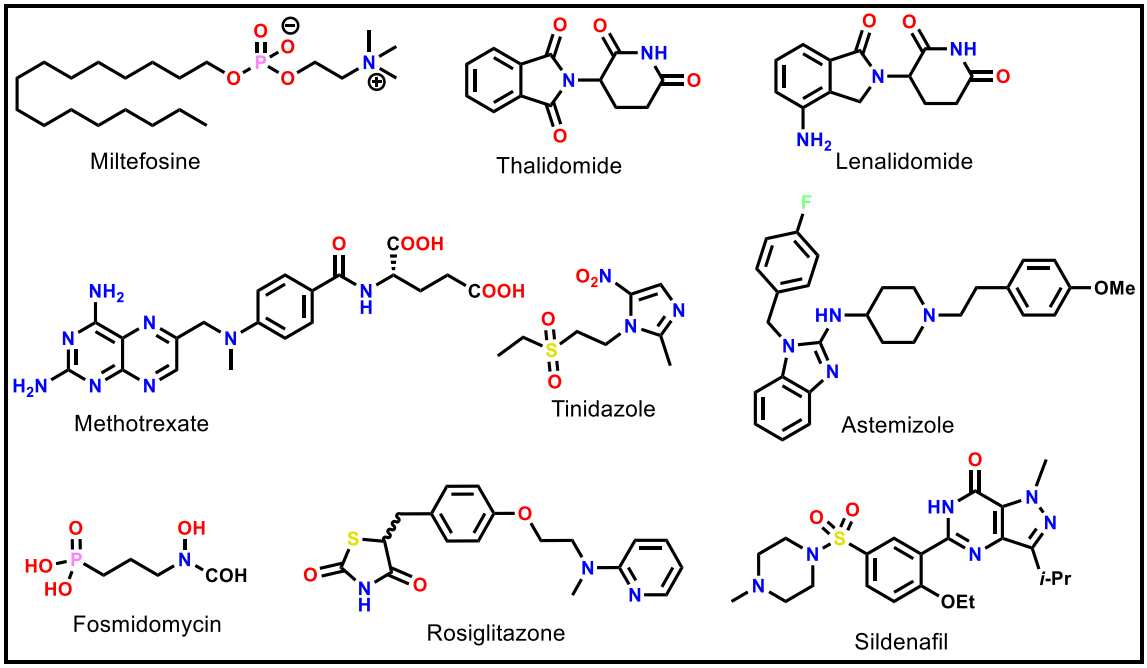

Figure 1.10: Structures of selected drugs repurposed and repositioned for malaria and other indications

Drug repositioning may deliver a drug to the market in much quicker time. In contrast, *de novo* drug discovery is a lengthy process, optimistically taking 10–17 years, with a realistically low

probability of success.[115] Lately, immense focus has shifted to this approach in delivery of antimalarial clinical candidates. This includes the recent completion of Phase II clinical trials of the anticancer drug, imatinib, explored in triple combination with dihydroartemisinin and piperaquine.[125] Other examples include methylene blue, an antianemia, **fosmidomycin**, a natural *Streptomyces* antibiotic, **rosiglitazone**, a drug initially developed for the management of diabetes (**Figure 1.10**), and sevuparin, a polysaccharide-based drug used to treat sickle-cell disease.[126]

1.9 Biological targets in antimalarial drug discovery

1.9.1 Well-established antimalarial targets

The life-cycle of the *Plasmodium* parasite is complex and involves both host and vector, and parasite progression through sexual and asexual stages of development.[12,127] Vital enzyme-mediated pathways in critical organelles are often targeted by antimalarials to disrupt the *Plasmodium* life-cycle (**Figure 1.11**). Classical targets of many existing antimalarial drug regimens include hemozoin formation, DHFR, and DHPS. Newly discovered targets include DHODH, ATP4-ase, and more recently, *Plasmodium* kinases such as PI4Kβ inhibitors.[35,80,128]

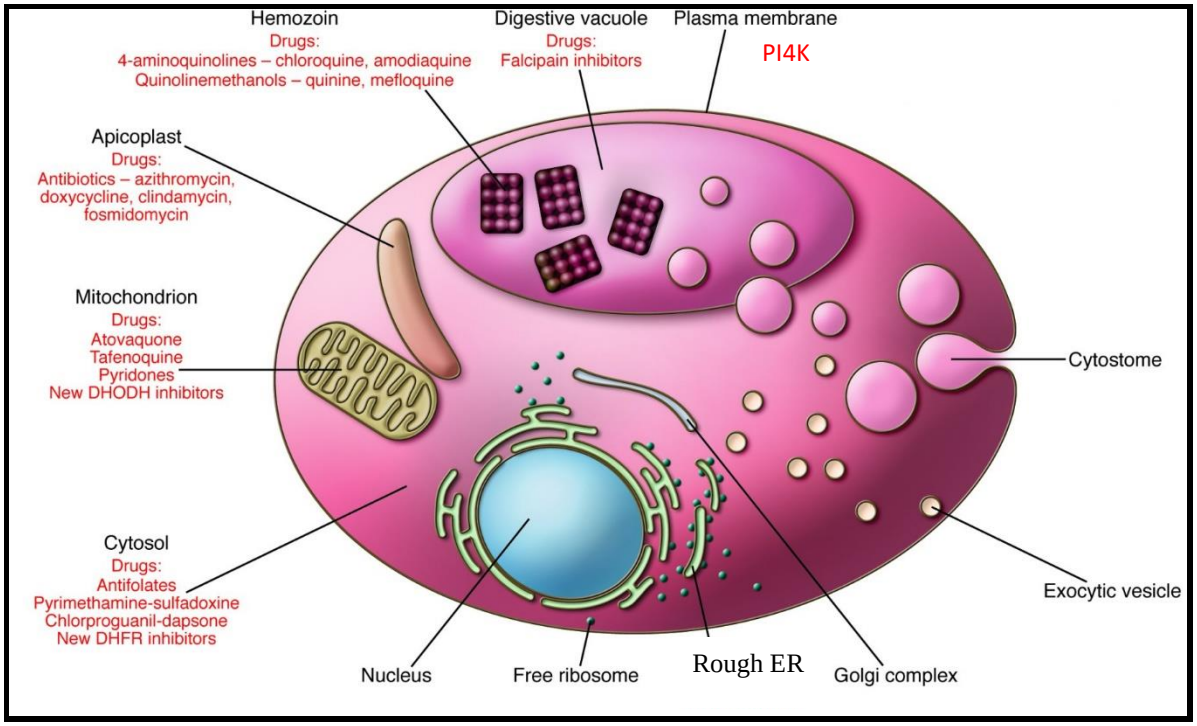

Figure 1.11: Organelle-specific targets of antimalarial drugs and leads. Figure adapted from Greenwood *et al.*[129]

The indispensable heme degradation pathway has been extensively explored in the design and development of classical antimalarials. It is a validated target for aminoquinoline antimalarial drugs such as quinine, CQ, amodiaquine, mefloquine, and mepacrine. Moreover, it continues to be exploited in the development of new antimalarial drugs and other anti-parasitic agents such as in *Schistosomiasis*.[130,131] Unfortunately, aminoquinolines are only active against specific stages of the parasite life cycle and widespread resistance has hampered their use in the development of future antimalarials. Resistance against aminoquinolines is associated with mutations in the *Pf*CQ resistance transporter (*Pf*CRT), a transmembrane protein involved in drug efflux out of the parasite's food vacuole. Therefore, although they are highly active against the asexual blood stage, their use as blood schizonticides is limited with some finding use in combination therapy.[36]

In addition, the use of novel antimalarials targeting mitochondrial DHODH is ideally motivated by their application in the management of human autoimmune diseases such as rheumatoid arthritis. DHODH is a key flavin-dependent mitochondrial electron transport enzyme that catalyzes oxidation of dihydroorotate to orotate in the fourth step of the *de novo* pyrimidine biosynthesis pathway. This step is crucial in the biosynthesis of ubiquinone (CoQ), which acts as an electron sink in the pyrimidine biosynthesis pathway.[132]

Despite pyrimidines being precursors for the formation of genetic materials such as DNA and RNA, *Plasmodium* parasites are incapable of scavenging these from the human host and rely entirely on *de novo* synthesis. Furthermore, *Plasmodium* DHODH performs only a single function, reinforcing its importance for parasite survival and thus presenting a druggable target in *Plasmodium* and other parasitic pathogens including *Leishmania* and *Trypanosoma* species.[133] Genetic information and X-ray studies of DHODH with known inhibitors are often used to provide insight into structural differences between species and host isoforms to achieve specificity. Significant progress has been made in the discovery of *Pf*DHODH inhibitors with the development and progression of **DSM265**, the first DHODH inhibitor to reach clinical development for the treatment of malaria and several pre-clinical inhibitors of this enzyme [116,134]

1.9.2 *Plasmodium* kinases as drug targets

The success of human kinase inhibitors as anticancer drugs has motivated the design and development of similar agents for the treatment of malaria and other parasitic infections.[135] Kinases are diverse enzymes present in all organisms that catalyze the transfer of a γ phosphate

from ATP to a specific substrate such as a protein, lipid, carbohydrate, or other molecules. Phosphorylation is key to metabolism and the localization of these substrates is crucial to the formation of secondary messengers used in intracellular signaling.[136,137] Protein kinases form one of the major foci in anticancer drug development because of their role in cell proliferation and survival. Significant overexpression of protein kinases is highly associated with malignant growth and tumors.[138,139] To date, the major clinical niche of kinase inhibitors is cancer therapy, with 52 anticancer kinase inhibitor drugs currently approved by the FDA.[140]

Kinase inhibitors are normally classified based on their targeted kinase binding site as type I – IV. Type 1 such as **sunitinib** (**Figure 1.12**) binds to the highly conserved ATP- and proximal regions in the active conformation (DFG-in) while type II binds to the inactive form.[141] A classic example of type II compound is the TK inhibitor, **imatinib** (Gleevac; **Figure 1.12**). The other types (III and IV) are referred to as the allosteric binding kinases with III binding to the sites adjacent to the ATP binding sites while type IV occupy distant allosteric sites such as in the C-, N-lobe and pockets on the surface of the kinase domain. More elaborate classifications include inhibitors binding to multiple sections of the active site (type V) and covalent inhibitors (VI).[140] Other relevant kinase inhibitors approved as drugs are represented in **Figure 1.12**.[142]

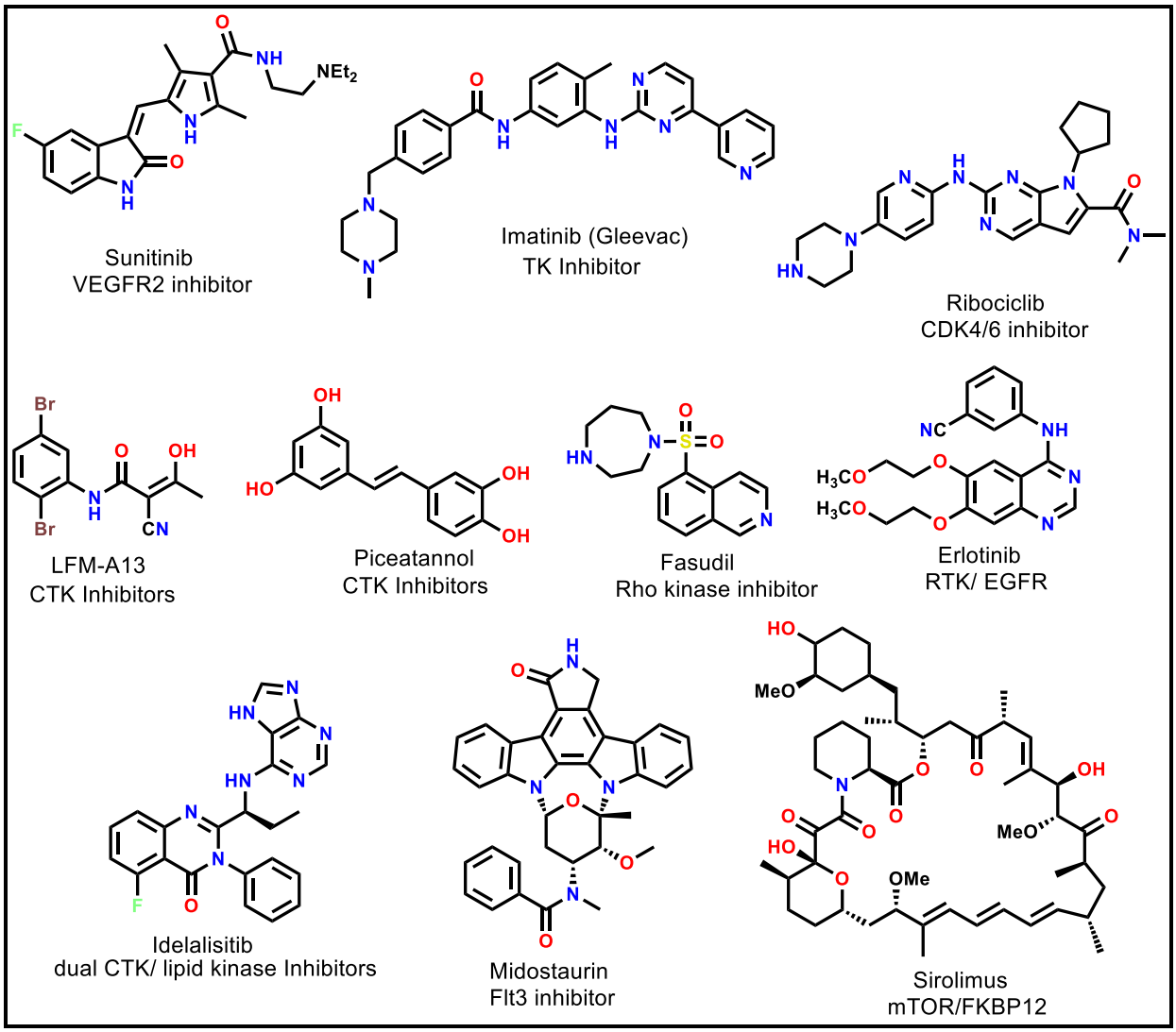

Figure 1.12: Structures of representative anticancer kinase inhibitors

Lipid kinases play an equally significant role in fundamental pathways essential for membrane trafficking, growth, and development in both humans and pathogens. Dysregulation of host lipid phosphoinositide kinases is associated with the proliferation of viral infections and several human diseases including cancer, and are thus explored extensively as targets in drug discovery.[143,144]

Exploitation of the homologous nature of human kinases targeted for cancer therapy and other indications and parasite kinases offers a viable niche for the development of antiparasitic drugs. This is commonly referred to as target repurposing. Likewise, clinically validated human kinase inhibitors can be repurposed for application in a different disease.[116] Such approaches have resulted in extensive kinase-target based research for brucellosis, *schistosomiasis*, cryptosporidiosis, and malaria.[145,146] The *Plasmodium* kinome comprises of 86–99 protein

kinases and a smaller set of lipid kinases.[147] Targeting these kinases has a clear-cut advantage in achieving selectivity over the host due to distinct structural differences in the regulatory regions, absence of some classes such as the tyrosine kinases (TK) in the parasite, and absence of some mammalian orthologues, for instance in the CDPK families.[148]

Currently, it is estimated that about 30% of global drug discovery programs target kinases.[149] Accordingly, *Plasmodium* protein and lipid kinases such as cyclic guanosine monophosphate (cGMP)-dependent protein kinase (*Pf*PKG) and lipid *Pf*PI4K offer a hitherto underutilized chemical space for the discovery of novel antimalarials.[150,151]

1.9.2.1 *Pf* Protein Kinase G

*Pf*PKG is a cGMP-activated serine/threonine protein kinase that is involved in the phosphorylation of proteins required for various processes in the sexual and asexual stages of the *Plasmodium* life cycle. This 97.5-kDa complex comprising 853 amino acid residues is localized in the parasitic endoplasmic reticulum (ER). Functionally, it is associated with the phosphorylation of at least 69 protein substrates dictating their mobility and thereby influencing numerous stages of the parasite's development.

*Pf*PKG contains several regulatory domains and one catalytic domain that collectively facilitate its enzymatic functions (**Figure 1.13**).[152] The regulatory domain of *Pf*PKG comprises four cGMP binding domains (A-D) with C being degenerate. Although all the three non-degenerate cGMP-binding sites are involved in kinase regulation, domain-D has been demonstrated to have the strongest influence on *Pf*PKG activation. In comparison, the regulatory domain of mammalian PKGs differs significantly due to possession of two cGMP binding domains (A and B).[153]

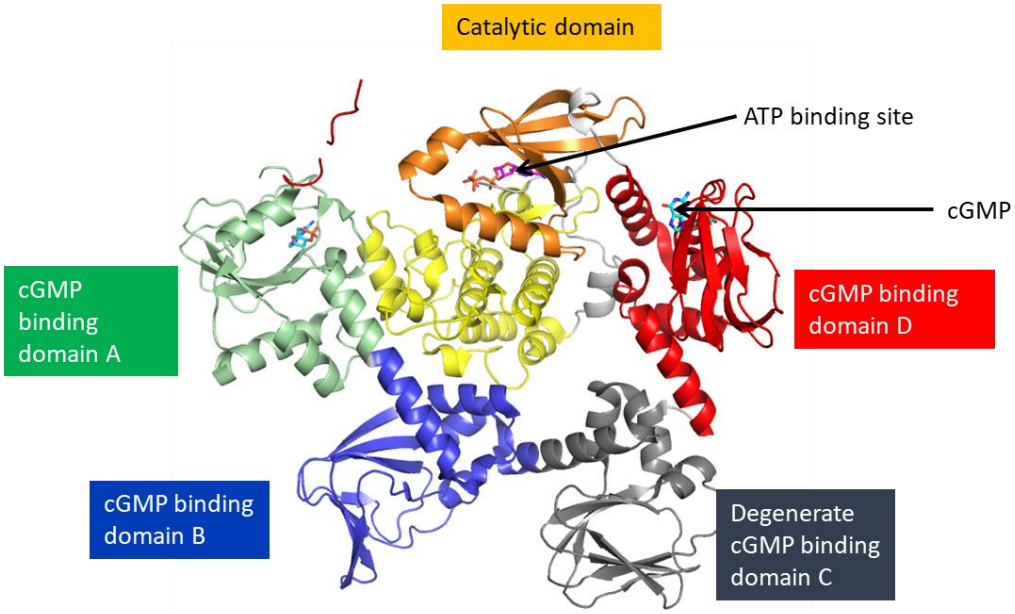

Figure 1.13: The main domain components of the *Pf*PKG crystal structure[154]

*Pf*PKG is an important kinase in multiple key stages of the parasite's life cycle in both the human host and mosquito vector. In the host, it acts as a signalling hub in the pre-erythrocytic liver stage invasion by sporozoites and merozoites invasion and egression in the asexual blood stage. It is also involved in the initiation of gametogenesis towards the formation of the transmissible sexual forms.[127,155,156] In the vector, *Pf*PKG is involved in both gametogenesis and ookinete motility.[157] Although gametocytes are developmentally arrested in human RBCs, transfer of gametocytes from an infected person to the mosquito during a blood meal results in a rapid change in environment. This includes a concomitant drop in temperature and a rise in pH, which are optimal for gamete egression and fertilization. This process is rapid (< 10 min) and is therefore highly energy-intensive.[22] *Pf*PKG is also involved in this activation process via phosphorylation of lipids used as precursors for phosphoinositide synthesis, which triggers rapid mobilization of intracellular calcium.[158]

Fertilization of the female macrogamete results in the formation of a zygote, which develops over 24 h to a slow motile ookinete. The gliding motility of these ookinetes to the epithelial monolayer of the mosquito midgut for further development requires a significant amount of intracellular Ca^{2+}. PKG is vital for these two processes and performs a function similar to that of essential calcium-dependent protein kinases (CDPKs).[159,160]

The first obligate step in the human host invasion process is the liver stage. Once sporozoites are inoculated into the host, these motile forms migrate through the host plasma and undergo a series of developmental stages upon reaching the liver, with eventual generation of hepatic

merozoites ready for blood-stage invasion.[161,162] Arresting the development of early-stage sporozoites would ideally offer protection against the disease. Unlike the asexual blood-stage form, hepatic sporozoites are immotile and, once inside hepatocytes, trigger a cascade of signaling events for acquisition of substrates necessary for nuclear division, cytoplasmic segmentation, and eventual maturation.[17,163]

*Pf*PKG is activated in *P. berghei* liver-stage parasites and its inhibition prevents progression of the disease to the symptomatic stage.[164] Concomitantly, merozoite development in infected hepatocytes triggers an increase in calcium sequestration from the host cytoplasm, indicating a similar role in both the mosquito and liver-stage invasion.[165,166]

The clinical manifestations of malaria are due to attack of RBCs by replicating merozoites in the asexual blood stages of the parasite. Each intraerythrocytic replication cycle results in merozoite egression and consequently rupture of RBCs, eventually leading to anemia.[167] Replication progresses via schizogony, a process in which up to five cycles of cell division occur to produce a multinucleated schizont bound by a single membrane. Thereafter, cytokinesis (division of cytoplasm) occurs, leading to the segmentation of the daughter merozoites and release from RBCs.[168]

*Pf*PKG also plays a key role in the maturation of these merozoites by regulating subtilisin-like serine protease 1 (*Pf*SUB1), an essential protease that facilitates modification of the parasitophorous vacuole and intracellular merozoite surface. This enzyme is also implicated in the breakdown and recycling of the host cell membrane.[169,170] Insufficient proteases hinders permeabilization of the erythrocytic membrane, denying the parasite access to vital substrates. Whilst schizogony may occur, inhibition of this enzyme predominantly results in premature development and unsuccessful erythrocytic rupture and release. Furthermore, the immature merozoites are typically non-invasive, even when released mechanically.[127,171] Resistance selection studies on several *Pf*PKG inhibitors raised no mutants, suggesting its potential as a target of low propensity for resistance.[172,173]

With the ever-increasing need for new targets for malaria, *Pf*PKG is a promising target for novel drug discovery programs. Despite its essentiality, a single PKG gene exists in *Plasmodium*. Furthermore, several *Pf*PKG crystal structures are available in PDB, and these highlight key features that can be targeted to promote antiparasitic activity and structural differences between human and host that can be exploited to achieve selectivity.[174] In addition,

inhibitors known to target PKG in other organisms, may be used as starting points for the development of selective *Plasmodium Pf*PKG inhibitors.[175,176]

Furthermore, PKG has been validated *in vivo* and through chemogenetic approaches across multiple pathogens including coccidiosis, toxoplasmosis, and *Plasmodium*, with exploitation of structural similarities between enzymes making them amenable to inhibitor repositioning.[177,178] For example, a scaffold-hopping repositioning approach with a tri-substituted pyrole lead compound, a known poultry *Eimeria tenella* PKG (*Et*PKG) inhibitor, led to the identification of a series of tri-substituted thiazoles showing high *Pf*PKG activity (**Figure 1.14**).[173,175,179] **MMV030084,** a tri-substituted imidazole compound also shows similar mechanistic activity, with these and related scaffolds explored as starting points in further medicinal chemistry programs.[180]

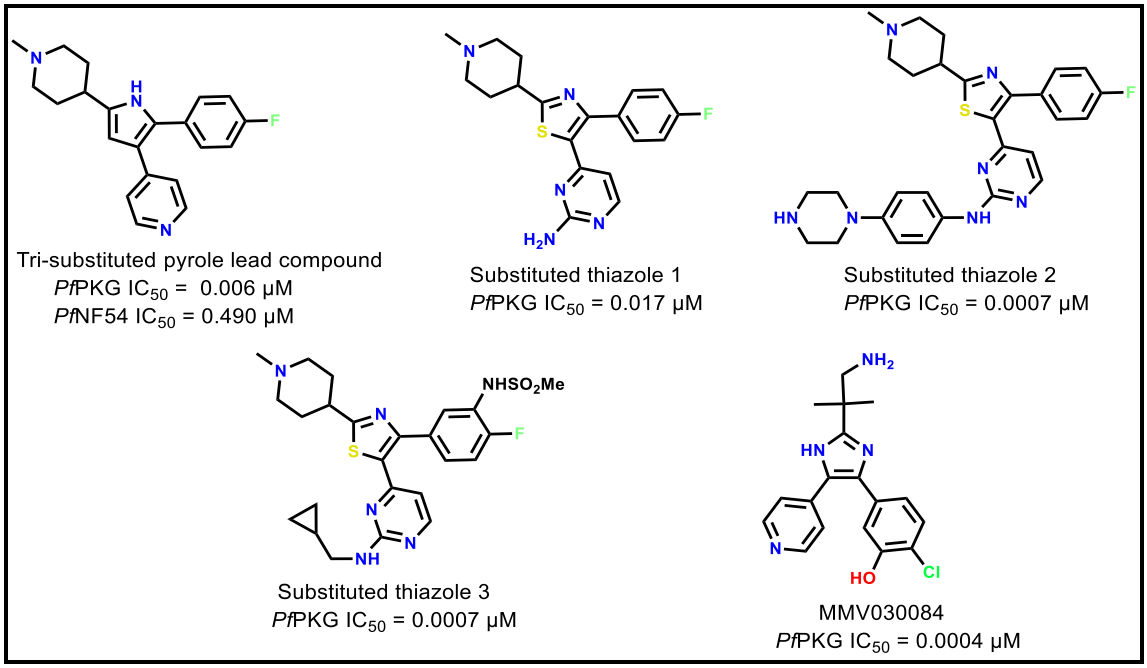

Figure 1.14: Anti-plasmodium compounds targeting cGMP dependent *Pf*PKG

1.9.2.2 *Pf* phosphatidylinositol 4-kinase

*Pf*PI4K is an essential lipid kinase primarily localized in the parasitic golgi apparatus and plasma membrane.[181] It is involved in the phosphorylation of lipids and regulates key intracellular signaling pathways, lipid metabolism, and trafficking. Structurally, it is larger than *Pf*PKG and comprises 1559 amino acid residues, translating to a molecular mass of 183 kDa. PI4Ks add a phosphate moiety on the D-4 position of the inositol ring of phosphatidylinositol to produce a series of phosphatidylinositol 4-phosphate (PI4P) derivatives.[181]

PI4Ps are lipid precursors that are instrumental secondary signalling messengers involved in intracellular signal transduction and localization of the parasites' cytoskeletal components. These biomolecules are clearly important during cytokinesis, the last step of cell division, for the delivery of daughter cells with appropriate cell morphology.[182] Inhibition of *Pf*PI4K causes irreparable defects in new plasma membranes after cell division with resulting daughter cells generally incapable of egression from the infected human RBCs at the asexual blood stage. Clinically, *Pf*PI4K inhibitors demonstrate potency against dormant and artemisinin-resistant ring-stage parasites, a distinctive morphological form associated with malaria recrudescence, monotherapy resistance and ultimate artemisinin treatment failure.[183]

Disruption of Rab11A-mediated membrane trafficking (**Figure 1.15**), a common synergistic effector, is the probable mechanism via which *Pf*PI4K inhibitors impair dividing daughter cells, resulting in deformities.[184] Similar effects lead to complete clearance of early-stage liver schizonts in *P. cynomolgi*-infected monkeys after hypnozoite reawakening, thereby delaying relapse.[185,186] Furthermore, *Pf*PI4K plays significant roles during the formation of gametocytes, ex-flagellation in the mosquito stage prior to fertilization, and oocyst development, providing a potential window for host-to-vector and vector-to-host transmission blocking.[187]

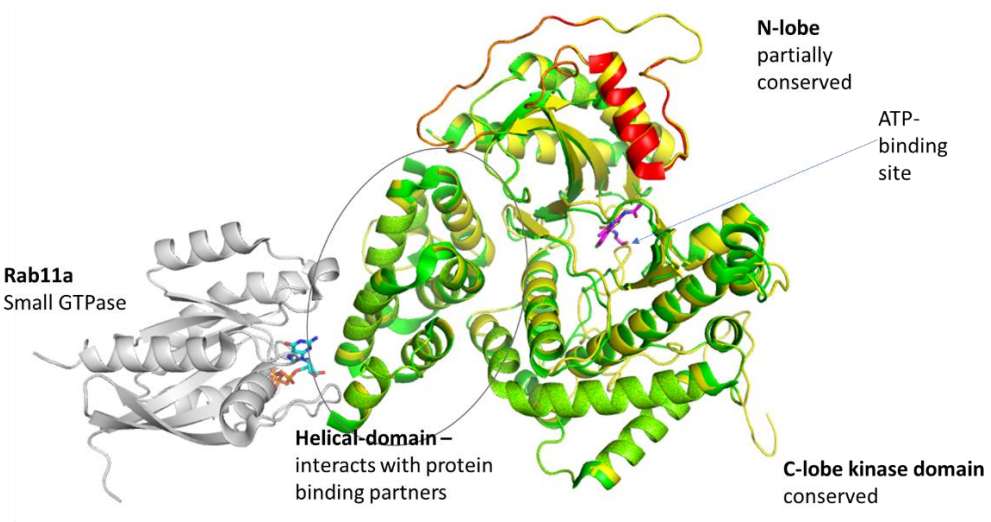

Figure 1.15: Crystal structure of human PI4KIIIβ (green) interacting with Rab11a (grey) (PDB **4D0L**)–PI4KIIIβ specific insert shown in red *Pf*PI4K homology model in yellow

Besides membrane delivery, PI4P is also directly involved in regulating cell polarity and consequently membrane trafficking and lipids dynamics.[188] This includes regulation of compartment identity and effector protein recruitment across key *Plasmodium* stages such as the asexual blood stages. Specifically, it is involved in schizont maturation, a critical stage prior

to merozoite egression from an infected RBC. Inhibitor-treated parasites undergo incomplete and disorganized cytokinesis with the resulting merozoites showing incomplete cell membranes and thus phenotypically disadvantaged.[189]

Moreover, *Pf*PI4K is involved in other catalytic and non-catalytic functions.[190] Its essentiality has been validated clinically,[191] the highest level of validation, and inhibitors achieved rapid parasite clearance in patients as opposed to the slow and moderate rate of clearance observed *in vitro* and *in vivo*, respectively. PI4K inhibition is therefore an effective mechanism against all vital stages of the parasite life cycle, with the exception of late liver hypnozoites (**Figure 1.16**). Accordingly, PI4K may be exploited as a curative and prophylactic target.[80]

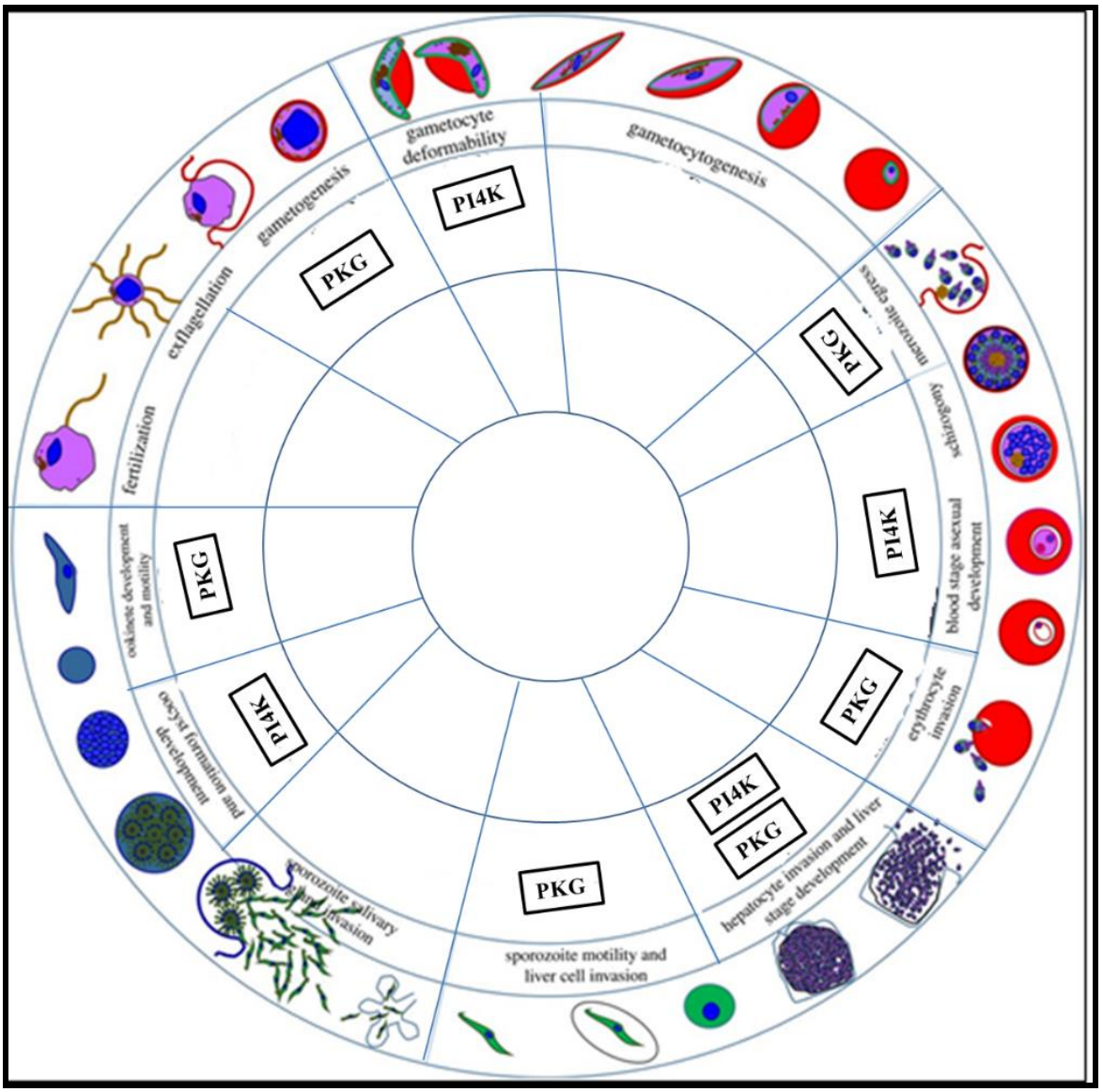

Figure 1.16: Pan *Plasmodium* life-stage specificity of *Pf*PI4K and *Pf*PKG kinases. Adopted with modifications from Baker *et al*.[168]

Collectively, *Plasmodium* protein and lipid kinases play crucial roles in the parasite life cycle and therefore represent attractive antimalarial targets.[192,193] However, no *Plasmodium* kinase inhibitors have been approved by the FDA to date, although the potential of such agents remains high as evidenced by **MMV390048** (**Figure 1.17**), a *Plasmodium* PI4K inhibitor showing high efficacy in patients.[80] Other pre-clinical lead compounds such as **KDU691**, **UCT943**, **KAI407**, **KAI715**, the quinoxaline compound **BQR695**, **LMV559** (structure undisclosed), and representative naphthyridine-based compounds (**Figure 1.17**) also function primarily via *Pf*PI4K inhibition.[75,194,195]

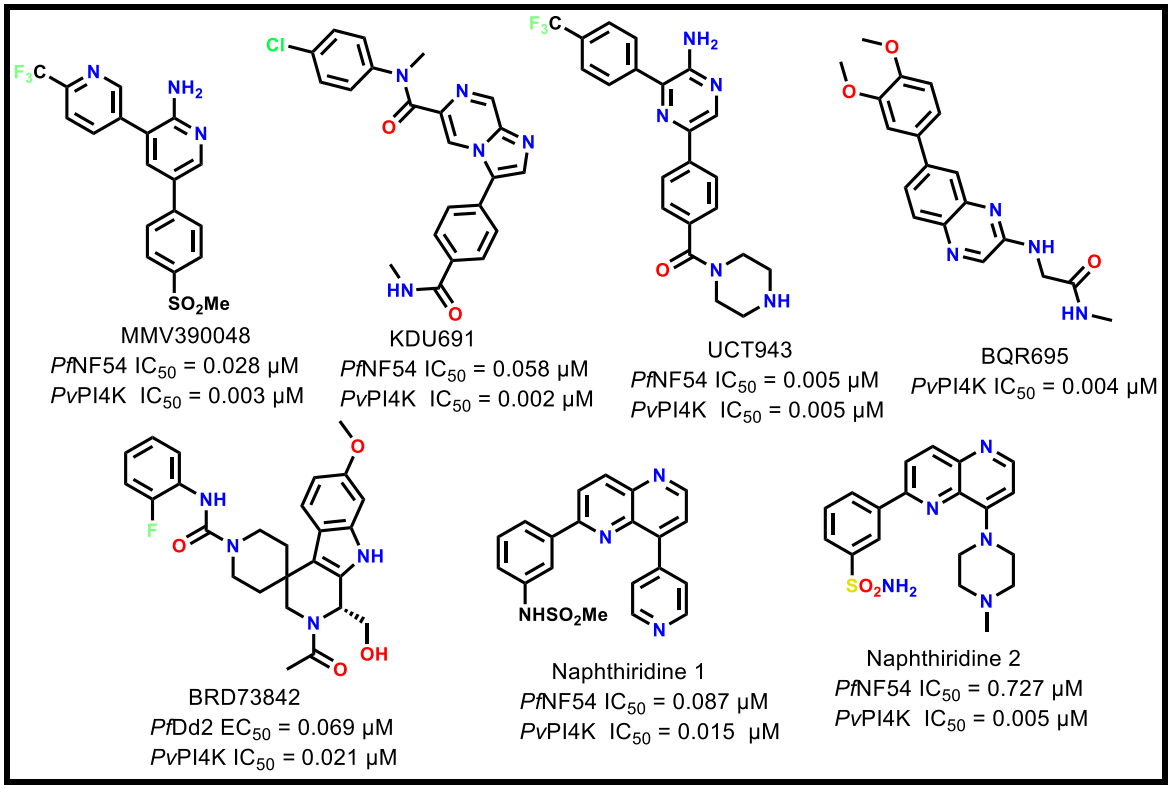

Figure 1.17: Chemical structures of selected clinical and pre-clinical *Pf*PI4K inhibitors

1.10 Poly-pharmacology in drug discovery and development

Traditionally, efforts in drug discovery were directed to finding the "magic bullet" i.e., a drug with high potency and selectivity towards a specific biological target in contrast to compounds with multiple targets/MoAs. Colloquially, referred to as the "magic shotgun", poly-pharmacology stimulates "out-of-the-box" thinking for the development of a single compound that simultaneously modulates multiple essential targets.[196] Such a compound would show reduced propensity for the development of resistance, as the likelihood of spontaneous resistance against multiple independent targets occurring at the same time is low. Furthermore, poly-pharmacologically relevant compounds may be more efficacious, particularly if

synergistic effects occur between multiple targets. In addition, this approach would offer the benefit of a reduced pill burden on patients, a problem currently encountered with combination therapies.[148]

In addition, toxicity emanating from drug-drug interactions during combination therapies would be offloaded in the early stages of drug discovery, since a single poly-pharmacological compound would be optimized. This would also promote simplified dosing schedules and consequently increases patient compliance in contrast with drugs cocktails employed in combination therapies. Moreover, it reduces drug attrition associated with acute and delayed clinical toxicities, which are common in combination therapies particularly if the drug partners are promiscuous.[148]

The molecular and genetic complexities of some diseases such as cancer also suggest that targeting a single pathway may not be sufficient to achieve durable remission in patients.[197] Poly-pharmacology is effective in mitigating drug resistance and improving efficacy, as use of combinational therapies as recommended by WHO, is driven by this concept. For example, antimalarial DHPS and DHFR inhibitors act synergistically on folate metabolism.[33] Currently, it is recognized that several approved drugs and clinical candidates exert their therapeutic effects through poly-pharmacology, although many are identified retrospectively. The *Plasmodium* PI4K inhibitor **MMV390048** was recently shown to inhibit the phosphatidylinositol 3-kinases (*Pf*PI3K), although the overall phenotypic contribution of this, and the effects on the compound's clinical efficacy remains unknown.[198] The MoAs of artemisinin derivatives also require further elucidation, with several lines of evidence suggesting multiple *Plasmodium* targets.[197] Other relevant representative examples of poly-pharmacology-based drug discovery are highlighted in **Figure 1.18**.[199]

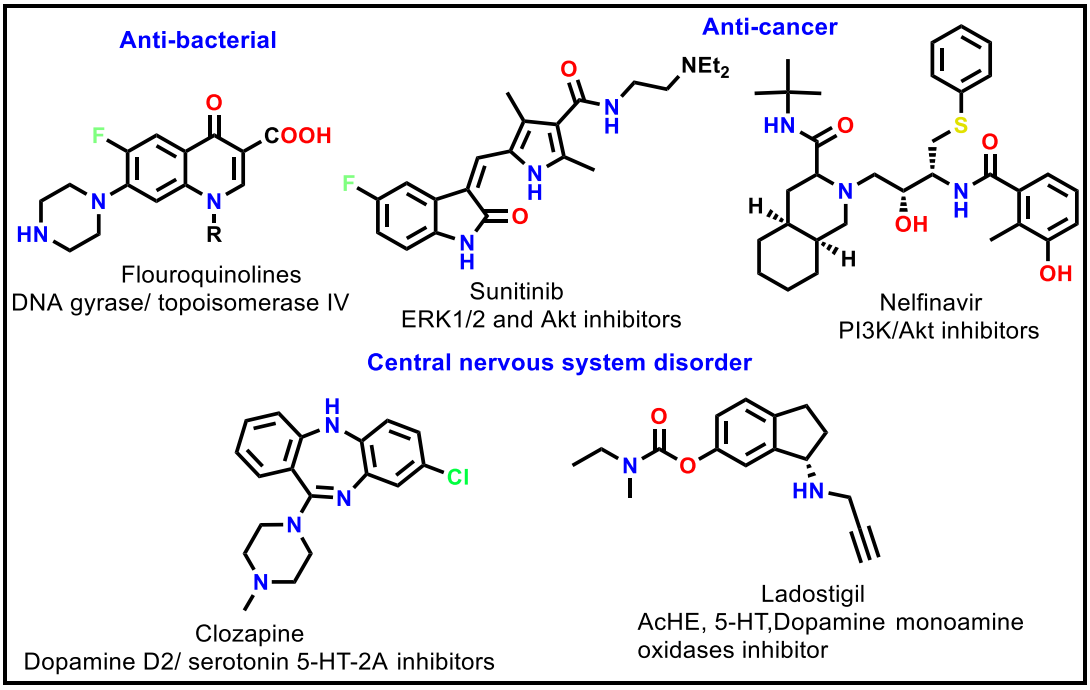

Figure 1.18: Chemical structures of selected poly-pharmacological drugs

Lately, the coherent design of single compounds targeting multiple pathways has drawn increasing attention. The ultimate challenge is to generate compounds with the desired poly-pharmacological profile and, more importantly, to mitigate promiscuity for the generation of safe therapeutics.[199] To this end, dedicated efforts through integrated approaches involving chemical biology, medicinal chemistry, and computational aspects are needed to successfully generate a selective multi-target inhibitor and provide a definitive evidence of synergy to curing diseases.[200] The paradigm shift has led to the development of computational and chemogenetic techniques to describe, design and ideally predict multi-target inhibitors across a wide range of parasitic, viral, autoimmune and neurodegenerative disorders. This multi-dimensional approach includes structure-multiple activity relationships, proteochemometric and pharmacophore modeling, data mining, target fishing and validation, and poly-pharmacology fingerprinting, of which a number of rich reviews have been published.[201–204]

1.11 Off-target considerations in antimalarial drug discovery

Selectivity studies on potential candidates are critical to the success of drug discovery programs. Indiscriminate host target interactions and associated toxicity remain a principal reason for the withdrawal or abandonment of numerous hits and lead compounds.[205] Off-target inhibition is often the result of structural similarities between host and parasite enzymes. In addition, repositioning of drugs targeting human lipid and protein kinases such as PI3Ks may

require the dysregulation of these critical host enzymes to avoid unwanted off-target effects. Several off-targets relevant to this study are discussed in the following sections.

1.11.1 Selected human off-targets

Typical small-molecule kinase inhibitors targeting the ATP-binding site mimic ATP. Such an approach has successfully been employed in the development of cancer drugs which directly target kinases involved in critical enzyme-mediated pathways such as mTOR and PI3K.[206] Although the merits of drug repositioning approaches such as optimizing PK and safety parameters are undeniable, this strategy is hampered by difficulties in mitigating the original human host kinase target and achieving selectivity over the 538 protein kinases encoded by the human genome.[207,208] Therefore, repositioning to a mono-selective inhibitor would be particularly challenging and in this regard, small molecules often exhibit some degree of promiscuity, often hitting 6–12 targets including their intended pharmacological one. To some extent, this contributes to host toxicity.[205]

Consequently, pharmaceutical companies and drug developers prefer to off-load this liability in the early stages of drug development. This is achieved by routine cross-screening of potential candidates against panels of human lipids and protein kinases to de-risk promiscuity.[209] Other common off-targets worthy of consideration in drug development include dopamine active transporter and cyclooxygenase 1 and 2. High attrition rates associated with human off-target promiscuity prevent many clinically relevant candidates from further development. Nonetheless, it is important to note that toxicity is dependent on a dose related manner and length of treatment, and that not all off-target activity will lead to toxicity. For instance, required dose and length of treatment may differ for malaria and other indications in comparison to oncological diseases.

1.11.2 Induced cardiotoxicity

Induced cardiotoxicity is a result of the inhibition of human ether-*a*-*go*-*go*-related gene (hERG), an important potassium ion channel that plays a critical role in cardiac potential repolarization.[210] Induced blockage of this channel by a drug can have serious repercussions including seizure, loss of consciousness, and death, and has led to the discontinuation and withdrawal of several marketed non-cardiac drugs such as antibiotics, antihistamines, and antipsychotics.[211]

Cardiotoxicity is a complex phenomenon attributed to many factors such as the chemical structure of a compound, its MoA, potential interactions with other ion channels, and its binding modes.[212] Often, cardiotoxicity risk is identified post-clinically as a heightened risk in particular patients. It has led to the withdrawal of **astemizole**, a long-acting and non-sedating antihistamine, **sertindole**, an antipsychotic drug used in the treatment of schizophrenia, **grepafloxacin**, a broad-spectrum fluoroquinolone antibiotic, and the antimalarial drug **halofantrine**, whose use is limited to patients without heart disease, despite its efficacy in treating severe and resistant forms of malaria (**Figure 1.19**).[212,213] Consequently, hERG toxicity needs to be routinely assessed in the early stages of the drug development process.[211]

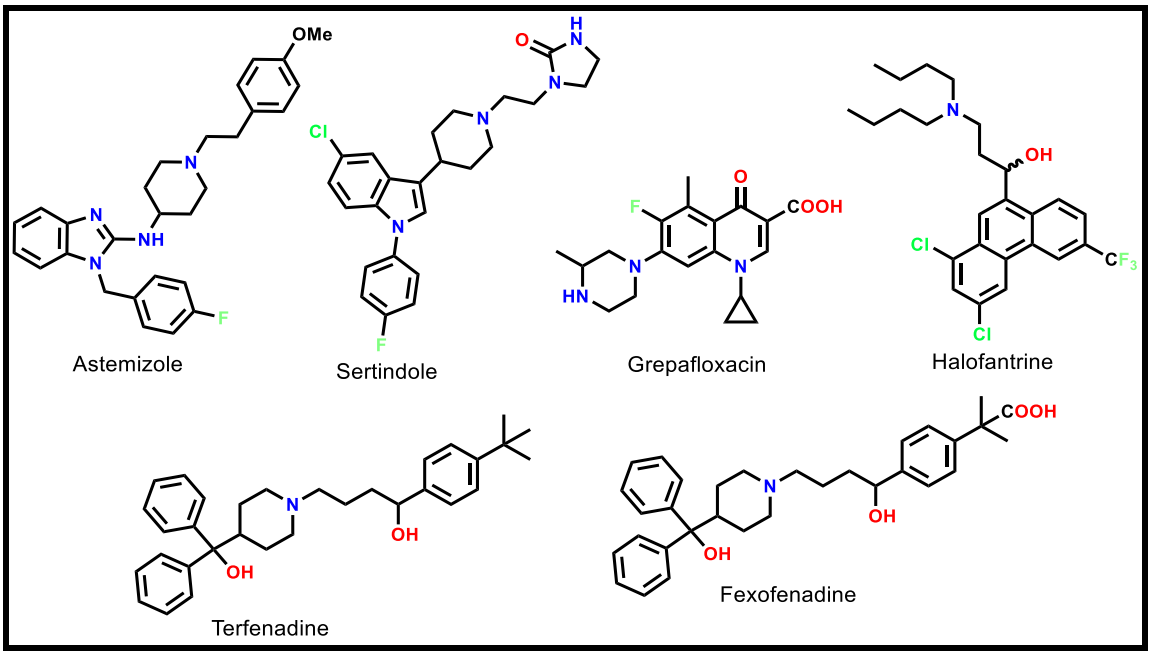

Figure 1.19: Chemical structures of selected drugs associated with induced hERG blockade

Synthetically, several approaches have been proposed to mitigate hERG activity in potential lead compounds. π-Stacking and hydrophobic interactions between aromatic constituents of the drug and the phenyl amino acid residues of proteins lining the cavity of the channel, such as Tyr-652 and Phe-656 in the S6 domain, contribute significantly to increased hERG-drug interactions.[212] Consequently, modification and disruption of the aromatic constituents of a drug can drastically reduce these interactions. Stereochemical variation of substituents, replacement of an electron-donating substituent, replacement of a fluorine atom within an aromatic moiety, and introduction of constraints within the molecule are strategies employed to detune hERG activity.[214,215] Other empirical approaches used to reduce hERG-drug interactions include the formation of zwitterions, control of log P, and attenuation of the ionization constant pKa.[216]

In addition, the presence of a basic nitrogen in a moiety may contribute to induced hERG activity attributable to π-cation interactions between the nitrogen and aromatic residues of the channel.[214] A basic amine is not a necessary prerequisite to hERG blockade but reduction of basicity generally destabilizes π-interactions, thus lowering the pKa of the molecule and reducing its affinity for hERG.[216] Generation of a zwitterionic system involves the introduction of a substituent that confers both positive and negative charges to a drug at physiological pH. This may be achieved by introducing an acid moiety into an amine-containing drug, an approach successfully used in the re-purposing of **terfenadine**, a hERG-active antihistamine withdrawn from the market but replaced with **fexofenadine**, its carboxylate derivative (**Figure 1.19**).[210,211] However, such an approach may also lead to reduced bioavailability associated with the presence of an acidic moiety.[216]

1.12 Physicochemical properties relevant to drug discovery and development

1.12.1 Solubility and strategies for its improvement

Solubility is an important physicochemical parameter in drug discovery. Low solubility often presents significant problems such as inconsistent correlations between *in vitro* and *in vivo* studies as the compound may precipitate out of solution, and varying solubilities in different media. It also increases cost in advanced stages of drug development and the risk of attrition. For example, over 75% of lead compounds exhibit low solubility, an issue responsible for many not advancing in drug development.[217,218] This is partly attributed to high MW, the method of identification, and drug target. For example, effective kinase inhibitors are typically highly aromatic compounds containing a flat hinge binding motif, multiple aromatic rings, and contains an array of hydrogen bond acceptors and donors. Consequently, they tend to be highly lipophilic with high MW. It is therefore not surprising that nearly half of the FDA-approved kinase inhibitors have a MW exceeding 500 Da.[219]

In animal models, the solubility of an oral drug defines its absorption and thus its bioavailability in the target organ. Insoluble compounds require formulations to achieve optimal *in vivo* PK and efficacy in an appropriate animal model.[218] Consequently, medicinal chemists aim to improve solubility in early stages through structural modifications. For instance, water-solubilizing polar groups and H-bonding motifs may be strategically embodied in a molecule to mitigate this issue. Effective polar functionalities include hydroxyl, amino, amide, carboxyl, sulfonic, pyridine, pyrazine, and phosphate groups. This strategy was employed in the lead compounds to deliver **UCT943**, an antimalarial lead compound (**Figure 1.20A**).[220-221]

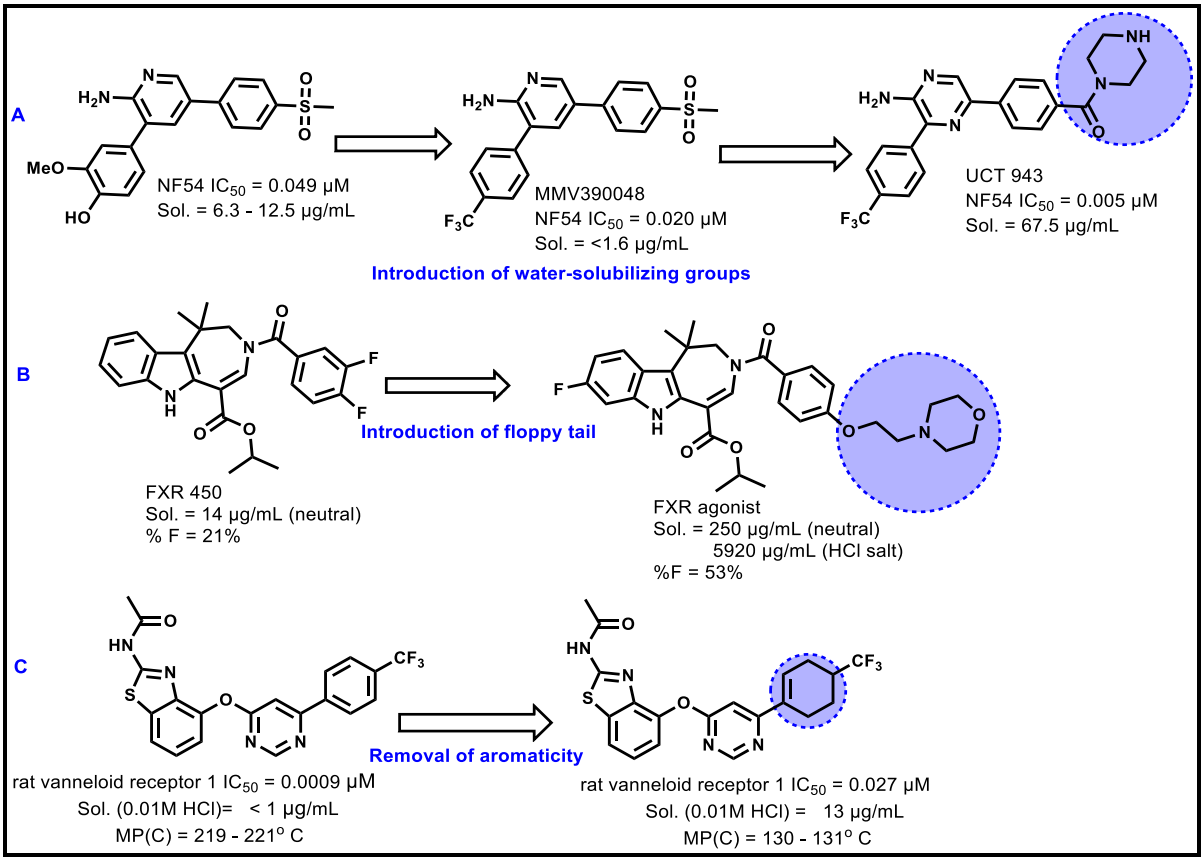

Figure 1.20: Successful chemical modification strategies employed to improve solubility of A) *Pf*PI4K inhibitor UCT943, B) farnesoid X receptor (FXR) agonist lead compound, C) lead vanilloid receptor 1 compound

Other strategies employed to improve solubility include molecular size reduction, structural changes to disrupt molecular planarity and symmetry, interruption of crystal packing, and formulation into salts.[222] These strategies may also improve other physicochemical parameters such as lipophilicity and associated ADME properties. For example, the introduction of a floppy tail in a farnesoid X receptor (FXR) agonist lead compound improved solubility (0.25 mg/mL; **Figure 1.20B**). In addition, reduced aromaticity in a lead vanilloid receptor 1 compound led to the discovery of a second-generation clinical candidate with improved solubility and other physicochemical parameters.[223] Solubility could be improved further by conversion of the candidate to an HCl salt, consequently improving bioavailability in animal models.[224] Similar approaches have also been successfully employed in the discovery of amlodipine, a drug with improved solubility relative to that of its original congeners.[225]

However, strategies employed to improve solubility may at times be detrimental to other ADME parameters such as efficacy and hepatic clearance. Consequently, structure-solubility relationships (SSRs) are normally undertaken to optimize activity. Utilization of predictive *in*

silico solubility models may also assist medicinal chemistry optimization and the development of an appropriate SAR. Computational models and numerous commercially available software packages such as Dragon, Optibrium StarDrop, and ChemSilico may be used for these predictions. However, virtual predictions by such tools may be unreliable, particularly for compounds whose solubility is crystal-dependent rather than associated with physicochemical parameters.[226]

1.12.2 Lipophilicity and permeability

Lipophilicity is another crucial physicochemical parameter with significant influence on ADME properties and thus on the success of a drug candidate. For a drug to show *in vivo* efficacy, it must traverse through several lipid bilayer membranes such as the gastro-intestinal tract, tissue, blood vessels, and blood-brain barrier to reach the target site of action. This process may be mediated by passive diffusion and/or transporter-mediated uptake and is thus at least partly dependent on lipophilicity. Lipophilicity therefore has an important impact on drug potency, metabolism, PK, and toxicity.[227]

Practically, lipophilicity is measured as a partition coefficient (LogP), which is the ratio of the affinity of non-ionized drug when partitioned between a lipid layer (usually n-octanol) and an aqueous one. The drug therefore mimics partition between a cell membrane and an aqueous phase. Alternatively, it is measured as a distribution coefficient (LogD), which is the ratio of ionized and un-ionized drug distributed between the two layers at equilibrium.[228] By comparing marketed drugs by Pfizer, Lipinski found that orally administered drugs with high lipophilicity (LogP > 5), MW (> 500 Da), and a high number of hydrogen-bond donors (HBD > 5) and hydrogen-bond acceptors (HBA > 10) showed low solubility, low absorption, and consequently low bioavailability. This became known as the Lipinski rule of five (Ro5; **Figure 1.21**).[229]

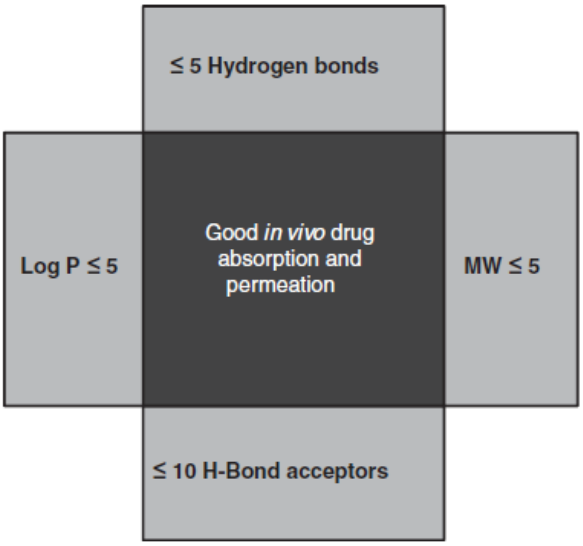

Figure 1.21: Summary of Lipinski's physicochemical parameters for successful oral drugs

In practice, highly lipophilic molecules show high plasma protein binding, resulting in relatively small free fractions of the unbound molecule and consequently low *in vivo* efficacy. This may also result in promiscuity-induced toxicity or fast metabolic breakdown of a compound, thus limiting its potential as a drug lead.[209] Toxicity associated with high lipophilicity arises from drug promiscuity in plasma protein binding, including unwanted drug targets.[230] For example, highly lipophilic bases can cause cardiotoxicity by binding to the hERG ion channel. These may also have high propensity to cause tissue toxicity via cellular phospholipidosis and increase the compound's susceptibility to metabolism by cytochrome P450 enzymes. Highly lipophilic drugs are typically favorable substrates that fit optimally within large hydrophobic binding pockets of drug metabolizing enzymes, resulting in high metabolic turnover. These enzymes are involved in phase 1 biotransformation of 70–80% of currently marketed drugs.[231]

Key mediators of numerous enzyme-drug interactions are guided by some degree of lipophilicity. It is therefore not surprising that over 30% of patented compounds from major pharmaceutical companies and FDA-approved drugs have a LogP > 5 and a MW > 500 Da.[140,219] This is often common for drugs which act as substrates for membrane transporters as is the case for most natural products and related derivatives. Nevertheless, an optimal balance between lipophilicity and permeability is necessary for optimal absorption and bioavailability.[232]

Several approaches are involved in the reduction of lipophilicity within a molecule, including decreasing the length of alkyl groups, replacing phenyl rings with saturated heterocyclic rings,

and removing or replacing halogens with more polar functionalities.[233] Noteworthy, these same properties have a direct positive correlation with aqueous solubility and other physicochemical properties such as solubility, as discussed earlier.[234]

1.13 Drug Metabolism and Pharmacokinetics (DMPK)

Potency of a compound and efficacy do not necessarily translate into successful drug development as this process is multi-parametric and encompasses a delicate balance between chemistry, pharmacology, and PK.[235] It involves understanding how a drug is absorbed, distributed within the body, metabolized, and finally eliminated out of the system. For instance, an orally administered drug first requires dissolution and absorption before going into circulation through the bloodstream. Here, various factors come into play such as chemical stability, solubility, membrane permeability, and stability in liver enzymes. All of these factors contribute towards the overall amount of drug available at the site of action.[236,237]

Drug metabolism has a significant effect on the overall bioavailability of a drug. Understanding biotransformation is important as it can lead to the formation of an inactive, toxic, or pharmacologically active metabolite. Such transformations are usually enzyme-catalyzed and include hydroxylation, oxidation, *N*–dealkylation, oxidative deamination, and conjugation reactions, which may make a drug less lipophilic and more easily excreted.[238,239]

Understanding ADME properties may aid drug design in blocking metabolite hotspots, improving undesirable characteristics such as low solubility and permeability, and understanding possible toxicities resulting from *in vivo* metabolism.[240] DMPK involves assessing PK parameters such as bioavailability, plasma clearance, half-life, and volume of distribution.[241] It assists in drug discovery by quantitatively predicting human drug PK and metabolism while acting as a guide in drug design, thus saving time and resources. By initially screening large numbers of compounds and optimizing these further, compounds with sub-optimal PK profiles can be eliminated. Henceforth, DMPK profiling becomes critical with the potential to deliver drug candidates capable of overcoming hurdles in further development.[242]

1.14 Chapter summary

This chapter introduced malaria as a disease and provided a foundation for the work undertaken in this study. It provided insight into epidemiology, current treatment modalities, and prevention options, as well as current drugs in the pipeline, with emphasis on novelty and considerations for the development of future antimalarials. This included important aspects in kinase drug discovery programs such as selectivity over host kinases and other relevant off-targets. Lastly, the need for optimal physicochemical and ADME properties was discussed in relation to their influence on *in vivo* studies and pharmacological outcomes for potential drugs. In the next sections, the rationale, and justifications for the repositioning approach of the anticancer Phase 1 clinical candidate (**MLN0128**; **Part 1**) and the optimization of the imidazopyridine scaffold (**Part 2**), as the main objectives of this research will be discussed.

References

1. CDC. Malaria biology https://www.dpd-cdc-gov/dpdx/malaria/about/biology/index.html.

2. Amir, A.; Cheong, F.; de Silva, J.; Liew, J.; Lau, Y. *Plasmodium knowlesi* malaria: Current research perspectives. *Infect. Drug Resist*. **2018**; 11: 1145 - 1155 doi:10.2147/IDR.S148664.

3. World Health Organization. *WHO World Malaria Report 2020; Years of Global Progress and Challenges*; **2020**: 1 - 299.

4. World Health Organization. World Malaria Report 2019. *World Health*. **2019**; WHO/HTM/GM(December):238. doi:ISBN 978 92 4 1564403.

5. World Health Organization. *World Malaria Report 2017*; **2017**. doi:http://www.who.int/malaria/ publications/world-malaria-report-2017/report/en/.

6. Global technical strategy for malaria 2016 - 2030. *World Heal. Organ*. **2015**: 1 - 35. http://apps.who.int/iris/bitstream/10665/176712/1/9789241564991_eng.pdf?ua=1.

7. The Global Fund. Result Report 2017. **2017**. 1 - 53.

8. Plebanski, M. and Flanagan, K. The Economics of Malaria Vaccine Development. *Trends Parasitol.* **2017**, 33 (3); 154 – 156. doi.org/10.1016/j.pt.2017.01.006.

9. World Health Organization. Global Malaria Control and Elimination : Malaria Control and Elimination: **2008**: 1 - 38.

10. WHO. *Report on Antimalarial Drug Efficacy, Resistance and Response: 10 Years of Surveillance (2010 - 2019).*; **2020**. https://www.who.int/publications/i/item/9789240012813.

11. Petersen, I.; Eastman, R. and Lanzer, M. Drug-resistant malaria: Molecular mechanisms and implications for public health. *FEBS Lett*. **2011**; 585 (11): 1551 - 1562. doi:10.1016/j.febslet.2011.04.042.

12. Na-Bangchang, K. and Karbwang, J. Current status of malaria chemotherapy and the role of pharmacology in antimalarial drug research and development. *Fundam. Clin. Pharmacol*. **2009**; 23 (4): 387 - 409. doi:10.1111/j.1472-8206.2009.00709.x.

13. Cowman, A.; Healer, J.; Marapana, D. and Marsh, K. Malaria: Biology and disease. *Cell*. **2016**; 167 (3): 610 - 624. doi:10.1016/j.cell.2016.07.055.

14. Trampuz, A.; Jereb, M.; Muzlovic, I.; Prabhu, R. Clinical Review: Severe Malaria. *Crit. Care* **2003**; 7 (4): 315 - 323. https://doi.org/10.1186/cc2183.

15. Prudêncio, M.; Rodriguez, A. and Mota, M. The silent path to thousands of merozoites: The *Plasmodium* liver stage. *Nature Reviews* **2006**; 4 (11): 849 - 856. doi:10.1038/nrmicro1529.

16. Hawkins, V.; Joshi, H.; Rungsihirunrat, K.; Na-Bangchang, K.; Sibley, C. Antifolates can have a role in the treatment of *Plasmodium vivax*. *Trends Parasitol*. **2007**; 23 (5): 213 - 222. doi:10.1016/j.pt.2007.03.002.

17. Coppi, A.; Tewari, R.; Bishop, J.; Bennett, B.; Lawrence, R. Heparan sulfate proteoglycans provide a signal to *Plasmodium* sporozoites to stop migrating and productively invade cells. *Cell Host Microbe*. **2008**; 2 (5): 316 - 327.

18. Liñares, G. and Rodriguez, J. Current status and progresses made in malaria chemotherapy. *Curr. Med. Chem*. **2007**; 14 (3): 289 - 314. doi:10.2174/092986707779941096.

19. Phillips, M.; Burrows, J.; Manyando, C.; Van Huijsduijnen, R.; Van Voorhis, W.; Wells, T. Malaria. *Nature Reviews* **2017**; 3: 1 - 24. doi:10.1038/nrdp.2017.50.

20. Doerig, C.; Rayner, J.; Scherf, A. and Tobin, A. Post-translational protein modifications in malaria parasites. *Nat. Publ. Gr*. **2015**; 1 - 13. doi:10.1038/nrmicro3402.

21. Schlitzer, M. Antimalarial drugs - What is in use and what is in the pipeline. *Arch. Pharm (Weinheim)*. **2008**; 341 (3): 149 - 163. doi:10.1002/ardp.200700184.

22. Nacer, M.; Underhill, A.; Carter, V.; Sinden, R.; Hurd, H. Minimum requirements for ookinete to oocyst transformation in *Plasmodium*. *Int. J. Parasitol.* **2007**; 37: 1221 - 1232. doi:10.1016/j.ijpara.2007.03.005.

23. Vlachou, D.; Zimmermann, T.; Cantera, R.; Janse, C.; Waters, A.; Kafatos, F. Real-time, *in vivo* analysis of malaria ookinete locomotion and mosquito midgut invasion.*Cellular. Microbio.* **2004**; 6: 671 - 685. doi:10.1111/j.1462-5822.2004.00394.x.

24. RTS,S Partnership, Clinical Trials Partnership. Efficacy and safety of RTS,S/AS01

malaria vaccine with or without a booster dose in infants and children in Africa: Final results of a phase 3, individually randomised, controlled trial. *Lancet*. **2015**; 386 (9988): 31 - 45. doi:10.1016/S0140-6736(15)60721-8.

25. WHO. Historic RTS,S/AS01 recommendation can reinvigorate the fight against malaria. https://www.who.int/news/item/06-10-2021-who-recommends-groundbreaking-malaria-vaccine-for-children-at-risk. Accessed October 29, 2021.

26. Bero, J.; Frédérich, M. and Quetin-Leclercq, J. Antimalarial compounds isolated from plants used in traditional medicine. *J. Pharm. Pharmacol*. **2009**; 61 (11): 1401 - 1433. doi:10.1211/jpp/61.11.0001.

27. Wongsrichanalai, C.; Pickard, A.; Wernsdorfer, W. and Meshnick, S. Epidemiology of drug-resistant malaria. *Lancet Infect. Dis*. **2002**; 2 (4): 209 - 218. doi:10.1016/S1473-3099(02)00239-6.

28. Schwikkard, S. and van Heerden, F. Antimalarial activity of plant metabolites. *Nat. Prod. Rep*. **2002**; 19 (6): 675 - 692. doi:10.1039/b008980j.

29. Solomon, V. and Lee, H. Chloroquine and its analogs: A new promise of an old drug for effective and safe cancer therapies. *Eur. J. Pharmacol*. **2009**; 625 (1-3): 220 - 233. doi:10.1016/j.ejphar.2009.06.063.

30. World Health Organization. World Health Organization Model List of Essential Medicines. *WHO*. **2019**; 21: 23 - 24.

31. Saifi, A. Antimalarial drugs: Mode of action and status of resistance. *African J. Pharm. Pharmacol*. **2013**; 7 (5): 148 - 156. doi:10.5897/AJPPX12.015.

32. Müller, I. and Hyde, J. Parasite Resistance. *Future Microbiol*. **2010**; 5 (12): 1857 - 1873. doi:10.2217/fmb.10.136.

33. Nzila, A. The past, present and future of antifolates in the treatment of *Plasmodium falciparum* infection. *J. Antimic. Chemotherapy* **2006**; 57: 1043 - 1054. doi:10.1093/jac/dkl104.

34. Siregar, J.; Kurisu, G.; Kobayashi, T.; Matsuzaki, M.; Sakamoto, K. Direct evidence for the atovaquone action on the *Plasmodium* cytochrome bc 1 complex. *Parasitol. Int.* **2015**; 64 (3): 295 - 300. doi:10.1016/j.parint.2014.09.011.

35. Winstanley, P. and Ward, S. Malaria chemotherapy. *Adv. Parasitol*. **2006**; 61 (05): 47 - 76. doi:10.1016/S0065-308X(05)61002-0.

36. World Health Organization. *Guidelines for the Treatment of Malaria*. **2015**: 1 - 88.

37. Eastman, R. and Fidock, D. Artemisinin-based combination therapies: A vital tool in efforts to eliminate malaria. *Nat. Rev. Microbiol*. **2009**; 7 (12): 864 - 874. doi:10.1038/nrmicro2239.

38. Bridgford, J.; Xie, S.; Cobbold, S.; Pasaje, C.; Herrmann, S.; Yang, T.; Gillett, D.; Dick, L,; Ralph, S.; Dogovski, C.; Spillman, N.; Tilley, L Artemisinin kills malaria parasites by damaging proteins and inhibiting the proteasome. *Nat. Commun*. **2018**; 9 (1): 1 - 9. doi:10.1038/s41467-018-06221-1.

39. Lu, F.; He, X.; Richard, C. and Cao, J. A brief history of artemisinin: Modes of action and mechanisms of resistance. *Chin. J. Nat. Med*. **2019**; 17 (5): 331 - 336. doi:10.1016/S1875-5364(19)30038-X.

40. Nagasundaram, N.; Doss, C.; Chakraborty, C.; Karthick V.; Thirumal, K.; Balaji, V.; Siva, R.; Aiping, L.; Zhang, G.; Hailong, Z. Mechanism of artemisinin resistance for malaria *Pf*ATP6 L263 mutations and discovering potential antimalarials: An integrated computational approach. *Sci. Rep*. **2016**; 6: 1 - 12. doi:10.1038/srep30106.

41. Naik, P.; Srivastava, M.; Bajaj, P.; Jain, S.; Dubey, A.; Ranjan, P.; Kumar, R.; Singh, H. The binding modes and binding affinities of artemisinin derivatives with *Plasmodium falciparum* Ca^{2+}-ATPase (*Pf*ATP6). *J. Mol. Model*. **2011**; 17 (2): 333 - 357. doi:10.1007/s00894-010-0726-4.

42. Krishna, S.; Pulcini, S.; Moore, C.; Teo, B.; Staines, H. Pumped up: Reflections on *Pf*ATP6 as the target for artemisinins. *Trends Pharmacol. Sci*. **2014**; 35 (1): 4 - 11. doi:10.1016/j.tips.2013.10.007.

43. Woodrow, C. and Krishna, S. Antimalarial drugs: Recent advances in molecular determinants of resistance and their clinical significance. *Cell Mol. Life Sci*. **2006**; 63 (14): 1586 - 1596. doi:10.1007/s00018-006-6071-1.

44. Nosten, F.; McGready, R.; d'Alessandro, U.; Bonell, A.; Verhoeff, F.; Menendez, C.; Mutabingwa, T.; Brabin, B. Antimalarial Drugs in Pregnancy: A Review. *Curr. Drug Saf*. **2006**; 1 (1): 1 - 15. doi:10.2174/157488606775252584.

45. Ambroise-Thomas, P. The tragedy caused by fake antimalarial drugs. *Mediterr. J. Hematol. Infect. Dis.* **2012**; 4 (1): 1 - 4. doi:10.4084/MJHID.2012.027.

46. Karunamoorthi, K. The counterfeit anti-malarial is a crime against humanity: A systematic review of the scientific evidence. *Malar. J.* **2014**; 13 (1): 1 - 13. doi:10.1186/1475-2875-13-209.

47. Shrivastava, S.; Shrivastava, P. and Ramasamy, J. Public health measures to fight counterfeit medicine market. *Int. J. Prev. Med.* **2014**; 5 (3): 370 - 371. doi:10.1136/bmjopen-2013-002923.

48. Fernandez, F.; Hostetler, D.; Powell, K.; Kaur, H.; Green, M.; Mildenhall, D.; Newton, P. Poor quality drugs: grand challenges in high throughput detection, countrywide sampling, and forensics in developing countries. *Analyst.* **2011**; 136 (15): 3073 - 3082. doi:10.1039/C0AN00627K.

49. Po, A. Too much, too little, or none at all: Dealing with substandard and fake drugs. *Lancet*. **2001**; 357 (9272): 1904. doi:10.1016/S0140-6736(00)05092-3.

50. Owens, S. Malaria and the millennium development goals. *Arch. Dis. Child.* **2015**; 100(Suppl 1): S53 - S56. doi:10.1136/archdischild-2013-305441.

51. Jin, G. and Wong, S. Toward better drug repositioning: Prioritizing and integrating existing methods into efficient pipelines. *Drug Discov. Today*. **2014**; 19 (5): 637 - 644. doi:10.1016/j.drudis.2013.11.005.

52. Muthyala, R. Orphan/rare drug discovery through drug repositioning. *Drug Discov. Today Ther. Strateg*. **2012**; 8 (3-4): 71 - 76. doi:10.1016/j.ddstr.2011.10.003.

53. Andrews, K.; Fisher, G. and Skinner-Adams, T. Drug repurposing and human parasitic protozoan diseases. *Int. J. Parasitol. Drugs Drug Resist.* **2014**; 4 (2): 95 - 111. doi:10.1016/j.ijpddr.2014.02.002.

54. Guiguemde, W.; Shelat, A.; Garcia-Bustos, J.; Diagana, T.; Gamo, F.; Guy, R. Global phenotypic screening for antimalarials. *Chem. Biol*. **2012**; 19 (1): 116 - 129. doi:10.1016/j.chembiol.2012.01.004.

55. Wells, T.; Van Huijsduijnen, R. and Van Voorhis, W. Malaria medicines: A glass half full? *Nat. Rev. Drug Discov*. **2015**; 14 (6): 424 - 442. doi:10.1038/nrd4573.

56. The malERA Consultative Group on Drugs. A research agenda for malaria eradication: Drugs. *PLoS Med*. **2011**; 8 (1): 1 - 9. doi:10.1371/journal.pmed.1000402.

57. Burrows, J.; Van Huijsduijnen, R.; Möhrle, J.; Oeuvray, C.; Wells, T. Designing the next generation of medicines for malaria control and eradication. *Malar. J*. **2013**; 12 (1): 1 - 20. doi:10.1186/1475-2875-12-187.

58. Burrows, J. Antimalarial drug discovery: Where next? *Future Med. Chem*. **2012**; 4 (18): 2233 - 2235. doi:10.4155/fmc.12.189.

59. Tiwari, M. and Chaudhary, S. Artemisinin-derived antimalarial endoperoxides from bench-side to bed-side: Chronological advancements and future challenges. *Med. Res. Rev*. **2020**: 1220 - 1275. doi:10.1002/med.21657.

60. Burrows, J.; Duparc, S.; Gutteridge, W.; van Huijsduijnen, R.; Kaszubska, W.; Macintyre, F.; Mazzuri, S,; Möhrle, J.; Wells, T. New developments in anti-malarial target candidate and product profiles. *Malar. J*. **2017**; 16 (1): 1 - 29. doi:10.1186/s12936-016-1675-x.

61. Burrows, J.; Leroy, D.; Lotharius, J. and Waterson, D. Challenges in antimalarial drug discovery. *Future Med. Chem*. **2011**; 3 (11): 1401 - 1412. doi:10.4155/fmc.11.91.

62. Fernando, D.; Rodrigo, C. and Rajapakse, S. Primaquine in *vivax* malaria: An update and review on management issues. *Malar. J*. **2011**; 10: 1 - 12. doi:10.1186/1475-2875-10-351.

63. Chu, C. and Freedman, D. Tafenoquine and g6pd: A primer for clinicians. *J. Travel Med*. **2019**; 26 (4): 1 - 11. doi:10.1093/jtm/taz023.

64. Antonova-Koch, Y.; Meister, S.; Abraham, M.; Luth, M.; Ottilie, S.; Lukens, A.; Sakata-Kato, T.; Vanaerschot, M.; Owen, E.; Jado, J.; Maher, S.; Calla, J.; Plouffe, D.; Zhong, Y.; Chen, K.; Chaumeau, V.; Conway, A.; McNamara, C.; Ibanez, M.; Gagaring, K.; Serrano, F.; Eribez, K.; Taggard, C.; Cheung, A.; Lincoln, C.; Ambachew, B.; Rouillier, M.; Siegel, D.; Nosten, F.; Kyle, D.; Gamo, F.; Zhou, Y.; Llinás, M.; Fidock, D.; Wirth, D.; Burrows, J.; Campo, B.; Winzeler, E. Open-source discovery of chemical leads for next-generation chemoprotective antimalarials. *Science*. **2018**; 362 (6419): 1 - 8. doi:10.1126/science.aat9446.

65. Meister, S.; Plouffe, D.; Kuhen, K.; Bonamy, G.; Tao Wu, T.; Barnes, W.; Bopp, S.;

Borboa, R.; Bright, T.; Che, J.; Cohen, S.; Dharia, N.; Gagaring, K.; Gettayacamin, M.; Gordon, P.; Groessl, T.; Kato, K.; Lee, M.; McNamara, C.; Fidock, D.; Nagle, A.; Nam, T.; Richmond, W.; Roland, J.; Rottmann, M.; Zhou, B.; Froissard, P.; Glynne, R.; Mazier, D.; Sattabongkot, J.; Schultz, P.; Tuntland, T.; Walker, J.; Zhou, Y.; Chatterjee, A.; Diagana, T.; Winzeler, E. Imaging of *Plasmodium* liver stages to drive next-generation antimalarial drug discovery. *Science* **2011**; 334 (6061): 1372 - 1377. doi:10.1126/science.1211936.

66. Alano, P. *Plasmodium falciparum* gametocytes: Still many secrets of a hidden life. *Mol. Microbiol*. **2007**; 66 (2): 291 - 302. doi:10.1111/j.1365-2958.2007.05904.x.

67. Bousema, T.; Okell, L.; Shekalaghe, S.; Griffin, J.; Omar, S.; Sawa, P.; Sutherland, C.; Sauerwein, R.; Ghani, A.; Drakeley, C. Revisiting the circulation time of *Plasmodium falciparum* gametocytes: Molecular detection methods to estimate the duration of gametocyte carriage and the effect of gametocytocidal drugs. *Malar. J.* **2010**; 9 (136): 1 - 11.

68. Tiburcio, M.; Niang, M.; Deplaine, G.; Perrot, S.; Bischoff, E.; Ndour, P.; Silvestrini, F.; Khattab, A.; Milon, G.; David, P.; Hardeman, M.; Vernick, K.; Sauerwein, R.; Preiser, P.; Mercereau-Puijalon, O.; Buffet, P.; Alano, P.; Lavazec, C. A switch in infected erythrocyte deformability at the maturation and blood circulation of *Plasmodium falciparum* transmission stages. *Blood* **2016**; 119 (24): e172 - e180 doi:10.1182/blood-2012-03-414557.

69. Delves, M. *Plasmodium* cell biology should inform strategies used in the development of antimalarial transmission-blocking drugs. *Future Med. Chem.* **2012**: 2251 - 2263.

70. Lucantoni, L. and Avery, V. Whole-cell *in vitro* screening for gametocytocidal compounds. *Future Med. Chem*. **2012**; 4 (18): 2337 - 2360. doi:10.4155/fmc.12.188.

71. Ebstie, Y.; Abay, S.; Tadesse, W. and Ejigu, D. Tafenoquine and its potential in the treatment and relapse prevention of *Plasmodium vivax* malaria: The evidence to date. *Drug Des. Devel. Ther*. **2016**; 10: 2387 - 2399. doi:10.2147/DDDT.S61443.

72. Taylor, W.; Naw, H.; Maitland, K.; Williams, T.; Kapulu, M.; D'Alessandro, U.; Berkley, J.; Bejon, P.; Okebe, J.; Achan, J.; Amambua, A.; Affara, M.; Nwakanma, D.; van Geertruyden J.; Mavoko, M.; Lutumba, P.; Matangila, J.; Brasseur, P.; Piola, P.;

Randremanana, R.; Lasry, E.; Fanello, C.; Onyamboko, M.; Schramm, B.; Yah, Z.; Jones, J.; Fairhurst, R.; Diakite, M.; Malenga, G.; Molyneux, M.; Rwagacondo, C.; Obonyo, C.; Gadisa, E.; Aseffa, A.; Loolpapit, M.; Henry, M.; Dorsey, G.; John, C.; Sirima, S.; Barnes, K.; Kremsner, P; Day, N.; White, N.; Mukaka, M. Single low-dose primaquine for blocking transmission of *Plasmodium falciparum* malaria - A proposed model-derived age-based regimen for sub-Saharan Africa. *BMC Med*. **2018**; 16 (1): 1 - 14. doi:10.1186/s12916-017-0990-6.

73. Burrows, J.; Slater, H.; Macintyre, F.; Rees, S.; Thomas, A.; Okumu, F.; Hooft Van Huijsduijnen, R.; Duparc, S.; Wells, T. A Discovery and development roadmap for new endectocidal transmission-blocking agents in Malaria. *Malar. J.* **2018**; 17 (1), 1 - 15. https://doi.org/10.1186/s12936-018-2598-5.

74. Chaccour, C.; Kobylinski, K.; Bassat, Q.; Bousema, T.; Drakeley, C.; Alonso, P.; Foy, B. Ivermectin to reduce malaria transmission: A research agenda for a promising new tool for elimination. *Malar. J*. **2013**; 12 (1): 1 - 8. doi:10.1186/1475-2875-12-153.

75. Okombo, J. and Chibale, K. Recent updates in the discovery and development of novel antimalarial drug candidates. *Med. chem. comm*. **2018**; 9 (3): 437 - 453. doi:10.1039/c7md00637c.

76. Held, J.; Jeyaraj, S. and Kreidenweiss, A. Antimalarial compounds in Phase II clinical development. *Expert Opin. Investig. Drugs* **2015**; 24 (4): 1 - 5. doi:10.1517/13543784.2015.1000483.

77. Rottmann, M.; McNamara, C.; Yeung, B.; Lee, M.; Zou, B.; Russell, B.; Seitz, P.; Plouffe, D.; Dharia, N.; Tan, J.; Cohen, S.; Spencer, K.; González-Páez, G.; Lakshminarayana, S.; Goh, A.; Suwanarusk, R.; Jegla, T.; Schmitt,E.; Beck, H.; Brun, R.; Nosten, F.; Renia, L.; Dartois, V.; Keller, T.; Fidock, D.; Winzeler, E.; Diagana, T. Spiroindolones, a potent compound class for the treatment of malaria. *Science* **2012**; 329 (1175): 1 - 15. doi:10.1126/science.1193225.

78. Spillman, N.; Allen, R.; McNamara, C.; Yeung, B.; Winzeler, E.; Diagana, T.; Kirk, K. Na^+ Regulation in the malaria parasite *Plasmodium falciparum* Involves the cation ATPase *Pf*ATP4 and is a target of the spiroindolone antimalarials. *Cell Host Microbe*. **2013**; 13 (2): 227 - 237. doi:10.1016/j.chom.2012.12.006.

79. Kublin, J.; Murphy, S.; Maenza, J.; Seilie, A.; Jain, J.; Berger, D.; Spera, D.; Zhao, R.; Soon, R.; Czartoski, J.; Potochnic, M.; Duke, E.; Chang, M.; Vaughan, A.; Kappe, S.; Leong, F.; Pertel, P.; Prince, W. Safety, pharmacokinetics, and causal prophylactic efficacy of KAF156 in a *Plasmodium falciparum* human infection study. *Clin. Infect. Dis*. **2021**; 73 (7): e2407 - e2414. doi:10.1093/cid/ciaa952.

80. Paquet, T.; Le Manach, C.; Cabrera, D.; Younis Y.; Henrich, P.; Abraham T.; Lee, M.; Basak R.; Ghidelli-Disse, S.; Lafuente-Monasterio, M.; Bantscheff, M.; Ruecker, A.; Blagborough, A.; Zakutansky, S.; Zeeman, A.; White, K.; Shackleford, D.; Mannila, J.; Morizzi, J.; Scheurer, C.; Angulo-Barturen, I.; Martínez, M.; Ferrer, S.; Sanz, L.; Gamo, F.; Reader, J.; Botha, M.; Dechering, K.; Sauerwein, R.; Tungtaeng, A.; Vanachayangkul, P.; Lim, C.; Burrows, J.; Witty, M.; Marsh, K.; Bodenreider, C.; Rochford, R.; Solapure, S.; Jiménez-Díaz, M.; Wittlin, S.; Charman, S.; Donini, C.; Campo, B.; Birkholtz, L.; Hanson, K.; Drewes, G.; Kocken, C.; Delves, M.; Leroy, D.; Fidock, D.; Waterson, D.; Street, L.; Chibale, K. Antimalarial efficacy of MMV390048, an inhibitor of *Plasmodium* phosphatidylinositol 4-kinase. *Sci. Transl. Med*. **2017**; 9 (387): 1 - 14. doi:10.1126/scitranslmed.aad9735.

81. Ashley, E. and Phyo, A. Drugs in development for malaria. *Drugs*. **2018**; 78 (9): 861 - 879. doi:10.1007/s40265-018-0911-9.

82. Peters, W.; Irare, S.; Ellis, D. Warhurst, D.; Robinson, B. The chemotherapy of rodent malaria, XXXVIII. Studies on the activity of three new antimalarials (WR 194,965, WR 228,258 and WR 225,448) against rodent and human malaria parasites (*Plasmodium berghei* and *P. falciparum*). *Ann. Trop. Med. Parasitol*. **1984**; 78 (6): 567 - 579.

83. Birrell, G.; Chavchich, M.; Ager, A.; Shieh, H.; Heffernan, G.; Zhao, W.; Krasucki, P.; Saionz, K.; Terpinski, J.; Schiehser, G.; Jacobus, L.; Shanks, G.; Jacobus, D.; Edstein, M. JPC-2997, a new aminomethylphenol with high *in vitro* and *in vivo* antimalarial activities against blood stages of *Plasmodium*. *Antimicrob. Agents Chemother*. **2015**; 59 (1): 170 - 177. doi:10.1128/AAC.03762-14.

84. Chavchich, M.; Birrell, G.; Ager, A.; MacKenzie, D.; Heffernan, G.; Schiehser, G. Jacobus, L.; Shanks, G.; Jacobus, D.; Edstein, M. Lead selection of a new aminomethylphenol, JPC-3210, for malaria treatment and prevention. *Antimicrob. Agents Chemother*. **2016**; 60 (5): 3115 - 3118. doi:10.1128/AAC.03066-15.

85. McCallum, F.; Birrell, G.; Chavchich, M.; Harris, I.; Obaldia, N.; Van Breda, K.; Heffernan, G.; Jacobus, D.; Shanks, D.; Edstein, M. *In vivo* efficacy and pharmacokinetics of the 2-aminomethylphenol antimalarial JPC-3210 in the Aotus monkey-human malaria model. *Antimicrob. Agents Chemother*. **2020**; 64 (3): e01538 - 19. doi:10.1128/AAC.01538-19.

86. Delves, M.; Angrisano, F. and Blagborough, A. Antimalarial transmission-blocking interventions: past, present, and future. *Trends Parasitol*. **2018**; 34 (9): 735 - 746. doi:10.1016/j.pt.2018.07.001.

87. Mathews, E. and Odom, J. Tackling resistance: Emerging antimalarials and new parasite targets in the era of elimination. *F1000Research*. **2018**; 7: 1 - 11. doi:10.12688/f1000research.14874.1.

88. Gamo, F.; Sanz, L.; Vidal, J.; de Cozar, C.; Alvarez, E.; Lavandera, J.; Vanderwall, D.; Green, D.; Kumar, V.; Hasan, S.; Brown, J.; Peishoff, C.; Cardon, L.; Garcia-Bustos, J. Thousands of chemical starting points for antimalarial lead identification. *Nature*. **2010**; 465 (7296): 305 - 310.doi:10.1038/nature09107.

89. Guiguemde, W.; Shelat, A.; Bouck, D.; Duffy, S.; Crowther, G.; Davis, P.; Smithson, D.; Connelly, M.; Clark, J.; Zhu, F.; Jiménez-Díaz, M.; Martinez, M.; Wilson, E.; Tripathi, A.; Gut, J.; Sharlow, E.; Bathurst, I.; El Mazouni, F.; Fowble, J.; Forquer, I.; McGinley, P.; Castro, S.; Angulo-Barturen, I.; Ferrer, S.; Rosenthal, P.; Derisi, L.; Sullivan, D.; Lazo, J.; Roos, D.; Riscoe, M.; Phillips, M.; Rathod, P.; Van Voorhis, W.; Avery, V.; Guy, R. Chemical genetics of *Plasmodium falciparum*. *Nature* **2010**; 465 (7296): 311 - 315. doi:10.1038/nature09099.Chemical.

90. Chatterjee, A. Cell-based medicinal chemistry optimization of high-throughput screening (HTS) hits for orally active antimalarials. Part 1: Challenges in potency and absorption, distribution, metabolism, excretion/pharmacokinetics (ADME/PK). *J. Med. Chem*. **2013**; 56 (20): 7741 - 7749. doi:10.1021/jm400314m.

91. Younis, Y.; Street, L.; Waterson, D.; Witty, M.; Chibale, K. Cell-based medicinal chemistry optimization of high throughput screening hits for orally active antimalarials. part 2: Hits from softfocus kinase and other libraries. *J. Med. Chem*. **2013**; 56 (20): 7750 - 7754. doi:10.1021/jm400279y.

92. Lee, J.; Uhlik, M.; Moxham, C.; Tomandl, D.; Sall, D. Modern phenotypic drug discovery is a viable, neoclassic pharma strategy. *J. Med. Chem*. **2012**; 55 (10): 4527 - 4538. doi:10.1021/jm201649s.

93. Swinney, D. and Anthony, J. How were new medicines discovered? *Nat. Rev. Drug Discov*. **2011**; 10 (7): 507 - 519. doi:10.1038/nrd3480.

94. Kotz, J. Phenotypic screening, take two. *Sci. Exch*. **2012**; 5 (15): 1 - 3. doi:10.1038/scibx.2012.380.

95. Tse, E.; Korsik, M. and Todd, M. The past, present and future of antimalarial medicines. *J. Korean Acad. Oral Heal*. **2019**; 18 (93): 1 - 21. doi:10.11149/jkaoh.2019.43.3.109.

96. Ashton, T.; Devine, S.; Möhrle, J.; Laleu, B.; Burrows, J.; Charman, S.; Creek, D.; Sleebs, B. The development process for discovery and clinical advancement of modern antimalarials. *J. Med. Chem*. **2019**; 62 (23): 10526 - 10562. doi:10.1021/acs.jmedchem.9b00761.

97. Buchholz, K.; Burke, T.; Williamson, K.; Wiegand, R.; Wirth, D.; Marti, M. A high-throughput screen targeting malaria transmission stages opens new avenues for drug development. *J. Infect. Dis*. **2011**; 203 (10): 1445 - 1453. doi:10.1093/infdis/jir037.

98. Cowell, A. and Winzeler, E. Advances in omics-based methods to identify novel targets for malaria and other parasitic protozoan infections. *Genome Med*. **2019**; 11 (1): 1 - 17. doi:10.1186/s13073-019-0673-3.

99. Gilbert, I. Drug discovery for neglected diseases: Molecular target-based and phenotypic approaches. *J. Med. Chem*. **2013**; 56 (20): 7719 - 7726. doi:10.1021/jm400362b.

100. Murithi, J.; Owen, E.; Istvan, E.; Lee, M.; Ottilie, S.; Chibale, K.; Goldberg, D.; Winzeler, E.; Llinas, M.; Fidock, D.; Vanaerschot, M. Combining stage specificity and metabolomic profiling to advance antimalarial drug discovery. *Cell Chem. Biol*. **2020**; 27 (2): 158 - 171.e3. doi:10.1016/j.chembiol.2019.11.009.

101. Doerig, C.; Billker, O.; Haystead, T.; Sharma, P.; Tobin, A.; Waters, N. Protein kinases of malaria parasites : An update. *Trends in Parasitology* **2008**; 24 (12): 570 - 577. doi:10.1016/j.pt.2008.08.007.

102. Luth, M.; Gupta, P.; Ottilie, S. and Winzeler, E. Using *in vitro* evolution and whole

genome analysis to discover next generation targets for antimalarial drug discovery. *ACS Infect. Dis*. **2018**; 4 (3): 301 - 314. doi:10.1021/acsinfecdis.7b00276.

103. Sykes, M. and Avery, V. Approaches to protozoan drug discovery: Phenotypic screening. *J. Med. Chem*. **2013**; 56 (20): 7727 - 7740. doi:10.1021/jm4004279.

104. Butera, J. Phenotypic screening as a strategic component of drug discovery programs targeting novel antiparasitic and antimycobacterial agents: An editorial. *J. Med. Chem*. **2013**; 56 (20): 7715 - 7718. doi:10.1021/jm400443k.

105. Yella, J. Yaddanapudi, S.; Wang, Y. and Jegga A. Changing trends in computational drug repositioning. *Pharmaceuticals*. **2018**; 11 (2): 1 - 21. doi:10.3390/ph11020057.

106. Leszczynski, J.; Kaczmarek-Kedziera, A.; Puzyn, T.; Papadopoulos, M.; Reis, H.; Shukla, M. *Handbook of Computational Chemistry*.; **2017**. doi:10.1007/978-3-319-27282-5.

107. Yu, W. and Jr MacKerell, A. Computer-aided drug design methods. *Antibiot. Methods Protoc*. **2017**; 1520: 85 - 106. doi:10.1007/978-1-4939-6634-9.

108. Zucca, M.; Scutera, S. and Savoia, D. New chemotherapeutic strategies against malaria, leishmaniasis and trypanosomiases. *Curr. Med. Chem*. **2013**; 20 (4): 502 - 526. doi:10.2174/0929867311320040003.

109. Duarte, Y.; Márquez-Miranda, V.; Miossec, M. and González-Nilo, F. Integration of target discovery, drug discovery and drug delivery: A review on computational strategies. *Wiley Interdiscip. Rev. Nanomedicine Nanobiotechnology*. **2019**; 11 (4): 1 - 22. doi:10.1002/wnan.1554.

110. Njogu, P.; Guantai, E.; Pavadai, E. and Chibale K. Computer-aided drug discovery approaches against the tropical infectious diseases malaria, tuberculosis, trypanosomiasis, and leishmaniasis. *ACS Infect. Dis*. **2016**; 2 (1): 8 - 31. doi:10.1021/acsinfecdis.5b00093.

111. Muhammed, M. and Aki-Yalcin, E. Homology modeling in drug discovery: Overview, current applications, and future perspectives. *Chem. Biol. Drug Des*. **2019**; 93 (1): 12 - 20. doi:10.1111/cbdd.13388.

112. Shaker, B.; Ahmad, S.; Lee, J.; Jung, C.; Na, D. *In Silico* methods and tools for drug

discovery. *Comput. Biol. Med.* **2021**; 137 (7); 1 - 15. 10.1016/j.compbiomed.2021.104851.

113. Bruno, A.; Costantino, G.; Sartori, L.; Radi, M. The *In Silico* drug discovery toolbox: Applications in lead discovery and optimization. *Curr. Med. Chem.* **2019**, 26 (21): 3838 -3873. doi.org/10.2174/0929867324666171107101035.

114. Lotharius, J.; Gamo-Benito, F.; Angulo-Barturen, I.; Clark, J.; Connelly, M.; Ferrer-Bazaga, S.; Parkinson, T.; Viswanath, P.; Bandodkar, B.; Rautela, N.; Bharath, S.; Duffy, S.; Avery, V.; Möhrle, J.; Guy, R.; Wells, T. Repositioning: The fast track to new anti-malarial medicines? *Malar. J.* **2014**; 13 (1): 1 - 15. doi:10.1186/1475-2875-13-143.

115. Ashburn, T. and Thor, K. Drug repositioning: Identifying and developing new uses for existing drugs. *Nature Reviews* **2004**; 3: 673 - 683. doi:10.1038/nrd1468.

116. Njoroge, M.; Njuguna, N.; Mutai, P.; Ongarora, D.; Smith, P.; Chibale, K. Recent approaches to chemical discovery and development against malaria and the neglected tropical diseases human African trypanosomiasis and schistosomiasis. *Chem. Rev*. **2014**; 114 (22): 11138 - 11163. doi:10.1021/cr500098f.

117. Sohraby, F.; Bagheri, M. and Aryapour, H. Performing an *in silico* repurposing of existing drugs by combining virtual screening and molecular dynamics simulation. *Methods Mol. Biol*. **2019**; 1903: 23 - 43. doi:10.1007/978-1-4939-8955-3_2.

118. Croft, S. and Engel, J. Miltefosine - Discovery of the antileishmanial activity of phospholipid derivatives. *Trans. of the Roy. Soc. of Trop. Med. and Hyg.* **2006**; S4 - S8. doi:10.1016/j.trstmh.2006.03.009.

119. Mehta, J.; Desikan, R.; Ayers, D.; Roberson, P.; Eddlemon, P.; Munshi, N.; Anaissie, E.; Wilson, C.; Dhodapkar, M.; Zeddis, J.; Barlogie, B. Antitumor activity of thalidomide in refractory multiple myeloma. *N. Engl. J. Med.* **1999**; 341 (21): 1565 - 1571.

120. Urquhart, L. Market watch: Top drugs and companies by sales in 2017. *Nat. Rev. Drug Discov.* **2018**; 17 (4): 232. doi:10.1038/nrd.2018.42.

121. Ghofrani, H.; Osterloh, I.; and Grimminger, F. Sildenafil: From angina to erectile dysfunction to pulmonary hypertension and beyond. **2006**; 5 (8), 689 - 702. https://doi.org/10.1038/nrd2030.

122. Nzila, A. and Chibale, K. Drug repositioning in the treatment of malaria and TB. *Future Med. Chem.* **2011**; 3 (11): 1413 - 1426.

123. Chong, C.; Chen, X.; Shi, L.; Liu, J. and Sullivan, D. A clinical drug library screen identifies astemizole as an antimalarial agent. *Nat. Chem. Biol*. **2006**; 2 (8): 415 - 416. doi:10.1038/nchembio806.

124. Musonda, C.; Whitlock, G.; Witty, M.; Brun, R. and Kaiser, M. Chloroquine-astemizole hybrids with potent in vitro and in vivo antiplasmodial activity. *Bioorganic Med. Chem. Lett*. **2009**; 19 (2): 481 - 484. doi:10.1016/j.bmcl.2008.11.047.

125. Chien, H.; Pantaleo, A.; Kesely, K,; Noomuna, P.; Putt, K.; Tuan, T.; Low, P.; Turrini, F. Imatinib augments standard Malaria combination therapy without added toxicity. *J. Exp. Med.* **2021**; 218 (10): 1 - 9. https://doi.org/10.1084/jem.20210724.

126. Yuthavong, Y.; Tarnchompoo, B.; Vilaivan, T. and Chitnumsub, P. Malarial dihydrofolate reductase as a paradigm for drug development against a resistance-compromised target. *Proc. Natl. Acad. Sci. USA.* **2012**; 109 (42): 16823 - 16828. doi:10.1073/pnas.1204556109.

127. Collins, C.; Hackett, F.; Strath, M.; Penzo, M.; Withers-Martinez, C.; Baker, D.; Blackman, M. Malaria parasite cGMP-dependent protein kinase regulates blood stage merozoite secretory organelle discharge and egress. *PLoS Pathog*. **2013**; 9 (5): 1 - 13. doi:10.1371/journal.ppat.1003344.

128. García-Echeverría, C. Protein and lipid kinase inhibitors as targeted anticancer agents of the Ras/Raf/MEK and PI3K/PKB pathways. *Purinergic Signal*. **2009**; 5 (1): 117 - 125. doi:10.1007/s11302-008-9111-5.

129. Greenwood, B.; Fidock, D.; Kyle, D.; Kappe, S.; Alonso, P.; Collins, F.; Duffy, P. Review series malaria : Progress, perils, and prospects for eradication. *J. Clin. Invest*. **2008**; 118 (4): 1266 - 1276. doi:10.1172/JCI33996.

130. De Villiers, K. and Egan, T. Heme detoxification in the Malaria parasite: A target for antimalarial drug development. *Acc. Chem. Res.* **2021**; 54 (11): 2649 - 2659. doi.org/10.1021/acs.accounts.1c00154.

131. Marker, E. and Debbert, S. Recent Advances in anti-schistosomiasis drug discovery. In *Parasitic Helminths and Zoonoses - From Basic to Applied Research*; IntechOpen:

Rijeka, **2022**; Ch. 2. https://doi.org/10.5772/intechopen.103056.

132. Phillips, M. and Rathod, P. *Plasmodium* dihydroorotate dehydrogenase: a promising target for novel anti-malarial chemotherapy. *Infect. Disord. Drug Targets*. **2010**; 10 (3): 226 - 239. https://www.ncbi.nlm.nih.gov/pmc/articles/PMC3624763/pdf/nihms412728.pdf.

133. Singh, A.; Maqbool, M.; Mobashir, M. and Hoda, N. Dihydroorotate dehydrogenase: A drug target for the development of antimalarials. *Eur. J. Med Chem*. **2017**; 125: 640 - 651. doi:10.1016/j.ejmech.2016.09.085.

134. Phillips, M.; Lotharius, J.; Marsh, K.; White, J.; Dayan, A.; White, K.; Njoroge, J.; El Mazouni, F.; Lao, Y.; Kokkonda, S.; Tomchick, D.; Deng, X.; Laird, T.; Bhatia, S.; March, S.; Ng, C .; Fidock, D.; Wittlin, S.; Lafuente-Monasterio, M.; Benito, F.; Alonso, L.; Martinez, M.; Jimenez-Diaz, M.; Bazaga, S.; Angulo-Barturen, I.; Haselden, J.; Louttit, J.; Cui, Y.; Sridhar, A.; Zeeman, A.; Kocken, I.; Sauerwein, R.; Dechering, K.; Avery, V.; Duffy, S.; Delves, M.; Sinden, R.; Ruecker, A.; Wickham, K.; Rochford, R.; Gahagen, J.; Iyer, L.; Riccio, E.; Mirsalis, J.; Bathhurst, I.; Rueckle, T.; Ding, X.; Campo, B.; Leroy, D.; Rogers, M.; Rathod, P.; Burrows, J.; Charman, S. A long duration dihydroorotate dehydrogenase inhibitor (DSM265) for prevention and treatment of malaria. *Sci. Transl. Med*. **2015**; 8 (5): 583 - 592. doi:10.1126/scitranslmed.aaa6645.A.

135. Huang, M.; Shen, A.; Ding, J. and Geng, M. Molecularly targeted cancer therapy: some lessons from the past decade. *Trends Pharmacol. Sci*. **2014**; 35 (1): 41 - 50. doi:10.1016/j.tips.2013.11.004.

136. Rauch, J.; Volinsky. N.; Romano, D. and Kolch, W. The secret life of kinases: Functions beyond catalysis. *Cell Commun. Signal*. **2011**; 9 (1): 1 - 23. doi:10.1186/1478-811X-9-23.

137. Deshmukh, K.; Anamika, K. and Srinivasan, N. Evolution of domain combinations in protein kinases and its implications for functional diversity. *Prog. Biophys. Mol. Biol.* **2010**; 102 (1): 1 - 15. doi:10.1016/j.pbiomolbio.2009.12.009.

138. Tsai, C. and Nussinov, R. The molecular basis of targeting protein kinases in cancer therapeutics. *Semin. Cancer Biol*. **2013**: 1 - 8. doi:10.1016/j.semcancer.2013.04.001.

139. Roskoski, R. The ErbB / HER family of protein-tyrosine kinases and cancer. *Pharmacol.*

Res. **2014**; 79: 34 - 74. doi:10.1016/j.phrs.2013.11.002.

140. Roskoski, R. Properties of FDA-approved small molecule protein kinase inhibitors: A 2020 update. *Pharmacol. Res*. **2020**; 152 (12): 1 - 15. doi:10.1016/j.phrs.2019.104609.

141. Zhao, Z. and Bourne, P. Overview of Current Type I/II Kinase Inhibitors. *Next Gener. Kinase Inhib*. **2020**; (434): 13 - 28. doi:10.1007/978-3-030-48283-1_2.

142. Cohen, P.; Cross, D. and Jänne, P. Kinase drug discovery 20 years after imatinib: progress and future directions. *Nat. Rev. Drug Discov*. **2021**; 20 (7): 551 - 569. doi:10.1038/s41573-021-00195-4.

143. Burke, J. Structural basis for regulation of phosphoinositide kinases and their involvement in human disease. *Mol. Cell*. **2018**; 71 (5): 653 - 673. doi:10.1016/j.molcel.2018.08.005.

144. Mejdrová, I.; Chalupská, D.; Plačková, P.; Müller, C.; Šála, M.; Klíma, M.; Baumlová, A.; Hřebabecký, H.; Procházková, E.; Dejmek, M.; Strunin, D.; Weber, J.; Lee, G.; Matoušová, M.; Mertlíková-Kaiserová, H.; Ziebuhr, J.; Birkus, G.; Boura, E.; Nencka, R. Rational design of novel highly potent and selective Phosphatidylinositol 4-kinase IIIβ (PI4KB) inhibitors as broad-spectrum antiviral agents and tools for chemical biology. *J. Med. Chem*. **2017**; 60 (1): 100 - 118. doi:10.1021/acs.jmedchem.6b01465.

145. Manjunatha, U.; Vinayak, S.; Zambriski, J.; Chao, A.; Sy, T.; Noble, C.; Bonamy, G.; Kondreddi, R.; Zou, B.; Gedeck, P.; Brooks, C.; Herbert, G.; Sateriale, A.; Tandel, J.; Noh, S.; Lakshminarayana, S.; Lim, S.; Goodman, L.; Bodenreider, C.; Feng, G.; Zhang, L.; Blasco, F.; Wagner, J.; Leong, F.; Striepen, B.; Diagana, T. A Cryptosporidium PI(4)K inhibitor is a drug candidate for cryptosporidiosis. *Nature*. **2017**; 546 (7658): 376 - 380. doi:10.1038/nature22337.

146. Dziwornu, G.; Attram, H.; Gachuhi, S. and Chibale, K. Chemotherapy for human schistosomiasis: how far have we come? What's new? Where do we go from here? *RSC Med. Chem*. **2020**; 11: 455 - 490. doi:10.1039/d0md00062k.

147. Cabrera, D.; Horatscheck, A.; Wilson, C.; Basarab, G.; Eyermann, C.; Chibale, K. *Plasmodial* Kinase Inhibitors: License to Cure? *J. Med. Chem*. **2018**; 61 (18): 8061 - 8077. doi:10.1021/acs.jmedchem.8b00329.

148. Arendse, L.; Wyllie, S.; Chibale, K. and Gilbert, I. *Plasmodium* kinases as potential drug

targets for malaria: Challenges and opportunities. *ACS Infect. Dis*. **2021**; 7 (3): 518 - 534. doi:10.1021/acsinfecdis.0c00724.

149. Attwood, M., Fabbro, D.; Sokolov, A.; Knapp, S.; Schiöth, H. Trends in kinase drug discovery: targets, indications and inhibitor design. *Nat. Rev. Drug Discov*. **2021**; 20 (11): 839 - 861. doi:10.1038/s41573-021-00252-y.

150. Lucet, I.; Tobin, A.; Drewry, D. and Wilks, A. *Plasmodium* kinases as targets for new-generation antimalarials. *Future Med Chem*. **2012**; 4 (18): 2295 - 2310.

151. Srinivasan, N. and Krupa, A. A genomic perspective of protein kinases in *Plasmodium falciparum*. *Proteins* **2005**; 189 (6): 180 - 189. doi:10.1002/prot.20278.

152. Deng, W.; Parbhu-patel, A.; Meyer, D. and Baker, D. The role of two novel regulatory sites in the activation of the cGMP-dependent protein kinase from *Plasmodium falciparum*. *Biochem. J.* **2003**; 374: 559 - 565.

153. Franz, E.; Knape, M. and Herberg, F. CGMP binding domain d mediates a unique activation mechanism in *Plasmodium falciparum* PKG. *ACS Infect. Dis*. **2018**; 4 (3): 415 - 423. doi:10.1021/acsinfecdis.7b00222.

154. Bakkaouri, M.; Kouidmi, I.; Wernimont, A.; Amani, M.; Hutchinson, A.; Loppnau, P. Structures of the cGMP-dependent protein kinase in malaria parasites reveal a unique structural relay mechanism for activation. *Proc. Natl. Acad. Sci.* **2019**; 116 (28): 14164 - 14173. doi:10.1073/pnas.1905558116.

155. Hopp, C.; Bowyer, P. and Baker, D. The role of cGMP signalling in regulating life cycle progression of *Plasmodium*. *Microbes Infect*. **2012**; 14 (10): 831 - 837. doi:10.1016/j.micinf.2012.04.011.

156. Baker, D. Cyclic nucleotide signalling in malaria parasites. *Cell Microbiol*. **2011**; 13 (3): 331 - 339. doi:10.1111/j.1462-5822.2010.01561.x.

157. Lakshmanan, V.; Fishbaughera, M.; Morrisona, B.; Baldwina, M.; Macarulaya, M.; Vaughana, A.; Mikolajczaka, S.; Kappea, S. Cyclic GMP balance is critical for malaria parasite transmission from the mosquito to the mammalian host. *mBiol.* **2015**; 6 (2): 1 - 10. doi:10.1128/mBio.02330-14.Editor.

158. Mcrobert, L.; Taylor, C.; Deng, W.; Fivelman, Q.; Cummings, R.; Polley, S.; Billker,

O.; Baker, D. Gametogenesis in malaria parasites is mediated by the cGMP-Dependent protein kinase. *PLoS Bio.* **2008**; 6 (6): 1 - 10. doi:10.1371/journal.pbio.0060139.

159. Ishino, T.; Orito, Y.; Chinzei, Y. and Yuda, M. A calcium-dependent protein kinase regulates Plasmodium ookinete access to the midgut epithelial cell. *Mol. Microbio.* **2006**; 59: 1175 - 1184. doi:10.1111/j.1365-2958.2005.05014.x.

160. Moon, R.; Taylor, C.; Bex, C.; Schepers, R.; Goulding, D.; Janse, C.; Waters, A.; Baker, D.; Billker, O. A Cyclic GMP signalling module that regulates gliding motility in a malaria parasite. *PLoS Pathog.* **2009**; 5 (9): 1 -14. doi:10.1371/journal.ppat.1000599.

161. Amino, R.; Thiberge, S.; Blazquez, S.; Baldacci, P.; Renaud, O.; Shorte, S.; Ménard, R. Imaging malaria sporozoites in the dermis of the mammalian host. *Nat. Protoc.* **2007**; 2 (7): 1705 - 1712. doi:10.1038/nprot.2007.120.

162. Thiberge, S.; Blazquez, S.; Baldacci, P.; Renaud, O.; Shorte, S.; Ménard, R.; Amino, R. *In vivo* imaging of malaria parasites in the murine liver. *Nat. Protoc.* **2007**; 2 (7): 1811 - 1818. doi:10.1038/nprot.2007.257.

163. Bhanot, P.; Schauer, K.; Coppens, I. and Nussenzweig, V. A Surface phospholipase is involved in the migration of *Plasmodium* sporozoites through cells. *J. Biol. Chem.* **2005**; 280 (8): 6752 - 6760. doi:10.1074/jbc.M411465200.

164. Falae, A.; Combe, A.; Amaladoss, A.; Carvalho, T.; Menard, R.; Bhanot, P. Role of *Plasmodium berghei* cGMP-dependent protein kinase in late liver stage development. *J. Biol. Chem.* **2010**; 285 (5): 3282 - 3288. doi:10.1074/jbc.M109.070367.

165. Taylor, H.; McRobert, L.; Grainger, M.; Sicard, A.; Dluzewski, A.; Hopp, C.; Holder, A.; Baker, D. The malaria parasite cyclic GMP-dependent protein kinase plays a central role in blood-stage schizogony. *Eukaryot. Cell* **2010**; 9 (1): 37 - 45. doi:10.1128/EC.00186-09.

166. Brochet, M.; Collins, M.; Smith, T.; Thompson, E.; Sebastian, S.; Volkmann, K.; Schwach, F.; Chappell, L.; Gomes, A.; Berriman, M.; Rayner, J.; Baker, D.; Choudhary, J.; Billker, O. Phosphoinositide metabolism links cGMP-dependent protein kinase G to essential Ca^{2+} signals at key decision points in the life cycle of malaria parasites. *PLoS Bio.* **2014**; 12 (3): 1 - 15. doi:10.1371/journal.pbio.1001806.

167. Cowman, A.; Healer. J.; Marapana, D. and Marsh, K. Review Malaria: Biology and

disease. *Cell* **2016**; 167: 610 - 624. doi:10.1016/j.cell.2016.07.055.

168. Baker, D.; Drought, L.; Flueck, C.; Nofal, S.; Patel, A.; Penzo, M.; Walker, E. Cyclic nucleotide signalling in malaria parasites. *Open Biol*. **2017**; 7 (12): 1 - 18. doi:10.1098/rsob.170213.

169. Absalon, S.; Blomqvist, K.; Rudlaff, R.; Delano, T.; Pollastri, M.; Dvorin, J. Calcium-dependent protein kinase 5 is required for egress-specific organelles in *Plasmodium falciparum*. *mBio.* **2018**; 9 (1): 1 - 16.

170. Yeoh, S.; O'Donnell, R.; Koussis, K.; Dluzewski, A.; Ansell, K.; Osborne, S.; Hackett, F.; Withers-Martinez, C.; Mitchell, G.; Bannister, L.; Bryans, J.; Kettleborough, C.; Blackman, M. Subcellular discharge of a serine protease mediates release of invasive malaria parasites from host erythrocytes. *Cell* **2007**: 1072 - 1083. doi:10.1016/j.cell.2007.10.049.

171. Govindasamy, K.; Jebiwott, S.; Jaijyan, D.; Davidow, A.; Ojo, K.; Van Voorhis, W.; Brochet, M.; Billker, O.; Bhanot, P. Invasion of hepatocytes by *Plasmodium* sporozoites requires cGMP-dependent protein kinase and calcium dependent protein kinase 4. *Mol. Microbiol.* **2016**; 102 (2): 349 - 363.

172. Baker, D.; Stewart, L.; Large, J.; Bowyer, P.; Ansell, K.; Jiménez-Díaz, M.; El Bakkouri, M.; Birchall, K.; Dechering, K.; Bouloc, N.; Coombs, P.; Whalley, D.; Harding, D.; Smiljanic-Hurley, E.; Wheldon, M.; Walker, E.; Dessens, J.; Lafuente, M.; Sanz, L.; Gamo, F.; Ferrer, S.; Hui, R.; Bousema, T.; Angulo-Barturén, I.; Merritt, A.; Croft, S.; Gutteridge, W.; Kettleborough, C.; Osborne, S. A potent series targeting the malarial cGMP-dependent protein kinase clears infection and blocks transmission. *Nat. Commun*. **2017**; 8 (1): 1 - 9. doi:10.1038/s41467-017-00572-x.

173. Vanaerschot, M.; Murithi, J.; Pasaje, C.; Ghidelli-Disse, S.; Dwomoh, L.; Bird, M.; Spottiswoode, N.; Mittal, N.; Arendse, L.; Owen, E.; Wicht, K.; Siciliano, G.; Bosche, M.; Yeo, T.; Kumar, T.; Mok, S.; Carpenter, E.; Giddins, M.; Sanz, O.; Ottilie, S.; Alano, P.; Chibale, K.; Llinas, M.; Uhlemann, A.; Delves, M.; Tobin, A.; Doerig, C.; Winzeler, E.; Lee, M.; Niles, J.; Fidock, D. Inhibition of resistance-refractory *P. falciparum* kinase PKG delivers prophylactic, blood stage, and transmission-blocking antiplasmodial activity. *Chembiol.* **2020**: 1 - 11. doi:10.1016/j.chembiol.2020.04.001.

174. Deng, W. and Baker, D. A novel cyclic GMP-dependent protein kinase is expressed in the ring stage of the *Plasmodium falciparum* life cycle. *Mol. Microbiol.* **2002**; 44: 1141 - 1151.

175. Gurnett, A.; Liberator, P.; Dulski, P.; Salowe, S.; Donald, R.; Anderson, J.; Wiltsie, J.; Diaz, C.; Harris, G.; Chang, B.; Darkin-Rattray, S.; Nare, B.; Crumley, T.; Blum, P.; Misura, A.; Tamas, T.; Sardana, M.; Yuan, J.; Biftu, T.; Schmatz, D. Purification and molecular characterization of cGMP-dependent protein kinase from *Apicomplexan* parasites. *J. Biol. Chem.* **2002**; 277 (18): 15913 - 15922. doi:10.1074/jbc.M108393200.

176. Penzo, M.; de las Heras-Dueña, L.; Mata-Cantero, L.; Diaz-Hernandez, B.; Vazquez-Muñiz, M.; Ghidelli-Disse, S.; Drewes, G.; Fernandez-Alvaro, E.; Baker, D. High-throughput screening of the *Plasmodium falciparum* cGMP-dependent protein kinase identified a thiazole scaffold which kills erythrocytic and sexual stage parasites. *Sci. Rep*. **2019**; 9 (1): 1 - 13. doi:10.1038/s41598-019-42801-x.

177. Donald, R. and Liberator, P. Molecular characterization of a coccidian parasite cGMP dependent protein kinase. *Mol. Biochem. Parasitol.* **2002**; 120 (2): 165 - 175.

178. Biftu, T.; Feng, D.; Ponpipom, M.; Girotra, N.; Liang, G.; Qian, X.; Bugianesi, R.; Simeone, J.; Chang, L.; Gurnett, A.; Liberator, P.; Dulski, P.; Leavitt, P.; Crumley, T.; Misura, A.; Murphy, T.; Rattray, S.; Samaras, S.; Tamas, T.; Mathew, J.; Brown, C.; Thompson, D.; Schmatz, D.; Fisher, M.; Wyvratt, M. Synthesis and SAR of 2,3-diarylpyrrole inhibitors of parasite cGMP-dependent protein kinase as novel anticoccidial agents. *Biorg. Med. Chem. Lett.* **2005**; 15: 3296 - 3301. doi:10.1016/j.bmcl.2005.04.060.

179. Donald, R.; Zhong, T.; Wiersma, H.; Nare, B.; Yao, D.; Lee, A.; Allocco, J.; Liberator, P. Anticoccidial kinase inhibitors: Identification of protein kinase targets secondary to cGMP-dependent protein kinase. *Mol. Biochem. Parasitol.* **2006**; 149: 86 - 98 doi:10.1016/j.molbiopara.2006.05.003.

180. Tsagris, D.; Birchall, K.; Bouloc, N.; Large, J.; Merritt, A.; Smiljanic-Hurley, E.; Wheldon, M.; Ansell, K.; Kettleborough, C.; Whalley, D.; Stewart, L.; Bowyer, P.; Baker, D.; Osborne, S. Trisubstituted thiazoles as potent and selective inhibitors of *Plasmodium falciparum* protein kinase G (*Pf*PKG). *Bioorg. Med. Chem. Lett*. **2019**; 28 (19): 3168 - 3173. doi:10.1016/j.bmcl.2018.08.028.Trisubstituted.

181. Hassett, M. and Roepe, P. PIK-ing new malaria chemotherapy. *Trends Parasitol*. **2018**; 34 (11): 925 - 927. doi:10.1016/j.pt.2018.06.003.

182. Balla, T. Phosphoinositides: Tiny lipids with giant impact on cell regulation. *Physiol. Rev*. **2013**; 93 (3): 1019 - 1137. doi:10.1152/physrev.00028.2012.

183. Dembele, L.; Ang, X.; Chavchich, M.; Bonamy, G.; Selva, J.; Yi-Xiu Lim, M.; Bodenreider, C.; Yeung, B.; Nosten, F.; Russell, B.; Edstein, M.; Straimer, J.; Fidock, D.; Diagana, T.; Bifani, P. The *Plasmodium* PI(4)K inhibitor KDU691 selectively inhibits dihydroartemisinin-pretreated *Plasmodium falciparum* ring-stage parasites. *Sci. Rep*. **2017**; 7 (1): 1 - 9. doi:10.1038/s41598-017-02440-6.

184. Campa, C. and Hirsch, E. Rab11 and phosphoinositides: A synergy of signal transducers in the control of vesicular trafficking. *Adv. Biol. Regul*. **2017**; 63: 132 - 139. doi:10.1016/j.jbior.2016.09.002.

185. Voorberg-van der Wel, A.; Zeeman, A.; Nieuwenhuis, I.; van der Werff, N.; Klooster, E.; Klop, O.; Vermaat, L.; Gupta, D.; Dembele, L.; Diagana, T.; Kocken, C. A dual fluorescent *Plasmodium* cynomolgi reporter line reveals *in vitro* malaria hypnozoite reactivation. *Commun. Biol*. **2020**; 3 (1): 1 - 9. doi:10.1038/s42003-019-0737-3.

186. Campo, B.; Vandal, O.; Wesche, D. and Burrows J. Killing the hypnozoite – drug discovery approaches to prevent relapse in *Plasmodium vivax*. *Pathog. Glob. Health*. **2015**; 109 (3): 107 - 122. doi:10.1179/2047773215Y.0000000013.

187. Zeeman, A.; Lakshminarayana, S.; van der Werff, N.; Klooster, E.; Voorberg-van der Wel, A.; Kondreddi, R.; Bodenreider, C.; Simon, O.; Sauerwein, R.; Yeung, B.; Diagana, T.; Kocken, C. PI4 Kinase is a prophylactic but not radical curative target in *Plasmodium vivax*-type malaria parasites. *Antimicrob. Agents Chemother*. **2016**; 60 (5): 2858 - 2863. doi:10.1128/AAC.03080-15.Address.

188. Sridhar, S.; Patel, B.; Aphkhazava, D.; Macian, F.; Santambrogio, L.; Shields, D.; Maria Cuervo, A. The lipid kinase PI4KIIIβ preserves lysosomal identity. *EMBO J*. **2013**; 32 (3): 324 - 339. doi:10.1038/emboj.2012.341.

189. McNamara, C.; Lee, M.; Lim, C.; Lim, S.; Roland, J.; Nagle, A.; Simon, O.; Yeung, B.; Chatterjee, A.; McCormack, S.; Manary, M.; Zeeman, A.; Dechering, K.; Kumar, T.; Henrich, P.; Gagaring, K.; Ibanez, M.; Kato, N.; Kuhen, K.; Fischli, C.; Rottmann, M.;

Plouffe, D.; Bursulaya, B.; Meister, S.; Rameh, L.; Trappe, J.; Haasen, D.; Timmerman, M.; Sauerwein, R.; Suwanarusk, R.; Russell, B.; Renia, L.; Nosten, F.; Tully, D.; Kocken, C.; Glynne, R.; Bodenreider, C.; Fidock, D.; Diagana, T.; Winzeler, E. Targeting *Plasmodium* PI(4)K to eliminate Malaria. *Nature* **2013**, 504 (7479), 248 - 253. https://doi.org/10.1038/nature12782.

190. Dornan, G.; McPhail. J. and Burke, J. Type III phosphatidylinositol 4 kinases: Structure, function, regulation, signalling and involvement in disease. *Biochem. Soc. Trans*. **2016**; 44: 260 - 266. doi:10.1042/BST20150219.

191. Sinxadi, P.; Donini, C.; Johnstone, H.; Langdon, G.; Wiesner, L.; Allen, E.; Duparc, S.; Chalon, S.; McCarthy, J.; Lorch, U.; Chibale, K.; Mohrle, J.; Barnes, K. Safety, tolerability, pharmacokinetics, and antimalarial activity of the novel *Plasmodium* phosphatidylinositol 4-kinase inhibitor MMV390048 in healthy volunteers. *Antimicrob. Agents Chemother*. **2020**; 64 (4): e01896 - 19.

192. Tewari, R.; Straschil, U.; Bateman, A.; Böhme, U.; Cherevach, I.; Gong, P.; Pain, A.; Billker, O. The systematic functional analysis of *Plasmodium* protein kinases identifies essential regulators of mosquito transmission. *Cell Host Microbe*. **2010**; 8 (4): 377 - 387. doi:10.1016/j.chom.2010.09.006.

193. Patterson, H.; Nibbs, R.; Mcinnes, I. and Siebert, S. Protein kinase inhibitors in the treatment of inflammatory and autoimmune diseases. *Clin. Exp. Immunol*. **2014**; 176 (1): 1 - 10. doi:10.1111/cei.12248.

194. Kato, N.; Comer, E.; Sakata-Kato, T.; Sharma, A.; Sharma, M.; Maetani, M.; Bastien, J.; Brancucci, N.; Bittker, J.; Corey, V.; Clarke, D.; Derbyshire, E.; Dornan, G.; Duffy, S.; Eckley, S.; Itoe, M.; Koolen, K.; Lewis, T.; Lui, P.; Lukens, A.; Lund, E.; March, S.; Meibalan, E.; Meier, B.; McPhail, J.; Mitasev, B.; Moss, E.; Sayes, M.; Yvonne Van Gessel, Y.; Mathias J. Wawer, M.; Yoshinaga, T.; Zeeman, A.; Avery, V.; Bhatia, S.; Burke, J.; Catteruccia, F.; Clardy, J.; Clemons, P.; Dechering, K.; Duvall, J.; Foley, M.; Gusovsky, F.; Kocken, C.; Marti, M.; Morningstar, M.; Munoz, B.; Neafsey, D.; Sharma, A.; Winzeler, E.; Wirth, D.; Scherer, C.; Schreiber, S. Diversity-oriented synthesis yields novel multistage antimalarial inhibitors. *Nature*. **2016**; 538 (7625): 344 - 349. doi:10.1038/nature19804.

195. Kandepedu, N.; Cabrera, D.; Eedubilli, S.; Taylor, D.; Brunschwig, C.; Gibhard, L.

Njoroge, M.; Lawrence, N.; Paquet, T.; Eyermann, C.; Spangenberg, T.; Basarab, G.; Street, L.; Chibale, K. Identification, characterization, and optimization of 2,8-disubstituted-1,5-naphthyridines as novel *Plasmodium falciparum* phosphatidylinositol-4-kinase inhibitors with *in vivo* efficacy in a humanized mouse model of malaria. *J. Med. Chem*. **2018**; 61 (13): 5692 - 5703. doi:10.1021/acs.jmedchem.8b00648.

196. Roth, B.; Sheffler, D. and Kroeze, W. Magic shotguns versus magic bullets: Selectively non-selective drugs for mood disorders and schizophrenia. *Nat. Rev. Drug Discov*. **2004**; 3: 353 - 359.

197. Eastman, R. and Fidock, D. Artemisinin-based combination therapies: A vital tool in efforts to eliminate malaria. *Nat. Rev. Microbiol.* **2009**; 7 (12): 864 - 874. doi:doi:10.1038/nrmicro2239.

198. Sternberg, A. and Roepe, P. Heterologous expression, purification, and functional analysis of the *Plasmodium falciparum* phosphatidylinositol 4-kinase IIIβ. *Biochemistry*. **2020**; 59 (27): 2494 - 2506. doi:10.1021/acs.biochem.0c00259.

199. Anighoro, A.; Bajorath, J. and Rastelli G. Polypharmacology: Challenges and opportunities in drug discovery. *J. Med. Chem*. **2014**; 57 (9): 7874 - 7887.

200. Hopkins, A.; Mason, J. and Overington, J. Can we rationally design promiscuous drugs? *Curr. Opin. Struct. Biol*. **2006**; 16 (1): 127 - 136. doi:10.1016/j.sbi.2006.01.013.

201. Ramsay, R.; Popovic-Nikolic, M.; Nikolic, K.; Uliassi, E.; Bolognesi, M. A Perspective on multi-target drug discovery and design for complex diseases. *Clin. Transl. Med.* **2018**; 7 (1). https://doi.org/10.1186/s40169-017-0181-2.

202. Chaudhari, R.; Fong, L.; Tan, Z.; Huang, B.; Zhang, S. An Up-to-date overview of computational polypharmacology in modern drug discovery. *Expert Opin. Drug Discov.* **2020**; 15 (9):1025–1044. https://doi.org/10.1080/17460441.2020.1767063.

203. Proschak, E.; Stark, H. and Merk, D. Polypharmacology by design: A medicinal chemist's perspective on multitargeting compounds. *J. Med. Chem.* **2019**; 62 (2): 420 - 444. https://doi.org/10.1021/acs.jmedchem.8b00760.

204. Méndez-Lucio, O.; Naveja, J.; Vite-Caritino, H.; Prieto-Martínez, F. Medina-Franco, J. L. Polypharmacology in drug discovery. *Drug Sel. An Evol. Concept Med. Chem.* **2017**; 1 - 29. https://doi.org/10.1002/9783527674381.ch1.

205. Miljković, F. and Bajorath, J. Exploring selectivity of multikinase inhibitors across the human kinome. *ACS Omega* **2018**, 3 (1): 1147 - 1153. https://doi.org/10.1021/acsomega.7b01960.

206. Bhullar, K.; Lagarón, N.; McGowan, E.; Parmar, I.; Jha, A.; Hubbard, B.; Rupasinghe, V. Kinase-targeted cancer therapies: Progress, challenges and future directions. *Mol. Cancer*. **2018**; 17 (1): 1 - 20. doi:10.1186/s12943-018-0804-2.

207. Wu, P.; Nielsen, T, and Clausen M. FDA-approved small-molecule kinase inhibitors. *Trends Pharmacol. Sci*. **2015**; 36 (7): 422 - 439. doi:10.1016/j.tips.2015.04.005.

208. Manning, G.; Whyte, D.; Martinez, R.; Hunter, T.; Sudarsanam, S. The protein kinase complement of the human genome. *Science*. **2002**; 298 (5600): 1912 - 1934. doi:10.1126/science.1075762.

209. Leeson, P. and Springthorpe, B. The influence of drug-like concepts on decision-making in medicinal chemistry. *Nat. Rev. Drug Discov*. **2007**; 6 (11): 881 - 890. doi:10.1038/nrd2445.

210. Priest, B.; Bell, I. and Garcia, M. Role of hERG potassium channel assays in drug development. *Channels*. **2008**; 2 (2): 87 - 93. doi:10.4161/chan.2.2.6004.

211. Kalyaanamoorthy, S. and Barakat, K. Development of safe drugs: The hERG challenge. *Med. Res. Rev*. **2018**; 38 (2): 525 - 555. doi:10.1002/med.21445.

212. Kratz, J.; Grienke, U.; Scheel, O.; Mann, S.; Rollinger, J. Natural products modulating the hERG channel: heartaches and hope. *Nat. Prod. Rep*. **2017**; 34 (8): 957 - 980. doi:10.1039/C7NP00014F.

213. Croft, A. A lesson learnt: the rise and fall of Lariam and Halfan. *J. R. Soc. Med*. **2007**; 100: 170 - 174.

214. Raschi, E.; Ceccarini, L.; De Ponti, F. and Recanatini, M. hERG-related drug toxicity and models for predicting hERG liability and QT prolongation. *Expert Opin. Drug Metab. Toxicol*. **2009**; 5 (9): 1005 - 1021. doi:10.1517/17425250903055070.

215. Pearlstein, R.; Vaz, R.; Kang, J.; Chen, X.; Preobrazhenskaya, M.; Shchekotikhin, A.; Korolev, A.; Lysenkova, L.; Miroshnikova, O.; Hendrix, J.; Rampe, D. Characterization of HERG potassium channel inhibition using CoMSiA 3D QSAR and homology

modeling approaches. *Bioorganic Med. Chem. Lett*. **2003**; 13 (10): 1829 - 1835. doi:10.1016/S0960-894X(03)00196-3.

216. Jamieson, C.; Moir, E.; Rankovic, Z. and Wishart, G. Medicinal chemistry of hERG optimizations: Highlights and hang-ups. *J. Med. Chem*. **2006**; 49 (17): 5029 - 5046. doi:10.1021/jm060379l.

217. Di, L.; Kerns, E. and Carter, G. Drug-like property concepts in pharmaceutical design. *Curr. Pharm. Des*. **2009**; 15 (19): 2184 - 2194. doi.org/10.2174/138161209788682479.

218. Di, L.; Fish, V. and Mano, T. Bridging solubility between drug discovery and development. *Drug Discovery Today* **2011**; 17 (9/10): 486 - 495. doi:10.1016/j.drudis.2011.11.007.

219. Roskoski, R. Properties of FDA-approved small molecule protein kinase inhibitors. *Pharmacol. Res*. **2019**; 144 (3): 19 - 50. doi:10.1016/j.phrs.2019.03.006.

220. Cheuka, P.; Mayoka, G.; Okombo, J. and Chibale, K. *Medicinal Chemistry Progression of Antimalarial Hits from Phenotypic Whole Cell Screening of SoftFocus Libraries*. 1st ed. Elsevier Inc.; **2019**. doi:10.1016/bs.armc.2019.04.001.

221. Le Manach C.; Nchinda, A.; Paquet, T.; Cabrera, D.; Younis, Y.; Han, Z.; Bashyam, S.; Zabiulla, M.; Taylor, D.; Lawrence, N.; White, K.; Charman, S.; Waterson, D.; Witty, M.; Wittlin, S.; Botha, M.; Nondaba, S.; Reader,J.; Birkholtz, L.; Jiménez-Díaz, M.; Martínez, M.; Ferrer, S.; Angulo-Barturen, I.; Meister, S.; Antonova-Koch, Y.; Winzeler, E.; Street, L.; Chibale, K. Identification of a potential antimalarial drug candidate from a series of 2 - aminopyrazines by optimization of aqueous solubility and potency across the parasite life cycle. *J. Med. Chem*. **2016**; 55 (7): 3478 - 3487. doi:10.1021/acs.jmedchem.6b01265.

222. Ishikawa, M. and Hashimoto, Y. Improvement in aqueous solubility in small molecule drug discovery programs by disruption of molecular planarity and symmetry. *J. Med. Chem*. **2011**; 54 (6): 1539 - 1554.

223. Wang, H.; Katon, J.; Balan, C.; Bannon, A.; Bernard, C.; Doherty, E.; Dominguez, C.; Gavva, N.; Gore, V.; Ma, V.; Nishimura, N.; Surapaneni, S.; Tang, P.; Tamir, R.; Thiel, O.; Treanor, J.; Norman, M. Novel vanilloid receptor-1 antagonists: 3. The identification of a second-generation clinical candidate with improved physicochemical and

pharmacokinetic properties. *J. Med. Chem.* **2007**; 50 (15): 3528 - 3539.

224. Doherty, E.; Fotsch, C.; Bannon, A.; Bo, Y.; Chen, N.; Dominguez, C.; Falsey, J.; Gavva, N.; Katon, J.; Nixey, T.; Ognyanov, V.; Pettus, L.; Rzasa, R.; Stec, M.; Surapaneni, S.; Tamir, R.; Zhu, J.; Treanor, J.; Norman, M. Novel vanilloid receptor-1 antagonists: 2. Structure-activity relationships of 4-oxopyrimidines leading to the selection of a clinical candidate. *J. Med. Chem.* **2007**; 50 (15): 3515 - 3527.

225. Sheraz, M.; Ahsan, S.; Khan, M.; Ahmed, S.; Ahmad, I. Formulations of amlodipine: A Review. *J. Pharm*. **2016**: 1 - 11. doi:10.1155/2016/8961621.

226. Hewitt, M.; Cronin, M.; Enoch, S.; Madden, J.; Roberts, D.; Dearden, J. *In silico* prediction of aqueous solubility: The solubility challenge. *J. Chem. Inf. Model*. **2009**; 49 (11): 2572 - 2587. doi:10.1021/ci900286s.

227. Woolf, T. *Handbook of Drug Metabolism*, 1st ed.; CRC Press, **1999**.

228. Arnott, J. and Planey, S. The influence of lipophilicity in drug discovery and design. *Expert Opin. Drug Discov*. **2012**; 7 (10): 863 - 875. doi:10.1517/17460441.2012.714363.

229. Lipinski, C.; Lombardo, F.; Dominy, B. and Feeney, P. Experimental and computational approaches to estimate solubility and permeability in drug discovery and development settings. *Adv. Drug Deliv. Rev*. **1997**; 23: 3 - 25.

230. Hughes, J.; Blagg, J.; Price, D.; Bailey, S.; DeCrescenzo, G.; Devraj, R.; Ellsworth, E.; Fobian, Y.; Gibbs, M.; Gilles, R.; Greene, N.; Huang, E.; Krieger-Burke, T.; Loesel, J.; Wager, T.; Whiteley, L.; Zhang, Y. Physiochemical drug properties associated with *in vivo* toxicological outcomes. *Bioorganic Med. Chem. Lett*. **2008**; 18 (17): 4872 - 4875. doi:10.1016/j.bmcl.2008.07.071.

231. Lewis, D.; Jacobs, M. and Dickins, M. Compound lipophilicity for substrate binding to human P450s in drug metabolism. *Drug Discov. Today*. **2004**; 9 (12): 530 - 537. doi:10.1016/S1359-6446(04)03115-0.

232. Benet, L.; Hosey, C.; Ursu, O. and Oprea, T. BDDCS, the Rule of 5 and drugability. *Adv Drug Deliv. Rev*. **2016**; 101: 89 - 98. doi:10.1016/j.addr.2016.05.007.

233. Wermurth, C.; Raboisson, P.; Aldous, D. and Rogman, D. *The Practise of Medicinal*

Chemistry. 4th ed. Academic Press; **2015**. doi:https://doi.org/10.1016/C2012-0-03066-9.

234. Jain, N. and Yalkowsky, S. Estimation of the aqueous solubility I: Application to organic nonelectrolytes. *J. Pharm. Sci*. **2001**; 90 (2): 234 - 252. doi:10.1002/1520-6017(200102)90:2<234::AID-JPS14>3.0.CO;2-V.

235. Hughes, J.; Rees, S.; Kalindjian, S. and Philpott, K. Principles of early drug discovery. *Br. J. Pharmacol*. **2011**; 162 (6): 1239 - 1249. doi:10.1111/j.1476-5381.2010.01127.x.

236. Doogue, M. and Polasek, T. The ABCD of clinical pharmacokinetics. *Ther. Adv. Drug Saf*. **2013**; 4 (1): 5 - 7. doi:10.1177/2042098612469335.

237. Alavijeh, M.; Chishty, M.; Qaiser, M. and Palmer, A. Drug metabolism and pharmacokinetics, the blood-brain barrier, and central nervous system drug discovery. *NeuroRx*. **2005**; 2 (4): 554 - 571. doi:10.1602/neurorx.2.4.554.

238. Sane, R. and Sinz, M. *Introduction of Drug Metabolism and Overview of Disease Effect on Drug Metabolism*. Elsevier Inc.; **2016.** doi:10.1016/B978-0-12-802949-7.00001-8.

239. Bachmann, K. *Drug Metabolism*, 1st ed.; Elsevier Inc., **2009**. https://doi.org/10.1016/B978-0-12-369521-5.00008-7.

240. Beaumont, C.; Young, G.; Cavalier, T. and Young, M. Human absorption, distribution, metabolism and excretion properties of drug molecules: A plethora of approaches. *Br. J. Clin. Pharmacol*. **2014**; 78 (6): 1185 - 1200. doi:10.1111/bcp.12468.

241. Kerns, E. and Di, L. Pharmaceutical profiling in drug discovery. *Drug Discov. Today*. **2003**; 8 (7): 316 - 323. doi:10.1016/S1359-6446(03)02649-7.

242. Li, Y.; Meng, Q.; Yang, M.; Liu, D.; Hou, X.; Tang, L.; Wang, X.; Lyu, Y.; Chen, X.; Liu, K.; Yu, A.; Zuo, Z.; Bi, H. Current trends in drug metabolism and pharmacokinetics. *Acta. Pharm. Sin. B*. **2019**; 9 (6): 1113 - 1144. doi:10.1016/j.apsb.2019.10.001.

PART 1: REPOSITIONING OF THE ANTICANCER CLINICAL CANDIDATE PYRAZOLOPYRIMIDINE MLN0128 FOR MALARIA

CHAPTER 2

RATIONALE, DESIGN, SYNTHESIS AND CHARACTERIZATION OF MLN0128 ANALOGUES

2.1 Chapter overview

This chapter will provide a brief account of the pharmacological profile of the anticancer drug MLN0128/ Sapanisertib and describes its activity with respect to its potential as an anti-malarial chemotype. At the onset, its anti-plasmodium multi-kinase inhibition including dual *Pf*PI4K and PKG inhibition will be highlighted, and thus, a statement of justification for part 1 of the research will be expressed. This will also include the aims and objectives of this study. The design and medicinal chemistry plans leading to the synthesis of target compounds will subsequently be provided. Lastly, the synthesis, reaction mechanisms and spectroscopic characterization of representative compounds generated in this study will be elaborated to confirm structures of the target compounds.

2.2 Anticancer activity of MLN0128

MLN0128 (also called Sapanisertib or INK128; **Figure 2.1**) is a synthetic 1*H*-pyrazolo[3,4-*d*]pyrimidin-4-amine derivative, a dual inhibitor of mammalian target of rapamycin complexes (mTORC1 and mTORC2) which if up-regulated contribute to the proliferation of malignant growths and tumours.[1,2] Structurally, it can be categorized as a 1*H*-pyrazolo[3,4-*d*]pyrimidin-4-amine or a benzoxazole derivative. The drug was developed by Intellikine LLC in 2009 and later taken over by Takeda Pharmaceutical, now called Millennium Pharmaceuticals, Inc. It is currently in phase II human clinical trials for the treatment of breast cancer, hematological malignancies and, solid tumors.[3]

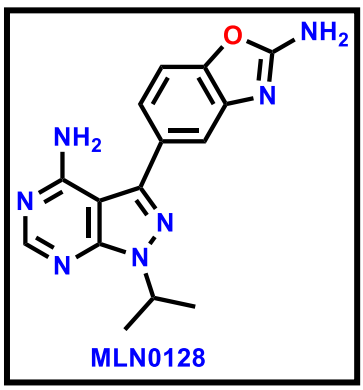

Figure 2.1: Chemical structure of **MLN0128**, the scaffold repositioned in this study

Pre-clinically, it demonstrated potent antitumor activity against prostate cancer, B-cell leukemia and renal cell carcinoma.[4,5] Recently, it was also shown to exhibit potent activity against bone and soft tissue sarcoma such as rhabdomyosarcoma, osteo-, and liposarcoma.[4] It also possesses strong antitumor activity against a broad range of solid and soft cancerous cells with potent inhibition against rapamycin-resistant forms.[6] It exhibits greater therapeutic potential because of the dual mTOR1/2 complexes inhibition in contrast to many rapamycin analogues that interfere with mTORC1 only, allowing feedback loops and an eventual augmentation in tumour growth.[5,7]

MLN0128 is administered orally, as a single dose or in combination with bevacizumab, aflibercept, or paclitaxel, to patients with glioblastoma multiforme, recurrent solid tumours and breast cancer, respectively.[6] It has a plasma half-life of 6 - 8 h and does not accumulate with repeated dosing which is ideal for both daily and intermittent administration schedules. It exhibits fast oral absorption with exposures generally increasing in a dose-dependent manner with the maximum plasma concentration achieved in one to two hours.[7] However, there are several side effects associated with **MLN0128** which include nausea, fatigue, mucosal inflammation, increased blood creatinine, hyperglycemia, thrombocytopenia and occasional rashes.[7]

The ability of **MLN0128** to inhibit kinases is attributed to the presence of a pyrazolopyrimidine scaffold which structurally resembles adenine in ATP, and consequently participates in competitive inhibition.[8] Although various mTOR inhibitors show exemplary cytostatic activity in many cell contexts such as tumour control,[5] they are often cytotoxic to human cells and many rarely progress beyond clinical trials in the treatment of non-oncological ailments.[9,10] However, considering the ever-emerging problem of parasite resistance to current antimalarials, few newly validated *Plasmodium* targets, and lengthy process of conventional drug optimization and validation of clinical candidates, one of the specific objectives of this study was to re-position **MLN0128** as a dual *P. falciparum* PI4K and PKG kinase inhibitor.

2.2.1 Human mammalian target of rapamycin (mTOR)

The mammalian target of rapamycin (mTOR) is a key regulator of many metabolic functions. It is a dual-specific protein kinase phosphorylating serine/threonine and tyrosine residues. Due to its atypical catalytic domain resemblance to that of lipid PI3K kinases, it forms part of the PI3K-related (PIKK) family.[11] Structurally, it exists as two multi-protein complexes, mTOR complex 1 (mTORC1) and mTORC2, each with different upstream activators and downstream

substrates. Generally, it converges various extracellular stimuli associated with the control of nutrients for cell growth. Conversely, it diverges other biochemical functions such as autophagy, translation, and lipid synthesis. The balance between these two functions regulates cell growth.[12]

For necessary growth and division, cells increase the production of required proteins and lipids while simultaneously suppressing catabolic processes such as autophagy. Under conditions permissive for growth, mTORC1 is activated, promoting protein translation and the synthesis of various biomolecules by phosphorylation of substrates. This may be achieved by promoting *de novo* fatty acid and cholesterol synthesis by activation of sterol regulatory element-binding protein (SREBP) transcription factors.[13]

Structurally, the main characteristic component of mTORC1 is raptor (**Figure 2.2**), a macromolecule responsible for protein assembly, substrate recognition, and conferring rapamycin-sensitive functions. Mammalian lethal with sec13 protein 8 (mLST8) is a protein found in both complexes and whose function is associated with protein assembly.[14] mTORC2 is not rapamycin-sensitive and regulates several protein kinases, thereby controlling cell growth and survival. Unlike mTORC1, it contains rictor, an important binding protein regulating its specificity to substrates. Similar to mLST8, MSIN1 also functions in regulating the assembly of the complex.[15]

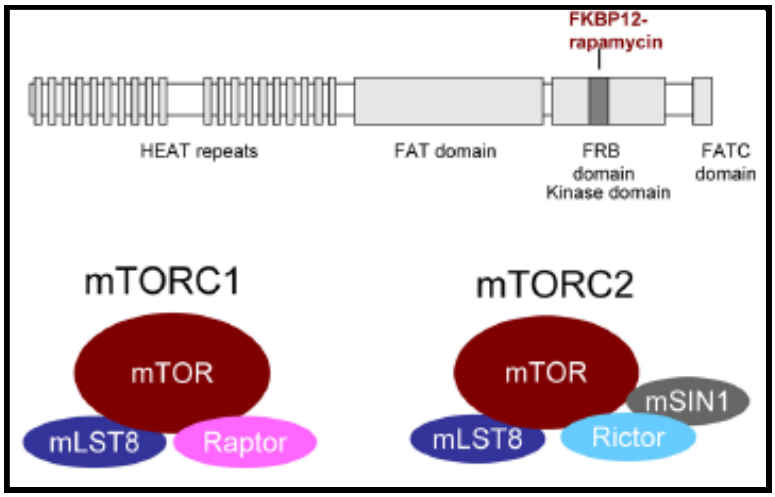

Figure 2.2: Graphical representation of the core components of human mTOR[14]

Several neurotransmitters, neuromodulators, and hormones are reported to activate mTOR. These include vascular endothelial growth factors and insulin, responsible for regulating the formation of blood vessels and sugars, respectively, as well as nutrients through the PI3K pathway. Consequently, dysregulation of the mTOR signaling pathway induces various

disorder such as cancer, diabetes, and cardiovascular and neurodegenerative diseases, confirming its potential as a relevant disease target.[16,17] Indeed, some mTOR inhibitors have been approved for the treatment of cancer, with many more not progressing beyond clinical stages.

Considering the structural similarities between kinases, repositioning of mTOR and other human kinase inhibitors such as **MLN0128** remains an attractive proposition and may contribute to overcoming challenges in PK parameter optimization, target selection, and validation, which are important in a target-based drug discovery program.

2.3 The anti-plasmodium activity of MLN0128

The anti-plasmodium activity of **MLN0128** was identified via Kino-bead screening studies performed by the GSK/Cellzome facility using a library of 84 clinically used human kinase inhibitors against a set of 89 *Pf* kinases. **MLN0128** was identified as a pan-kinase inhibitor showing putative inhibition of *Pf*PKG and *Pf*PI4K (IC_{50} of 20 and 35 nM, respectively). Based on the Kino-bead data, its pan-kinase activity extends to other *Plasmodium* kinases such as PI3K, cysteine-rich receptor-like protein kinase 5 (CRK5), casein kinase 1 (CK1) and CDPKs (**Figure 2.3**). Furthermore, it exhibited high anti-plasmodium activity in the 48- and 72-h parasite-based assay with *Pf*3D7 IC_{50} values of 200 and 78 nM, respectively.

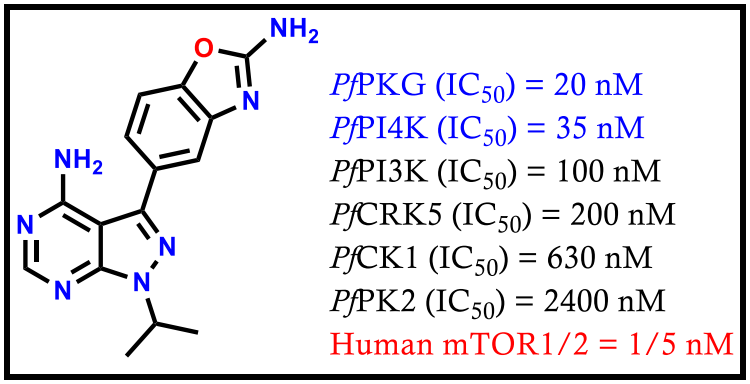

Figure 2.3: Human mTOR and *Plasmodium* kinase profile of **MLN0128**

However, the major limitation of **MLN0128** as an anti-malarial drug is its potential to inhibit several important human kinases, including transforming growth factor (TGF) beta Receptor 1, and Receptor-interacting serine/threonine-protein kinase 2 (RIPK2), which poses potential human toxicity besides its main oncological target. This study aimed to reposition **MLN0128** using a structure-based medicinal chemistry approach to maintain potency against both the

Plasmodium targets (*Pf*PKG and *Pf*PI4K) while potentially minimizing interactions with human mTOR and other human kinases.

2.4 Justification of the study

Developing unique compounds with novel mode of action remains crucial to the discovery of drugs that can be effectively administered either as a single-dose cure or active against multiple stages of the *Plasmodium* lifecycle to eradicate malaria.[18] Considering the successful approval of several kinase inhibitor drugs by the Food and Drug Administration (FDA) as anticancer agents, there is increased attention to reposition these compounds for the treatment of malaria and other parasitic diseases. Repositioning of known human kinase inhibitors is a good starting point for antimalarial drug discovery programs because of the optimized ADME properties.[19]

The major challenge to the drugability of kinase inhibitors is achieving selectivity, as the ATP-binding site is conserved across kinases in both humans and disease-causing pathogens. An in-depth understanding of structural differences between host and *Plasmodium* orthologues is crucial for the successful exploitation of kinases in drug discovery programs.[20] Comparative docking between human and *Plasmodium* phosphoinositide kinases (PIKs) may provide insight on strategies to de-risk human off-target kinase activity and associated toxicity.[20] Nonetheless, the discovery and successful development of **MMV390048** as a selective *Pf*PI4K inhibitor for the treatment of malaria and its progression to phase II human clinical trials is a major milestone towards realization of antimalarial kinase inhibitors in human therapeutics. Other advanced pre-clinical lead *Pf*PI4K-inhibitors include **UCT943** and **KDU691**.[21,22]

Besides *Pf*PI4K, *Pf*PKG is another promising *Plasmodium* kinase drug target in malaria and has been validated *in vivo* using **ML10**, a potent preclinical lead compound.[23] One drawback of specific PKG inhibitors is their narrow therapeutic temporal window (< 3 h) against the asexual blood-stage parasite.[24] Although *Pf*PKG plays essential role in the asexual blood-stage during schizont rupture and merozoite egression, its catalytic activity is not needed during the 48-h period of intraerythrocytic parasite development.[25] Consequently, such inhibitors show moderate to slow killing rates as observed in the Parasite Reduction Ratio (PRR) biochemical assay.[26]

Plasmodium pan-kinase inhibitors may have advantages over single-target therapeutics due to the added pan-stage activities, possible synergistic effects, minimized toxicity, and absence of PK mismatch during advanced clinical drug combinations studies. Essentially validated *Plasmodium* kinases also provides an opportunity to target the parasite at multiple stages, an

appealing characteristic for future antimalarials. Thus, poly-pharmacology studies of essential *Plasmodium* kinases coupled with *in silico* predictions provide a platform for discovery of such "magic shotgun" antimalarials which are selective against the host kinases.[18] Towards this end, the major focus of this project was to apply computer-aided drug design (CADD) and medicinal chemistry approaches to reposition the anticancer clinical candidate **MLN0128**, the second generation inhibitor of human mTORC1 (IC_{50} = 1 nM) and mTORC2 (IC_{50} = 5 nM),[4,6] as targeted dual *P. falciparum* PI4K and PKG inhibitors.

2.5 Objectives of the study

One of the main objectives of this study was to design and synthesize dual *Pf*PI4K/PKG inhibitors using **MLN0128** as a template, evaluate their multi-stage anti-plasmodium activities using drug-susceptible (*Pf*NF54) and -resistant (*Pf*K1) strains, investigate their physicochemical properties (*i.e.*, solubility), and carry out enzymatic screening against *Pf*PI4K, *Pf*PKG, off-target activity against selected human kinases, including mTOR, to evaluate selectivity. Accordingly, the aim was to derive SARs and structure-property relationships (SPRs) to further guide and inform our structure-based optimization campaign based on this, amongst other scaffolds.

2.5.1 Specific objectives

The specific objectives of this study were to:

i. re-synthesize **MLN0128**, validate its anti-plasmodium and dual PI4K/PKG activity, and establish *in vivo* proof-of-concept in an appropriate malaria infection model
ii. design, synthesize and characterize **MLN0128** analogues as potential anti-plasmodium dual *Pf*PI4K/PKG inhibitors.
iii. profile the *in vitro* inhibition potencies of synthesized analogues with respect to *Pv*PI4K, *Pf*PKG, and off-target human mTOR and PI4K lipid kinases.
iv. evaluate solubility and profile *in vitro* microsomal metabolic stability, cytotoxicity, gametocytocidal, and hERG activity of selected potent compounds.

2.6 General medicinal chemistry plan

The workflow adopted in this study is depicted in **Figure 2.4**. The initial step involved *in silico* design of dual *Pf*PI4K and PKG inhibitors based on the **MLN0128** scaffold. The hit compound, **MLN0128**, was re-synthesized and tested for *in vivo* efficacy in a non-obese diabetic severe combined immunodeficiency gamma (NOD SCID) *Pf* mouse model. Target compounds were

synthesized, characterized and tested for asexual blood-stage activity in the drug-sensitive *Pf*NF54 strain. Selected compounds were further tested against the multi drug resistant *Pf*K1 strain. Potent compounds (*Pf*NF54 IC_{50} < 0.5 µM) were selected and evaluated for transmission blocking ability in both early- and late-stage gametocytes. *In vitro* biochemical enzymatic studies (*Pv*PI4K and *Pf*PKG) were also performed to correlate results with the observed whole-cell anti-plasmodium activity, followed by off-target studies performed using human mTOR and human PI4KIIIβ as a prototype for evaluation of off-target host phosphoinositide kinase inhibition.

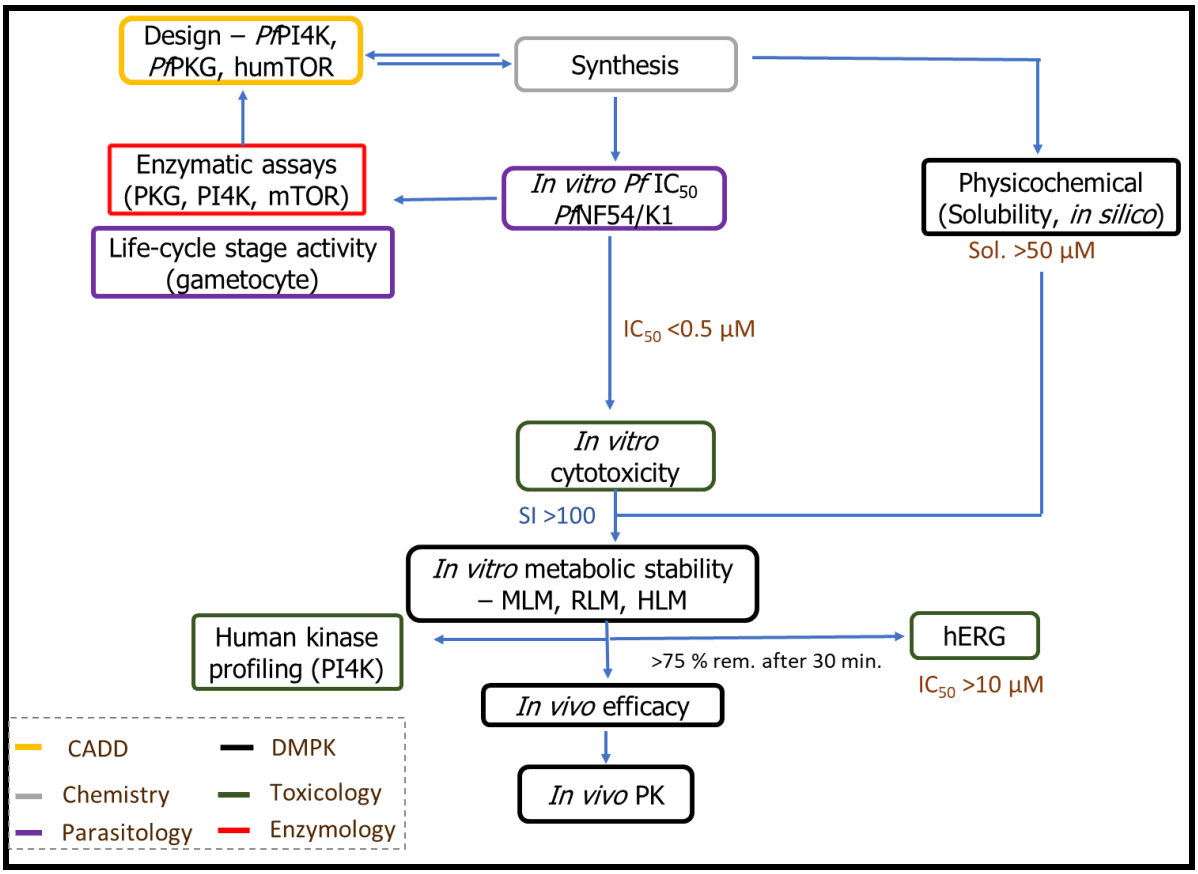

Figure 2.4: Working cascade for dual *Plasmodium* kinase inhibitors followed in this study

Additionally, physicochemical profiling of the analogues was undertaken in parallel to assess SARs and structure-property relationships (SPRs). This included experimentally determined properties including melting points and solubility vis-a-vis properties determined using *in silico* tools (cLogP and TPSA). *In vitro* cytotoxicity profiling of promising analogues (*Pf*NF54 IC_{50} < 0.5 µM) was conducted against Chinese Hamster Ovarian (CHO) and HepG2 cell lines for comparative studies. Compounds with high safety profiles based on high CHO selectivity

indices (SI; CHO CC_{50}/*Pf*NF54 IC_{50} > 100) were progressed to *in vitro* microsomal metabolic stability testing in human, rat, and liver microsomes.

Furthermore, inhibition studies for representative compounds across the series were undertaken on a hERG laboratory-adapted assay to highlight the effect of structural modifications made. This potassium ion channel controls the contractile activity of heart muscles with induced inhibition associated with a fatal heart condition called arrhythmia.[27,28] Although high solubility (> 50 µM at pH 6.5) was a desirable criteria for the progression of compounds in this series, it was unfortunately not achieved for promising **MLN0128** compounds, and may be an important consideration for future design and development. .

2.7 Design and synthesis of MLN0128 analogues

2.7.1 Rational design of MLN0128 analogues

Most kinase inhibitors bind to the conserved ATP-binding site. The ATP-binding pocket of any kinase is structurally characterized by a hinge region endowed with a backbone carbonyl H-acceptor and an amide donor which anchors the adenine core of ATP (**Figure 2.5**). It also contains a ribose binding pocket with two or three hydroxyls from serine or threonine amino acid residues. In addition, there is a phosphate channel (P-loop) containing both acidic and basic residues which acts as a lid over the phosphate channel to secure the ATP in position. A catalytic lysine/acid pair used to neutralize charge during phosphorylation is found at the end of the channel where the terminal phosphate is hydrolyzed (**Figure 2.5**).[29] Some kinase inhibitors also explore other portions of the protein, such as allosteric site,[30] regions which are not explored in this work.

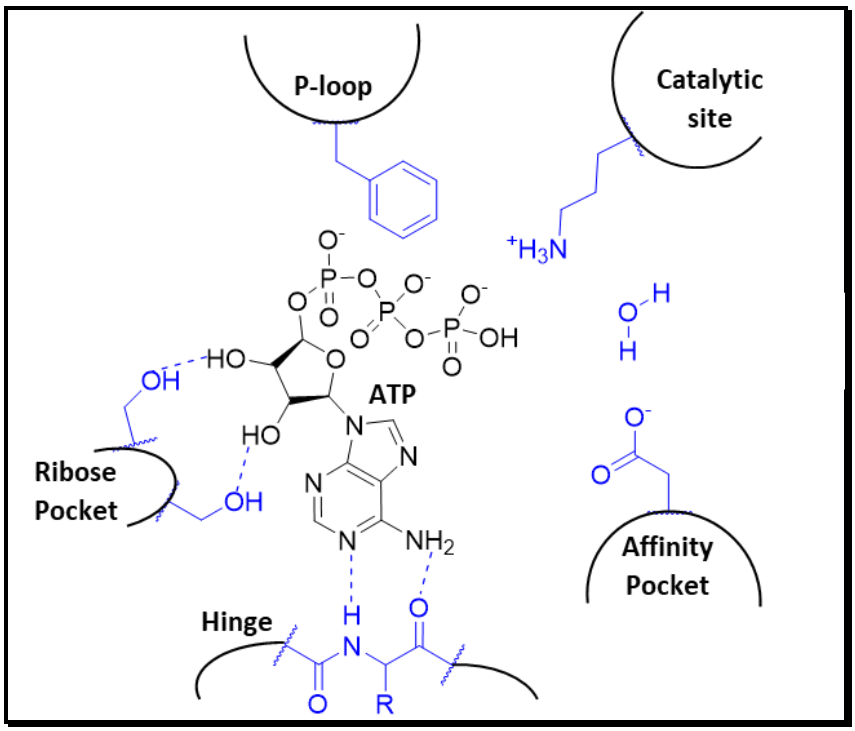

Figure 2.5: Generalized 2D schematic diagram of a kinase ATP-binding site[29]

The design of many ATP-competitive kinase inhibitors involves *in silico* studies of the ligands at the hydrophobic pocket adjoining the ATP-binding site. Access of inhibitors to the back pocket in protein kinases is regulated by a gate-keeper residue, such as threonine (Thr) in *Plasmodium* PKG.[23] In contrast, mammalian PKGs and most serine/threonine kinases possess a different gate-keeper residue, such as glutamine or histidine, a property that can be judiciously explored by small molecules to achieve selectivity.[23,31]

Contrary to *Plasmodium* PI4K, the structures of *P. vivax* and *P. falciparum* PKG are well characterized, and their crystal structures are available in the Protein Data Bank (PDB). Typically, PI4Ks have numerous disordered regions where heavy truncation is required to form well-ordered diffracting crystals, as was the case for crystallization of human PI4KIIIβ.[32] Moreover, *Plasmodium* PI4K contains approximately 1600 residues with significantly more unstructured regions than human orthologues (approximately 816 residues). Compounded by the presence of long low complexity regions and asparagine and aspartic acid repeats, typical of *P. falciparum* proteins and particularly prevalent in *Pf*PI4K, high-resolution crystal structures of the *Plasmodium* PI4K remain elusive to date.[32–34] However, homology models have been developed and continue to be exploited as substitutes in the discovery of new chemical matter targeting the enzyme.[35] Similarly, a locally developed *Pf*PI4K homology

model and available *Pv*PKG and human mTOR crystal structures were employed in the design of compounds for this project.

The *Pf*PI4K homology model used for docking was prepared by the H3D computational team using a target sequence obtained from PlasmoDB (PDB, **PF3D7_0509800**), as described by Fienberg *et al*.[29] Homology modeling involved a sequence similarity search and protein preparation (sequence alignment, loop refinement at the ATP-binding site, and energy minimization) using Maestro software v.11.5.011 (Schrodinger, LLC, New York, NY, USA). The crystal structures of *Pv*PKG (PDB code **5EZR**) and human mTOR (**6ZWM**) were selected for modeling due to the analogous nature of their co-crystallized ligands with MLN0128. Despite availability of the *Pf*PKG structure in PDB (**5DYK**), the *Pv*PKG crystal structure (**5EZR**) was deemed a more suitable model for use because of its ATP-motif inhibitor-bound structure, as opposed to the apo form. The catalytic domain of *Pv*PKG and *Pf*PKG are homologous to each other and hence display high similarity in their amino acid sequences (92%) with equally conserved ATP-binding site.[36]

Thus, computational docking of selected ligands based on the *Pf*PI4K homology model, *Pv*PKG crystal structure (**5EZR**), and human mTOR (**6ZWM**) was employed to further determine the appropriate SAR to be explored on the **MLN0128** scaffold. Test docking using known inhibitors such as MMV390048 and published imidazopyridazines for PI4K and ML10 for *Pv*PKG were employed for appropriate geometry, binding pose approximation, and investigation of interactions crucial for binding.

In the *Pf*PI4K homology model, the hinge binding motif of **MLN0128** was predicted to bind via a H-bond from the backbone amide of Val 1357 to the 5-*N*-heteroatom within the pyrazolopyrimidine hinge binding motif (**Figure 2.6**). The benzoxazole moiety extends into the lipophilic affinity pocket with the oxazole imine and amine aligned as H-bond acceptor and donor to the Asp 1430 amide and carbonyl, respectively (**Figure 2.6**). The isopropyl group is positioned in the ribose pocket although no feasible interactions were made in this region. Interestingly, the hinge binding motif is proximally positioned to Tyr 1356 possibly π-stacking with the aromatic sidechain, further strengthening binding. This is analogous to the docking alignments of **MMV390048** and other PIK inhibitors.[29]

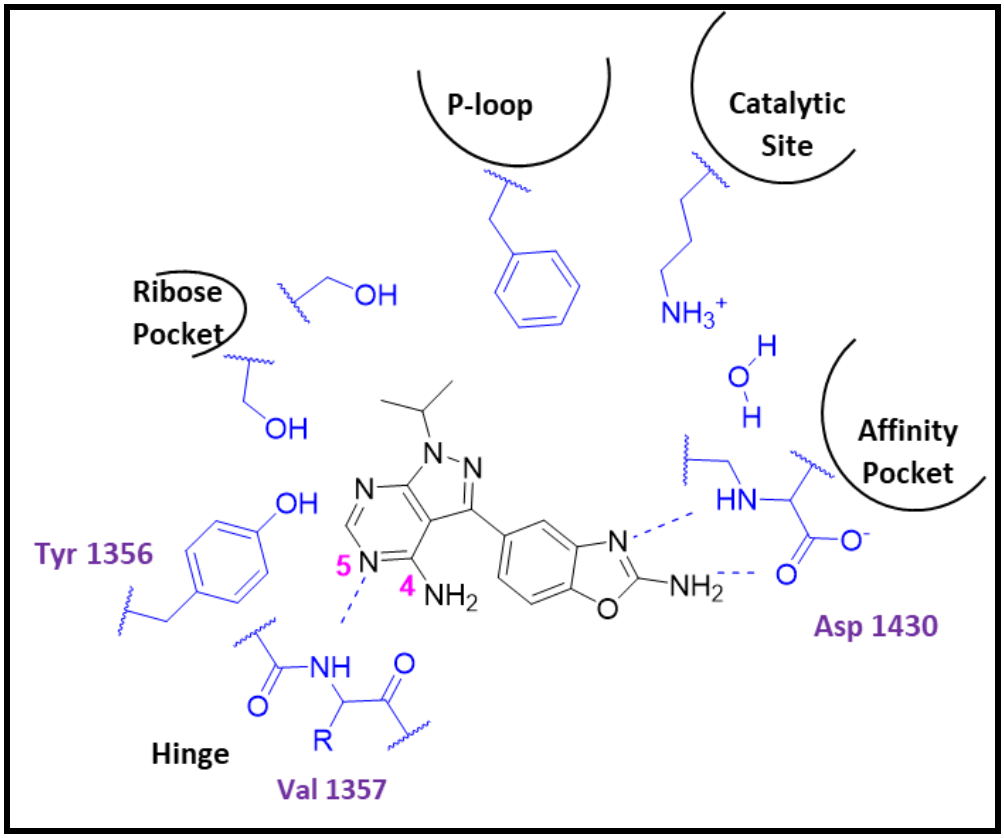

Figure 2.6: Generalized 2D schematic of **MLN0128** at the ATP-binding site of the *Pf*PI4K homology model

Docking of **MLN0128** into the *Pf*PKG crystal structure (**5EZR**) suggests that the 5-N of the core scaffold accepts a H-bond from Val 614 in the hinge while 4-NH_2 donates a H-bond to the carbonyl of Glu 612 (**Figure 2.7**). Like the interactions in the *Pf*PI4K homology model, the benzoxazole extends into the protein kinase back pocket, forming a putative H bond with Asp 675. Generally, the *Pv*PKG back pocket is structurally analogous to the PI4K affinity pocket and equally accessible due to a small gatekeeper Thr 611 residue, albeit deeper in nature. Strikingly, the aromatic benzoxazole part of the molecule also extends towards the catalytic lysine (Lys 563) to form a π - cation interaction at the catalytic site (**Figure 2.7**; interaction not shown). On the other hand, the isopropyl group is positioned in the ribose pocket and forms no interactions with any amino acid residues in this region. Notably, this hydrophobic pocket is endowed with acidic residues such as Glu 661 and Glu 618 which a small inhibitor could explore for potency improvement.[31]

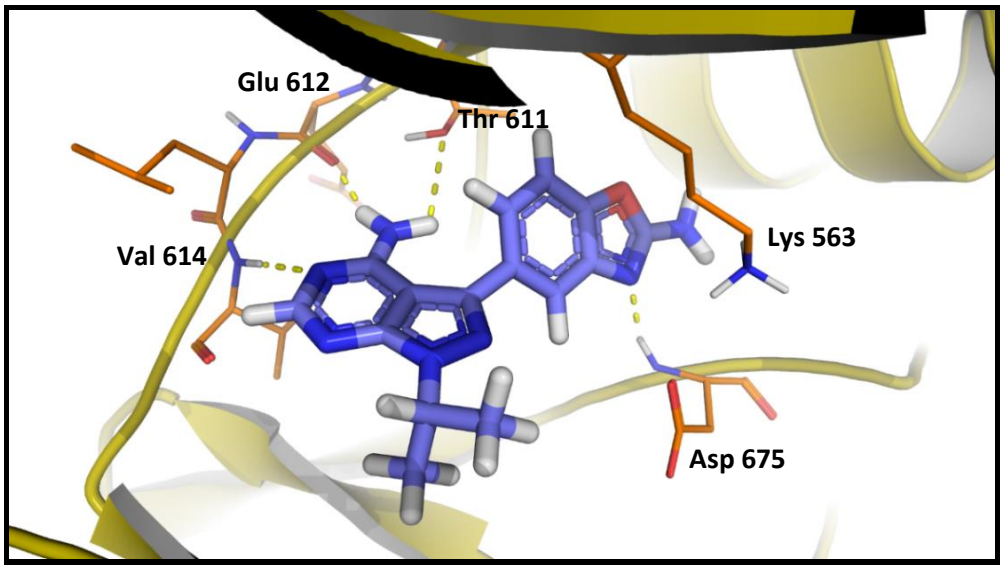

Figure 2.7: Docking pose of **MLN0128** on the *Pf*PKG crystal structure (code **5EZR**) with H-bonds shown as yellow dashed lines

In the human mTOR crystal structure (**6ZWM**), the **MLN0128** core was predicted to accept an H-bond from the backbone amide of the hinge (Val 2240; **Figure 2.8**) and donate one through the pyrimidine amide to Gly 2238 in a PI4K-like manner. This was attributed to the typical resemblance of the catalytic domain of mTOR to that of phosphoinositide kinases. π-π interactions occurred between the core and the Trp 2239 residue extending from the hinge (interaction not shown). Furthermore, the benzoxazole imine extended to interact with the conserved catalytic Lys (2187) with the amine positioned near Asp 2195 in the affinity pocket for binding. In addition, π - π stacking occurred between the phenyl ring and Tyr 2225 (interaction not displayed in **Figure 2.8**). Indeed, these multiple interactions rationalized the particularly high potency of MLN0128 against the oncological targets (mTOR1/2 IC_{50} = 1/5 nM).

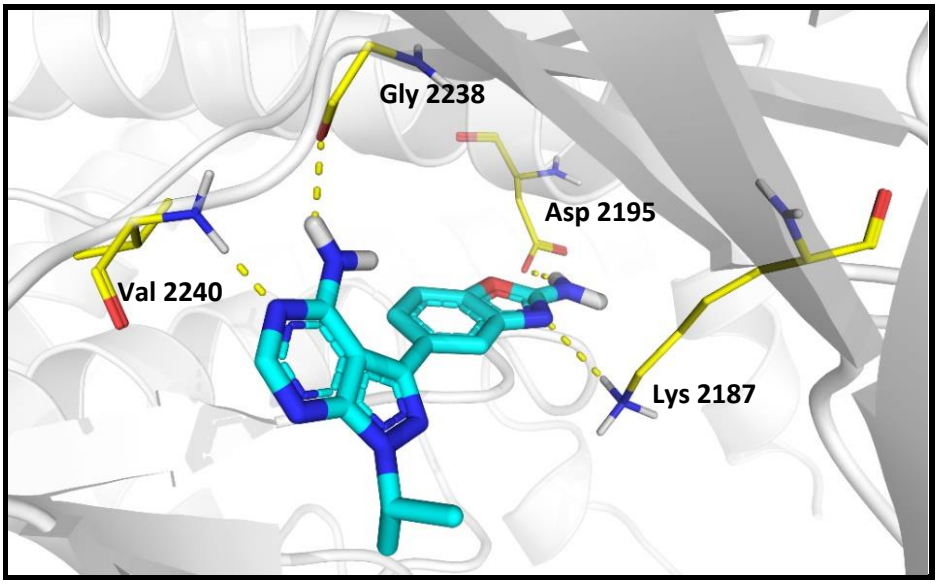

Figure 2.8: Docking pose of **MLN0128** on human mTOR crystal structure (code **6ZWM**) displaying H-bonds only (as yellow dotted lines)

The major difference between PI4K and mTOR is the smaller ribose pocket in PI4K where no feasible interactions were observed for **MLN0128** against the three targets. PI4K possesses robust amino acid residues such as Ser 1362 and aromatic Phe 827/828 residues extending towards the P-loop,[29] while the human mTOR ribose pocket lies exposed to a solvent front. Conversely, *Plasmodium* PKG is more hydrophilic because of an abundance of serine, threonine, and acidic amino acids (mostly Glu and Asp). These are appealing features which judicious design can exploit for selectivity.[37]

Molecular docking studies to enhance these interactions at the ribose pocket of the *Plasmodium* targets were desirable to produce dual *Pf*PI4K/PKG inhibitors. It was thought that the strong interactions of the benzoxazole moiety at the affinity/back pocket of the *Plasmodium* targets could be retained for potency with substitutions directed at the ribose binding pocket for initial SAR exploration aimed at introducing selectivity. Furthermore, the hydrophobic pocket is smaller in size and the benzoxazole moiety thus fitted optimally in the affinity/back pocket of the *Plasmodium* models and extended to the catalytic region. This suggested a limited SAR for exploration on this side of the molecule.

To virtually test this hypothesis, two points of diversity on the pyrazolo[3,4-*d*]pyrimidine core (**SAR 1** and **SAR 2**; **Figure 2.9**) were employed to generate a library of compounds for docking analysis. **SAR2** involved maintaining the pyrazolo[3,4-*d*]pyrimidine core and the isopropyl part of the molecule and introducing structural changes to the benzoxazole component. Diverse

structural changes were explored such as six-membered phenyls, heteroaromatic pyridyls, five-membered pyrrole, and aliphatic cyclohexyls with the rings tethered with 1–2 carbon spacers for free-rotation and flexibility. **SAR1** involved similar substitutions while fixing the core scaffold and the benzoxazole moiety, while varying substituents on the rings as guided by the Craig plot.

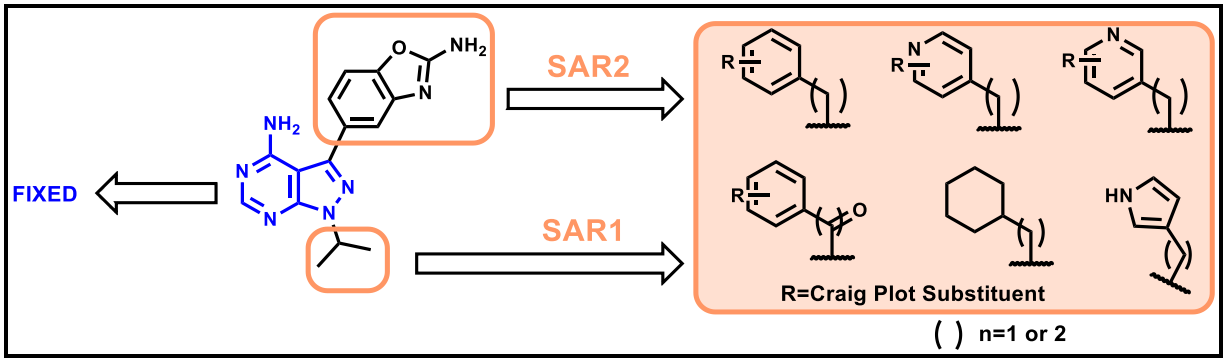

Figure 2.9: Design plan for **MLN0128** analogues

The Craig plot (**Figure 2.10**) is a commonly employed medicinal chemistry tool used in SAR investigation for the selection of substituents with diverse physicochemical properties. It is a 2D plot of substituents with differing electronic (σ) and lipophilic (π) characters with each quadrant comprising closely related substituents of similar bio-isosteric effect.[38] The choice of substituents in **SAR1** and **2** (**Figure 2.9**) was made by investigating binding of selected substituents from across the four quadrants of the Craig plot to *Plasmodium* targets and human mTOR. In this regard, F, Cl, and CF_3 (1st quadrant), CN (2nd), NH_2 and OMe (3rd), and Me and NMe_2 (4th) were selected.

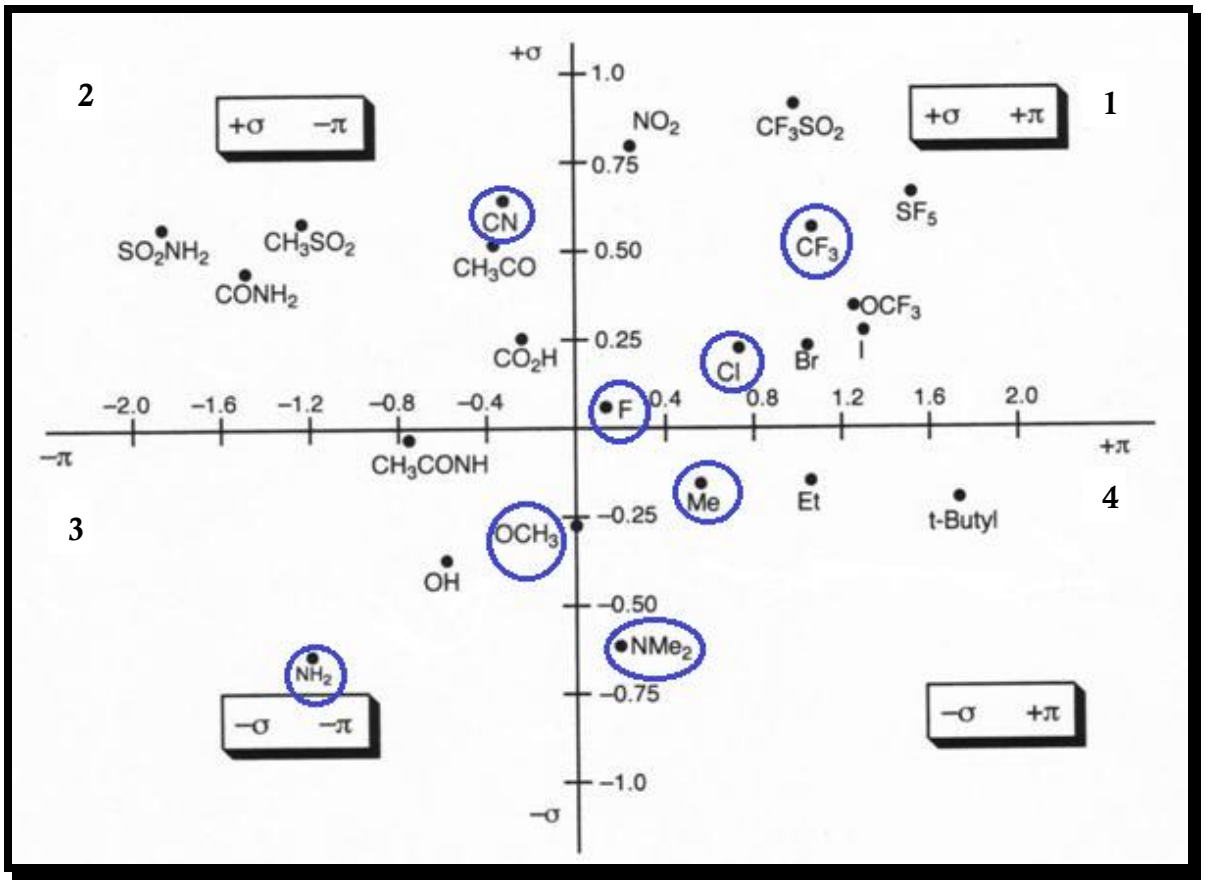

Figure 2.10: Craig plot capturing selected substituents on the structures of **SAR1** and **2**

An iterative approach was employed in the rationalization of compounds based on the **MLN0128** scaffold as illustrated in **Figure 2.11**. Promising ligands showing high Glide XP docking scores, net molecular mechanics/generalized Born surface area energy change (ΔΔMMGBSA) values (>-15 kcal/mol relative to MLN0128), and conforming docking poses were identified and used to generate a subsequent set of ligands for redocking. Similar evaluations were performed against *Pv*PKG and human mTOR crystal structures with **MLN0128** as a reference.

Disruptive interactions in the binding site were trackable using calculated binding energy by making use of the generalized Born Surface Area (MMGBSA) implicit solvent model, as exemplified in **Table 2.1**. These energy changes indicated ease of the ligand-protein complex formation by calculating the net receptor and ligand conformational energy changes needed to form the complex although the results are often unreliable.[39] In addition, physical inspection of ligand and protein anomalies such as abnormal torsions, bond angles, peptide planarity, and geometry were also employed to track unfavorable interruptions.[29]

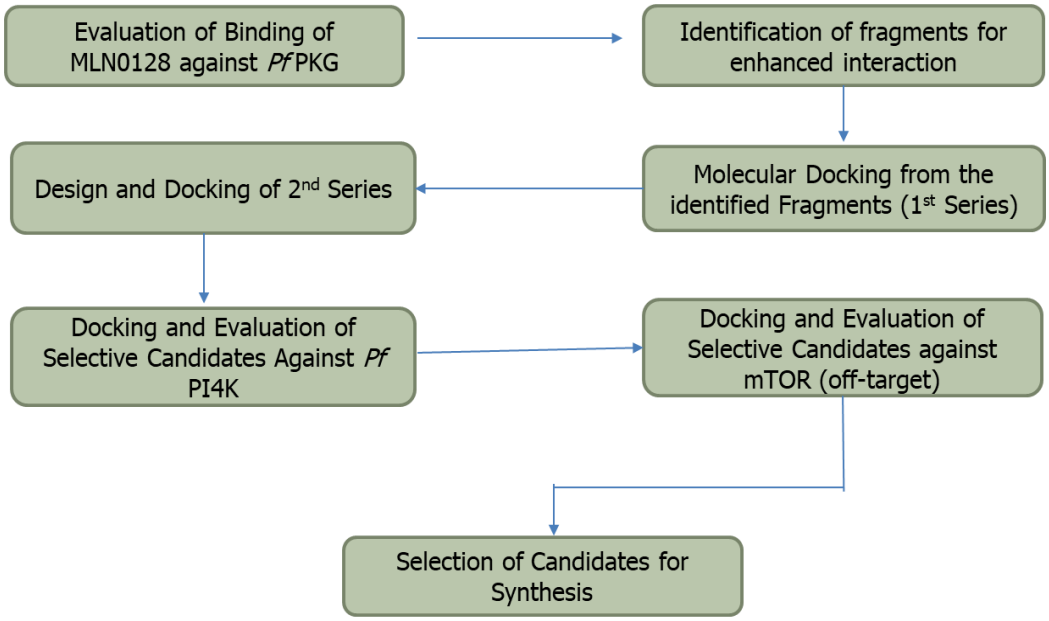

Figure 2.11: Flow diagram of the design approach for selective dual *Pf*PKG/PI4K inhibitors

Ideally, these docking experiments would de-risk potent inhibition of human mTOR, and potentially reduce off-target effects on other human kinases. Promiscuity in kinase inhibitors is often attributed to the conserved ATP-binding found in all kinases[40] so differences on the periphery of the ATP-binding site need to be identified and exploited for selectivity. It was hypothesized that replacement of the isopropyl group in **MLN0128** with aromatic sidechains might hinder the ligand from effectively accessing the binding pocket in human mTOR which is apparently widely exposed to the bulk solvent (**Figure 2.12**). This may consequently lead to proportionate disruption of interactions between the pyrazolopyrimidine and benzoxazole moieties with the associated amino acid residues in mTOR relative to the *Plasmodium* targets, thereby achieving selectivity.

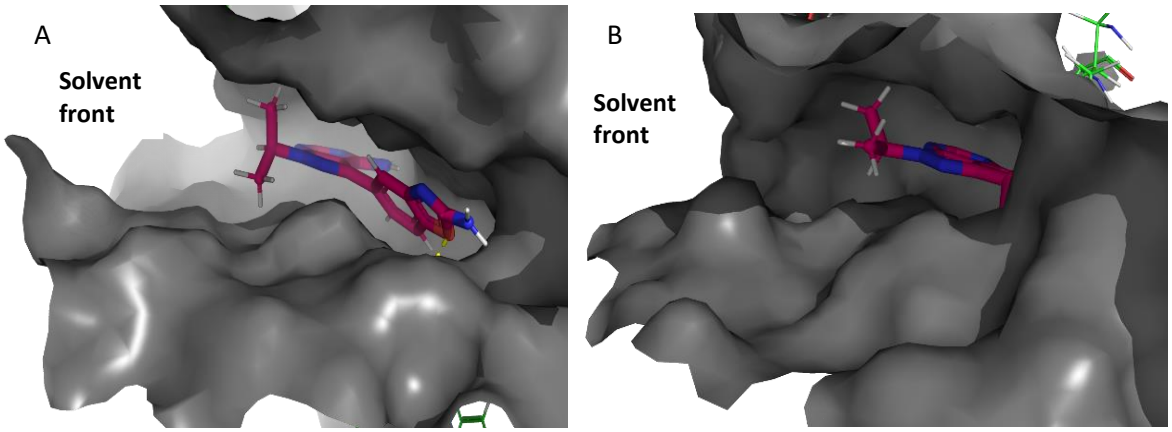

Figure 2.12: A; Predicted surface binding mode of MLN0128 in ATP-binding site of human mTOR, suggesting proximity to the solvent front, and B; Docked MLN0128 in the *Pf*PKG crystal structures

Substitutions in the benzyl or pyridyl moiety could also be adapted to create facile diversity for interactions with specific non-conserved residual amino acids in the *Pf*PI4K and PKG ribose pockets, thereby improving or retaining dual potency. Moreover, the ATP binding site of *Plasmodium* PI4K is largely lipophilic and aromatic ligands are likely to enhance π - stacking and edge-to-π bonding with several Phe and Tyr residues. This consequently promotes potency as observed in most potent *Pf*PI4K inhibitors.[41] MMGBSA outputs of selected ligands from docking experiments (**Table 2.1**) also supported this hypothesis with expected poor binders exhibiting low negative or positive net binding energies. Additionally, these results suggested that a single-carbon (n = 1) alkyl chain linker was optimal for *Plasmodium* kinase activity retention as exemplified by representative compounds docked in the *Pf*PI4K homology model and human mTOR crystal structure (**Table 2.1**).

Table 2.1: Calculated MMGBSA ΔG (in kcal. /mol) of selected **MLN0128** ligands

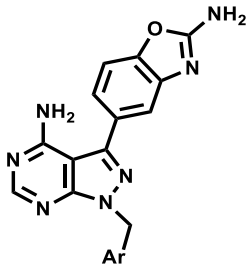

R	*Pf*PI4K MMGBSA	*Pf*PI4K MLN0128 ΔΔG	Human mTOR MMGBSA ΔG	mTOR MLN0128 ΔΔG	*Pf*PI4K ΔΔG – mTOR ΔΔG
MLN0128	-41.76	0.00	-53.22	0.00	0.00
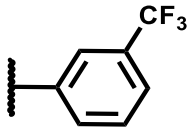	-60.23	-18.47	-51.85	1.37	-19.84
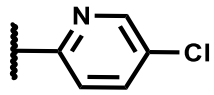	-57.6	-15.84	-49.46	3.76	-19.60
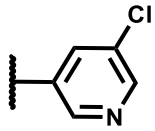	-63.58	-21.82	-50.55	-3.08	-18.74
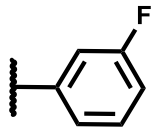	-56.39	-14.63	-52.41	0.81	-15.44
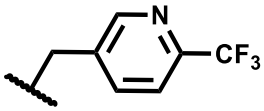	-38.22	3.54	-53.60	-6.13	9.67

As a result, a series of compounds was proposed for synthesis as summarized in **Figure 2.13**. Docking exploration studies of **SAR2** (replacement of the benzoxazole part of the molecule) suggested significant disruptive interactions against the *Plasmodium* targets. **SAR1** was thus prioritized for synthesis. Furthermore, substituted benzyl and pyridyl analogues could be easily accessed using a straightforward synthetic route from commercially available bromo- or chlorobenzyl and pyridyl chemicals based on synthetic protocols like those of **MLN0128**. At the same time, this divergent SAR could be employed to investigate physicochemical properties such as solubility which were likely to decrease in response to the added lipophilicity.

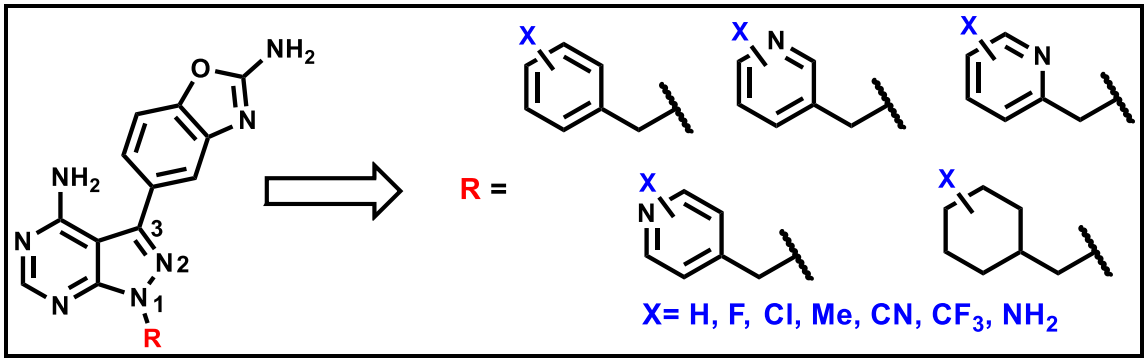

Figure 2.13: Outline of the proposed SAR exploration on MLN0128 scaffold

2.7.2 Synthesis of MLN0128 and related analogues

Part of the first objective of this study involved the re-synthesis of the hit compound **MLN0128** for biological re-testing, confirmation of structural assignments, verification of the synthetic steps, and generation of key intermediates for subsequent SAR studies. Several synthetic methods for the realization of **MLN0128** and other pyrazolo[3,4-*d*] pyrimidine compounds have been previously reported.[42] However, the re-synthesis of the hit compound and subsequent SAR studies were performed using modified methods from the work of Ren *et al*.[43]

Exploration of the target SAR commenced with the condensation of 5-amino-1*H*-pyrazole-4-carbonitrile (**1**) to form the core scaffold (**2**). This was followed by the selective iodination to **3**. To minimize synthetic steps and cost of goods, Suzuki cross-coupling reaction in appropriate boronic acid/ester to yield the intermediate **2.1a** (**Scheme 2.1**) was seen as an ideal synthetic protocol. Thus, it was hypothesized that this monosubstituted pyrazolopyrimidine intermediate (**2.1a**) would be a versatile and ideal candidate for this exploration, after which structural diversification at N-1 would be explored via nucleophilic substitution reactions.

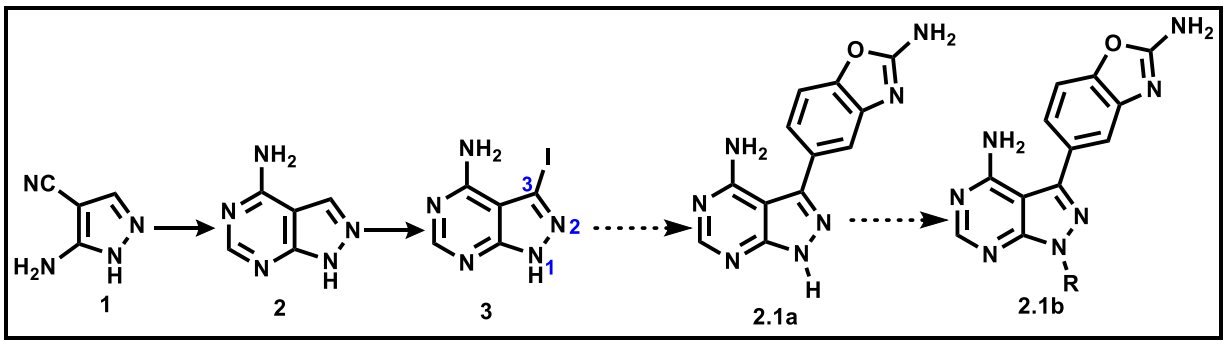

Scheme 2.1: Proposed route for effective incorporation of benzyl substituents at N^1

However, obtaining the monosubstituted pyrazolo[3,4-*d*]pyrimidine intermediate, **2.1a**, was more difficult than was initially anticipated. For instance, when intermediate **3** was subjected

to a Suzuki-cross coupling reaction under standardized conditions (*i.e.*, catalytic $Pd(PPh_3)_4$ and Na_2CO_3 in dioxane/water (3:1 v/v) at 100°C), no desired product was detected via liquid chromatography-mass spectrometry (LC-MS) although the starting material was consumed as confirmed by LC-MS. Attempted systematic modifications of the reaction conditions including use of various catalysts and ligands such as $PdCl_2(PPh_3)$, $Pd(dba)_2$ with $(C_6H_{11})_3P$ was unsuccessful. Changes of experimental reaction conditions such as microwave irradiation, extended reaction times under conventional heating (3 days) or change of solvent to DMF only resulted in trace amount of product or no formation at all. Similar unsuccessful coupling reactions on the same scaffold have also been previously observed by Todorovic *et al*.[44]

It is well-accepted that derivatization of certain heterocycles containing a basic centre such as amines, thiols, and alcohols by Suzuki-cross coupling reaction is more challenging compared to other substrates.[45,46] This is mainly due to binding of the basic centre to a Pd (ii) intermediate formed during the catalytic cycle, resulting in catalyst deactivation or poisoning. The use of bidentate ligands such as XPhos and SPhos has been suggested as a plausible strategy to overcome this phenomenon. Protection of the basic centre is also envisaged as a feasible alternative.[47]

With this in mind, protection of the pyrazole basic nitrogen with *para*-methoxybenzyl (PMB) group enabled a successful Suzuki cross-coupling reaction. Unfortunately, deprotection of PMB protecting group required the use of harshly acidic trifluoroacetic acid (TFA), conditions which caused decomposition of the benzoxazole ring. Other PMB deprotecting reagents such as 2,3-dichloro-5,6-dicyano-1,4-benzoquinone (DDQ) were not successful, possibly due to the steric demands of the deprotection process.[48] Other recommended protection strategies to overcome such synthetic challenges involves 2-(trimethylsilyl)ethoxymethyl (SEM) or tosyl groups, which can be deprotected under basic conditions.[49] However, such approaches were not exhaustively explored in this study.

Consequently, the synthetic protocol undertaken involved the generation of a series of directly *N*-alkylated intermediates (**6a**–**62a**) prior to Suzuki cross-coupling with the boronic ester (**5**) prepared in-house. The synthetic protocol was therefore derived from the commercially sourced 5-amino-1*H*-pyrazole-4-carbonitrile (**1**) and 5-bromobenzo[*d*]oxazol-2-amine (**4**), using methods previously described with some modifications (**Scheme 2.2**).[50] Additionally, unsubstituted aniline derivatives explored in this series were synthesized via reduction of nitro

intermediates under standard conditions (*i.e.*, using iron dust in HCl followed by Suzuki cross-coupling) using reported methods.[51]

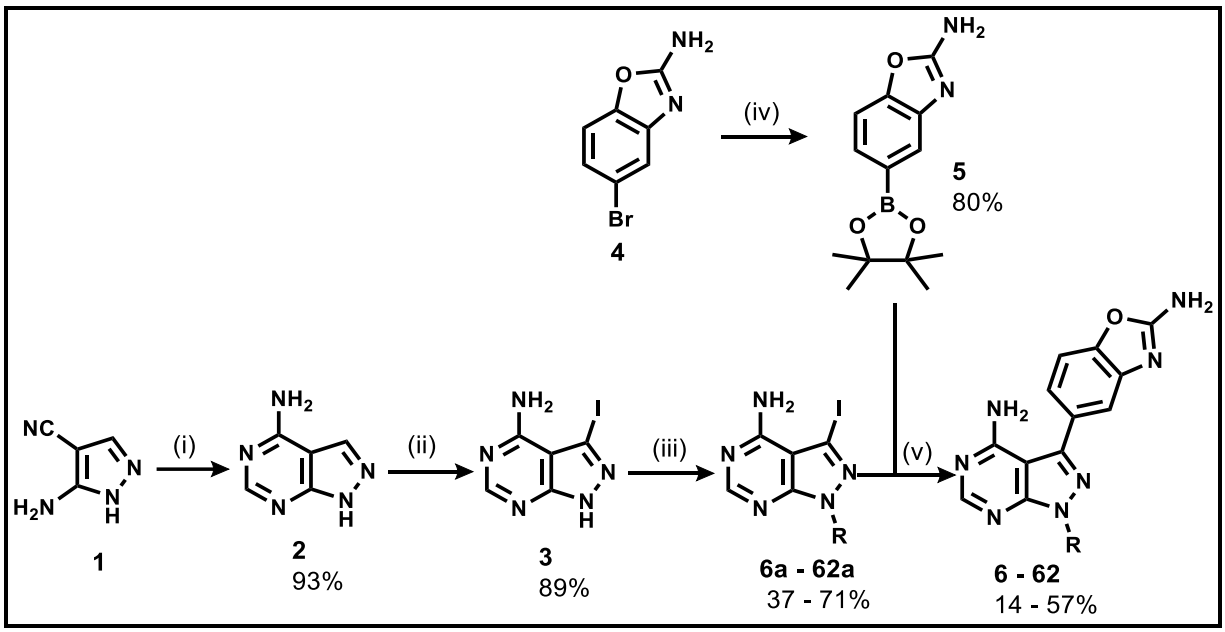

Scheme 2.2: Synthetic protocol for substituted MLN0128 analogues

Reagents and reaction conditions: (i) $HCONH_2$, DMF, 180°C, 15 h; (ii) NIS, DMF, 80°C, 15 h; (iii) RBr or RCl, K_2CO_3, DMF, 30°C for RBr and 70°C for RCl, 2 h; (iv) bis(pinacolato)diborane, $Pd(dppf)Cl_2$, KOAc, dioxane, 100°C, 15 h; (v) $Pd(PPh_3)_4$, Na_2CO_3, dioxane/ H_2O (3:1), 100°C, 15 h.

Certain 2-chloromethyl pyridyl precursors (2-(chloromethyl)-5-fluoropyridine, 2-(chloromethyl)-6-fluoropyridine, and 2-(chloromethyl)-6-(trifluoromethyl)pyridine) were not commercially available. As a result, these were produced in-house using their corresponding alcohols under standard conditions (*i.e.*, chlorination with $SOCl_2$) or carboxylic acid derivatives. For instance, 3-(chloromethyl)-5-fluoropyridine (**2.3b**) was synthesized from its carboxylic acid derivative through reduction to an alcohol intermediate (**2.3a**) with lithium aluminum hydride (LAH), followed by chlorination (**Scheme 2.3**).[52,53]

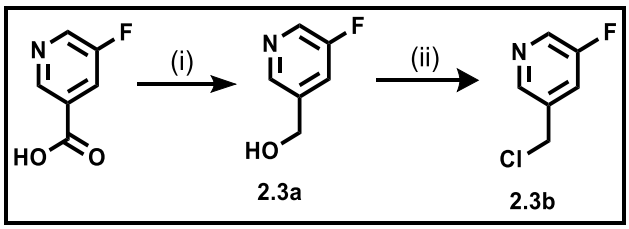

Scheme 2. 3: Synthetic scheme for conversion of a nicotinic acid derivative to **2.3b**

Reagents and reaction conditions; (i) LAH, THF, 4°C, 3 h; (ii) $SOCl_2$, DCM, 2°C, 15h.

Overall, *N* alkylation proceeded with moderate to high yield (37–71%), while lower yields (14–57%) were obtained in Suzuki cross-coupling reactions. A summary of the isolated yields for intermediates **6a**–**62a** and the target compounds **6**–**62** is provided in **Table 2.2**.

Table 2.2: Synthetic yields of intermediate and target compounds

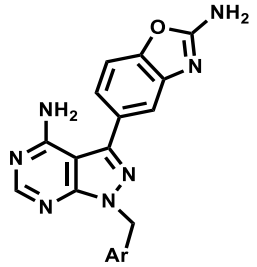

Ar	R	Intermediate	% yield	Target compound	% yield	Ar	R	Intermediate	% yield	Target compound	% yield
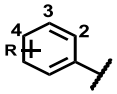	H	**6a/ GS 76**	54	**6/ GS 77**	36	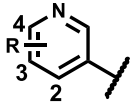	4-CF_3	**39a/ GS 98**	65	**39/ GS 99**	36
	4-Cl	**7a/ GS 54**	43	**7/ GS 55**	42		4-Cl	**40a/ GS 120**	53	**40/ GS 121**	21
	4-F	**8a/ GS 64**	44	**8/ GS 65**	54		4-F	**41a/ GS 134**	47	**41/ GS 135**	24
	4-CN	**9a/ GS 62**	44	**9/ GS 63**	32		4-Me	**42a/ GS 136**	47	**42/ GS 137**	40
	4-CF_3	**10a/ GS 58**	51	**10/ GS 59**	37	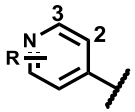	H	**43a/ GS 79**	56	**43/ GS 79B**	39
	4-Me	**11a/ GS 68**	44	**11/ GS 69**	49		3-Cl	**44a/ GS 156**	47[a]	**44/ GS 157**	17
	4-OMe	**12a/ GS 41**	51	**12/ GS 42**	57		3-F	**45a/ GS 164**	44	**45/ GS 165**	14
	4-NH_2	**13a/ GS 148***	40	**13/ GS 149**	17		3-CF_3	**46a/ GS 186**	44	**46/ GS 187**	29
	3-F	**14a/ GS 72**	50	**14/ GS 73**	34		3-Me	**47a/ GS 188**	54	**47/ GS 189**	48
	3-CF_3	**15a/ GS 70**	47	**15/ GS 71**	34	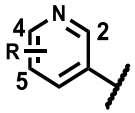	H	**48a/ GS 82**	50	**48/ GS 83**	50
	3-Me	**16a/ GS 66**	51	**16/ GS 67**	53		5-Me	**49a/ GS 166**	43	**49/ GS 167**	18
	3-Cl	**17a/ GS 56**	48	**17/ GS 57**	53		5-Cl	**50a/ GS 202**	56	**50/ GS 203**	28
	3-NH_2	**18a/ GS 154***	41	**18/ GS 155**	28		5-F	**51a/ GS 198**	49	**51/ GS 199**	24
	3-$N(Me)_2$	**19a/ GS 174**	40	**19/ GS 175**	24	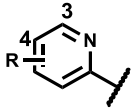	H	**52a/ GS 86**	52	**52/ GS 87**	32
	2-Me	**20a/ GS 96**	67	**20/ GS 97**	34		4-Cl	**53a/ GS 184**	49	**53/ GS 185**	28
	2-F	**21a/ GS 90**	51	**21/ GS 91**	43		4-F	**54a/ GS 182**	53	**54/ GS 183**	27
	2-Cl	**22a/ GS 114**	65	**22/ GS 115**	18		4-CF_3	**55a/ GS 190**	46	**55/ GS 191**	25
	2-CF_3	**23a/ GS 112**	58	**23/ GS 113**	21	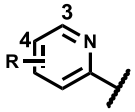	3-Cl	**56a/ GS 180**	43	**56/ GS 181**	24
	3,4-Cl	**24a/ GS 100**	60	**24/ GS 101**	37		3-Me	**57a/ GS 176**	45	**57/ GS 177**	31
	2,4-Cl	**25a/ GS 102**	44	**25/ GS 103**	38		3-F	**58a/ GS 192**	58	**58/ GS 193**	23
	2-F, 4-Cl	**26a/ GS 110**	53	**26/ GS 111**	19		3-CF_3	**59a/ GS 194**	48	**59/ GS 195**	26

2-CN, 4-Cl	**27a/ GS 106**	71	**27/ GS 107**	18	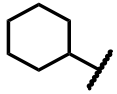	H	**60a/ GS 124**	59	**60/ GS 125**	24
3-F, 4-Cl	**28a/ GS 104**	66	**28/ GS 105**	17		4-*di* F	**61a/ GS 196**	47	**61/ GS 197**	45
3-CF_3, 4-Cl	**29a/ GS 116**	56	**29/ GS 117**	23						
2-F, 4-F	**30a/ GS 122**	57	**30/ GS 123**	23	**MLN0128**		**62a/ GS 19**	54	**62/ GS 20b**	53
2-Cl, 4-F	**31a/ GS 126**	40	**31/ GS 127**	20						
2-CF_3, 4-F	**32a/ GS 128**	52	**32/ GS 129**	24						
2-CN, 4-F	**33a/ GS 130**	43	**33/ GS 131**	16						
2-Me, 4-F	**34a/ GS 132**	45	**34/ GS 133**	27						
3-Cl, 4-F	**35a/ GS 138**	40	**35/ GS 139**	27						
3-CN, 4-F	**36a/ GS 140**	41	**36/ GS 141**	17						
3-F, 4-F	**37a/ GS 142**	44	**37/ GS 143**	16						
3-CF_3, 4-F	**38a/ GS 144**	37	**38/ GS 145**	19						

*Synthesized via reduction of their corresponding nitro derivatives; [a] crude form, used with no further purification

2.7.3 Reaction mechanisms and spectroscopic analysis of MLN0128 analogues

A combination of 1D proton and carbon nuclear magnetic resonance spectroscopy (^{1}H and ^{13}C-NMR, respectively), 2D heteronuclear multiple bond correlation (HMBC), and heteronuclear single quantum coherence (HSQC) spectroscopy were used for peak assignment and to confirm the structures of crucial intermediates and target final compounds. In addition, thin-layer chromatography (TLC) and high-performance liquid chromatography coupled with mass spectrometry (HPLC-MS) were used to monitor the reaction progress and confirm the purity of the final products after purification.

Synthesis of 1*H*-pyrazolo[3,4-*d*]pyrimidin-4-amine (**2**) proceeded via Leuckart reaction of 5-amino-1*H*-pyrazole-4-carbonitrile (**1**) with formamide acting as the solvent and a reactant. The consecutive steps involved in this condensation reaction required for the formation of **2** (**Scheme 2.4**) were initiated by a nucleophilic attack of the carbonyl carbon of formamide to **2.4a**. Charge stabilization of **2.4a** via intramolecular proton abstraction produced an amino alcohol intermediate **2.4b**, whose dehydration yielded an imine (**2.4c**). High heat (160–180°C) was required to accomplish this E_2 elimination reaction step in the sequence.

The imine readily tautomerized, activating an intramolecular ring closure involving the amine form (Schiff base; **2.4d**) and the electrophilic cyano carbon. Proton transfer and energetically favored tautomerism of the imine intermediate **2.4f** ensured the delivery of the required pyrazolo[3,4-*d*] pyrimidine intermediate **8**. Imine-amine tautomerism has previously been demonstrated through computational methods to energetically favor the amine form in nucleic acid bases and related derivatives.[54] Overall, the cyclization/condensation reaction produced the necessary product in high yield (93%) with minimal purification.

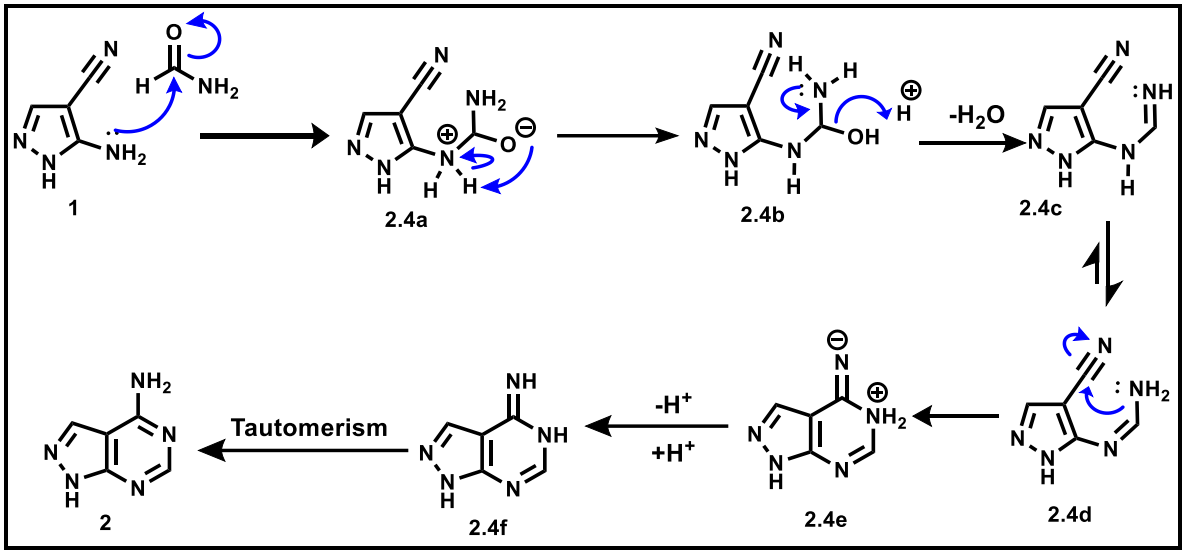

Scheme 2.4: Proposed reaction mechanism for condensation of **7** in formamide

The structure of **2** was confirmed spectroscopically by ^{1}H-NMR. The spectrum (**Figure 2.14**) de-convoluted the diagnostic highly de-shielded pyrazole proton H-1 resonating downfield at δ_H 13.30 ppm as a broad singlet. Additionally, the aromatic protons H-6 and H-3 in the pyrazole and pyrimidine rings, were identified as singlets at δ_H 8.22 and 8.06 ppm, respectively. As expected, each peak integrated for a single proton. Furthermore, a less pronounced broad singlet identified downfield at δ_H 7.56 ppm integrated for two protons, typically corresponding to the amine functionality of the pyrimidine core.

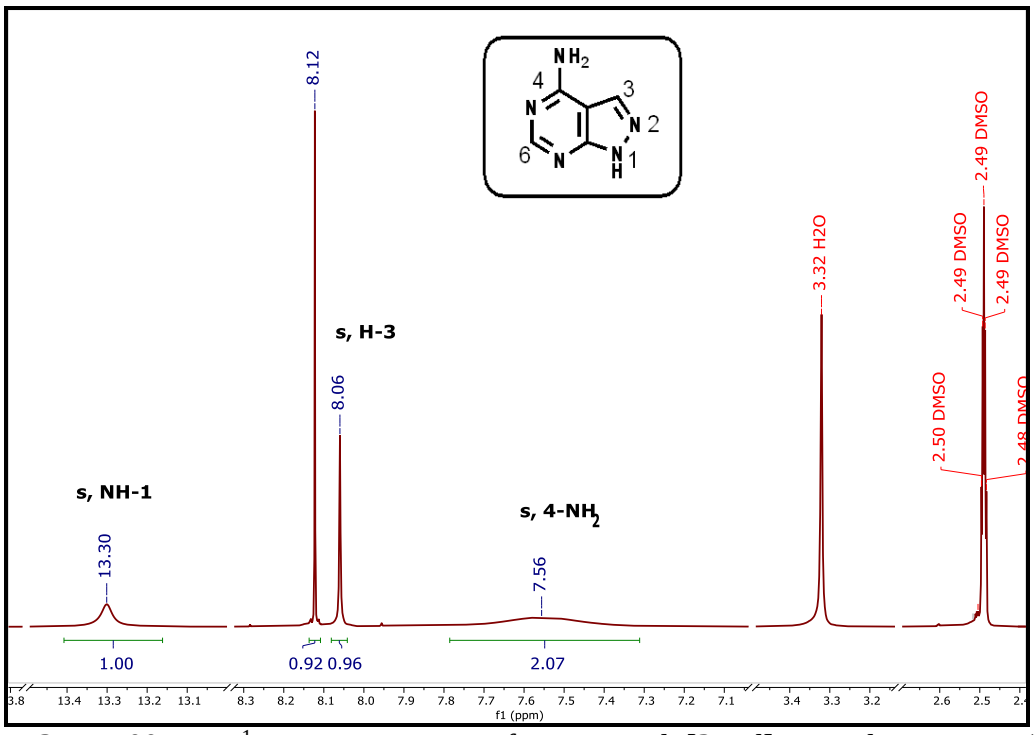

Figure 2.14: 400 MHz ^{1}H NMR spectrum of 1*H*-pyrazolo[3,4-d]pyrimidin-4-amine (**2**) in DMSO-d_6

Selective iodination of 1*H*-pyrazolo[3,4-*d*]pyrimidin-4-amine (**2**) at C-3 occurred via a high yielding (89%) aromatic nucleophilic substitution, hypothesized to proceed via the reaction mechanism illustrated in **Scheme 2.5**. The progression of this reaction was ensured by the electron-donating pyrazole nitrogen, which supplied a non-bonding pair of electrons, thereby pushing C-3 towards electrophilic substitution and consequent regioselective iodination with high yield. In the end, aromatization and charge stabilization is ensured by abstraction of a proton in the intermediate **2.5a** by the resonance-stabilized succinimide anion with release of succinimide as a by-product.[55]

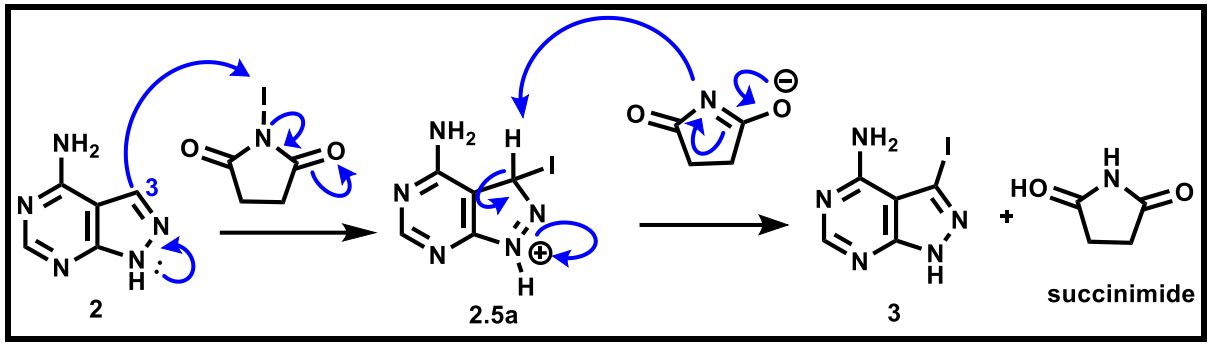

Scheme 2.5: Reaction mechanism for iodination in *N*-iodosuccinimide (NIS)

Successful iodination was confirmed via ^{1}H-NMR of **3**, with the most diagnostic feature being the loss of the pyrazole proton at C-3 resonating at δ_H 8.06 ppm for the initial precursor (**Figure 2.15**). As expected, the pyrimidine proton H-6 resonated as a singlet generally in the same aromatic region as observed in the starting compound and equally integrated for a single proton. Formation of this intermediate was also confirmed by HPLC-MS (atmospheric pressure chemical ionization $(APCI)^+$/electrospray ionization $(ESI)^+$- m/z; $[M + H]^+ = 262.0$; calculated exact mass = 261.0265), with low retention time (t_R) of 0.24 min and purity of 98% in the reversed-phase HPLC (Figure not displayed).

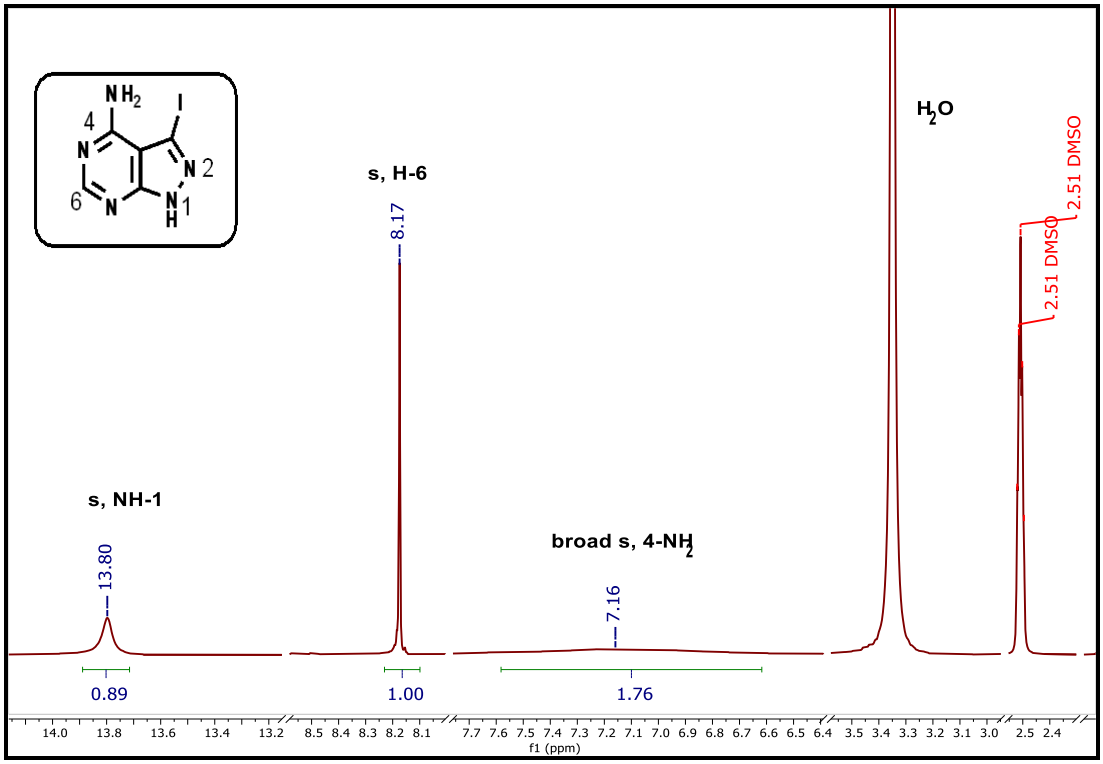

Figure 2.15: 400 MHz ^{1}H-NMR spectrum of the iodinated product, **3** in DMSO-d_6

Relevant *N*-alkylated intermediates such as **7a** (**GS 54**) were furnished in moderate yields (37-71%) via bimolecular nucleophilic substitution (S_N2) with the appropriate alkyl halide under basified conditions. To describe relevant reaction mechanisms resulting from this SAR exploration at N-1 position, compounds resulting from *N*-alkylation of 3-iodo-1*H*-pyrazolo[3,4-*d*]pyrimidin-4-amine (**3**) with 4-chlorobenzyl bromide to obtain **7a** (**GS 54**) and the target compound **7** (**GS 55**) will be used as illustrative examples.

In several instances, the required alkyl halides for *N*-alkylation were not commercially available and were synthesized from either their corresponding alcohols or carboxylic acids based on standard chlorination and reduction reactions. For example, the synthesis of intermediate **51a** (**GS 198**) commenced with the reduction of 5-fluoronicotinic acid in lithium aluminium hydride (LAH) to its corresponding alcohol, followed by chlorination using thionyl chloride in quantitative yields.[52,53] With the necessary alkyl halides at hand, the *N*-alkylation coupling reaction with the pyrazolo[3,4-*d*]pyrimidine were then initiated successfully. The mechanisms of these basic reactions have not been illustrated here but are standard and well-known.[56]

Among the key signals identified in the ^{1}H-NMR spectrum of **7a** (**GS 54**; **Figure 2.16**) are two sets of symmetrical doublets (d) observed at δ_H 7.35 and 7.23 ppm, each with J = 9.0 Hz. These

are indicative of *ortho* spin-spin coupling of the two sets of symmetrically aromatic protons, H-7, and H-8 (**Figure 2.16**), of the newly introduced *para*-substituted phenyl group. In addition, further diagnostics reveal presence of two electronically equivalent up-field protons appearing as a singlet at δ_H 5.46 ppm indicating presence of the methylene linker. These methylene protons resonate at higher frequencies than the expected range of 1.5–3.0 ppm due to the de-shielding effects of the α-nitrogen of the core.

Furthermore, and as theoretically expected, this resulted in the consequent disappearance of the down-fielded pyrazole proton which appeared at δ_H 13.30 ppm for the unsubstituted pyrazolopyrimidine intermediate. Accordingly, insertion of the various aromatic or aliphatic functionalities at N-1 of the pyrazolo[3,4-*d*]pyrimidine core led to the relevant peaks that were identified in the spectra of intermediates **6a**–**62a**.

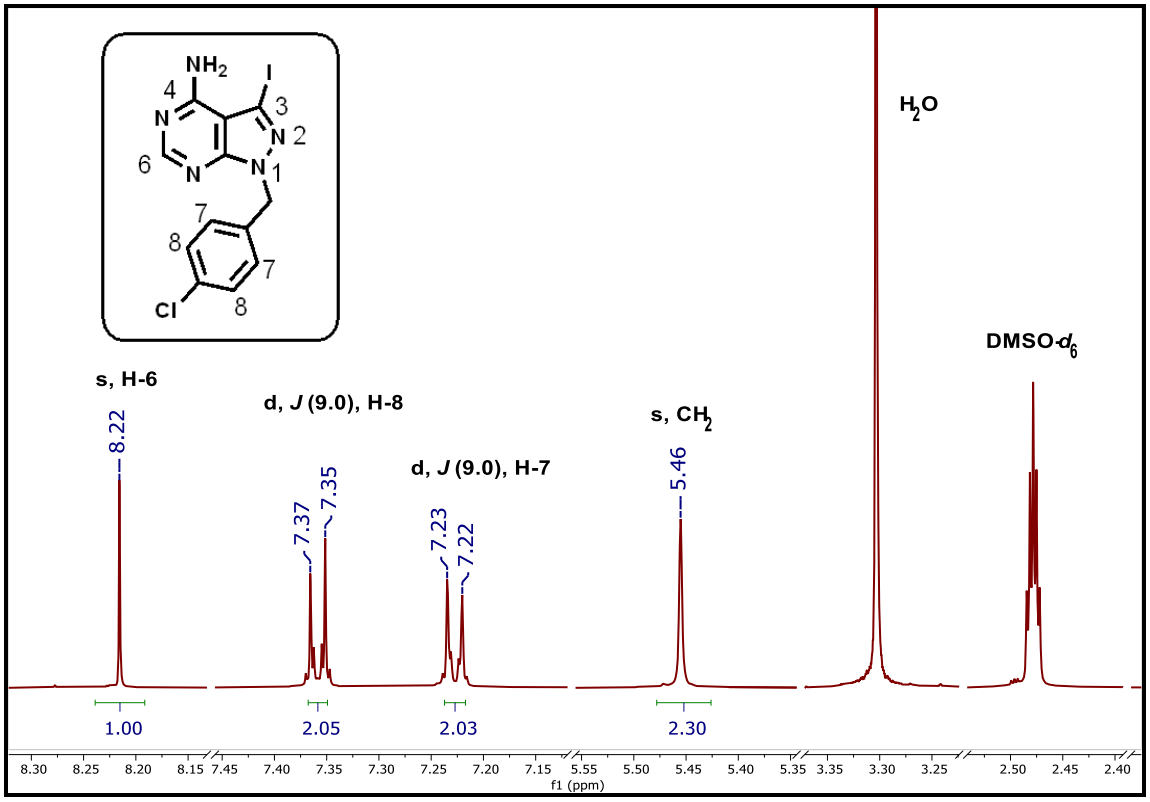

Figure 2.16: ^{1}H-NMR spectrum of *N*-alkylation product, **7a** (**GS 54**)

Generation of the important boronic ester intermediate **5** and the final target compounds was achieved via Suzuki-Boronation and Suzuki-Miyaura cross-coupling of the appropriate aryl halides and boronic acids/bis(pinacolato)diboron (B_2pin_2), respectively.[57] Suzuki-Miyaura cross-coupling of biaryl organoboron compounds with organic halides is an important C–C cross-coupling reactions, particularly at sp^2 and sp carbons where typical nucleophilic

substitution cannot occur. Indeed, the impact of this tremendously enabling reaction was recognized by its inclusion in the 2010 Nobel Prize in Chemistry. Its widespread application in organic synthesis is attributed to factors such as commercial availability of a wide variety of boronic acids/esters and Pd catalysts, compatibility with aqueous conditions, ease of product separation, and environmentally benign reaction conditions.[58] Suzuki boronation reaction, a closely related Pd-catalyzed cross-coupling reaction between an organic halide and B_2pin_2, was used to furnish the benzoxazole ester with a yield of 80%. Both reactions proceed via a similar mechanism as illustrated in **Figure 2.17**.[57]

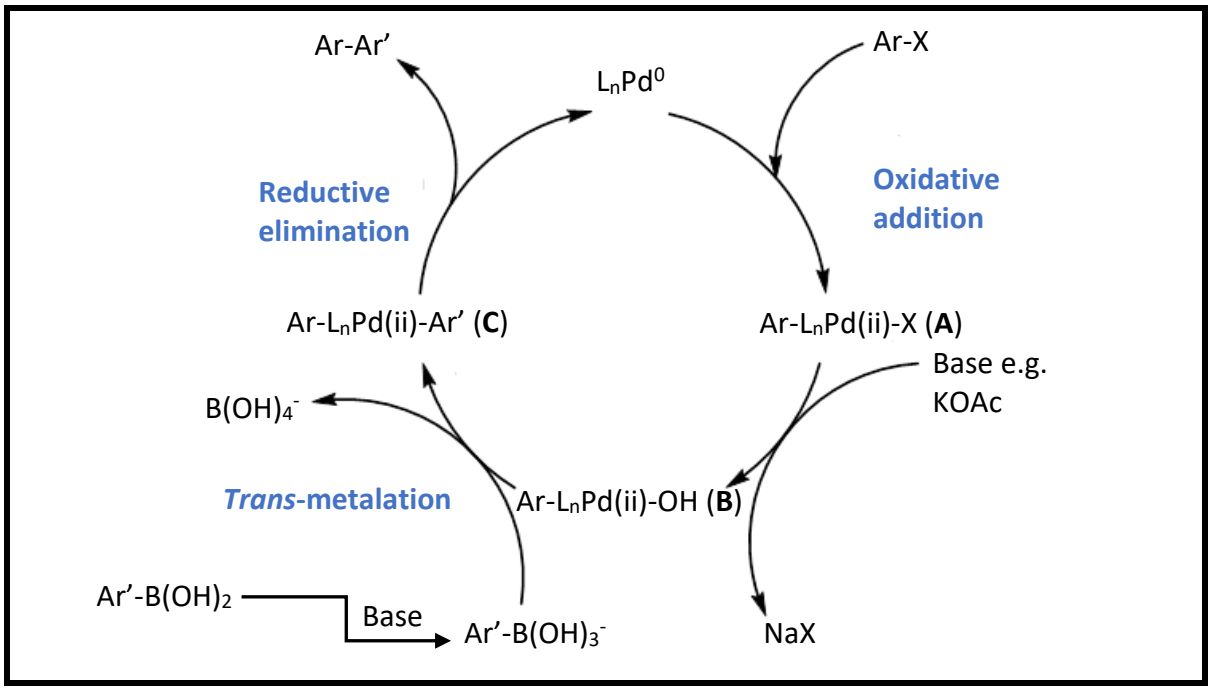

Figure 2.17: Catalytic cycle for Pd-catalyzed Suzuki-Miyaura cross-coupling reaction

A standard cross-coupling reaction proceeds via a catalytic cycle involving three major steps: oxidative addition, *trans*-metalation, and reductive elimination (**Figure 2.17**; **blue**). Oxidative addition of an aryl halide to a Pd(0) complex produces a stable *trans*-σ-Pd(II) complex **A** in an S_N2 reaction. In this case, either $Pd(PPh_3)_4$ or $Pd(dppf)Cl_2$ was used as the catalyst. This step is the rate-determining step for the reaction following the C–X strength bond order of I <Br <<Cl. Subsequently, displacement of the halide from complex **A** by a base, in this case KOAc, yields a more reactive basic organopalladium complex **B**, which then undergoes *trans*-metalation with the boronic acid. In case a boronic ester is used, it is hydrolyzed first in the basified conditions to its corresponding acid and used in the *trans*-metalation step. This is then

followed by isomerization to complex **C**. Ultimately, the biaryl product is expelled via reductive amination with regeneration of the Pd(0) catalyst to continue the cycle.[57]

The generated key intermediate **5** was identified via ^{1}H-NMR spectrum (**Figure 2.18**) displaying key signals associated with the transformation, with the most significant being the singlet at δ_H 0.55 ppm integrating for 12 protons. This accounted for the methyl hydrogens of the introduced pinacol ester. Additionally, three mutually coupled aromatic protons were observed resonating at δ_H 6.82 (d, J = 2.4 Hz), 6.68 (dd, J = 8.4 and 2.4 Hz), and 6.82 (d, J = 8.4 Hz) ppm accounting for H-6, H-4, and H-3, respectively. However, purification of this compound by column chromatography and trituration was difficult possibly due to partial hydrolysis to the corresponding boronic acid, with consequent generation of mixtures.

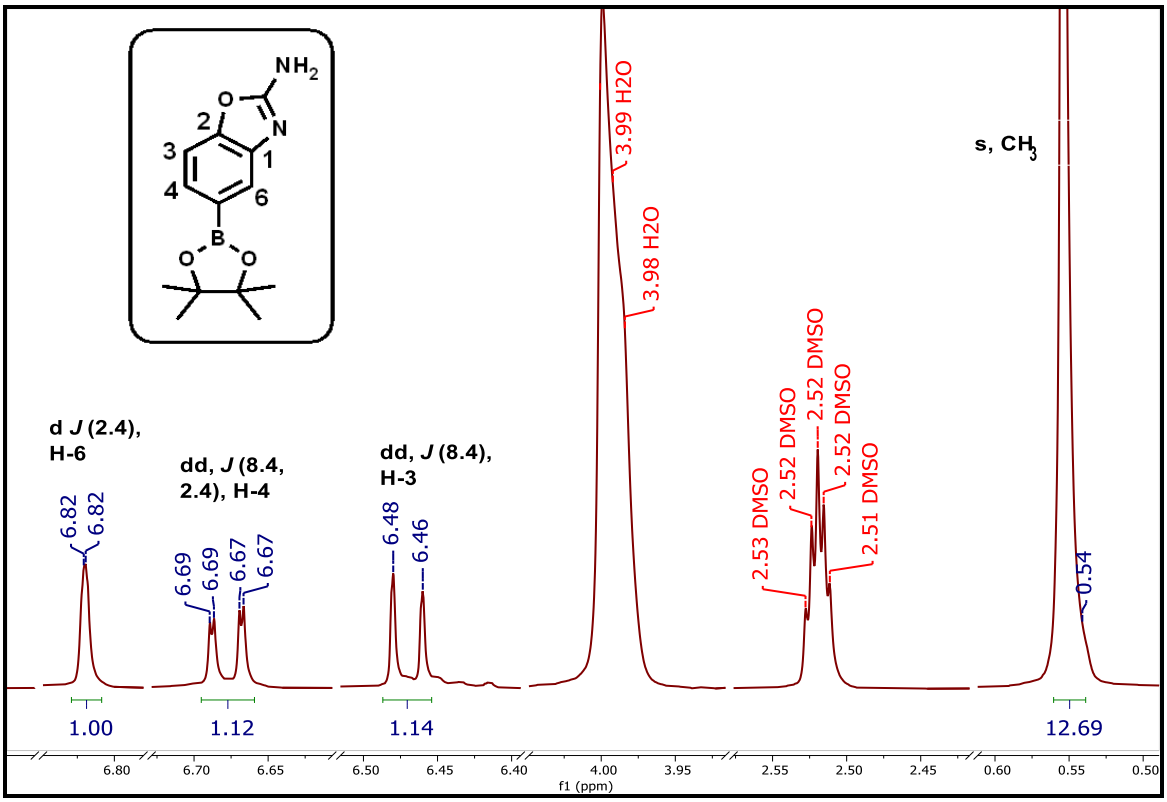

Figure 2.18: ^{1}H-NMR spectrum of the Suzuki boronation product, **5**

Overall, the Suzuki-Miyaura cross-coupling reaction performed to obtain the final compounds proceeded with the lowest yields (14–53%). Frequent low yields are encountered in this reaction because of self-coupling of reagents and products emanating from the phosphine-bound aryls of the catalyst producing scrambled derivatives.[59] Nevertheless, successful execution of this reaction to produce the target compounds, such as **7** (**GS 55**), was confirmed spectroscopically. Of particular note, the ^{1}H-NMR spectrum of this target compound (**Figure**

2.19) displays the presence of three, finely resolved mutually coupled aromatic protons resonating at δ_H 7.46 (d, *J* = 8.1 Hz), 7.40 (d, *J* = 1.7 Hz), and 7.23 ppm (dd, *J* = 8.1 and 1.7 Hz), which were assigned to H-3, H-6, and H-4, respectively, and a broad singlet at δ_H 7.52 ppm integrating for 2 protons. This was assigned to the amine protons (2H, NH_2-2'') of the benzoxazole part of the molecule. Additionally, the expected protons for the core scaffold and the benzyl component of the molecule were observed, resonating in a manner similar to that of the important precursor **7a** (**GS 54**; **Figure 2.16**), previously described.

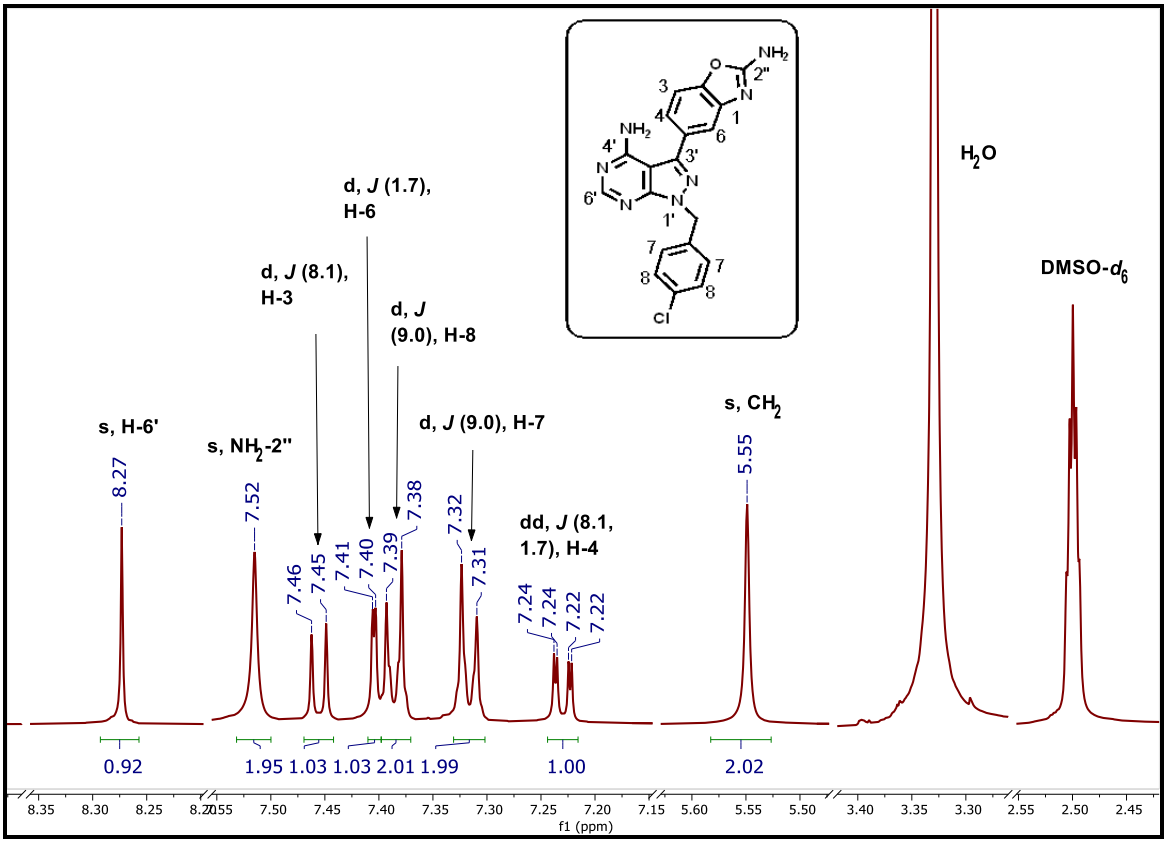

Figure 2.19: ^{1}H-NMR spectrum of target compound, **7** (**GS 55**)

However, additional multiplicity splitting in the ^{1}H-NMR spectrum was observed in fluorine-containing compounds, inclusive of trifluoromethyl pyridyl and benzyl compounds. For instance, the H-9 signal of the fluoropyridyl analogue **51** (**GS 199**; **Figure 2.20**) appeared at δ_H 7.60 ppm as a doublet of triplets (dt) with coupling constants 9.0 and 2.4 Hz. This unusual coupling pattern in ^{1}H-NMR spectra was associated with the *meta* coupling with H-7 and H-8 (*J* = 2.4 Hz), and *ortho* fluorine coupling (*J* = 9.0 Hz). Interestingly, the ^{1}H-^{19}F coupling was not observed for H-8 in **51** (**GS 199**), which appears as an up-field doublet (*J* = 2.4 Hz) at δ_H 8.47 ppm in this case and was equally absent in several other such analogues. This may be associated to the π- donating nitrogen adjacent to H-8 which suppresses ^{1}H-^{13}F coupling.

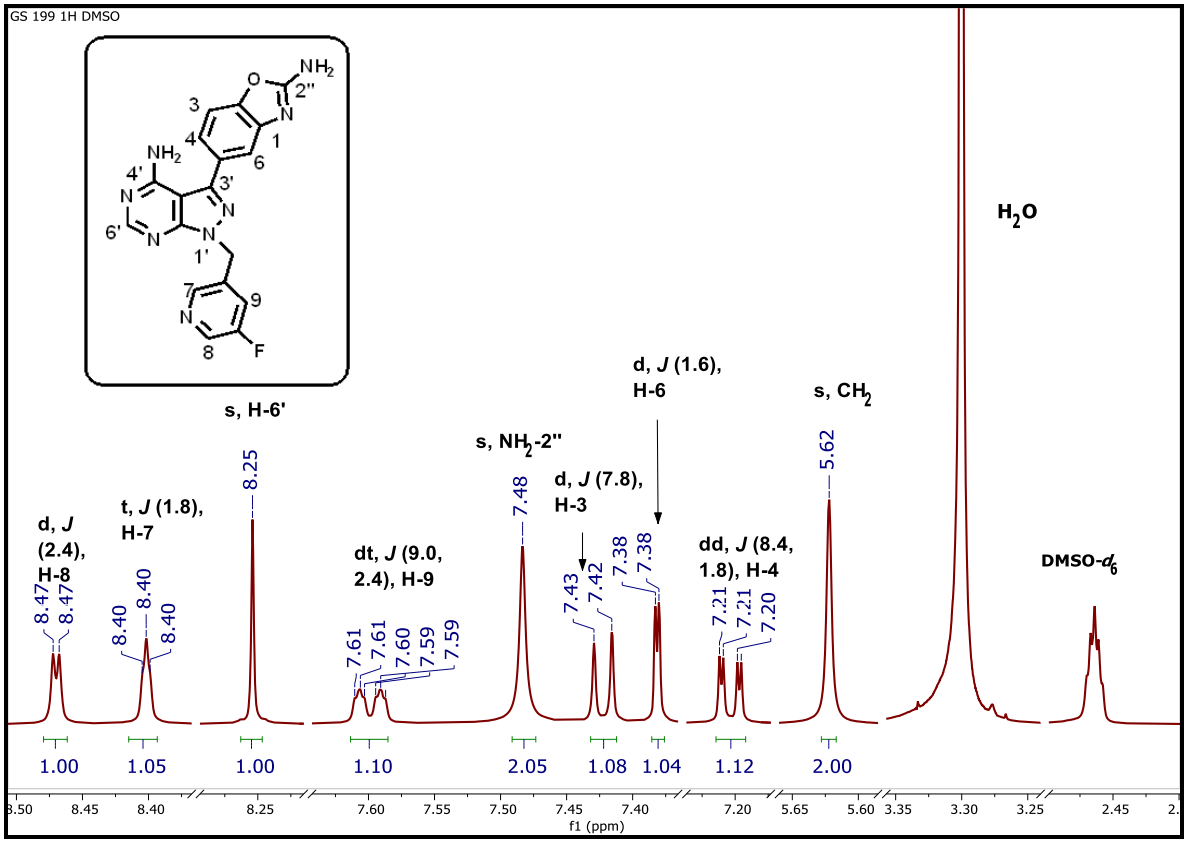

Figure 2.20: ^{1}H-NMR spectrum of target compound **51** (**GS 199**)

This fluorine coupling was also observed in the ^{13}C-NMR spectrum for all fluorine-containing compounds. For example, the spectrum of **51** (**GS 199**; **Figure 2.21**) delineates C-8' resonating as an overlapping doublet at δ_C 159.31 ppm with a large coupling constant (J = 253.7 Hz) typical of $^{1}J_{C\text{-}F}$ coupling.[60] Long range C–F coupling (3 to 4 bonds away) was also observed with four carbons signals resonating as doublets (d) at δ_C 145.61 ppm (J = 4.5 Hz, $^{4}J_{C\text{-}F}$), 137.52 ppm (J = 22.7 Hz, $^{2}J_{C\text{-}F}$), 135.21 ppm (J = 3.0 Hz, $^{3}J_{C\text{-}F}$), and 122.84 ppm (J = 19.6 Hz, $^{2}J_{C\text{-}F}$), assigned to C-7, C-8, C-7', and C-9, respectively.

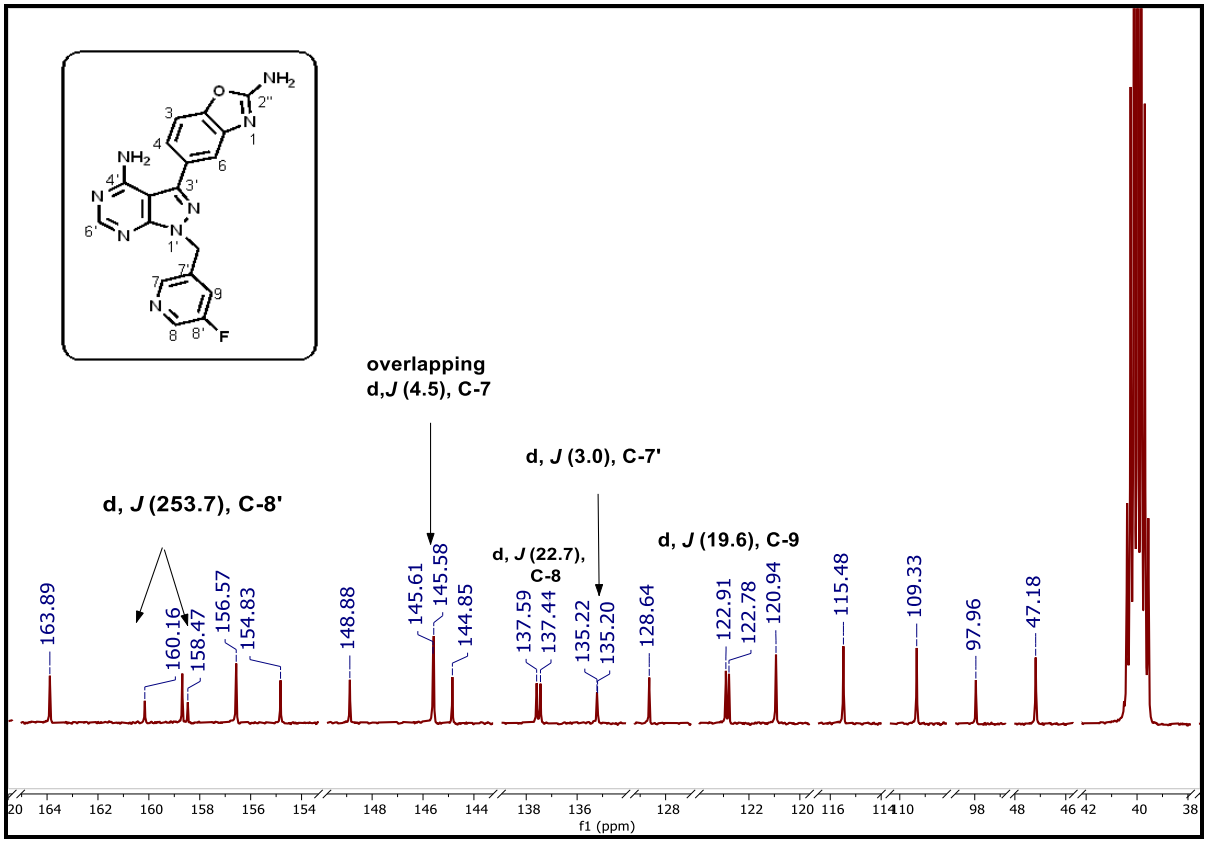

Figure 2.21: ^{13}C-NMR spectrum of target compound **51** (**GS 199**)

More sophisticated 2D NMR experiments, particularly HSQC and HMBC experiments, also provided insight into the observed fluorine coupling. For example, short-range (^1J) coupling was observed between H-9 resonating at δ_H 7.60 ppm (dt, J = 9.0 and 2.4 Hz) and C-9 at δ_C 122.84 ppm (d, J = 19.6 Hz). Long-range coupling (^3J) between the methylene carbon resonating down-field at δ_C 47.18 ppm with both C-7 and C-9 resonating as doublets at δ_C 145.61 ppm (J = 4.5 Hz) and δ_C 122.84 ppm (J = 19.6 Hz), respectively (**Figure 2.22**), further confirmed the assignment. Ultimately, the observed ^{13}C-NMR spectrum was resolved accounting for the 18 carbons of analogue **51**. Employing these 2D correlation experiments enabled assignment and accountment for all the expected carbons and protons of the synthesized compounds.

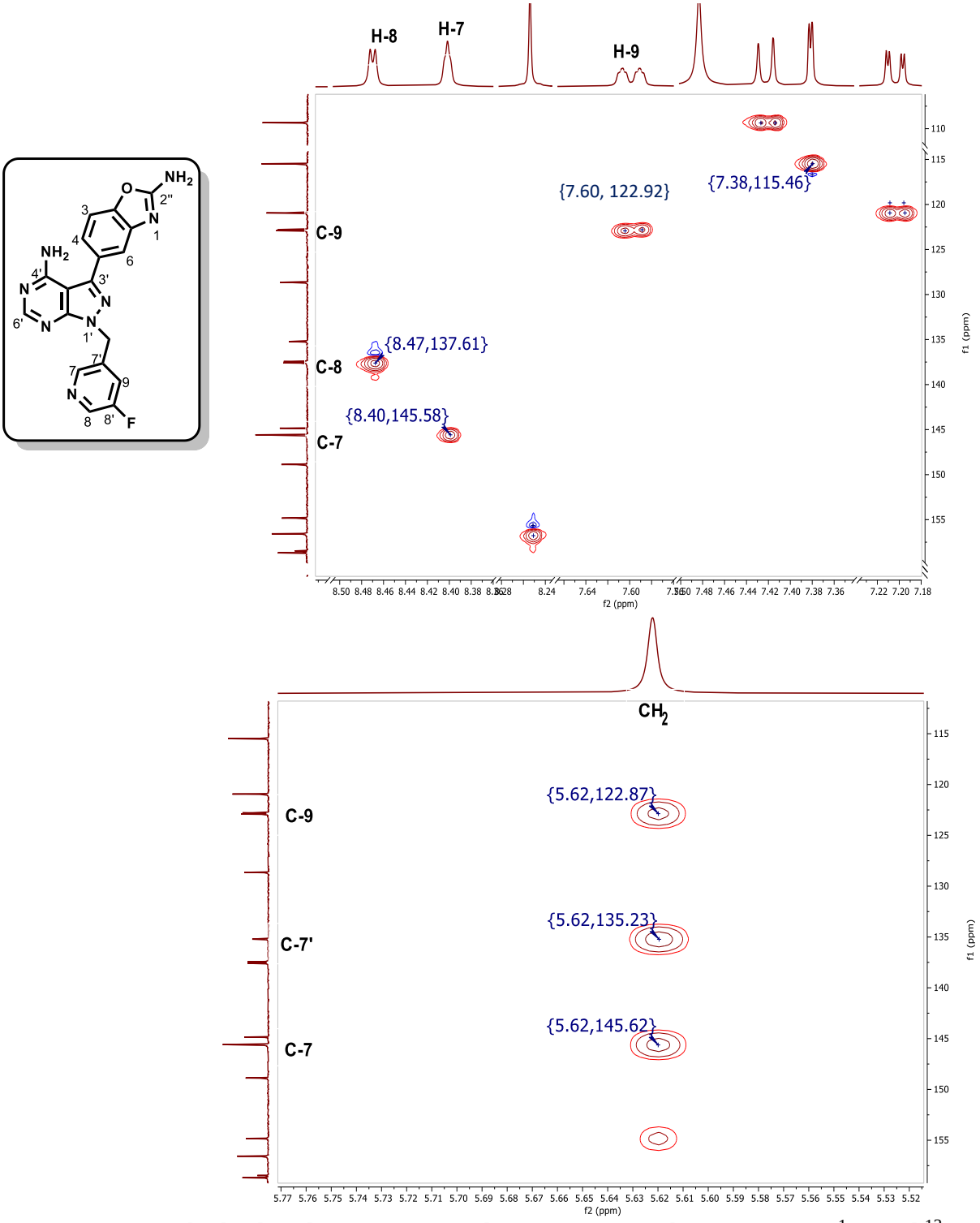

Figure 2.22: Partly displayed HSQC (top) and HMBC spectra showing various ^{1}H- and ^{13}C-NMR short- and long-range coupling for **51** (**GS 199**)

HPLC-MS analysis of these analogues further confirmed their successful synthesis with pseudo-molecular ion $[M+H]^+$ *m/z* peaks observed for all the compounds. As an example, a protonated molecular ion for the representative compound, **51** (**GS 199**), (calculated exact mass = 376.1196 g.mol^{-1}) was observed at 377.1 with a retention time (t_R) of 2.26 min (**Figure 2.23**).

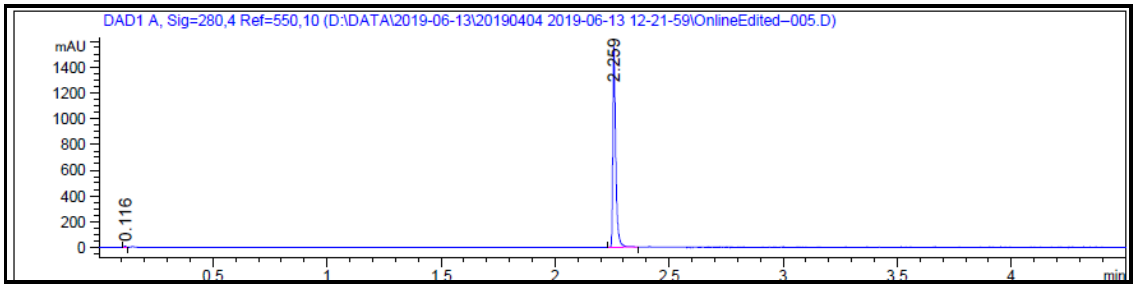

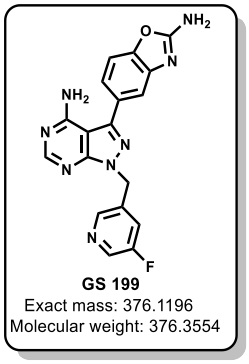

Signal 1: DAD1 A, Sig=280,4 Ref=550,10

Peak #	RetTime [min]	Type	Width [min]	Area [mAU*s]	Height [mAU]	Area %
1	0.116	BB	9.79e-3	5.29249	9.09375	0.3787
2	2.259	BV	0.0135	1392.26782	1540.68921	99.6213

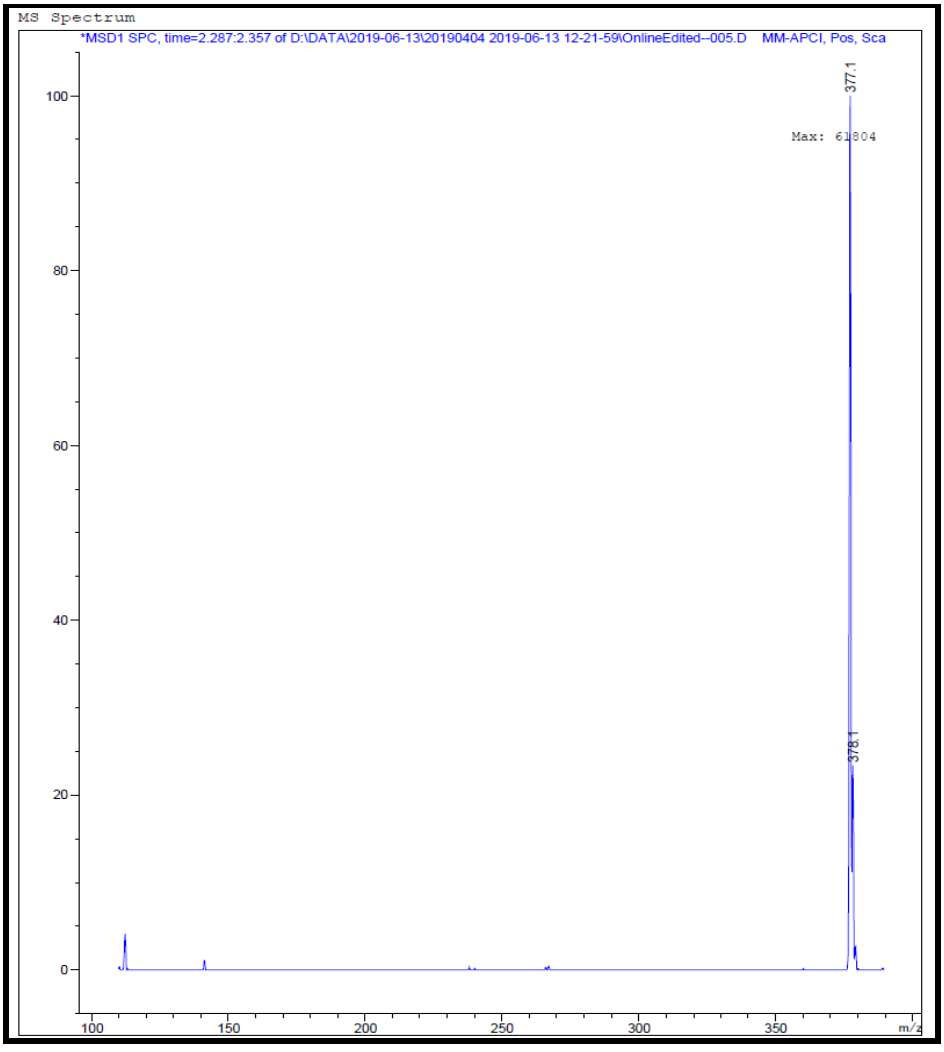

Figure 2.23: HPLC chromatogram and atmospheric pressure chemical ionization ($APCI^+$) mass spectrum of **51** (**GS 199**)

Overall, a small library of 57 target compounds (including MLN0128 compound) were successfully synthesised and fully characterised by ^{1}H-NMR, ^{13}C NMR, and selected 2D-NMR experiments (HSQC and HMBC). Their masses were then confirmed by the LC-MS for SAR and SPR studies. HPLC was used to assess purity with the satisfactory threshold for biological and physicochemical evaluation set at 95% under UV wavelength of 280 nM. Further characterization details of each compound and crucial intermediates are outlined in the experimental section (Chapter 10).

2.8 Chapter summary

In this chapter, the biochemical activities, as well as the liability of the hit compound as an antimalarial scaffold, were described laying ground for the rationale to reposition MLN0128 as explored in this study. Consequently, the broad aim and specific objectives of this part of the study have also been highlighted. The rational approach to the design and medicinal chemistry strategy employed in this work has been provided. Furthermore, the synthesis, spectroscopic characterization, and reaction mechanisms of intermediates and selected target compounds generated for this work have been described. In the next Chapter, the biological results of these compounds will be discussed.

References

1. Zeng, Z.; Wang, R.; Qiu, Y.; Mak, D.; Coombes, K.; Yoo, S.; Zhang, Q.; Jessen, K.; Liu, Y.; Rommel, C.; Fruman, D.; Kantarjian, H.; Kornblau, S.; Andreeff, M.; Konopleva, M. MLN0128, a novel mTOR kinase inhibitor, disrupts survival signaling and triggers apoptosis in AML and AML stem/ progenitor cells. *Oncotarget*. **2016**; 7 (34): 55083 - 55097. doi:10.18632/oncotarget.10397.

2. Rad, E.; Murray, J. and Tee A. Oncogenic signalling through mechanistic target of rapamycin (mTOR): A driver of metabolic transformation and cancer progression. *Cancers* **2018**; 10 (1): 1 - 17. doi:10.3390/cancers10010005.

3. DeSchuytner, B.; Kuvalanka, K.; Hibner, B. and Bolen, J. Takeda's oncology discovery strategy. *Jpn. J. Clin. Oncol*. **2013**; 43 (4): 357 - 361. doi:10.1093/jjco/hyt023.

4. Slotkin, E.; Patwardhan, P.; Vasudeva, S.; de Stanchina, E.; Tap, W.; Schwartz, G. MLN0128, an ATP-Competitive mTOR kinase inhibitor with potent *in vitro* and *in vivo* antitumor activity, as potential therapy for bone and soft-tissue sarcoma. *Mol. Cancer Ther*. **2015**; 14 (2): 395 - 406. doi:10.1158/1535-7163.MCT-14-0711.

5. Janes, M.; Vu, C.; Mallya, S.; Shieh, M.; Limon, J.; Li, L.; Jessen, K.; Martin, M.; Ren, P.; Lilly, M.; Sender, L.; Liu, Y.; Rommel, C.; Fruman, D. Efficacy of the investigational mTOR kinase inhibitor MLN0128/INK128 in models of B-cell acute lymphoblastic leukemia. *Leukemia*. **2013**; 27 (3): 586 - 594. doi:10.1038/leu.2012.276.

6. Moore, K.; Bauer, T.; Falchook, G.; Chowdhury, S.; Patel, C.; Neuwirth, R.; Enke, A.; Zohren, F.; Patel, M. Phase I study of the investigational oral mTORC1/2 inhibitor sapanisertib (TAK-228): tolerability and food effects of a milled formulation in patients with advanced solid tumours. *ESMO Open*. **2018**; 3 (2): e000291. doi:10.1136/esmoopen-2017-000291.

7. Ghobrial, I.; Siegel, D.; Vij, R.; Berdeja, J.; Richardson, P.; Neuwirth, R.; Patel, C.; Zohren, F,; Wolf, J. TAK-228 (formerly MLN0128), an investigational oral dual TORC1/2 inhibitor: A phase I dose escalation study in patients with relapsed or refractory multiple myeloma, non-Hodgkin lymphoma, or Waldenström's macroglobulinemia. *Am. J. Hematol*. **2016**; 91 (4): 400 - 405. doi:10.1002/ajh.24300.

8. Ismail, N.; Ali, G.; Ibrahim, D. and Elmetwali, A. Medicinal attributes of pyrazolo[1,5-a]pyrimidine based scaffold derivatives targeting kinases as anticancer agents. *Futur. J.*

Pharm. Sci. **2016**; 2 (2): 60 - 70. doi:10.1016/j.fjps.2016.08.004.

9. Schenone, S.; Brullo, C.; Musumeci, F.; Radi, M. and Botta, M. ATP-competitive inhibitors of mTOR: An update. *Curr. Med. Chem*. **2011**; 18 (20): 2995 - 3014. doi:10.2174/092986711796391651.

10. Ingels, A.; Zhao, H.; Thong, A.; Saar, M.; Valta, M.; Nolley, R.; Santos, J.; Peehl, D. Pre-clinical trial of a new dual mTOR inhibitor, MLN0128, using renal cell carcinoma tumorgrafts. *Int. J. Cancer*. **2014**; 134 (10): 2322 - 2329. doi:10.1002/ijc.28579.

11. Imseng, S.; Aylett, C. and Maier, T. Architecture and activation of phosphatidylinositol 3-kinase related kinases. *Curr. Opin. Struct. Biol*. **2018**; 49: 177 - 189. doi:10.1016/j.sbi.2018.03.010.

12. Saxton, R. and Sabatini, D. mTOR signaling in growth, metabolism, and disease. *Cell*. **2017**; 168 (6): 960 - 976. doi:10.1016/j.cell.2017.02.004.

13. Laplante, M. and Sabatini, D. mTOR signaling at a glance. *J. Cell. Sci*. **2009**; 122 (20): 3589 - 3594. doi:10.1242/jcs.051011.

14. Takei, N. and Nawa, H. mTOR signaling and its roles in normal and abnormal brain development. *Front. Mol. Neurosci*. **2014**; 7 (4): 1 - 12. doi:10.3389/fnmol.2014.00028.

15. Kim, J. and Guan, K. mTOR as a central hub of nutrient signalling and cell growth. *Nat. Cell Biol*. **2019**; 21 (1): 63 - 71. doi:10.1038/s41556-018-0205-1.

16. Zou, Z.; Tao, T.; Li, H. and Zhu, X. MTOR signaling pathway and mTOR inhibitors in cancer: Progress and challenges. *Cell Biosci*. **2020**; 10 (1): 1 - 11. doi:10.1186/s13578-020-00396-1.

17. Martelli, A.; Buontempo, F. and McCubrey, J. Drug discovery targeting the mTOR pathway. *Clin. Sci*. **2018**; 132 (5): 543 - 568. doi:10.1042/CS20171158.

18. Arendse, L.; Wyllie, S.; Chibale, K. and Gilbert, I. *Plasmodium* kinases as potential drug targets for malaria: Challenges and opportunities. *ACS Infect. Dis*. **2021**; 12 (7): 518 - 534. doi:10.1021/acsinfecdis.0c00724.

19. Lucet, I.; Tobin, A.; Drewry, D. and Wilks, A. *Plasmodium* kinases as targets for new-generation antimalarials. *Future Med. Chem*. **2012**; 4 (18): 2295 - 2310.

20. Cabrera, D.; Horatscheck, A.; Wilson, C.; Basarab, G.; Eyermann, C.; Chibale, K.

Plasmodial kinase inhibitors: License to cure? *J. Med. Chem*. **2018**; 61 (18): 8061 - 8077. doi:10.1021/acs.jmedchem.8b00329.

21. Paquet, T.; Le Manach, C.; Cabrera, D.; Younis Y.; Henrich, P.; Abraham T.; Lee, M.; Basak R.; Ghidelli-Disse, S.; Lafuente-Monasterio, M.; Bantscheff, M.; Ruecker, A.; Blagborough, A.; Zakutansky, S.; Zeeman, A.; White, K.; Shackleford, D.; Mannila, J.; Morizzi, J.; Scheurer, C.; Angulo-Barturen, I.; Martínez, M.; Ferrer, S.; Sanz, L.; Gamo, F.; Reader, J.; Botha, M.; Dechering, K.; Sauerwein, R.; Tungtaeng, A.; Vanachayangkul, P.; Lim, C.; Burrows, J.; Witty, M.; Marsh, K.; Bodenreider, C.; Rochford, R.; Solapure, S.; Jiménez-Díaz, M.; Wittlin, S.; Charman, S.; Donini, C.; Campo, B.; Birkholtz, L.; Hanson, K.; Drewes, G.; Kocken, C.; Delves, M.; Leroy, D.; Fidock, D.; Waterson, D.; Street, L.; Chibale, K. Antimalarial efficacy of MMV390048, an inhibitor of *Plasmodium* phosphatidylinositol 4-kinase. *Sci. Transl. Med*. **2017**; 9 (387): 1 - 15. doi:10.1126/scitranslmed.aad9735.

22. Okombo, J. and Chibale, K. Recent updates in the discovery and development of novel antimalarial drug candidates. *Med. Chem. Comm*. **2018**; 9 (3): 437 - 453. doi:10.1039/c7md00637c.

23. Baker, D.; Stewart, L.; Large, J.; Bowyer, P.; Ansell, K.; Jiménez-Díaz, M.; El Bakkouri, M.; Birchall, K.; Dechering, K.; Bouloc, N.; Coombs, P.; Whalley, D.; Harding, D.; Smiljanic-Hurley, E.; Wheldon, M.; Walker, E.; Dessens, J.; Lafuente, M.; Sanz, L.; Gamo, F.; Ferrer, S.; Hui, R.; Bousema, T.; Angulo-Barturén, I.; Merritt, A.; Croft, S.; Gutteridge, W.; Kettleborough, C.; Osborne, S. A potent series targeting the malarial cGMP-dependent protein kinase clears infection and blocks transmission. *Nat. Commun*. **2017**; 8 (1): 1 - 9. doi:10.1038/s41467-017-00572-x.

24. Baker, D.; Matralis, A.; Osborne, S.; Large, J. and Penzo, M. Targeting the malaria parasite cGMP-dependent protein kinase to develop new drugs. *Front. Microbiol*. **2020**; 11 (12): 1 - 8. doi:10.3389/fmicb.2020.602803.

25. Koussis, K.; Withers-Martinez, C.; Baker, D. and Blackman, M. Simultaneous multiple allelic replacement in the malaria parasite enables dissection of PKG function. *Life Sci. Alliance*. **2020**; 3 (4): 1 - 14. doi:10.26508/LSA.201900626.

26. Matralis, A.; Malik, A.; Penzo, M.; Moreno, I.; Almela, M.; Camino, I.; Crespo, B.; Saadeddin, A.; Ghidelli-Disse, S.; Rueda, L.; Calderon, F.; Osborne, S.; Drewes, G.;

Böesche, M.; Fernández-Á lvaro, E.; Hernando, J.; Baker, D. Development of chemical entities endowed with potent fast-killing properties against *Plasmodium falciparum* malaria parasites. *J. Med. Chem*. **2019**; 62 (20): 9217 - 9235. doi:10.1021/acs.jmedchem.9b01099.

27. Kelleni, M. Drug induced cardiotoxicity: Mechanism, prevention and management. In: Tan MAE-W, ed. Rijeka: IntechOpen; **2018**: Ch. 7. doi:10.5772/intechopen.79611.

28. Kalyaanamoorthy, S. and Barakat, K. Development of safe drugs: The hERG challenge. *Med. Res. Rev*. **2018**; 38 (2): 525 - 555. doi:10.1002/med.21445.

29. Fienberg, S.; Eyermann, C.; Arendse, L.; Basarab, G.; McPhail, J.; Burke, J.; Chibale, K. Structural basis for inhibitor potency and selectivity of *plasmodium falciparum* phosphatidylinositol 4-kinase inhibitors. *ACS Infect. Dis*. **2020**; 6 (11): 3048 - 3063. doi:10.1021/acsinfecdis.0c00566.

30. Zuccotto, F.; Ardini, E.; Casale, E. and Angiolini, M. Through the "gatekeeper door": Exploiting the active kinase conformation. *J. Med. Chem*. **2010**; 53 (7): 2681 - 2694. doi:10.1021/jm901443h.

31. Huang, D.; Zhou, T.; Lafleur, K.; Nevado, C. and Caflisch, A. Kinase selectivity potential for inhibitors targeting the ATP binding site: A network analysis. *Bioinformatics*. **2010**; 26 (2): 198 - 204. doi:10.1093/bioinformatics/btp650.

32. Dornan, G.; McPhail, J. and Burke, J. Type III phosphatidylinositol 4 kinases: Structure, function, regulation, signalling and involvement in disease. *Biochem. Soc. Trans*. **2016**; 44: 260 - 266. doi:10.1042/BST20150219.

33. Babu, M. The contribution of intrinsically disordered regions to protein function, cellular complexity, and human disease. *Biochem. Soc. Trans*. **2016**; 44 (5): 1185 - 1200. doi:10.1042/BST20160172.

34. Boura, E. and Nencka, R. Phosphatidylinositol 4-kinases: Function, structure, and inhibition. *Exp. Cell Res*. **2015**; 337 (2): 136 - 145. doi:10.1016/j.yexcr.2015.03.028.

35. Njogu, P.; Guantai, E.; Pavadai, E. and Chibale, K. Computer-Aided drug discovery approaches against the tropical infectious diseases malaria, tuberculosis, trypanosomiasis, and leishmaniasis. *ACS Infect. Dis*. **2016**; 2 (1): 8 - 31. doi:10.1021/acsinfecdis.5b00093.

36. Bakkaouri, M.; Kouidmi, I.; Wernimont, A.; Amani, M.; Hutchinson, A.; Loppnau, P. Structures of the cGMP-dependent protein kinase in malaria parasites reveal a unique structural relay mechanism for activation. *Proc. Natl. Acad. Sci.* **2019**: 1 - 10. doi:10.1073/pnas.1905558116.

37. Cheuka, P.; Centani, L.; Arendse, L.; Fienberg, S.; Wambua, L.; Renga, S.; Dziwornu, G.; Kumar, M.; Lawrence, N.; Taylor, D.; Wittlin, S.; Coertzen, D.; Reader, J.; van der Watt, M.; Birkholtz, L.; Chibale, K. New amidated 3,6-diphenylated imidazopyridazines with potent antiplasmodium activity are dual inhibitors of *Plasmodium* phosphatidylinositol-4-kinase and cGMP-dependent protein kinase. *ACS Infect. Dis*. **2021**; 7 (1): 34 - 46. doi:10.1021/acsinfecdis.0c00481.

38. Craig, P. Interdependence between physical parametess and selection of substituent groups for correlation studies. *J. Med. Chem*. **1971**; 14 (8): 680 - 684. doi:10.1021/jm00290a004.

39. Pantsar, T. and Poso, A. Binding affinity via docking: Fact and fiction. *Molecules*. **2018**; 23 (8): 1 - 11. doi:10.3390/molecules23081899.

40. Miljković, F. and Bajorath, J. Exploring selectivity of multikinase inhibitors across the human kinome. *ACS Omega*. **2018**; 3 (1): 1147 - 1153. doi:10.1021/acsomega.7b01960.

41. Moolman, C.; Sluis, R.; Beteck, R. and Legoabe, L. An update on development of small-molecule *Plasmodial* kinase inhibitors. *Molecules*. **2020**; 25 (21): 1 - 45. doi:10.3390/molecules25215182.

42. Schenone, S.; Radi, M.; Musumeci, F.; Brullo, C. and Botta, M. Biologically driven synthesis of pyrazolo[3,4- *d*]pyrimidines as protein kinase inhibitors: An old scaffold as a new tool for medicinal chemistry and chemical biology studies. *Chem. Rev*. **2014**; 114 (14): 7189 - 7238. doi:10.1021/cr400270z.

43. Ren, P.; Liu, Y.; Troy, W.; Li, L. and Chan, K. Benzoxazole kinase inhibitors and method of use. US Patent. No. 8476282 B2. *USA Pat*. **2013**; 1: 1 - 182.

44. Todorovic, N.; Awuah, E.; Shakya, T.; Wright, G. and Capretta, A. Microwave-assisted synthesis of N1- and C3-substituted pyrazolo[3,4-*d*] pyrimidine libraries. *Tetrahedron Lett*. **2011**; 52 (44): 5761 - 5763. doi:10.1016/j.tetlet.2011.08.103.

45. Gunda, P.; Russon, L. and Lakshman, M. Pd-Catalyzed amination of nucleoside

arylsulfonates to yield N6-aryl-2,6-diaminopurine nucleosides. *Angew Chem. Int. Ed. Engl.* **2004**; 43: 6372 - 6377. doi:10.1002/anie.200460782.

46. Thompson, A.; Hughes, G.; Batsanov, A.; Bryce, M.; Parry, P.; Tarbit, B. Palladium-catalyzed cross-coupling reactions of pyridylboronic acids with heteroaryl halides bearing a primary amine group: Synthesis of highly substituted bipyridines and pyrazinopyridines. *J. Org. Chem*. **2005**; 70 (1): 388 - 390. doi:10.1021/jo0402226.

47. Itoh, T. and Mase, T. Direct synthesis of hetero-biaryl compounds containing an unprotected NH_2 group via Suzuki–Miyaura reaction. *Tetrahedron Lett.* **2005**; 46: 3573 - 3577. doi:10.1016/j.tetlet.2005.03.053.

48. Nair, R. and Bannister, T. Tale of two protecting groups - Boc vs SEM - For directed lithiation and C-C bond formation on a pyrrolopyridazinone core. *Org. Process Res. Dev*. **2016**; 20 (7): 1370 - 1376. doi:10.1021/acs.oprd.6b00128.

49. Greene, T. and Wuts, P. *Greene's Protective Groups in Organic Synthesis*. 4th ed. New Jersey, USA: John Wiley and Sons, Inc.; **2007**.

50. Shaw, I. and Francisco, S. (12) United States Patent (10) Patent No.: (45) Date of patent: **2014**; 1 (12). doi:10.1021/n10602701.

51. Hartwig, J.; Shekhar, S.; Shen, Q. and Barrios-Landeros, F. *Synthesis of Anilines*.; **2009**. doi:10.1002/9780470682531.pat0391.

52. Mao, L.; Zhao, L.; Liu, J.; Wang, X. and Xu, X. Pyrazolopyrimidine derivatives and their preparation and use as anticancer agents; PCT 2012097196. **2012**: 1 - 89.

53. Škalamera, D.; Blažek Bregović, V.; Antol, I.; Bohne, C. and Basarić, N. Hydroxymethylaniline photocages for carboxylic acids and alcohols. *J. Org. Chem.* **2017**; 82 (23): 12554 - 12568. doi:10.1021/acs.joc.7b02314.

54. Hasanein, A. and Senior, S. DFT calculations of amine-imine tautomerism in some pyrimidine derivatives and their 1:1 and 1:2 complexes with water. *Int. J. Quantum Chem*. **2011**; 111: 3993 - 4010. doi:10.1002/qua.22739.

55. Carreno, M.; Ruano, J.; Sanz, G.; Toledo, M. and Urbano, A. Mild and regiospecific nuclear iodination of methoxybenzenes and napthalenes with *N*-iodosuccinimide in acetonitrile. *Tetrahedron Lett*. **1996**; 37 (23): 4081 - 4084.

56. Smith, M. and March, J. *March's Advanced Organic Chemistry*. 6th ed. John Wiley and Sons; **2006**. doi:10.1002/0470084960.

57. Miyaura, N. and Suzuki, A. Palladium-catalyzed cross-coupling reactions of organoboron compounds. *Chem. Rev*. **1995**; 95 (7): 2457 - 2483. doi:10.1021/cr00039a007.

58. Rocard, L. and Hudhomme, P. Recent developments in the Suzuki–Miyaura reaction using nitroarenes as electrophilic coupling reagents. *Catalysts* **2019**; 9 (3): 4 - 11. doi:10.3390/catal9030213.

59. Kotha, S., Lahiri, K. and Kashinath, D. Recent applications of the Suzuki-Miyaura cross-coupling reaction in organic synthesis. *Tetrahedron* **2002**; 58 (48): 9633 - 9695. doi:10.1016/S0040-4020(02)01188-2.

60. Gierczyk, B.; Kaźmierczak, M.; Popenda, Ł.; Sporzyński, A.; Schroeder, G.; Jurga, S. Influence of fluorine substituents on the NMR properties of phenylboronic acids. *Magn. Reson. Chem*. **2014**; 52 (5): 202 - 213. doi:10.1002/mrc.4051.

CHAPTER 3

BIOLOGICAL ACTIVITY OF MLN0128 AND RELATED ANALOGUES

3.1 Chapter overview

In this chapter, the biological and biochemical activities of the synthesized target compounds will be discussed. The chapter begins with a discussion on the *in vivo* antimalarial efficacy and mechanism of action studies for the lead compound, MLN0128, highlighting its antimalarial potential and generally that of the series. The *in vitro* asexual blood stage and the *Plasmodium* PI4K and PKG inhibitory activity of MLN0128 and related analogues is then presented. The gametocytocidal activity of the synthesized compounds generated in this study is then discussed, as well as cytotoxicity, microsomal metabolic stability, and off-target inhibitory activity against the human orthologue PI4KIIIβ and human mTOR. Progressively, the anti-plasmodium and enzymatic inhibitory activities of the compounds are rationalized using the homology model of *Pf*PI4K and crystal structures of *Pv*PKG and human mTOR and PI4KIIIβ kinases.

3.2 Biological evaluation of MLN0128 and related analogues

3.2.1 *In vivo* antimalarial blood stage activity of MLN0128 in a *Pf*SCID mouse model

Pre-clinical studies of MLN0128 as an mTOR inhibitor for oncology showed its favorable ADME and oral PK properties in xenograft solid tumor mouse models (*in vivo* anti-tumor efficacy): 90% effective dose (ED_{90}), po, qd = 1.0 $mg.kg^{-1}$; bioavailability (% F) = 90%; fast oral absorption profile with T_{max} = 0.25–0.5 h; and an observed half-life ($t_{1/2}$) of 1.5 h. These appealing ADME/PK parameters ultimately led to its progression to human clinical studies as an oncological drug.[1] Accordingly, and further warranted by the recent discovery of its anti-plasmodium potency, an antimalarial proof-of-concept study was performed in a non-obese diabetic severe combined immunodeficiency gamma (NOD-SCID IL2Rγ^{null}) murine malaria model of *Pf* infection. Although it is expensive and logistically demanding, this murine model provides a platform for *in vivo* investigation of therapeutic efficacy against *Pf*, which almost exclusively infects human erythrocytes.[2]

NOD-SCID IL2Rγ^{null} (NSG) mice possess innate immune deficiencies such as immature T and B cells, while the null mutation of the interleukin 2 receptor γ (IL2Rγ) chain blocks mature natural killer (NK) cell development.[2] As a result, the model supports engraftment with human erythrocytes and *Pf* infection. Additionally, despite accommodating high infection burdens,

this model shows low incidences of early thymic lymphomas with long lifespan, thus allowing extensive PK/PD studies. It therefore offers a clear advantage of better efficacy prediction for human malaria than the alternative rodent-adapted *P. berghei* infection model.[3]

The *in vivo* proof-of-concept study on the NSG mouse model was conducted at the UCT's Holistic Drug Discovery and Development (H3D) Centre, Division of Clinical Pharmacology, Department of Medicine, according to methods previously described.[4] In brief, a cohort of age-matched, female, NSG mice grafted with human erythrocytes in peripheral circulation were initially prepared. The mice were then intravenously infected with *Pf*3D70087/N9-infected erythrocytes on day 0. On day 3, mice selected randomly were administered a daily dose of the formulated compound (0, 0.05, 0.1, 0.5, 1.0, or 10 $mg.kg^{-1}$) for four consecutive days via oral gavage (n = 2 per dose group). Parasitemia was measured in blood samples harvested every 24 h until assay completion via flow cytometry. A detailed description of this experiment is provided in Chapter 10.

Following this *in vivo* experiment, an impressive reduction in parasitemia (98%) was observed in the *Pf*-infected NSG mice treated with MLN0128 at a single daily dose of 1.0 $mg.kg^{-1}$ (**Figure 3.1**). Single doses of 0.05, 0.1, and 0.5 $mg.kg^{-1}$ were less effective. The compound achieved a satisfactory ED_{90} of 0.88 $mg.kg^{-1}$ at day 7 in this model. This result provided the vital proof-of-concept that the test compound achieved systemic exposure following oral administration and displayed antimalarial activity in an experimental animal model. However, a complete parasite clearance was not achieved by administration of 1.0 $mg.kg^{-1}$ compound, possibly because of the slow killing kinetics of the drug and unfortunately, both animals in the 10 $mg.kg^{-1}$ group reached a humane endpoint before day 7 of the study (weight loss > 15%). This is likely due to the narrow safety margin of the compound as evaluated in CHO (SI = 2) and HepG2 cells (SI = 100). The efficacy study also suggested that plasma saturation was reached with administration of this dose.

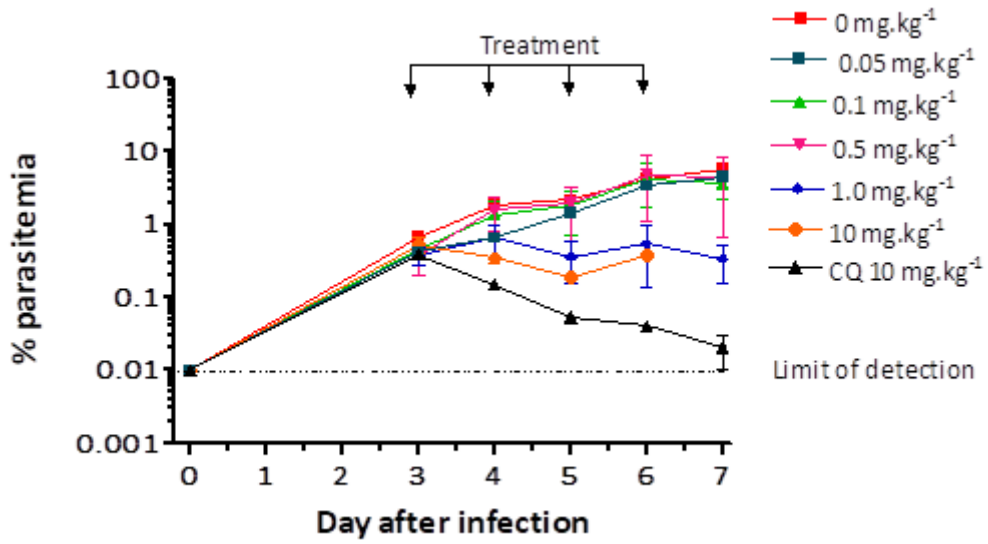

Figure 3.1: *In vivo* efficacy of **MLN0128** (**62**; **GS 20b**) in a non-obese diabetic (NOD)-severe combined immunodeficiency (SCID) mouse model of *P. falciparum* infection

3.2.2 *In vivo* PK profile of MLN0128 (62; GS 20b)

To rationalize the observed efficacy, mouse plasma PK snapshot studies were undertaken on infected mice. Following the first oral administration, PK parameters were assessed by monitoring compound concentrations in blood via LC-MS. A detailed description of this method is provided in the experimental chapter. Briefly, serial samples of peripheral blood (25 µL) were obtained via tail puncture from mice included in the efficacy experiment at 0.25, 0.5, 1, 3, 6, 8, 18, and 23 h after administration and prepared.

Efficacy was estimated from drug concentrations over 24 h (**Figure 3.2**) and was expressed as the daily exposure (area under the curve (AUC), µg.h/mL/day) of the drug in whole-blood required to reduce parasitemia at day 7 by 90% relative to that in vehicle-treated mice.

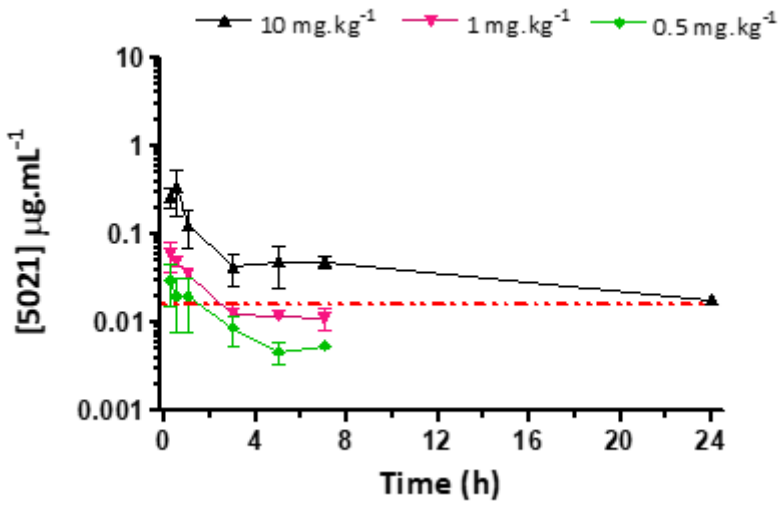

Figure 3.2: Plasma concentrations of **MLN0128** (**62**) following oral administration in a non-obese diabetic (NOD)-severe combined immunodeficiency (SCID) mouse model of *P. falciparum* infection

Compound exposure increased with increasing dose, as indicated by the $AUC_{(0-24)}$ at the various doses (**Table 3.1**). The compound displayed relatively fast absorption with the maximum concentration (C_{max}) reached in 0.38 h (T_{max}) for both 1- and 10-mg.kg^{-1} doses. However, the estimated average daily exposure in whole-blood necessary to achieve the ED_{90}, denoted as $AUCED_{90}$, could not be calculated because exposure levels in the 0.1 and 0.05 mg.kg^{-1} groups were below the limit of quantification. Furthermore, PK studies on healthy mice were not undertaken for comparative studies, as the *in vivo* PK data on the infected mice was deemed as a better indicator of observed antimalarial efficacy. The fact that the compound is in the advanced stages of human clinical trials also indicates it possesses favorable PK parameters.

Table 3.1: Mean pharmacokinetic parameters of MLN0128 (**62**) after dosing in a non-obese diabetic (NOD)-severe combined immunodeficiency (SCID) mouse model

Parameter	Oral dose administered		
	10 mg.kg^{-1}	**1 mg.kg^{-1}**	**0.5 mg.kg^{-1}**
C_{max} (µg.mL^{-1})	0.43 (0.14)	0.07 (0.02)	0.03 (0.02)
$AUC_{(0-24)}$ (µg.h.mL^{-1})	0.84 (0.19)	0.14 (0.01)	0.07 (0.05)
T_{max} (h)	0.38 (0.18)	0.38 (0.18)	0.25 (0.00)

3.2.3 Metabolomic studies of MLN0128, (62; GS 20b)

Metabolomic studies of MLN0128 were performed to further investigate the antimalarial mode-of-action (MoA) of this compound using methods described by Allman *et al*.[5] This work was performed at the Department of Chemistry and Molecular Biology, Pennsylvania State University, USA. These studies investigate changes in metabolite levels via ultra-high-performance liquid chromatography-mass spectrometry (UHPLC-MS) as signatures of a biochemical pathway perturbation after pharmacological intervention, which are then correlated with the observed phenotypic effect. Drug-induced changes to the metabolome (collection of small molecules produced during metabolism) can provide insight into the biochemical pathways affected by a drug and the possible MoA.[6] Although the technique relies on established reference drugs, it may also contribute to the elucidation of novel elements of *Plasmodium* biology and discovery of chemical matter with novel MoA.[7,8]

MLN0128 was metabolically profiled in 3D7 *P. falciparum* trophozoites and normalized targeted metabolites evaluated using log2 fold-change values after treatment. Accordingly, metabolite clusters were organized into eight generalized metabolic pathways based on drugs with known MoA, which were further stratified into supra-hexagonal metabolomic fingerprints (metaprints) (**Figure 3.3**).[5] Metaprints were then assembled and interpreted using a combination of hierarchical clustering, metaprint analysis, and *a priori* biochemical knowledge.[9] The metabolite fingerprint of MLN0128 at the asexual stage of the parasite is shown in **Figure 3.3**.

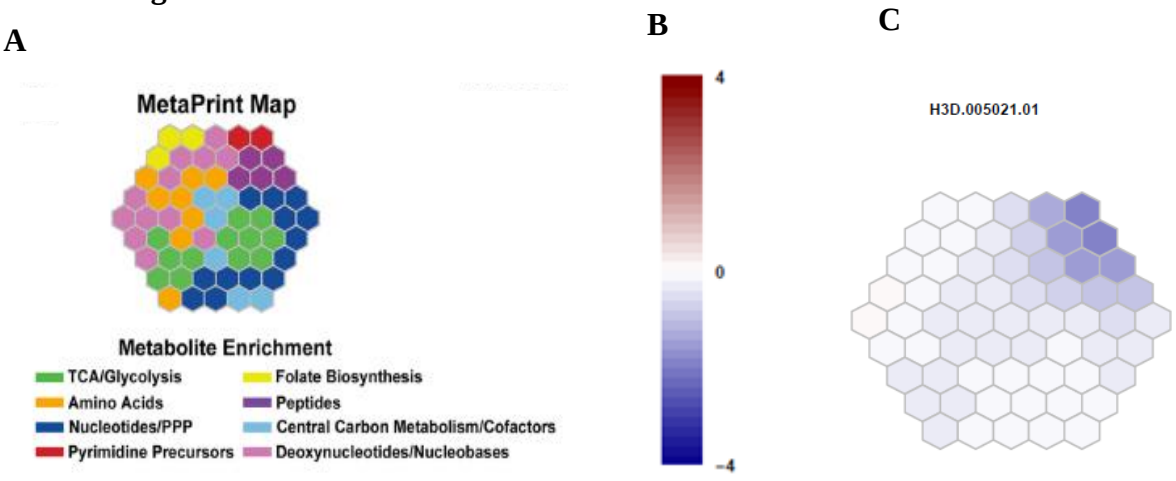

Figure 3.3: A) Metaprint of eight general metabolic pathways; B) color code for log2 fold-change in targeted metabolites relative to the untreated control (indicated as zero); C) metabolomic fingerprint analysis of MLN0128 (**62**, **GS 20b**)

Unique signature changes in hemoglobin-derived peptides and amino acid derivatives were evident, suggesting that MLN0128 acts via perturbation of the parasite's hemoglobin catabolism pathway. Characteristic metabolite changes included reduction in the hemoglobin-derived peptides like aspartyl-leucyl-histidine (DLH), prolyl-glutamate (PE), and prolyl-aspartate (PD). A similar pattern was reported for the *Pf*PI4K inhibitor MMV390048 and CQ, despite their different predicted molecular targets.[5] Thus, the hemoglobin catabolism pathway was likely implicated as a hallmark for the inhibition of *Pf*PI4K and *Pf*PI3K (*in vitro* IC_{50} = 100 nM). *Pf*PI3K is a genetically validated enzyme localized in vesicles near the parasite's membrane and food vacuole and is involved in endocytosis from the host and trafficking of hemoglobin in the parasite.[10] MMV390048 has recently been reported to inhibit *Pf*PI3K *in vitro* (IC_{50} = 1 nM), in addition to its primary target *Pf*PI4K.[11]

Additionally, metabolites perturbation on several pyrimidine nucleotides was observed. For example, decline in the pyrimidine precursors *N*-carbamoyl-L-aspartate and dihydroorotate were recorded. This is in contrast to the metabolic effects of atovaquone, a known bc_1 complex inhibitor on the *de novo* pyrimidine biosynthesis pathway.[5] Evidently, these metabolites were affected as a downstream effect of the inhibition of the hemoglobin-derived peptides' pathway which was significantly inhibited by this compound. Furthermore, despite MLN0128 inhibiting *Pf*PKG *in vitro*, it displayed no significant differences in peptide disruptions relative to MMV390048 possibly due to this effect being superseded by the *Pf*PI4Kβ targeting. Nonetheless, the metabolic profile similarity with CQ, despite the latter acting on the heme-degradation pathway, emphasizes the need for in-depth investigation of biochemical pathways and use of multiple techniques to elucidate the MoA of a compound. In addition, the *Plasmodium* pan-kinase activity of this compound will likely lead to perturbations of multiple pathways.

3.2.4 *In vitro* asexual blood stage anti-plasmodium activity of MLN0128 and its derivatives

In line with the outlined workflow and the specific objectives of this study, the *in vitro* anti-plasmodium activities of MLN0128 (**62**, **GS 20b**) and target compounds were evaluated against a CQ-sensitive *Pf* strain (NF54) using a modified lactate dehydrogenase (LDH) assay.[12] Selected compounds were also assessed against a multidrug-resistant *Pf* strain (K1). These experiments were carried out at H3D in the Division of Clinical Pharmacology, Department of Medicine, UCT. Several compounds were also assessed at the Swiss Tropical and Public Health

Institute (STPH), University of Basel, Switzerland, using a modified tritium [^{3}H]-hypoxanthine incorporation assay.[13] These assays are described in detail in Chapter 10.

The LDH assay involves incubating asexual erythrocytic parasites with varying concentrations of the compound and monitoring the production of nicotinamide adenine dinucleotide (NADH) in the last step of the parasitic glycolytic pathway, as an indicator of metabolic activity in response to parasite inhibition.[12] By using a probe substrate, the inhibitor concentration-response relationship is spectrophotometrically quantified and can be used to deduce half-maximum concentrations (IC_{50} values). In the case of the modified [^{3}H]-hypoxanthine incorporation assay, an isotopic hypoxanthine is added to the parasite culture where it is taken up for nucleic acid biosynthesis in *de novo* DNA synthesis.[12] Despite pyrimidines being precursors for the formation of genetic materials such as DNA and RNA, *Plasmodium* species are incapable of biosynthesis and wholly rely on host scavenging for their acquisition. Consequently, parasite viability can be monitored by incorporating radiolabeled precursors that can be measured using a scintillating counter for IC_{50} extrapolation.[13]

MLN0128 displayed high anti-plasmodium whole-cell potency (*Pf*NF54 IC_{50} = 0.058 µM; **Table 3.2**). This is consistent with the results obtained from the GSK/Cellzome facility using *Pf*3D7strain (IC_{50} = 0.078 µM). For the analogues, the first set of compounds synthesized was an assortment of mono-atomic benzyls designed to investigate the effect of various Craig plot substituents and their orientations, on anti-plasmodium activity. These substitutions were made at the *meta*, *para*, and *ortho* positions with non-substituted benzyl used as a control. Potent activity (*Pf*NF54 IC_{50} < 0.5 µM) was observed for all analogues with Cl, F, CN, NH_2, CF_3 or Me substituents at the *para* and *meta* positions relative to their *ortho* counterparts. All *ortho*-substituted analogues synthesized showed poor activity (IC_{50} > 1 µM; **Table 3.2**), while the non-substituted benzyl **6** (**GS 77**) displayed modest activity (IC_{50} = 0.750 µM) highlighting the importance of a protruding lipophilic or hydrophilic group to increase anti-plasmodium activity.

Table 3.2: Anti-plasmodium activities (IC_{50} values) of target compounds against *Pf*NF54 and K1 strains

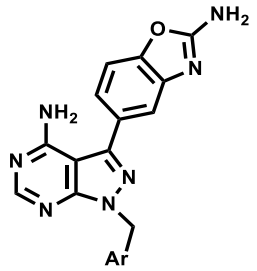

Ar	R	Code	[a]*Pf*NF54 (IC_{50}, µM)	[a]*Pf*K1 (µM)	RI[b]	[c]Sol.	Ar	R	Code	[a]*Pf*NF54 (IC_{50}, µM)	[a]*Pf*K1 (µM)	RI[b]	[c]Sol.
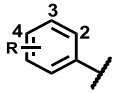	H	**6/ GS 77**	0.719	-	-	< 5	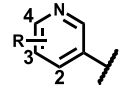	4-CF_3	**39 (GS 99)**	0.375	0.219	0.6	< 5
	4-Cl	**7/ GS 55**	0.029	0.035	1	< 5		4-Cl	**40 (GS 121)**	0.081	0.060	1	< 5
	4-F	**8/ GS 65**	0.141	0.106	1	< 5		4-F	**41 (GS 135)**	0.184	-	-	10
	4-CN	**9/ GS 63**	0.198	-	-	< 5		4-Me	**42 (GS 137)**	0.340	-	-	< 5
	4-CF_3	**10/ GS 59**	0.221	-	-	-	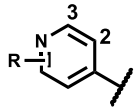	H	**43 (GS 79B)**	0.950	-	-	30
	4-Me	**11/ GS 69**	0.178	-	-	< 5		3-Cl	**44 (GS 157)**	0.104	2.500	24	< 5
	4-OMe	**12/ GS 42**	0.329	-	-	< 5		3-F	**45 (GS 165)**	3.350	-	-	5
	4-NH_2	**13/ GS 149**	0.068	2.690	40	-		3-CF_3	**46 (GS 187)**	> 6	0.283	-	< 5
	3-F	**14/ GS 73**	0.297	0.206	1	-		3-Me	**47 (GS 189)**	-	0.698	-	85
	3-CF_3	**15/ GS 71**	0.191	0.143	1	< 5	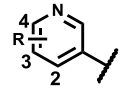	H	**48 (GS 83)**	0.795	-	-	20
	3-Me	**16/ GS 67**	0.418	-	-	-		3-Me	**49 (GS 167)**	0.189	0.304	2	10
	3-Cl	**17/ GS 57**	0.129	0.134	1	< 5		3-Cl	**50 (GS 203)**	0.151	0.133	1	< 5
	3-NH_2	**18/ GS 155**	0.345	1.400	4	< 5		3-F	**51 (GS 199)**	0.250	-	-	< 5
	3-$N(Me)_2$	**19/ GS 175**	0.411	3.680	9	< 5	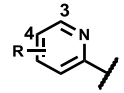	H	**52 (GS 87)**	-	-	-	65
	2-Me	**20/ GS 97**	1.260	1.410	0.5	-		4-Cl	**53 (GS 185)**	-	0.099	-	< 5
	2-F	**21/ GS 91**	2.655	1.280	0.5	-		4-F	**54 (GS 183)**	-	0.273	-	< 5
	2-Cl	**22/ GS 115**	1.345	-	-	< 5		4-CF_3	**55 (GS 191)**	-	0.334	-	< 5
	2-CF_3	**23/ GS 113**	3.595	-	-	-	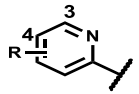	3-Cl	**56 (GS 181)**	-	0.341	-	< 5
	3,4-Cl	**24/ GS 101**	0.039	0.035	1	< 5		3-Me	**57 (GS 177)**	0.336	1.060	3	< 5
	2,4-Cl	**25/ GS 103**	0.520	0.448	1	-		3-F	**58 (GS 193)**	0.682	-	-	< 5
	2-F, 4-Cl	**26/ GS 111**	0.100	0.082	1	< 5		3-CF_3	**59 (GS 195)**	0.278	-	-	< 5
	2-CN, 4-Cl	**27/ GS 107**	0.165	0.153	1	< 5	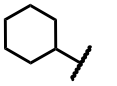	H	**60 (GS 125)**	0.384	-	-	< 5
	3-F, 4-Cl	**28/ GS 105**	0.020	0.018	1	< 5		4-*di* F	**61 (GS 197)**	0.169	-	-	< 5
	3-CF_3, 4-Cl	**29/ GS 117**	0.157	0.093	0.6	< 5							
	2-F, 4-F	**30/ GS 123**	0.207	-	-	-							

2-Cl, 4-F	**31/ GS 127**	0.834	-	-	-	**MLN0128**	**62 (GS 20b)**	0.058	-	-	115
2-CF_3, 4-F	**32/ GS 129**	-	-	-	-	**Controls**:					
2-CN, 4-F	**33/ GS 131**	0.389	-	-	15	Chloroquine		0.010	0.194	12	
2-Me, 4-F	**34/ GS 133**	0.520	-	-	-	Artesunate		0.008	0.003	0.8	
3-Cl, 4-F	**35/ GS 139**	0.086	-	-	< 5						
3-CN, 4-F	**36/ GS 141**	0.080	-	-	< 5						
3-F, 4-F	**37/ GS 143**	0.044	-	-	< 5						
3-CF_3, 4-F	**38/ GS 145**	0.191	-	-	< 5						

- = Not determined, [a]asexual blood stage IC_{50} values are a mean of n ≥ 2 determinations, [b]RI = resistance index i.e., *Pf*K1 IC_{50}/*Pf*NF54 IC_{50}; [c]HPLC kinetic solubility in μM (at pH 6.5) determined using the HPLC-based DMSO "dry-down" method

Generally, analogues with small electron-withdrawing groups (EWGs) at the *para* position were more potent than their corresponding *meta* isomers. Notably, the *para*-Cl analogue **7** (**GS 55**) was the most potent showing exemplary nanomolar activity (*Pf*NF54 IC_{50} = 0.029 µM). In comparison, the *meta*-Cl-containing compound **17** (**GS 57**) displayed a four-fold reduction in activity (IC_{50} = 0.129 µM). Similarly, *meta*-Me and *meta*-F containing analogues (**16**, **GS 67**, IC_{50} = 0.418 µM and **14**, **GS 73**, IC_{50} = 0.297 µM, respectively), displayed an insignificant two-fold reduction in activity relative to their more potent *para*-substituted counterparts (**11**, **GS 69**, IC_{50} = 0.178 µM; and **8**; **GS 65**, *Pf*NF54 IC_{50} = 0.141 µM).

In contrast, trifluoromethyl-containing compounds showed equipotency for both the *meta* and *para* positions as seen in **15** (**GS 71**; IC_{50} = 0.191) and **10** (**GS 59**; IC_{50} = 0.221 µM). However, as expected, improved activity came at the expense of solubility due to increased lipophilicity. All front-runner compounds showed intrinsic solubility < 5 µM at pH 6.5 (**Table 3.2**). Solubility and its relationships with other physicochemical parameters for these compounds are discussed in Chapter 4.

The encouraging anti-plasmodium activity of the monosubstituted analogues identified in the initial SAR warranted further structural modifications. The first approach (**SAR 1a**; **Figure 3.4**) involved di-substitution of the benzyls with various electron-withdrawing and -donating groups while maintaining Cl or F in the *para* position. This approach was prioritized for anti-plasmodium potency retention. **SAR 1b** involved introduction of *para*- and *meta*-substituted pyridyls also aimed at potency retention, as previous results on benzyl compounds suggested that these positions were crucial for potency. This approach also had the potential to mitigate poor solubility, a liability necessitating optimization for the front-runner compounds.

In another approach (**SAR 1c**; **Figure 3.4**), aliphatic groups were introduced, aiming to mimic ribose at the ATP-binding site, although only a few compounds were pursued (**60**; **GS 125** and **61**; **GS 197**) as they were anticipated to be promiscuous. Nevertheless, this strategy also increased sp^3 character in a molecule, a property associated with disruption of aromatic π-stacking interactions, thereby potentially improving solubility and associated ADME properties.[14]

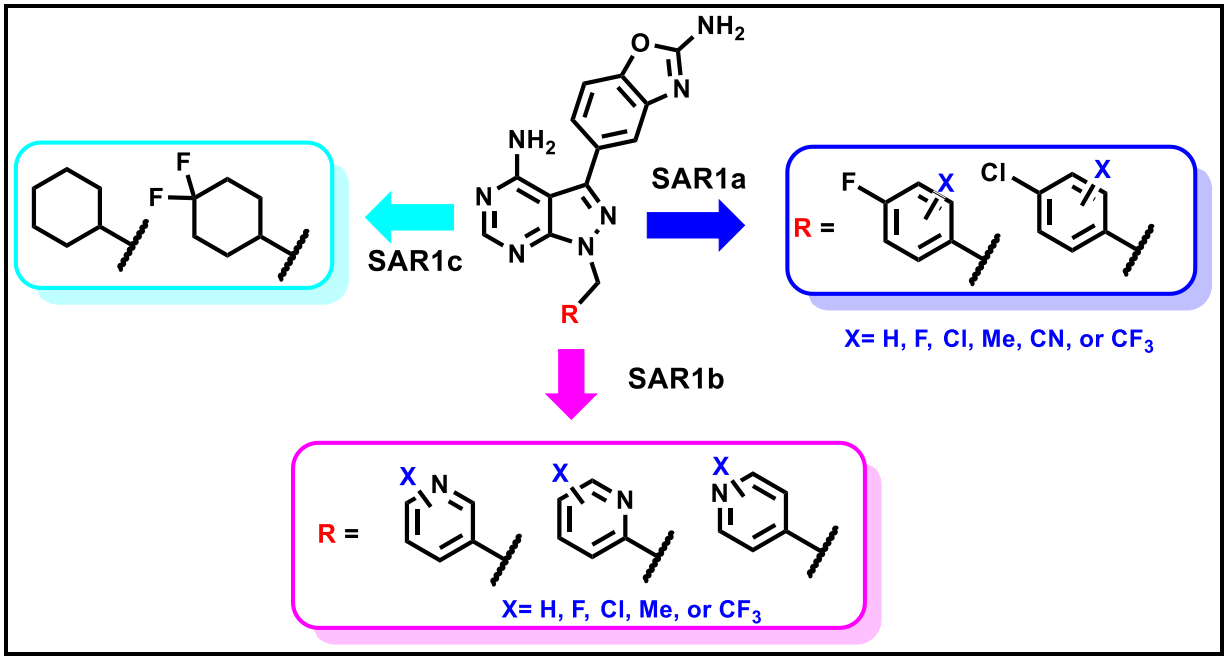

Figure 3.4: SARs explored by substituting the isopropyl group on the MLN0128 scaffold

Anti-plasmodium whole-cell potency was retained by keeping either Cl and F in the *para* position and introducing di-substitution on the benzyl moiety. Introduction of EWGs such as F and Cl in the *meta* position while maintaining Cl in the *para* position led to equipotency as observed in **24** (**GS 101**; *Pf*NF54 IC_{50} = 0.039 µM) and **28** (**GS 105**; IC_{50} = 0.020 µM) relative to the lead monochlorinated compound **7** (**GS 55**; IC_{50} = 0.029 µM). In contrast, the *ortho* position was detrimental to potency as 2,4-disubstitution of the same compounds led to respective > 10- and 3-fold decrease in potency for analogues **25** (**GS 103**; IC_{50} = 0.520 µM) and **26** (**GS 111**; IC_{50} = 0.100 µM), relative to analogue **7**.

Similarly, maintaining F in the *para* position ensured potency for 3,4-disubstituted compounds (IC_{50} = 0.044–0.191 µM), with showed superior or comparable activity to that of the lead compound **8** (**GS 65**; IC_{50} = 0.141 µM). Of note is the more potent 3,4 - difluoro analogue **37** (**GS 143**; IC_{50} = 0.044 µM) and 3-Cl, 4-F-substituted congener **35** (**GS 139**; IC_{50} = 0.086 µM). Interestingly, isomerism may heavily impact anti-plasmodium activity as epitomized by the four-fold difference in activity observed for analogue **35** (**GS 139**; IC_{50} = 0.086 µM) and its isomer **28** (**GS 105**; IC_{50} = 0.020 µM). However, substitution at the *ortho* position while maintaining the fluorine atom at the *para* position was generally detrimental to potency, as demonstrated by **30** (**GS 123**; IC_{50} = 0.207 µM), **31** (**GS 127**; IC_{50} = 0.834 µM), and **34** (**GS 133**; IC_{50} = 0.520 µM).

Introducing a pyridyl while maintaining Cl and F at the *meta* or *para* position was generally tolerated, although activity was slightly reduced (~3-fold) as in the case of **40** (**GS 121**) relative to the *para-Cl* substituted benzyl **7 (GS 55)**. The pyridine position appeared to have a minimal impact on potency, as observed in the *meta*-substituted Cl analogues **44** (**GS 157**; *Pf*NF54 IC_{50} = 0.104 µM) and **50** (**GS 203**; IC_{50} = 0.151 µM). This strategy also led to some improvement in aqueous solubility at the physiologically relevant pH of 6.5, particularly regarding the non-substituted pyridyls **52** (**GS 87**; 65 µM), **48** (**GS 83**; 20 µM), and **43** (**GS 79b**; 30 µM; **Table 3.2**). However, these compounds also showed reduced antiparasitic activity (*Pf*NF54 IC_{50} > 0.5 µM). Moreover, substitution on the pyridyl ring negated the improved solubility as all substituted pyridyls tested showed low solubility (< 5 µM) except for **47** (**GS 189**; 85 µM), **41** (**GS 135**; 10 µM), and **49** (**GS 167**; 10 µM), because of the addition of lipophilic groups.

In addition, potency was maintained by introduction of a cyclohexyl moiety as seen in **60** (**GS 125**; IC_{50} = 0.384 µM) in comparison to the non-substituted benzyl **6** (**GS 77**; IC_{50} = 0.719 µM) and pyridyl analogues **43** (**GS 79b**; IC_{50} = 0.950 µM) and **48** (**GS 83**; IC_{50} = 0.795 µM). However, similarly poor solubility (< 5 µM) was observed for these compounds suggesting that increase in sp^3 character may not be an effective strategy to mitigate this issue for the series. However, as pointed out earlier, greater diversity on aliphatic sidechains was deemed undesirable because of a heightened risk of promiscuity despite the observed favorable anti-plasmodium potency.

Most analogues tested against both the CQ-sensitive (*Pf*NF54) and multidrug-resistant (*Pf*K1) parasite strains were equipotent, suggesting the absence of cross-resistance. CQ resistance has been associated with the *Pf*CQ resistance transporter (*Pf*CRT), a membrane protein responsible for decreased accumulation of the drug in the parasite's food vacuole.[15] The activity observed against *Pf*K1 parasites indicated that the compounds tested were able to access the parasite via a potentially novel mechanism, different to that of CQ.

In contrast, some compounds showed lower activity against the multi-drug resistant *Pf*K1 strain relative to the drug sensitive *Pf*NF54 strain. Notable is the aniline **13** (**GS 149**; *Pf*K1 IC_{50}/*Pf*NF54 IC_{50} (resistance index; RI) = 40), **19** (**GS 175**; RI = 9), and **18** (**GS 155**; RI = 4; **Table 3.2**), and several pyridyl analogues such as **44** (**GS 157**; RI = 24). Worth noting is that all the compounds showing cross-resistance against *Pf*K1 had basic sidechains or ionizable basic centers, suggesting similar MoA(s). This cross-resistance is hypothesized to emanate

from *Pf*CRT recognizing amphipathic amines as transport substrates with consequent out-of-cellar efflux in a manner to that of CQ.

3.2.5 *In vitro Pv*PI4K activity of MLN0128 analogues

To validate these compounds as PI4K inhibitors, *in vitro* PI4K inhibition was assessed using purified *Pv*PI4K recombinant protein in an ADP detection assay using the ADP-Glo Kinase assay (Promega).[16] The procedure involved initiating a kinase reaction in standardized conditions and in the presence of PI substrate and 10 µM ATP. The reaction was then terminated using ADP-Glo reagent which quenched any remaining ATP and converted the ADP generated in the kinase reaction to ATP, which was then used in a luciferase-coupled reaction to generate light. Luminescence measurements were then recorded as a quantifier of ADP formed during the kinase reaction and used to calculate the % inhibition and IC_{50} values.

Whilst evaluation against *Pf*PI4K would have been more desirable, *Pv*PI4K is the only recombinantly expressed and purified *Plasmodium* PI4K available. Notwithstanding, the catalytic domains of *Pf*PI4K and *Pv*PI4K are well conserved and share over 97% sequence similarity. Consequently, *Pv*PI4K serves as an adequate surrogate for *Pf*PI4K which is more challenging to express recombinantly. In support of this, inhibition assays using a heavily truncated *Pf*PI4K construct demonstrated comparable IC_{50} values for a number of ATP-competitive inhibitors previously tested against *Pv*PI4K.[11]

Initially, single-point % inhibition (inhibitor concentration = 0.1 µM; **Table 3.3**) was evaluated as a progression criterion for the more laborious dose-response studies. This inhibitor concentration was selected after a single-point assay performed with a higher dose (1 µM) indicated > 95% inhibition for all compounds assayed. This suggested that PI4K inhibition was an important MoA for this series. Furthermore, 44/46 compounds showed > 50% inhibition in the assay performed at a lower concentration (0.1 µM; **Table 3.3**), providing a possible explanation for the high anti-plasmodium potency generally observed for this series.

Selected compounds representing some potent anti-plasmodium compounds (*Pf*NF54 IC_{50} < 0.2 µM), moderately potent (IC_{50} = 0.2–1 µM) and poorly active ones (IC_{50} > 1 µM) were then progressed to dose response studies. All the compounds tested in this assay (10 point, three-fold serial dilutions from 10 µM stock; n ≥ 2 determinations), exhibited potent *Pv*PI4K inhibition with IC_{50} values ranging from 1 to 113 nM (**Table 3.3**). Small EWGs in the *para*

and *meta* positions favored PI4K inhibition, and the presence of a Cl group appeared more favored than a F, which also translated to high parasite whole-cell potency. Compound **50** (**GS 203**) showed the highest *Pv*PI4K inhibition (IC_{50} = 0.002 µM), which translated to modest potency (IC_{50} = 0.151 µM) against the drug-sensitive strain NF54. Compounds **28** (**GS 105**; *Pf*NF54 IC_{50} = 0.020 µM) and **7** (**GS 55**; IC_{50} = 0.029 µM) that displayed the most potent anti-plasmodium activity, also exhibited potent *in vitro Pv*PI4K inhibition (IC_{50} = 0.021 and 0.007 µM, respectively).

Furthermore, all tested pyridyl compounds with *para*- and *meta*-F and -Cl substituents also showed good *Pf*PI4K potency (IC_{50} < 0.010 µM) regardless of the pyridine position. Notable compounds include the *para*-Cl pyridyl analogues **40** (**GS 121**; *Pv*PI4K IC_{50} = 8 nM), **53** (**GS 185**; *Pv*PI4K IC_{50} = 3 nM), *meta*-F **58** (**GS 193**; IC_{50} = 6 nM), and *meta*-Cl analogue **50** (**GS 203**; IC_{50} = 1 nM), which was the most potent compound against this enzyme. Similarly, the anti-plasmodium activity of benzyl Cl-containing compounds revealed a moderate benefit posed by the *para* position, as indicated by **7** (**GS 55**; *Pv*PI4K IC_{50} = 7 nM) over the *meta* **17** (**GS 57**; *Pv*PI4K IC_{50} = 18 nM) and *ortho* **22** (**GS 115**; *Pv*PI4K IC_{50} = 41 nM), which showed three- and six-fold reductions in activity, respectively.

Table 3.3: *In vitro Pv*PI4K inhibition activities (IC_{50} values) of selected target compounds

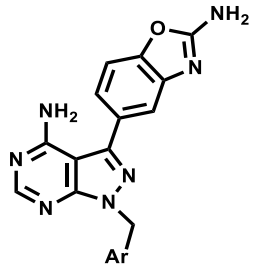

Ar	R	Code	[a]*Pf*NF54 (IC_{50}, µM)	[b]% PI4K Inh. (0.1 µM)	*Pv*PI4K (IC_{50}, µM)	Ar	R	Code	[a]*Pf*NF54 (IC_{50}, µM)	[b]% PI4K Inh. (0.1 µM)	[c]*Pv*PI4K (IC_{50}, µM)
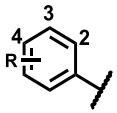	H	**6/ GS 77**	0.719	83.2	-	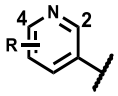	4-CF_3	**39 (GS 99)**	0.375	41.2	-
	4-Cl	**7/ GS 55**	0.029	91.8	0.007		4-Cl	**40 (GS 121)**	0.081	-	0.008
	4-F	**8/ GS 65**	0.141	90.3	0.006		4-F	**41 (GS 135)**	0.184	82.6	0.012
	4-CN	**9/ GS 63**	0.198	92.6	-		4-Me	**42 (GS 137)**	0.340	85.4	-
	4-CF_3	**10/ GS 59**	0.221	57.4	-	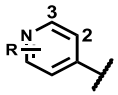	H	**43 (GS 79B)**	0.950	81.9	0.013
	4-Me	**11/ GS 69**	0.178	77.1	-		3-Cl	**44 (GS 157)**	0.104	-	0.004
	4-OMe	**12/ GS 42**	0.329	85.3	0.016		3-F	**45 (GS 165)**	3.350	84.8	-
	4-NH_2	**13/ GS 149**	0.068	-	0.024		3-CF_3	**46 (GS 187)**	> 6	92.1	-
	3-F	**14/ GS 73**	0.297	87.8	-		3-Me	**47 (GS 189)**	0.698-K1	-	0.013
	3-CF_3	**15/ GS 71**	0.191	95.9	-	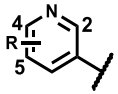	H	**48 (GS 83)**	0.795	87.5	0.007
	3-Me	**16/ GS 67**	0.418	71.6	0.005		5-Me	**49 (GS 167)**	0.189	-	0.006
	3-Cl	**17/ GS 57**	0.129	87.9	0.018		5-Cl	**50 (GS 203)**	0.151	-	0.001
	3-NH_2	**18/ GS 155**	0.345	-	0.010		5-F	**51 (GS 199)**	0.250	98.0	-
	3-$N(Me)_2$	**19/ GS 175**	0.411	-	0.011	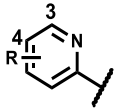	H	**52 (GS 87)**	-	89.0	-
	2-Me	**20/ GS 97**	1.260	74.1	-		4-Cl	**53 (GS 185)**	0.099-K1	-	0.003
	2-F	**21/ GS 91**	2.655	81.2	0.027		4-F	**54 (GS 183)**	0.273-K1	96.9	-
	2-Cl	**22/ GS 115**	1.345	60.0	0.041		4-CF_3	**55 (GS 191)**	0.334-K1	92.2	-
	2-CF_3	**23/ GS 113**	3.595	53.4	0.113	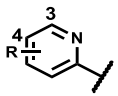	3-Cl	**56 (GS 181)**	0.341-K1	92.8	-
	3,4-Cl	**24/ GS 101**	0.039	58.2	-		3-Me	**57 (GS 177)**	0.336	89.7	-
	2,4-Cl	**25/ GS 103**	0.520	80.0	0.027		3-F	**58 (GS 193)**	0.682	-	0.006
	2-F, 4-Cl	**26/ GS 111**	0.100	91.3	-		3-CF_3	**59 (GS 195)**	0.278	-	0.005
	2-CN, 4-Cl	**27/ GS 107**	0.165	91.4	-						
	3-F, 4-Cl	**28/ GS 105**	0.020	73.9	0.021						

3-CF_3, 4-Cl	**29/ GS 117**	0.157	54.5	-	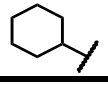	H	**60** (**GS 125**)	0.384	89.5	-
2-F, 4-F	**30/ GS 123**	0.207	93.5	-		4-*di* F	**61** (**GS 197**)	0.169	92.6	-
2-Cl, 4-F	**31/ GS 127**	0.834	84.5	0.025						
2-CF_3, 4-F	**32/ GS 129**	-	48.1	-	**MLN0128**		**62** (**GS 20b**)	0.058	100	0.005
2-CN, 4-F	**33/ GS 131**	0.389	55.3	-	**Controls**:					
2-Me, 4-F	**34/ GS 133**	0.520	80.0	0.020	Chloroquine			0.010		
3-Cl, 4-F	**35/ GS 139**	0.086	89.4	0.008	Artesunate			0.008		
3-CN, 4-F	**36/ GS 141**	0.080	89.6	0.004						
3-F, 4-F	**37/ GS 143**	0.044	91.2	0.004						
3-CF_3, 4-F	**38/ GS 145**	0.191	68.0	-						

- = Not determined; [a]asexual blood stage IC_{50} values are means of n ≥ 2 determinations, all the data is obtained against *Pf*NF54 strain unless otherwise stated; [b]*in vitro Pv*PI4K percentage inhibition are means of n ≥ 2 (in triplicate) determinations; [c]mean of n ≥ 2 (in duplicate) determinations.

A reduction in potency against the recombinant protein was also observed in the *para*-F benzyl isomer **8** (**GS 65**; *Pv*PI4K IC_{50} = 6 nM) relative to its *ortho*-F counterpart, translating to a four-fold decline in potency in **21** (**GS 91**; IC_{50} = 27 nM). Evidently, the pyridyl nitrogen favors potency against the enzyme, possibly due to enhanced interactions through increased H-bonds. In contrast, incorporation of the larger and more lipophilic CF_3 group at the *ortho* position resulted in the least potent benzyl analogue (**23**, **GS 113**; IC_{50} = 113 nM). This observation further confirms that *Pv*PI4K inhibition and anti-plasmodium activity is dependent on the electronic properties and size of the substituent.

In addition, both the enzymatic and the anti-plasmodium data, spanned through a meaningful range for quantitative statistical analysis. A plot of *Pf*NF54 pEC_{50} vs *Pv*PI4K pIC_{50} (**Figure 3.4**) for compounds whose IC_{50} values were determined, revealed a strong positive correlation (R^2 = 0.63), which further suggests that these compounds elicited the whole cell anti-plasmodium activity via PI4K inhibition. Strong correlations between antiparasitic and enzymatic potencies have also been reported in other *Pf*PI4K inhibitor series.[4]

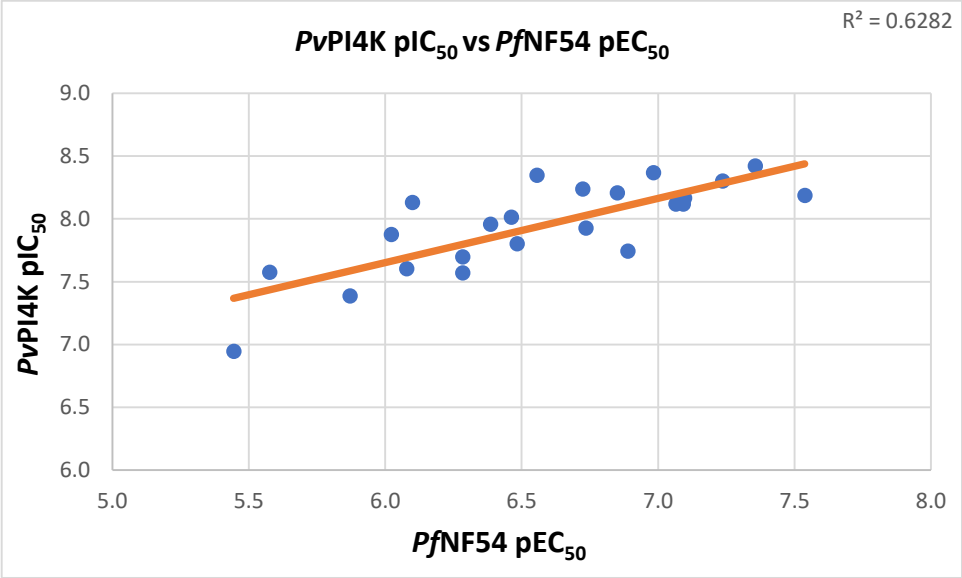

Figure 3.5: Correlation plot between *Pf*NF54 (expressed as pEC50) and *in vitro Pv*PI4K activity (pIC50)

Very strong correlations (> 0.8) are unlikely to be achieved due to poly-pharmacological effects against other *Plasmodium* targets, such as *Pf*PKG (as discussed later) and *Pf*PI3K as observed for MLN0128, which may possibly drive anti-plasmodium potency in a synergistic manner. Furthermore, physicochemical properties such as aqueous solubility affect compound

permeation across host red blood cells and parasitic cell membranes, which may also contribute to general variability.

3.2.5.1 Rationalization of *Pv*PI4K inhibition data using the *Pf*PI4K homology model

To rationalize the observed *Pv*PI4K inhibition, putative protein-inhibitor interactions for selected ligands were re-investigated using the *Pf*PI4K homology model.[17] All the active analogues docked well into the homology model, consistently forming H-bonds and at times π - π stacking interactions in the hinge, ribose, and affinity pockets. The most potent *Pv*PI4K inhibitor in the biochemical assay **50** (**GS 203**; IC_{50} = 1 nM) docked in the *Pf*PI4K homology model with a similar pose to MLN0128 with the 5'-N of the pyrazolopyrimidine core accepting a H-bond from Val 1357, and the amine group of the core donating a H-bond to the backbone carbonyl Glu 1355, also located in the hinge region (**Figure 3.5**).

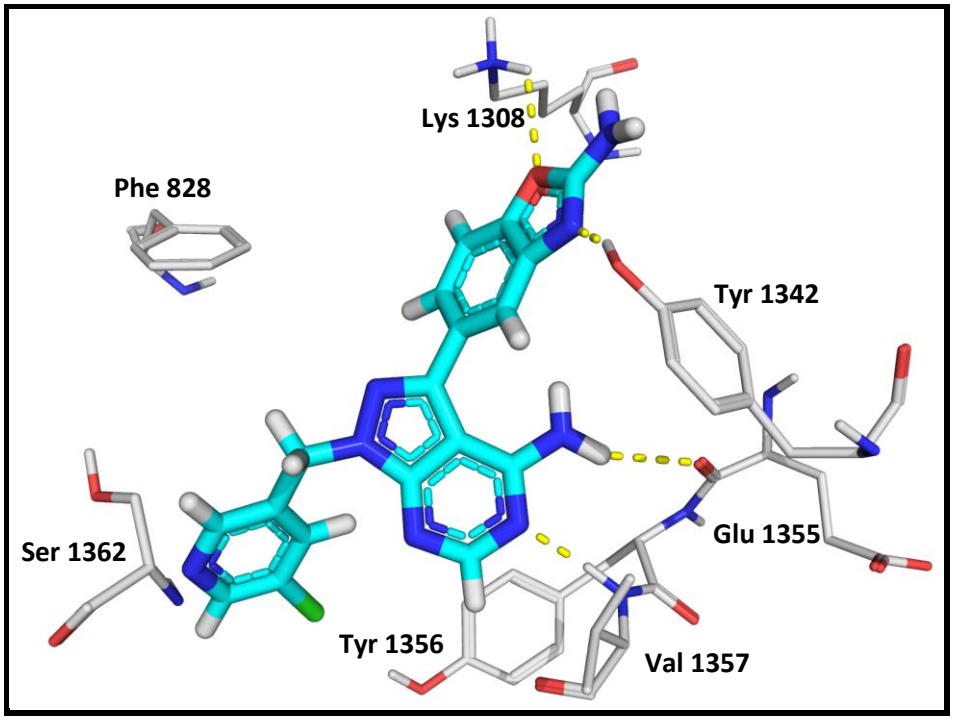

Figure 3.6: 3-D representation of **50** (**GS 203**) docked into the ATP-biding site of the *Pf*PI4K homology model

The benzoxazole imine was predicted to extend into the affinity pocket accepting a H-bond from Tyr 1342, showing docking like that of MLN0128. The pyridyl moiety situated in the ribose pocket forming a putative halogen-bond interaction with the hydroxyl of Tyr 1356 via the *meta*-chloro group (interaction not shown in **Figure 3.5**). These additional interactions result in the compound being more potent than MLN0128. In addition to the halogen bond, the extended aromatic pyridyl motif could also form a H-bond with Ser 1362 via the pyridyl

nitrogen, and/or π-stacking interactions with nearby Tyr and/or Phe residues (such as Phe 828 due to a ligand flip), accounting for the particularly high potency observed for this and other closely related compounds against *Pv*PI4K.

The closely related pyridyl **44** (**GS 157**) lacked a halogen bond interaction in the pyridyl moiety, although this was compensated by a face-to-face π-stacking interaction between the aromatic pyridyl part of the molecule and Phe 828 in the homology model, explaining the equipotency of this compound against the enzyme (*Pv*PI4K IC_{50} = 4 nM). Other equally potent analogues with favorable π-π interactions were **53** (**GS 185**; *Pv*PI4K IC_{50} = 3 nM) and **40** (**GS 121**; *Pv*PI4K IC_{50} = 8 nM) with consistent π-stacking interactions between the pyrazole and the pyridyl moiety of the analogue and Phe 828 or Phe 827 on the P-loop of the model.

In other cases, the reasons for moderate differences in potency between analogues were less apparent. For example, a modest three-fold decline in *Pv*PI4K potency was observed for the *meta*-Cl benzyl analogue **17** (**GS 57**; IC_{50} = 18 nM) and a five-fold decline in activity of the *ortho*-substituted congener **22** (**GS 115**; IC_{50} = 41 nM) relative to that of the *para*-analogue **7** (**GS 55**; IC_{50} = 7 nM). Similar observations were noted for the *para*-fluoro substituted benzyl **8** (**GS 65**; IC_{50} = 6 nM) relative to the less potent *ortho* isomer **21** (**GS 91**; IC_{50} = 27 nM).

Quantitative binding energy (MMGBSA) calculations offered little insight due to poor correlations with the *in vitro* enzymatic activity (R^2 = 0.07; **Figure 3.6**). MMGBSA correlations with *in vitro* antiparasitic activity have previously been demonstrated to occur only under highly controlled circumstances. This is because of the large number of variables involved in these calculations.[18] Also, inaccurate predictions are more likely to occur when relying on a homology model, as employed in this case. Furthermore, the narrow range of *Pv*PI4K data for this set of compounds may be insufficient to give any meaningful correlation. Thus, a qualitative binding pose analysis for each ligand was deemed a more reasonable approach while consecutively staying cognizant of the MMGBSA binding energies.

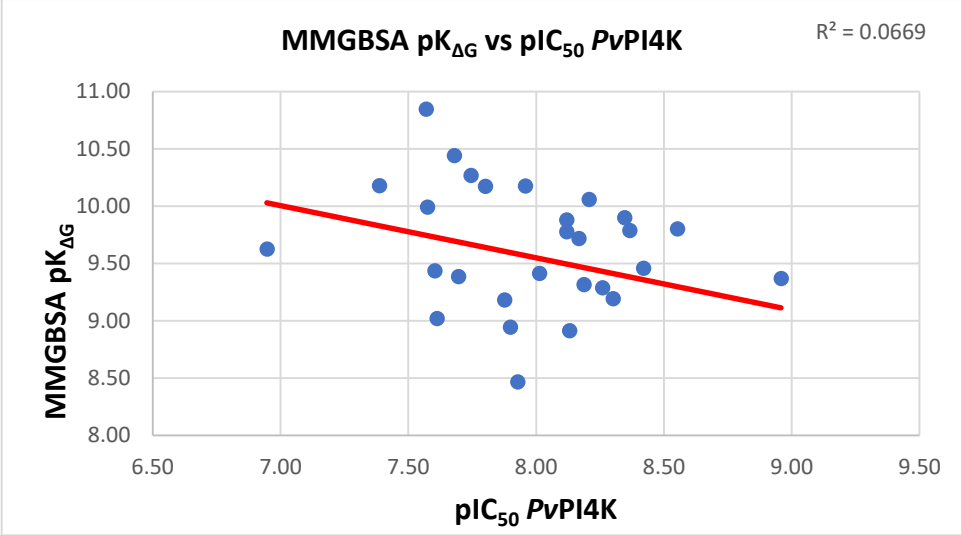

Figure 3 7: Correlation plot between *in vitro Pv*PI4K activity (pIC_{50}) and the calculated MMGBSA binding energies

Indeed, visual inspection identified a slight but avoidable ribose pocket clash between **17** (**GS 57**) and Tyr 1356 (ligand positioned within a minimization radius of 5.0 Å), while a more significant one was observable between **22** (**GS 115**) and Ser 1362 due to the occupation of the *ortho* Cl group in the space near the solvent edge. This corroborated well with the observed *in vitro* enzymatic activities of these compounds. In contrast, the *para*-Cl congener **7** (**GS 55**) fitted well in the ribose pocket with no observable anomalies auguring with its' slightly higher PI4K potency (IC_{50} = 7 nM).

Likewise, docking modes for the *meta* and *para* substituted pyridyls consistently accounted for their high *in vitro* potencies due to their structural similarities. For example, **49** (**GS 167**) docked well with the seemingly well-tolerated *meta*-methyl pyridyl lying close to Phe 828 of the model, in a manner similar to that of the benzyl compound **16** (**GS 67**). Satisfactorily, both compounds were equipotent with respective *Pv*PI4K IC_{50} values of 6 nM. Though the model predicted no Phe 828-pyridyl interaction for these compounds, this compound is likely to form π - π interactions, as observed in **58** (**GS 193**) and **59** (**GS 195**; *Pv*PI4K IC_{50} = 6 and 5 nM, respectively) accounting for the particularly high PI4K potency of these compounds.

Ortho positioning of the relatively large tri-fluoromethyl substituent on the benzyl ring resulted in a significant clash with Tyr 1356 for **23** (**GS 113**), and an associated decrease in potency (*Pv*PI4K IC_{50} = 113 nM) in the biochemical assay. Indeed, this compound showed the lowest *in vitro* PI4K inhibitory potency amongst all the compounds tested for this series. However, *ortho*-substituted pyridyls were not synthesized for comparative studies.

3.2.6 *In vitro Pf*PKG inhibition studies of MLN0128 analogues

The potential of this class of compounds to act as dual *Plasmodium* inhibitors was evaluated by testing selected compounds against full-length recombinant *Pf*PKG (PF3D7_1436600) expressed and purified according to methods previously described.[19,20] The assay was performed in the presence of kinase-activator cGMP and peptide substrate (GRTGRRNSI-NH2). ADP formation was detected using the ADP Glo Kinase assay.

Percentage PKG inhibition (10 µM dose) was initially evaluated for the hit compound and selected analogues. Compounds showing high inhibition at this concentration were progressed to IC_{50} determination against the recombinant protein. From the single-point assay, 12/50 compounds (**Table 3.4**) showed > 90% inhibition at 10 µM, generally indicating modest *in vitro* potency against the parasite enzyme. From the dose-response plots, the hit compound, **62** (**GS 20b**) was found to have an IC_{50} of 0.020 µM, in close agreement with the GSK/Cellzome Kino-bead data (apparent dissociation constant ± standard deviation; K_d^{app} = 0.007 ± 0.003µM).

The 4-amino benzyl analogue **13** (**GS 149**) and the cyclohexyl-substituted analogue **60** (**GS 125**) were the most potent compounds (IC_{50} values = 0.053 and 0.074 µM, respectively). Furthermore, all analogues with basic sidechains displayed moderate *Pf*PKG potencies as exemplified by **18** (**GS 155**; *Pf*PKG IC_{50} = 0.116 µM) and **19** (**GS 175**; *Pf*PKG IC_{50} = 0.126 µM), suggesting the importance of this to *Pf*PKG inhibition. Similarly, the *ortho*-F and Me benzyls **21** (**GS 91**) and **20** (**GS 97**) also displayed moderate potency with respective IC_{50} values of 0.17 and 0.23 µM.

Compounds with aliphatic groups exhibited good enzymatic potency as exemplified by the cyclohexyl-substituted analogue **60** (**GS 125**; IC_{50} = 0.062 µM). Difluorination of the cyclohexyl substituent in **61** (**GS 197**) resulted in a four-fold decline in potency (IC_{50} = 0.258 µM). This was also the case for the parent compound, MLN0128 (**GS 20b**; IC_{50} = 0.020 µM), which was the most potent of all the compounds assayed. However, all pyridyls tested displayed moderate *in vitro* potency (IC_{50} < 1 µM) against the recombinant protein. Pyridyl compound **50** (**GS 203**) showed the highest potency against the enzyme with an IC_{50} of 0.145 µM. Other notable potent pyridyls included the *meta*-substituted analogues **63** (**GS 177**; IC_{50} = 0.186 µM), **58** (**GS 193**; IC_{50} = 0.187 µM), and **59** (**GS 195**; IC_{50} = 0.196 µM), which were equipotent despite their different Me, F, and trifluoromethyl substitutions.

Table 3.4: *In vitro Pf*PKG activity (% inhibition at 10 µM inhibitor concentration and IC_{50} values) of selected target compounds

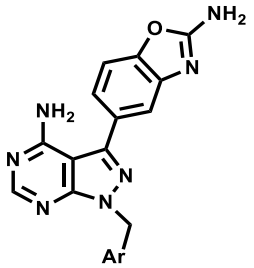

Ar	R	Code	[a]*Pf*NF54 (IC_{50}, µM)	[b]% PKG Inh. (10 µM)	*Pf*PKG (IC_{50}, µM)	Ar	R	Code	[a]*Pf*NF54 (IC_{50}, µM)	[b]% PKG Inh. (10 µM)	*Pf*PKG (IC_{50}, µM)
	H	**6/ GS 77**	0.719	85.5[c]	0.502	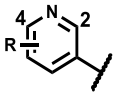	4-CF_3	**39 (GS 99)**	0.375	74.8	-
	4-Cl	**7/ GS 55**	0.029	53.5[c]	>2		4-Cl	**40 (GS 121)**	0.081	84.9	0.554
	4-F	**8/ GS 65**	0.141	60.0[c]	>2		4-F	**41 (GS 135)**	0.184	100.0	0.623
	4-CN	**9/ GS 63**	0.198	67.4	-		4-Me	**42 (GS 137)**	0.340	97.1	0.245
	4-CF_3	**10/ GS 59**	0.221	40.4	>10		H	**43 (GS 79B)**	0.950	94.8[c]	0.485
	4-Me	**11/ GS 69**	0.178	43.5[c]	>10	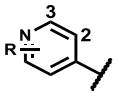	3-Cl	**44 (GS 157)**	0.104	72.0	0.834
	4-OMe	**12/ GS 42**	0.329	80.1	-		3-F	**45 (GS 165)**	3.350	89.8	0.711
	4-NH_2	**13/ GS 149**	0.068	-	0.053		3-CF_3	**46 (GS 187)**	> 6	70.5	-
	3-F	**14/ GS 73**	0.297	-	-		3-Me	**47 (GS 189)**	-	91.4	0.883
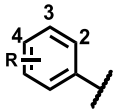	3-CF_3	**15/ GS 71**	0.191	82.8	-		H	**48 (GS 83)**	0.795	96.0[c]	0.350
	3-Me	**16/ GS 67**	0.418	66.4	0.630	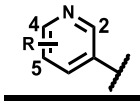	5-Me	**49 (GS 167)**	0.189	90.6	0.384
	3-Cl	**17/ GS 57**	0.129	49.1[c]	3.200		5-Cl	**50 (GS 203)**	0.151	86.7	0.145
	3-NH_2	**18/ GS 155**	0.345	-	0.116		5-F	**51 (GS 199)**	0.250	83.5	-
	3-$N(Me)_2$	**19/ GS 175**	0.411	-	0.155		H	**52 (GS 87)**	-	75.6	-
	2-Me	**20/ GS 97**	1.260	77.1	0.225	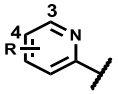	4-Cl	**53 (GS 185)**	0.099[d]	-	0.289
	2-F	**21/ GS 91**	2.655	89.9	0.100		4-F	**54 (GS 183)**	0.273[d]	70.3	-
	2-Cl	**22/ GS 115**	1.345	78.8	0.320		4-CF_3	**55 (GS 191)**	0.334[d]	63.1	-
	2-CF_3	**23/ GS 113**	3.595	90.9	0.230		3-Cl	**56 (GS 181)**	-	65.5	-
	3,4-Cl	**24/ GS 101**	0.039	33.9	>10	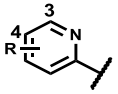	3-Me	**57 (GS 177)**	0.336	83.5	0.186
	2,4-Cl	**25/ GS 103**	0.520	72.3	-		3-F	**58 (GS 193)**	0.682	92.1	0.186
	2-F, 4-Cl	**26/ GS 111**	0.100	74.9	-		3-CF_3	**59 (GS 195)**	0.278	87.2	0.196
	2-CN, 4-Cl	**27/ GS 107**	0.165	83.0	-		H	**60 (GS 125)**	0.384	-	0.062
	3-F, 4-Cl	**28/ GS 105**	0.020	49.7	10	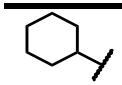	4-*di* F	**61 (GS 197)**	0.169	-	0.258
	3-CF_3, 4-Cl	**29/ GS 117**	0.157	68.1	-						
	2-F, 4-F	**30/ GS 123**	0.207	81.4	-						

2-Cl, 4-F	**31/ GS 127**	0.834	69.4	-
2-CF_3, 4-F	**32/ GS 129**	-	76.7	-
2-CN, 4-F	**33/ GS 131**	0.389	79.2	-
2-Me, 4-F	**34/ GS 133**	0.520	83.2	-
3-Cl, 4-F	**35/ GS 139**	0.086	42.9	>10
3-CN, 4-F	**36/ GS 141**	0.080	94.0	0.763
3-F, 4-F	**37/ GS 143**	0.044	70.1	-
3-CF_3, 4-F	**38/ GS 145**	0.191	48.1	>10

MLN0128	**62 (GS 20b)**	0.058	99.7	0.020
Controls:				
Chloroquine		0.010		
Artesunate		0.008		

- = Not determined, [a]asexual blood-stage IC_{50} values are means of n ≥ 2 determinations, [b]*in vitro* PKG percentage inhibitions are means of n ≥ 2 (in triplicate) determinations, [c]mean of n = 1 (in duplicate) determinations; [d]asexual blood-stage IC_{50} values against *Pf*K1.

In contrast to PI4K, a significant number of *para*- and *meta*-substituted benzyls displayed a complete loss of activity in this PKG biochemical assay. For example, the *para*-Cl analogue **7** (**GS 55**) and *para*-F **8** (**GS 65**) which previously showed high *Pv*PI4K potency displayed low activity (IC_{50} > 2 µM) against this recombinant protein. Similarly, *para*-substituted methyl **11** (**GS 69**) and trifluoromethyl **10** (**GS 59**) compounds showed an $1C_{50}$ >10 µM. By comparison, the unsubstituted benzyl **6** (**GS 77**) exhibited an IC_{50} of 0.502 µM, suggesting that substitution with a partially negatively charged group is generally unfavorable for *in vitro* PKG potency. Similar observations were made with substitution on the *meta* position, as exemplified by **17** (**GS 57**; IC_{50} = 3.2 µM). Indeed, neutral groups such as Me were better tolerated in this position, as demonstrated by analogue **16** (**GS 67**; IC_{50} = 0.630 µM).

In addition, correlation between the *Plasmodium* PKG inhibition and *Pf*NF54 activity was poor, with the most potent anti-plasmodium analogues exhibiting low *in vitro* PKG activity. For example, analogues **28** (**GS 105**; *Pf*NF54 IC_{50} = 0.020), **7** (**GS 55**; *Pf*NF54 IC_{50} = 0.029 µM), and **24** (**GS 101**; *Pf*NF54 IC_{50} = 0.039 µM) showed low enzymatic activity with respective inhibitory values of 10, > 2, and > 10 µM. Also, certain potent PKG inhibitors were devoid of good activity against this strain, as exemplified by the *meta*-fluoro benzyl **21** (**GS 91**; *Pv*PKG IC_{50} = 0.17 µM) and *meta*-trifluoromethyl congener **23** (**GS 113**; *Pv*PKG IC_{50} = 0.23 µM) having respective anti-parasitic activities of 2.655 and 3.595 µM against the drug-sensitive strain. In addition, there was no significant correlation between *Pf*NF54 pEC_{50} vs *Pf*PKG pIC_{50} (**Figure 3.7**; R^2 = 0.04) further confirming this observation.

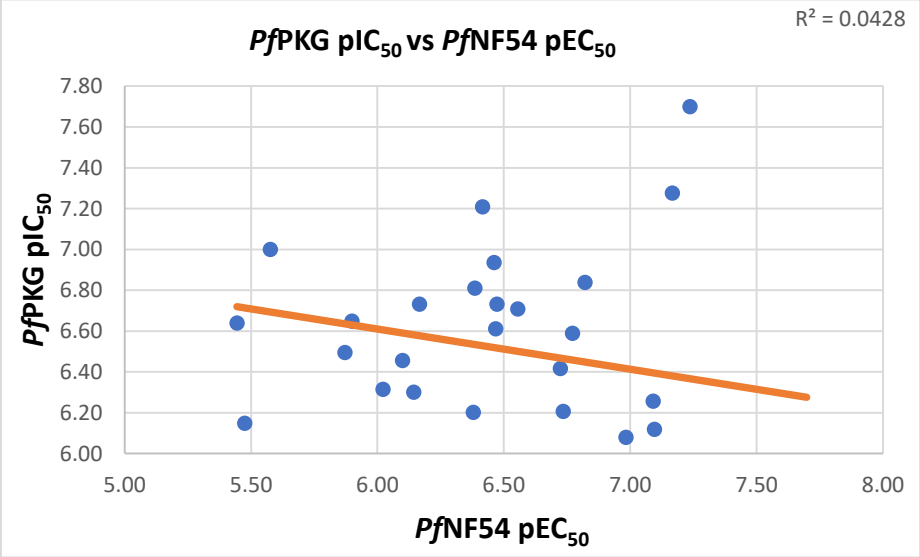

Figure 3.8: Correlation plot of anti-plasmodium activity (*Pf*NF54 pEC50) and *in vitro* *Pv*PKG activity (pIC50)

*Pf*PKG is a validated target as demonstrated by ML10 and other compounds in the series using a plethora of techniques such as chemoproteomics, mutant cell-lines and *in vivo* efficacy in a *Pf*SCID mouse model of malaria.[19] However, a compound must possess suitable properties to overcome cell barriers in a cellular setting, and reach the site of action contrary to *in vitro* conditions. Furthermore, different levels of inhibition are required in various targets to achieve whole cell antiparasitic activity. Indeed, picomolar *Pf*PKG inhibitors have previously been implicated for significant anti-plasmodium correlation although the compounds were occasionally incriminated with a secondary target.[20,21] By comparison, the inhibitory potency of compounds explored in this series ranged from 0.053 to > 10 μM. Collectively, these issues may account for the low correlation between PKG activity, and the anti-plasmodium potency as observed in this series.

3.2.6.1 Rationalization of MLN0128 analogues by *Pv*PKG crystal structure docking

To rationalize the experimental *in vitro* PKG potencies, the binding modes of selected compounds were investigated using a *Pv*PKG crystal structure (PDB code **5EZR**), as described by Cheuka and co-workers.[16] The compound with the most potent enzymatic activity **13** (**GS 149**; IC_{50} = 0.053 μM) docked into the ATP-binding site with a similar binding pose to MLN0128 with the core nitrogen at position 5' of the hinge-binding motif accepting a H-bond from Val 614 and 4-NH_2 donating a H-bond to the backbone carbonyl of Glu 612 (**Figure 3.8**), just like MLN0128.

Similarly, the benzoxazole amine extended to the PKG back pocket, forming multiple H-bonds with the conserved catalytic Asp 675, Glu 582, and Thr 586. In addition, a π - cation interaction formed between the aromatic oxazole and Lys 563 (interaction not displayed in **Figure 3.8**). Furthermore, the aromatic benzyl amine, oriented optimally towards the Glu 618 residue in the ribose pocket and was thought to donate a H-bond to the electron-deficient carbonyl of Glu 618 residue, accounting for the particularly high potency of this compound.

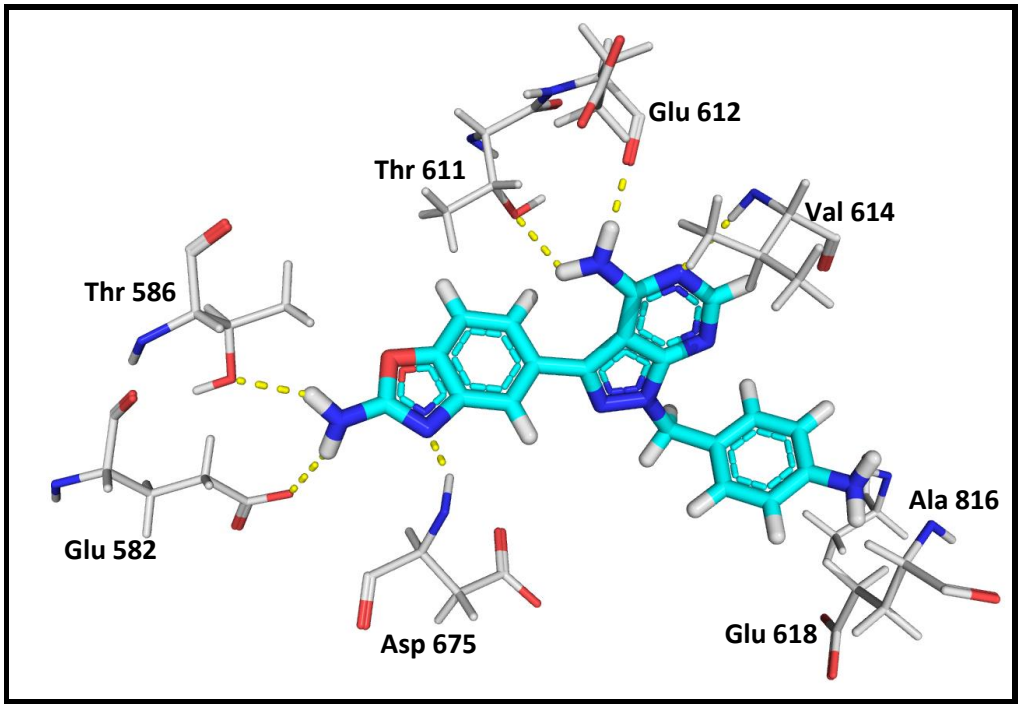

Figure 3.9: Docking pose of the most potent analogue **13** (**GS 149**) in the ATP-binding site of *Pv*PKG (PDB code **5EZR)**

Unlike PI4K, the ribose and back pocket of PKG are rich in acidic amino acid residues (mainly Glu and Asp), which basic centers such as amines can target. Accordingly, the *meta*-substituted aniline **18** (**GS 155**) also exhibited good *Pf*PKG inhibition (IC_{50} = 0.116 µM), comparable to the *para* isomer. Compound **18** (**GS 155**) showed a docking pose similar to that of **13** (**GS 149**), with the typical H-bond acceptor/donor interaction at the hinge and back pocket of the crystal structure. However, although the π-cation interaction was lost, it was compensated by π-stacking with an adjacent Phe 609 residue. The slight decline in potency was likely due to a slight clash between the benzyl and Glu 618 in the ribose pocket (ligand positioned within a minimization radius of 5.0 Å). In parallel, compound **19** (**GS 175**; *Pf*PKG IC_{50} = 0.155 µM) was predicted to sit deep and extend towards the catalytic Lys 563 with an equally observable clash with Glu 618. This possibly accounted for its equipotent activity.

Aliphatic substitution was beneficial to PKG inhibition as exemplified by the potent cyclohexyl substituted analogue **60** (**GS 125**; IC_{50} = 0.074 µM), which sat optimally in the ribose pocket. The ribose pocket of PKG is less accessible to solvent, unlike that of PI4K, and consequently favours aliphatic groups as highlighted by the *in vitro* potency of this analogue. However, di-fluoro substitution as in **61** (**GS 197**), led to a three-fold loss in affinity due to significant clashes with Glu 618, Ala 816, and Ile 540 residues of the crystal structure.

Generally, incorporation of a potentially ionizable pyridyl structure was favorable to enzymatic potency as highlighted by the single-point assays at 10 µM, with most analogues exhibiting ≥70% inhibition (**Table 3.4**). Additionally, all pyridyls tested in the dose-response assay displayed IC_{50} < 1 µM. The most potent pyridyls were **50** (**GS 203**; IC_{50} = 0.145 µM), **57** (**GS 177**; IC_{50} = 0.186 µM), **58** (**GS 193**; IC_{50} = 0.186 µM), and **59** (**GS 195**; IC_{50} = 0.196 µM), which were all equipotent against the recombinant protein.

Although the compounds docked well with the common hinge and back pocket binding, no additional interactions were observed with the pyridyl group for these compounds. It is likely that the good potency is ensured by H-bond interactions with Ala 816, as observed in the unsubstituted pyridyl **48** (**GS 83**; IC_{50} = 0.350 µM; **Figure 3.9**), or a halogen bond with Glu 618 of the crystal structure as observed in **53** (**GS 185**; IC_{50} = 0.289 µM). Other analogues with moderate potency bound in the same fashion, with two- to three-fold reductions attributed to possible clashes with Ala 816, Glu 618, and/or Ile 540 of the model as observed in **45** (**GS 165**; IC_{50} = 0.711 µM).

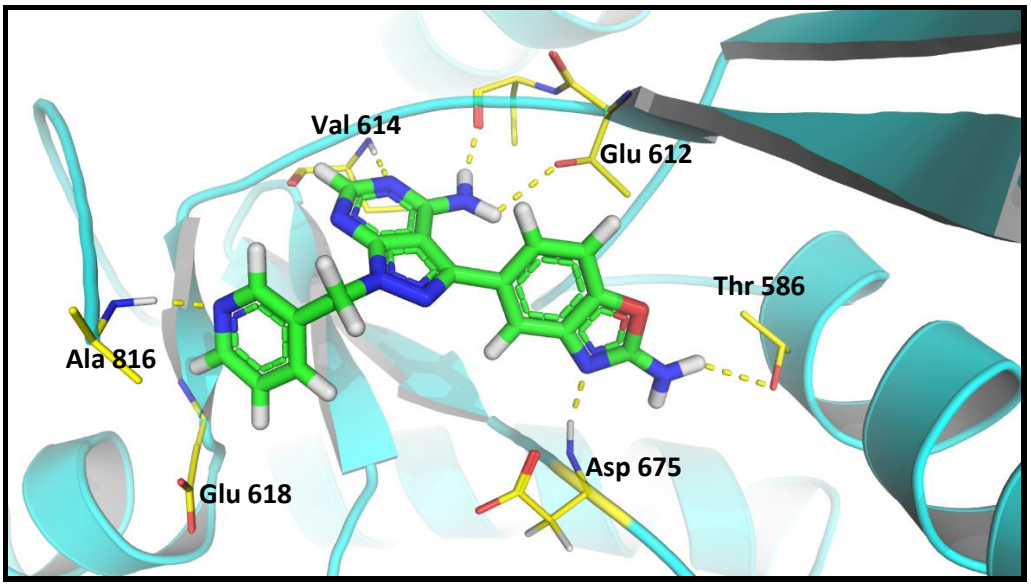

Figure 3.10: Docking pose of analogue **48** (**GS 83**) within the *Pv*PKG binding site showing additional H-bond with Ala 816 and the position of Glu 618, a residue which is responsible for clash with several analogues

Docking of **7** (**GS 55**) and **8** (**GS 65**) with *Pv*PKG (IC_{50} > 2 µM) revealed the unfavorable placement of the partially negatively charged halogen atom in a relatively non-polar region near Glu 618 of the ribose pocket but not within reach for H-bond formation (**Figure 3.10**). Compound **7** (**GS 55**) was also subject to a significant clash of the benzyl ring with Ala 816.

This, together with the lack of π-stacking, provides an explanation for the low PKG potency observed for these compounds. A similar observation was noted for the *para*-trifluoromethyl analogue **10** (**GS 59**), while a significant clash of the methyl group in the *para* position of **11** (**GS 69**) with Glu 618 accounted for decreased enzymatic activity (*Pv*PKG IC_{50} > 10 µM for each). Furthermore, appending multiple partially negatively charged or bulky substituents as in **38** (**GS 145**; *Pv*PKG IC_{50} > 10 µM) resulted in unfavorable interactions and/or significant steric clashes causing a loss of activity.

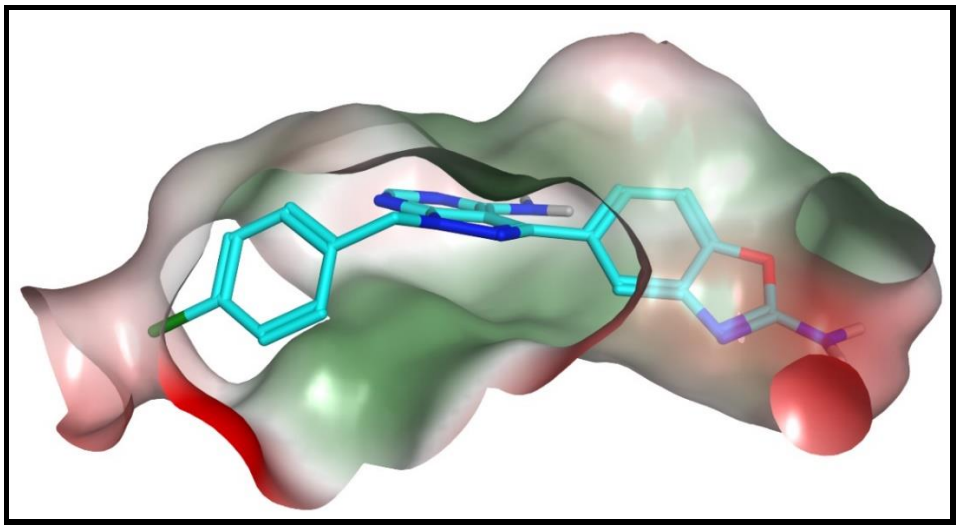

Figure 3.11: Polar (green) and non-polar (red) surface depicting the docking pose of **7** (**GS 55,** cyan) in the *Pv*PKG binding site

The predicted binding modes were also analyzed quantitatively using MMGBSA calculations. The calculated MMGBSA values, and energy change for a selected set of compounds relative to that of the reference compound are listed in **Table 3.5**. From this experiment, most compounds with large negative MMGBSA dG values (-55.86 to -57.34 kcal/mol) exhibited moderate inhibitory activity (IC_{50} = 0.35–0.8 µM, **Table 3.5**). Docking experiments also revealed significantly lower negative energy for some compounds such as **11** (**GS 69**; -54.70 kcal/mol) in agreement with the observed poor *Pv*PKG inhibition ($IC_{50} \geq 10$ µM). However, in contrast, poor correlation was also observed in a significant number of compounds. For example, **17** (**GS 57**) displayed a good binding pose with high binding energy (MMGBSA dG = -62.05 Kcal/mol; **Table 3.5**) and was expected to be a potent inhibitor contrary to its experimental result (*Pf*PKG IC_{50} = 3.20 µM).

Table 3.5: Calculated energy changes (kcal/mol) of selected ligands in the *Pv*PKG crystal structure

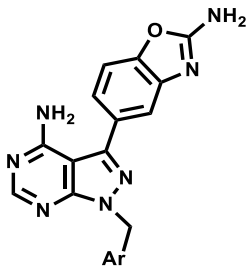

Ar	R	Code	*Pf*NF54 (IC_{50}, µM)	*Pf*PKG (IC_{50}, µM)	MMGBSA dG*	MMGBSA $pK_{\Delta G}$
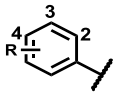	4-Cl	**7 (GS 55)**	0.029	> 2	-60.65	10.63
	2-Cl	**22(GS 115)**	1.345	0.32	-61.02	10.70
	3-Cl	**17 (GS 57)**	0.129	3.20	-62.05	10.88
	2-CF_3	**23(GS 113)**	3.595	0.23	-57.83	10.14
	4-F	**8 (GS 65)**	0.141	> 2	-59.64	10.45
	2-Me	**20 (GS 97)**	1.260	0.23	-58.52	10.26
	3-Me	**16 (GS 67)**	0.418	0.63	-57.47	10.07
	2-F	**21 (GS 91)**	2.655	0.10	-57.83	10.14
	H	**6 (GS 77)**	0.719	0.50	-58.41	10.24
	4-Me	**11 (GS 69)**	0.178	> 10	-54.70	9.59
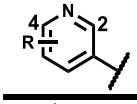	H	**48 (GS 83)**	0.795	0.35	-60.26	10.56
	4-Me	**42(GS 137)**	0.340	0.25	-56.27	9.86
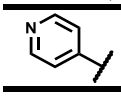	-	**43(GS 79B)**	0.950	0.49	-55.86	9.79
	62 (MLN0128)		0.058	0.02	-51.81	9.08

* Calculated energy changes in kcal/mol

Furthermore, an unexpected non-positive correlation (negative slope) was observed between the calculated change in binding energy and *Pf*PKG inhibition (**Figure 3.11**), with a rather surprising R^2 value (0.42) suggesting favorable MMGBSA binding energies for poor target binders. However, the minimized binding modes used to calculate the MMGBSA dG values for a compound was qualitatively analyzed and hence may be inaccurate for certain compounds. This further highlights the limitations of the *in-silico* methods employed and the importance of generating experimental data in biochemical assays to guide the SAR.

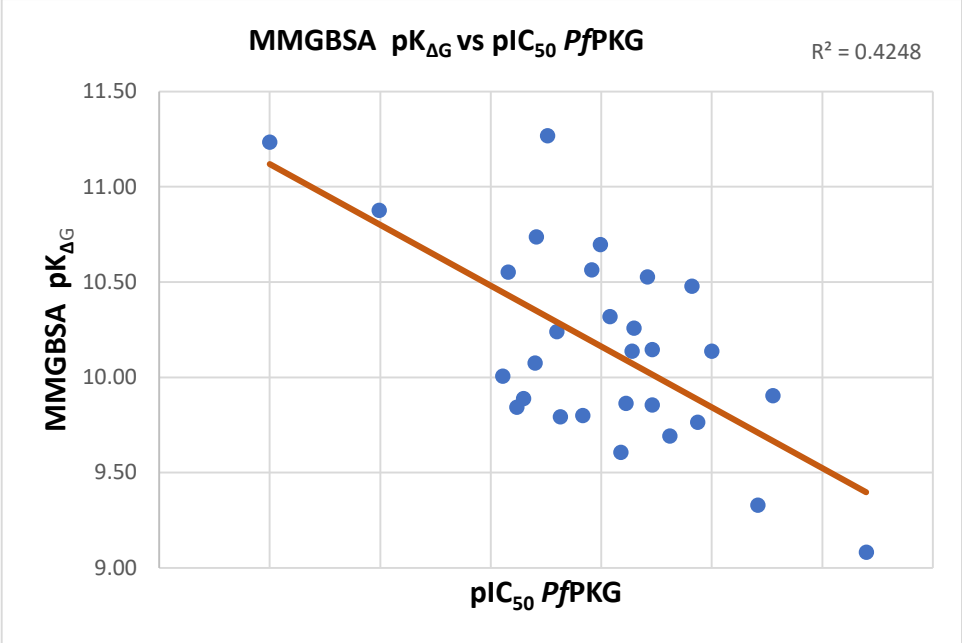

Figure 3.12: Correlation plot of *in vitro Pv*PI4K activity (pIC50) and calculated MMGBSA values

Furthermore, fixed core docking experiments as undertaken in this study postulate a rigid hydrogen bonding interaction, for example between the backbone carbonyl of Glu 612 and Val 614 with the pyrazolo[3,4-*d*] pyrimidine core, which may not be the case in a biochemical or cellular setting. In addition, all PKG crystal structures have a break at Ala 816, presumably for a disordered region which could not be resolved via crystal structure assessment. Because this disordered region is near the ribose pocket explored in this series, fixing this residue during the MMGBSA calculations could have led to unreliable results for some compounds, skewing the correlation plot for this limited data set and range of IC_{50} values.

3.2.7 Identification of dual and single target *Plasmodium* PI4K/PKG inhibitors

This study aimed to identify MLN0128 analogues with high anti-plasmodium potency and dual *Plasmodium* PI4K/PKG inhibitors. In this regard, analogues showing sub-nanomolar potency against both *Plasmodium* targets of interest were identified. Compounds in this series generally possessed high *in vitro Pv*PI4K potency (IC_{50} < 0.02 µM), and variable *Pf*PKG potency (between 0.053 and > 10 µM). Consequently, *Pf*PKG activity was selected as an appropriate indicator to monitor dual potency. A cut-off for PKG IC_{50} < 0.2 µM was set for the sake of identifying dual inhibitors in this thesis, whereas compounds exhibiting > 2 µM were categorized as single PI4K inhibitors (Class: PI4K). Towards this end, a summary of selected compounds highlighting the associated properties is shown in **Table 3.6**.

Table 3.6: Dual/single target classification of selected MLN0128 analogues

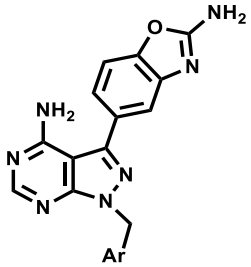

Code	Ar	R	*Pf*NF54 (IC_{50}, µM)	*Pv*PI4K (IC_{50}, µM)	*Pf*PKG (IC_{50}, µM)	Class
7 (GS 55)		4-Cl	0.029	0.007	> 2	PI4K
8 (GS 65)		4-F	0.141	0.006	> 2	PI4K
35(GS 139)	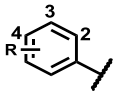	3-Cl, 4-F	0.086	0.008	> 10	PI4K
28(GS 105)		3-F, 4-Cl	0.020	0.021	10	PI4K
13(GS 149)		4-NH_2	0.068	0.024	0.053	Dual
18(GS 155)		3-NH_2	0.345	0.010	0.116	Dual
19(GS 175)		3-$N(Me)_2$	0.411	0.011	0.155	Dual
21 (GS 91)		2-F	2.655	0.027	0.100	Dual
58(GS 193)	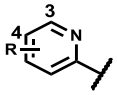	3-F	0.682	0.006	0.186	Dual
59(GS 195)		3-CF_3	0.278	0.005	0.196	Dual
50(GS 203)	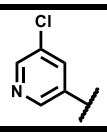	-	0.151	0.001	0.145	Dual
62(GS 20b)	MLN0128		0.058	0.005	0.020	Dual

This data highlights the potential of this series as dual *Plasmodium* kinase inhibitors. As previously discussed, poly-pharmacological compounds are likely to be less prone to drug resistance because of the limited risk of spontaneous emergence of resistance against two essential parasitic targets simultaneously.[22] Inhibition of multiple targets simultaneously may also offer improved efficacy as a result of synergistic effects and a wider window of activity across the life cycle. Furthermore, PK parameters of such compound would be optimized in early stages of drug development reducing risk of toxicity and PK mismatch as encountered in combinational therapies at advanced clinical studies. Poly-pharmacological drugs can potentially present more long-term benefits to patients through reduction of pill burden and cost of goods as the WHO recommends the administration of multiple compounds with different MoA and PK parameters to treat malaria.[23]

3.2.8 *In vitro* gametocytocidal activity of MLN0128 analogues

To assess the transmission-blocking potential of this series, the *in vitro* gametocytocidal activity of selected compounds showing high asexual blood-stage activity (*Pf*NF54 $IC_{50} \leq 0.5$ µM) was tested at the Department of Biochemistry, Institute for Sustainable Malaria Control, University of Pretoria (UP), South Africa, using the luciferase-reporter NF54 line of *P. falciparum.* Gametocytes were produced according to methods previously described.[24] This luciferase assay measures luminescence signal generated when a luciferin substrate is added to a parasite expressing the luciferase enzyme. In this case, stage-specific action against the early and late gametocyte transgenic parasite cell line marker NF54-*Pf*S16-GFP-Luc. was quantified according to methods previously described.[24,25]

Each compound was tested at concentrations of 1 and 5 µM with methylene blue (1 µM) and MMV390048 (1 µM) as positive controls. Initially, 36 compounds were screened against early-stage gametocytes (EG, contains > 90% stage I-III) and late-stage gametocytes (LG, > 90% stage IV/V; **Table 3.7**). The series was specific for LGs, with 18 compounds exhibiting > 70% inhibition of LGs at 5 µM. None of the tested compounds showed dual activity (> 50% inhibition) against the two sexual stages of development at 1 µM drug dose concentration. Encouragingly, the LG specificity demonstrated that these compounds potentially inhibited an essential target pre-dominant in LGs. Compounds with reproducibly high single-point inhibition at 1 µM (> 75%; **Table 3.7**), were tested in dose-response assays for IC_{50} determination (n = 1 experiment in technical duplicates).

Table 3.7: *In vitro* gametocytocidal activity of compounds on *Pf* early- and late-stage gametocytes, at 1 and 5 µM

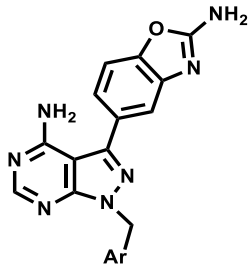

Ar	R	Code	*Pf*NF54 (IC_{50}, µM)	[a]% Inh. (EG) at 1 and 5 µM		[a]% Inh. (LG) at 1 and 5 µM		[b]LG IC_{50}	Ar	R	Code	*Pf*NF54 (IC_{50}, µM)	[a]% Inh. (EG) at 1 and 5 µM		[a]% Inh. (LG) at 1 and 5 µM		[b]LG IC_{50}
				1	5	1	5						1	5	1	5	
	H	**6**	0.719	-	-	-	-	-	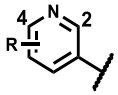	4-CF_3	**39**	0.375	0.0	30.2	16.6	78.0	-
	4-Cl	**7**	0.029	8.1	39.5	68.3	84.8	0.63		4-Cl	**40**	0.081	16.0	56.1	57.2	88.8	0.52
	4-F	**8**	0.141	0.0	0.0	1.2	76.9	-		4-F	**41**	0.184	0.0	41.6	21.7	61.1	-
	4-CN	**9**	0.198	0.0	5.2	10.4	73.9	-		4-Me	**42**	0.340	1.8	36.7	12.7	53.3	-
	4-CF_3	**10**	0.221	0.0	0.0	2.7	57.4	-	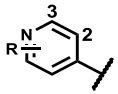	H	**43**	0.950	-	-	-	-	-
	4-Me	**11**	0.178	0.0	0.0	0.0	67.8	-		3-Cl	**44**	0.104	0.0	0.0	23.9	73.1	-
	4-Ome	**12**	0.329	0.0	0.0	7.9	69.0	-		3-F	**45**	3.350	-	-	-	-	-
	4-NH_2	**13**	0.068	0.0	5.6	0.0	0.0	-		3-CF_3	**46**	> 6	-	-	-	-	-
	3-F	**14**	0.297	0.0	23.8	9.2	57.4	-		3-Me	**47**	-	-	-	-	-	-
	3-CF_3	**15**	0.191	5.1	0.0	0.0	68.7	-	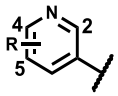	H	**48**	0.795	-	-	-	-	-
	3-Me	**16**	0.418	-	-	-	-	-		5-Me	**49**	0.189	0.0	0.0	22.5	70.9	-
	3-Cl	**17**	0.129	0.0	14.6	5.4	68.6	-		5-Cl	**50**	0.151	0.0	0.0	51.0	79.3	2.25
	3-NH_2	**18**	0.345	0.0	0.0	12.5	39.0	-		5-F	**51**	0.250	0.0	0.0	17.8	71.6	-
	3-$N(Me)_2$	**19**	0.411	0.0	0.0	0.0	5.8	-	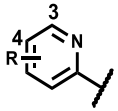	H	**52**	-	-	-	-	-	-
	2-Me	**20**	1.260	-	-	-	-	-		4-Cl	**53**	0.099[c]	-	-	-	-	-
	2-F	**21**	2.655	-	-	-	-	-		4-F	**54**	0.273[c]	-	-	-	-	-
	2-Cl	**22**	1.345	-	-	-	-	-		4-CF_3	**55**	0.334[c]	-	-	-	-	-
	2-CF_3	**23**	3.595	-	-	-	-	-									
	3,4-Cl	**24**	0.039	0.0	4.7	34.7	80.7	-	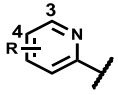	3-Cl	**56**	-	-	-	-	-	-
	2,4-Cl	**25**	0.520	-	-	-	-	-		3-Me	**57**	0.336	0.0	0.0	1.5	39.7	-
	2-F, 4-Cl	**26**	0.100	7.1	18.6	45.6	88.2	-		3-F	**58**	0.682	-	-	-	-	-
	2-CN, 4-Cl	**27**	0.165	0.0	24.5	19.4	81.5	-		3-CF_3	**59**	0.278	0.0	0.0	29.0	73.8	-
	3-F, 4-Cl	**28**	0.020	0.4	50.5	71.9	88.5	-									

3-CF_3, 4-Cl	**29**	0.157	0.0	0.0	13.6	75.5	-
2-F, 4-F	**30**	0.207	0.0	1.6	18.4	78.7	-
2-Cl, 4-F	**31**	0.834	-	-	-	-	-
2-CF_3, 4-F	**32**	-	-	-	-	-	-
2-CN, 4-F	**33**	0.389	3.2	31.8	5.3	43.8	-
2-Me, 4-F	**34**	0.520	-	-	-	-	-
3-Cl, 4-F	**35**	0.086	2.3	49.2	31.5	68.0	-
3-CN, 4-F	**36**	0.080	0.0	43.1	40.6	70.9	-
3-F, 4-F	**37**	0.044	5.5	61.9	55.0	76.0	1.95
3-CF_3, 4-F	**38**	0.191	0.0	37.7	9.1	45.3	-

	H	**60**	0.384	0.0	56.6	8.4	61.3	-
	4-*di* F	**61**	0.169	0.0	0.0	29.4	73.0	-
MLN0128		**62**	0.058	2.7	29.6	68.0	83.9	0.54
Controls:								
Methylene blue				95		92		
MMV390048				56		86		

"-" = Not determined, [a]% inhibition at the specified drug dose, n = 1, one biological assay with technical triplicates; [b] mean of duplicates for n = 3 determinations; [c]asexual blood stage IC_{50} values against *Pf*K1.

Compounds **40** (**GS 121**) and **7** (**GS 55**) demonstrated high potency against LGs (IC_{50} = 0.517 and 0.623 µM, respectively). Similarly, MLN0128 (**62**) exhibited high gametocytocidal activity against LGs (IC_{50} = 0.538 µM). This is in addition to the three compounds exhibiting potent asexual blood stage activity (**40** (**GS 121**), **7** (**GS 55**), and **62** (**GS 20b**); *Pf*NF54 IC_{50} = 0.081, 0.029, and 0.058 µM, respectively) and *in vitro Pv*PI4K potencies (*Pf*PI4K IC_{50} = 0.008, 0.007, and 0.005 µM, respectively; **Figure 3.12**). However, despite meeting the pre-set criteria, compound **28** (**GS 105**) was not evaluated as there was not enough solid sample available at the time of the assay.

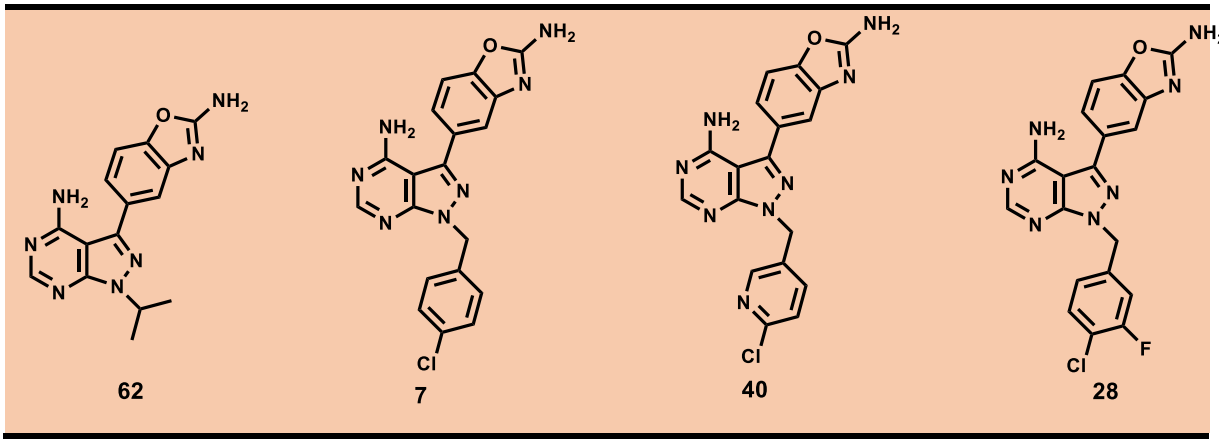

Figure 3.13: Compounds showing high late stage gametocytocidal activity

The results indicated the potential of these compounds as novel gametocytocidal agents possibly emanating from the inhibition of *Pf*PI4K as a main contributor to their MoA.[26] Late stage IV/V gametocytes undergo a membrane deformation step adopting a crescent (falciform or banana) shape, a transformation that adaptively enables them to fit in the mosquito's proboscis during a blood meal on an infected human to ensure progressive development in the mosquito vector.[27] *Pf*PI4K is highly associated with proper assembly of morphologically functioning cell membrane in this step of the *Plasmodium* life-cycle.[28]

Furthermore, the gametocytocidal activity of MLN0128 and front-runner compounds indicated that this class of compounds was more active against asexual blood-stage parasites than against those in the sexual gametocyte stage, an observation consistent with published PI4K inhibitors.[4] In addition to inhibition of *Pf*PI4K and PKG, it is likely that the compounds inhibited other *Pf* kinases strongly associated with LGs, such as CRK5, as observed in the GSK Kino-bead study. Also, other kinases not necessarily targeted by the parent compound may be implicated after subtle changes during the design of the analogues, due to the highly conserved

nature of the ATP-binding site across this superfamily of enzymes. For example, inhibition of *Pf*CDPK4 by closely related pyrazolopyrimidine-based compounds, has been strongly associated with the suppression of gametocytes.[29]

Taken together, these results indicated that compounds in this series present other potential benefits besides activity against the asexual blood-stage of the parasite in line with the newly defined TCPs for future antimalarials. Amongst other benefits, the next generation of drugs should exhibit gametocytocidal activity for host-vector transmission blockade.[30]

3.2.9 *In vitro* cytotoxicity screening of MLN0128 analogues

The cytotoxicity of selected compounds was determined based on the well-established colorimetric 3-(4,5-dimethylthiazol-2-yl)-2,5-diphenyltetrazolium bromide (MTT) assay in CHO cells.[31] This work was conducted at H3D within the Division of Clinical Pharmacology, Department of Medicine, UCT. The full methodology employed is described in Chapter 10. Selected compounds were also evaluated against HepG2 cells using a CytoSelect™ cytotoxicity assay kit (CBA-241; Cell Biolabs Inc.) at 2 µM, according to methods previously described.[32] This assay was performed at the Department of Biochemistry, Institute for Sustainable Malaria Control, University of Pretoria (UP), South Africa. The % inhibition and IC_{50} values (from a dose-response model at four concentrations in triplicates) were determined and selectivity indices (SI) were calculated (**Table 3.8**).

In principle, SI is an indicator of the rate at which a compound eliminates the *Plasmodium* parasite relative to healthy human cells or other viable surrogates. A high SI is desirable as an indicator that the drug preferentially targets the parasite over the human cells. In this study, a minimum SI (CHO IC_{50}/*Pf*NF54 IC_{50}) of 100 was considered as a reasonable indicator of selectivity and was set as a cut-off for the progression of compounds.

Table 3.8: *In vitro* mammalian cytotoxicity profiling of selected analogues

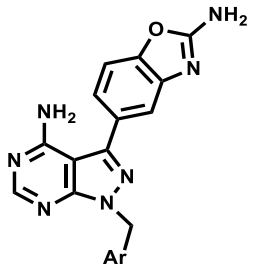

Ar	R	Code	[a]*Pf*NF54 (IC_{50}, µM)	[b]CHO (µM)	[d]SI	[e]% Inh.* HepG2 (2 µM)	Ar	R	Code	[a]*Pf*NF54 (IC_{50}, µM)	[b]CHO (µM)	[d]SI	[e]% Inh.* HepG2 (2 µM)
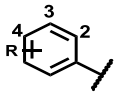	H	**6**	0.719	-	-	-	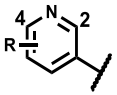	4-CF_3	**39**	0.375	> 50	>133	19.1
	4-Cl	**7**	0.029	1.19	40	9.9		4-Cl	**40**	0.081	3.48	44	17.4
	4-F	**8**	0.141	9.04	108	15.2		4-F	**41**	0.184	1.94	11	11.9
	4-CN	**9**	0.198	4.18	21	11.8		4-Me	**42**	0.340	15.25	45	12.0
	4-CF_3	**10**	0.221	> 50	> 226	5.6	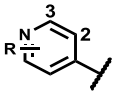	H	**43**	0.950	1.35	1	-
	4-Me	**11**	0.178	> 50	> 281	8.7		3-Cl	**44**	0.104	40.82	408	35.8
	4-OMe	**12**	0.329	> 50	> 152	15.5		3-F	**45**	3.350	0.63	-	-
	4-NH_2	**13**	0.068	-	-	9.0		3-CF_3	**46**	> 6	-	-	-
	3-F	**14**	0.297	> 50	> 168	21.0		3-Me	**47**	0.698[f]	-	-	-
	3-CF_3	**15**	0.191	> 50	> 262	8.1	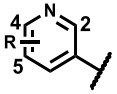	H	**48**	0.795	2.91	4	-
	3-Me	**16**	0.418	8.37	20	-		5-Me	**49**	0.189	39.85	210	41.2
	3-Cl	**17**	0.129	> 50	> 388	7.5		5-Cl	**50**	0.151	0.60	4	69.0
	3-NH_2	**18**	0.345	-	-	38.6		5-F	**51**	0.250	0.69	2	52.2
	3-$N(Me)_2$	**19**	0.411	1.57	4	48.3	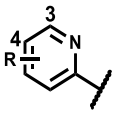	H	**52**	-	-	-	-
	2-Me	**20**	1.260	-	-	-		4-Cl	**53**	0.099[f]	-	-	-
	2-F	**21**	2.655	-	-	-		4-F	**54**	0.273[f]	-	-	-
	2-Cl	**22**	1.345	-	-	-		4-CF_3	**55**	0.334[f]	-	-	-

2-CF_3	**23**	3.595	-	-	-
3,4-Cl	**24**	0.039	> 50	>1250	6.9
2,4-Cl	**25**	0.520	-	-	-
2-F, 4-Cl	**26**	0.100	1.17	12	14.2
2-CN, 4-Cl	**27**	0.165	2.24	13	11.3
3-F, 4-Cl	**28**	0.020	1.98	99	8.9
3-CF_3, 4-Cl	**29**	0.157	1.84	12	13.5
2-F, 4-F	**30**	0.207	0.61	3	7.5
2-Cl, 4-F	**31**	0.834	-	-	-
2-CF_3, 4-F	**32**	-	-	-	-
2-CN, 4-F	**33**	0.389	4.73	12	9.4
2-Me, 4-F	**34**	0.520	-	-	-
3-Cl, 4-F	**35**	0.086	24.0	267	7.9
3-CN, 4-F	**36**	0.080	5.66	71	21.6
3-F, 4-F	**37**	0.044	0.62	15	10.7
3-CF_3, 4-F	**38**	0.191	8.67	46	4.3

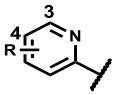	3-Cl	**56**	0.341[f]	-	-	-
	3-Me	**57**	0.336	1.66	5	55.7
	3-F	**58**	0.682	5.66	8	-
	3-CF_3	**59**	0.278	2.00	7	60.2
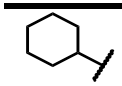	H	**60**	0.384	5.67	15	19.6
	4-*di* F	**61**	0.169	0.22	1.2	71.8
MLN0128		**62**	0.058	0.13	2	34.3
Controls:						
Chloroquine			0.010			
Artesunate			0.008			

* Average for technical triplicates for n = 1 experiments; "-" = not determined, [a]asexual blood stage IC_{50} values are means of n ≥ 2 determinations; [b] CHO = Chinese hamster ovarian cell line; [d]SI = selectivity index i.e. CHO IC_{50}/*Pf*NF54 IC_{50}; [e]% inhibition at 2 µM, average for technical triplicates (n = 1); [f]anti-plasmodium data generated using the *Pf*K1 strain.

A significant number of mono-substituted *para* and *meta* benzyl analogues exhibited SI > 100 as exemplified by **16** (**GS 59**), **17** (**GS 69**), and **23** (**GS 57**) with CHO IC_{50} > 50 µM, translating to SI > 226, > 281, and > 338, respectively (**Table 3.8**). Exceptions to this included *para*-Cl analogue **13** (**GS 55**), *para*-CN **15** (**GS 63**), *meta*-methyl **22** (**GS 67**), and the *N*, *N*-di-methylated compound **25** (**GS 175**) with SI = 40, 21, 20, and 4, respectively. Data for *ortho*-substituted benzyl analogues were not available for comparison at the time of writing. In contrast, di-substitution increased the potential for inducing cytotoxicity against CHO cells as all disubstituted benzyls showed poor SIs (< 100), except for 3,4 di-chloro in **30** (**GS 101**; SI > 1250) and 3-Cl, 4-F substitution in **41** (**GS 139**; SI = 267). Interestingly, the 3,4-di-chlorinated analogue **30** (**GS 101**) showed the most favorable safety profile (SI > 1250) of all analogues tested.

Additionally, no significant improvement was achieved through regio-isomerism, except for the 3-F, 4-Cl modification in analogue **28** (**GS 105**; SI = 99) lying just within the defined threshold for CHO selectivity. A head-to-head comparison with its isomeric congener **35** (**GS 139**; SI = 267) showed a dramatic shift in SI, suggesting that minor modifications can impact heavily on the cytotoxicity profile of compounds. None of the pyridyl analogues tested met the selectivity criteria, except for compounds **39** (**GS 99**; SI > 133), **44** (**GS 157**; SI = 393), and **49** (**GS 167**; SI = 210), suggesting that pyridyls generally showed low safety profiles in this series.

Furthermore, there appeared to be no favored pyridyl position for enhanced selectivity as no specific SAR could be deduced. Equally, replacement of the aromatic moiety with an aliphatic cyclohexyl was not beneficial, as evidenced by the low SI of **60** (**GS 125**; SI = 15) and **61** (**GS 197**; SI = 1.2). In addition, cytotoxicity of **MLN0128** (**62**; **GS 20b**) was 0.126 µM (SI = 2), indicative of high toxicity against CHO cells. Overall, these data show that the cytotoxicity profile of compounds against this cell line is amenable to modulation with subtle changes resulting in significant changes in SI, an indication that *in vitro* cytotoxicity is compound-specific and not an intrinsic issue for the series.

Based on high anti-plasmodium potency (*Pf*NF54 IC_{50} < 0.5 µM), 35 compounds were also triaged for cytotoxicity testing in the HepG2 cell line assay. Certain compounds that met the criteria could not be tested because of missing *Plasmodium* data or solid samples were unavailable at the time of the assay. The structures of the specific compounds and the results of these assay are included in **Table 3.8**. All benzyls and a significant number of pyridyl compounds tested against HepG2 displayed low cytotoxicity as indicated by their % inhibitions

at 2 µM (< 50%). Exceptions to these included compounds **57** (**GS 177**), **59** (**GS 195**), **61** (**GS 197**), **51** (**GS 199**), and **50** (**GS 203**), which displayed modest inhibitions of 55, 60, 72, 52, and 69%, respectively, against this cell line at the same concentration. The same compounds also showed low SI (< 10) against CHO cells, as previously discussed. A structural investigation indicated that most of these compounds possessed pyridyl moieties except for compound **61** (**GS 197**) comprising a di-fluoro-substituted cyclohexyl ring.

Overall, cytotoxicity is dependent on the cell line employed in a study, emphasizing the need to evaluate potential candidates against multiple host and surrogate cell lines. Such a strategy is often employed for the progression of pre-clinical candidates before their advancement to human trials. It is also important to note that cytotoxicity may be species related. Moreover, combination therapies in oncological drug discovery are often employed to achieve antagonistic effects by one drug on normal human cells, allowing another drug to selectively eliminate rapidly dividing tumor cells.[33] This may explain why MLN0128 is currently explored in human clinical studies despite its low safety margin in the mammalian CHO cell line.

3.2.10 Microsomal metabolic stability of MLN0128 analogues

Compounds exhibiting high *in vitro* anti-plasmodium activity (IC_{50} < 0.5 µM) and low cytotoxicity against the CHO cell line (SI > 100) were selected for *in vitro* microsomal metabolic stability testing against human (HLM), rat (RLM), and mouse liver microsomes (MLM). This assay was performed at the H3D Centre, Division of Clinical Pharmacology, Department of Medicine, UCT. Although all compounds progressed showed low solubility according to the pre-determined cut-off (> 50 µM), it was argued that other strategies such as co-formulation may be adopted in advanced stages or optimized together with any other emerging issues. The microsomal metabolic stability assay involved incubation of the compounds in liver microsomes at optimized conditions for 30 min, before evaluating the amount of compound remaining via LC-MS. For this study, a single-point metabolic stability assay at a compound concentration of 0.1 µM was used in preparations of liver microsomes from the three species of interest.[34] Compounds not tested despite meeting these pre-determined criteria had pending cytotoxicity results at the time of the assay.

Even though a drug is ultimately intended for human use, studies using rat and mouse microsomes are necessary to progress compounds to *in vivo* efficacy studies in mouse models of disease and assist in understanding and interpreting ADME data emanating from studies in these models.[35] Furthermore, PK studies are often undertaken in rats because of the higher

blood volume available compared to that in mice. Highly active but metabolically labile compounds would be expected to achieve low systemic exposure and thus compromised pharmacological outcomes particularly if they generate inactive metabolites.[36]

Compounds showing low metabolic stability in animal models often result in rapid hepatic clearance, poor exposure and low efficacy and may potentially lead to the termination of a series which would otherwise be promising and worthy of pursuit. Thus, scrutiny of drug metabolism across multiple species is important to make judicious choices of *in vivo* proof-of-concept animal models.[36] Consequently, this study was employed to identify hotspots and guide metabolically stable substituents for the preliminary triaging of compounds for *in vivo* efficacy and PK studies.

For this study, microsomal metabolic stability criteria were determined based on the amount of compound remaining after a 30-min incubation with liver microsomal preparations. Compounds were classed as highly stable (> 75% remaining), moderately stable (50–74%), or poorly stable (< 50%). *In vitro* half-lives (t½) and hepatic extraction ratios (E_H), which are estimates of expected first-pass metabolism in animal models and clinical conditions, were also evaluated. The half-life of a compound indicates the time it takes for 50% disappearance of the parent drug whereas E_H is the fraction of the metabolized drug relative to the initial concentration of the parent drug. Thus, large t½ and low E_H values are desirable, as indicators of low metabolism and projected high bioavailability.[37]

Encouragingly, four of five compounds assayed showed high microsomal metabolic stability across all species (> 85%; **Table 3.9**). Compounds **35** (**GS 139**), **44** (**GS 157**), and **49** (**GS 167**) displayed very high stability (> 90%) across the three species translating to high t½ of > 150 min and low E_H in human liver microsomal preparations.

Table 3.9: *In vitro* microsomal metabolic stability data for selected MLN0128 analogues

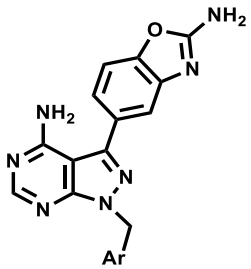

Code	Ar	*Pf*NF54 (IC_{50}, µM)	CHO (SI)	% rem. after 30 min.	Projected $^{d}t_{½}$ (min)	Hepatic extraction ratio (E_H)
				^{a}H/^{b}R/^{c}M	^{a}H/^{b}R/^{c}M	^{a}H/^{b}R/^{c}M
24 (**GS 101**)	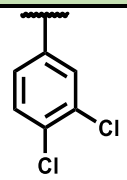	0.039	>1250	95.9/68.2/59.7	>150/54.2/40.2	<0.42/0.4/0.65
28 (**GS 105**)	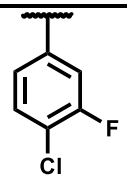	0.020	99	89.2/87.0/85.5	>150/146.2/130.7	<0.42/<0.3/0.37
35 (**GS 139**)	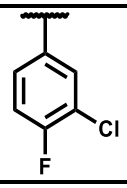	0.086	267	94.7/93.5/96.6	>150/>150/>150	<0.42/<0.3/<0.33
44 (**GS 157**)	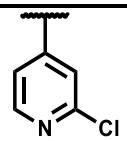	0.104	408	97.2/95.2/94.5	>150/>150/>150	<0.42/<0.3/<0.33
49 (**GS 167**)	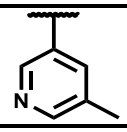	0.189	210	97.3/97.7/95.5	>150/>150/>150	<0.42/<0.3</0.33

^{a}H = Human liver microsomes; ^{b}R = Rat liver microsomes; ^{c}M = Mouse liver microsomes; $^{d}t_{½}$ = half-life

According to the percentage parent drug remaining after 30 min incubation, regio-isomerism appeared to impact microsomal stability as **28** (**GS 105**; H/R/M = 89.2/87.0/85.5%) was slightly disadvantaged compared to **35** (**GS 139**; H/R/M = 94.7/93.5/96.6%) across the three species. The di-chlorinated analogue **24** (**GS 101**) displayed moderate stability in RLMs (68.2% remaining after 30 min) and MLMs (59.7%), although it displayed high stability in HLMs (95.9%), suggesting species differences in its metabolism. However, metabolite identification studies for this compound in RLM and MLMs were not undertaken.

Despite these encouraging results, it is important to emphasize that although this study indicates the expected *in vivo* microsomal metabolism of a drug in the liver, microsomes are only hepatic sub-cellular fractions containing drug-metabolizing enzymes, chiefly CYP450 involved in Phase I metabolism.[38] Thus, the results do not account for Phase II metabolism, which often involves hydrophilic conjugation thereby facilitating faster renal or hepatobiliary excretion.[39] Moreover, other potential metabolism sites such as blood, intestinal walls, kidneys,

lungs, and skin are not considered.[40] Additionally, the compounds tested showed low solubility (< 50 µM) and this may have an impact on metabolic stability assay results, particularly if they are unavailable to liver microsomes.

3.2.11 Cardiotoxicity (hERG) risk assessment profile

Although MLN0128 has been reported as a compound of significantly low risk on the hERG potassium ion channel (IC_{50} = 175 µM), the contribution of the structural modifications undertaken in this work was investigated to determine the risk arising from the added aromaticity and potentially ionizable nitrogen centers.[1,41] Representative benzyls; (**24**; **GS 101** and **28** (**GS 105**), pyridyls (**44**; **GS 157** and **49**; **GS 167**) and a saturated ring-containing compound **60** (**GS 125**) were tested. The experimental study was outsourced to B'SYS GmbH, Witterswil, Switzerland and was conducted based on the whole-cell patch-clamp technique on channels stably expressed in CHO cells. Details of the assay procedure, cell systems, and voltage pulses conditions have been provided in the Experimental Chapter.

In brief, the samples were prediluted in extracellular solution from a DMSO stock of 10 mM to test concentrations of 1, 3, 10 and 30 µM from which electrophysiology profile was assessed in triplicate assays using the QPatch HTX automated patch-clamp system. By recording the hERG tail current amplitudes, the normalized concentration-dose response curves were generated and fitted in the Hill equation from which the IC_{50} values were determined. E-4031, a known hERG channel blocker was included for quality control in the experiment. In several instances where the average percentage inhibition from the cells was higher than 50% at the maximum test concentration (30 µM), extrapolated IC_{50} values were obtained, hence are rough estimates or otherwise reported as > 30 µM. The data and structures for the tested compounds is summarized in **Table 3.10**.

Table 3.10: *In vitro* hERG inhibition activity of selected MLN0128 analogues

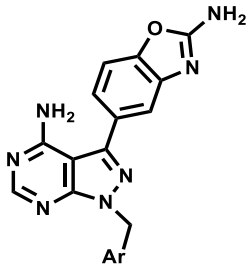

Code	Ar	*Pf*NF54 (IC_{50}, µM)	CHO (SI)	IC_{50} (µM)	IC_{20} (µM)	Hill coefficient

24 (**GS 101**)	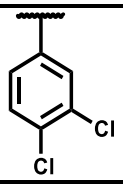	0.039	> 1250	> 30[a]	-	-
28 (**GS 105**)	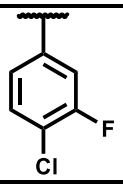	0.020	99	> 30[a]	-	-
44 (**GS 157**)	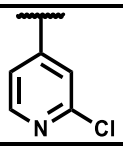	0.104	408	21.62	5.07	0.96
49 (**GS 167**)	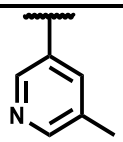	0.189	210	78.99[b]	8.61	0.63
60 (**GS 125**)	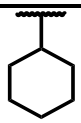	0.384	15	13.74[c]	6.49	1.85

[a]Remaining current at highest concentration > 70%, no curve was fitted; [b]remaining current at highest concentration 50–70%; [c]precipitation at the highest concentration; E-4031 used as reference compound at a concentration of 100 nM, with the hERG tail current blockade of 5.22 ± 0.95% relative remaining current for n = 2 experiments

The tested compounds showed no potential to cause cardiotoxicity with the IC_{50} values obtained higher than the pre-set cut-off (IC_{50} > 10 µM). All the compounds possessing the additional aromaticity including the pyridyls exhibited a clean profile. Pyridyl analogue **49** (**GS 167**) displayed low activity against the channel with IC_{50} of 79.0 µM and a hill co-efficient of 0.6. For hERG and other channel-compound interactions, an independent binding of the ligand is expected, hence a hill co-efficient of 1. However, in practice, this may deviate due to solubility issues as observed in several compounds, unideal clamp conditions and differences in series resistance.

To circumvent crashing out of compounds, lower inhibitory determinations (IC_{20}) were evaluated. Modest activity against the cardiac channel was obtained for **44** (**GS 157**), **49** (**GS 167**), **60** (**GS 125**) with respective IC_{20} values of 5.1, 8.6, and 6.5 µM further confirming low risk to cause cardiotoxicity for the tested compounds and generally the series. Overall, this data encouragingly offers confidence in future optimization of the compounds generated from this series as anti-plasmodium leads.

3.2.12 Human off-target kinase evaluation of MLN0128 analogues

3.2.12.1 *In vitro* human mTOR inhibition and rationalization of selected compounds

To assess human mTOR mitigation for selectivity in line with the specific objectives of this study, the *in vitro* enzyme inhibition activity of selected compounds was evaluated against the recombinant human protein FK506-binding protein 12-rapamycin-associated protein 1 (FRAP1) using the "HotSpot" assay platform.[42] This assay was outsourced to Reaction Biology® Corporation Laboratories, Pennsylvania, USA. Initially, six compounds (**7** (**GS 55**), **29** (**GS 117**), **30** (**GS 123**), **38** (**GS 145**), **44** (**GS 157**), and **19** (**GS 175**); **Table 3.11**) and the reference compound **62** (**GS 20b**) were evaluated based on a fixed-dose percentage inhibition assay at a concentration of 1 µM.

Additional compounds were later evaluated in dose-response studies (**Table 3.11)**. The full details of the methodology used in this assay are provided in the experimental section (Chapter 10).

Table 3.11: *In vitro* human mTOR data and MMGBSA values for selected MLN0128 analogues

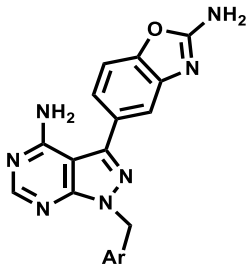

Code	Ar	R	*Pf*NF54 (IC_{50}, µM)	[a]% mTOR inh. (1 µM)	[a]mTOR IC_{50} (nM)	MMGBSA $pK_{\Delta G}$
12 (**GS 42**)	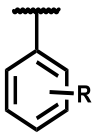	4-OMe	0.329	-	2.3	8.42
29 (**GS 117**)		4-Cl, 3-CF_3	0.157	93.5	32.7	7.48
36 (**GS 141**)		4-F, 3-CN	0.080	-	4.1	8.96
7 (**GS 55**)		4-Cl	0.029	95.2	-	-
30 (**GS 123**)		2,4-*di*-F	0.207	98.0	-	-
19 (**GS 175**)		3-N(Me)$_2$	0.411	95.1	-	-
38 (**GS 145**)		4-F, 3-CF_3	0.191	97.4	-	-
39 (**GS 99**)	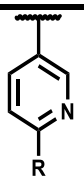	4-CF_3	0.375	-	13.6	8.30
40 (**GS 121**)		4-Cl	0.081	-	4.6	8.25
41 (**GS 135**)		4-F	0.184	-	0.7	7.18
49 (**GS 167**)		3-CH_3	0.189	-	< 0.5	7.61
50 (**GS 203**)		3-Cl	0.151	-	< 0.5	7.59

53 (**GS 185**)	Ar = 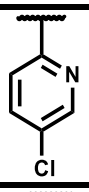	0.099[b]	-	1.8	8.30
44 (**GS 157**)	Ar = 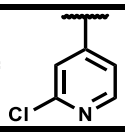	0.104	99.3	-	-
61 (**GS 197**)	Ar = 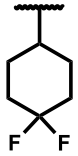	0.169	-	1.4	7.60
62 (**GS 20b**)	MLN0128	0.058	99.4	7.2	6.95

[a] n = 1, in technical triplicates; [b]anti-plasmodium data based on the *Pf*K1 strain

All analogues tested in the single-point assay exhibited high % inhibition (> 95%) at the maximum concentration of test compound (i.e., 1 µM; **Table 3.11**). In the dose-response IC_{50} determination, only two compounds (**39**; **GS 99**) and **29**; **GS 117**), showed a significant reduction with respective IC_{50} values of 14 and 33 nM. MLN0128 had an IC_{50} value of 7 nM based on this assay. Conversely, compounds **40** (**GS 121**), **36** (**GS 141**), **53** (**GS 185**), **61** (**GS 197**), and **41** (**GS 135**) displayed high potency against the human enzyme with respective IC_{50} values of 4.6, 4.1, 1.8, 1.4, and 0.7 nM, despite the clustered substitution. More discouragingly, the inhibitory potencies of *meta*-substituted pyridyl analogues **49** (**GS 167**) and **50** (**GS 203**) were low (picomolar). Ultimately, no specific SAR could be deduced in contrast to the initial hypothesis.

Docking of the disubstituted analogue **29** (**GS 117**), which showed a slight decrease in mTOR activity (IC_{50} = 33 nM), with the crystal structure (PDB code **6ZWM**) revealed an interaction between the hinge-binding motif and the benzoxazole. This is similar to that observed in the docked MLN0128: two hinge pairs of H-bond with Val 2240 and Gly 2238, two pairs of π-stacking with Trp 2239 (**Figure 3.13**; π-π interactions not displayed, in the hinge region) and Tyr 2225 (affinity pocket), and a H-bond between the sp^3 nitrogen of the benzoxazole and Asp 2195 of the model. However, the interaction between the sp^2 benzoxazole nitrogen and the catalytic lysine (Lys 2187) is missing while the disubstituted benzyl extended from the ribose pocket into the bulk solvent with no observable interactions. Thus, due to the observed loss in interactions, the ligand may be expected to show a decline in affinity.

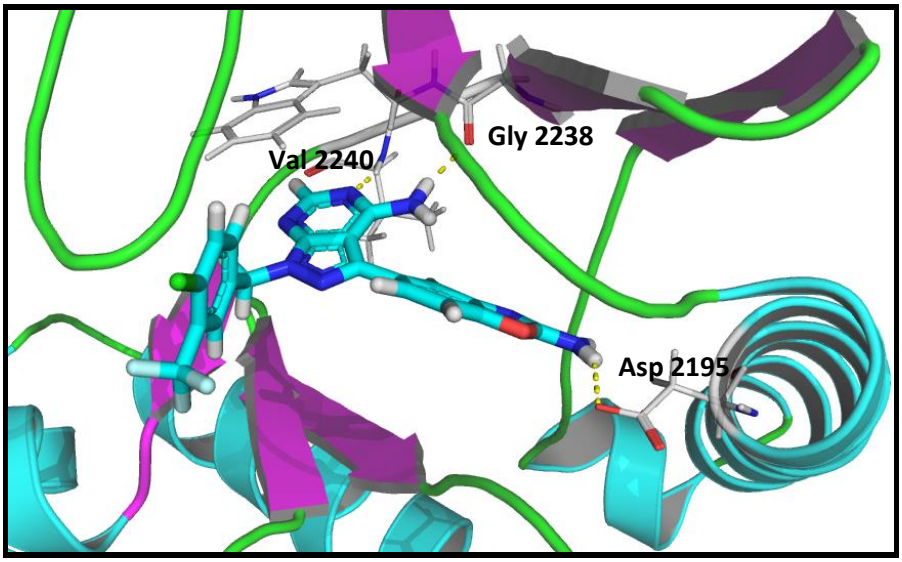

Figure 3.14: Docking pose of analogue **29** (**GS 117**) in the human mTOR binding site

In contrast, several docked ligands such as **53** (**GS 185**; IC_{50} = 1.8 nM) and **41** (**GS 135**; IC_{50} = 0.7 nM) displayed additional π-stacking of the pyridyl part of the molecule with Trp 2239, a π-cation bond with the catalytic lysine as in **7** (**GS 55**; 95.2% inhibition at 1 µM), **39** (**GS 99**; IC_{50} = 13.6 nM), and **49** (**GS 167**; IC_{50} < 0.5 nM), or a halogen bond as observed in **50** (**GS 203**; IC_{50} < 0.5 nM). However, several analogues docked with the substituted appendage lying extensively in the bulk solvent with loss in several H-bond interactions, yet no significant loss in mTOR potency was recorded. The benzyl analogue **29** (**GS 117**; IC_{50} = 33 nM), pyridyls **39** (**GS 99**; **Figure 3.14**), **36** (**GS 141**; IC_{50} = 4.1 nM), and **40** (**GS 121**; IC_{50} = 4.6 nM), and the saturated analogue **61** (**GS 197**; IC_{50} = 1.4 nM) all showed unexpectedly high potency despite the loss in interactions and the important structural differences between these compounds.

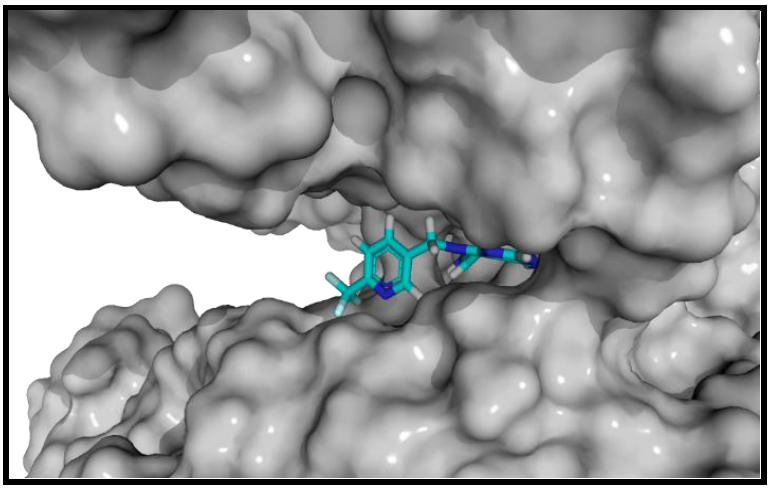

Figure 3.15: Surface binding mode of the pyridyl analogue **39** (**GS 99**) in the human mTOR crystal structure

Unsurprisingly, poor correlations were also observed between the calculated binding energies (MMGBSA) and potency (R^2 = 0.02; chart not displayed), as with PI4K and PKG. Overall, these data suggest that it is difficult to rationalize the observed mTOR activity based on binding energy calculations and the docking method employed. This data also suggested significant contribution of the bulk solvent to mTOR potency. Molecular dynamics which involve complex binding energy calculations by considering energetics of de-solvating both the target and the ligand, and evaluating the overall energy change of the complex has been suggested as a better quantifier for such non-covalent thermodynamic systems.[43–45] However, these laborious, slow, but more accurate calculations were beyond the scope of this work. Nonetheless, physicochemical correlations may also provide some insight.

To this end, strong correlations (R^2 = 0.40–0.79) were observed between mTOR activity and several physicochemical parameters such as lipophilicity (LogP), melting points (MP), molecular weight (MW), and turbidimetric solubility at pH 7.4. Correlation plots and further discussion regarding SPR studies are provided in **Chapter 4**. As expected, these observations further confirmed the predicted docking poses and, also suggested a preference for lipophilic groups on the explored part of the molecule due to unfavorable interactions with aqueous media. As with other biochemical assays, mTOR experiments were conducted in standardized conditions that mimic physiological conditions, and therefore the ligand would be expected to interact similarly at the cellular site of action.

It was also evident that the strong binding of the benzoxazole moiety at the affinity pocket was also responsible for the high activity observed against the human kinase. Going forward, further SAR exploration on this part of the molecule may mitigate this issue. However, docking studies suggested that this was likely to result in a significant reduction in activity against the *Plasmodium* targets of interest, but an optimal balance needs to be ultimately achieved. Modification to the hinge-binding motif should be explored for kinase selectivity in addition to improving the sub-optimal physicochemical properties of these analogues (including solubility), as discussed later in **Chapter 4**. For example, minor structural modifications such as single-atom changes in the hinge-binding motif have recently been demonstrated to impact heavily on selectivity and the physicochemical profiles of this series.[46] This warrants further investigation in future optimization of this scaffold.

Overall, the results indicated that mTOR potency remains an issue for these analogues, a hurdle that must be overcome for the progression of this series. Nevertheless, it is also worth noting that not all *in vitro* off-target activity necessarily leads to toxicity *in vivo*.

3.2.12.2 *In vitro* human PI4Kβ off-target assessment of selected compounds

Although the parent compound MLN0128 has been reported to possess no inhibition against human PI4Kβ and α isoforms at 1 μM, obtaining selectivity over host kinases often becomes an issue following subtle structural changes.[1] This is principally due to the high conservation of the ATP binding site in *Plasmodium* PI4K and related human phosphoinositide kinases.[23] Consequently off-target activity needs to be constantly monitored in early stages of a repositioning drug discovery program to highlight the effects of the structural modifications undertaken. Towards this end, two compounds were selected to investigate the off-target activity against the human PI4KIIIβ orthologue. This work was outsourced to Reaction Biology® laboratories and assays were based on a single-dose duplicate method (ADP-Glo assay) at a maximum concentration of 1 μM. The results and the structures of the specific compounds are summarized in **Table 3.12**.

Table 3.12: *In vitro* human PI4Kβ data and MMGBSA values for selected MLN0128 analogues

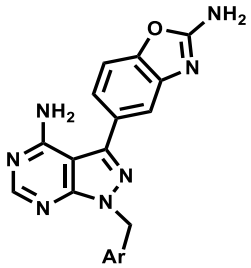

Code	Ar	*Pf*NF54 (IC_{50}, μM)	[a]% human PI4Kβ inh. at 1 μM	MMGBSA ΔG ($pK_{\Delta G}$)	*Pv*PI4K IC_{50} (nM)	MMGBSA ΔG ($pK_{\Delta G}$)
44 (**GS 157**)	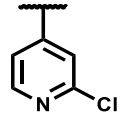	0.104	4.9	-46.73 (8.19)	4.3	-55.84 (9.79)
19 (**GS 175**)	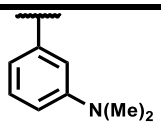	0.411	2.4	-46.50 (8.15)	11.0	-58.05 (10.18)

[a]n = 1, one biological assay with technical triplicates

Both compounds analyzed showed poor activity (< 5% inhibition at 1 µM) against the human orthologue, suggesting that the series possessed selectivity for the *Plasmodium* PI4Kβ enzyme. Toxicity resulting from off-target host kinase inhibition has been associated with the termination of numerous target-based drug discovery programs because of the conserved nature of kinase ATP-binding sites.[47] Retaining selectivity against the human PI4Kβ orthologue, a key host lipid kinase, was an appealing property for the representative compounds tested in this series.

Docking studies highlighted key binding site differences responsible for the low *in vitro* affinity and calculated binding energies (**Table 3.12**) with the human PI4KIIIβ crystal structure (PDB code **6GL3**). An overlay with the *Pf*PI4K homology model (**Figure 3.15**) indicated a change of Tyr 1356 to Pro 612 in the human PI4KIIIβ, Phe 827 to Leu 389, and Ser 1365 to Gln 621 at the ATP-binding site. The change in Phe 827 resulted in a loss of aromaticity, which disrupted π-stacking with the benzyl or pyridyl moiety of the analogues in the human target. Furthermore, the change to the large polar glutamine in the human protein made the ribose pocket tighter resulting in a significant clash between the bulky benzoxazole group, Asp 689, and the *N*, *N*-dimethyl amino benzyl moiety of **19** (**GS 175**) and Asn 390 and Ser 618 of the crystal structure (**Figure 3.15**).

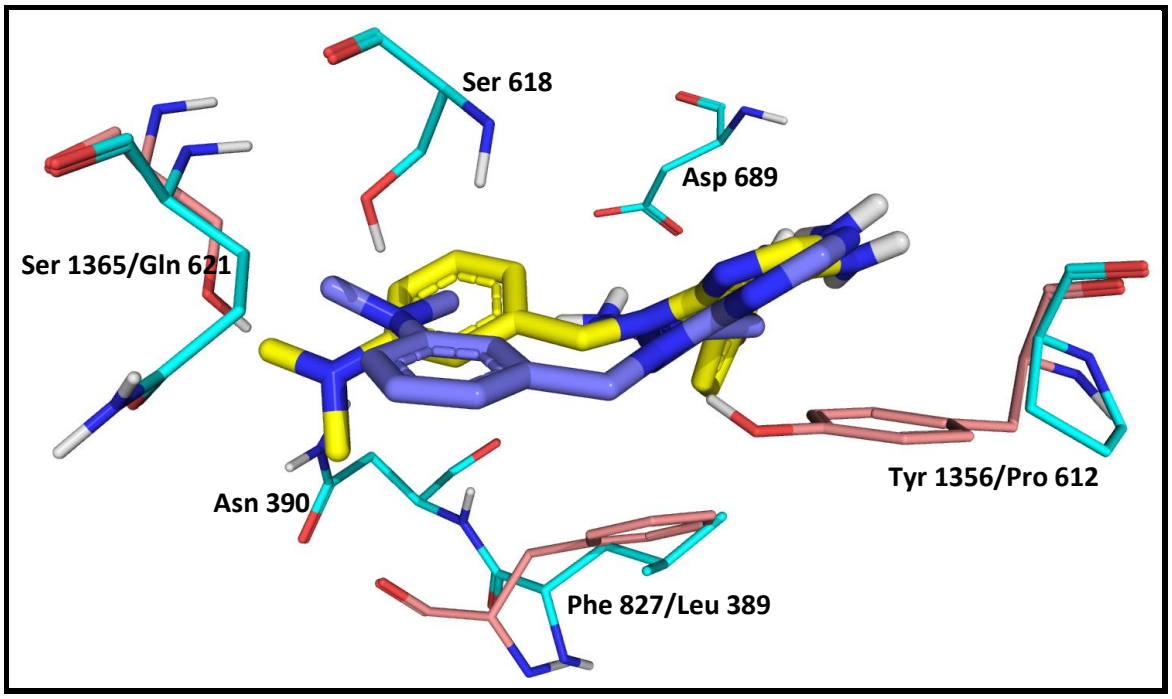

Figure 3.16: A binding-site overlay of **19** (**GS 175**) in the *Pf*PI4K homology model (pink; ligand in dark blue) and the HuPI4Kβ crystal structure (blue; ligand in yellow) highlighting structural differences and residues responsible for the reduced humPI4K affinity.

Going forward, although human PI4KIIIβ is not likely to be a key off-target for this series as demonstrated by the compounds tested, it will also be necessary to evaluate compound selectivity relative to other human phosphoinositide and protein kinases.

3.3 Chapter summary

In summary, the antimalarial efficacy of MLN0128 in the *Pf*SCID mouse model (98% reduction in parasitaemia) has been shown and analogues with dual *Pf*PI4K and PKG inhibition identified. Molecular features responsible for the high affinity to their mechanistic targets have been rationalized using *in silico* tools. Non-cytotoxic compounds against the CHO cell line and some with high gametocytocidal activity (< 1 μM) have been identified. Additionally, four out of five of the analogues evaluated for microsomal metabolic stability across human, rat and mouse liver microsomes were stable. Cardiotoxicity hERG profiling of five compounds suggested low risk against the cardiac channel. In addition, off-target kinase selectivity displayed low affinity for the two analogues tested against human PI4K enzyme (< 5% inhibition) although a high affinity to mTOR remains an issue. In the next chapter, physicochemical profiling for these analogues and the relationships with the reported biological and biochemical results will be assessed.

References

1. Hsieh, A.; Liu, Y.; Edlind, M.; Ingolia, N.; Janes, M.; Sher, A.; Shi, E.; Stumpf, C.; Christensen, C.; Bonham, M.; Wang, S.; Ren, P.; Martin, M.; Jessen, K.; Feldman, M.; Weissman, J.; Shokat, K.; Rommel, C.; Ruggero, D. The translational landscape of mTOR signalling steers cancer initiation and metastasis. *Nature*. **2012**; 485 (7396): 55 - 61. doi:10.1038/nature10912.

2. Jiménez-Díaz, M., Mulet, T.; Viera, S.; Gomez, V.; Garuti, H.; Ibanez, J.; Alvarez-Doval, A.; Shultz, L.; Martinez, A.; Gargallo-Viola, D.; Angulo-Barturen, I. Improved murine model of malaria using *Plasmodium falciparum* competent strains and non-myelodepleted NOD-scid IL2Rγnull mice engrafted with human erythrocytes. *Antimicrob. Agents Chemother*. **2009**; 53 (10): 4533 - 4536. doi:10.1128/AAC.00519-09.

3. Angulo-Barturen, I.; Jiménez-Díaz, M.; Mulet, T.; Rullas, J.; Herreros, E.; Ferrer, S.; Jimenez, E.; Mendoza, A.; Regadera, J.; Rosenthal, P.; Bathurst, I.; Pompliano, D.; Heras, F.; Gargallo-Viola, D. A murine model of *falciparum*-malaria by *in vivo* selection of competent strains in non-myelodepleted mice engrafted with human erythrocytes. *PLoS One*. **2008**; 3 (5). 1 - 14. doi:10.1371/journal.pone.0002252.

4. Paquet, T.; Le Manach, C.; Cabrera, D.; Younis Y.; Henrich, P.; Abraham T.; Lee, M.; Basak R.; Ghidelli-Disse, S.; Lafuente-Monasterio, M.; Bantscheff, M.; Ruecker, A.; Blagborough, A.; Zakutansky, S.; Zeeman, A.; White, K.; Shackleford, D.; Mannila, J.; Morizzi, J.; Scheurer, C.; Angulo-Barturen, I.; Martínez, M.; Ferrer, S.; Sanz, L.; Gamo, F.; Reader, J.; Botha, M.; Dechering, K.; Sauerwein, R.; Tungtaeng, A.; Vanachayangkul, P.; Lim, C.; Burrows, J.; Witty, M.; Marsh, K.; Bodenreider, C.; Rochford, R.; Solapure, S.; Jiménez-Díaz, M.; Wittlin, S.; Charman, S.; Donini, C.; Campo, B.; Birkholtz, L.; Hanson, K.; Drewes, G.; Kocken, C.; Delves, M.; Leroy, D.; Fidock, D.; Waterson, D.; Street, L.; Chibale, K. Antimalarial efficacy of MMV390048, an inhibitor of *Plasmodium* phosphatidylinositol-4-kinase. *Sci. Transl. Med*. **2017**; 9 (387): 1 - 14. doi:10.1126/scitranslmed.aad9735.

5. Allman, E.; Painter, H.; Samra, J.; Carrasquilla, M. and Llinás, M. Metabolomic profiling of the Malaria box reveals antimalarial target pathways. *Antimicrob. Agents*

Chemother. **2016**; 60 (11): 6635 - 6643. doi:10.1128/aac.01224-16.

6. Murithi, J.; Owen, E.; Istvan, E.; Lee, M.; Ottilie, S.; Chibale, K.; Goldberg, D.; Winzeler, E.; Llinas, M.; Fidock, D.; Vanaerschot, M. Combining stage specificity and metabolomic profiling to advance antimalarial drug discovery. *Cell Chem. Biol*. **2020**; 27 (2): 158 - 171.e3. doi:10.1016/j.chembiol.2019.11.009.

7. Patti, G.; Yanes, O. and Siuzdak, G. Innovation: Metabolomics: the apogee of the omics trilogy. *Nat. Rev. Mol. Cell Biol*. **2012**; 13 (4): 263 - 269. doi:10.1038/nrm3314.

8. Vincent, I. and Barrett, M. Metabolomic-based strategies for anti-parasite drug discovery. *J. Biomol. Screen*. **2015**; 20 (1): 44 - 55. doi:10.1177/1087057114551519.

9. Yang, T.; Ottilie, S.; Istvan, E.; Godinez-Macias, K.; Lukens, A.; Baragana, B.; Campo, B.; Walpole, C.; Niles, J.; Chibale, K.; Dechering, K.; Llinas, M.; Lee, M.; Kato, N.; Wyllie, S.; McNamara, C.; Gamo, F.; Burrows, J.; Fidock, D.; Goldberg, D.; Gilbert, I.; Wirth, D.; Winzeler, E.; MalDA, Accelerating Malaria Drug Discovery. *Trends Parasitol*. **2021**; 37 (6): 493 - 507. doi:10.1016/j.pt.2021.01.009.

10. Vaid, A.; Ranjan, R.; Smythe, W.; Hoppe, H. and Sharma, P. *Pf*PI3K, a phosphatidylinositol-3 kinase from *Plasmodium falciparum* is exported to the host erythrocyte and is involved in hemoglobin trafficking. *Blood*. **2010**; 115 (12): 2500-2507.

11. Sternberg, A. and Roepe, P. Heterologous expression, purification, and functional analysis of the *Plasmodium falciparum* phosphatidylinositol 4-kinase IIIβ. *Biochemistry*. **2020**; 59 (27): 2494 - 2506. doi:10.1021/acs.biochem.0c00259.

12. Makler, M. and Hinrichs, D. Measurement of the lactate dehydrogenase activity of *Plasmodium falciparum* as an assessment of parasitemia. *Am. J. Trop. Med. Hyg*. **1993**; 48 (2): 205 - 210. doi:10.4269/ajtmh.1993.48.205.

13. Huber, W. and Koella, J. A comparison of three methods of estimating EC_{50} in studies of drug resistance of malaria parasites. *Acta. Trop*. **1993**; 55 (4): 257 - 261. doi:10.1016/0001-706X(93)90083-N.

14. Ishikawa, M. and Hashimoto, Y. Improvement in aqueous solubility in small molecule drug discovery programs by disruption of molecular planarity and symmetry. *J. Med.*

Chem. **2011**; 54: 1539 - 1554.

15. Kim, J.; Tan, Y.; Wicht, K.; Erramilli, S.; Dhingra, S.; Okombo, J.; Vendome, J.; Hagenah, L.; Giacometti, S.; Warren, A.; Nosol, K.; Roepe, P.; Potter, C.; Carragher, B.; Kossiakoff, A.; Quick, M.; Fidock, D.; Mancia, F. Structure and drug resistance of the *Plasmodium falciparum* transporter *Pf*CRT. *Nature*. **2019**; 576: 315 - 320. doi:10.1038/s41586-019-1795-x.

16. Cheuka, P.; Centani, L.; Arendse, L.; Fienberg, S.; Wambua, L.; Renga, S.; Dziwornu, G.; Kumar, M.; Lawrence, N.; Taylor, D.; Wittlin, S.; Coertzen, D.; Reader, J.; van der Watt, M.; Birkholtz, L.; Chibale, K. New amidated 3,6-diphenylated imidazopyridazines with potent anti-plasmodium activity are dual inhibitors of *Plasmodium* phosphatidylinositol-4-kinase and cGMP-dependent protein kinase. *ACS Infect. Dis*. **2021**; 7 (1): 34 - 46. doi:10.1021/acsinfecdis.0c00481.

17. Fienberg, S.; Eyermann, C.; Arendse, L.; Basarab, G.; McPhail, J.; Burke, J.; Chibale, K. Structural basis for inhibitor potency and selectivity of *Plasmodium falciparum* phosphatidylinositol 4-kinase inhibitors. *ACS Infect. Dis*. **2020**; 6 (11): 3048 - 3063. doi:10.1021/acsinfecdis.0c00566.

18. Greenidge, P.; Kramer, C.; Mozziconacci, J. and Wolf, R. MM/GBSA binding energy prediction on the PDB-bind data set: successes, failures, and directions for further improvement. *J. Chem. Inf. Model*. **2013**; 53 (1): 201 - 209. doi:10.1021/ci300425v.

19. Baker, D.; Stewart, L.; Large, J.; Bowyer, P.; Ansell, K.; Jiménez-Díaz, M.; El Bakkouri, M.; Birchall, K.; Dechering, K.; Bouloc, N.; Coombs, P.; Whalley, D.; Harding, D.; Smiljanic-Hurley, E.; Wheldon, M.; Walker, E.; Dessens, J.; Lafuente, M.; Sanz, L.; Gamo, F.; Ferrer, S.; Hui, R.; Bousema, T.; Angulo-Barturén, I.; Merritt, A.; Croft, S.; Gutteridge, W.; Kettleborough, C.; Osborne, S. A potent series targeting the malarial cGMP-dependent protein kinase clears infection and blocks transmission. *Nat. Commun.* **2017**, 8 (1), 1 - 9. doi.org/10.1038/s41467-017-00572-x.

20. Vanaerschot, M.; Murithi, J.; Pasaje, C.; Ghidelli-Disse, S.; Dwomoh, L.; Bird, M.; Spottiswoode, N.; Mittal, N.; Arendse, L.; Owen, E.; Wicht, K.; Siciliano, G.; Bosche, M.; Yeo, T.; Kumar, T.; Mok, S.; Carpenter, E.; Giddins, M.; Sanz, O.; Ottilie, S.; Alano, P.; Chibale, K.; Llinas, M.; Uhlemann, A.; Delves, M.; Tobin, A.; Doerig, C.; Winzeler,

E.; Lee, M.; Niles, J.; Fidock, D. Inhibition of resistance-refractory *P* . *falciparum* Inhibition of resistance-refractory *P. falciparum* kinase PKG delivers prophylactic, blood stage, and transmission-blocking anti-plasmodial activity. *Cell Chem. Bio.* **2020**: 1 - 11. doi:10.1016/j.chembiol.2020.04.001.

21. Baker, D.; Matralis, A.; Osborne, S.; Large, J. and Penzo, M. Targeting the malaria parasite cGMP-dependent protein kinase to develop new drugs. *Front. Microbiol*. **2020**; 11: 1 - 8. doi:10.3389/fmicb.2020.602803.

22. Anighoro, A., Bajorath, J., and Rastelli, G. Polypharmacology: Challenges and opportunities in drug discovery. *J. Med. Chem*. **2014**; 57 (9): 7874 - 7887.

23. Arendse, L.; Wyllie, S.; Chibale, K. and Gilbert, I. *Plasmodium* kinases as potential drug targets for malaria: Challenges and opportunities. *ACS Infect. Dis*. **2021**; 7 (3): 518 - 534. doi:10.1021/acsinfecdis.0c00724.

24. Reader, J.; Botha, M.; Theron, A.; Lauterbach, S.; Rossouw, C.; Englebrecht, D.; Wepener, M.; Smit, A.; Leroy, D.; Mancama, D.; Coetzer, T.; Birkholtz, L. Nowhere to hide: Interrogating different metabolic parameters of *Plasmodium falciparum* gametocytes in a transmission blocking drug discovery pipeline towards malaria elimination. *Malar. J*. **2015**; 14 (1): 1 - 17. doi:10.1186/s12936-015-0718-z.

25. Adjalley, S.; Johnston, G.; Li, T.; Eastman, R.; Ekland, E.; Eappen, A.; Richman, A.; Sim, B.; Lee, M.; Hoffman, S.; Fidock, D. Quantitative assessment of *Plasmodium falciparum* sexual development reveals potent transmission blocking activity by methylene blue. *Proc. Natl. Acad. Sci. USA*. **2011**; 108 (47): E1214 - E1223. doi:10.1073/pnas.1112037108.

26. van der Watt, M.; Reader, J.; Churchyard, A.; Nondaba, S.; Lauterbach, S.; Niemand, J.; Abayomi, S.; van Biljon, R.; Connacher, J.; van Wyk, R.; Le Manach, C.; Paquet, T.; González Cabrera, D.; Brunschwig, C.; Theron, A.; Lozano-Arias, S.; Rodrigues, J.; Herreros, E.; Leroy, D.; Duffy, J.; Street, L.; Chibale, K.; Mancama, D.; Coetzer, T.; Birkholtz, L. Potent *Plasmodium falciparum* gametocytocidal compounds identified by exploring the kinase inhibitor chemical space for dual active antimalarials. *J. Antimicrob. Chemother*. **2018**; 73 (5): 1279 - 1290. doi:10.1093/jac/dky008.

27. Dixon, M.; Dearnley, M.; Hanssen, E.; Gilberger, T.; and Tilley, L. Shape-shifting

gametocytes: How and why does *P. falciparum* go banana-shaped? *Trends Parasitol*. **2012**; 28 (11): 471 - 478. doi:10.1016/j.pt.2012.07.007.

28. McNamara, C.; Lee, M..; Lim, C.; Lim, S.; Roland, J.; Nagle, A.; Simon, O.; Yeung, B.; Chatterjee, A.; McCormack, S.; Manary, M.; Zeeman, A..; Dechering, K.; Kumar, T.; Henrich, P.; Gagaring, K.; Ibanez, M.; Kato, N.; Kuhen, K.; Fischli, C.; Rottmann, M.; Plouffe, D.; Bursulaya, B.; Meister, S.; Rameh, L.; Trappe, J.; Haasen, D.; Timmerman, M.; Sauerwein, R.; Suwanarusk, R.; Russell, B.; Renia, L.; Nosten, F.; Tully, D.; Kocken, C.; Glynne, R.; Bodenreider, C.; Fidock, D.; Diagana, T.; Winzeler, E. Targeting Plasmodium PI(4)K to Eliminate Malaria. *Nature* **2013**, 504 (7479), 248 - 253. https://doi.org/10.1038/nature12782.

29. Billker, O.; Dechamps, S.; Tewari, R.; Wenig, G.; Franke-fayard, B.; Brinkmann, V. Calcium and a calcium-dependent protein kinase regulate gamete formation and mosquito transmission in a malaria parasite. *Cell* **2004**; 117: 503 - 514.

30. Burrows, J.; Hooft Van Huijsduijnen, R.; Möhrle, J.; Oeuvray, C. and Wells, T. Designing the next generation of medicines for malaria control and eradication. *Malar. J*. **2013**; 12 (1): 1 - 20. doi:10.1186/1475-2875-12-187.

31. Liu, Y.; Peterson, D.; Kimura, H.; and Schubert, D. Mechanism of cellular 3-(4,5-Dimethylthiazol-2-yl)-2,5-diphenyltetrazolium bromide (MTT) reduction. *J. Neurochem*. **1997**; 69 (2): 581 - 593.

32. Verlinden, B.; Niemand, J.; Snyman, J.; Sharma, S.; Beattie, R.; Woster, P.; Birkholtz, L. Discovery of novel alkylated (bis)urea and (bis)thiourea polyamine analogues with potent antimalarial activities. *J. Med. Chem*. **2011**; 54 (19): 6624 - 6633. doi:10.1021/jm200463z.

33. Van Leeuwen, I.; Rao, B.; Sachweh, M. and Laín, S. An evaluation of small-molecule p53 activators as chemoprotectants ameliorating adverse effects of anticancer drugs in normal cells. *Cell Cycle*. **2012**; 11 (9): 1851 - 1861. doi:10.4161/cc.20254.

34. Kandepedu, N.; Cabrera, D.; Eedubilli, S.; Taylor, D.; Brunschwig, C.; Gibhard, L. Njoroge, M.; Lawrence, N.; Paquet, T.; Eyermann, C.; Spangenberg, T.; Basarab, G.; Street, L.; Chibale, K. Identification, characterization, and optimization of 2,8-disubstituted-1,5-naphthyridines as novel *Plasmodium falciparum* phosphatidylinositol-

4-kinase inhibitors with *in vivo* efficacy in a humanized mouse model of Malaria. *J. Med. Chem*. **2018**; 61 (13): 5692 - 5703. doi:10.1021/acs.jmedchem.8b00648.

35. Siramshetty, V.; Shah, P.; Kerns, E.; Nguyen, K.; Yu, K.; Kabir, M.; Williams, J.; Neyra, J.; Southall. N.; Nguyen, D.; Xu, X. Retrospective assessment of rat liver microsomal stability at NCATS: Data and QSAR models. *Sci. Rep*. **2020**; 10 (1): 1 - 14. doi:10.1038/s41598-020-77327-0.

36. Słoczyńska, K.; Gunia-Krzyzak, A.; Koczurkiewicz, P.; Wojcik-Pszczola, K, Zelaszczyk, D.; Popiol, J.; Pekala, E. Metabolic stability and its role in the discovery of new chemical entities. *Acta. Pharm*. **2019**; 69 (3): 345 - 361. doi:10.2478/acph-2019-0024.

37. Priyadharshini, A.; Ahalya, S.; Vaishnavi, P.; Pavithra, S.; Rosario, A. A review on benefits and toxicity of Orlistat therapy. *Drug Invent. Today*. **2019**; 12 (3): 550 - 553. http://ezproxy.libraries.wright.edu/login?url=https://search.ebscohost.com/login.aspx?direct=true&db=a9h&AN=135900222&site=eds-live.

38. Guengerich, F. P. Cytochrome P450s and other enzymes in drug metabolism and toxicity. *AAPS J*. **2006**; 8 (1): E101 - E111.

39. Jancova, P. and Siller, M. Phase II Drug Metabolism. *Topics on Drug Metabolism*. ISBN: 978-953-51-0099-7, InTech, **2012**. doi:10.5772/29996.

40. Rogers, J.; Nafziger, A. and Bertino, J. Pharmacogenetics affects dosing, efficacy and toxicity of Cytochrome P450–metabolized drugs. *Am. J. Med*. **2002**; 113 (9): 746 - 750.

41. Patel, C.; Goel, S.; Patel, M.; Rangachari, L.; Wilbur, J.; Shou, Y.; Venkatakrishnan, K.; Lockhart, C. Phase 1 study to evaluate the effect of the investigational anticancer agent Sapanisertib on the QTc interval in patients with advanced solid tumors. *Clin. Pharmacol. Drug Dev*. **2020**; 9 (7): 876 - 888. doi:10.1002/cpdd.808.

42. Anastassiadis, T.; Deacon, S.; Devarajan, K.; Ma, H. and Peterson, J. Comprehensive assay of kinase catalytic activity reveals features of kinase inhibitor selectivity. *Nat. Biotechnol*. **2011**; 29 (11): 1039 - 1045. doi:10.1038/nbt.2017.

43. Maffucci, I.; Hu, X.; Fumagalli, V. and Contini, A. An efficient implementation of the Nwat-MMGBSA method to rescore docking results in medium-throughput virtual

screenings. *Front. Chem*. **2018**; 6 (43): 1 - 14. doi:10.3389/fchem.2018.00043.

44. Barelier, S.; Boyce, S.; Fish, I.; Fischer, M.; Goodin, D.; Shoichet, B. Roles for ordered and bulk solvent in ligand recognition and docking in two related cavities. *PLoS One*. **2013**; 8 (7): 1 - 11. doi:10.1371/journal.pone.0069153.

45. Zhang, H.; Tan, T.; Hetényi, C. and Van Der Spoel, D. Quantification of solvent contribution to the stability of non-covalent complexes. *J. Chem. Theory Comput*. **2013**; 9 (10): 4542 - 4551. doi:10.1021/ct400404q.

46. Ouvry, G.; Clary, L.; Tomas, L.; Aurelly, M.; Bonnary, L.; Borde, E.; Bouix-Peter, C.; Chantalat, L.; Defoin-Patel, C.; Deret, S.; Forissier, M.; Harris, C.; Isabet, T.; Lamy, L.; Luzy, A.; Pascau, J.; Soulet, C.; Taddei, A.; Taquet, N.; Thoreau, E.; Varvier, E.; Vial, E.; Hennequin, L. Impact of minor structural modifications on properties of a series of mTOR inhibitors. *ACS Med. Chem. Lett*. **2019**; 10 (11): 1561 - 1567. doi:10.1021/acsmedchemlett.9b00401.

47. Cabrera, D.; Horatscheck, A.; Wilson, C.; Basarab, G.; Eyermann, J.; Chibale, K. Plasmodial kinase inhibitors: License to cure? *J. Med. Chem*. **2018**; 61 (18): 8061 - 8077. doi:10.1021/acs.jmedchem.8b00329.

CHAPTER 4

PHYSICOCHEMICAL EVALUATION AND STRUCTURE-PROPERTY RELATIONSHIPS OF MLN0128 ANALOGUES

4.1 Chapter overview

This chapter describes the physicochemical profiles of the MLN0128 analogues reported in Chapter 3. At the onset, SPRs are investigated to establish the effects of structural changes on various physicochemical attributes. Furthermore, the interrelationships between experimentally and/or virtually derived physicochemical parameters and biological activity presented in Chapter 3 are described. This is done to shed light on the effects of physicochemical properties on the intrinsic biological activity and to identify any overlapping or diverging chemical and biological spaces suitable for further exploration. In addition, the profiled attributes are compared to those of marketed drugs and superior lead compounds showing optimal PK, PD, and safety properties, further adding value to a hit-to-lead campaign for the anti-plasmodium compounds explored in this study.

4.2 Influence of physicochemical properties on drug-likeness

The physicochemical properties of a molecule influence the PK and PD properties of a potential drug candidate as well as its safety profile. Despite huge financial investment, many compounds designated to be administered orally fail midstream in the drug discovery process due to poor oral bioavailability.[1] Special attention is given to factors of a compound that influence bioavailability in a particular disease model. These factors include solubility, permeability, and metabolic stability. However, these factors are interrelated as change in one parameter consequentially affects others.[2] In addition, physicochemical and ADME(T) properties need to be considered with target affinity in mind. High-molecular weight compounds are likely to exhibit a high degree of lipophilicity and consequently low solubility, with significant impact on ADME(T) properties for orally administered drugs, ultimately resulting in low bioavailability. In contrast, key mediators of numerous enzyme-drug interactions such as kinase inhibitors are guided by some degree of lipophilicity. Most are multi-aromatic and consequently often display suboptimal physicochemical properties.[3]

High lipophilicity often results in undesirable ADME(T) properties such as promiscuity-induced toxicity (tissue toxicity and cardiotoxicity) and fast metabolic breakdown associated with a high affinity for CYP450 enzymes. Such paradigms indicate that it is appropriate to adopt a balance in drug-like properties in accordance with experience from drug discovery enterprises.[4] Towards this end, simple rules that define boundaries of fundamental properties considered acceptable for potential drug candidates have been adopted. However, these rules only act as a guide to identify hits with a high probability of success with regard to PK and safety considerations.[3]

For instance, Lipinski's rule of five (Ro5)[5] identifies molecular features in oral drugs responsible for poor oral absorption and permeation, and defines simple guidelines for triaging potential drug candidates. These include a physical count of the number of hydrogen-bond donors (HBD < 5) and acceptors (HBA < 10), MW (< 500 Da), and lipophilicity (LogP < 5). Further modifications to consider other physical characteristics affecting ADME properties for potential drug candidates have been proposed. Veber *et al*.[6] established that the ideal number of rotatable bonds should not exceed 10 and that the TPSA of a compound should be 65–140 $Å^2$ for successful permeation. Other extensions to these rules have also been proposed including the exemption of natural products and refinement to the rule of three (Ro3) for fragment-based drug discovery programs.[7,8]

In this study, some intrinsic properties that affect solubility such as LogP, TPSA, MW, melting point (MP), and HPLC retention times in a standardized buffer and solvent system were evaluated and their potential contribution to observed biochemical/biological activities were assessed.

4.3 Physicochemical profiling of MLN0128 analogues

Several parameters were calculated (MW, TPSA, cLogP, and number of HBDs and HBAs), while MP and aqueous solubility were experimentally determined. TPSA, HBD, HBA, and cLogP values were calculated using commercial StarDrop® 64 software and MW values were obtained using ChemDraw® Professional 16.0 software. These calculated and experimentally determined physicochemical parameters are summarized in **Table 4.1**.

Table 4.1: Physicochemical evaluation and structure-property relationships of the target compounds

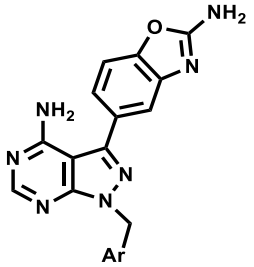

Ar	R		Calculated				Experimental			Ar	R		Calculated				Experimental		
			MW	cLogP	TPSA	HBD/ HBA	[a]MP	[b]Solubility	[c]Solubility				MW	cLogP	TPSA	HBD/ HBA	[a]MP	[b]Solubility	[c]Solubility
	H	**6**	357.38	2.78	121.67	2/8	288.0	20	<5		4-CF_3	**39**	426.36	2.86	134.56	2/9	299.5	-	<5
	4-Cl	**7**	391.82	3.30	121.67	2/8	293.0	80	<5		4-Cl	**40**	392.81	2.60	134.56	2/9	290.0	80	<5
	4-F	**8**	375.37	2.86	121.67	2/8	299.0	20	<5		4-F	**41**	376.36	2.21	134.56	2/9	275.5	160	10
	4-CN	**9**	382.39	2.62	145.46	2/9	309.5	20	<5		4-Me	**42**	372.39	2.47	134.56	2/9	279.5	40	<5
	4-CF_3	**10**	425.38	3.55	121.67	2/8	307.5	20	-		H	**43**	358.37	2.12	134.56	2/9	299.5	>200	30
	4-Me	**11**	371.40	3.15	121.67	2/8	277.0	40	<5		3-Cl	**44**	392.81	2.60	134.56	2/9	292.5	80	<5
	4-OMe	**12**	387.40	2.67	130.90	2/9	286.0	80	<5		3-F	**45**	376.36	2.21	134.56	2/9	-	160	5
	4-NH_2	**13**	372.39	2.10	147.69	3/9	282.5	160	-		3-CF_3	**46**	426.36	2.86	134.56	2/9	280.5	160	<5
	3-F	**14**	375.37	2.86	121.67	2/8	306.0	10	-		3-Me	**47**	372.39	2.47	134.56	2/9	273.5	>200	85
	3-CF_3	**15**	425.38	3.55	121.67	2/8	282.0	-	<5	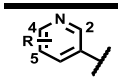	H	**48**	358.37	2.12	134.56	2/9	286.5	>200	20
	3-Me	**16**	371.40	3.12	121.67	2/8	300.0	5	-		5-Me	**49**	372.39	2.47	134.56	2/9	285.5	80	10
	3-Cl	**17**	391.82	3.30	121.67	2/8	311.0	10	<5		5-Cl	**50**	392.81	2.60	134.56	2/9	274.5	-	<5
	3-NH_2	**18**	372.39	2.10	147.69	3/9	286.5	80	<5		5-F	**51**	376.36	2.21	134.56	2/9	285.5	-	<5
	3-$N(Me)_2$	**19**	400.45	2.71	124.91	2/9	269.5	-	<5		H	**52**	358.37	2.12	134.56	2/9	272.0	-	65
	2-Me	**20**	371.40	3.15	121.67	2/8	300.5	-	-		4-Cl	**53**	392.81	2.60	134.56	2/9	289.5	40	<5
	2-F	**21**	375.37	2.86	121.67	2/8	296.5	-	-		4-F	**54**	376.36	2.21	134.56	2/9	274.5	40	<5
	2-Cl	**22**	391.82	3.30	121.67	2/8	293.5	10	<5		4-CF_3	**55**	426.36	2.86	134.56	2/9	304.0	20	<5
	2-CF_3	**23**	425.38	3.55	121.67	2/8	279.5	20	-		3-Cl	**56**	392.81	2.60	134.56	2/9	280.5	80	<5
	3,4-Cl	**24**	426.26	3.80	121.67	2/8	288.5	-	<5		3-Me	**57**	372.39	2.47	134.56	2/9	279.5	80	<5
	2,4-Cl	**25**	422.26	3.80	121.67	2/8	271.5	-	-		3-F	**58**	376.36	2.21	134.56	2/9	293.5	>200	<5
	2-F, 4-Cl	**26**	409.81	3.37	121.67	2/8	272.5	5	<5		3-CF_3	**59**	426.36	2.86	134.56	2/9	257.5	-	<5
	2-CN, 4-Cl	**27**	416.83	3.13	145.46	2/9	280.5	20	<5											

3-F, 4-Cl	**28**	409.81	3.37	121.67	2/8	318.5	20	<5
3-CF_3, 4-Cl	**29**	459.82	3.98	121.67	2/8	285.5	20	<5
2-F, 4-F	**30**	393.36	2.91	121.67	2/8	294.5	10	-
2-Cl, 4-F	**31**	409.81	3.37	121.67	2/8	277.5	5	-
2-CF_3, 4-F	**32**	443.37	3.63	121.67	2/8	289.5	5	-
2-CN, 4-F	**33**	400.38	2.71	145.46	2/9	288.0	40	15
2-Me, 4-F	**34**	389.39	3.23	121.67	2/8	282.5	10	-
3-Cl, 4-F	**35**	409.81	3.37	121.67	2/8	285.5	5	<5
3-CN, 4-F	**36**	400.38	2.71	145.46	2/9	259.5	20	<5
3-F, 4-F	**37**	393.36	2.91	121.67	2/8	289.5	10	<5
3-CF_3, 4-F	**38**	443.37	3.63	121.67	2/8	290.0	5	<5

 H	**60**	363.43	3.41	121.67	2/8	285.5	20	<5
4-*di* F	**61**	399.41	3.34	121.67	2/8	288.5	-	<5
MLN0128 (GS 20b)	**62**	309.33	2.21	121.67	2/8	273.5	>200	115

-, Not determined; MW, molecular weight in g.mol^{-1} calculated using ChemDraw Professional 16.0; TPSA, topological polar surface area in Å^2; HBD, hydrogen-bond donors; HBA, hydrogen-bond acceptors; cLogP, calculated log P calculated using StarDrop™; [a]MP, melting point in °C as an average between the start and end of melting process; [b]turbidimetric solubility in µM (pH 7.4); [c]High-performance liquid chromatography (HPLC) solubility in µM (pH 6.5), determined via HPLC-based DMSO "dry-down" method.

4.3.1 Solubility evaluation

Solubility is a key physicochemical parameter in drug discovery because of its impact on oral absorption and consequent ramifications on drug bioavailability at the site of action.[9] Generally, aqueous solubility is a measure of solute-solvent interactions and the main contributors of a compound are lipophilicity, hydrogen bonding, and the energetics of the solid state, particularly crystal lattice energy.[10] Solubility is also majorly dependent on solvent conditions such as pH, temperature, and ionic strength. Consequently, for relevance in the drug discovery context, the solubility of a compound is determined under conditions that mimic the biological environment and the intended mode of administration.[11] As the compounds explored in this study were intended for oral administration, two methods of evaluating solubility were employed and are described in the following sections.

4.3.1.1 Turbidimetric kinetic solubility

Aqueous solubility of compounds must be reliably evaluated in drug discovery programs for medicinal chemistry optimization, as poorly soluble drugs often result in low oral bioavailability whereas highly polar drugs encounter difficulty permeating through cell membranes.[11] Generally, turbidimetric methods are employed in the initial stages of the drug discovery process as they have high-throughput capability and are more labor- and cost-effective than thermodynamic methods. Although less accurate, turbidimetric methods allow fast generation of data that can assist in evaluating biological/biochemical results and triaging compounds for the more meaningful thermodynamic assays.[12]

In this study, a classical turbidimetric kinetic assay was employed.[13] This involves the comparative evaluation of a compound's solubility in phosphate buffered saline (PBS) relative to that in a highly dissolving organic solvent (DMSO), at physiological temperature (37 °C) and pH (7.4). Turbidity is observed at some concentration in PBS and is detected using a UV-Vis spectrophotometer at 620 nM, a wavelength at which most synthetic compounds do not absorb. Concentration-absorbance graphs at varying compound concentration (200–0 µM in eight dilutions) are thus generated and the aqueous solubility of the compound is determined as the point of inflection from the DMSO plot. In addition, hydrocortisone, a highly soluble drug in both solvents, and reserpine, a poor soluble drug in PBS, are employed as internal controls. Thus, the approximate solubility of selected compounds is evaluated from the plots generated (**Figure 4.1**).

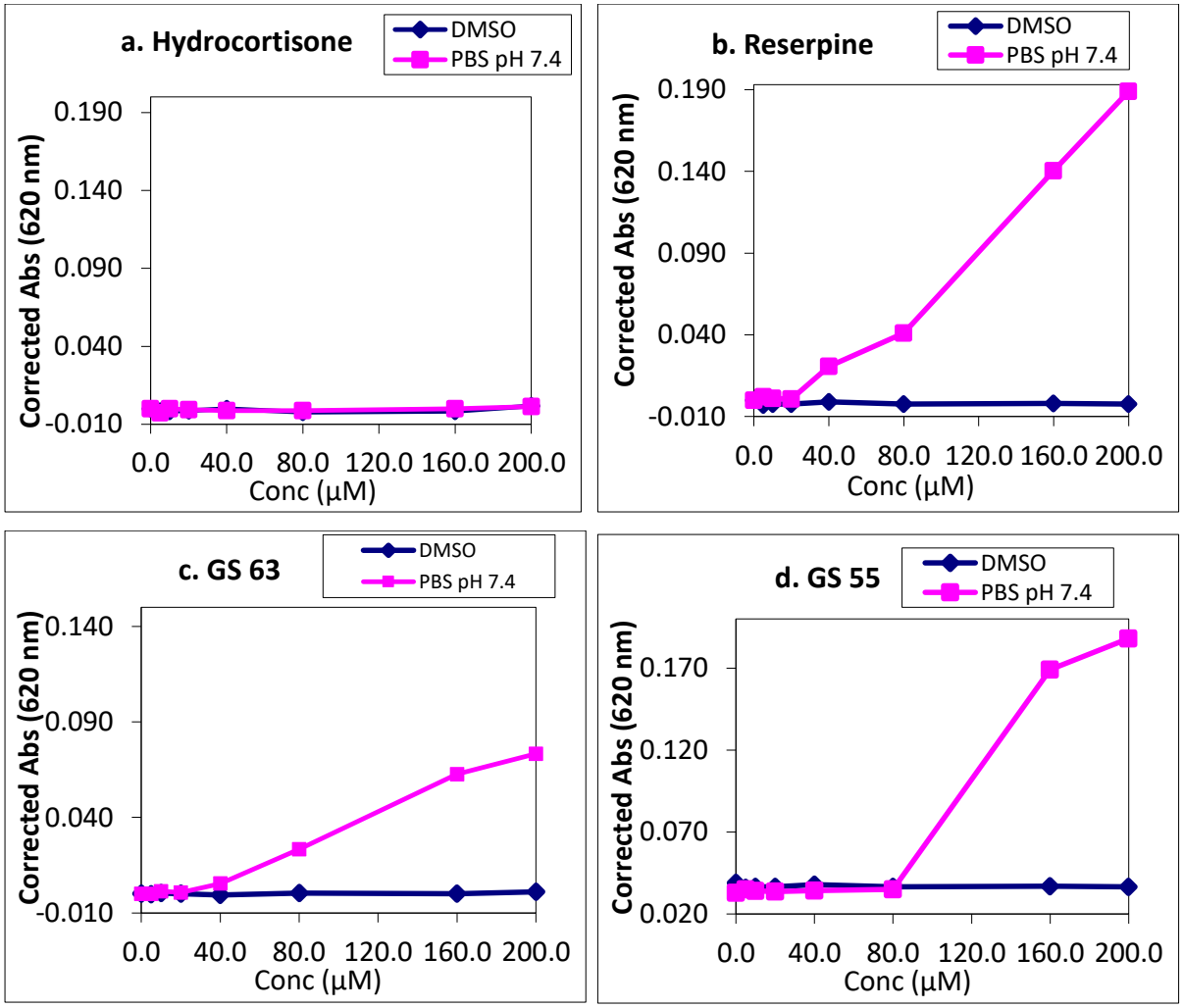

Figure 4.1: Plots of the solubility of the controls (a) hydrocortisone, (b) reserpine, and (c, d) compounds **9** (**GS 63**) and **8** (**GS 55**) in DMSO (**blue**) and PBS (**purple**)

Overall, the solubility of 44/57 analogues (including MLN0128) was evaluated using this method. Pyridyls were generally highly soluble, with most showing solubility between 40 and > 200 µM. In contrast, most benzyls exhibited lower solubility (5–80 µM), with the exception of the aniline compound **13** (**GS 149**;160 µM). As expected, MLN0128 (**62**; **GS 20b**) exhibited high solubility (> 200 µM) in this assay.

4.3.1.2 HPLC-based DMSO "dry-down kinetic solubility

The accurate determination of solubility via turbidimetric assays is hampered by pre-assay dissolution of the test compounds in powerful solvents such as DMSO. This results in overestimated solubility because of enhanced co-solvent effects. Hence, thermodynamic solubility methods are universally considered the 'gold standard' for solubility determination,

as co-solvent effect does not come into play in this case.[14] These methods involve supersaturation of the test compound in aqueous media simulating *in vivo* physiological conditions (37°C and pH 6.5), equilibrating with shaking for 24–72 h, filtering, and analyzing the analyte concentration via HPLC or other quantitative techniques. The exact concentration is then extrapolated by comparison with a constructed standard curve. However, although this method is devoid of co-solvent effects, it is tedious and relatively insusceptible to automation.[15]

Consequently, a modified kinetic solubility method described by Zhou *et al*.,[16] has been adapted for use at H3D. This involves drying off the DMSO solution, reconstituting the test material in buffer, and determining the concentration of the sample using HPLC as in thermodynamic methods. It is therefore referred to as the HPLC-based DMSO "dry-down" method. This adapted method is quick (30 min incubation) and provides more meaningful results as co-solvent effects are eliminated. Accordingly, the solubility of selected compounds was determined. The full methodology for this assay is described in the experimental section (Chapter 10).

In summary, the kinetic solubility of 44/57 compounds (including MLN0128) was evaluated using this method. Pyridyl analogues generally showed greater solubility than benzyl derivatives. The pyridyl compounds **47** (**GS 189**), **52** (**GS 87**), and **43** (**GS 79b**) showed particularly high solubility (85, 65, and 30 µM, respectively; **Figure 4.2**). As expected, MLN0128 (**62**; **GS 20b**) also displayed high solubility (115 µM). In contrast and unsurprisingly, all benzyl derivatives tested retained poor aqueous solubility at pH 6.5 (< 5 µM), with the exception of **33** (**GS 131**, 15 µM; **Figure 4.2**). The modest solubility of **33** (**GS 131**) may be attributed to the water-solubilizing capacity of its cyano group leading to increased interactions with the aqueous media.

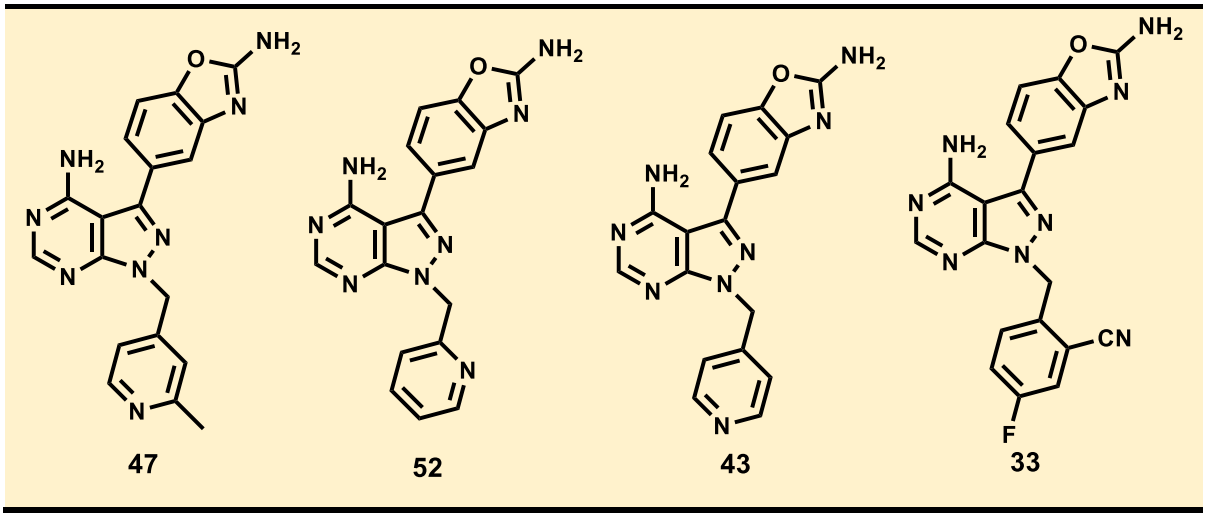

Figure 4.2: MLN0128 analogues with improved aqueous solubility

Overall, and as expected, the turbidimetric solubility method based on the UV-Vis spectrophotometry method was found to be a relatively high over-estimation of solubility compared to the HPLC-based method, although different pH conditions were employed in each assay.

4.3.2 Melting point (MP)

The melting point of a compound is a general indicator of the strength of its inter- and intra-molecular forces. Thus, it is dependent on factors such as molecular flexibility and size, which play a pivotal role in the extent of these forces. A compound's MP is also an indicator of the energy required to break up its crystal structure and is associated with other physicochemical parameters. For example, a compound with a high MP will also have a high crystal packing energy, which reduces its ability to dissolve in an aqueous medium.[17]

For this study, MPs were determined using a Reichert-Jung Thermovar hot-stage microscope coupled with a digital thermometer (20–350 °C). Temperatures were recorded from the start of the melting process to its end and the uncorrected average was reported. These data are included in **Table 4.1**. All analogues synthesized were evaluated using this method, with the exception of analogue **45** (**GS 165**), whose solid material was unavailable at the time of the experiment. All the tested compounds, including MLN0128, displayed high MPs with values greater than 250°C. This is not surprising due to the extended aromaticity of these compounds with the potential to enhance strong π - π interactions requiring huge amounts of energy to break apart their molecular crystal packing.

4.4 Assessment of factors influencing the solubility of MLN0128 analogues

To investigate statistical correlations, the turbidimetric kinetic solubility of the compounds was expressed as a function of cLogP, MW, MP, and TPSA, and the contributory effects of these factors were statistically evaluated. Although it would have been more accurate to assess these correlations using results from the H3D-adapted HPLC method, most of the analogues displayed low solubility (< 5 µM) in this assay. Hence results from the robust UV-Vis thermodynamic solubility were employed to produce statistical plots. For the sake of discussion of the correlation strength (R^2 value) for these plots, Evan's guidelines were employed *i.e.*, R^2 of 0.00–0.19 is categorized as very weak, 0.20–0.39; weak, 0.40–0.59; moderate, 0.60–0.79; strong and 0.80–1.00; as very strong.[18]

A moderate negative correlation ($R^2 = 0.52$) was observed between turbidimetric solubility and cLogP for selected compounds was observed (**Figure 4.3**). In line with literature precedence,[19] this was expected as a highly lipophilic drug (hence high LogP) is likely to interact unfavorably with aqueous media, resulting in an inverse relationship as observed in this case. A stronger correlation may have been observed if definite values of 200 µM had not been arbitrary assigned to compounds whose solubility was beyond the upper limit of determination.

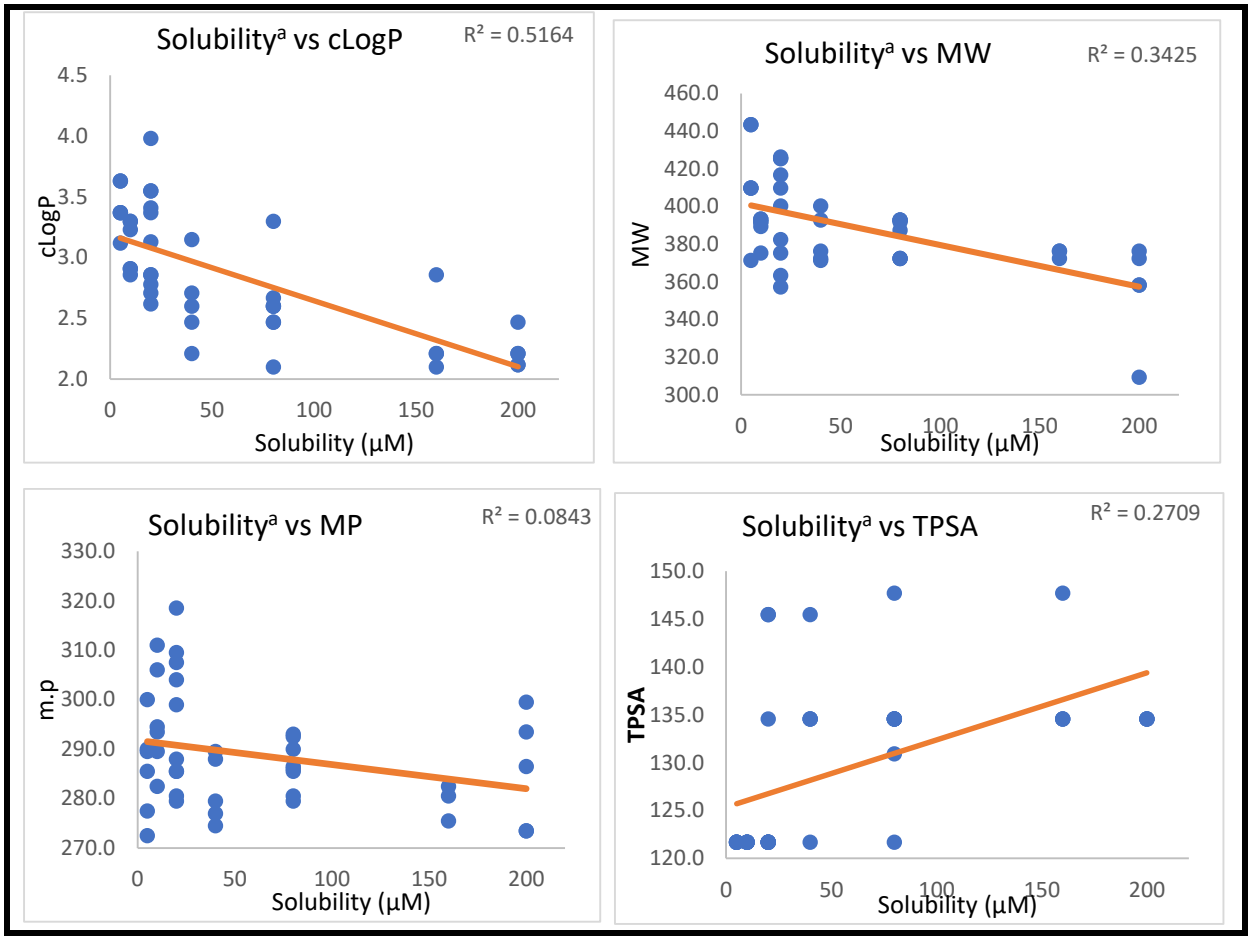

Figure 4.3: Correlations between turbidimetric solubility and MW, cLogP, TPSA, and MP for selected MLN0128 analogues

[a]Turbidimetric solubility determined via UV-Vis spectrophotometry at pH 7.4

In addition, there was a weak positive correlation between solubility and TPSA (R^2 = 0.27). TPSA is a measure of all the polar surfaces of a molecule including oxygen, nitrogen, and their attached hydrogens. It is consequently expected to display a strong positive correlation with solubility, contrary to what was observed here. However, the data points contributing most significantly to this weak correlation correspond to the cyanobenzyls **27** (**GS 107**; solubility = 20 µM), **33** (**GS 131**; 40 µM), and **36** (**GS 141**; 20 µM), which showed high TPSA (145.46 $Å^2$) due to the additional nitrogen atom but exhibited unexpected low solubility which tends to skew the trendline. In contrast, compounds with an additional nitrogen as a pyridyl display greater solubility and slightly lower TPSA (134.56 $Å^2$). Elimination of the cyanobenzyl data

points resulted in a realistically higher R^2 value (0.49; Figure not shown), suggesting that pyridyls facilitated more favorable hydrogen bonding interactions with water molecules.

Similarly, a weak inverse correlation was observed between solubility and MW (R^2 = 0.34). This was expected as an increase in MW corresponds to an increase in molecular size, volume, and lipophilicity, factors likely to result in decreased aqueous solubility. Additionally, arbitrary assignment of a value of 200 µM to solubility for compounds exceeding the upper limit of determination is likely to affect the strength of these correlations.

No correlation was observed between solubility and MP (R^2 = 0.08). In theory, a converse relationship is expected as MP is an indication of the strength of hydrophobic forces that hold molecules together. For instance, highly aromatic molecules would be expected to show high lipophilicity and high MP due to π-π stacking, properties which decrease solubility. In contrast, high solubility may arise due to enhanced polarity, resulting in greater capacity for hydrogen-bond interactions with aqueous media.[20] However, in this case, no apparent relationship could be deduced, suggesting that improvement in the solubility of compounds in this series would not be realized by focusing solely on MP. The observed trend is likely influenced by inherent properties such as the presence of polar functionalities, isomerism, and differences in molecular planarity.

4.5 Correlations between the physicochemical properties and biochemical activities of MLN0128 analogues

The biochemical property of a ligand is a fundamental effect arising from the interactions between the chemical matter and target parasitic or human enzyme. These protein-ligand interactions are determined by the intrinsic physicochemical properties of the compound which controls its ability to interact, for instance with the protein in an *in vitro* set-up. In addition, access to the target in a biological setting requires the compound to cross the host and parasite membranes in a process that requires optimal physicochemical properties.[21] Consequently, it is imperative to evaluate the interrelationships between the physicochemical properties of a compound and the observed biological activities. This enables comparison of the ensuing trends and provides insight for further medicinal chemistry optimization. Towards this end, a section of the experimental and calculated physicochemical parameters (cLogP, TPSA, MW and MP) were chosen for regression analysis with selected biochemical and biological properties.

First, the potential associations between these physicochemical features and anti-plasmodium whole-cell activity (*Pf*NF54 IC_{50}) for selected compounds were investigated. Graphs of the anti-plasmodium activity (expressed as pEC_{50}) for selected MLN0128 analogues as a function of the aforementioned physicochemical parameters were generated (**Figure 4.4**). R^2 values were low (0.00–0.13) and ultimately, no specific relationships could be deduced.

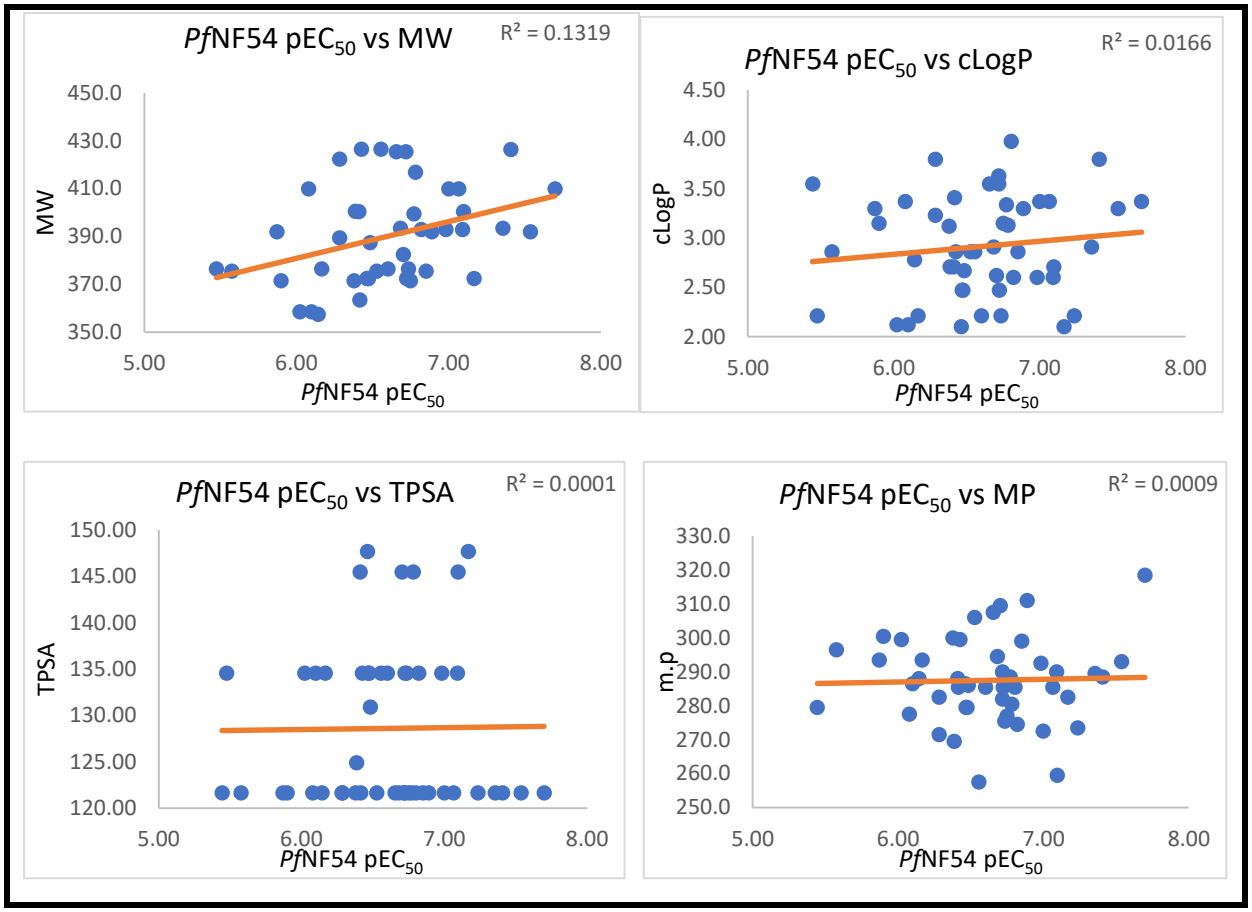

Figure 4.4: Correlations between *Pf*NF54 (pEC_{50}) activity and MW, cLogP, TPSA, and MP

The endeavor to further elucidate the SPRs for these compounds also involved analyzing anti-parasitic *in vitro* enzymatic activity with regard to selected physicochemical parameters. One observation noted in potent *Pf*PKG inhibitors was the presence of basic sidechains that appeared crucial for binding to the parasitic target and consequently influence the biochemical property. At the same time, basicity of a molecule contributes essentially to multiple experimental and calculated physicochemical properties including cLogP, MP, TPSA and MW.[22]

However, it was evident from the correlational plots that no meaningful correlation between *Pf*PKG and these physicochemical parameters could be deduced based on the low R^2 values (0.00–0.22; **Figure 4.5**). This was expected as high *Pf*PKG potency is dependent on the position of the substituent for optimal interactions with the *Plasmodium* target, yet these physicochemical parameters are characteristics of the whole molecule. Therefore, they were unable to distinguish isomers, whose different effects on the *Plasmodium* target were significant.

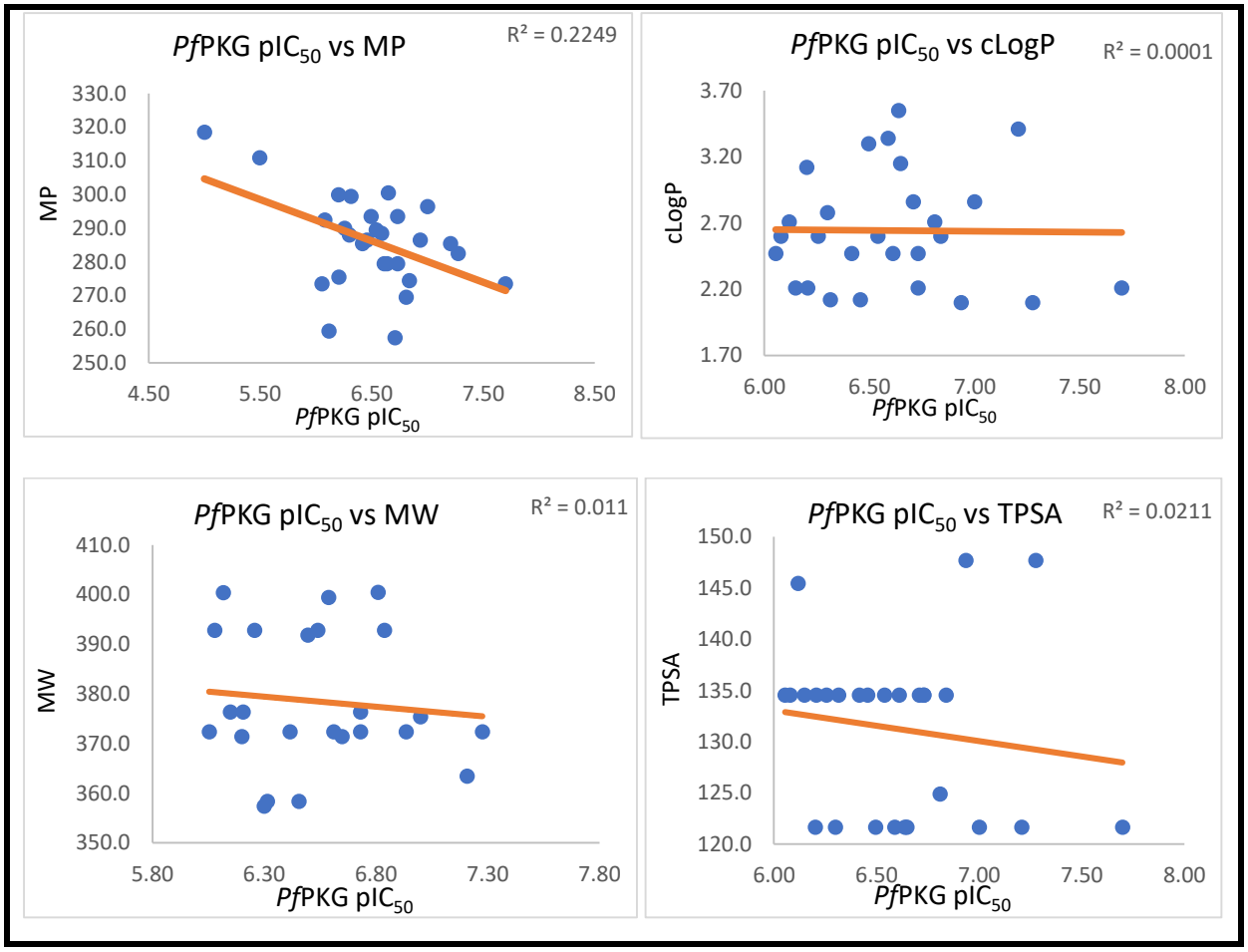

Figure 4.5: Correlation charts of *Pf*PKG (pIC_{50}) with MW, cLogP, TPSA and MP

Similar correlation analysis was undertaken for *Pv*PI4K activity (expressed as pIC_{50}) and the said physicochemical parameters. Generally, as previously alluded, the catalytic site of *Pf*PI4K is more lipophilic and likely to interact better with multi-aromatic compounds[23] hence *Pv*PI4K activity is conjectured to assume an inverse relationship with most of the aforementioned physicochemical parameters. However, in contrast, the plots (**Figure 4.6**) apparently revealed no correlations as indicated by the insignificant R^2 values (0.00–0.17).

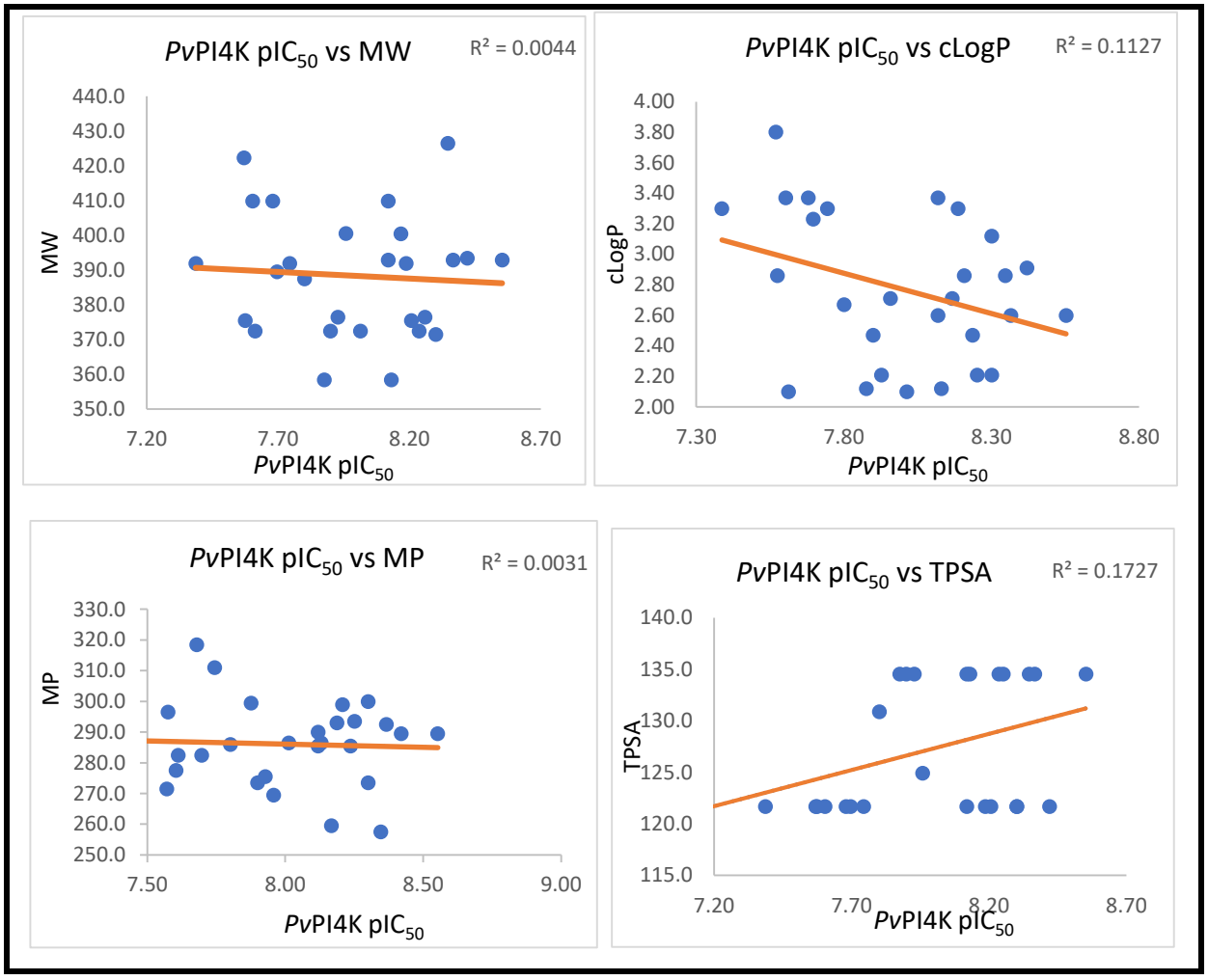

Figure 4.6: Correlations between *Pv*PI4K (pIC_{50}) and MW, cLogP, TPSA and MP

This observation was likely due to the variation in residual amino acids that were targeted as revealed by docking in the *Pf*PI4K homology model. Therefore, although an increase in lipophilicity would be expected to impart favourably on the *Pv*PI4K activity through enhanced π–π stacking, other compound-specific factors such as the nature of the substituent, orientation, solubility, charge at physiological pH, and overall geometry of the molecule, contribute to effective binding against the recombinant protein. In addition, other binding forces such as H-bonds, halogen bonds, π–cation and salt bridges with ionizable centres also promote binding against the *Plasmodium* target. Collectively, these factors reduced the likelihood of any possible correlations.

4.6 Correlation between mTOR activity and physicochemical properties of MLN0128 analogues

De-risking human mTOR in the design of these analogues was a desirable objective of this study, which unfortunately was not achieved. Certainly, a handful of compounds portrayed exemplary *in vitro* anti-plasmodium activity and *Pv*PI4K inhibition. However, these compounds also showed high activity against the recombinant human mTOR as discussed in Chapter 3. To establish the possible underlying causes, the relationships between mTOR potency and the chosen physicochemical parameter (MW, cLogP, MP, and turbidimetric solubility) were investigated. Moderate to very strong correlations were observed between mTOR activity (expressed as pIC_{50}), and these parameters as highlighted by their R^2 values (0.40–0.79; **Figure 4.7**).

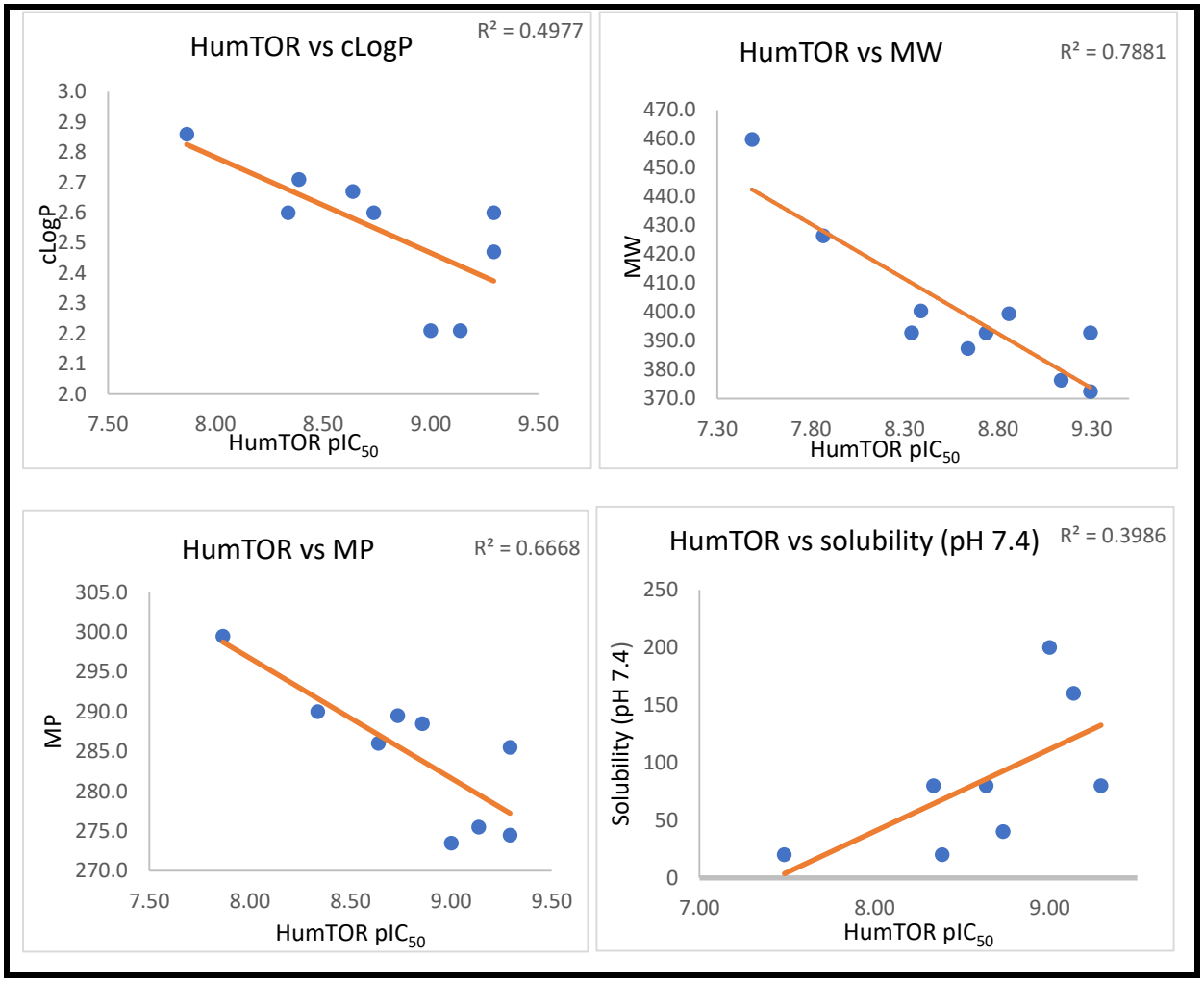

Figure 4.7: Correlations between human mTOR (pIC_{50}) and MW, cLogP, TPSA and MP

These results reflect the interactions between the groups added and the bulk solvent in human mTOR. As expected, these plots indicated some meaningful correlations with increasing lipophilicity (cLogP; $R^2 = 0.50$), MW ($R^2 = 0.79$), and MP ($R^2 = 0.67$). For instance, an increase in MW and lipophilicity should result in a decreased in favorable interactions with aqueous media. Therefore, this would result in poor interactions with the ligand at the mTOR ATP-binding site. Similarly, an inverse relationship would be expected between ligand potency against mTOR and solubility, as observed in this case.

Docking experiments relied heavily on binding energy calculations and unfavorable interactions with the residual amino acids of the human target. These correlations support the inference that substituent interactions with the solvent were best rationalized using physicochemical parameters rather than through molecular docking. Furthermore, it is likely that a significantly higher correlation between mTOR activity and solubility would have been observed in the presence of accurate data points for compounds whose solubility were uncertain. As already mentioned, compounds with solubility < 5 and > 200 µM were arbitrarily assigned definite respective values of 5 and 200 µM, and this might have affected the strength of the correlations observed. However, these trends should be interpreted with caution as only a modest number of data points were available for the plots and only one general SAR was explored in this study. Therefore, these observations will likely not apply if modifications are made to other parts of the molecule.

4.7 Assessment of drug-likeness of the MLN0128 analogues

Assessment for compliance to drug-likeness was gauged based on the well-established Lipinski's Ro5 and Veber's rule on TPSA. In addition, molecular flexibility (expressed as the number of rotatable bonds), a descriptor highly associated with good oral absorption and bioavailability was also determined.[5,6] From the results, (included in **Table 4.1**, previously highlighted), all the analogues were found to conform with the Ro5 with MWs ranging between 363.43–459.82 $g.mol^{-1}$. In addition, other parameters also conformed to this rule (cLogP = 2.10–3.98, HBDs = 2–3, and HBAs of 8–9). Furthermore, all the analogues had 3 or 4 rotatable bonds as determined by StarDrop™ Optibrium 2019 Software. MLN0128 (**62**; **GS 20b**) had 2 rotatable bonds, the lowest count for compounds in this series.

All the analogues also conformed to the Veber's rule on TPSA (< 140 $Å^2$) with the exception of the anilines **13** (**GS 149**; 147.69 $Å^2$) and **18** (**GS 155**; 147.69 $Å^2$), and the cyano-containing

benzyls **9** (**GS 63**), **27 (GS 107**) and **33** (**GS 131**) each with a value 145.46 Å^2 (**Figure 4.9**). In terms of the number of HBDs and HBAs, Veber's rule proposed that the sum of the two as a better indicator of predicting "drug-likeness", with an acceptable cut-off of ≤ 12. In this regard, all the analogues conformed to this important guideline.

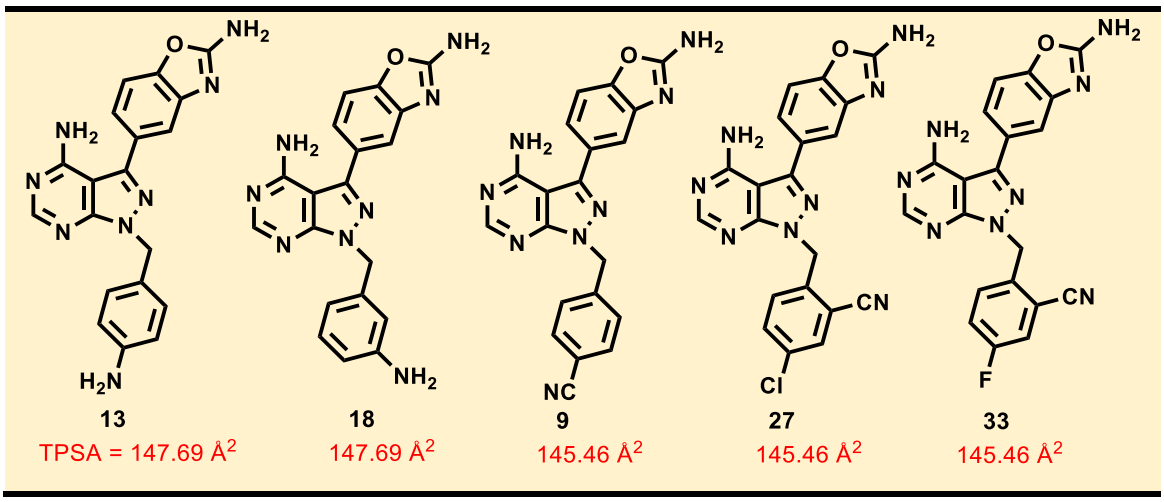

Figure 4.8: MLN0128 analogues in violation of Veber's rule on TPSA

4.8 Chapter summary

In summary, the experimentally (MP and solubility) and computationally derived physicochemical parameters (MW, LogP, TPSA, and number of HBDs, HBAs, and rotatable bonds) of synthesized MLN0128 analogues have been discussed. The relationships between these parameters and the observed biological and biochemical properties have also been evaluated. In addition, parameters that influence aqueous dissolution have been assessed for these compounds. Finally, the "drug-likeness" and conformity of these compounds with Lipinski and Veber's rules have been discussed.

References

1. Di, L.; Kerns, E. and Carter, G. Drug-like property concepts in pharmaceutical design. *Curr. Pharm. Des*. **2009**; 15 (19): 2184 - 2194. doi:10.2174/ 138161209788682479.

2. Fasinu, P; Pillay, V.; Ndesendo, V.; Toit, L.; Choonara, Y. Review: Diverse approaches for the enhancement of oral drug bioavailability. *Biopharm. Drug Dispos*. **2011**; 32: 185 - 209. doi:10.1002/bdd.

3. Roskoski, R. Properties of FDA-approved small molecule protein kinase inhibitors. *Pharmacol Res*. **2019**; 144 (3): 19 - 50. doi:10.1016/j.phrs.2019.03.006.

4. Arnott, J. and Planey, S. The influence of lipophilicity in drug discovery and design. *Expert Opin Drug Discov*. **2012**; 7 (10): 863 - 875. doi:10.1517/17460441.2012.714363.

5. Lipinski, C.; Lombardo, F.; Dominy, B. and Feeney, P. Experimental and computational approaches to estimate solubility and permeability in drug discovery and development settings. *Adv. Drug Deliv. Rev.* **1997**; 23: 3 - 25.

6. Veber, F.; Johnson, S.; Cheng, H.; Smith, B.; Ward, K.; Kopple, K. Molecular properties that influence the oral bioavailability of drug candidates. *J. Med. Chem*. **2002**; 45 (12): 2615 - 2623. doi:10.1021/jm020017n.

7. Congreve, M.; Carr, R.; Murray, C.; Jhoti, H. A "Rule of Three" for fragment-based lead discovery? *Drug Discov. Today*. **2003**; 8 (19): 876 - 877. doi:10.1016/S1359-6446(03)02831-9.

8. Benet, L.; Hosey, C.; Ursu, O. and Oprea, T. BDDCS, the Rule of 5 and drugability. *Adv. Drug Deliv. Rev*. **2016**; 101: 89 - 98. doi:10.1016/j.addr.2016.05.007.

9. Ishikawa, M. and Hashimoto, Y. Improvement in aqueous solubility in small molecule drug discovery programs by disruption of molecular planarity and symmetry. *J. Med. Chem.* **2011**; 54 (6): 1539 - 1554.

10. Kerns, E. and Di, L. Drug-like properties: Concepts, structure design and methods from ADME to toxicity optimization. In: San Diego: Academic Press; **2008**: 56 - 85. doi:https://doi.org/10.1016/B978-012369520-8.50008-5.

11. Di, L.; Fish, P. and Mano, T. Bridging solubility between drug discovery and development. **2011**; 17 (9/10): 486 - 495. doi:10.1016/j.drudis.2011.11.007.

12. Saal, C. and Petereit, A. Optimizing solubility: Kinetic versus thermodynamic solubility temptations and risks. *Eur. J. Pharm. Sci*. **2012**; 47 (3): 589 - 595. doi:10.1016/j.ejps.2012.07.019.

13. Pan, L.; Ho, Q.; Tsutsui, K. and Takahashi, L. Comparison of chromatographic and spectroscopic methods used to rank compounds for aqueous solubility. *J. Pharm. Sci*. **2001**; 90 (4): 521 - 529. doi:10.1002/1520-6017(200104)90:4<521:AID - JPS1009>3.0.CO;2-B.

14. Colclough, N.; Ruston, L. and Tam, K. Physicochemical aspects of drug dissolution and solubility aqueous solubility in drug discovery chemistry, DMPK, and biological assays. In: *Methods and Principles in Medicinal Chemistry*; **2009**: 9 - 31. doi:10.1002/9783527623860.ch2.

15. Veseli, A.; Žakelj, S. and Kristl, A. A review of methods for solubility determination in biopharmaceutical drug characterization. *Drug Dev. Ind. Pharm*. **2019**; 45 (11): 1717 - 1724. doi:10.1080/03639045.2019.1665062.

16. Zhou, L., Yang, L., Tilton, S. and Wang, J. Development of high throughput equilibrium solubility assay using miniaturized shake-flask method in early drug discovery. *J. Pharm. Sci*. **2007**; 96 (11): 3052 - 3071. doi:10.1002/jps.

17. Katritzky, A.; Jain, R.; Lomaka, A.; Petrukhin, R.; Maran, U.; Karelson, M. Perspective on the relationship between melting points and chemical structure. *Cryst. Growth Des*. **2001**; 1 (4): 261 - 265.

18. Evans, J. *Straightforward Statistics for the Behavioral Sciences*. Brooks/Cole Publishing Company; **1996**. https://books.google.co.za/books?id=8Ca2AAAAIAAJ.

19. Rutkowska, E.; Pająk, K. and Jóźwiak, K. Lipophilicity - Methods of determination and its role in medicinal chemistry. *Acta. Pol. Pharm - Drug Res*. **2013**; 70 (1): 3 - 18.

20. Tetko, I.; Yan, A. and Gasteiger, J. Prediction of physicochemical properties of compounds. *Appl. Chemoinformatics*. **2018**: 53 - 81. doi:10.1002/9783527806539.ch3.

21. Meanwell, N. Improving drug design: An update on recent applications of efficiency metrics, strategies for replacing problematic elements, and compounds in nontraditional drug space. *Chem. Res. Toxicol*. **2016**; 29 (4): 564 - 616. doi:10.1021/acs.chemrestox.6b00043.

22. Manallack, D.; Prankerd, R.; Yuriev, E.; Oprea, T.; Chalmers, D. The significance of acid/base properties in drug discovery. *Chem. Soc. Rev*. **2013**; 42 (2): 485 - 496. doi:10.1039/c2cs35348b.

23. Fienberg, S.; Eyermann, C.; Arendse, L.; Basarab, G.; McPhail, J.; Burke, J.; Chibale, K. Structural basis for inhibitor potency and selectivity of *Plasmodium falciparum* phosphatidylinositol 4-kinase inhibitors. *ACS Infect. Dis*. **2020**; 6 (11): 3048 - 3063. doi:10.1021/acsinfecdis.0c00566**.**

CHAPTER 5

SUMMARY, CONCLUSIONS AND RECOMMENDATIONS FOR FUTURE WORK ON THE MLN0128 TEMPLATE

5.1 Summary on the MLN0128 series

The GSK Cellzome facility identified anticancer clinical candidate, MLN0128 as a potent hit compound with anti-plasmodium activity. Multiple putative *Plasmodium* kinase targets of MLN0128 were identified from *P. falciparum* asexual blood stage extracts using the Kino-bead technology. In this study, the potent *in vitro* asexual blood stage anti-plasmodium activity of MLN0128 was confirmed, late-stage specific gametocytocidal activity and *in vivo* efficacy in a *Pf*SCID mouse model of the human malaria parasite was demonstrated. An impressive reduction in parasitemia (98%) was observed at a daily per oral dose of 1 $mg.kg^{-1}$ displaying the potential of this chemotype as an antimalarial scaffold. In addition, metabolomics studies revealed a metabolite perturbation profile characteristic of PI4K inhibition.

In silico techniques were then employed to reposition the scaffold as a dual *Plasmodium* PI4K and PKG inhibitor, with potentially reduced human mTOR inhibitory activity. Medicinal chemistry iterations were carried out by appending substituted benzyl and pyridyl moiety with representative substituents chosen across the four quadrants of the Craig plot (**Figure 5.1)**. Several cyclohexyl substituents were also explored.

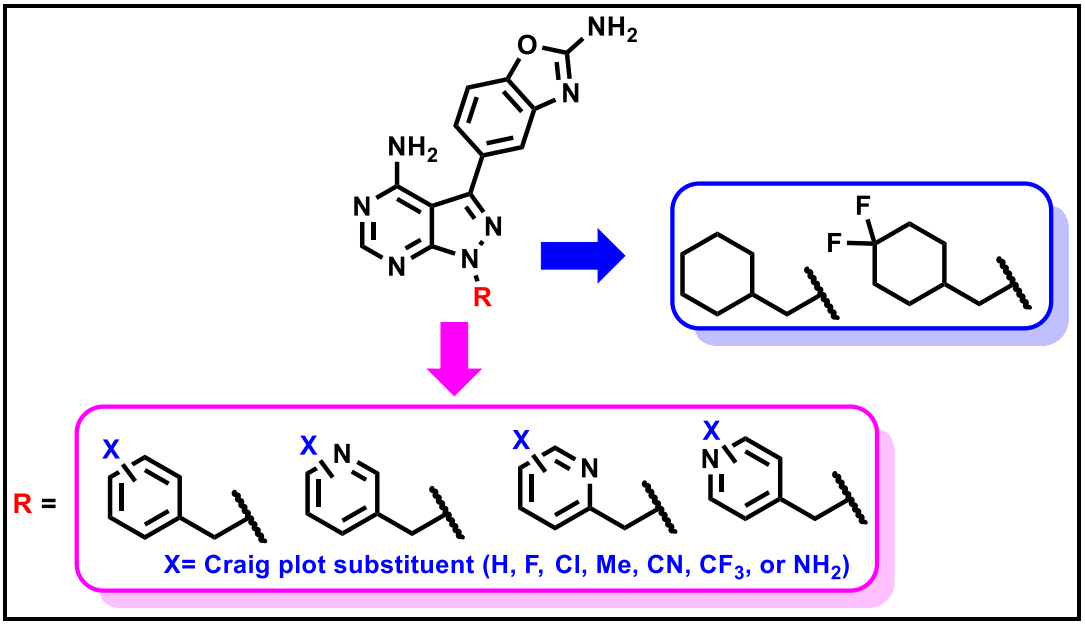

Figure 5.1: Structural modifications explored in this study on the MLN0128 scaffold

Delivery of the target compounds was ensured through adapted Leuckart condensation, iodination by aromatic nucleophilic substitution, *N*-alkylation, and Suzuki cross-coupling reactions. Arising from this work, analogues with sub-nanomolar potency against the asexual blood stage parasites of both the chloroquine sensitive (*Pf*NF54) and multi-drug resistant (*Pf*K1) strains were identified. Equipotency against both strains suggested low risk of cross-resistance for this series. An exception to this were several analogues possessing pyridyl or benzyl basic sidechains suggesting potentially increased recognition by *Pf*CRT as substrates. Progression of selected compounds for gametocytocidal evaluation identified potent molecules with high specificity against late-stage gametocytes (IC_{50} < 1 µM). This important finding suggest that the series has the potential for transmission blocking by elimination of gametocytes, the transmissible form of the parasite, in line with the recently launched TCPs (TCP 5) for future antimalarials.

Subsequent profiling of the compounds for *in vitro* *Pv*PI4K and *Pf*PKG inhibitory activity revealed compounds with sub-micromolar dual potency (IC_{50} < 0.2 µM) against these essential *Plasmodium* targets of interest. The explored SARs further highlighted molecular features that promoted differential selectivity. Docking studies using a *Pf*PI4K homology model and *Pv*PKG crystal structure were used to predict key inhibitor binding interactions within the ATP-binding site, providing insight into the SAR observed in the *in vitro* enzyme inhibition assays. A summary of the anti-plasmodium activity and the *in vitro* enzymatic data is provided **Figure 5.2**.

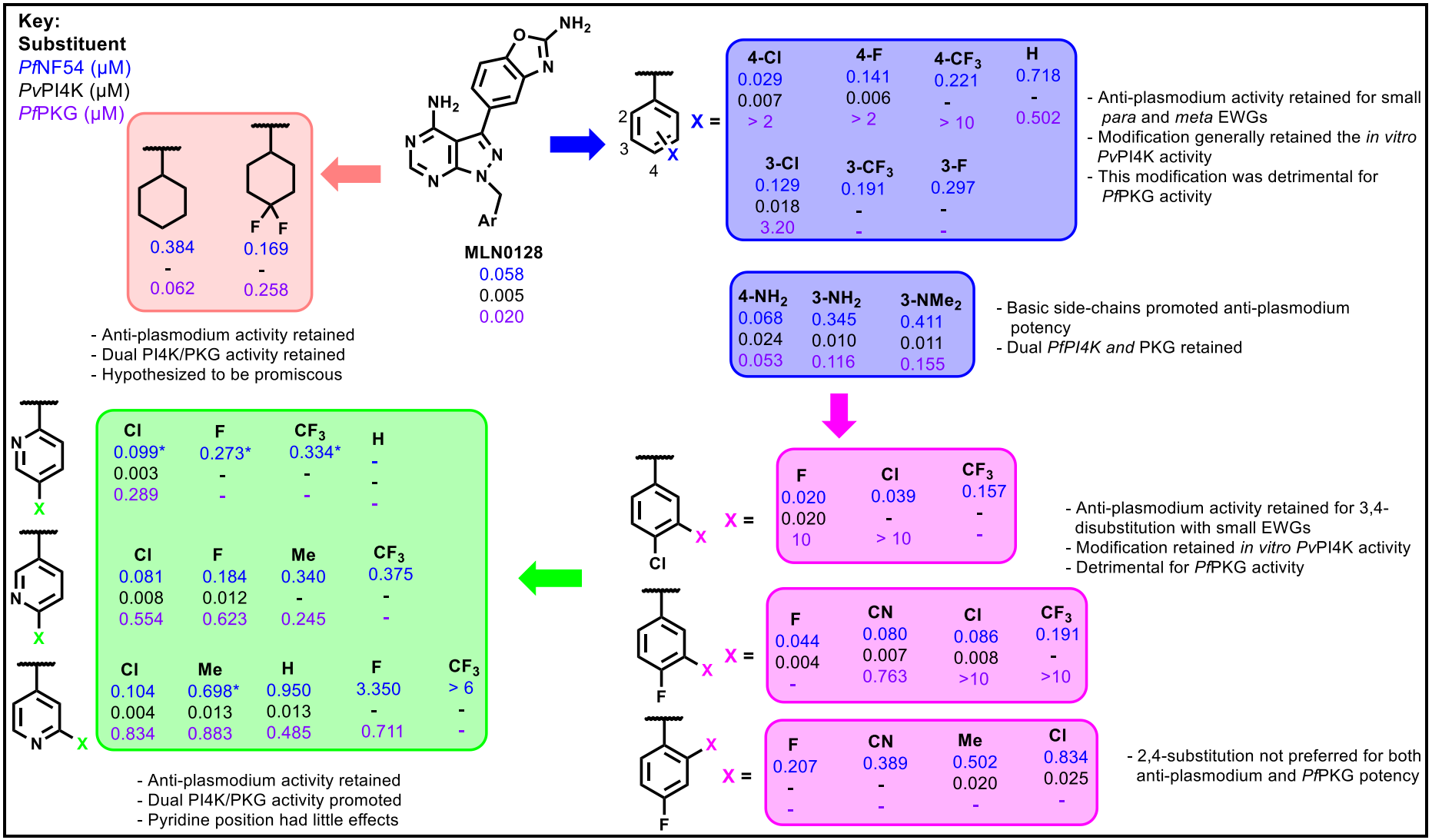

Figure 5. 2: SAR summary of the asexual blood stage *Pf*NF54 activity and biochemical profile for representative MLN0128 analogues

*Asexual blood-stage IC50 values were obtained against the multi-drug resistant *Pf*K1 strain

Towards probing the safety profile for the series, selected analogues with potent anti-plasmodium activity (*Pf*NF54 IC_{50} < 0.5 µM) were examined for cytotoxicity using the CHO cell line. Based on the selectivity indices (SI) obtained (SI = 1 to > 1250), thirteen compounds displayed an acceptable safety margin (≥ 100) suggesting that CHO cytotoxicity is compound specific and not a general issue for the series. Furthermore, hERG assessment using laboratory adapted methods suggested that the series possess limited risk against the cardiac channel. In terms of microsomal metabolic stability, all analogues evaluated were found to be stable across the microsomal preparations of the three (mouse, rat and human) species of interest.

Two representative compounds were assessed for off-target inhibition of human PI4KIIIβ. As has been reported for the parent compound MLN0128, both compounds demonstrated low affinity for human PI4KIIIβ, maintaining selectivity for the *Plasmodium* orthologue. However, evaluation against recombinant human mTOR, revealed that this remains a key human off-target for this series and selectively may need to be further optimized. The extent of human mTOR inhibition *in vivo* and any attendant implications will be dependent on the required dose and the duration of treatment and will need to be evaluated in the context of PK/PD modelling.

Examination of physicochemical properties showed all analogues complied with Lipinski's rule of five (Ro5) with regard to MW, LogP, and number of HBDs and HBAs in addition to Veber's guideline on the number of rotatable bonds (≤ 10).[1,2] Apart from five analogues, the compounds synthesized also complied with the guideline on TPSA (< 141 $Å^2$), a parameter that is useful in predicting high permeation and oral bioavailability in animal models.[2] However, kinetic aqueous solubility emerged as a critical property requiring further optimization to improve anticipated solubility-limited absorption *in vivo*. Ultimately, several promising compounds were identified, providing a starting point for further optimization and identification of potential drug leads from this series (**Figure 5.3**).

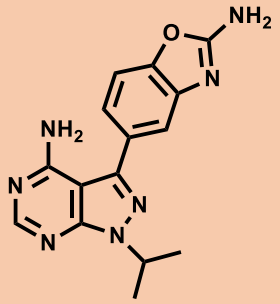

62

*Pf*NF54 IC_{50} = 0.058 μM
*Pv*PI4K IC_{50} = 0.005 μM
*Pf*PKG IC_{50} = 0.020 μM
LG IC_{50} = 0.54 μM
CHO SI = 2
MMS[b] H/R/M = ND
HumTOR IC_{50} = 0.007 μM
HumPI4K IC_{50} = ND
hERG IC_{50} = 175 μM[a]

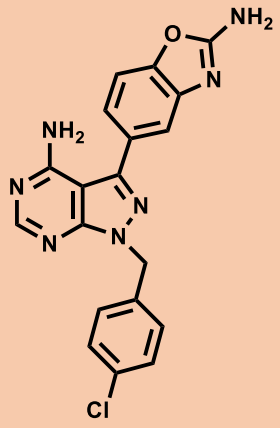

7

*Pf*NF54 IC_{50} = 0.029 μM
*Pv*PI4K IC_{50} = 0.0065 μM
*Pf*PKG IC_{50} > 2 μM
LG IC_{50} = 0.63 μM
CHO SI = 40
MMS[b] H/R/M = ND
HumTOR % Inh. @ 1 μM = 95%
HumPI4K IC_{50} = ND
hERG IC_{50} = ND

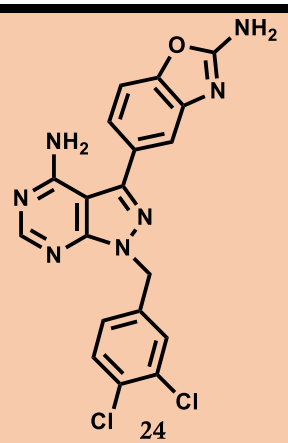

24

*Pf*NF54 IC_{50} = 0.039 μM
*Pv*PI4K IC_{50} = ND
*Pf*PKG IC_{50} >10 μM
LG IC_{50} = ND
CHO SI > 1250
MMS[b] H/R/M = 96/68/60
Human mTOR IC_{50}= ND
Human PI4K IC_{50} = ND
hERG IC_{50} > 30 μM

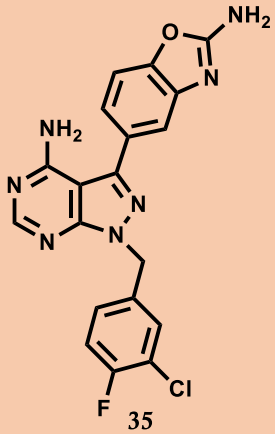

35

*Pf*NF54 IC_{50} = 0.086 μM
*Pv*PI4K IC_{50} =0.0076 μM
*Pf*PKG IC_{50} >10 μM
LG IC_{50} = ND
CHO SI = 267
MMS[b] H/R/M =95/94/97
HumTOR IC_{50} = ND
HumPI4K IC_{50} = ND
hERG IC_{50} = ND

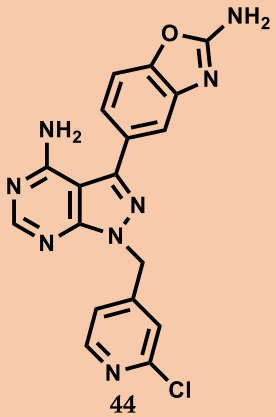

44

*Pf*NF54 IC_{50} = 0.104 μM
*Pv*PI4K IC_{50} =0.0043 μM
*Pf*PKG IC_{50} = 0.834 μM
LG IC_{50} = ND
CHO SI = 408
MMS[b] H/R/M = 97/95/95
HumTOR % Inh. @ 1 μM = 99%
HumPI4K % Inh. @ 1 μM = 4 %
hERG IC_{50} = 21.6 μM

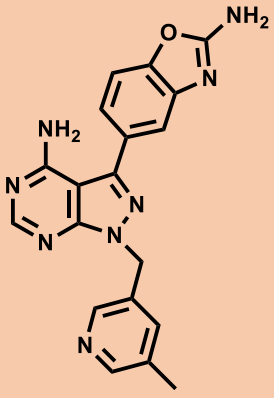

49

*Pf*NF54 IC_{50} = 0.189 μM
*Pv*PI4K IC_{50} =0.0058 μM
*Pf*PKG IC_{50} = 0.384 μM
LG IC_{50} = ND
CHO SI = 210
MMS[b] H/R/M = 95/87/86
HumTOR % Inh. IC_{50} < 0.51 nM
HumPI4K % Inh. @ 1 μM = ND
hERG IC_{50} = 79.0 μM*

Figure 5.3: Structure, biological and biochemical profiles of MLN0128 and selected front-runner compounds

[a]Data obtained from Hsieh *et al.*[3] [b]Microsomal metabolic stability against human, rat, and mouse liver microsomes; *hERG data obtained by extrapolation.

5.2 Conclusions

In conclusion, the work pursued here provides preliminary data for further optimization of the oncological MLN0128 scaffold as an antimalarial chemotype. This highlights the utility of the particularly appealing drug repositioning approach in antimalarial drug discovery program. *In silico* docking has been employed to rationalize the observed *in vitro* enzymatic activity against *Plasmodium* PI4K and PKG forming the basis for a potentially more structured target-based drug discovery program for this series. The possibility of targeting two essentially validated *Plasmodium* kinases with a single molecule based on this chemotype has been demonstrated in this study. Finally, the compounds synthesized also show other benefits such as blocking transmission via inhibition of gametocytes in addition to eliminating asexual-stage *Plasmodium* parasites, an appealing characteristic for future antimalarials.

5.3 Recommendations for future exploration of the MLN0128 template

A summary of the proposed SAR (pSAR) for future studies focusing on the MLN0128 series is shown in **Figure 5.4**. So far, the primary liabilities of the series as an anti-malarial chemotype include high activity against human mTOR and sub-optimal aqueous solubility. These issues need to be addressed for further progression of this chemotype as an anti-plasmodium series. Corroborated by *in silico* techniques and physicochemical correlations, the introduction of a floppier lipophilic group (as proposed in pSAR1) may de-risk potency against the recombinant human mTOR protein. Both benzyls and pyridyls must be investigated in tandem. In addition, optimal retention of *Pf*PI4K potency may be achieved by incorporating small EWGs such as Cl and F in the *ortho* and *meta* positions. Furthermore, introduction of basic groups such as substituted and unsubstituted amines on the pyridyl or benzyl moiety may maintain dual potency against the *Plasmodium* targets and should be investigated going forward. In addition, correlation plots of mTOR activity with other physicochemical metrics relevant to lipophilicity such as the lipophilic ligand efficiency (LLE) need to be investigated to highlight possible effects of these structural changes to protein binding.

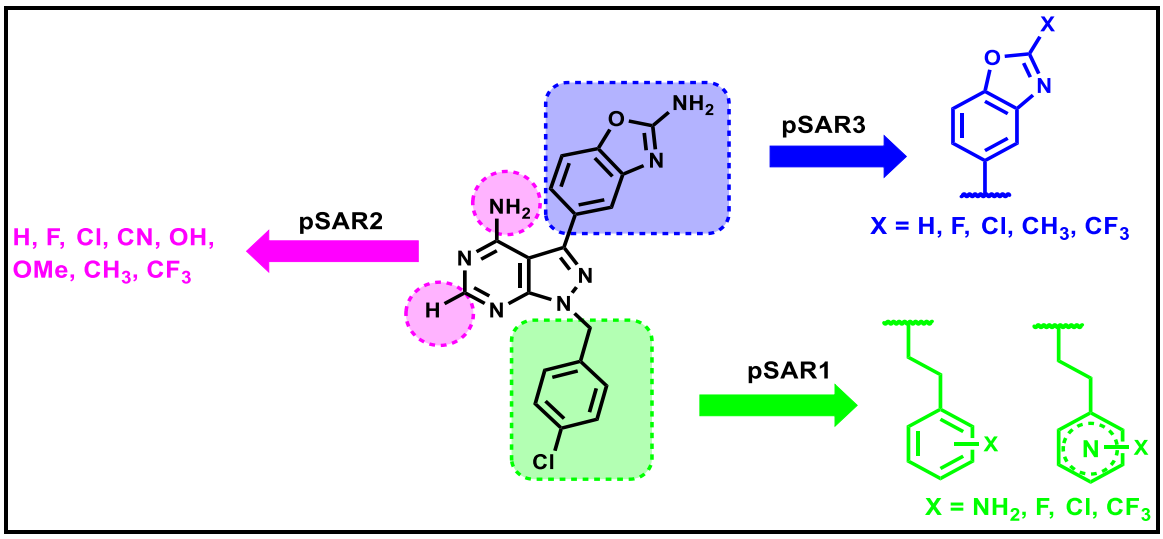

Figure 5.4: Proposed SAR for future exploration on the MLN0128 scaffold

However, pSAR1 is unlikely to mitigate the issue of sub-optimal aqueous solubility due to the further increase in lipophilicity. In this case, other strategies may need to be employed. For example, the formulation of amines to hydrochloride salts, introduction of water-solubilizing functionalities, disruption of molecular planarity and introduction of chiral centers are some medicinal chemistry methodologies previously employed that may mitigate the issue.[4–7] In this regard, guided by molecular docking, introduction of a methyl, hydroxyl, amine and carbonyl substituents at the benzylic position of the scaffold need to be experimentally explored (**Figure 5.5**).

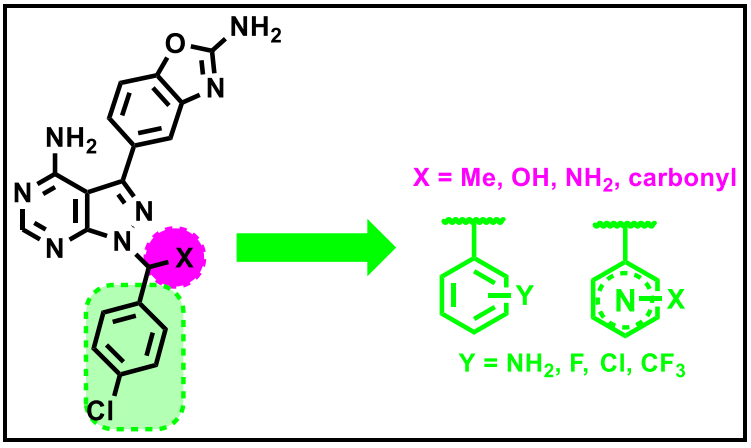

Figure 5.5: Proposed modifications capable of improving solubility on the MLN0128 scaffold

Some of the strategies proposed in **Figure 5.5** will result in the introduction of a chiral center, warranting biological investigation of the racemic and respective enantiomers. Molecular docking coupled with experimental data would assist in guiding and understanding the effects

of these modifications on the *Plasmodium* and human targets. Furthermore, a balance between solubility and lipophilicity will be needed for optimal permeation, as a requirement for effective drug movement through cell membranes. In addition, industrial techniques such as formulation may also be adopted to improve drug solubility, although such approaches are often expensive.[5]

With regard to human mTOR activity, molecular docking suggests that strong binding to the hinge is ensured by the pyrazolopyrimidine acceptor-donor pairs with Val 2240 and Gly 2238, resulting in high potency against the recombinant protein. Interestingly, recent repositioning endeavors of MLN0128 as a topical human PI3K inhibitor for the management of dermatological conditions by Nestle® Skin Health highlighted the impact of subtle structural modifications on the hinge binding motif with high impact on physicochemical and kinase selectivity profiles, including mTOR.[8] Parallel to this campaign, further medicinal chemistry iterations should be explored as proposed in pSAR2. Incorporating substituents with hydrogen-bonding capacity such as OH, OMe, and CN in either of these positions should be explored to improve aqueous solubility and other physicochemical properties, in addition to potential mTOR activity attenuation.

In silico studies suggest that the benzoxazole side of the molecule is also a key driver of the observed mTOR potency. Although modification of the sp^3-hybridized amine is predicted to result in partial loss of affinity against the *Plasmodium* targets, this needs to be confirmed experimentally, and an optimal balance between the antiparasitic and human mTOR activity is required. In this regard, deletion of the benzoxazole amine or substitution with small neutral groups or EWGs, as suggested in pSAR3, should be pursued. However, although one or more of the above-mentioned strategies may improve solubility and/or mitigate mTOR activity, potency against the *Plasmodium* targets must be enhanced and not compromised.

References

1. Lipinski, C.; Lombardo, F.; Dominy, B. and Feeney, P. Experimental and computational approaches to estimate solubility and permeability in drug discovery and development settings. *Adv. Drug Deliv. Rev.* **1997**; 23: 3 - 25.

2. Veber, F.; Johnson, S.; Cheng, H.; Smith, B.; Ward, K.; Kopple, K. Molecular properties that influence the oral bioavailability of drug candidates. *J. Med. Chem*. **2002**; 45 (12): 2615 - 2623. doi:10.1021/jm020017n.

3. Hsieh, A.; Liu, Y.; Edlind, M.; Ingolia, N.; Janes, M.; Sher, A.; Shi, E.; Stumpf, C.; Christensen, C.; Bonham, M.; Wang, S.; Ren, P.; Martin, M.; Jessen, K.; Feldman, M.; Weissman, J.; Shokat, K.; Rommel, C.; Ruggero, D. The translational landscape of mTOR signalling steers cancer initiation and metastasis. *Nature*. **2012**; 485 (7396): 55 - 61. doi:10.1038/nature10912.

4. Doherty E.; Fotsch, C.; Bannon, A.; Bo, Y.; Chen, N.; Dominguez, C.; Falsey, J.; Gavva, N.; Katon, J.; Nixey, T.; Ognyanov, V.; Pettus, L.; Rzasa, R.; Stec, M.; Surapaneni, S.; Tamir, R.; Zhu, J.; Treanor, J.; Norman, M. Novel vanilloid receptor-1 antagonists : 2 Structure - activity relationships of 4-oxopyrimidines leading to the selection of a clinical candidate. *J. Med. Chem.* **2007**; 50 (15): 3515 - 3527.

5. Di, L.; Fish, P. and Mano, T. Bridging solubility between drug discovery and development. **2011**; 17 (9/10): 486 - 495. doi:10.1016/j.drudis.2011.11.007.

6. Ishikawa, M. and Hashimoto, Y. Improvement in aqueous solubility in small molecule drug discovery programs by disruption of molecular planarity and symmetry. *J. Med. Chem.* **2011**; 54 (6): 1539 - 1554.

7. Wang, H.; Katon, J.; Balan, C.; Bannon, A.; Bernard, C.; Doherty, E.; Dominguez, C.; Gavva, N.; Gore, V.; Ma, V.; Nishimura, N.; Surapaneni, S.; Tang, P.; Tamir, R.; Thiel, O.; Treanor, J.; Norman, M. Novel vanilloid receptor-1 antagonists :3, the identification of a second-generation clinical candidate with improved physicochemical and pharmacokinetic properties. *J. Med. Chem.* **2007**; 50 (15): 3528 - 3539.

8. Ouvry, G.; Clary, L.; Tomas, L.; Aurelly, M.; Bonnary, L.; Borde, E.; Bouix-Peter, C.; Chantalat, L.; Defoin-Patel, C.; Deret, S.; Forissier, M.; Harris, C.; Isabet, T.; Lamy, L.; Luzy, A.; Pascau, J.; Soulet, C.; Taddei, A.; Taquet, N.; Thoreau, E.; Varvier, E.; Vial,

E.; Hennequin, L. Impact of minor structural modifications on properties of a series of mTOR inhibitors. *ACS Med. Chem. Lett*. **2019**; 10 (11): 1561 - 1567.

PART 2: *PLASMODIUM* PI4K/PKG, SOLUBILITY, AND CARDIOTOXICITY RISK OPTIMIZATION OF ANTI-MALARIAL IMIDAZOPYRIDINES

CHAPTER 6

DESIGN AND SYNTHESIS OF IMIDAZOPYRIDINES AS *PLASMODIUM* PI4K/PKG INHIBITORS WITH IMPROVED CARDIOTOXICITY RISK AND SOLUBILITY PROFILES

6.1 Chapter overview

This chapter will provide a brief account of the pharmacological spectrum of imidazopyridazines and imidazopyridines which includes a brief description of their potential as antimalarial chemotypes. Next, a brief background of this part of research work will be described after which the objectives of the study will ensue. The design of hypothesized dual *Pf*PI4K/PKG inhibitors leading to the synthesis of target compounds based on the imidazopyridine scaffold will subsequently be provided. Lastly, reaction mechanisms and characterization of representative intermediates and target compounds will be elaborated.

6.2 Antimalarial imidazopyridazines and imidazopyridines

Imidazopyridazines and imidazopyridines are related classes of compounds which display a plethora of pharmacological properties such as anticancer, anti-arthritic, hypnotic, antiviral, and anti-parasitic activities. Their mechanistic action has been attributed to their ability to inhibit multiple oncological and parasite-relevant kinases such as mTOR, PI3Ks, CRKs, and AKT receptors.[1-3] For example, an imidazopyridazine compound, **ponatinib** (**Figure 6.1**), was approved as a multi-tyrosine kinase inhibitor for the treatment of chronic myeloid leukaemia.[4] Additionally, numerous lead compounds for non-oncological and kinase-targeting oncological indications have progressed to various stages of development. Several representative imidazopyridazines and imidazopyridines compounds are captured in **Figure 6.1**.[5-9]

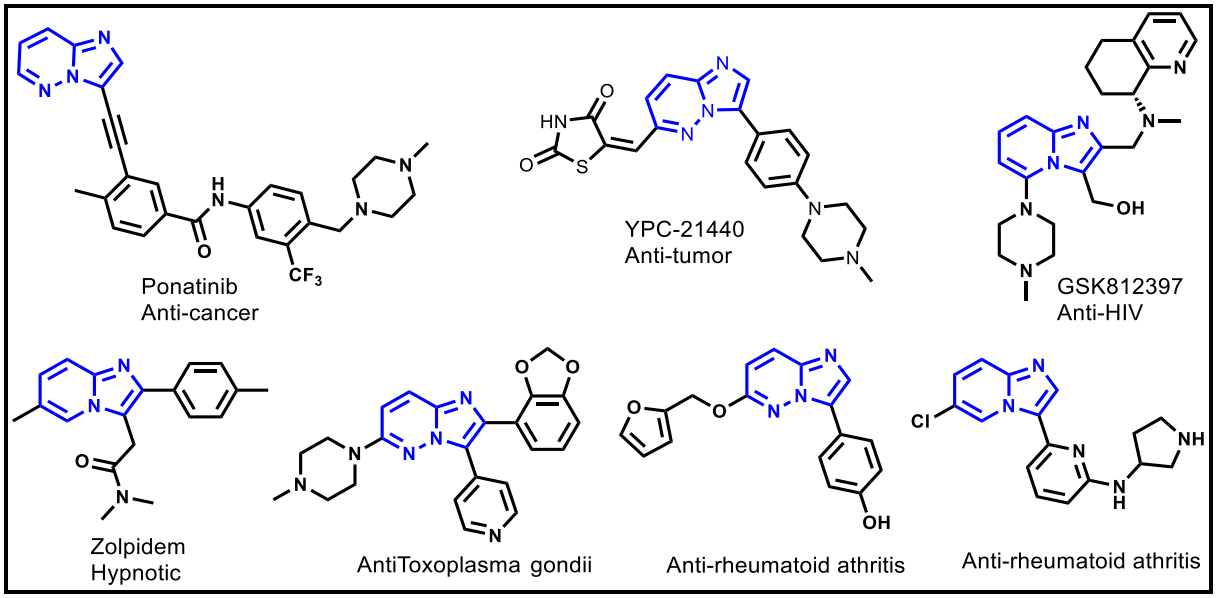

Figure 6.1: Pharmacological properties of selected imidazopyridine/ imidazopyridazines

Although the development of antimalarial kinase inhibitors is still in its infancy, it has the potential to produce novel drugs with activity against multiple stages of the *Plasmodium* parasite life cycle.[10] For instance, several publications have reported imidazopyridazines as novel antimalarial kinase inhibitors targeting CDPK1, protein kinase 7 (*Pf*PK7), PKG, PI4K, and Cdc2-like kinase 1 (CLK1).[11-13]

A structure-based approach guided by a *Pf*CDPK1 homology model led to the discovery of imidazopyridazine 1 (**Figure 6.2**) showing high enzymatic activity (*Pf*CDPK1 IC_{50} = 0.012 µM) and *Pf* potency (*Pf*3D7 EC_{50} = 0.080 µM), albeit this compound showed low *in vivo* efficacy in a *P. berghei* mouse model (51% reduction in parasitemia after administration of 4 × 50 mg/kg doses).[14] CDPK1 is involved in *Plasmodium* calcium signaling and is an appealing target due to the absence of human orthologues and the presence of a small gatekeeper residue that can be exploited for selectivity.[15] However, it's essentiality is contentious since additional targets, such as PKG and heat shock protein 90, have been identified for potent CDPK1 inhibitors.[16] Other CDPK1 inhibitors comprising an imidazopyridine scaffold are highlighted in **Figure 6.2**.[11,17,18]

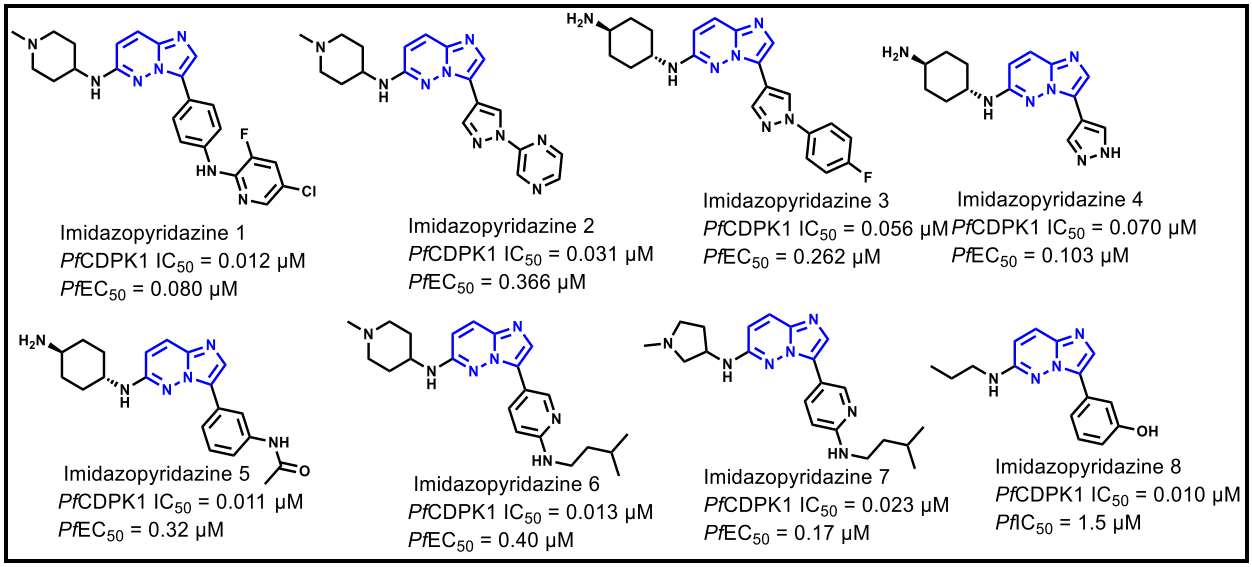

Figure 6.2: Examples of anti-plasmodium CDPK1-inhibitor imidazopyridines

Inhibition of *Pf*PKG has also been associated with the anti-plasmodium activity of imidazopyridazines. Inhibitor-resistant parasite transgenic lines and engineered strains generated by the mutation of threonine 618 to glutamine (T618Q) have been used as indispensable validation tools for *Pf*PKG inhibitors.[19] Using this approach, PKG was identified as the primary target of a series of 3,6-disubstituted imidazopyridazines displaying potent anti-plasmodium activity. Amongst these was the lead compound (**Compound A**; **Figure 6.3**), showing high potency against the recombinant *Pf*PKG (IC_{50} = 0.002 μM) and high activity against the wild-type CQ-sensitive *Pf*3D7 strain (EC_{50} = 0.012 μM), but was significantly less potent against the mutant enzyme (*Pf*PKG T618Q IC_{50} = 10.96 μM) and engineered *Pf*3D7 PKG T618Q line (IC_{50} = 0.901 μM).[16,20]

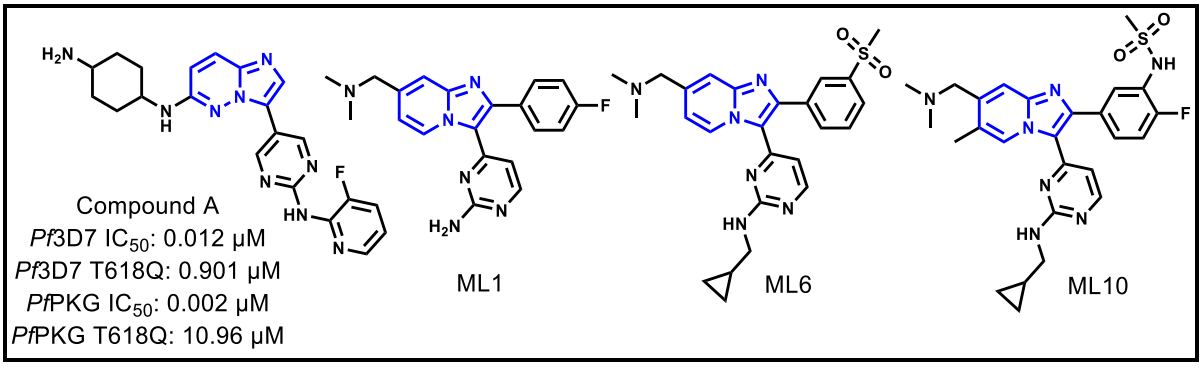

Figure 6.3: Structure of anti-plasmodium *Pf*PKG-inhibitor imidazopyridines/pyridazines

Related imidazopyridines have also been shown to inhibit *Pf*PKG. A repositioning approach initiated on a potent inhibitor of *Eimeria*, **ML1**, led to the discovery of potent *Pf*PKG inhibitors such as **ML6** and **ML10** (**Figure 6.3**).[19,21] *Eimeria* is an apicomplexan parasite that causes

coccidiosis in poultry but is genetically closely related to the *Plasmodium* parasite. *Pf*PKG was confirmed as the primary mode of action for these inhibitors based on their reduced potency against the PKG T618Q mutant enzyme and engineered 3D7 parasite strain relative to the wild-types (**Table 6.1**).[19]

Table 6.1: Potency of *Pf*PKG inhibitors in kinase and cell-based assays

	***Pf*PKG IC_{50} WT (nM)**	***Pf*PKG T618Q IC_{50} (nM)**	**IC_{50} fold shift**	***Pf*3D7 EC_{50} WT (nM)**	***Pf*3D7 T618Q EC_{50} (nM)**	**EC_{50} fold shift**
ML1	3.1	8440	2722	395	5952	15
ML6	0.13	52500	>400,000	102.3	1855	18
ML10	0.16	29,540	184,625	2.1	2430	1157

Recently, *Pf*PI4K has also been implicated as the primary MoA for some antimalarial imidazopyridazines and related imidazopyridine scaffolds. For example, the discovery of the antimalarial compound **KDU691** by scientists from Novartis from a potential hit to **KAI407** (**Figure 6.4**) and subsequent medicinal chemistry optimizations to improve PK properties demonstrated that the lead compound **KDU691** and the rest of the series acted primarily via *Pf*PI4K inhibition.[22,23]

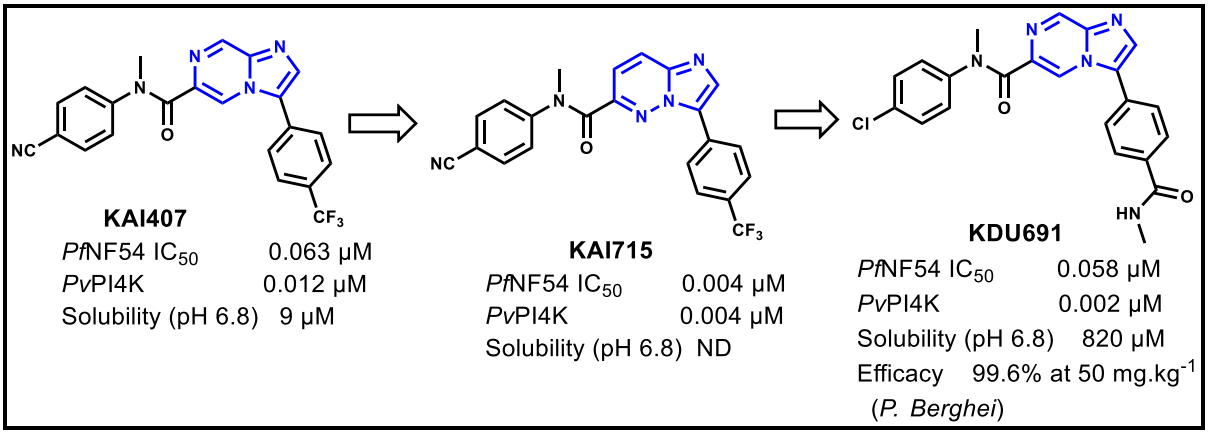

Figure 6.4: Lead optimization strategies employed in the discovery of **KDU691**

6.3 Research background and objectives

Phenotypic high-throughput screening (HTS) of a BioFocus DPI® SoftFocus Kinase library, led to the identification of a series of hit compounds containing the 3,6-diarylimidazo[1,2-*b*] pyridazine core, commonly referred to as the SFK52 series, with potent anti-plasmodium activity.[24] Generally, SoftFocus libraries contain small-drug-like molecules related to a particular gene family.[25] Based on these hits, extensive SAR exploration was carried out at

UCT to optimize ADME/PK parameters such as poor metabolic stability, solubility and efficacy. Imidazopyridazine sulfones such as **63** and **64** demonstrated exemplary *in vitro* anti-plasmodium potency and *in vivo* efficacy (> 98% at 4 × 50 mg/kg per oral, p.o.) or cure in the *P. berghei* mouse model. However, the compounds were plagued with the hERG liability and poor kinetic solubility at the physiologically relevant pH of 6.5 (**Figure 6.5**).[26]

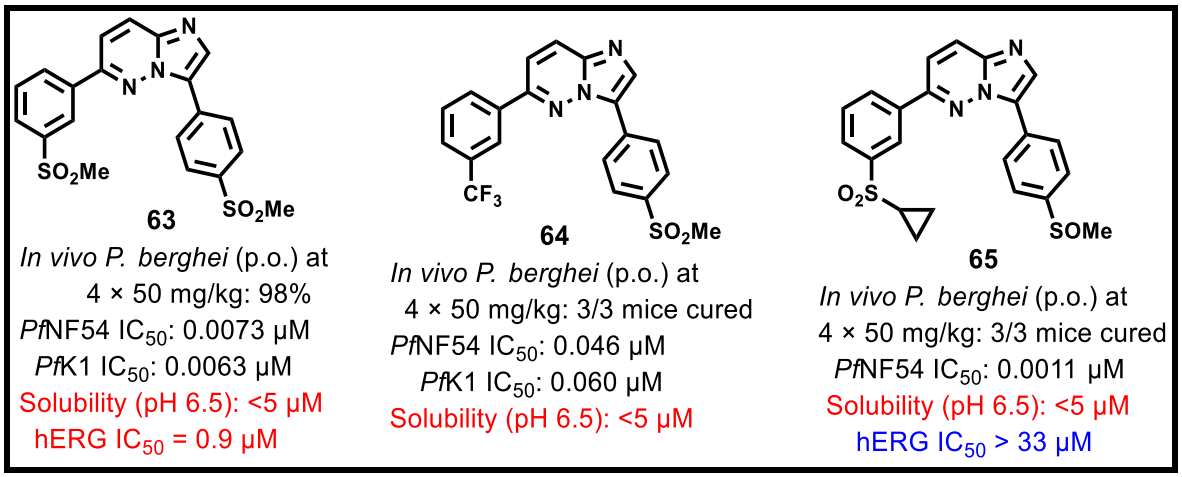

Figure 6.5: Examples of imidazopyridazines with high *in vivo* efficacy

To address these issues, SAR studies such as conversion of the sulfone to sulfoxide on either side of the core scaffold were investigated. Most sulfoxides showed reduced *in vitro* hERG inhibition, as exemplified by **65**, but this did not mitigate the cardiotoxicity risk due to the anticipated *in vivo* cytochrome P450-mediated bio-transformation to the corresponding sulfones.[27] Changes in the heterocyclic core scaffold were also investigated, leading to the identification of the sulfone imidazopyridine analogue **66** (**Figure 6.6**), which demonstrated high *in vitro* efficacy and a modest reduction in hERG inhibition (IC_{50} = 4.8 µM) but retained low solubility (< 5 µM).[24,26]

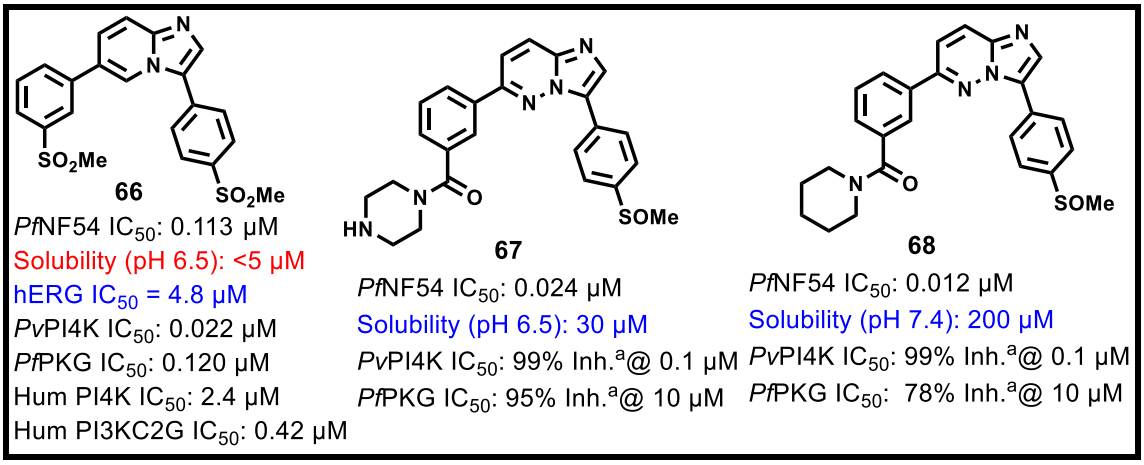

Figure 6.6: Examples of imidazopyridazines with improved solubility as dual *Plasmodium* kinase inhibitors

Introduction of aminated polar functionality on the imidazopyridazine core proved an effective strategy for disrupting lipophilic drug-hERG channel interactions.[28] Subtle changes such as the reduction of the sulfoxide on the left hand side ring also enhanced solubility while maintaining high *in vitro* anti-plasmodium potency, although the prodrug conversion remains an issue.[28] More recently, Cheuka and co-workers[29] expanded the imidazopyridazine SAR further and demonstrated that this series potently inhibit *Plasmodium* PI4K, with several compounds also showing activity against PKG. Introduction of carboxyl amination on left-hand side phenyl ring of the core scaffold delivered analogues such as **67** and **68** (**Figure 6.6**), that showed high solubility, *in vitro* efficacy, and dual potency against the *Plasmodium* kinase targets. In addition, enzymatic screening at H3D has recently identified the imidazopyridine compound **66** as a potent dual *Pv*PI4K and *Pf*PKG inhibitor (**Figure 6.6**; unpublished work).

Imidazopyridazines and closely related compounds had also been shown to inhibit essential *Plasmodium* kinases such PKG, CDPK1, and Cdc2-like kinase 1 (CLK1).[1] It is well acknowledged that achieving selectivity between *Plasmodium* and human kinases is a major challenge due to highly conserved kinase ATP-binding.[30] However, the imidazopyridine compound **66** encouragingly possesses modest parasitic selectivity over human phosphatidylinositol 4-phosphate β (PI4KIIIβ) and phosphatidylinositol 4-phosphate 3-kinase C2 domain-containing subunit γ (PI3KC2G) kinases (SI, *hu*PI4KIIIβ/*Pf*PI4KIIIβ > 100 and huPI3Kγ/*Pf*PI3Kγ = 19, respectively; **Figure 6.6**).[31]

Drugs with multi-target activity on the parasite life cycle and of low propensity for resistance are highly desirable, since they are capable of treatment and prevention of transmission and relapse, as set in TCPs.[32,33] Physicochemical properties such as high aqueous solubility also remain part of the crucial requirements that must be met for a drug to achieve optimal therapeutic efficacy.[34-35] In this regard, and based on their appealing anti-plasmodium and kinase selectivity profiles, the objective of this part of the study was to design and synthesize dual *Plasmodium* PI4K/PKG inhibitors with potentially improved solubility, and reduced hERG activity based on the imidazo[1,2-*a*]pyridine core (**Figure 6.7**).

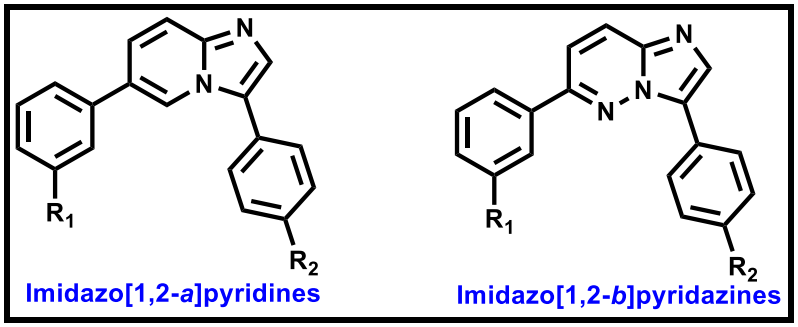

Figure 6.7: General structure of 3,6 -diaryl imidazo[1,2-*a*]pyridine and imidazo[1,2-*b*] pyridazine (SFK52) scaffolds

6.4 Design and synthesis of imidazo [1,2-*a*]pyridines

6.4.1 Design of imidazo [1,2-*a*]pyridine analogues through molecular docking studies

Molecular docking studies on the 3,6-diaryl-imidazopyridazine (SFK52) series into both the *Pf*PI4K homology model and *Pf*PKG crystal structure (**5F0A**) resulted in a favorable docking pose, with interactions between the core and the hinge binding region of the ATP-binding site. For simplicity, the structures and docking results of one imidazopyridazine (**69**) and the matched imidazopyridine (**72**; **Figure 6.8**) will be employed to highlight the rationale employed in the design of compounds for synthesis.

Figure 6.8: Structure of the imidazopyridazine compound (**69**) and the related imidazopyridine

The docking experiments highlighted the importance of the sulfone or sulfinyl in the interaction with various amino acids residues, as exemplified by **69** with the catalytic Lys 570 of the crystal structure (**Figure 6.9**). The PKG docking studies predicted a key interaction between N-1 of the imidazopyridazines core and backbone carbonyl of the conserved valine residue within the hinge region (Val 621 in *Pv*PKG; **Figure 6.9A**) as the most important for binding in the hinge region. This is analogous to Val 614 in the *Pv*PKG structure (**5EZR**) reported by Cheuka and co-workers.[29] The importance of the sulfone or sulfinyl in the interaction with various amino acids residues, such as the sulfone of **69** with the catalytic Lys 570 of the crystal structure was

also highlighted (**Figure 6.9B**). This is besides additional H-bond interactions of the carbonyl and the hydroxyl group of the ligand with Arg 549 and the conserved Asp 682 in the back-pocket of the *Pv*PKG crystal structure.

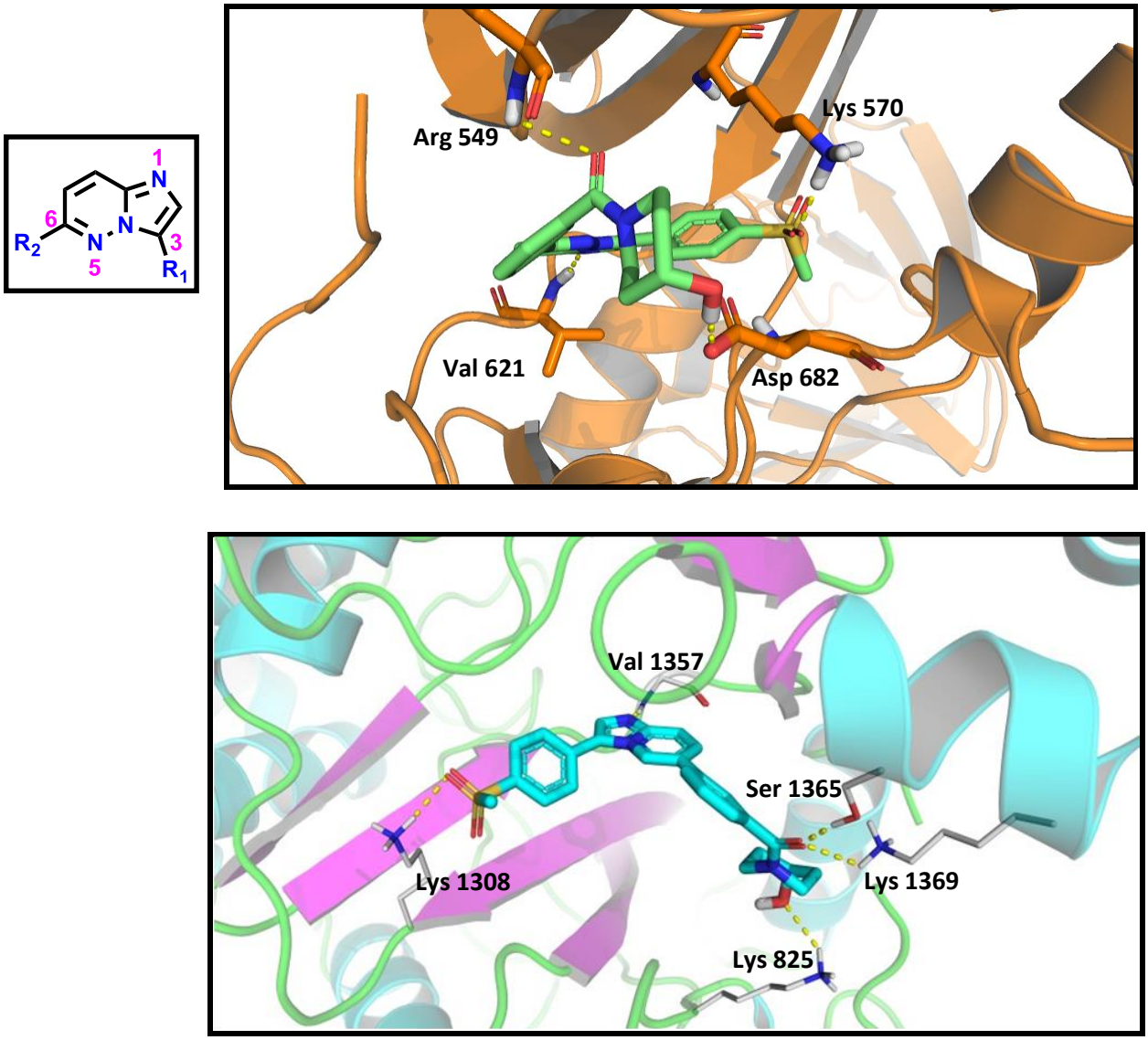

Figure 6.9: (A), 3,6-diaryl-imidazopyridazine (SFK52) scaffold; (B), 3-dimensional representation of **69** docked into the crystal structure of *Pv*PKG (**5F0A**); (C), 3-D homology model docking of the related sulfone imidazopyridine analogue with the *Pf*PI4K homology model.

Docking studies using the *Pf*PI4K homology model[31] predicted similar interactions to those predicted for PKG, as exemplified by the imidazopyridazine analogue **72** (**Figure 6.8C**), with plausible H-bond interaction between N-1 with Val 1357 and the sulfinyl group and the catalytic Lys 1308. A similar docking pose was recently reported by Fienberg *et al*.[31] These docking studies suggested that deletion of the nitrogen in position 5 of the core scaffold (N-5; **Figure 6.9A**) would not interfere with binding to *Pf*PKG and *Pf*PI4K. Additionally, this deletion would be advantageous in potentially de-tuning hERG liability and reducing TPSA as exemplified by **72** and **73** in comparison to the corresponding imidazopyridazine compounds **69** and **70** (**Table 6.2**).

Veber's rule sets a threshold of 140Å^2 for compounds intended for oral administration, with lower values indicative of the propensity to increase permeation and oral bioavailability.[36] Pharmacologically relevant compounds also show significant correlations between high TPSA values and adverse toxicological *in vivo* outcomes.[37] In addition, comparative energy docking scores of selected imidazopyridines was observed in comparison to the corresponding SFK52 compounds, suggesting retention of the interaction with *Pv*PI4K and *Pf*PKG (**Table 6.2**). Swapping the position of the methylsulfonylphenyl group on the LHS of the scaffold with the phenyl carboxamide was detrimental to *Pf*PKG potency, as exemplified by **71** (inhibition of 30% at 10 μM; **Table 6.2**).

Based on the molecular docking studies and enzymatic data from the SFK52 series, this study aimed to explore a series of dual PI4K/PKG inhibitors based on the imidazopyridine core and employ strategies to mitigate poor solubility and detune hERG binding. Accordingly, introduction of water-solubilizing groups such as the sulfinylmethyl and carboxamides was expected to increase the strength of hydrogen-bonding interactions between the resultant compounds and aqueous media, thus improving DMPK properties while retaining potency against the targeted *Plasmodium* kinases.

Table 6.2: TPSA, enzymatic and molecular docking parameters for selected SFK52 and imidazopyridine compounds

Compound	Code	TPSA[a] (Å^2)	*Pv*PI4K		*Pf*PKG	
			IC_{50} (µM)	MMGBSA[b]	IC_{50} (µM)	MMGBSA[b]
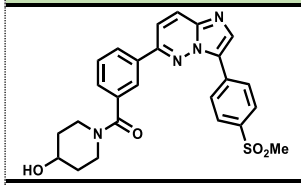	**69**	104.9	0.002	ND	0.183	-82.21
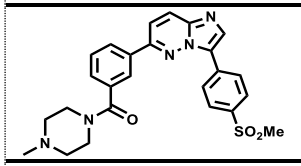	**70**	87.9	0.001	ND	0.292	-67.65
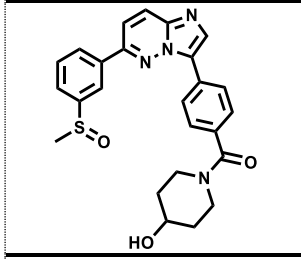	**71**	87.8	96 % inh. @ 1 µM[c]	ND	31 % inh. @ 10 µM[c]	ND
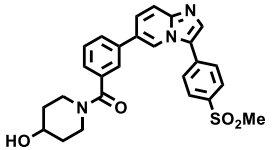	**72**	92.0	-	-59.10	-	-63.48
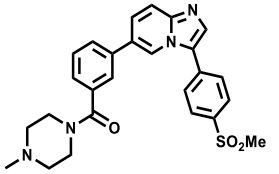	**73**	75.0	-	-	-	-77.25

[a] TPSA, topological polar surface area in Å^2 and calculated using StarDrop™; [b] MMGBSA, calculated molecular mechanics/generalized Born surface area energy change in kcal/mol; [c] Enzymatic data previously reported by Cheuka *et al*.[38]

Furthermore, introduction of the solubility-enhanced aliphatic carboxamides was expected to significantly disrupt π-stacking and hydrophobic interactions between aromatic residues lining the cavity of the hERG channel, hereby potentially mitigating cardiotoxic risk.[27] Incorporation of the nitrogen α to the carbonyl group would further reduce the basicity of potentially ionizable centers at physiological pH, thus lowering the pKa of the molecule, destabilizing π-cation interactions, and thereby reducing affinity for the channel. Finally, shielding of the nitrogen centers may further destabilize putative interactions with the channel. In this study, these strategies were deemed worthy of pursuit to potentially reduce hERG binding affinity.[39]

It was also deemed desirable to investigate both the sulfone and sulfoxide moiety on the RHS of the scaffold in anticipation of the CYP-mediated *in vivo* metabolism where oxidation of sulfones would occur. CYP-450 enzymes reside primarily in liver cells and are responsible for > 90% of phase I metabolism of drugs on the market.[40] Investigating sulfoxide/sulfone in tandem would assist in interrogating primary ADME data in preparation for *in vivo* efficacy studies. Consequently, a series of imidazopyridine compounds hypothesized to address these issues were proposed for synthesis (**Figure 6.10**).

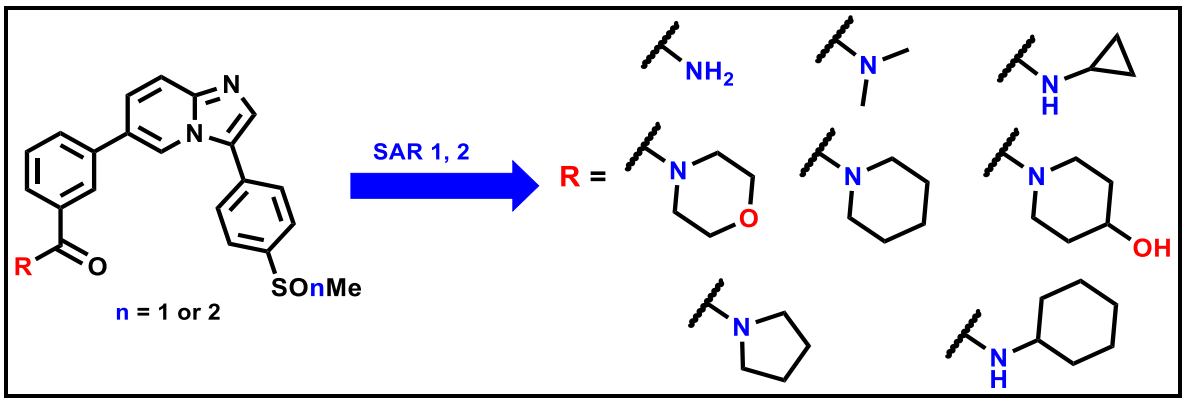

Figure 6.10: Target SAR exploration on the imidazopyridine scaffold

6.4.2 Synthesis, selected mechanisms and spectroscopy of imidazo[1,2-*a*]pyridine analogues

The synthetic methods used to produce target imidazo[1,2-*a*]pyridine compounds were similar to those used for MLN0128 compounds previously described, and related mechanistic steps are therefore not repeated. Analogues were synthesized using the generic synthetic approach outlined in **Scheme 6.1**. The initial step involved regioselective electrophilic aromatic iodination of commercially available 6-bromoimidazo[1,2-*a*]pyridine (**74**) in *N*-iodosuccinimide (NIS), which afforded the iodinated intermediate **75**.

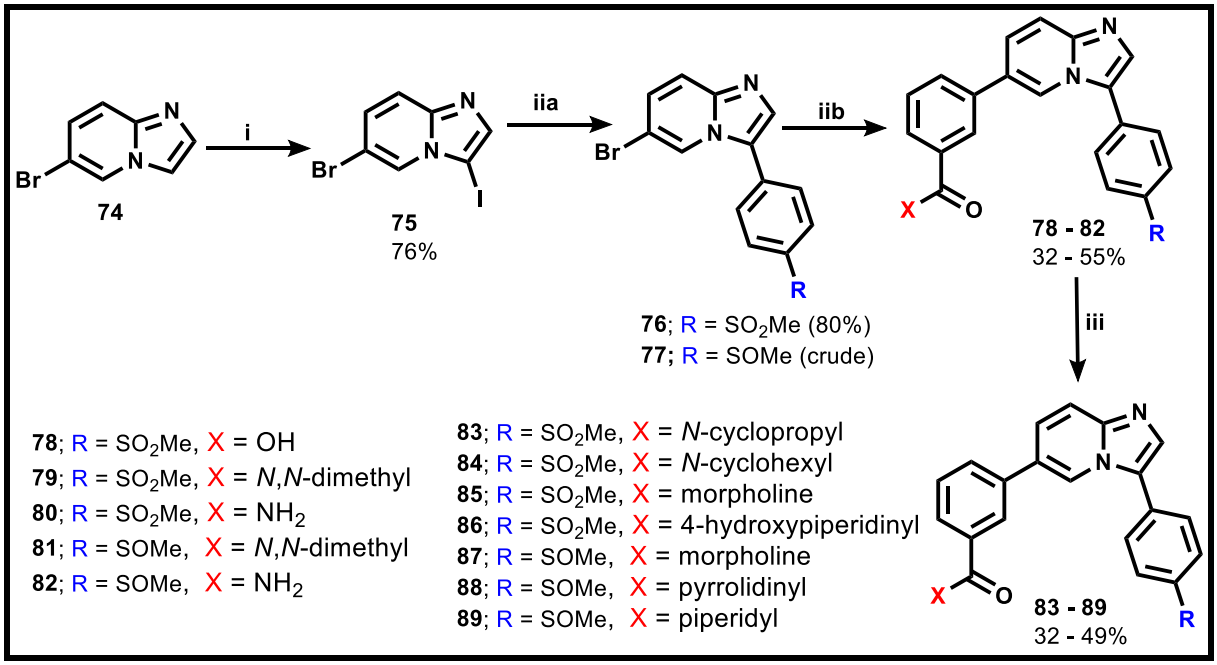

Scheme 6.1: Synthetic protocol for imidazopyridine analogues

Reagents and reaction conditions; (i) NIS, DMF, 20°C, 15 h; (ii) (a) and (b) appropriate boronic acid, $Pd(PPh_3)_2Cl_2$, K_2CO_3, dioxane/ H_2O (3:1), 90°C, 15 h; (iii) appropriate amine, HATU, DIPEA, DMF, 50°C, 15 h.

Next, the key intermediate **75** (**Scheme 6.1**) was subjected to a series of Suzuki-Miyaura cross coupling reaction to yield mono-halogenated sulfinyl or sulfonyl intermediates such as **76** then the carboxylic acid intermediate **78,** and several target compounds such as the demethylated analogue **79** and free amide **80**. In the final step, the carboxylic acid derivative was subjected to an amide cross coupling reaction to furnish other target molecules.

The rapid formation of the di-halogenated intermediate **75** (precipitated immediately upon addition of NIS and was then stirred overnight) proceeded via the known NIS-mediated electrophilic aromatic iodination and was postulated to occur as previously described. The π electrons of the imidazo ring system act as the nucleophile attacking the electrophilic iodine in NIS to displace the good leaving succinimide anion whose stability is ensured by resonance.[41] Eventually, the succinimide anion deprotonates the heteroarenium ion intermediate to form the expected molecule in decent yield (76%) and succinimide as a by-product.

At first glance, one may have anticipated that this reaction would yield isomeric mixtures. However, the fast rate and regioselectivity of this reaction can be explained by the large number of resonance structures of the positively charged heteroarenium intermediate **6.2a** favouring iodination at C-3 relative to C2 (**6.2e**–**f**) of the imidazo ring (**Scheme 6.2**). Iodination in the

pyridine side of the molecule was less feasible as the pyrrole core has a higher electron density and consequently reacted favourably as a stronger nucleophile.[41]

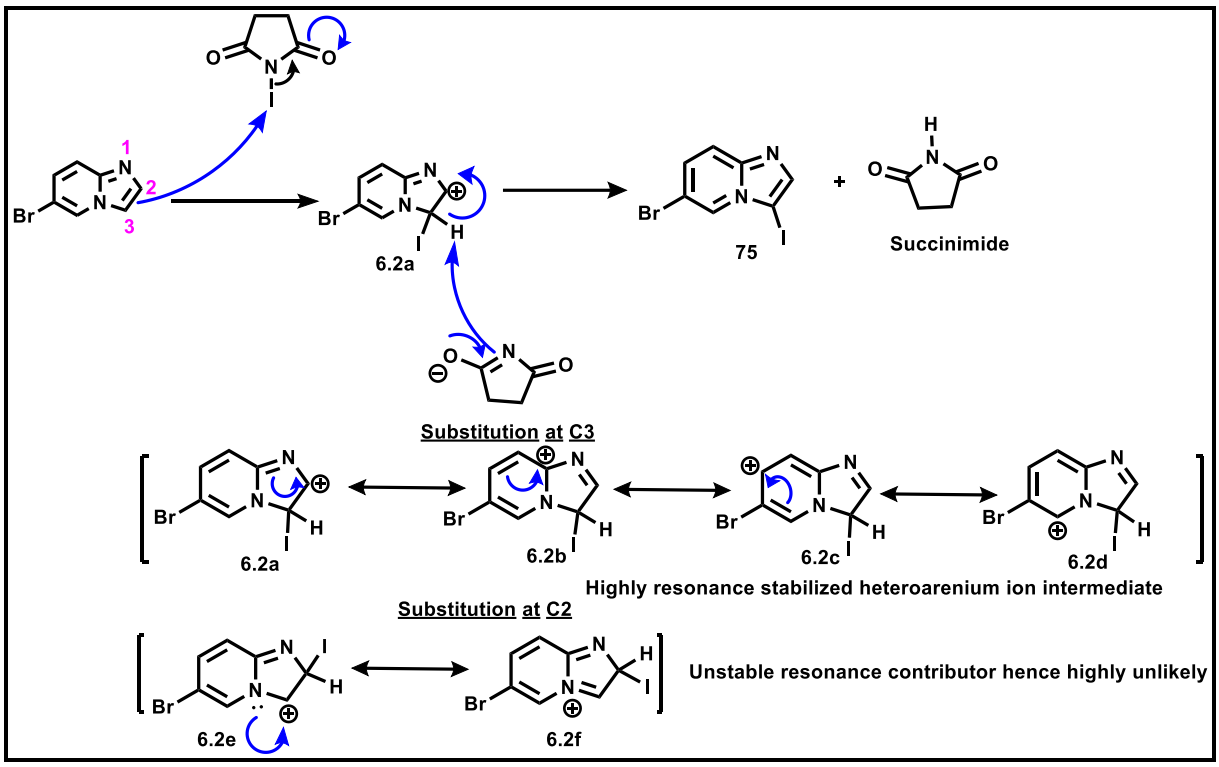

Scheme 6.2: Postulated mechanistic steps for selective electrophilic aromatic iodination

One dimensional ^{1}H-NMR spectroscopy confirmed the successful synthesis of **75** (**Figure 6.11**) with the mutually coupling H-5 and H-8 proton signals appearing as two pairs of well resolved doublets at chemical shifts δ_H 8.30 (J = 1.8 Hz) and 7.54 ppm (J = 9.6 Hz), respectively. The signal resonating at 7.32 ppm as doublets of doublet was assigned to H^7 while the H-2 peak is observed slightly down-field in the aromatic region as a singlet at δ_H 7.72 ppm. As anticipated, all the proton signals integrated for a single proton each. Additionally, successful synthesis of this intermediate was further confirmed via HPLC-MS (ESI$^+$/APCI$^+$: m/z [M + H]$^+$ = 322.8, calculated exact mass = 321.8603, with retention time (t_R) of 2.36 min) (spectrum not shown).

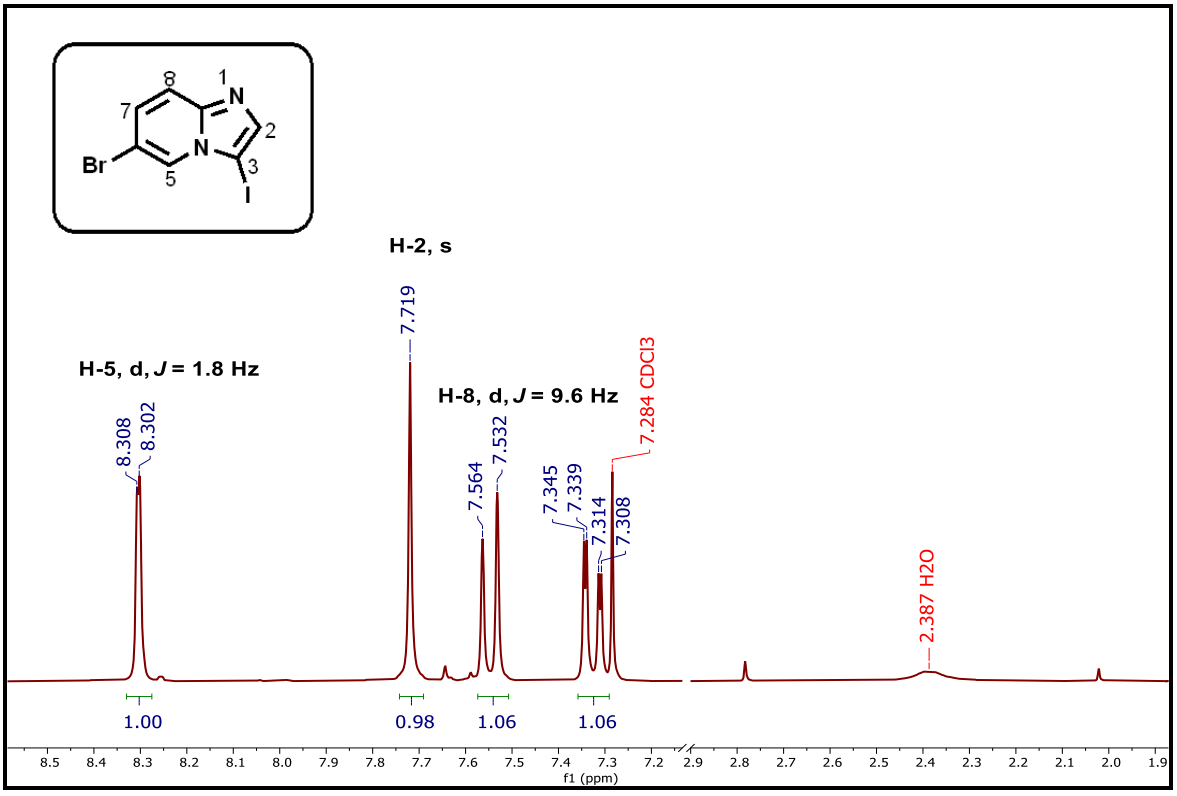

Figure 6.11: ^{1}H-NMR spectrum of the di-halogenated intermediate **20**

The next step involved a Suzuki-Miyaura cross coupling reaction of the crucial di-halogenated precursor **75** with 4-(methylsulfonyl)- or (sulfinyl)phenyl boronic acid, to produce the necessary compounds such as the sulfonyl intermediate **76**. No purification was undertaken for the sulfinyl counterpart **77**, which was used in its crude form. Nonetheless, the reaction mechanism proceeds as previously described, with high specificity to the C–I bond, as no iodo-substituted derivative was detected via LC-MS in both reactions. However, isomeric mixtures would be expected to form in the presence of excess boronic acid, but 1.3 equivalents were employed in this case.

As a representative, characterization of **76** via HPLC-MS revealed a characteristic quasi-molecular ion peak $[M+H]^+$ at *m/z* = 350.97 (calculated exact mass = 350.9725). The successful incorporation of the 4-methylsulfonylphenyl moiety was also evident in the ^{1}H-NMR spectrum (**Figure 6.12**) with an up-field singlet peak integrating for three protons (δ_H = 3.21 ppm) corresponding to the relatively shielded and uncoupled methyl of the sulfonyl moiety. H-9 and H-10 proton signals, were observed as two sets of doublets, integrating for two protons each, in the downfield aromatic region (δ_H 8.14 and 8.02 ppm, respectively) of the NMR spectrum (**Figure 6.12**).

Interestingly, all the proton signals for H-5, H-8, and H-7, appeared as sets of doublets of doublet resonating at δ_H 8.82 (dd, J = 2.0 and 0.8 Hz), 7.64 (dd, J = 9.6 and 0.8 Hz), and 7.46 ppm (dd, J = 9.6 and 2.0 Hz), respectively (**Figure 6.12**). The small, unusual J value of 0.8 Hz for H-5 and H-8 was ascribed to mutual *para* coupling between the three protons. As expected, the signal for H-2 corresponded to a singlet integrating for one proton in the aromatic region of the NMR spectrum.

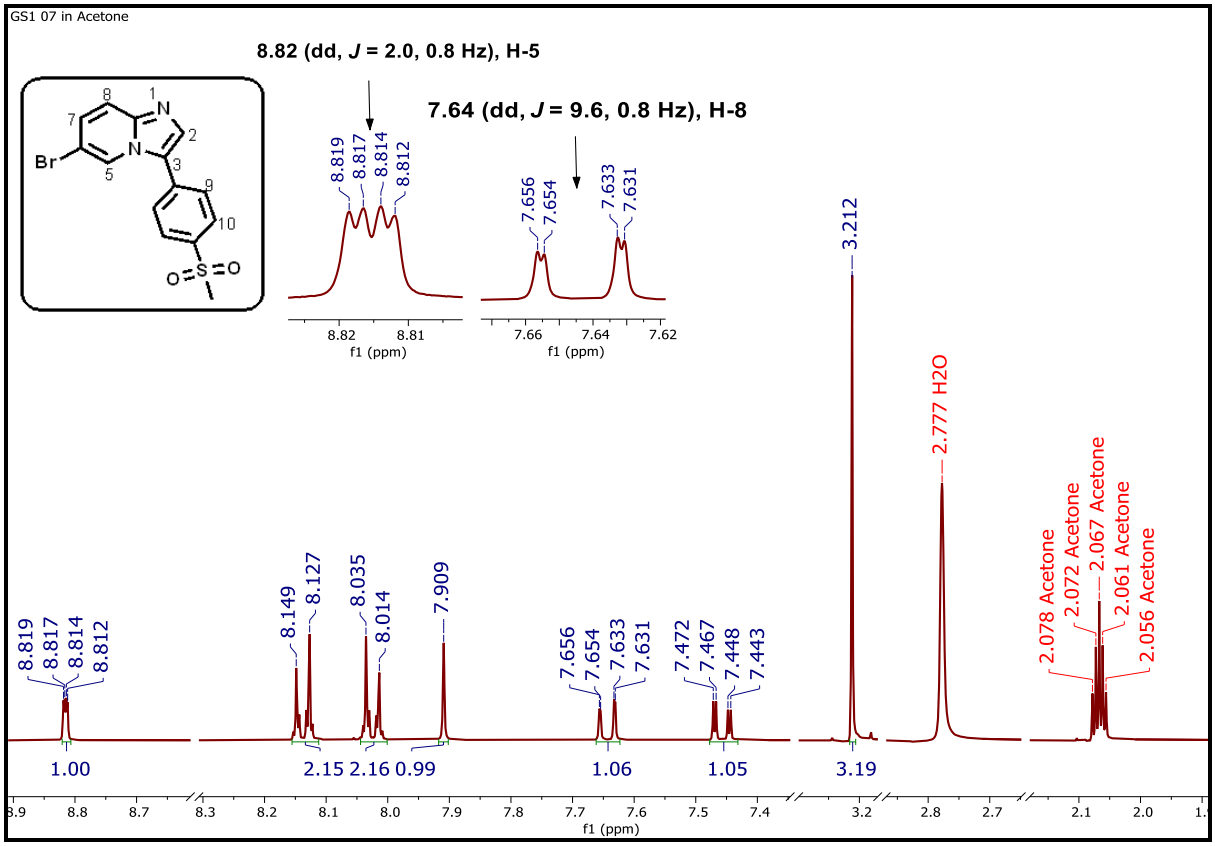

Figure 6.12: Expanded ^{1}H-NMR spectrum of intermediate **76** in acetone-d_6

Subsequent Suzuki-Miyaura cross coupling of intermediate **76** with various arylboronic acids, yielded the carboxylic acid derivative **78,** several sulfoxides, and some target sulfones in moderate yields (32–55%). Similarly, all the target molecules obtained in this step were spectroscopically characterized via ^{1}H-, ^{13}C-NMR, and HPLC-MS. As anticipated, the ^{1}H NMR spectrum of the carboxylic acid intermediate (**78**) (**Figure 6.13**), showed four additional well-resolved mutually coupled aromatic signals at δ_H 7.96 (dt, J = 7.8 and 1.8 Hz), 7.64 (t, J = 7.8 Hz), 8.16 (dt, J = 7.8 and 1.8 Hz), and 8.37 ppm (t, J = 1.8 Hz) each integrating for a single proton, corresponding to H-5, H-6, H-7 and H-8 of the newly introduced phenyl carboxylic acid moiety.

This is in addition to the splitting pattern of the protons in the imidazopyridine core and the phenyl sulfone moiety which resonate in a manner similar to that of the precursor compound **76** *i.e.*, δ_H 8.21 (s, 1H, H-1), 8.28 (d, *J* = 9.0 Hz, 1H, H-2), 8.13 (dd, *J* = 9.0 and 1.8 Hz, 1H, H-3), 8.89 (broad s, 1H, H-4), 8.19 (d, *J* = 8.4 Hz, 2H, H-9), and 8.03 ppm (d, *J* = 8.4 Hz, 2H, H-10), all in the aromatic region and 3.20 ppm (s, 3H, SO_2Me) in the up-field region of the NMR spectrum.

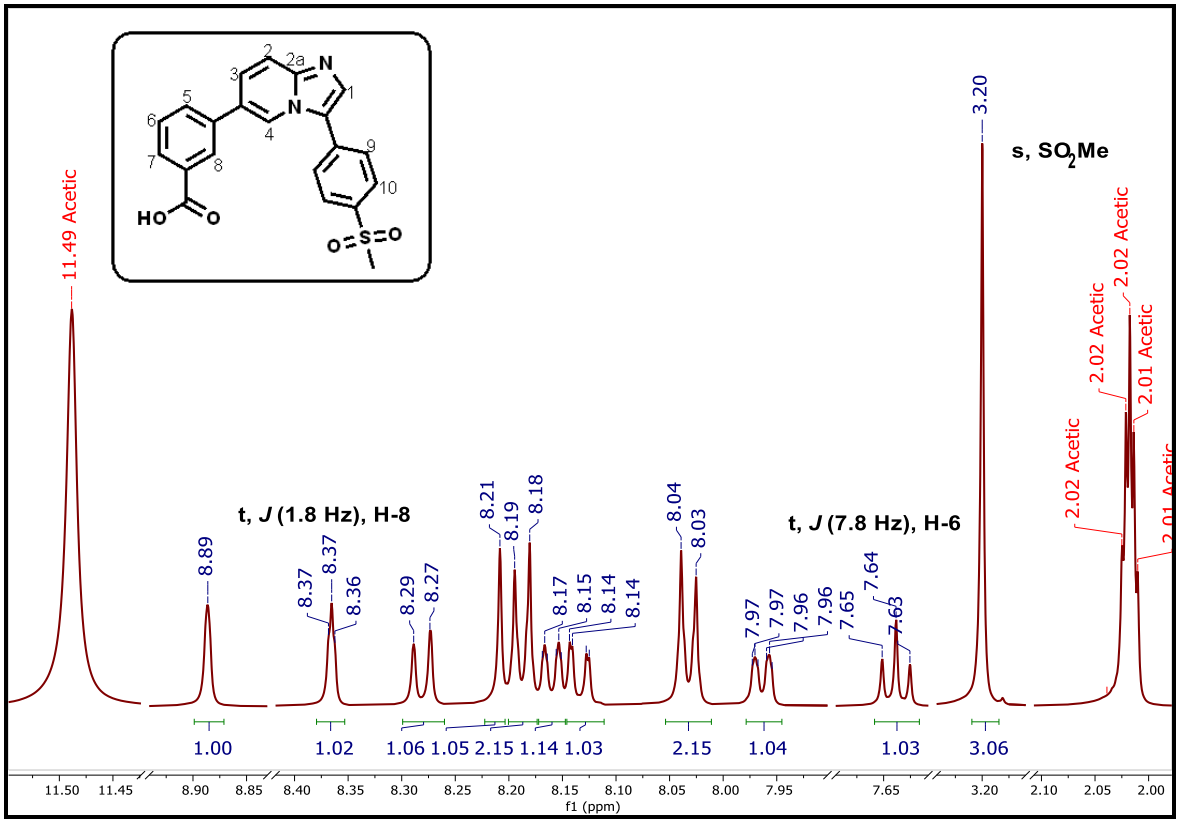

Figure 6.13: ^{1}H-NMR spectrum of the carboxylic acid intermediate **78**

The last step towards the realization of water-solubilizing carboxamides involved derivatization of the crucial carboxylic acid intermediate **78**, through a hexafluorophosphate azabenzotriazole tetramethyl uranium- (HATU) mediated amide coupling reaction in di-isopropyl ethylamine (DIPEA) as a base. In practice, DIPEA and other sterically hindered bases is preferentially used in this reaction due to poor nucleophilicity hence limited competition with the coupling amine required in the reaction.[42] This mechanism is well-known,[43] and hence will not be included in the discussion. Overall, the reaction occurred in moderate yields in the range of 32–49%.

A cassette of 7 analogues was eventually synthesized using this reaction. The characterization of the *N* - cyclopropyl analogue **83** is used here as a representative for the series of compounds.

As expected, the ^{1}H-NMR of this compound (**Figure 6.14**) displays the splitting pattern of the protons in the imidazopyridine scaffold (H-1, H-2, H-3, and H-4) and the embodied phenyl sulfone (H-9, H-10, and SO_2Me) moiety as in analogue **78** (**Figure 6.13**), earlier described.

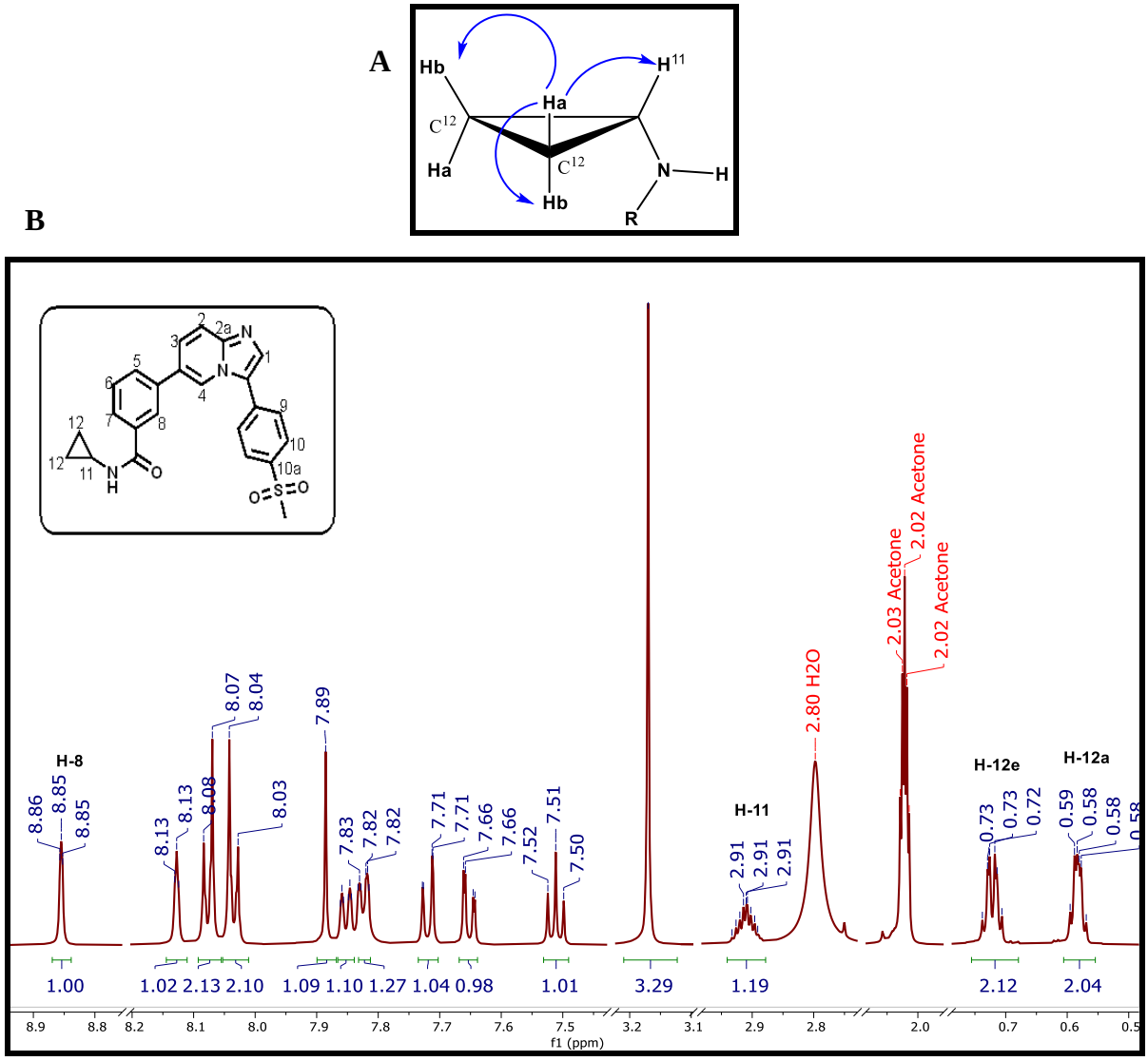

Figure 6.14: A, Coupling interactions of Ha with protons in geminal and adjacent carbons; B, ^{1}H-NMR spectrum of the final target **83**

The most diagnostic peaks in the spectra (**Figure 6.14**) were identified up-field in the aliphatic region as a distinct doublet of pentet (quintet, dp) at δ_H 2.91 ppm (J = 10.0 and 3.3 Hz) integrating for a single proton and an unclearly resolved multiplet at 0.61–0.52 ppm for 2H. In addition, a well-resolved triplet of doublets (td) was observed at 0.72 ppm (J = 7.0 and 4.9 Hz) integrating for two protons.

This splitting pattern originates from differences in the chemical environment created by a 3-D puckered conformation of the cyclopropyl moiety, making the protons non-equivalent. Proton H-11 was thus expected to couple with two sets of axial and equatorial protons in the adjacent carbons appearing as a dp peak with a large vicinal J_{HaHa} value of 10.0 Hz and a smaller J_{HaHe} value of 3.3 Hz. Furthermore, this peak appears slightly down-field compared to the other cyclopropyl protons (0.58–0.73 ppm) because of the de-shielding effects of the adjacent nitrogen atom. Likewise, splitting between vicinal axial, equatorial and geminal protons in C-12 (**Figure 6.14**) results in the observed dt and multiplet (m) patterns for protons attached to C-12 in the ^{1}H-NMR spectrum.

The accompanying ^{13}C-NMR spectrum for the representative compound **83** in deuterated acetone is shown in **Figure 6.15**. As anticipated, three signals were identified in the aliphatic region at δ_C 43.43, 22.97, and 22.84 ppm which were assigned to the sulfone methyl and the low-field methylene carbons of the *N* - cyclopropyl group. The carbon signal appearing at δ_C 22.97 ppm has higher intensity and was arbitrarily assigned to the two aliphatic carbons C-12 of the *N* - cyclopropyl moiety which are likely to resonate in the same chemical environment and are hence equivalent. Also notable are signals of higher intensity appearing in the aromatic region at δ_C 128.31 and 127.89 ppm, which were assigned with the assistance of HSQC experiment to the chemically equivalent phenyl carbons C-9 and C-10 with two carbons for each.

Generally, carbons attached to protons are more intense and with assistance of the 2D experiments, signals such as those resonating at δ_C 128.58, 129.00, 126.56, and 134.91 ppm were respectively assigned to C-5, C-6, C-7, and C-1. The relatively weak carbon signals appearing in the aromatic region were attributed to the quaternary carbons of the compound. For example, the relatively down-field peaks at δ_C 146.22 and 140.21 ppm were assigned to C-2a and C-10a carbons (**Figure 6.15**), respectively. In addition, a relatively down-field peak was observed at δ_C 167.25 ppm, highlighting evidence of the characteristic carbonyl signal which appears in this region (165–180 ppm). In total, 21 distinct carbon signals were observed accounting for all the carbons in this compound.

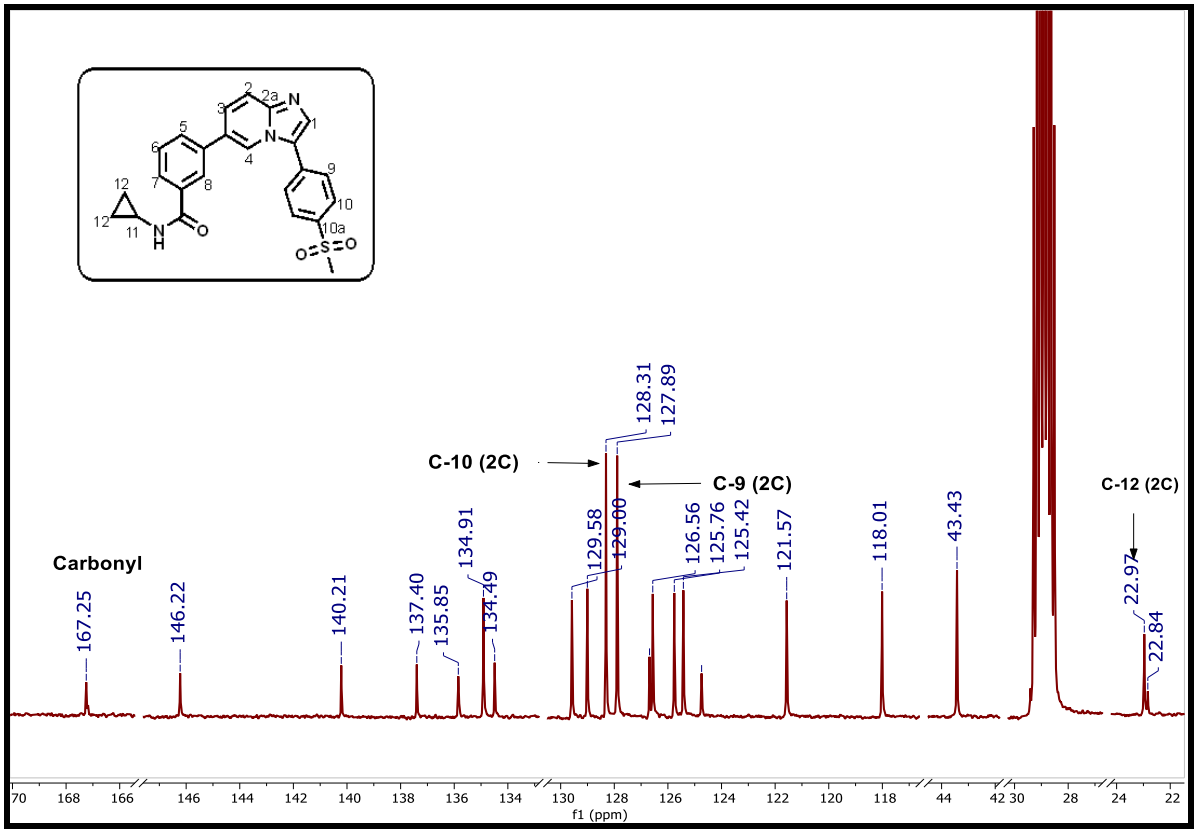

Figure 6.15: ^{13}C-NMR spectrum of the representative final target **83**

Further diagnostic investigations via by HPLC-MS analysis also revealed successful acquisition of this compound with a pseudo-molecular ion $[M+H]^+$ *m/z* peak observed at 432.1 (calculated exact mass = 431.1304 g.mol^{-1}). The peak associated with this compound on the reversed-phase column eluted at a retention time (t_R) of 2.37 min (**Figure 6.16**). In addition, assessment of contaminants highlighted a purity of 98.6% under a UV absorption wavelength of 280 nM.

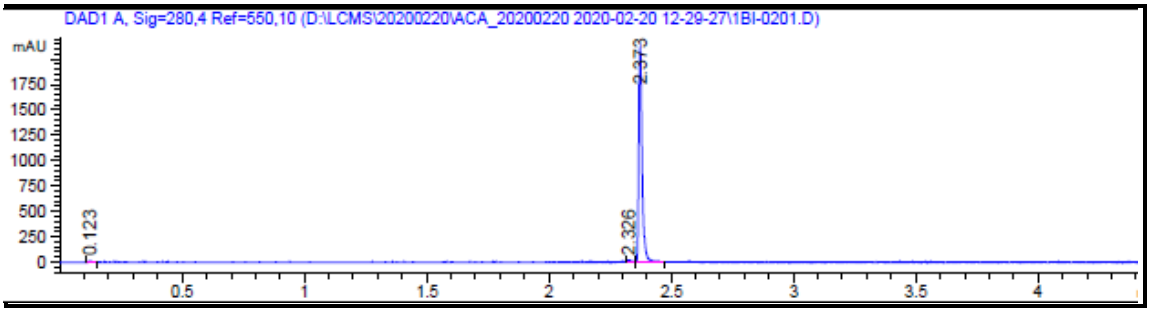

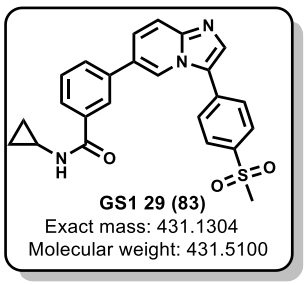

Signal 1: DAD1 A, Sig=280,4 Ref=550,10

Peak #	RetTime [min]	Type	Width [min]	Area [mAU*s]	Height [mAU]	Area %
1	0.123	BBA	0.0138	8.97737	9.72182	0.4522
2	2.326	VV	0.0168	17.81999	15.64312	0.8976
3	2.373	VB	0.0139	1958.43689	2100.12427	98.6502

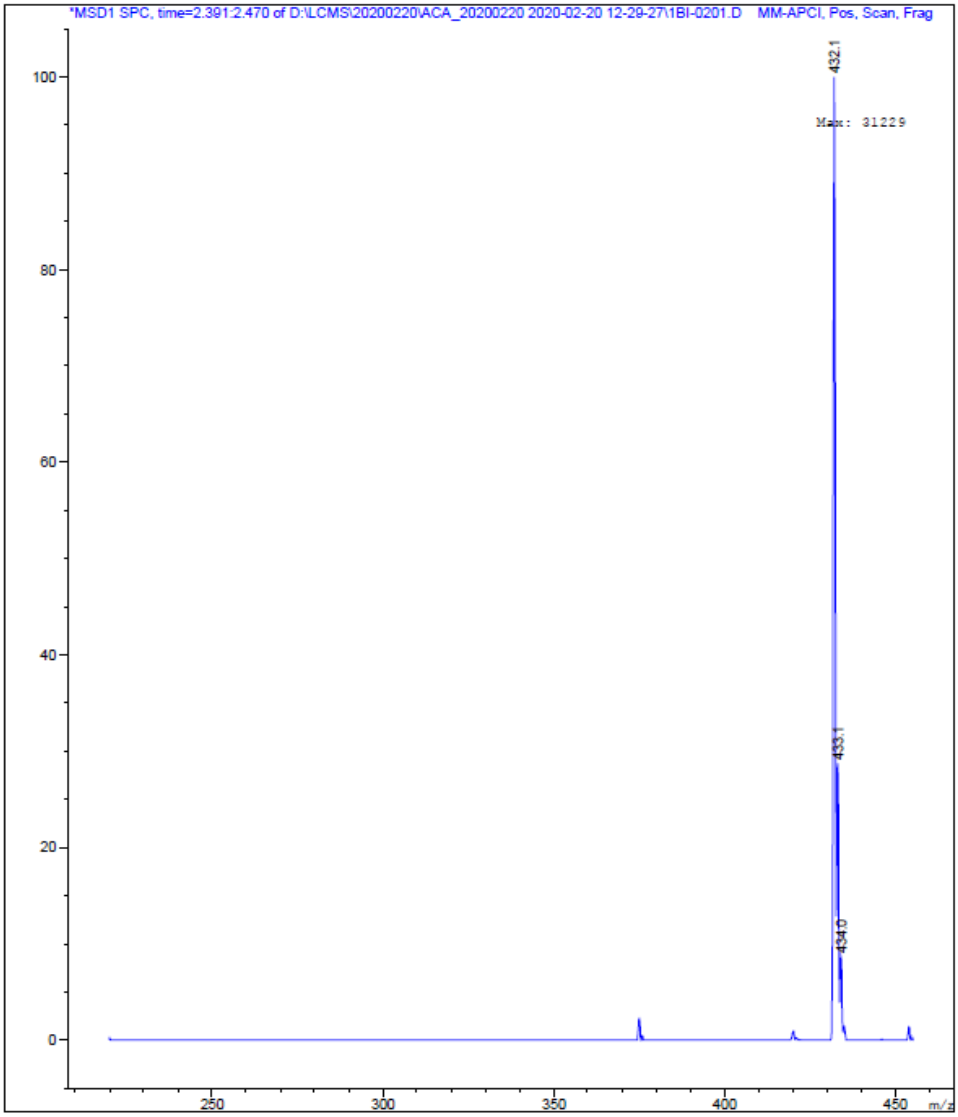

Figure 6.16: HPLC chromatogram and atmospheric pressure chemical ionization ($APCI^+$) mass spectrum of **83**

In total, 12 analogues were synthesized in this series, and characterized using 1D and 2D NMR spectroscopy. Purity was assessed via HPLC coupled with MS. Ultimately, all the expected carbons and protons for the synthesized compounds were accounted for. The comprehensive characterization details of all the compounds synthesized are summarized in the Experimental section (Chapter 10) whereas the biological evaluation of all the synthesized analogues is discussed in Chapter 7 of this thesis.

6.5 Chapter summary

In summary, previous research work undertaken on imidazopyridines and imidazopyridazines as antimalarial series has been described, providing a framework for this study. A rational approach to the design and medicinal chemistry strategy employed in this work has been provided. Furthermore, the synthesis, spectroscopic characterization, and reaction mechanisms of key intermediates and selected target compounds generated have been described. Specific details of the synthesis and characterization of each compound reported in this study is provided in the Experimental Chapter. In the next Chapter the biological properties of these compounds will be described.

References

1. Peterson E.; Boezio, A.; Andrews, P.; Boezio, C.; Bush, T.; Cheng, A.; Choquette, D.; Coats, J.; Colletti, A.; Copeland, K.; DuPont, M.; Graceffa, R.; Grubinska, B.; Kim, J. L.; Lewis, R.; Liu, J.; Mullady, E.; Potashman, M.; Romero, K.; Shaffer, P.; Stanton, M.; Stellwagen, J.; Teffera, Y.; Yi, S.; Cai, T.; La, D. Discovery and optimization of potent and selective imidazopyridine and imidazopyridazine mTOR inhibitors. *Bioorganic Med. Chem. Lett*. **2012**; 22 (15): 4967 - 4974. doi:10.1016/j.bmcl.2012.06.033.

2. WO2012136776-PAMPH-20121011-2419 Imidazopyridines as AKT Inhibitors.pdf. **2012**: 1 - 199.

3. Merritt, C.; Silva, L.; Tanner, A.; Stuart, K.; Pollastri, M. Kinases as druggable targets in trypanosomatid protozoan parasites. *Chem. Rev*. **2014**; 114 (22): 11280 - 11304. doi:10.1021/cr500197d.

4. Tan, F.; Putoczki, T.; Stylli, S. and Luwor, R. Ponatinib: A novel multi-tyrosine kinase inhibitor against human malignancies. *Onco. Targets Ther*. **2019**; 12: 635 - 645. doi:10.2147/OTT.S189391.

5. Roskoski, R. Properties of FDA-approved small molecule protein kinase inhibitors: A 2020 update. *Pharmacol Res*. **2020**; 152 : 1 - 15. doi:10.1016/j.phrs.2019.104609.

6. Sawaguchi, Y.; Yamazaki, R.; Nishiyama, Y.; Mae, M.; Abe, A.; Nishiyama, H.; Nishisaka, F.; Ibuki, T.; Sasai, T.; Matsuzaki, T. Novel pan-pim kinase inhibitors with imidazopyridazine and thiazolidinedione structure exert potent antitumor activities. *Front. Pharmacol*. **2021**; 12: 1 - 12. doi:10.3389/fphar.2021.672536.

7. Spyvee, M.; Hawkins, L. and Ishizaka, S. *Chapter 12 - Modulators of Toll-Like Receptor (TLR) Signaling*. Vol. 45. Elsevier Inc.; **2010**. doi:10.1016/S0065-7743(10)45012-5.

8. Jenkinson, S.; Thomson, M.; McCoy, D.; Edelstein, M.; Danehower, S.; Lawrence, W.; Wheelan, P.; Spaltenstein, A.; Gudmundsson, K. Blockade of X4-tropic HIV-1 cellular entry by GSK812397, a potent noncompetitive CXCR4 receptor antagonist. *Antimicrob. Agents Chemother*. **2010**; 54 (2): 817 - 824. doi:10.1128/AAC.01293-09.

9. Dymin, L. Imidazopyridines as a source of biological activity and their pharmacological potentials - Infrared and Raman spectroscopic evidence of their content in

pharmaceuticals and plant materials. *Bioorg. Med. Chem*. **2015**; 23: 6087 - 6099. doi:10.1016/j.bmc.2015.07.045.

10. Doerig, C.; Billker, O.; Haystead, T.; Sharma, P.; Tobin, A.; Waters, N. Protein kinases of malaria parasites : an update. *Trends in Parasitology* **2008**; 24 (12): 570 - 577. doi:10.1016/j.pt.2008.08.007.

11. Chapman T.; Osborne, S.; Bouloc, N.; Large, J.; Wallace, C.; Birchall, K.; Ansell, K. H.; Jones, H.; Taylor, D.; Clough, B.; Green, J.; Holder, A. Substituted imidazopyridazines are potent and selective inhibitors of *Plasmodium falciparum* calcium-dependent protein kinase 1 (*Pf*CDPK1). *Bioorg. Med. Chem. Lett*. **2013**; 23: 3064 - 3069. doi:10.1016/j.bmcl.2013.03.017.

12. Moolman, C.; van der Sluis, R.; Beteck, R. and Legoabe, L. An update on development of small-molecule *Plasmodial* kinase inhibitors. *Molecules*. **2020**; 25 (21): 1 - 45. doi:10.3390/molecules25215182.

13. Cabrera, D.; Horatscheck, A.; Wilson, C.; Basarab, G.; Eyermann, C.; Chibale, K. *Plasmodial* kinase inhibitors: License to cure? *J. Med. Chem*. **2018**; 61 (18): 8061 - 8077. doi:10.1021/acs.jmedchem.8b00329.

14. Chapman, T.; Osborne, S.; Wallace, C.; Birchall, K.; Bouloc, N.; Jones, H.; Ansell, K.; Taylor, D.; Clough, B.; Green, J.; Holder, A. Optimization of an imidazopyridazine series of inhibitors of *Plasmodium falciparum* calcium-dependent protein kinase 1 (*Pf*CDPK1). *Med. Chem.* **2014**; 8 (4): 636 - 648.

15. Doerig, C. and Tobin, A. Previews parasite protein kinases : At home and abroad. *Cell Host Microbe*. **2010**; 8 (4): 305 -307. doi:10.1016/j.chom.2010.10.002.

16. Green, J.; Moon, R.; Whalley, D.; Bowyer, P.; Wallace, C.; Rochani, A.; Nageshan, R.; Howell, S.; Grainger, M.; Jones, H.; Ansell, K.; Chapman, T.; Taylor, D.; Osborne, S.; Baker, D.; Tatu, U.; Holder, A. Imidazopyridazine inhibitors of *Plasmodium falciparum* calcium- dependent protein kinase 1 also target cyclic GMP-dependent protein kinase 1 also target cyclic GMP-dependent protein kinase and heat shock protein 90 to kill the parasite at different stages. *Antimicrob. Agents Chemotherap.* **2016**; 60 (3): 1464 - 1475. doi:10.1128/AAC.01748-15.Address.

17. Ansell, K.; Jones, H.; Whalley, D.; Hearn, A.; Taylor, D.; Patin, E.; Chapman, T.;

Osborne, S.; Wallace, C.; Birchall, K.; Large, J.; Bouloc, N.; Smiljanic-Hurley, E.; Clough, B.; Moon, R.; Green, J.; Holder, A. Biochemical and antiparasitic properties of inhibitors of the *Plasmodium falciparum* calcium-dependent protein kinase *Pf*CDPK1. *Antimicrob. Agents Chemotherap.* **2014**; 58 (10): 6032 - 6043. doi:10.1128/AAC.02959-14.

18. Lemercier, G.; Fernandez-Montalvan, A.; Shaw, J.; Kugelstadt, D.; Bomke, J.; Domostoj, M.; Schwarz, M.; Scheer, A.; Kappes, B.; Leroy, D. Identification and characterization of novel small molecules as potent inhibitors of the *Plasmodial* calcium-dependent protein kinase 1. *Biochem.* **2009**; 48 (27): 6379 - 6389. doi:10.1021/bi9005122.

19. Baker, D.; Stewart, L.; Large, J.; Bowyer, P.; Ansell, K.; Jiménez-Díaz, M.; El Bakkouri, M.; Birchall, K.; Dechering, K.; Bouloc, N.; Coombs, P.; Whalley, D.; Harding, D.; Smiljanic-Hurley, E.; Wheldon, M.; Walker, E.; Dessens, J.; Lafuente, M.; Sanz, L.; Gamo, F.; Ferrer, S.; Hui, R.; Bousema, T.; Angulo-Barturén, I.; Merritt, A.; Croft, S.; Gutteridge, W.; Kettleborough, C.; Osborne, S. A potent series targeting the malarial cGMP-dependent protein kinase clears infection and blocks transmission. *Nat. Commun.* **2017**; 8 (1): 1 - 9. doi:10.1038/s41467-017-00572-x.

20. Large, J.; Birchall, K.; Bouloc, N.; Merritt, A.; Smiljanic-Hurley, E.; Tsagris, D.; Wheldon, M.; Ansell, K.; Coombs, P.; Kettleborough, C.; Whalley, D.; Stewart, L.; Bowyer, P.; Baker, D.; Osborne, S. Potent inhibitors of malarial *P. falciparum* protein kinase G: Improving the cell activity of a series of imidazopyridines. *Bioorganic Med. Chem. Lett.* **2019**; 29 (3): 509 - 514. doi:10.1016/j.bmcl.2018.11.039.

21. Donald, R.; Zhong, T.; Wiersma, H.; Nare, B.; Yao, D.; Lee, A.; Allocco, J.; Liberator, P. Anticoccidial kinase inhibitors: Identification of protein kinase targets secondary to cGMP-dependent protein kinase. *Mol. Biochem. Parasitol.* **2006**; 149: 86 - 98. doi:10.1016/j.molbiopara.2006.05.003.

22. McNamara, C.; Lee, M.; Lim, C.; Lim, S.; Roland, J.; Nagle, A.; Simon, O.; Yeung, B.; Chatterjee, A.; McCormack, S.; Manary, M.; Zeeman, A.; Dechering, K.; Kumar, T.; Henrich, P.; Gagaring, K.; Ibanez, M.; Kato, N.; Kuhen, K.; Fischli, C.; Rottmann, M.; Plouffe, D.; Bursulaya, B.; Meister, S.; Rameh, L.; Trappe, J.; Haasen, D.; Timmerman, M.; Sauerwein, R.; Suwanarusk, R.; Russell, B.; Renia, L.; Nosten, F.; Tully, D.; Kocken, C.; Glynne, R.; Bodenreider, C.; Fidock, D.; Diagana, T.; Winzeler, E.

Targeting *Plasmodium* PI(4)K to eliminate malaria. *Nature*. **2013**; 504 (7479): 248 - 253. doi:10.1038/nature12782.

23. Zou, B.; Nagle, A.; Chatterjee, A.; Leong, S.; Tan, L.; Sim, W.; Mishra, P.; Guntapalli, P.; Tully, D.; Lakshminarayana, S.; Lim, C.; Tan, Y.; Abas, S.; Bodenreider, C.; Kuhen, K.; Gagaring, K.; Borboa, R.; Chang, J.; Li, C.; Hollenbeck, T.; Tuntland, T.; Zeeman, A.; Kocken, C.; McNamara, C.; Kato, N.; Winzeler, E.; Yeung, B.; Diagana, T.; Smith, P.; Roland, J. Lead optimization of imidazopyrazines: A new class of antimalarial with activity on *Plasmodium* liver stages. *ACS Med. Chem. Lett*. **2014**; 5 (8): 947 - 950. doi:10.1021/ml500244m.

24. Le Manach, C.; Cabrera, D.; Douelle, F.; Nchinda, A.; Younis, Y.; Taylor, D.; Wiesner, L.; White, K.; Ryan, E.; March, C.; Duffy, S.; Avery, V.; Waterson, D.; Witty, J.; Wittlin, S.; Charman, S.; Street, L.; Chibale, K. Medicinal chemistry optimization of antiplasmodial imidazopyridazine hits from high throughput screening of a softfocus kinase library: Part 1. *J. Med. Chem*. **2014**; 57: 2789 - 2798.

25. John Harris, C.; Hill, R.; Sheppard, D.; Slater, M.; and Stouten, P. The design and application of target-focused compound libraries. *Comb. Chem. High Throughput Screen*. **2011**; 14 (6): 521 - 531. doi:10.2174/138620711795767802.

26. Le Manach, C.; Paquet, T.; Brunschwig, C.; Njoroge, M.; Han, Z.; Cabrera, D.; Bashyam, S.; Dhinakaran, R.; Taylor, D.; Reader, J.; Botha, M.; Churchyard, A.; Lauterbach, S.; Coetzer, T.; Birkholtz, L.; Meister, S.; Winzeler, E.; Waterson, D.; Witty, M.; Wittlin, S.; Jiménez-Díaz, M.; Martínez, M.; Ferrer, S.; Angulo-Barturen, I.; Street, L.; Chibale, K. A novel pyrazolopyridine with *in vivo* activity in *Plasmodium* berghei- and *Plasmodium falciparum*-infected mouse models from structure-activity relationship studies around the core of recently identified antimalarial imidazopyridazines. *J. Med. Chem*. **2015**; 58 (21): 8713 - 8722. doi:10.1021/acs.jmedchem.5b01605.

27. Le Manach, C.; Paquet, T.; Cabrera, D.; Younis, Y.; Taylor, D.; Wiesner, L.; Lawrence, N.; Schwager, S.; Waterson, D.; Witty, M.; Wittlin, S.; Street, L.; Chibale, K. Medicinal chemistry optimization of antiplasmodial imidazopyridazine hits from high throughput screening of a softfocus kinase library: Part 2. *J. Med. Chem*. **2014**; 57 (21): 8839 - 8848. doi:10.1021/jm500887k.

28. Cheuka, P.; Lawrence, N.; Taylor, D.; Wittlin, S.; Chibale, K. Antiplasmodial imidazopyridazines; structure activity relationship studies lead to the identification of analogues with improved solubility and hERG profiles. *Med. Chem. Comm.* **2018**: 1733 - 1745. doi:10.1039/c8md00382c.

29. Cheuka, P.; Centani, L.; Arendse, L.; Fienberg, S.; Wambua, L.; Renga, S.; Dziwornu, G.; Kumar, M.; Lawrence, N.; Taylor, D.; Wittlin, S.; Coertzen, D.; Reader, J.; van der Watt, M.; Birkholtz, L.; Chibale, K. New amidated 3,6-diphenylated imidazopyridazines with potent antiplasmodium activity are dual inhibitors of *Plasmodium* phosphatidylinositol-4-kinase and cGMP-dependent protein kinase. *ACS Infect. Dis*. **2021**; 7 (1): 34 - 46. doi:10.1021/acsinfecdis.0c00481.

30. Solyakov, L.; Halbert, J.; Alam, M.; Semblat, J.; Dorin-Semblat, D.; Reininger, L.; Bottrill, A.; Mistry, S.; Abdi, A.; Fennell, C.; Holland, Z.; Demarta, C.; Bouza, Y.; Sicard, A.; Nivez, M.; Eschenlauer, S.; Lama, T.; Thomas, D.; Sharma, P.; Agarwal, S.; Kern, S.; Pradel, G.; Graciotti, M.; Tobin, A.; Doerig, C. Global kinomic and phospho-proteomic analyses of the human malaria parasite *Plasmodium falciparum*. *Nat. Commun*. **2011**; 2 (565): 1 - 12.

31. Fienberg, S.; Eyermann, C.; Arendse, L.; Basarab, G.; McPhail, J.; Burke, J.; Chibale, K. Structural basis for inhibitor potency and selectivity of *plasmodium falciparum* phosphatidylinositol 4-kinase inhibitors. *ACS Infect. Dis*. **2020**; 6 (11): 3048 - 3063. doi:10.1021/acsinfecdis.0c00566.

32. Sinden, R. Developing transmission-blocking strategies for malaria control. *PLoS Pathog*. **2017**; 13 (7): 1 - 12. doi:10.1371/journal.ppat.1006336.

33. Burrows, J.; Huijsduijnen R.; Möhrle, J.; Oeuvray, C.; Wells, T. Designing the next generation of medicines for malaria control and eradication. *Malar. J*. **2013**; 12 (1): 1 - 20. doi:10.1186/1475-2875-12-187.

34. Meanwell, N. A. Improving Drug Design: An update on recent applications of efficiency metrics, strategies for replacing problematic elements, and compounds in non-traditional drug space. *Chem. Res. Toxicol*. **2016**; 29 (4): 564 - 616. doi:10.1021/acs.chemrestox.6b00043.

35. Hopkins, A.; Keserü, G.; Leeson, P.; Rees, D. and Reynolds, C. The role of ligand efficiency metrics in drug discovery. *Nat. Rev. Drug Discov*. **2014**; 13 (2): 105 - 121.

doi:10.1038/nrd4163.

36. Veber, D.; Johnson, S.; Cheng, H.; Smith, B.; Ward, K.; Kopple, K. Molecular properties that influence the oral bioavailability of drug candidates. *J. Med. Chem*. **2002**; 45 (12): 2615 - 2623. doi:10.1021/jm020017n.

37. Hughes, J.; Blagg, J.; Price, D.; Bailey, S.; DeCrescenzo, G.; Devraj, R.; Ellsworth, E.; Fobian, Y.; Gibbs, M.; Gilles, R.; Greene, N.; Huang, E.; Krieger-Burke, T.; Loesel, J.; Wager, T.; Whiteley, L.; Zhang, Y. Physiochemical drug properties associated with *in vivo* toxicological outcomes. *Bioorganic Med. Chem. Lett*. **2008**; 18 (17): 4872 - 4875. doi:10.1016/j.bmcl.2008.07.071.

38. Cheuka, P.; Mayoka, G.; Okombo, J. and Chibale, K. *Medicinal Chemistry Progression of Antimalarial Hits from Phenotypic Whole Cell Screening of SoftFocus Libraries*. 1st ed. Elsevier Inc.; **2019**. doi:10.1016/bs.armc.2019.04.001.

39. Kalyaanamoorthy, S. and Barakat K. Development of safe drugs: The hERG challenge. *Med. Res. Rev*. **2018**; 38 (2): 525 - 555. doi:10.1002/med.21445.

40. Deodhar, M.; Rihani, S.; Arwood, M.; Darakjian, L.; Dow, P.; Turgeon, J.; Michaud, V. Mechanisms of CYP-450 inhibition: Understanding drug-drug interactions due to mechanism-based inhibition in clinical practice. *Pharmaceutics*. **2020**; 12 (9): 1 - 18. doi:10.3390/pharmaceutics12090846.

41. Carreno, M.; Ruano, J.; Sanz, G.; Toledo, M.; Urbano, A. Mild and regiospecific nuclear iodination of methoxybenzenes and napthalenes with *N*-iodosuccinimide in acetonitrile. *Tetrahedron Lett*. **1996**; 37 (23): 4081 - 4084.

42. Carpino, L.; Ionescu, D. and El-Faham, A. Peptide coupling in the presence of highly hindered tertiary amines. *J. Org. Chem*. **1996**; 61 (7): 2460 - 2465. doi:10.1021/jo950912x.

43. Smith, M. and March, J. *March's Advanced Organic Chemistry*. 6th ed. John Wiley and Sons; **2006**. doi:10.1002/0470084960.

CHAPTER 7

BIOLOGICAL PROPERTIES OF THE SYNTHESIZED IMIDAZOPYRIDINE COMPOUNDS

7.1 Chapter overview

In this chapter, the biological and biochemical activities of the synthesized imidazopyridine compounds will be discussed. First, the anti-plasmodium activity, *Plasmodium* PI4K and PKG inhibitory activity will be discussed. The kinase inhibition data will then be rationalized using *in silico* tools. Finally, cytotoxicity, microsomal metabolic stability and hERG profiling of selected compounds generated in the study will be discussed.

7.2 Biological activity of the synthesized imidazopyridines

7.2.1 Anti-plasmodium activity of imidazopyridines

As with the MLN0128 series, the *in vitro* asexual blood-stage anti-plasmodium activities of synthesized imidazopyridines were tested against the CQ-sensitive strain of *P. falciparum* (NF54) using the previously described parasite LDH assay.[1] Chloroquine and artesunate were included as positive controls. Compounds displaying high potency (*Pf*NF54 IC_{50} < 1 µM) were progressed for testing against the multidrug-resistant strain (K1) using the same protocol. In parallel, evaluation of kinetic turbidimetric solubility was undertaken for all synthesized imidazopyridines, except for analogue **84** (**GS1 31**), for which anti-plasmodium data was pending at the time of the assay. A summary of the anti-plasmodium activity (IC_{50} values) and kinetic solubility (based on the modified HPLC DMSO "dry-down" method) is provided in **Table 7.1**.

Table 7.1: Anti-plasmodium activity (IC_{50} values) of target imidazopyridines

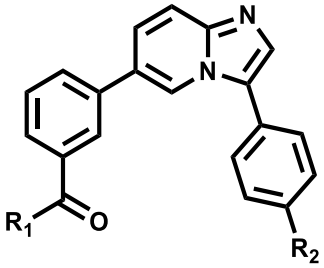

Code	R_1	R_2	[a]*Pf*NF54 (IC_{50}, µM)	[a]*Pf*K1 (IC_{50}, µM)	[b]RI	*Solubility (µM, pH 6.5)
78 (GS1 08)		SO_2Me	> 6	-	-	195
79 (GS1 09)		SO_2Me	0.432	0.687	2	195
80 (GS1 11)		SO_2Me	0.569	0.803	1	150
83 (GS1 29)	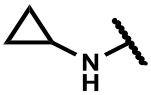	SO_2Me	1.870	-	-	100
84 (GS1 31)	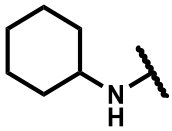	SO_2Me	2.020	-	-	-
85 (GS1 12)	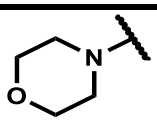	SO_2Me	0.214	0.405	2	195
86 (GS1 16)	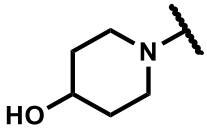	SO_2Me	0.063	0.100	2	195
81 (GS1 21)		SOMe	0.602	0.846	1	200
82 (GS1 22)		SOMe	0.489	0.817	2	190
87 (GS1 25)	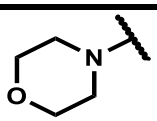	SOMe	0.275	0.478	2	200
88 (GS1 26)	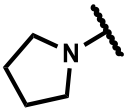	SOMe	0.502	0.819	2	195
89 (GS1 27)	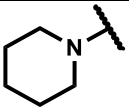	SOMe	0.126	0.226	2	200

"-" = Not determined, [a]asexual blood stage IC_{50} values are means of n ≥ 2 determinations; Artesunate [IC_{50} = 4 nM (*Pf*NF54), 3 nM (*Pf*K1)] and chloroquine [IC_{50} = 10 nM (*Pf*NF54), 194 nM (*Pf*K1)] were

used as reference drugs; [b]RI = resistance index i.e., *Pf*K1 IC_{50}/*Pf*NF54 IC_{50}; *HPLC solubility in µM (pH 6.5); determined via HPLC-based DMSO "dry-down" method

Most compounds showed potent activity against the drug-sensitive strain of the parasite (*Pf*NF54 IC_{50} < 1 µM). Furthermore, low cross-resistance (RI ≤ 2) against the multidrug-resistant (K1) strain was observed for all compounds tested. Compound **86** (**GS1 16**) was the most potent with *Pf*NF54 IC_{50} = 0.063 µM. The piperidine moiety was also well-tolerated as displayed by the high potency of the sulfone compound **89** (**GS1 27**; *Pf*NF54 IC_{50} = 0.126 µM). Substitution of a sulfoxide with a sulfone had little effect on anti-plasmodium activity, as exemplified by the *N*,*N*-dimethyl analogue **79** (**GS1 09**; *Pf*NF54 IC_{50} = 0.432 µM), the free amide **80** (**GS1 11**; *Pf*NF54 IC_{50} = 0.569 µM), and **85** (**GS1 12**; *Pf*NF54 IC_{50} = 0.214 µM) containing the morpholine appendage (**Table 7.1**), all of which were equipotent relative to their reduced counterparts **81** (**GS1 21**; *Pf*NF54 IC_{50} = 0.602 µM), **82** (**GS1 22**; *Pf*NF54 IC_{50} = 0.489 µM), and **87** (**GS1 25**; *Pf*NF54 IC_{50} = 0.275 µM). However, incorporation of a cyclopropyl appendage as in **83** (**GS1 29**) or a cyclohexyl one like in **84** (**GS1 31**), was detrimental to potency (*Pf*NF54 IC_{50} = 1.87 and 2.02 µM, respectively), while the introduction of a free carboxylic acid in **78** (**GS1 08**) led to a complete loss in activity at the maximum concentration tested (*Pf*NF54 IC_{50} > 6 µM).

Introduction of the water-solubilizing carboxamide group proved to be an effective strategy to mitigate poor solubility, as all analogues synthesized exhibited high solubility (≥ 100 µM) based on the H3D-adapted HPLC method (**Table 7.1**). Although the conversion of sulfones to sulfoxides was also predicted to improve solubility, the carboxamide strategy proved superior since the pro-drugs displayed comparable activity to the sulfones. However, the solubility of compound **84** (**GS1 31**) was not tested due to its poor anti-plasmodium activity (*Pf*NF54 IC_{50} = 2.02 µM). The inter-relationship between solubility and other physicochemical parameters is further elaborated in the next chapter.

The observed sulfone/sulfoxide equipotency in matched pairs suggested that only a single hydrogen bond acceptor on the LHS of the molecule is needed for anti-plasmodium activity, in congruence with previous findings.[2] However, it is worth emphasizing that sulfoxide racemates were used to generate the anti-plasmodium whole-cell data, but the activity may differ for individual enantiomers or be solely due to one enantiomer. It is also possible that the presence of both enantiomers could antagonize biological activity.[3,4] Furthermore, chirality encompasses unique PK and PD properties that render medicinal investigation of separate

enantiomers important, as exemplified by the successful marketing of esomeprazole.[5] Nevertheless, as previously mentioned, the synthesized sulfoxides were tested as racemates in this study.

Even so, the equipotency of the sulfones and sulfoxides is of significance importance in prodrug strategies in which oxidation would be expected to occur *in vivo* resulting in a compound with desirable pharmacological effects. Such a strategy may be employed to circumvent undesirable PK properties such as low aqueous solubility, limited bioavailability, poor oral absorption, and toxicity.[6] For example, some sulfoxides in the 3,5-diaryl-2-aminopyrazine series were more soluble than their corresponding sulfones and have been successfully employed to achieve higher *in vivo* plasma exposures with subsequent greater antimalarial efficacy in the humanized *Pf*SCID mouse model.[7]

7.2.2 *In vitro Pv*PI4K inhibition studies and *in silico* docking of selected imidazopyridines

To gain insight into the observed anti-plasmodium activity, *in vitro Pv*PI4K inhibition assays and *in silico* docking studies were carried out using methods previously described for MLN0128 analogues. The *Pv*PI4K inhibition data for selected compounds is summarized in **Table 7.2**.

Table 7.2: *In vitro Pv*PI4K activity (IC_{50} values) of the target imidazopyridines

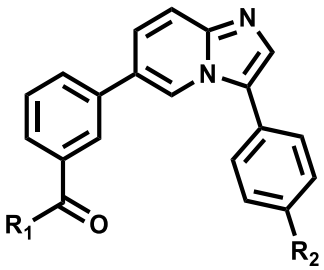

Code	R_1	R_2	*Pf*NF54 (IC_{50}, µM)	[a]*Pv*PI4K (IC_{50}, nM)
78 (**GS1 08**)		SO_2Me	> 6	11
79 (GS1 09)		SO_2Me	0.432	14
80 (**GS1 11**)	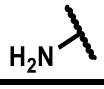	SO_2Me	0.569	17
83 (**GS1 29**)	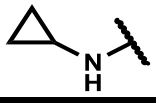	SO_2Me	1.870	29

85 (**GS1 12**)	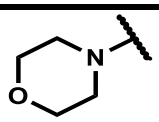	SO_2Me	0.214	15
86 (**GS1 16**)	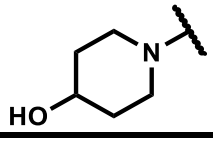	SO_2Me	0.063	3
81 (**GS1 21**)	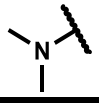	SOMe	0.602	11
82 (**GS1 22**)		SOMe	0.489	12
87 (**GS1 25**)	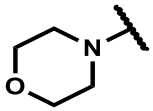	SOMe	0.275	7
88 (**GS1 26**)	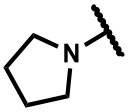	SOMe	0.502	26
89 (**GS1 27**)	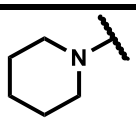	SOMe	0.126	5

[a] n ≥ 2, minimum of two independent assays in duplicates

Generally, the enzymatic data augured well with the observed anti-plasmodium activity with the most potent compound against *Pf*NF54, **86** (**GS1 16**; IC_{50} = 0.063 µM), also possessing superior activity against the recombinant protein (IC_{50} = 3 nM). Docking of this compound in the *Pf*PI4K homology model predicted a single H-bond pair interaction between N1 of the hinge binder and the Val 1357 residue of the model (**Figure 7.1**). Additionally, the sulfone appendage made an important interaction with the conserved catalytic lysine (Lys 1308; **Figure 7.1**). Crucially, the amide carbonyl on the left-hand side of the molecule was well configured to interact with Ser 1365 in the ribose pocket while the phenyl made a π–π interaction with Phe 827 (interaction not shown in **Figure 7.1**) in the P-loop region of the model. Furthermore, the location of the piperidine hydroxyl was judged optimal for H-bond interactions with the solvent-exposed Lys 825, further highlighting its contribution to potency.

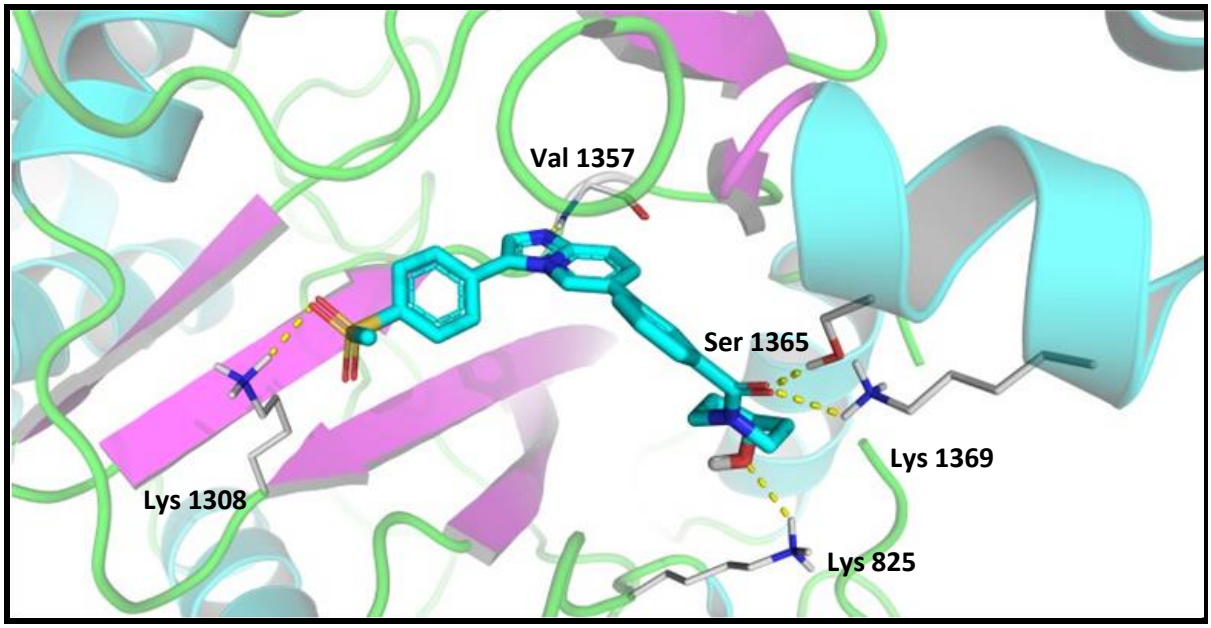

Figure 7.1: Docking representation of analogue **86** (**GS1 16**) in the *Pf*PI4K homology model

Analogue **89** (**GS1 27**; *Pv*PI4K IC_{50} = 5 nM) was equally potent although the observed interaction with Lys 825 was lost after deletion of the hydroxyl in the compound. However, this compound was tested as a racemic mixture, but individual enantiomers employed in docking. The docked *R*-sulfoxide was better positioned for H-bond interaction with the catalytic lysine, and thus showed a slight advantage over the *S*-stereoisomer, as both enantiomers were used for docking. The high biochemical activity of **87** (**GS1 25**; racemate IC_{50} = 5 nM) was attributed to the extra duo H-bond of the morpholine with Lys 825 and Ser 921 in the preferred *R*-stereoisomer. In contrast, this interaction was not observed in the sulfone congener **85** (**GS1 12**), explaining the three-fold decline in potency (IC_{50} = 15 nM).

N, *N*-dimethylated and unsubstituted sulfones and sulfoxides were generally well tolerated because of optimal occupation of the ribose pocket by the phenyl amide appendage with Ser 1362, Ser 1365, Lys 1369 and Cys 1361 of the model playing a pivotal role in retention of H bond interactions at this site. This explained the high potency of **79** (**GS1 09**; IC_{50} = 14 nM), **80** (**GS1 11**; IC_{50} = 17 nM), **81** (**GS1 21**; IC_{50} = 11 nM) and **82** (**GS1 22**; IC_{50} = 12 nM) in the *Pv*PI4K assay.

The free carboxylic acid **78** (**GS1 08**; IC_{50} = 11 nM) was also highly potent and docking experiments at pH 7 revealed the negatively charged oxygen atom of the carboxylate functionality positioned between Lys 825 and Lys 1369, consequently forming two salt-bridge bonds in addition to the putative H-bond with Cys 1361. In contrast, no additional advantages

were provided by a cyclopropyl or a pyrrolidine group in **83** (**GS1 29**; IC_{50} = 29 nM; **Figure 7.2**) or *R*/*S* isomers of **88** (**GS1 26**; IC_{50} = 26 nM), accounting for a slight decrease in enzymatic activity (**83** (**GS1 29**) shown as a representative compound). However, the docked *R* isomer of **88** (**GS1 26**) was preferred as it retained π-stacking with Phe 827 of the model.

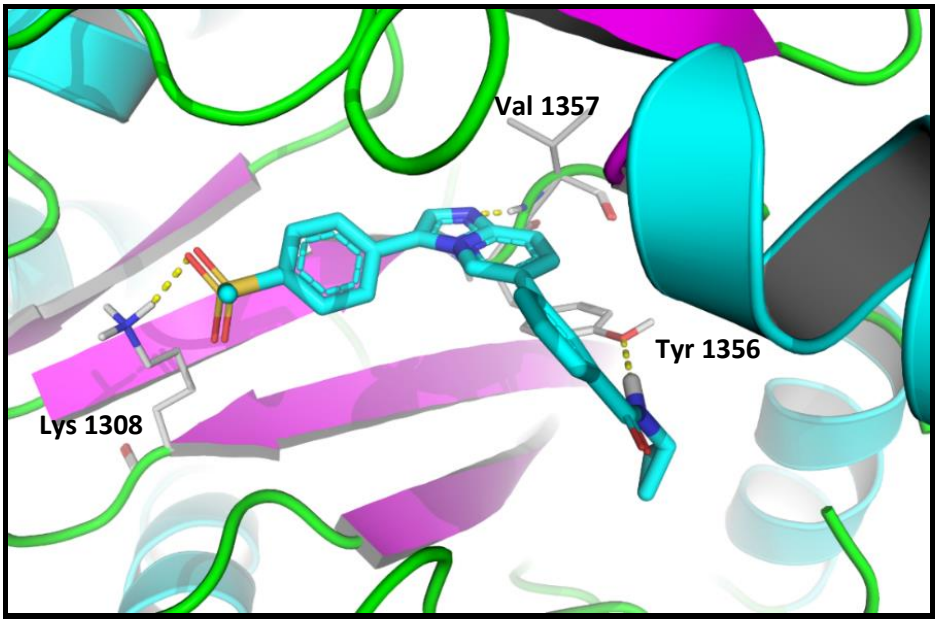

Figure 7.2: Binding modes of analogue **83** (**GS1 29**) depicting loss of interaction in the *Pf*PI4K homology model with the cyclopropyl appendage

Overall, the data suggests that the anti-plasmodium activity observed for these imidazopyridines is achieved via inhibition of *Pf*PI4K, which is likely a primary contributing target. This was also illustrated by a plot of *Pf*NF54 pEC_{50} vs *Pv*PI4K pIC_{50} for selected compounds (**Figure 7.3**) where a statistically significant correlation was observed (R^2 = 0.75), although this is based on a limited number of data points covering a narrow range of *Pv*PI4K activity. In the case of **78**, the single outlier excluded from the correlation plot, anti-plasmodium activity was lost despite high *in vitro* activity against the enzyme (**GS1 08**; *Pf*NF54 IC_{50} > 6 µM; *Pv*PI4K = 11 nM). This could be due to inability of the compound to reach the site of action.

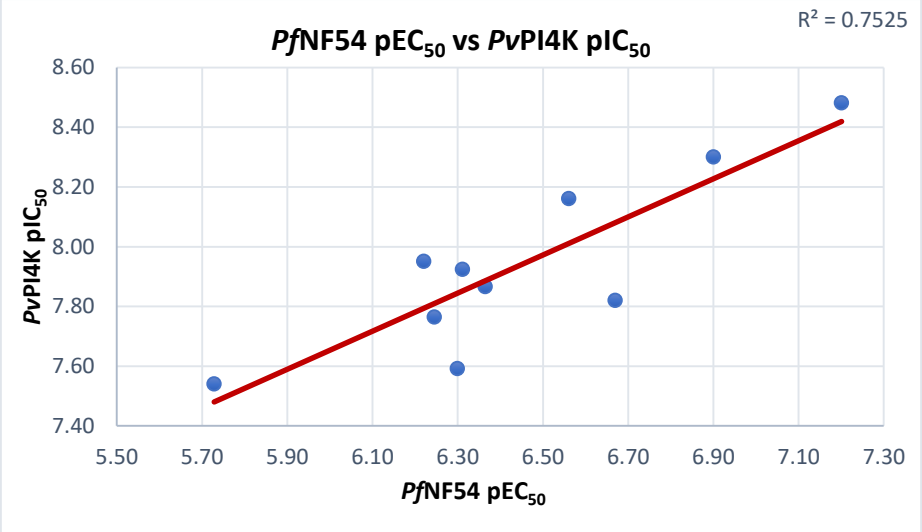

Figure 7.3: Correlation plot of *Pf*NF54 (pEC_{50}) and *in vitro Pv*PI4K activity (pIC_{50}) for imidazopyridines with elimination of except **78**, whose *Pf*NF54 IC_{50} value was indefinite

However, the synthesized imidazopyridines showed a 10- to 20-fold reduction in anti-plasmodium potency and a significant decline in *in vitro Pf*PI4K activity compared to that in reported matched imidazopyridazine compounds.[8] This suggests that deletion of N5 interferes with optimal hinge-binding in the core, contrary to *in silico* predictions. This may be attributed to the fixed-core docking methodology employed in this study, which assumes a rigid protein-ligand interaction and may not accurately predict binding of the core scaffold in the hinge region. Although notoriously laborious, quantum molecular dynamic (QMD) methodology may be more accurate for such predictions.

7.2.3 *In vitro Pf*PKG inhibition studies and *in silico* docking of selected imidazopyridines

To further investigate the MoA associated with this class of compounds, the *in vitro Pf*PKG inhibitory activities of selected analogues were investigated using the ADP-Glo kinase method previously described. The % inhibition (at 10 µM) and IC_{50} values of selected compounds are listed in **Table 7.3**. Most compounds showed low inhibition (≤ 50%) at the maximum concentration tested (10 µM) except for **86** (**GS1 16**; 77% inhibition at 10 µM), **80** (**GS1 11**; 61.7%), and **83** (**GS1 29**; 58.9%). IC_{50} determination indicated that all compounds explored in this series showed inhibitory concentrations > 2 µM, and eight of the eleven compounds synthesized had an $IC_{50} \geq 10$ µM.

Table 7.3: *In vitro Pf*PKG activity of selected imidazopyridines

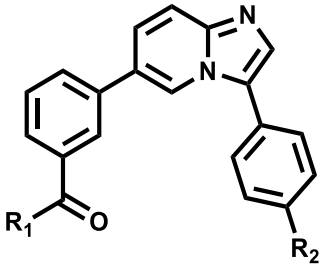

Code	R_1	R_2	*Pf*NF54 (IC_{50}, µM)	[a]% Inh. (10 µM)	[b]*Pf*PKG (IC_{50}, µM)
78 (**GS1 08**)	HO	SO_2Me	> 6	32.9	> 10
79 (GS1 09)	N	SO_2Me	0.432	53.4	10
80 (**GS1 11**)	H_2N	SO_2Me	0.569	61.7	> 2
83 (**GS1 29**)	N H	SO_2Me	1.870	58.5	> 2
85 (**GS1 12**)	N O	SO_2Me	0.214	36.1	> 10
86 (**GS1 16**)	N HO	SO_2Me	0.063	76.7	4.3
81 (**GS1 21**)	N	SOMe	0.602	53.5	10
82 (**GS1 22**)	H_2N	SOMe	0.489	50.0	10
87 (**GS1 25**)	N O	SOMe	0.275	20.8	> 10
88 (**GS1 26**)	N	SOMe	0.502	41.2	> 10
89 (**GS1 27**)	N	SOMe	0.126	50.5	10

[a]*In vitro Pf*PKG percentage inhibitions are a mean value of n ≥ 2 (in duplicate) determinations, [b]mean of values of n ≥ 2 (in duplicate) determinations

Molecular docking studies showed that the inactive compound **86** (**GS1 16**; *Pf*PKG IC_{50} = 4.3 µM) docked favorably into the ATP-binding site of the *Pv*PKG crystal structure (**PDB code 5EZR**; **Figure 7.4**). The imidazopyridine core was predicted to accept a single H-bond from

Val 614 while the phenyl sulfone interacted with Asp 675 of the model. In addition, the carbonyl on the phenyl carboxamide was deemed spatially favored to interact with Arg 542 while the piperidine hydroxyl interacted with the sidechain of the conserved Asp 675 residue, explaining its modest inhibitory activity. A similar binding pose was recently reported by Cheuka *et al*.[8] using related analogues based on the imidazopyridazine scaffold.

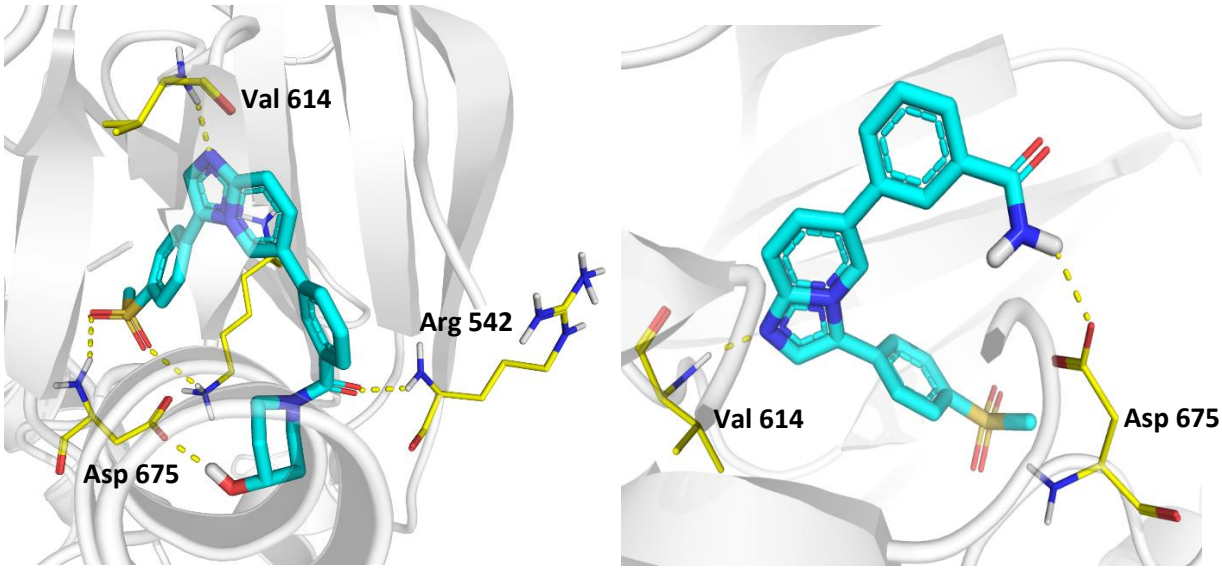

Figure 7.4: A, Docking pose of analogue **86** (**GS1 16**) in the *Pv*PKG crystal structure (**5EZR**); B, similar representation of **80** (**GS1 11**) depicting loss of interaction on the phenyl sulfonyl side of the molecule

The other inactive analogue **80** (**GS1 11**; 61.7% inhibition at 10 µM) was predicted to bind in a similar way with the amide donating a H bond to Asp 675, but the binding was deemed less favorable due to loss of interactions between the sulfone and carboxamide carbonyl and Asp 675 residue in the ATP-binding site (**Figure 7.4**). A complete loss of interactions was observed for several compounds such as **83** (**GS1 29**; IC_{50} > 2 µM) and **85** (**GS1 12**; IC_{50} > 10 µM), explaining the loss in PKG activity.

Additionally, every enantiomer/diastereomer of the synthesized sulfoxides was docked in the crystal structure. For analogue **87** (**GS1 25**), the *S*-sulfoxide showed a slight binding advantage over the *R*-isomer, with a contrary observation for **88** (**GS1 26**) enantiomers. This also highlighted the importance of biological and biochemical evaluation of individual chiral compounds, which was not undertaken in this study. This loss of interactions, occasional clash with Glu 612 or Asp 675 (as noted in **81**, **GS1 21**; *R*-isomer), and lack of π-stacking

interactions, as observed in *Pf*PI4K, provided an explanation for the loss in affinity observed in the *Pf*PKG biochemical assay for compounds in this series.

7.2.4 Cytotoxicity studies of selected imidazopyridines

To investigate the cytotoxicity profile of the imidazopyridine series, the cytotoxicity of compounds exhibiting high anti-plasmodium potency (*Pf*NF54 < 1 µM) was evaluated based on the previously described colorimetric MTT assay in the CHO cell line. This work was conducted at H3D within the Division of Clinical Pharmacology, Department of Medicine, UCT. The IC_{50} values were determined and selectivity indices (SI) were derived as summarized in **Table 7.4**.

Table 7.4: CHO cytotoxicity profile (IC_{50} values) of selected imidazopyridines

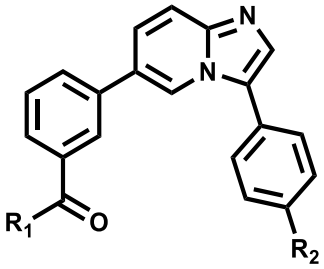

Code	R_1	R_2	*Pf*NF54 (IC_{50}, µM)	*Solubility (pH 6.5)	[a]CHO (µM)	[b]SI
80 (**GS1 11**)		SO_2Me	0.569	150	> 50	> 88
85 (**GS1 12**)	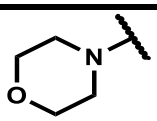	SO_2Me	0.214	195	> 50	> 233
86 (**GS1 16**)	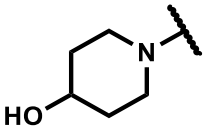	SO_2Me	0.063	195	> 50	> 793
81 (**GS1 21**)		SOMe	0.602	200	> 50	> 83
82 (**GS1 22**)		SOMe	0.489	190	> 50	> 102
87 (**GS1 25**)	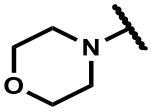	SOMe	0.275	200	> 50	> 180
88 (**GS1 26**)	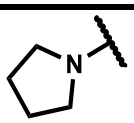	SOMe	0.502	195	> 50	> 100

89 (**GS1 27**)	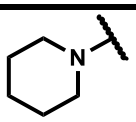	SOMe	0.126	200	34.8	277

[a]CHO = Chinese hamster ovarian cell line; average for technical duplicates (n = 1); [b]SI = selectivity index i.e., CHO IC_{50}/*Pf*NF54 IC_{50}

All compounds tested demonstrated a low cytotoxicity profile (CHO IC_{50} > 50 µM), except for the racemate **89** (**GS1 27;** IC_{50} = 34.8 µM). Analogue **86** (**GS1 16**) exhibited both high anti-plasmodium potency (*Pf*NF54 IC_{50} = 0.063 µM) and low CHO cytotoxicity, resulting in the most favorable safety profile (CHO IC_{50} > 50 µM; SI > 793) of all compounds in this series.

Modification to the sulfoxide appeared to have had no impact on the cytotoxicity profile, as exemplified by all sulfone-sulfoxide matched pairs (e.g., **85** (**GS1 12**) and **87** (**GS1 25**); CHO IC_{50} > 50 µM for each), although one sulfoxide enantiomer may display greater biological activity than the other. Overall, this data shows that cytotoxicity may not be a challenge for this series going forward. However, it will also be essential to evaluate the cytotoxicity of this series in other cell lines.

7.2.5 Microsomal metabolic stability and hERG inhibition assessment

Representative compounds exhibiting sub-micromolar *in vitro* asexual blood stage anti-plasmodium (*Pf*NF54 IC_{50} ˷ 0.5 µM), low cytotoxicity and acceptable solubility (> 50 µM) were progressed to microsomal metabolic stability assay profiling. Compounds were incubated with human (H), rat (R), and mouse (M) liver microsomes using methods previously described for the MLN0128 analogues. These included the sulfones **85** (**GS1 12**) and **86** (**GS1 16**) and the sulfoxides **87** (**GS1 25**) and **89** (**GS1 27**) which would potentially highlight the anticipated *in vivo* oxidative biotransformation and shed light on the envisaged pro-drug strategy. The microsomal metabolic stability data for the compounds is summarized in **Table 7.5**.

Table 7.5: Microsomal metabolic stability (% remaining) of selected imidazopyridines

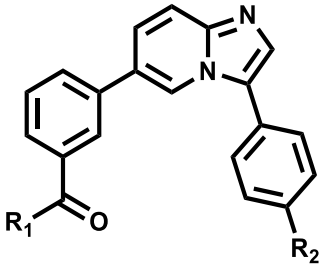

Code	R_1	R_2	% rem. after 30 min.	Projected $^{d}t_{½}$ (min)	Hepatic extraction ratio (E_H)
			^{a}H/^{b}R/^{c}M	^{a}H/^{b}R/^{c}M	^{a}H/^{b}R/^{c}M
85 (**GS1 12**)	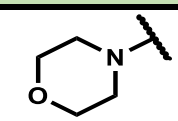	SO_2Me	98.4/ 98.4 /92.7	>150/>150/> 150	<0.42/<0.30/< 0.33
86 (**GS1 16**)	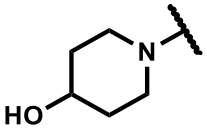	SO_2Me	95.6/ 85.3 /87.5	>150/130.4/> 150	<0.42/<0.30/< 0.33
87 (**GS1 25**)	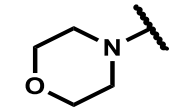	SOMe	97.3/ 97.7/ 97.1	>150/>150/> 150	<0.42/<0.30/< 0.33
89 (**GS1 27**)	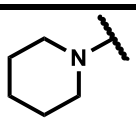	SOMe	16.3/7.11/ 0.24	11.4/ 7.9/ 3.4	0.90/ 0.82/ 0.96

^{a}H = Human liver microsomes; ^{b}R = Rat liver microsomes; ^{c}M = Mouse liver microsomes; $^{d}t_{½}$ = Half-life

Both the sulfones **85** and **86** were metabolically stable (> 75% remaining after a 30-minute incubation) in liver microsomes of the three species translating to a high projected half-life ($t_{½}$ > 150 min) and low hepatic extraction ratios (E_H). Interestingly, the sulfoxide **87** (**GS1 25**), was also stable across the liver preparations of the three species (H/R/M = 97.3/97.7/97.1%). In contrast, the sulfoxide congener **89** (**GS1 27**), was rapidly metabolized in microsomal preparations of the three species (H/R/M = 11.4/7.9/3.4%), suggesting similar metabolism amongst them. However, metabolite identification studies were not undertaken to decipher the hotspot and confirm the nature of the metabolites. In future, this may need to be undertaken to highlight if this metabolism occurs via oxidation of the sulfone group, as previously reported in sulfoxide-substituted imidazopyridazines.[9] Overall, the results indicates that the pro-drug conversion may be compound specific and could be overcome in this series.

In addition, representative compounds highlighting the structural modifications undertaken in this study, were progressed to hERG inhibition studies. These included the sulfones (**80**; **GS1 11**, **79**; **GS1 09** and **86**; **GS1 16**) and sulfoxides (**87**; **GS1 25** and **89**; **GS1 27**). The study was performed at B'SYS GmbH, Witterswil, Switzerland based on the QPatch clamp platform. **Table 7.6** summarizes the results for the analogues tested.

Table 7.6: hERG inhibition results for selected imidazopyridines

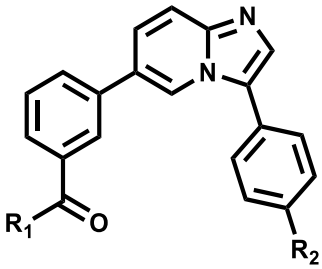

Code	R_1	R_2	hERG (IC_{50}, µM)	hERG (IC_{20}, µM)	Hill coefficient
80 (GS1 11)	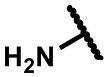	SO_2Me	19.66	8.55	1.7
79 (GS1 09)		SO_2Me	21.72	5.99	1.1
86 (GS1 16)	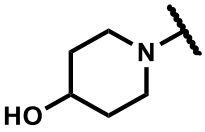	SO_2Me	44.80*	22.88	2.1
87 (GS1 25)	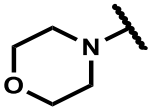	SOMe	51.03*	17.07	1.3
89 (GS1 27)	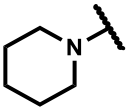	SOMe	12.96	4.25	1.2

*50–70% remaining current at highest concentration (30 µM)

All the tested compounds displayed favourable hERG inhibition activity with IC_{50} values above the pre-set cut-off (IC_{50} > 10 µM) in the screening cascade employed in this study. The sulfoxide **87** (**GS1 25**) and the sulfone **86** (**GS1 16**) displayed a clean profile against the cardiac channel with projected IC_{50} values of 51.0 and 44.8 µM, respectively. However, a high hill coefficient of 2.1 for **86** (**GS1 16**) was recorded due to a slightly higher current remaining (50–70%) at a dose of 30 µM. Since the projected values were obtained by extrapolation, the lower and more accurate IC_{20} values were generated. Both compounds exhibited respective IC_{20} = 17.1 and 22.9 µM. The low hERG activity on the tested sulfoxides including **89** (**GS1 27**; IC_{50}

= 12.96 µM) suggest that the hERG liability may be overcome on the imidazopyridine scaffold by the strategies employed.

The adopted strategies included the core change, masking of potentially ionizable nitrogen centers, reduction of sulfone group and introduction of water solubilizing carboxamides, properties which have the potential to disrupt π - cation and aromatic stacking between a drug and the cardiac channel.[10] Though, this reduction in hERG inhibition relative to the parent imidazopyridine compound and related imidazopyridines is encouraging, it may be difficult to pin-point the main contribution to this mitigation and is likely due to the additive contribution of the stated strategies.

7.3 Chapter summary

In summary, potent anti-plasmodium imidazopyridine analogues with high microsomal metabolic stability profile were identified. Although the modifications undertaken retained *Plasmodium* PI4K potency, compounds displayed poor *Pf*PKG inhibition (IC_{50} > 2 µM). However, significant improvement in the hERG profiles and aqueous solubility has been achieved. In the next chapter, physicochemical profiling for these analogues and their relationships with the biological and biochemical data will be assessed.

References

1. Makler, M. and Hinrichs, D. Measurement of the lactate dehydrogenase activity of *Plasmodium falciparum* as an assessment of parasitemia. *Am. J. Trop. Med. Hyg*. **1993**; 48 (2): 205 - 210. doi:10.4269/ajtmh.1993.48.205.

2. Cheuka, P.; Mayoka, G.; Okombo, J. and Chibale, K. *Medicinal Chemistry Progression of Antimalarial Hits from Phenotypic Whole Cell Screening of SoftFocus Libraries*. 1st ed. Elsevier Inc.; **2019**.doi:10.1016/bs.armc.2019.04.001.

3. Chhabra, N.; Aseri, M. and Padmanabhan, D. A review of drug isomerism and its significance. *Int. J. Appl. Basic Med. Res*. **2013**; 3 (1): 1 - 16. doi:10.4103/2229-516x.112233.

4. Hardikar, M. Chiral non-steroidal anti-inflammatory drugs - A review. *J. Indian Med. Assoc*. **2008**; 106 (9): 615 - 624.

5. Niazi, M.; Ahlbom, H.; Bondarov, P.; Karlsson, A.; Hassan-Alin, M.; Rydholm, H.; Röhss, K. Pharmacokinetics of esomeprazole following varying intravenous administration rates. *Basic Clin. Pharmacol. Toxicol*. **2005**; 97 (6): 351 - 354. doi:10.1111/j.1742-7843.2005.pto_150.x.

6. Surur, A.; Schulig, L. and Link A. Interconnection of sulfides and sulfoxides in medicinal chemistry. *Arch. Pharm. (Weinheim)*. **2019**; 352 (1): 1 - 11. doi:10.1002/ardp.201800248.

7. Gibhard, L.; Njoroge, M.; Paquet, T.; Brunschwig, C.; Taylor, D.; Lawrence, N.; Abay, E.; Wittlin, S.; Wiesner, L.; Street, L.; Chibale, K.; Basarab, G. Investigating sulfoxide-to-sulfone conversion as a prodrug strategy for a phosphatidylinositol 4-kinase inhibitor in a humanized mouse model of malaria. *Antimicrob. Agents Chemother*. **2018**; 62 (12): 1 - 11. doi:10.1128/AAC.00261-18.

8. Cheuka, P.; Centani, L.; Arendse, L.; Fienberg, S.; Wambua, L.; Renga, S.; Dziwornu, G.; Kumar, M.; Lawrence, N.; Taylor, D.; Wittlin, S.; Coertzen, D.; Reader, J.; van der Watt, M.; Birkholtz, L.; Chibale, K. New amidated 3,6-diphenylated imidazopyridazines with potent anti-plasmodium activity are dual inhibitors of *Plasmodium* phosphatidylinositol-4-kinase and cGMP-dependent protein kinase. *ACS Infect. Dis*. **2021**; 7 (1): 34 - 46. doi:10.1021/acsinfecdis.0c00481.

9. Le Manach, C.; Paquet, T.; Brunschwig, C.; Njoroge, M.; Han, Z.; Gonzàlez Cabrera, D.; Bashyam, S.; Dhinakaran, R.; Taylor, D.; Reader, J.; Botha, M.; Churchyard, A.; Lauterbach, S.; Coetzer, T.; Birkholtz, L.; Meister, S.; Winzeler, E.; Waterson, D.; Witty, M.; Wittlin, S.; Jiménez-Díaz, M.; Santos Martínez, M.; Ferrer, S.; Angulo-Barturen, I.; Street, L.; Chibale, K. A novel pyrazolopyridine with *in vivo* activity in *Plasmodium berghei*- and *Plasmodium falciparum*-infected mouse models from Structure-Activity Relationship studies around the core of recently identified anti-malarial imidazopyridazines. *J. Med. Chem*. **2015**; 58 (21): 8713 - 8722. doi:10.1021/acs.jmedchem.5b01605.

10. Jamieson, C.; Moir, E.; Rankovic, Z.; and Wishart, G. Medicinal chemistry of hERG optimizations: Highlights and hang-ups. *J. Med. Chem*. **2006**; 49 (17): 5029 - 5046. doi:10.1021/jm060379l.

CHAPTER 8

PHYSICOCHEMICAL PROPERTIES OF IMIDAZOPYRIDINE ANALOGUES

8.1 Chapter overview

This chapter describes selected experimental and virtually derived physicochemical properties of the target imidazopyridines compounds presented in this study. Physicochemical properties relationships are then investigated to establish physicochemical attributes influencing solubility of the generated imidazopyridines. In addition, the profiled attributes are compared for conformity to those of marketed drugs.

8.2 Physicochemical profiling of imidazopyridine analogues

The experimental (MP and solubility) and calculated (MW, cLogP, TPSA, and the number of HBDs and HBAs) physicochemical data for the imidazopyridine analogues synthesized were determined based on similar methods as those employed for MLN0128 analogues. One of the objectives for SAR exploration on the imidazopyridine scaffold was to improve aqueous solubility, while retaining good anti-plasmodium activity, as poor solubility was a key liability for the parent compound.[1] However, turbidimetric solubility determination using the UV-Vis spectrophotometry method was not performed as these compounds were anticipated to possess high solubility like previously reported imidazopyridazines.[2] Hence, they were assessed directly using the more meaningful H3D-adapted kinetic solubility method described earlier. These results are summarized in **Table 8.1**.

Introducing water-solubilizing carboxamides while retaining the sulfone/sulfoxide on the RHS of the core scaffold resulted in analogues with improved solubility (> 50 µM at pH 6.5). Most of the analogues tested showed high solubility (150–200 µM; **Table 8.1**) which was attributed to increased H-bonding of the carboxamide and the introduced sulfone/sulfoxide groups with water. Introduction of the carboxamide group was sufficient to improve solubility as highlighted by the sulfone morpholine **85** (**GS1 12**) and piperidin-4-ol **86** (**GS1 16**) analogues (solubility = 195 µM for both). Additionally, and as expected, the carboxylic acid derivative **78** (**GS1 08**) was also highly soluble (195 µM) due to the presence of the water solubilizing carboxylic acid moiety. However, this modification led to compromised anti-plasmodium activity (*Pf*NF54 IC_{50} > 6 µM).

Table 8.1: Physicochemical properties results of the target imidazopyridines

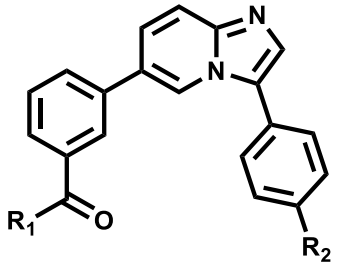

			Calculated properties				Experimental properties	
Code	**R_1**	**R_2**	**MW**	**cLogP**	**TPSA**	**HBD/ HBA**	**[a]MP (°C)**	**[b]Solubility (pH 6.5)**
78		SO_2Me	392.43	3.04	88.7	1/6	298.0	195
79		SO_2Me	419.50	2.58	71.8	0/6	99.0	195
80		SO_2Me	391.45	2.54	94.5	1/6	140.0	150
83	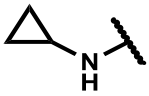	SO_2Me	431.51	3.25	80.5	1/6	151.5	100
84	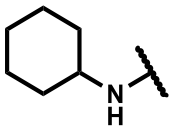	SO_2Me	473.59	4.38	80.5	1/6	217.0	-
85	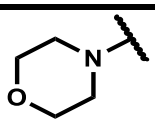	SO_2Me	461.54	2.61	81.0	0/7	120.0	195
86	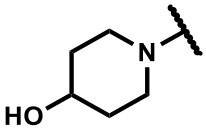	SO_2Me	475.56	2.57	92.0	1/7	217.5	195
81		SOMe	403.50	3.08	54.7	0/5	75.0	200
82		SOMe	375.45	2.71	77.5	1/5	214.0	190
87	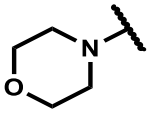	SOMe	445.54	3.14	63.9	0/6	108.0	200
88	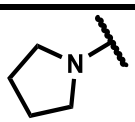	SOMe	429.54	3.67	54.7	0/5	82.0	195
89	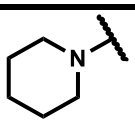	SOMe	443.57	4.27	54.7	0/5	98.0	200

"-", Not determined; MW, molecular weight in g.mol^{-1} calculated using ChemDraw Professional 16.0; TPSA, topological polar surface area in Å^2; HBD, hydrogen-bond donor; HBA, hydrogen-bond acceptor; cLogP, calculated log P, calculated using StarDrop™; [a]MP, melting point in °C as an average between the start temperature and end of melting process; [b]HPLC solubility in µM (pH 6.5), determined via HPLC-based DMSO "dry-down" method.

8.3 Assessment of factors influencing the solubility of imidazopyridines

Considering the high aqueous solubility observed in the compounds generated in this series, correlations between solubility and different physicochemical factors were investigated to identify their potential influence on solubility. These data also provide insights that can be extended to other series prospectively. Correlations between solubility based on the H3D-adapted method at pH 6.5 and selected physicochemical properties (MW, cLogP, TPSA, and MP) are shown in **Figure 8.1.**

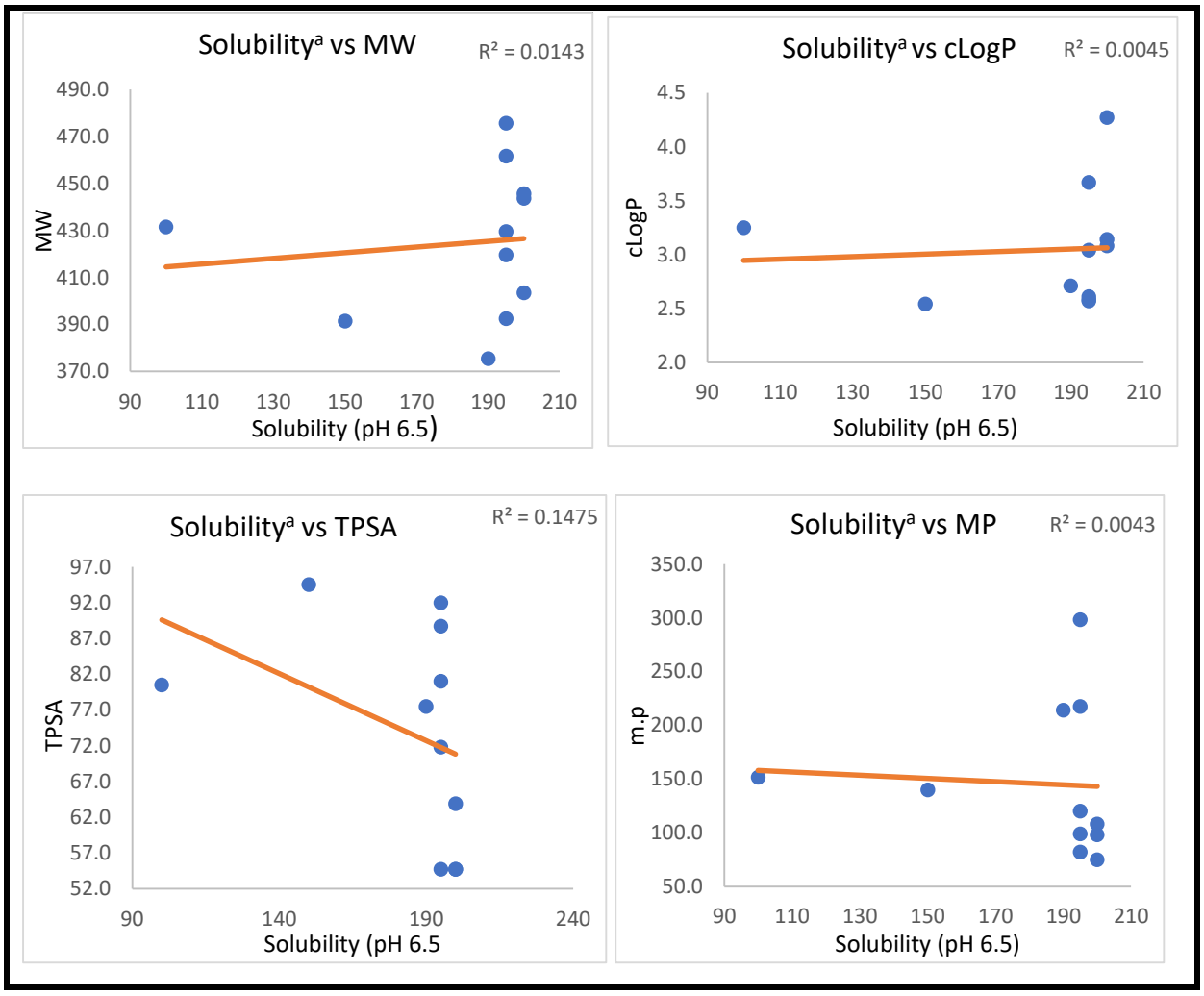

Figure 8.1: Correlations between solubility for selected imidazopyridines with various physicochemical parameters

[a]HPLC solubility in μM (pH 6.5), determined via HPLC-based DMSO "dry-down" method.

Weak correlations (R^2 = 0.004–0.148) were unexpectedly observed when solubility was expressed as a function of physicochemical parameters. One major reason to explain these weak correlations is that sulfoxides generally exhibit higher LogP values than sulfones yet they possess higher solubility due to the presence of more energetically favored HBAs that interact positively in aqueous media.[3] Apparently, sulfoxide formulation results in higher dipole moments and dielectric constants than in sulfones, which indicates improved polarity. This in turn elevates the water solubility of sulfoxides, despite sulfones having more oxygen binding sites.[4,5]

Experimental data such as HPLC retention time (t_R) and TLC retardation factor (R_f) also provide insight into the relative polarity. The t_Rs of matched sulfone-sulfoxide pairs were determined under similar experimental conditions such as buffer composition and solvent systems for the runs. This was ensured by using a generic fast gradient reversed phase HPLC analysis (octadecylsilane (C_{18})) as the stationary phase, aqueous ammonium acetate buffer as the mobile phase, and methanol as the organic modifier. The t_Rs obtained were then evaluated and the trends for selected matched imidazopyridine pairs generated are highlighted in **Figure 8.2**.

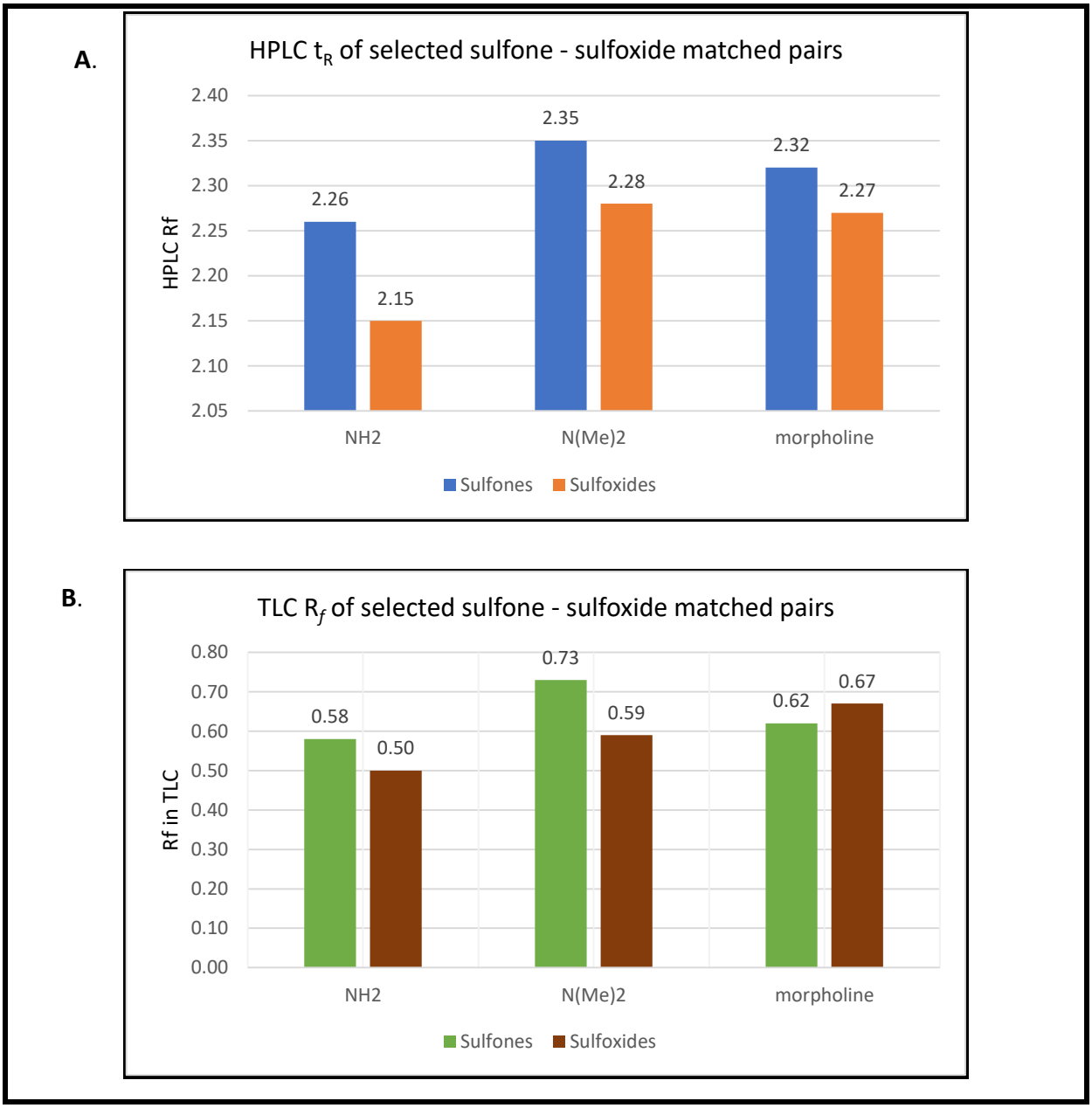

Figure 8.2: Clustered columns depicting **A**, HPLC retention times (t_R) of matched sulfone/sulfoxide pairs; and **B**, TLC retardation factor (R_f) values of matched sulfone/sulfoxide pairs

The sulfones (**Figure 8.2A**; in blue) consistently displayed higher retention times in the reversed phase HPLC column, an indicator of greater engagement with the non-polar C_{18} stationary phase hence lower polarity. In these experiments, the mobile phase is more polar than the stationary phase of the column and each gradient run starts with a high percentage of the aqueous medium to allow more water-soluble hence highly polar compounds to elute first. Details of the HPLC specifications, gradient mobile-phase composition and t_Rs of these

compounds and others explored in this study are provided in the Experimental section (Chapter 10) of this thesis.

As expected, there was also evidence of sulfoxides being more polar than sulfones based on the TLC R_f (10% MeOH/DCM, as the mobile phase) for the sulfone-sulfoxide pairs (**Figure 8.2B**), although morpholine sulfoxide deviated from this observation. R*f* represents the ratio of the distance moved by a compound relative to the solvent front.[6] In principle, polar compounds exhibit lower R_f values as the silica employed in this case contains polar silanol which interacts strongly with hydrophilic compounds and reduces the distance moved, in contrast to the reversed-phase HPLC.

Nonetheless, both the sulfones and sulfoxides were found to possess high and comparable solubility in this case (100–200 µM), suggesting a significant contribution of the carboxamide appendage of the molecules to aqueous dissolution. Consequently, a plot of a dataset comprising of sulfones and sulfoxides will tend to skew the trendline, leading to deviation from theoretical expectation as observed in this case. Additionally, limited diversity in solubility of the analogues analyzed potentially affected the strength of the observed trend, as most analogues from this series showed a solubility of 195–200 µM.

8.4 Compliance to drug-likeness of the synthesized imidazopyridines

Like the MLN0128 analogues, the imidazopyridines were subjected to assessment for conformity with the Veber's and Lipinski's Ro5. With regard to virtually-derived physicochemical parameters, all the imidazopyridine analogues were found to conform to the Lipinski's rule of 5:[7] MW range of 375.45–475.56 $g.mol^{-1}$, cLogP = 2.54–4.38, number of HBDs = 0–1, and number of HBAs = 5–7. All the compounds also conformed with the Veber's rule on TPSA lying in the range 54.7 to 94.5 $Å^2$ while the total sum of HBDs and HBAs was < 12 for all the analogues.

In addition, the analogues possessed 4–6 rotatable bonds, in line with the required threshold (≤ 12), a descriptor for predicted good permeation in animal models.[8] Interestingly, five analogues (**79**; **GS1 09**, **80**; **GS1 11**, **85**; **GS1 12**, **86**; **GS1 16**, and **82**; **GS1 22**; **Figure 8.3**) also conformed to the stricter Rule of 3 with regard to LogP and number of HBD (LogP ≤ 3, HBD ≤ 3) which, as already mentioned, are extensions of significant relevance in fragment-based drug discovery programs.[9] However, the compounds did to meet the guideline on MW (*i.e.*, ≤ 300 Da).

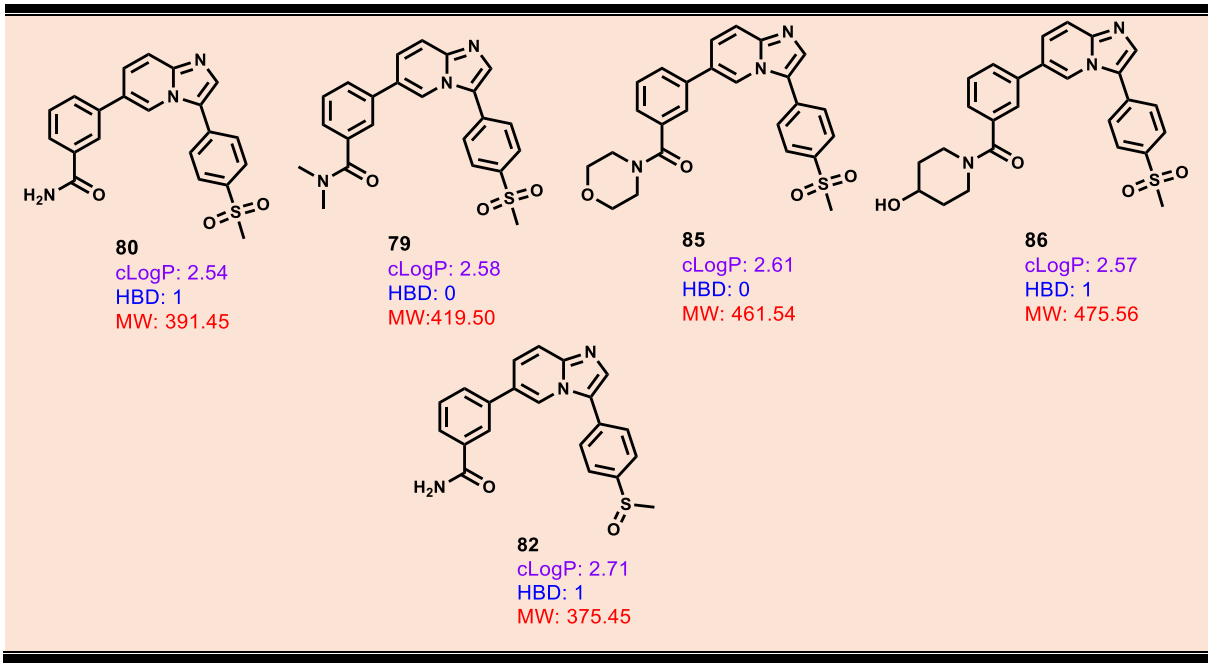

Figure 8.3: Chemical structures of imidazopyridines that conformed with Lipinski's rule of three on LogP and number of HBDs

8.5 Chapter summary

In summary, the experimentally (MP and solubility) and virtually derived physicochemical parameters (MW, LogP, TPSA, and number of HBDs, HBAs, and rotatable bonds) of the synthesized imidazopyridine analogues have been discussed. Physicochemical attributes that influence aqueous dissolution have been assessed for compounds. Finally, the "drug-likeness" and conformity of these compounds with Lipinski and Veber's rules have been discussed.

References

1. Le Manach, C.; Paquet, T.; Brunschwig, C.; Njoroge, M.; Han, Z.; Gonzàlez Cabrera, D.; Bashyam, S.; Dhinakaran, R.; Taylor, D.; Reader, J.; Botha, M.; Churchyard, A.; Lauterbach, S.; Coetzer, T.; Birkholtz, L.; Meister, S.; Winzeler, E.; Waterson, D.; Witty, M.; Wittlin, S.; Jiménez-Díaz, M.; Santos Martínez, M.; Ferrer, S.; Angulo-Barturen, I.; Street, L.; Chibale, K. A novel pyrazolopyridine with *in vivo* activity in *Plasmodium berghei*- and *Plasmodium falciparum*-infected mouse models from structure-activity relationship studies around the core of recently identified anti-malarial imidazopyridazines. *J. Med. Chem*. **2015**; 58 (21): 8713 - 8722. doi:10.1021/acs.jmedchem.5b01605.

2. Cheuka, P.; Centani, L.; Arendse, L.; Fienberg, S.; Wambua, L.; Renga, S.; Dziwornu, G.; Kumar, M.; Lawrence, N.; Taylor, D.; Wittlin, S.; Coertzen, D.; Reader, J.; van der Watt, M.; Birkholtz, L.; Chibale, K. New amidated 3,6-diphenylated imidazopyridazines with potent anti-plasmodium activity are dual inhibitors of *Plasmodium* phosphatidylinositol-4-kinase and cGMP-dependent protein kinase. *ACS Infect. Dis*. **2021**; 7 (1): 34 - 46. doi:10.1021/acsinfecdis.0c00481.

3. Surur, A.; Schulig, L. and Link, A. Interconnection of sulfides and sulfoxides in medicinal chemistry. *Arch Pharm (Weinheim)*. **2019**; 352 (1): 1 - 11. doi:10.1002/ardp.201800248.

4. Kingsbury CA. Why are the Nitro and Sulfone Groups Poor Hydrogen Bonders? *Fac Publ -- Chem Dep 81, Univ Nebraska-Lincoln*. **2015**. https://digitalcommons.unl.edu/cgi/viewcontent.cgi?referer=https://www.google.co.za/&httpsredir=1&article=1080&context=chemfacpub. Accessed: 2018-07-18. (Archived by WebCite® at http://www.webcitation.org/7107YWmgd).

5. Clark, T.; Murray, J.; Lane, P. and Politzer, P. Why are dimethyl sulfoxide and dimethyl sulfone such good solvents? *J. Mol. Model*. **2008**; 14 (8): 689 - 697. doi:10.1007/s00894-008-0279-y.

6. Rutkowska, E.; Pająk, K. and Jóźwiak, K. Lipophilicity - Methods of determination and its role in medicinal chemistry. *Acta. Pol. Pharm - Drug Res*. **2013**; 70 (1): 3 - 18.

7. Lipinski, C.; Lombardo, F.; Dominy, B. and Feeney, P. Experimental and computational approaches to estimate solubility and permeability in drug discovery and development

settings. *Adv. Drug Deliv. Rev.* **1997**; 23: 3 - 25.

8. Veber, F.; Johnson, S.; Cheng, H.; Smith, B.; Ward, K.; Kopple, K. Molecular properties that influence the oral bioavailability of drug candidates. *J. Med. Chem*. **2002**; 45 (12): 2615 - 2623. doi:10.1021/jm020017n.

9. Congreve, M.; Carr, R.; Murray, C.; Jhoti, H. A "Rule of Three" for fragment-based lead discovery? *Drug Discov. Today*. **2003**; 8 (19): 876 - 877. doi.org/10.1016/S1359-6446(03)02831-9.

CHAPTER 9

SUMMARY ON IMIDAZOPYRIDINES, CONCLUSIONS AND RECOMMENDATIONS FOR FUTURE WORK

9.1 Summary on imidazopyridines

Previous concerted SARs and phenotypic whole-cell screening led to the identification of the imidazopyridazines, a class of compounds, which showed high anti-plasmodium potency, promising PK properties, and high *in vivo* efficacy in *P. berghei*- and *Pf*-infected mouse models. However, the front-runner lead compounds identified were plagued with poor solubility and hERG liabilities.[12] Attempts to address these issues included alteration of the compound core by scaffold-hopping to obtain the imidazopyridine chemotype, but the issues still persisted.[3] Ensuing SAR on the imidazopyridazine scaffold produced sulfoxide analogues with improved aqueous solubility and devoid of hERG liability, although by inference, these were prone to *in vivo* metabolism of the sulfoxide group to sulfone.[4]

Recently, further iterations have resulted in the identification of a class of imidazopyridazines as dual *Pf*PI4K and PKG inhibitors, although the hERG activity of these compounds was not reported.[5] Inspired by these discoveries, this study, embarked on introducing molecular features on the imidazopyridine scaffold to improve aqueous solubility, de-risk hERG inhibition activity, and preserve dual parasitic kinase activity and anti-plasmodium potency.

The synthesis, pharmacological profiling, and physicochemical assessment of a series of compounds embodying the imidazopyridine core was successfully conducted in this study. Analogues equipotent against the asexual blood stages of both CQ-sensitive (*Pf*NF54) and multi-drug resistant (*Pf*K1) strains were identified, suggesting limited risk of cross-resistance. After investigating the anti-plasmodium mechanism of these compounds, PI4K was identified as the main driver of antiparasitic activity (IC_{50} = 0.001–0.113 µM against the recombinant protein). However, the modifications undertaken proved detrimental to *Pf*PKG activity as all the analogues were inactive (≤ 50% inhibition at 2 µM). An SAR summary of the anti-plasmodium and enzymatic data is captured in **Figure 9.1**.

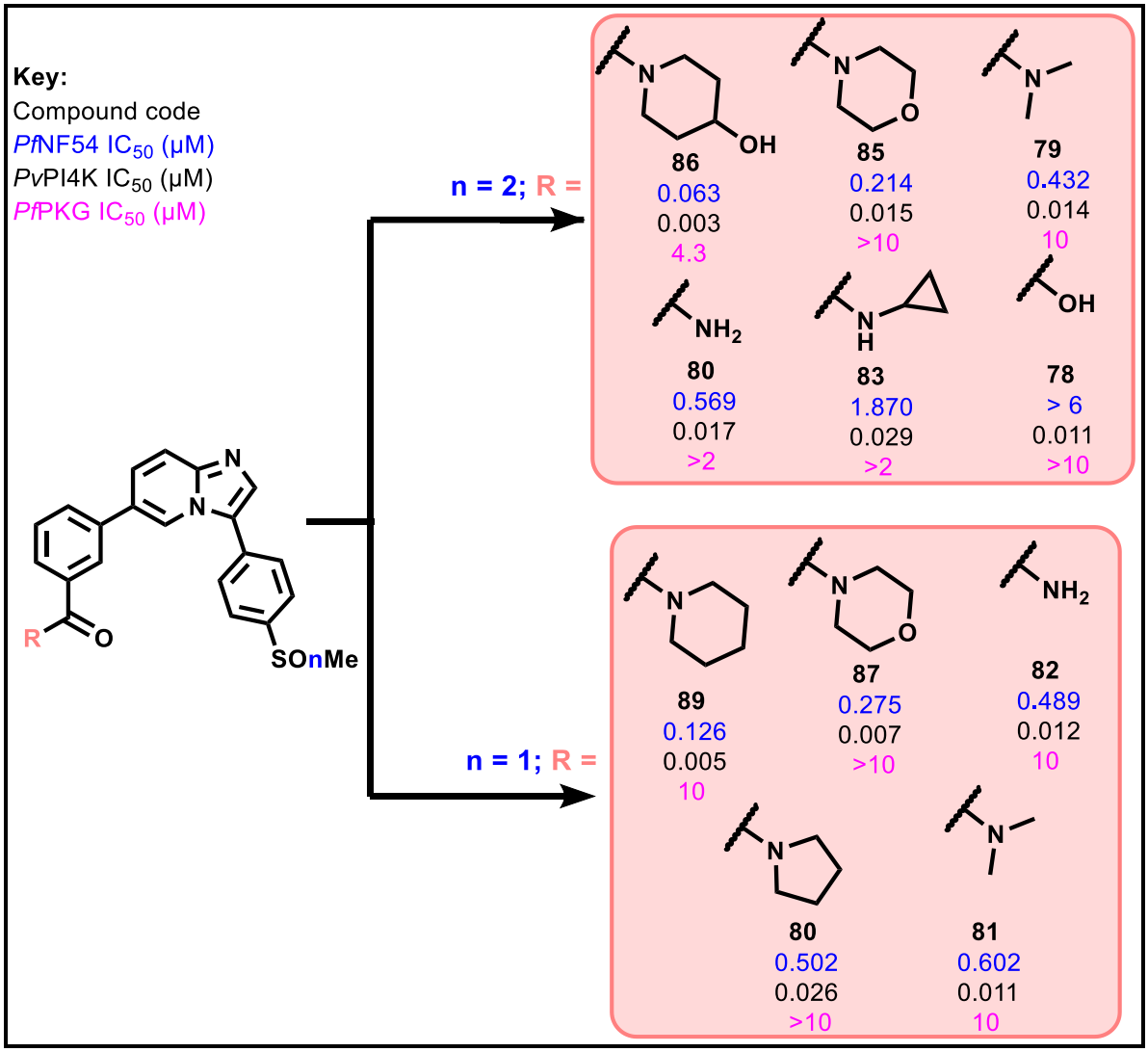

Figure 9.1: SAR summary of activity against asexual blood-stage *Pf*NF54 and enzymatic data for the synthesized imidazopyridines

Subsequent cytotoxicity and microsomal metabolic stability profiling identified several compounds with acceptable selectivity profiles (SI ≥ 100) and stability in HLMs, RLMs, and MLMs. In addition, the structural modifications introduced resulted in analogues showing high aqueous solubility (≥ 100 µM) and devoid of hERG activity (IC_{50} ≥ 10 µM), issues previously reported in related imidazopyridine and imidazopyridazine compounds. High conformity with both Lipinski and Veber's rules was also observed, suggesting favorable projected absorption and high oral bioavailability in animal models.[6,7]

Eventually, one analogue emerged as the most attractive with regard to biological and biochemical characteristics (**86**; **GS1 16**). It was the most potent against *Pf*NF54 (IC_{50} = 0.063 µM) and exhibited exemplary *in vitro* activity against the recombinantly expressed *Pv*PI4K protein (IC_{50} = 0.003 µM). Furthermore, it was devoid of hERG liability at 30 µM and showed

high solubility (195 µM) according to results obtained using the H3D-adapted HPLC method. It also showed other attractive physicochemical parameters, as listed in **Table 9.1**. Therefore, it conformed with all pre-set criteria in the pre-determined screening cascade and may thus be worthy of further pursuit as a potential anti-malarial lead compound.

Table 9.1: Biological and physicochemical profile of the front-runner imidazopyridine (**86**; **GS1 16**) identified in this study

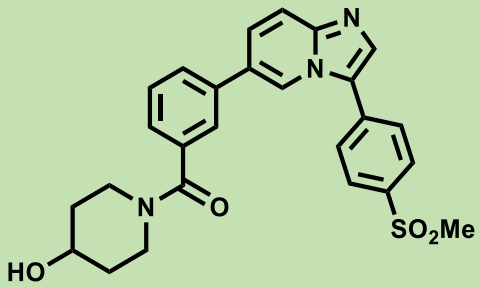

Biological properties		Physicochemical properties	
*Pf*NF54 (IC_{50}, µM)	0.063	Solubility[c] (µM)	195
*Pf*K1 (IC_{50}, µM)	0.100	MW ($g.mol^{-1}$)	475.56
*Pv*PI4K/*Pf*PKG (IC_{50}, µM)	0.003/ 4.3	TPSA ($Å^2$)	92.0
Microsomal stability (H/R/M)[a]	95.6/ 85.3 /87.5	cLogP	2.57
CHO (IC_{50}, µM)/ SI	> 50/ > 793	MP	217.5
hERG (IC_{50}, µM)	44.80[b]	HBD/ HBA	1/7

[a]Percentage compound remaining after 30 min incubation in human (H), rat (R), and mouse (M) liver microsomes; [b]value obtained via extrapolation; [c]measured using the UCT-adapted HPLC method.

9.2 Recommendations for future work on imidazopyridines

In this study, the anti-plasmodium potency, and drug-like properties of the front-runner sulfone analogue **86** (**GS1 16**) were demonstrated. It is recommended that the compound be upscaled and subjected to *in vivo* proof-of-concept studies in a relevant mouse model to establish its efficacy and PK properties. With regard to the microsomal metabolic instability of the racemate sulfoxide **87** (**GS1 25**), contrary to **89** (**GS1 27**), chiral separation and metabolite identification studies should be undertaken to decipher the metabolic hot-spot(s) and guide future modifications. It is also essential to investigate the potential multi-stage (gametocytocidal and liver-stage) activities of these compounds to determine their transmission blockade and chemoprotection potential, which are important target products profiles (TPPs) to support efforts towards malaria eradication.[8]

A summary of the pSAR, for future structural exploration for this series, is captured in **Figure 9.2**. To address the loss in anti-plasmodium *Pv*PKG activity as observed in this series relative

to the related imidazopyridazines (10- to 20-fold), future SAR studies should focus on introducing bio-isosteric substituents on the RHS of the molecule to compensate for this decline. Primary, secondary, and tertiary amides on the imidazopyridazine core have previously been demonstrated by Cheuka and co-workers to retain anti-plasmodium activity with dual inhibition of the *Plasmodium* targets of interest.[5]

Following on from this study, it is recommended that substitution patterns with basic sidechains, as in pSAR1, should be investigated through molecular docking and explored further to investigate activity in both parasite-based and enzymatic assays. Introduction of carboxamides, sulfonamides, and sulfonamide swap on the RHS of the molecule, as suggested in pSAR1, should be probed further to retain enzymatic activity and physicochemical properties.

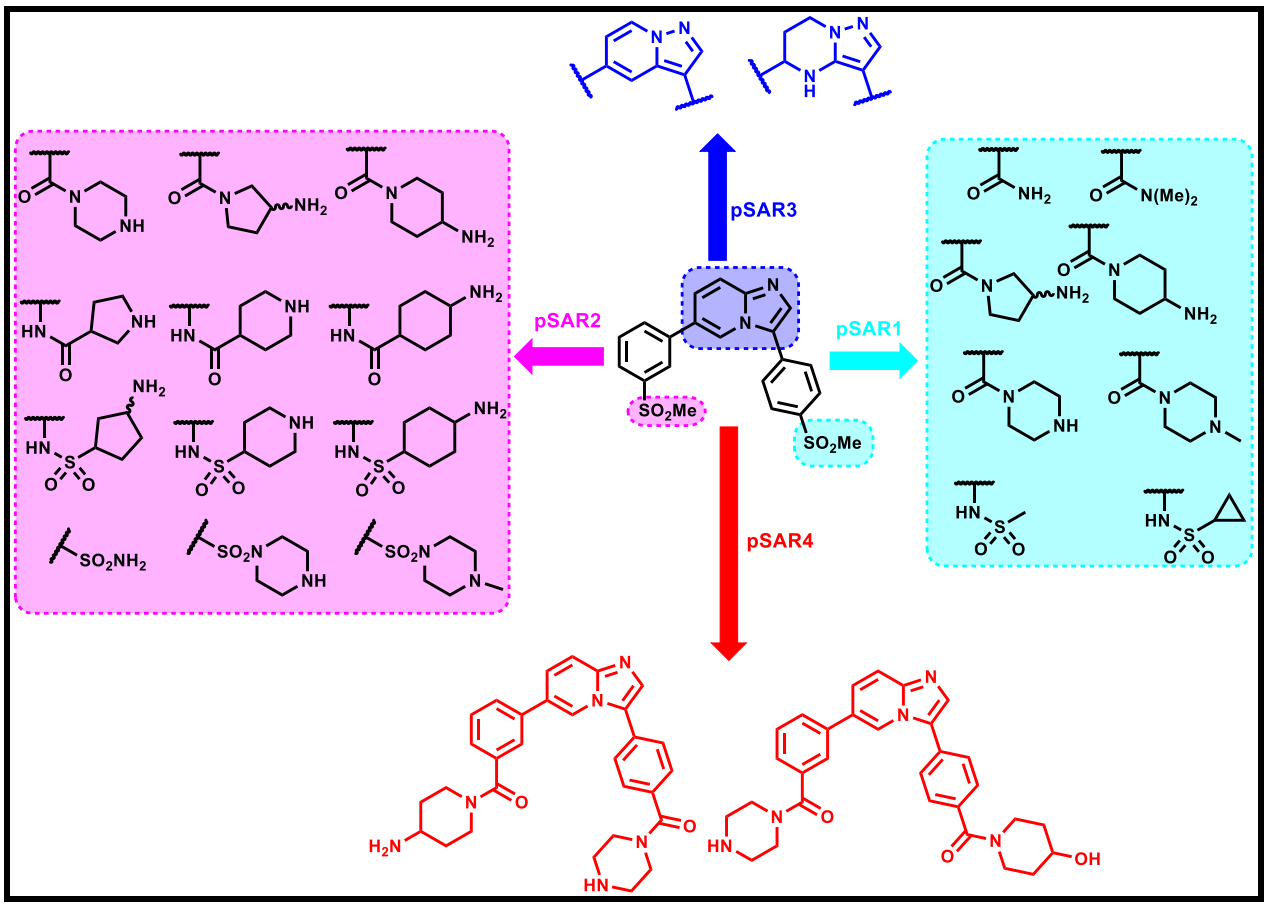

Figure 9.2: Proposed SAR for future exploration of the imidazopyridine scaffold

pSAR2 proposes incorporation of carboxamides on the LHS of the core scaffold with more basic sidechains in the *para* and *meta* positions. This is predicted to ensure stronger binding with Asp and Glu amino acid residues in the catalytic site of *Pf*PKG and improve activity against PI4K. Ideally, the sulfone and sulfoxide on the RHS should be investigated in tandem

in a pro-drug approach. The proposed substitutions on the LHS should also retain optimal solubility and anti-plasmodium activity. At the same time, docking studies should be utilized to guide appropriate substitutions and avoid any disruption of key interactions in the hinge-binding site. To increase diversity in the basic sidechains, amide swap and introduction of diverse sulfonamides as suggested in this pSAR should also be investigated. Similar sulfoxide and amide swap strategies have previously been exploited in the imidazopyridazine scaffold by Le Manach and colleagues to deliver a library of highly potent compounds, although the associated mechanistic studies were not explored.[1,2]

In addition, pSAR4 proposes the replacement of the imidazopyridine core-scaffold with other fused ring heterocyclics which will potentially preserve binding to the hinge region of the *Plasmodium* targets. These include the pyrazolo[1,5-*a*] pyridine and tetrahydro-pyrazolopyrimidines. This is also in agreement with previous exploration of these cores, although the targets of these chemotypes were not fully elucidated.[3] For example, 3,6-diarylated compounds based on these cores have previously been shown to possess good *in vitro* anti-plasmodium activity, albeit no enzymatic data was generated.[3] Ultimately, a combo recommendation applies for pSAR5 explorations where both phenyl rings on the scaffold would be simultaneously replaced by two phenyl carboxamide rings. At every point, computational modelling, synthesis, and enzymatic screening against wild-type and mutant-generated strains are important aspects to consider in driving future antimalarial programs based on these scaffolds and kinase targets. Off-target kinase activity will also need to be assessed going forward.

9.3 Conclusions on imidazopyridines

The work pursued on hERG and solubility optimization on the anti-malarial imidazopyridine chemotype has led to the identification of potent, highly soluble, and metabolically stable imidazopyridine compounds devoid of the hERG liability. Their associated MoA has been strongly linked to *Pv*PI4K inhibition with the strategies proving detrimental to *Pf*PKG inhibition. Eventually, a potential lead compound worthy of further pursuit has been identified.

References

1. Le Manach. C.; Cabrera, D.; Douelle, F.; Nchinda, A.; Younis, Y.; Taylor, D.; Wiesner, L.; White, K.; Ryan, E.; March, C.; Duffy, S.; Avery, V.; Waterson, D.; Witty, J.; Wittlin, S.; Charman, S.; Street, L.; Chibale, K. Medicinal chemistry optimization of antiplasmodial imidazopyridazine hits from high throughput screening of a softfocus kinase library: Part 1. *J. Med. Chem*. **2014**; 57: 2789 - 2798.

2. Le Manach, C.; Paquet, t.; Cabrera, D.; Younis, Y.; Taylor, D.; Wiesner, L.; Lawrence, N.; Schwager, S.; Waterson, D.; Witty, M.; Wittlin, S.; Street, L.; Chibale, K. Medicinal chemistry optimization of antiplasmodial imidazopyridazine hits from high throughput screening of a softfocus kinase library: Part 2. *J. Med. Chem*. **2014**; 57 (21): 8839 - 8848 doi:10.1021/jm500887k.

3. Le Manach, C.; Paquet, T.; Brunschwig, C.; Njoroge, M.; Han, Z.; Gonzàlez Cabrera, D.; Bashyam, S.; Dhinakaran, R.; Taylor, D.; Reader, J.; Botha, M.; Churchyard, A.; Lauterbach, S.; Coetzer, T.; Birkholtz, L.; Meister, S.; Winzeler, E.; Waterson, D.; Witty, M.; Wittlin, S.; Jiménez-Díaz, M.; Santos Martínez, M.; Ferrer, S.; Angulo-Barturen, I.; Street, L.; Chibale, K. A novel pyrazolopyridine with *in vivo* activity in *Plasmodium berghei*- and *Plasmodium falciparum*-infected mouse models from Structure-Activity Relationship studies around the core of recently identified anti-malarial imidazopyridazines. *J. Med. Chem*. **2015**; 58 (21): 8713 - 8722. doi:10.1021/acs.jmedchem.5b01605.

4. Cheuka, P.; Lawrence, N.; Taylor, D.; Wittlin, S.; Chibale, K. Antiplasmodial imidazopyridazines; structure activity relationship studies lead to the identification of analogues with improved solubility and hERG profiles. *Med. Chem. Comm.* **2018**: 1733 - 1745.. doi:10.1039/c8md00382c.

5. Cheuka P.; Centani, L.; Arendse, L.; Fienberg, S.; Wambua, L.; Renga, S.; Dziwornu, G.; Kumar, M.; Lawrence, N.; Taylor, D.; Wittlin, S.; Coertzen, D.; Reader, J.; van der Watt, M.; Birkholtz, L.; Chibale, K. New amidated 3,6-diphenylated imidazopyridazines with potent anti-plasmodium activity are dual inhibitors of *Plasmodium* phosphatidylinositol-4-kinase and cGMP-dependent protein kinase. *ACS Infect. Dis*. **2021**; 7 (1): 34 - 46. doi:10.1021/acsinfecdis.0c00481.

6. Lipinski, C.; Lombardo, F.; Dominy, B. and Feeney, P. Experimental and computational approaches to estimate solubility and permeability in drug discovery and development

settings. *Adv. Drug Deliv. Rev.* **1997**; 23: 3 - 25.

7. Veber, F.; Johnson, S.; Cheng, H.; Smith, B.; Ward, K.; Kopple, K. Molecular properties that influence the oral bioavailability of drug candidates. *J. Med. Chem*. **2002**; 45 (12): 2615 - 2623. doi:10.1021/jm020017n.

8. Burrows, J.; Duparc, S.; Gutteridge, W.; van Huijsduijnen, R.; Kaszubska, W.; Macintyre, F.; Mazzuri, S,; Möhrle, J.; Wells, T. New developments in anti-malarial target candidate and product profiles. *Malar. J*. **2017**; 16 (1): 1 - 29. doi:10.1186/s12936-016-1675-x.

CHAPTER 10

EXPERIMENTAL SECTION

10.1 Reagents, solvents, chromatography, and instrumentation

All commercially available chemicals and reagents were purchased from either Merck/Sigma-Aldrich (South Africa, SA) or Combi-Blocks (USA) and used without purification. The intermediate and target molecules were synthesized in glass flasks and subjected to appropriate purification techniques such as column chromatography (CC) and re-crystallization. Gravity CC was performed using Merck silica gel 60 (70–230 mesh) as the stationary phase while flash CC was conducted using a Biotage Isolera™ system. Analytical thin layer chromatography (TLC), performed on Merck silica gel 60 F_{254} pre-coated aluminium plates, was used to monitor the profile of reaction mixtures, fractions eluting from the columns, and compound purity . Chromatographic components were visualized under UV light at 254 nm whilemobile phase analytical-reagent (AR) grade solvents for TLC and column/flash chromatography were used as purchased.

Intermediates and the target compounds were characterized by ^{1}H-NMR, ^{13}C-NMR, high-performance liquid chromatography-mass spectrometry (HPLC-MS). Melting points (MP) were determined for the final target compounds using a Reichert-Jung Thermovar hot-stage microscope coupled with a digital thermometer (20–350 °C). ^{1}H-NMR spectra were recorded on either Varian® Mercury (300 MHz), Bruker® Ultrashield-Plus (400 MHz), or Bruker® (600 MHz) spectrometers against tetramethylsilane (TMS) as internal standard. ^{13}C-NMR spectra were recorded on the same instruments at 101 or 151 MHz. Deuterated DMSO (DMSO-d_6), methanol (MeOD), chloroform ($CDCl_3$), acetone or acetic acid (Sigma-Aldrich, South Africa) were used to dissolve the samples for the NMR experiments. Chemical shifts (δ) were reported in parts per million (ppm) and rounded to two decimal places. Coupling constants (J) were reported in Hertz (Hz) and rounded to one decimal place. Standard abbreviations were used in assigning ^{l}H-NMR signals such as d (doublet), dd (doublet of doublets), ddd (doublet of doublet of doublets), m (multiplet), q (quartet), s (singlet), t (triplet), or td (triplet of doublets). For chemical bond connectivity, results from HSQC and HMBC spectra were acquired using the 400 or 600 MHz Bruker® NMR equipment and processed using MestReNova® v.14 software.

The peak purities and mass spectra of the intermediate and target compounds were acquired on an Agilent reversed phase HPLC system. This was equipped with Agilent 1260® Infinity Binary Pump, Agilent 1260® Infinity Diode Array Detector, Agilent 1290® Infinity Column Compartment, Agilent 1260® Infinity Autosampler, Agilent 6120® Quadrupole LC/MS, and Peak Scientific® Genius 1050 Nitrogen Generator. The column used was a Kinetex® C_{18} (2.6 μm, 2.1 mm (internal diameter, ID) × 30 mm (length)) maintained at 35°C. The mobile phase flow rate was maintained at 0.7 mL/min, and the composition and fast gradient conditions and run times used are summarized in **Table 10.1**. HPLC grade MeOH (Sigma Aldrich) was used as the organic modifier. The injection volume was 1 μL. All target compounds used in physicochemical and biological profiling were determined to be >95% pure.

Mass spectra were obtained using electron spray ionization (ESI) and atmospheric pressure chemical ionization (APCI). The diode array detector was programmed to scan eluents at an absorption wavelength range of 210–640 nm. Data acquisitions were performed on IBM-compatible PC with HP Chemstation software (Hewlett-Packard Co., Amsterdam, The Netherlands). All spectroscopic analyses were undertaken at the Department of Chemistry, UCT.

Table 10.1: Summary of the mobile phase conditions used in high-performance liquid chromatography (HPLC) employed in this study

Time (Min)	Percentage composition (%)	
	10 mM NH_4OAc buffer in H_2O	10 mM NH_4OAc buffer in MeOH (90%)
0.00–0.30	85	15
0.30–1.20	85	15
1.20–4.50	0	100

10.2 Synthesis and characterization

10.2.1 Synthetic methods and characterization of MLN0128 analogues

10.2.1.1 Synthesis of 5-(4,4,5,5-tetramethyl-1,3,2-dioxaborolan-2-yl-)benzo[*d*]oxazol-2-amine, 5 (GS-19)

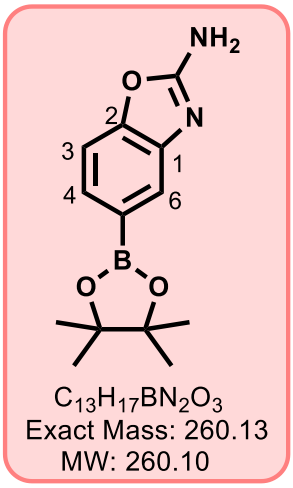

$C_{13}H_{17}BN_2O_3$
Exact Mass: 260.13
MW: 260.10

A solution of 3-bromobenzo[*d*]oxazol-2-amine (0.50 g, 2.35 mmol) in dioxane (3.5 mL) was purged with N_2 for 5 min and to this solution, bis(pinacolato)diboron (1.2 eq.), KOAc (3 eq.) and Pd(dppf)Cl_2 (1 mol%) were sequentially added. The resulting mixture was then heated at 100°C for 15 h with stirring. After completion of the reaction, the mixture was cooled to 20°C, EtOAc added (50 mL) and the mixture filtered through celite. Silica was added to the filtrate and concentrated *in vacuo*. The residue was then purified by flash CC (EtOAc: Hexane 0–55% v/v) to afford the crude product which was later triturated in diethyl ether to furnish the crucial intermediate. The product was obtained as an off-white solid (0.49 g, 80%); MP 161–162°C; R_f (40% EtOAc/hexane) 0.36; ^{1}H-NMR (MeOD, 400 MHz): δ_H 6.82 (d, J = 0.8 Hz, 1H, H^6), 6.68 (dd, J = 8.0 and 0.8 Hz, 1H, H^4), 6.47 (d, J = 8.0 Hz, 1H, H^3), and 0.55 (s, 12H, CH_3). ^{13}C-NMR (101 MHz, DMSO-d_6): δ_C 162.55, 149.84, 141.27, 126.90, 120.30, 115.70, 107.09, 82.86, and 22.97. HPLC-MS (APCI/ESI): purity 95%, t_R = 2.43 min, (*m*/*z*) $[M+H]^+$ = 261.1.

10.2.1.2 Synthesis of 1*H*-pyrazolo[3,4-*d*]pyrimidin-4-amine, 2 (GS-12)

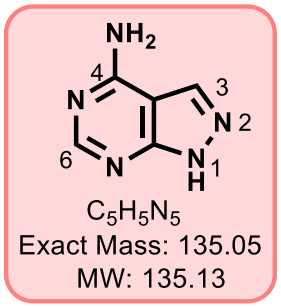

$C_5H_5N_5$
Exact Mass: 135.05
MW: 135.13

A suspension of 5-amino-1*H*-pyrazole-4-carbonitrile (3.0 g, 27.75 mmol) and formamide (15 mL) was heated at 180°C under N_2 atmosphere for 15 h. After completion of the reaction, the mixture was cooled to 20°C forming a brown precipitate, which was filtered off, washed with water (50 mL) and allowed to dry affording the product as a pale-brown solid (3.49 g, 93%); MP > 350°C; R_f (15% MeOH/DCM) 0.3; ^{1}H-NMR (DMSO-d_6, 400 MHz): δ_H 13.31 (broad s, 1H, NH^1), 8.12 (s, 1H, H^6), 8.07 (s, 1H, H^3), and 7.56 (broad s, 2H, 4-NH_2). ^{13}C-NMR (151 MHz, DMSO): δ_C 158.44, 156.26, 155.23, 133.05, and 100.04. HPLC-MS (APCI/ESI): purity 95%, t_R = 0.14 min, (*m*/*z*) $[M+H]^+$ = 136.0.

10.2.1.3 Synthesis of 3-iodo-1*H*-pyrazolo[3,4-*d*]pyrimidin-4-amine, 3 (GS-13)

A suspension of 1*H*-pyrazolo[3,4-*d*]pyrimidin-4-amine (**2**) (1.50 g, 11.11 mmol) in anhydrous DMF (13 mL) was charged with *N*-iodosuccinimide (1.5 eq.). The resulting reaction mixture was then heated at 80°C under N_2 atmosphere for 15 hours. After completion of the reaction, the mixture was then cooled to 20°C forming a precipitate which was filtered off, washed with EtOH (50 mL), and allowed to dry affording the product as a pale yellow solid (2.58 g, 89%); MP >350°C; R_f (10% MeOH/DCM) 0.6; ^{1}H-NMR (DMSO-d_6, 400 MHz): δ_H 13.31 (broad s, 1H, NH^1), 8.14 (s, 1H, H^6), 8.07 (s, 1H, H^3) and 7.16 (broad s, 2H, 4-NH_2). ^{13}C-NMR (101 MHz, DMSO-d_6): δ_C 158.03, 156.48, 155.49, 102.96, and 90.10. HPLC-MS (APCI/ESI): purity 97%, t_R = 0.24 min, (*m*/*z*) $[M+H]^+$ = 262.0.

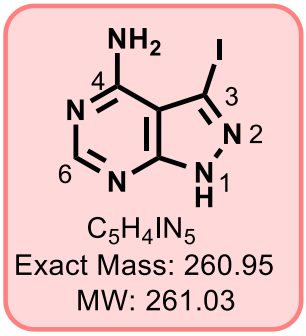

Synthesis of (5-fluoropyridin-3-yl)methanol

5-Fluoronicotinic acid (1 g, 7.1 mmol.) was dissolved in anhydrous THF (10 mL), cooled to 0°C and $LiAlH_4$ (1.6 eq.) added in small portions over a period of about 20 min. The mixture was then stirred under ice for 4 hours until the reaction was completed. The reaction mixture was quenched with water (5 mL), extracted in EtOAc (50 mL × 2), dried over anhydrous Na_2SO_4 and the solvent evaporated to afford the expected product which was used without further purification. The product was obtained as a red oil (0.6 g, 67%); R_f (10% MeOH/DCM) 0.5; ^{1}H-NMR (600 MHz, methanol-d_4): δ_H 8.40 (broad s, 1H, H^6), 8.37 (d, *J* = 2.8 Hz, 1H, H^2), 7.64 (broad dd, *J* = 9.6 and 2.4 Hz, 1H, H^4), and 4.71 (s, 2H, CH_2).^{13}C-NMR (101 MHz, methanol-d_4): δ_C 159.95 (d, *J* = 255.5 Hz, $^1J_{C\text{-}F}$, 1C), 143.49 (d, *J* = 4.0 Hz, $^4J_{C\text{-}F}$, 1C), 140.12 (d, *J* = 4.0 Hz, $^3J_{C\text{-}F}$, 1C), 135.69 (d, *J* = 24.2 Hz, $^2J_{C\text{-}F}$, 1C), 121.57 (d, *J* = 18.2 Hz, $^2J_{C\text{-}F}$, 1C), and 60.34. HPLC-MS (APCI/ESI): purity 95%, t_R = 0.18 min, (*m*/*z*) $[M+H]^+$ = 128.0.

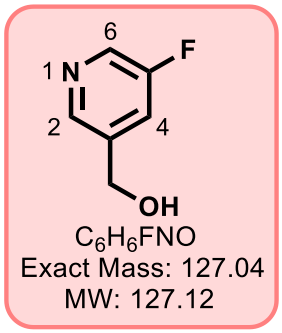

10.2.1.4 General procedure 1: Synthesis of chloromethyl pyridyl precursors

The appropriate phenylmethanol derivative (1 eq.) was dissolved in anhydrous DCM (8 mL), cooled to 0°C, and $SOCl_2$ (6.6 eq.) was added. The mixture was stirred at 0°C for 20 min and then overnight at 22°C. The reaction mixture was diluted with DCM (50 mL) and washed with saturated $NaHCO_3$ (50 mL × 2) to neutralize excess $SOCl_2$. The organic layer was dried over

anhydrous Na_2SO_4, filtered and the solvent evaporated to afford the expected product which was used without further purification.

3-(Chloromethyl)-5-fluoropyridine

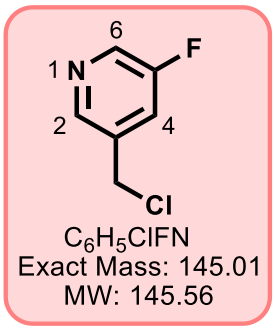

Using the general procedure 1 and a reaction mixture containing (5-fluoropyridin-3-yl)methanol (0.94 g, 7.39 mmol), the product was obtained as a brown solid (0.76 g, 71%); R_f (15% EtOAc/hexane) 0.5; ^{1}H-NMR (600 MHz, methanol-d_4): δ_H 8.44 (t, J = 1.8 Hz, 1H, H^6), 8.40 (d, J = 3.0 Hz, 1H, H^2), 7.70 (dt, J = 9.0 and 2.4 Hz, 1H, H^4), and 4.71 (s, 2H, CH_2). ^{13}C-NMR (151 MHz, methanol-d_4): δ_C 159.56 (d, J = 256.2 Hz, $^1J_{C\text{-}F}$, 1C), 144.93 (d, J = 4.1 Hz, $^4J_{C\text{-}F}$, 1C), 137.03 (d, J = 24.3 Hz, $^2J_{C\text{-}F}$, 1C), 136.32 (d, J = 4.1 Hz, $^3J_{C\text{-}F}$, 1C), 123.36 (d, J = 19.2 Hz, $^2J_{C\text{-}F}$, 1C), and 41.28. HPLC-MS (APCI/ESI): purity > 99%, t_R = 0.21 min, (m/z) $[M+H]^+$ = 146.0.

2-(Chloromethyl)-5-fluoropyridine

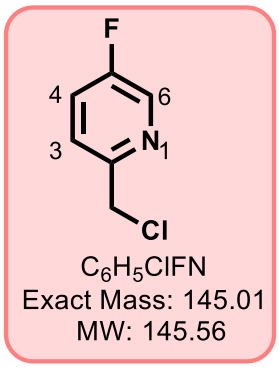

Using the general procedure 1 and a reaction mixture containing (5-fluoropyridin-2-yl)methanol (1 g, 7.87 mmol), the product was obtained as an off-white powder (0.85 g, 74%); R_f (15% EtOAc/hexane) 0.4; ^{1}H-NMR (600 MHz, methanol-d_4) δ_H 8.39 (d, J = 2.4 Hz, 1H, H^6), 7.61 (td, J = 8.4 and 2.4 Hz, 1H, H^4), 7.58 (dd, J = 8.4 and 4.8 Hz, 1H, H^3), and 4.67 (s, 2H, CH_2). ^{13}C-NMR (151 MHz, methanol-d_4) δ_C 159.19 (d, J = 255.2 Hz, $^1J_{C\text{-}F}$, 1C), 153.02 (d, J = 3.0 Hz, $^4J_{C\text{-}F}$, 1C), 136.90 (d, J = 24.2 Hz, $^2J_{C\text{-}F}$, 1C), 124.62 (d, J = 4.5 Hz, $^3J_{C\text{-}F}$, 1C), 124.10 (d, J = 19.6 Hz, $^2J_{C\text{-}F}$, 1C), and 44.88. HPLC-MS (APCI/ESI): purity < 95%, t_R = 0.18 min, (m/z) $[M+H]^+$ = 146.0.

2-(Chloromethyl)-6-fluoropyridine

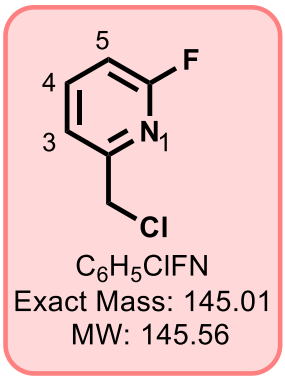

Using the general procedure 1 and a reaction mixture containing (6-fluoropyridin-2-yl)methanol (0.95 g, 7.47 mmol), the product was obtained as an off-white powder (0.75 g, 69%); R_f (15% EtOAc/hexane) 0.5; ^{1}H-NMR (600 MHz, methanol-d_4): δ_H 7.93 (td, J = 8.4 and 7.8 Hz, 1H, H^4), 7.41 (dd, J = 7.8 and 2.4 Hz, 1H, H^3), 6.99 (dd, J = 8.4 and 2.4 Hz, 1H, H^5), and 4.59 (s, 2H, CH_2). ^{13}C-NMR (151 MHz, methanol-d_4): δ_C 162.98 (d, J = 240.1 Hz, $^1J_{C\text{-}F}$, 1C), 155.51 (d, J = 13.0 Hz, $^3J_{C\text{-}F}$, 1C), 142.67 (d, J = 7.9 Hz, $^4J_{C\text{-}F}$, 1C), 120.26 (d, J = 4.1 Hz, $^2J_{C\text{-}F}$, 1C), 108.71 (d, J = 36.5 Hz, $^2J_{C\text{-}F}$, 1C), and 44.78. HPLC-MS (APCI/ESI): purity < 95%, t_R = 0.25 min, (m/z) $[M+H]^+$ = 146.0.

2-(Chloromethyl)-6-(trifluoromethyl)pyridine

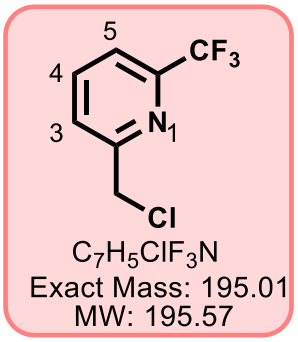

Using the general procedure 1 and a reaction mixture containing (6-(trifluoromethyl)pyridin-2-yl)methanol (0.80 g, 4.52 mmol), the product was obtained as an off-white solid (0.77 g, 87%); R_f (15% EtOAc/hexane) 0.46; ^{1}H-NMR (400 MHz, methanol-d_4): δ_H 8.08 (t, J = 8.0 Hz, 1H, H^4), 7.83 (broad d, J = 8.0 Hz, 1H, H^3), 7.77 (broad d, J = 8.0 Hz, 1H, H^5), and 4.78 (s, 2H, CH_2). ^{13}C-NMR (101 MHz, methanol-d_4): δ_C 157.94, 147.38 (q, J = 35.0 Hz, $^2J_{C\text{-}F}$, 1C), 139.05, 125.97, 121.42 (q, J = 274.0 Hz, $^1J_{C\text{-}F}$, 1C), 119.56 (broad q, J = 2.2 Hz, $^3J_{C\text{-}F}$, 1C), and 45.12. HPLC-MS (APCI/ESI): purity 96%, t_R = 0.19 min, (m/z) $[M+H]^+$ = 196.0.

10.2.1.5 General procedure 2: Synthesis of intermediates 6a–62a

A suspension of 3-iodo-1*H*-pyrazolo[3,4-*d*] pyrimidin-4-amine (**3**) (1 eq.) and K_2CO_3 (2 eq.) in DMF (6 mL) was treated with the appropriate bromobenzyl derivative (1.2 eq.) or chlorobenzyl derivative and resulting mixture stirred at 30°C or 50°C, respectively for 2h. The reaction mixture was then cooled to room temperature (20°C), diluted with water (50 mL) and extracted with EtOAc (50 mL × 2). The combined organic layer was dried over anhydrous Na_2SO_4 and concentrated *in vacuo* to obtain the crude product, which was then purified on column or flash chromatography (0–8% MeOH/DCM) to furnish the required intermediates.

3-Iodo-1-isopropyl-1*H*-pyrazolo[3,4-*d*]pyrimidin-4-amine, 62a (GS 14)

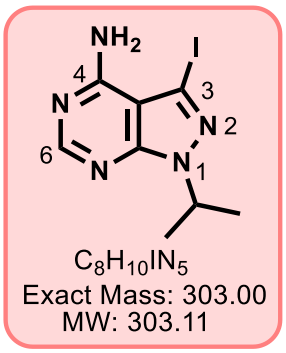

Using the general procedure 2 and a reaction mixture containing **3** (0,40 g, 1.53 mmol) and isopropyl bromide (1.2 eq.), the product was obtained as an off-white solid (0.25 g, 54%); MP 203–204°C; R_f (10% MeOH/DCM) 0.6; ^{1}H-NMR (DMSO-d_6, 600 MHz): δ_H 8.18 (s, 1H, H^6), 4.95 (1H, septet, CH), and 1.41 (d, J = 6.6 Hz, 6H, CH_3). ^{13}C-NMR (DMSO-d_6, 151 MHz): δ_C 158.10, 156.19, 153.01, 103.67, 88.59, 49.27, and 22.24. HPLC-MS (APCI/ESI): purity 98%, t_R = 2.23 min, (m/z) $[M+H]^+$ = 304.0.

1-Benzyl-3-iodo-1H-pyrazolo[3,4-*d*]pyrimidin-4-amine, 6a (GS 76)

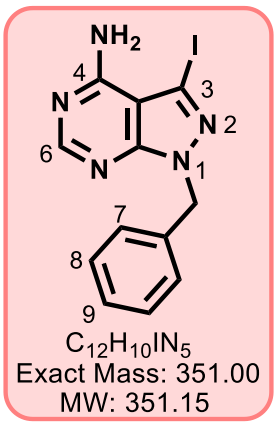

Using the general procedure 2 and a reaction mixture containing **3** (0.35 g, 1.15 mmol), K_2CO_3 (2 eq.) and benzyl chloride (1.2 eq.) the product was obtained as an off-white powder (0.22 g, 46%); MP 207–208°C; R_f (10% MeOH/DCM) 0.5; ^{1}H-NMR (DMSO-d_6, 600 MHz): δ_H 8.22 (s, 1H, H^6), 7.31–7.28 (m, 2H, H^8), 7.26–7.24 (m, 1H, H^9), 7.22–7.20 (m, 2H, H^7), and 5.46 (s, 2H, CH_2). ^{13}C-NMR (DMSO-d_6, 151 MHz): δ_C 158.20, 156.76, 153.99, 137.33, 129.06 (2C), 128.89, 128.14, 128.08 (2C), 103.59, 89.91, and 50.49. HPLC-MS (APCI/ESI): purity > 99%, t_R = 2.38 min, (m/z) $[M+H]^+$ = 352.0.

1-(4-Chlorobenzyl)-3-iodo-1*H*-pyrazolo[3,4-*d*]pyrimidin-4-amine, 7a (GS 54)

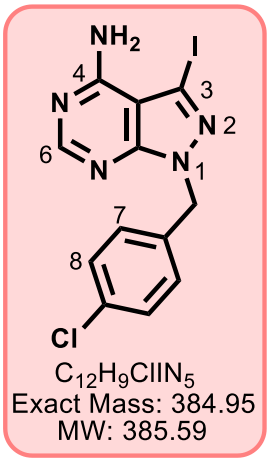

Using the general procedure 2 and a reaction mixture containing **3** (0.40 g, 1.53 mmol), K_2CO_3 (2 eq.) and 4-chlorobenzyl bromide (1.2 eq.) the product was obtained as a yellow powder (0.25 g, 43%); MP 246–247°C; R_f (10% MeOH/DCM) 0.4; ^{1}H-NMR (DMSO-d_6, 600 MHz): δ_H 8.22 (s, 1H, H^6), 7.35 (d, J = 9.0 Hz, 2H, H^8), 7.23 (d, J = 9.0, Hz 2H, H^7), and 5.46 (s, 2H, CH_2). ^{13}C-NMR (DMSO-d_6, 151 MHz): δ_C 158.21, 156.81, 154.00, 136.30, 132.84, 129.99 (2C), 129.07 (2C), 103.63, 90.17, and 49.75. HPLC-MS (APCI/ESI): purity > 99%, t_R = 2.51 min, (m/z) $[M+H]^+$ = 385.9

1-(4-Flourobenzyl)-3-iodo-1*H*-pyrazolo[3,4-*d*]pyrimidin-4-amine, 8a (GS 64)

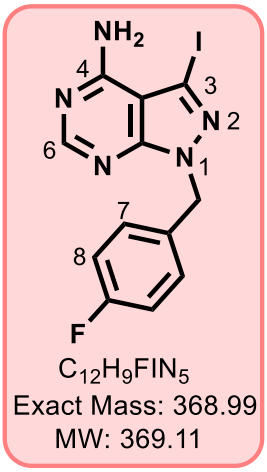

$C_{12}H_9FIN_5$
Exact Mass: 368.99
MW: 369.11

Using the general procedure 2 and a reaction mixture containing **3** (0.40 g, 1.53 mmol), K_2CO_3 (2 eq.) and 4-fluorobenzyl bromide (1.2 eq.), the product was obtained as an off-white solid (0.26g, 44%); MP 194–195°C R_f (10% MeOH/DCM) 0.6; ^{1}H-NMR (DMSO-d_6, 600 MHz): δ_H 8.23 (s, 1H, H^6), 7.28 (pseudo dd, J = 9.0 and 6.0 Hz, 2H, H^8), 7.13 (t, J = 9.0 Hz, 2H, H^7), and 5.46 (s, 2H, CH_2). ^{13}C-NMR (DMSO-d_6, 151 MHz): δ_C 162.08 (d, J = 244.6 Hz, $^1J_{C\text{-}F}$, 1C), 158.27, 156.79, 153.92, 133.53 (d, J = 3.0 Hz, $^4J_{C\text{-}F}$, 1C), 130.28 (d, J = 7.6 Hz, $^3J_{C\text{-}F}$, 2C), 115.88 (d, J = 22.7 Hz, $^2J_{C\text{-}F}$, 2C), 103.62, 90.03, and 49.74. HPLC-MS (APCI/ESI): purity 98%, t_R = 2.43 min, (*m*/*z*) $[M+H]^+$ = 370.0.

1-(4-Cyanobenzyl)-3-iodo-1*H*-pyrazolo[3,4-*d*]pyrimidin-4-amine, 9a (GS 62)

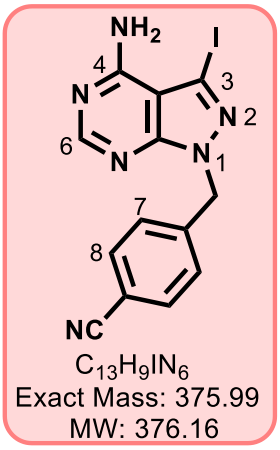

$C_{13}H_9IN_6$
Exact Mass: 375.99
MW: 376.16

Using the general procedure 2 and a reaction mixture containing **3** (0.50 g, 1.92 mmol), K_2CO_3 (2 eq.) and 4-(bromomethyl)benzonitrile (1.2 eq.), the product was obtained as an off-white solid (0.32g, 44%); MP 246–247°C; R_f (10% MeOH/DCM) 0.5; ^{1}H-NMR (DMSO-d_6, 600 MHz): δ_H 8.22 (s, 1H, H^6), 7.79 (d, J = 8.4 Hz, 2H, H^8), 7.37 (d, J = 8.4 Hz, 2H, H^7), and 5.58 (s, 2H, CH_2). ^{13}C-NMR (DMSO-d_6, 151 MHz): δ_C 158.24, 156.90, 154.19, 142.85, 133.07 (2C), 128.82 (2C), 119.05, 110.98, 103.66, 90.59, and 49.99. HPLC-MS (APCI/ESI): purity 98%, t_R = 2.30 min, (*m*/*z*) $[M+H]^+$ = 377.0.

3-Iodo-1-(3-(trifluoromethyl)benzyl)-1*H*-pyrazolo[3,4-*d*]pyrimidin-4-amine, 10a (GS 58)

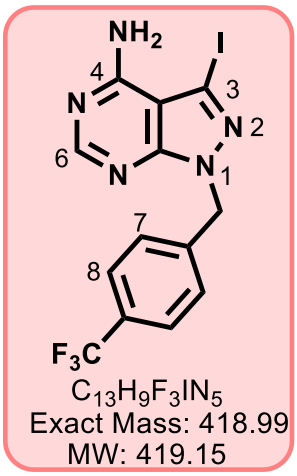

$C_{13}H_9F_3IN_5$
Exact Mass: 418.99
MW: 419.15

Using the general procedure 2 and a reaction mixture containing **3** (0.40 g, 1.53 mmol), K_2CO_3 (2 eq.) and 4-(trifluoromethyl)benzyl bromide (1.2 eq.), the product was obtained as an off-white solid (0.33 g, 51%); MP 227–228°C; R_f (10% MeOH/DCM) 0.5; ^{1}H-NMR (DMSO-d_6, 600 MHz): δ_H 8.23 (s, 1H, H^6), 7.68 (d, J = 7.8 Hz, 2H, H^8), 7.41 (d, J = 8.4 Hz, 2H, H^7), and 5.58 (s, 2H, CH_2). ^{13}C-NMR (DMSO-d_6, 151 MHz): δ_C 158.24, 156.88, 154.15, 141.98, 128.86 (q, J = 31.7 Hz, $^2J_{C\text{-}F}$, 1C), 128.76 (2C), 126.03 (broad q, J = 3.02 Hz, $^3J_{C\text{-}F}$, 2C), 126.03 (q, J = 273.3 Hz, $^1J_{C\text{-}F}$, 1C), 103.65, 90.46, and 49.93. HPLC-MS (APCI/ESI): purity 98%, t_R = 2.51 min, (*m*/*z*) $[M+H]^+$ = 419.9.

3-Iodo-1-(4-methylbenzyl)-1*H*-pyrazolo[3,4-*d*]pyrimidin-4-amine, 11a (GS 68)

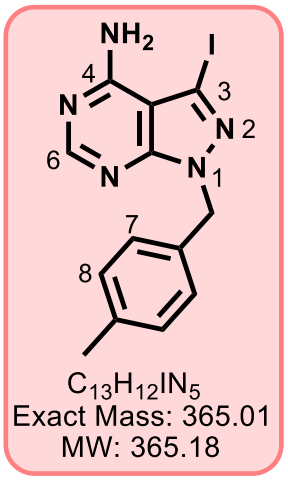

Using the general procedure 2 and a reaction mixture containing **3** (0.40 g, 1.53 mmol), K_2CO_3 (2 eq.) and 4-methylbenzyl bromide (1.2 eq.), the product was obtained as an off-white solid (0.25 g, 44%); MP 220–221°C; R_f (10% MeOH/DCM) 0.5; ^{1}H NMR (DMSO-d_6, 400 MHz): δ_H 8.25 (s, 1H, H^6), 7.13 (s, 4H, $H^{7,8}$), 5.43 (s, 2H, CH_2), and 2.26 (s, 3H, CH_3). ^{13}C-NMR (DMSO-d_6, 101 MHz): δ_C 158.19, 156.71, 153.93, 137.40, 134.33, 129.57 (2C), 128.13 (2C), 103.61, 89.65, 50.32, and 21.12. HPLC-MS (APCI/ESI): purity 95%, t_R = 2.50 min, (*m*/*z*) $[M+H]^+$ = 366.0

3-Iodo-1-(3-methoxybenzyl)-1*H*-pyrazolo[3,4-*d*]pyrimidin-4-amine, 12a (GS 38)

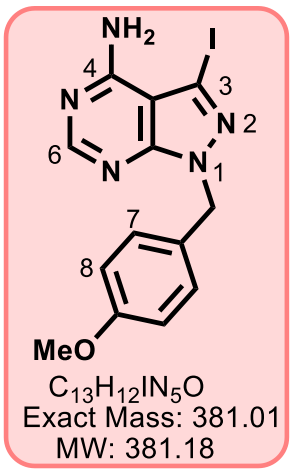

Using the general procedure 2 and a reaction mixture containing **3** (0.50 g, 1.92 mmol), K_2CO_3 (2 eq.) and 4-methoxybenzyl bromide (1.2 eq.), the product was obtained as an off-white solid (0.37 g, 51%); MP 192–193°C; R_f (10% MeOH/DCM) 0.3; ^{1}H-NMR (DMSO-d_6, 600 MHz): δ_H 8.23 (s, 1H, H^6), 7.20 (d, *J* = 9.0 Hz, 2H, H^8), 6.86 (d, *J* = 8.4 Hz, 2H, H^7), 5.38 (s, 2H, CH_2), and 3.70 (s, 3H, OMe). ^{13}C-NMR (DMSO-d_6, 151 MHz): δ_C 159.28, 158.16, 156.69, 153.79, 129.66 (2C), 129.28, 114.44 (2C), 103.58, 89.65, 55.55, and 50.03. HPLC-MS (APCI/ESI): purity > 99%, t_R = 2.38 min, (*m*/*z*) $[M+H]^+$ = 382.0.

1-(3-Fluorobenzyl)-3-iodo-1*H*-pyrazolo[3,4-*d*]pyrimidin-4-amine, 14a (GS 72)

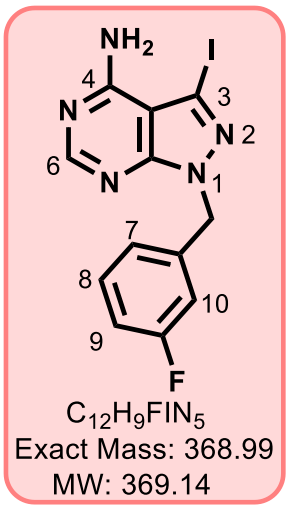

Using the general procedure 2 and a reaction mixture containing **3** (0.50 g, 1.92 mmol), K_2CO_3 (2 eq.) and 3-fluorobenzyl bromide (1.2 eq.), the product was obtained as an off-white powder (0.35 g, 50%); MP 176–177°C; R_f(8% MeOH/DCM) 0.5; ^{1}H-NMR (DMSO-d_6, 600 MHz): δ_H 8.22 (s, 1H, H^6), 7.35 (ddd *J* = 7.8, 6.0 and 1.8 Hz, 1H, H^8), 7.10 (ddd, *J* = 8.4, 3.0 and 1.2 Hz, 1H, H^9), 7.05–7.03 (m, 1H, H^{10}), 7.03–7.00 (m, 1H, H^7), and 5.49 (s, 2H, CH_2). ^{13}C-NMR (DMSO-d_6, 151 MHz): δ_C 163.36 (d, *J* = 244.6 Hz, $^1J_{C\text{-}F}$, 1C), 158.23, 156.84, 154.07, 140.10 (d, *J* = 7.6 Hz, $^3J_{C\text{-}F}$, 1C), 131.19 (d, *J* = 9.1 Hz, $^3J_{C\text{-}F}$, 1C), 124.08 (d, *J* = 3.0 Hz, $^4J_{C\text{-}F}$, 1C), 115.07, (d, *J* = 19.6 Hz, $^2J_{C\text{-}F}$, 1C), 114.91 (d, *J* = 21.1

Hz, $^{2}J_{C\text{-}F}$, 1C), 103.63, 90.28, and 49.85. HPLC-MS (APCI/ESI): purity 97%, t_R = 2.42 min, (*m*/*z*) $[M+H]^+$ = 370.0.

3-Iodo-1-(3-(trifluoromethyl)benzyl)-1*H*-pyrazolo[3,4-*d*]pyrimidin-4-amine, 15a (GS 70)

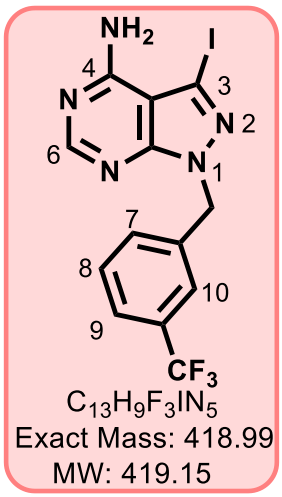

Using the general procedure 2 and a reaction mixture containing **3** (0.40 g, 1.53 mmol), K_2CO_3 (2 eq.) and 3-(trifluoromethyl)benzyl bromide (1.2 eq.), the product was obtained as an off-white solid (0.44 g, 68%); MP 190–191°C; R_f (10% MeOH/DCM) 0.5; ^{1}H NMR (DMSO-d_6, 600 MHz): δ_H 8.23 (s, 1H, H^6), 7.65–7.63 (m, 2H, $H^{9, 10}$), 7.55 (pseudo t, *J* = 7.8 Hz, 1H, H^8), 7.47–7.45 (m, 1H, H^7), and 5.58 (s, 2H, CH_2). ^{13}C-NMR (DMSO-d_6, 151 MHz): δ_C 158.24, 156.89, 154.12, 138.72, 132.20, 130.31, 129.82 (q, *J* = 31.7 Hz, $^{2}J_{C\text{-}F}$, 1C), 125.40 (q, *J* = 273.3 Hz, $^{1}J_{C\text{-}F}$, 1C), 124.99 (q, *J* = 4.5 Hz, $^{3}J_{C\text{-}F}$, 1C), 124.72 (q, *J* = 3.0 Hz, $^{3}J_{C\text{-}F}$, 1C), 103.65, 90.44, and 49.85. HPLC-MS (APCI/ESI): purity 98%, t_R = 2.50 min, (*m*/*z*) $[M+H]^+$ = 420.0.

1-(3-Methylbenzyl)-3-iodo-1*H*-pyrazolo[3,4-*d*]pyrimidin-4-amine, 16a (GS 66)

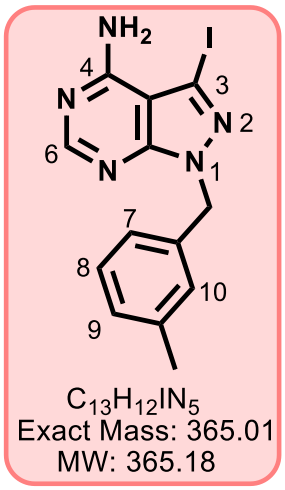

Using the general procedure 2 and a reaction mixture containing **3** (0.40 g, 1.53 mmol), K_2CO_3 (2 eq.) and 3-methylbenzyl bromide (1.2 eq.), the product was obtained as an off-white powder (0.28 g, 51%); MP 190–191°C; R_f (10% MeOH/DCM) 0.5; ^{1}H-NMR (DMSO-d_6, 600 MHz): δ_H 8.22 (s, 1H, H^6), 7.35 (pseudo t, *J* = 7.8 Hz, 1H, H^8), 7.07–7.05 (m, 1H, H^7), 7.05–7.04 (m, 1H, H^{10}), 7.00–6.98 (m, 1H, H^9), 5.41 (s, 2H, CH_2), and 2.23 (s, 3H, CH_3). ^{13}C-NMR (DMSO-d_6, 151 MHz): δ_C 158.19, 156.75, 153.96, 138.24, 137.25, 128.98, 128.80, 128.67, 125.24, 103.57, 89.84, 50.46, and 21.41. HPLC-MS (APCI/ESI): purity 97%, t_R = 2.46 min, (*m*/*z*) $[M+H]^+$ = 366.0.

1-(3-Chlorobenzyl)-3-iodo-1*H*-pyrazolo[3,4-*d*]pyrimidin-4-amine, 17a (GS 56)

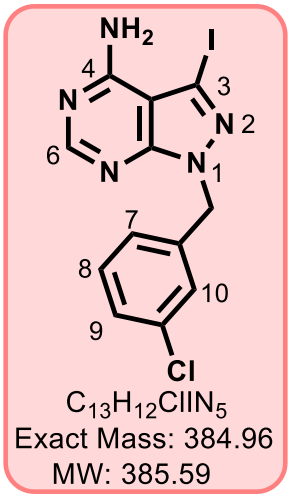

Using the general procedure 2 and a reaction mixture containing **3** (0.40 g, 1.53 mmol), K_2CO_3 (2 eq.) and 3-chlorobenzyl bromide (1.2 eq.), the product was obtained as an off-white powder (0.23 g, 39%); MP 177–178°C; R_f (10% MeOH/DCM) 0.5; ^{1}H-NMR (DMSO-d_6, 600 MHz): δ_H 8.24 (s, 1H, H^6), 7.36–7.33 (m, 2H, $H^{8,9}$), 7.30–7.29 (m, 1H, H^{10}), 7.15 (ddd, J = 5.4, 4.2 and 1.8 Hz, 1H, H^7), and 5.49 (s, 2H, CH_2). ^{13}C-NMR (DMSO-d_6, 151 MHz): δ_C 158.23, 156.86, 154.05, 139.73, 133.60, 131.05, 128.17, 127.92, 126.76, 103.63, 90.32, and 49.78. HPLC-MS (APCI/ESI): purity 98%, t_R = 2.50 min, (*m*/*z*) $[M+H]^+$ = 385.9.

1-(3-(Dimethylamino)benzyl)-3-iodo-1*H*-pyrazolo[3,4-*d*]pyrimidin-4-amine, 19a

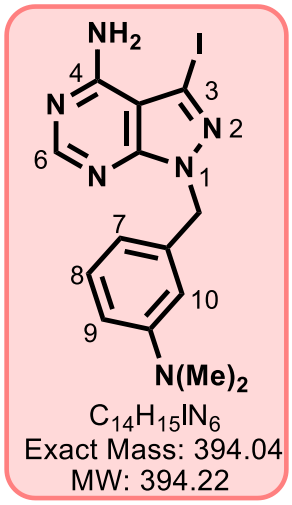

Using the general procedure 2 and a reaction mixture containing **3** (0.80 g, 3.06 mmol), K_2CO_3 (2 eq.) and 3-(chloromethyl)-*N*,*N*-dimethylaniline (1.2 eq.), the product was obtained as an off-white powder (485 mg, 40%); R_f (10% MeOH/DCM) 0.5; ^{1}H-NMR (DMSO-d_6, 400 MHz): δ_H 8.25 (s, 1H, H^6), 7.09 (t, J = 8.0 Hz, 1H, H^8), 6.68 (t, J = 2.0 Hz, 1H, H^{10}), 6.62 (dd, J = 8.4 and 2.4 Hz, 1H, H^7), 6.44 (broad d, J = 7.6 Hz, 1H, H^9), 5.40 (s, 2H, CH_2), and 2.85 (s, 6H, CH_3). ^{13}C-NMR (DMSO-d_6, 101 MHz): δ_C 158.19, 156.68, 154.01, 150.99, 137.96, 129.58, 115.66, 112.13, 112.07, 103.59, 89.51, 51.05, and 40.46 (2C). HPLC-MS (APCI/ESI): purity 95%, t_R = 2.41 min, (*m*/*z*) $[M+H]^+$ = 395.0.

1-(2-Methylbenzyl)-3-iodo-1*H*-pyrazolo[3,4-*d*]pyrimidin-4-amine, 20a (GS 96)

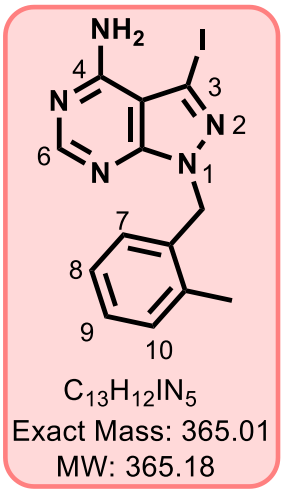

Using the general procedure 2 and a reaction mixture containing **3** (0.40 g, 1.53 mmol), K_2CO_3 (2 eq.) and 2-methylbenzyl bromide (1.2 eq.), the product was obtained as an off-white powder (0.37 g, 67%); MP 145–146°C; R_f (10% MeOH/DCM) 0.6; ^{1}H-NMR (DMSO-d_6, 400 MHz): δ_H 8.25 (s, 1H, H^6), 7.20–7.19 (m, 1H, H^{10}), 7.15–7.13 (m, 1H, H^8), 7.12–7.10 (m, 1H, H^9), 6.95 (broad d, J = 7.6 Hz, 1H, H^7), 5.48 (s, 2H, CH_2), and 2.35 (s, 3H, CH_3). ^{13}C-NMR (DMSO-d_6, 101 MHz): δ_C 158.23, 156.67, 154.08, 136.31, 135.32, 130.68, 128.80, 128.18, 126.45, 103.51, 89.76, 48.39, 19.31. HPLC-MS (APCI/ESI): purity 95%, t_R = 2.46 min, (m/z) $[M+H]^+$ = 366.0.

1-(2-Fluorobenzyl)-3-iodo-1*H*-pyrazolo[3,4-*d*]pyrimidin-4-amine, 21a (GS 90)

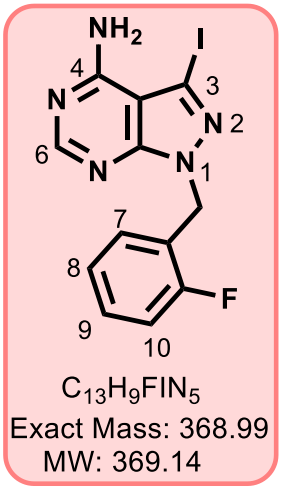

Using the general procedure 2 and a reaction mixture containing **3** (0.50 g, 1.92 mmol), K_2CO_3 (2 eq.) and 2-fluorobenzyl bromide (1.2 eq.), the product was obtained as an off-white powder (0.36 g, 51%); MP 205–207°C; R_f (10% MeOH/DCM) 0.5; ^{1}H-NMR (DMSO-d_6, 600 MHz): δ_H 8.22 (s, 1H, H^6), 7.35–7.31 (m, 1H, H^9), 7.20–7.18 (m, 1H, H^{10}), 7.17–7.15 (m, 1H, H^7), 7.12 (td, J = 7.8 and 1.2 Hz, 1H, H^8), and 5.59 (s, 2H, -CH_2). ^{13}C-NMR (DMSO-d_6, 151 MHz): δ_C 161.33 (d, J = 246.1 Hz, $^1J_{C\text{-}F}$, 1C), 158.20, 156.76, 154.10, 130.85, 130.76 (d, J = 3.0 Hz, $^4J_{C\text{-}F}$, 1C), 130.52 (d, J = 7.6 Hz, $^3J_{C\text{-}F}$, 1C), 125.09 (d, J = 4.5 Hz, $^3J_{C\text{-}F}$, 1C), 123.98 (d, J = 13.6 Hz, $^2J_{C\text{-}F}$, 1C), 115.92 (d, J = 21.1 Hz, $^2J_{C\text{-}F}$, 1C), 103.55, 90.23, and 44.23 (d, J = 4.5 Hz, $^3J_{C\text{-}F}$, 1C). HPLC-MS (APCI/ESI): purity 97%, t_R = 2.42 min, (m/z) $[M+H]^+$ = 370.0.

1-(2-Chlorobenzyl)-3-iodo-1*H*-pyrazolo[3,4-*d*]pyrimidin-4-amine, 22a

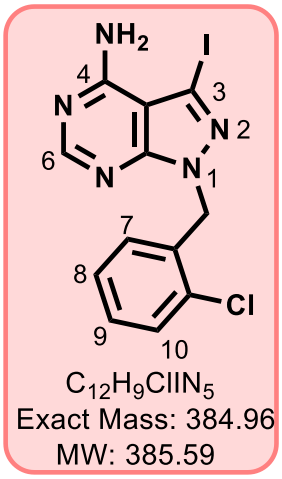

Using the general procedure 2 and a reaction mixture containing **3** (0.39 g, 1.49 mmol), K_2CO_3 (2 eq.) and 2-fluorobenzyl bromide (1.2 eq.), the product was obtained as an off-white powder (375 mg, 65%); R_f (10% MeOH/DCM) 0.54; ^{1}H-NMR (DMSO-d_6, 600 MHz): δ_H 8.22 (s, 1H, H^6), 7.47 (broad dd, J = 7.2 and 1.2 Hz, 1H, H^{10}), 7.32 (td, J = 7.8 and 1.8 Hz, 1H, H^9), 7.27 (td, J = 7.8 and 1.2 Hz, 1H, H^8), 6.98 (dd, J = 8.4 and 1.8 Hz, 1H, H^7), and 5.56 (s, 2H, CH_2). ^{13}C-NMR (DMSO-d_6, 151 MHz): δ_C 157.73, 156.29, 153.80, 133.96, 131.97, 129.65, 129.55, 129.40, 127.45, 103.06, 89.91, and 47.51. HPLC-MS (APCI/ESI): purity 97%, t_R = 2.45 min, (m/z) $[M+H]^+$ = 386.0.

3-Iodo-1-(2-(trifluoromethyl)benzyl)-1*H*-pyrazolo[3,4-*d*]pyrimidin-4-amine, 23a

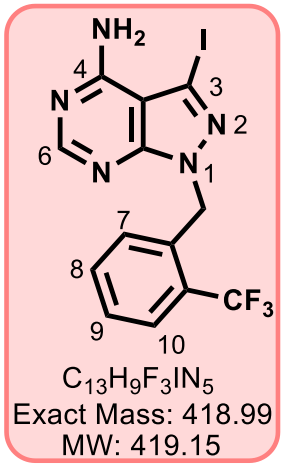

Using the general procedure 2 and a reaction mixture containing **3** (0.51 g, 1.95 mmol), K_2CO_3 (2 eq.) and 2-trifluorobenzyl bromide (1.2 eq.), the product was obtained as an off-white powder (0.47 g, 58%); R_f (10% MeOH/DCM) 0.50; ^{1}H-NMR (DMSO-d_6, 600 MHz): δ_H 8.22 (s, 1H, H^6), 7.77 (dd, J = 7.8 and 1.2 Hz, 1H, H^7), 7.57 (td, J = 7.8 and 1.2 Hz, 1H, H^8), 7.50 (broad t, J = 7.8 Hz, 1H, H^9), 6.88 (broad d, J = 7.8 Hz, 1H, H^{10}), and 5.66 (s, 2H, CH_2). ^{13}C-NMR (DMSO-d_6, 151 MHz): δ_C 157.78, 156.45, 154.02, 134.84, 132.97, 128.86, 128.20, 126.17 (q, J = 30.2 Hz, $^2J_{C\text{-}F}$, 1C), 126.02 (q, J = 6.0 Hz, $^3J_{C\text{-}F}$, 1C), 125.11 (q, J = 273.3 Hz, $^3J_{C\text{-}F}$, 1C), 103.18, 90.30, and 46.45. HPLC-MS (APCI/ESI): purity 98%, t_R = 2.50 min, (m/z) $[M+H]^+$ = 420.0.

1-(3,4-Dichlorobenzyl)-3-iodo-1*H*-pyrazolo[3,4-*d*]pyrimidin-4-amine, 24a (GS 100)

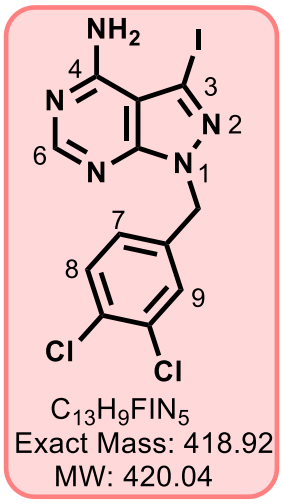

Using the general procedure 2 and a reaction mixture containing **3** (0.50 g, 1.92 mmol), K_2CO_3 (2 eq.) and 3,4-dichlorobenzyl bromide (1.2 eq.), the product was obtained as an off-white powder (0.48 g, 60%); MP 146–147°C; R_f (10% MeOH/DCM) 0.6; ^{1}H-NMR (DMSO-d_6, 400 MHz): δ_H 8.32 (s, 1H, H^6), 7.64 (d, J = 2.0 Hz, 1H, H^9), 7.59 (d, J = 8.4 Hz, 1H, H^8), 7.20 (dd, J = 8.4 and 2.0 Hz, 1H, H^7), and 5.53 (s, 2H, CH_2). ^{13}C NMR (101 MHz, DMSO-d_6): δ_C 158.25, 156.64, 153.86, 131.36, 130.94, 130.25, 129.74, 128.52, 128.08, 104.08, 89.65, and 49.31. HPLC-MS (APCI/ESI): purity 97%, t_R = 2.57 min, (m/z) $[M+H]^+$ = 419.9.

1-(2,4-Dichlorobenzyl)-3-iodo-1*H*-pyrazolo[3,4-*d*]pyrimidin-4-amine, 25a (GS 102)

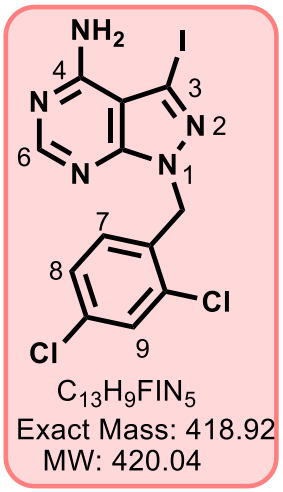

Using the general procedure 2 and a reaction mixture containing **3** (0.40 g, 1.53 mmol), K_2CO_3 (2 eq.) and 2,4-dichlorobenzyl bromide (1.2 eq.), the product was obtained as an off-white powder (0.39 g, 60%); MP 203–205°C; R_f (10% MeOH/DCM) 0.5; ^{1}H-NMR (400 MHz, DMSO-d_6): δ_H 8.24 (s, 1H, H^6), 7.66 (d, J = 2.0 Hz, 1H, H^9), 7.39 (dd, J = 8.4 and 2.0 Hz, 1H, H^8), 7.07 (d, J = 8.4 Hz, 1H, H^7), and 5.56 (s, 2H, CH_2). ^{13}C-NMR (101 MHz, DMSO-d_6): δ_C 158.26, 156.83, 154.33, 133.80, 133.64, 133.57, 131.70, 129.42, 128.16, 103.61, 90.58, and 47.58. HPLC-MS (APCI/ESI): purity 97%, t_R = 2.56 min, (m/z) $[M+H]^+$ = 419.9.

1-(4-Chloro-2-fluorobenzyl)-3-iodo-1H-pyrazolo[3,4-d]pyrimidin-4-amine, 26a (GS 110)

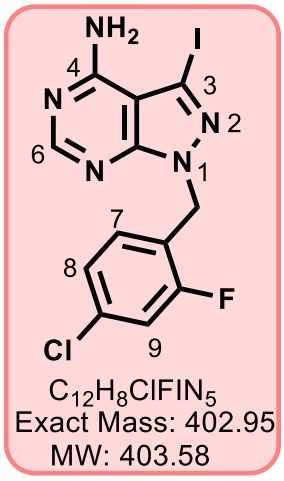

Using the general procedure 2, a reaction mixture containing **3** (0.60 g, 2.30 mmol), K_2CO_3 (2 eq.) and 4-chloro-2-fluorobenzyl bromide (1.2 eq.), the product was obtained as an off-white powder (0.49 g, 53%); R_f (10% MeOH/DCM) 0.54; ^{1}H-NMR (DMSO-d_6, 400 MHz): δ_H 8.25 (s, 1H, $H^{6'}$), 7.45 (dd, J = 10.0 and 1.6 Hz, 1H, H^9), 7.27 (dd, J = 8.4 and 2.0 Hz, 1H, H^8), 7.23 (pseudo t, 1H, J = 8.4 Hz, H^7), and 5.52 (s, 2H, CH_2). ^{13}C-NMR (DMSO-d_6, 101 MHz): δ_C 160.28 (d, J = 251.0 Hz, $^1J_{C\text{-}F}$, 1C), 158.22, 156.81, 154.14, 134.00 (d, J = 10.7 Hz, $^3J_{C\text{-}F}$, 1C), 132.14 (d, J = 4.7 Hz, $^3J_{C\text{-}F}$, 1C), 125.41 (d, J = 3.7 Hz, $^4J_{C\text{-}F}$, 1C), 123.21 (d, J = 14.9 Hz, $^2J_{C\text{-}F}$, 1C), 116.63 (d, J = 25.0 Hz, $^2J_{C\text{-}F}$, 1C), 103.60, 90.37, and 43.90 (d, J = 3.8 Hz, $^3J_{C\text{-}F}$, 1C). HPLC-MS (APCI/ESI): purity 96%, t_R = 2.50 min, (m/z) $[M+H]^+$ = 404.0.

2-((4-Amino-3-iodo-1*H*-pyrazolo[3,4-*d*]pyrimidin-1-yl)methyl)-5-chlorobenzonitrile, 27a

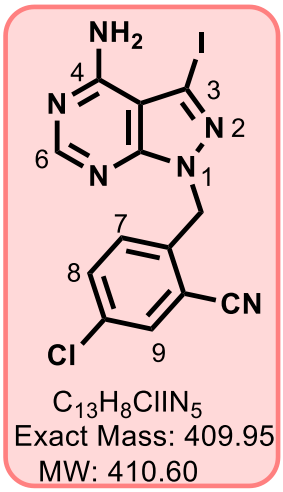

Using the general procedure 2 and a reaction mixture containing **3** (0.42 g, 1.61 mmol), K_2CO_3 (2 eq.) and 4-chloro-2-cyanobenzyl bromide (1.2 eq.), the product was obtained as a pink powder (0.47 g, 71%); R_f (10% MeOH/DCM) 0.60; ^{1}H NMR (DMSO-d_6, 600 MHz): δ_H 8.25 (s, 1H, H^6), 8.07 (d, J = 2.4 Hz, 1H, H^9), 7.74 (dd, J = 8.4 and 2.4 Hz, 1H, H^8), 7.28 (d, J = 8.4 Hz, 1H, H^7), and 5.66 (s, 2H, CH_2). ^{13}C-NMR (DMSO-d_6, 151 MHz): δ_C 158.22, 156.87, 154.39, 139.31, 134.20, 133.58, 133.08, 131.34, 116.18, 113.09, 103.63, 91.00, and 48.13. HPLC-MS (APCI/ESI): purity 96%, t_R = 2.35 min, (*m*/*z*) $[M+H]^+$ = 410.9.

1-(4-Chloro-3-fluorobenzyl)-3-iodo-1*H*-pyrazolo[3,4-d]pyrimidin-4-amine, 28a (GS 104)

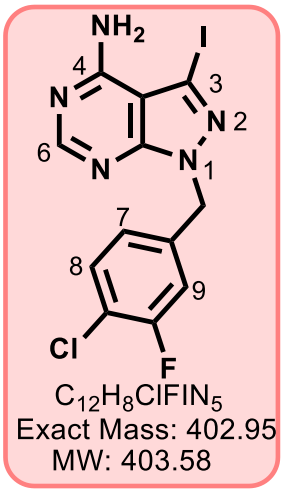

Using the general procedure 2 and a reaction mixture containing **3** (0.45 g, 1.72 mmol), K_2CO_3 (2 eq.) and 4-chloro-3-fluorobenzyl bromide (1.2 eq.), the product was obtained as an off-white powder (0.46 mg, 66%); R_f (10% MeOH/DCM) 0.66; ^{1}H-NMR (DMSO-d_6, 600 MHz): δ_H 8.25 (s, 1H, H^6), 7.54 (t, J = 8.4 Hz, 1H, H^8), 7.30 (dd, J = 10.1 and 1.8 Hz, 1H, H^9), 7.06 (dd, J = 8.4 and 1.8 Hz, 1H, H^7), and 5.51 (s, 2H, CH_2). ^{13}C-NMR (DMSO-d_6, 151 MHz): δ_C 158.24, 157.49 (d, J = 247.6 Hz, $^1J_{C\text{-}F}$, 1C), 156.87, 154.10, 138.94 (d, J = 6.0 Hz, $^3J_{C\text{-}F}$, 1C), 131.36, 125.29 (d, J = 4.5 Hz, $^3J_{C\text{-}F}$, 1C), 119.24 (d, J = 16.6 Hz, $^2J_{C\text{-}F}$, 1C), 116.55 (d, J = 22.7 Hz, $^2J_{C\text{-}F}$, 1C), 103.68, 90.50, and 49.38. HPLC-MS (APCI/ESI): purity 96%, t_R = 2.52 min, (*m*/*z*) $[M+H]^+$ = 404.0.

1-(4-Chloro-2-(trifluoromethyl)benzyl)-3-iodo-1*H*-pyrazolo[3,4-*d*]pyrimidin-4-amine 29a (GS 116)

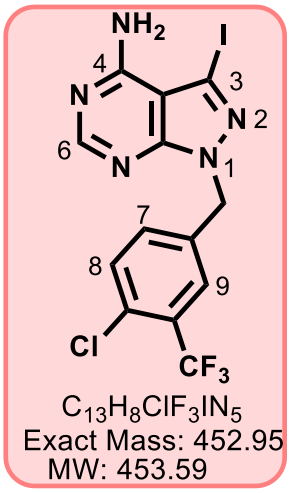

Using the general procedure 2 and a reaction mixture containing **3** (425 mg, 1.63 mmol), K_2CO_3 (2 eq.) and 4-chloro-3-trifluorobenzyl bromide (1.2 eq.), the product was obtained as an off-white powder (0.41 g, 56%); R_f (10% MeOH/DCM) 0.47; ^{1}H-NMR (DMSO-d_6, 600 MHz): δ_H 8.26 (s, 1H, H^6), 7.83 (d, J = 2.1 Hz, 1H, H^9), 7.69 (d, J = 8.1 Hz, 1H, H^8), 7.47 (dd, J = 8.1 and 2.1 Hz, 1H, H^7), and 5.60 (s, 2H, CH_2). ^{13}C-NMR (DMSO-d_6, 151 MHz): δ_C 157.76, 156.42, 153.64, 136.90, 133.32, 132.02, 130.02, 127.11 (q, J = 6.0 Hz, $^3J_{C\text{-}F}$, 1C), 126.65 (q, J = 30.2 Hz, $^2J_{C\text{-}F}$, 1C), 122.65 (d, J = 273.3 Hz, $^1J_{C\text{-}F}$, 1C), 103.19, 90.15, and 48.77. HPLC-MS (APCI/ESI): purity > 99%, t_R = 2.38 min, (*m*/*z*) $[M+H]^+$ = 453.9.

1-(2,4-Difluorobenzyl)-3-iodo-1*H*-pyrazolo[3,4-*d*]pyrimidin-4-amine, 30a (GS 130)

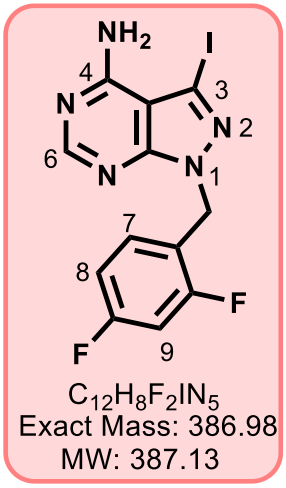

Using the general procedure 2 and a reaction mixture containing **3** (0.60 g, 2.30 mmol), K_2CO_3 (2 eq.) and 2,4-difluorobenzyl bromide (1.2 eq.), the product was obtained as an off-white powder (0.41 g, 57%); R_f (10% MeOH/DCM) 0.60; ^{1}H-NMR (DMSO-d_6, 400 MHz): δ_H 8.25 (s, 1H, H^6), 7.33–7.29 (m, 1H, H^7), 7.28–7.23 (m, 1H, H^9), 7.06 (tdd, J = 8.4, 2.4 and 1.2 Hz, 1H, H^8), and 5.51 (s, 2H, CH_2). ^{13}C-NMR (DMSO-d_6, 101 MHz): δ_C 162.73 (dd, J = 195.9 and 12.1 Hz, 1C), 160.26 (dd, J = 199.0 and 13.1 Hz, 1C), 158.22, 156.78, 154.08, 132.25 (dd, J = 10.1 and 6.1 Hz, 1C), 132.23, 132.18, 120.40 (dd, J = 15.2 and 3.0 Hz, 1C), 120.31, 112.22 (dd, J = 21.2 and 4.0 Hz, 1C), 104.52 (t, J = 25.3 Hz, 1C), 103.59, 90.25, and 43.83 (d, J = 4.0 Hz, 1C). HPLC-MS (APCI/ESI): purity 95%, t_R = 2.06 min, (*m*/*z*) $[M+H]^+$ = 387.9.

1-(2-Chloro-4-fluorobenzyl)-3-iodo-1*H*-pyrazolo[3,4-d]pyrimidin-4-amine, 31a

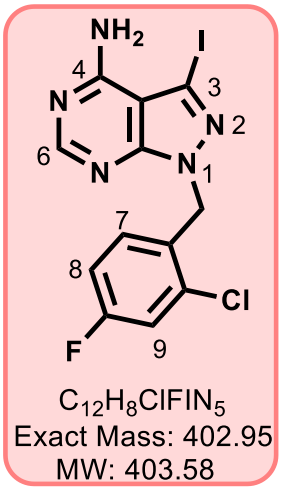

Using the general procedure 2 and a reaction mixture containing **3** (0.80 g, 3.06 mmol), K_2CO_3 (2 eq.) and 2-chloro-4-fluorobenzyl bromide (1.2 eq.), the product was obtained as an off-white powder (495 mg, 40%); R_f (10% MeOH/DCM) 0.60; ^{1}H-NMR (DMSO-d_6, 600 MHz): δ_H 8.20 (s, 1H, H^6), 7.44 (dd, J = 8.4 and 2.4 Hz, 1H, H^9), 7.15 (td, J = 8.4 and 2.4 Hz, 1H, H^8), 7.10 (dd, J = 8.4 and 6.0 Hz, 1H, H^7), and 5.51 (s, 2H, CH_2). ^{13}C-NMR (DMSO-d_6, 151 MHz): δ_C 161.89 (d, J = 247.6 Hz, $^1J_{C\text{-}F}$, 1C), 158.21, 156.78, 154.23, 133.45 (d, J = 10.6 Hz, $^3J_{C\text{-}F}$, 1C), 132.00 (d, J = 9.1 Hz, $^3J_{C\text{-}F}$, 1C), 130.88 (d, J = 4.5 Hz, $^4J_{C\text{-}F}$, 1C), 117.24 (d, J = 25.7 Hz, $^2J_{C\text{-}F}$, 1C), 115.13 (d, J = 21.7 Hz, $^2J_{C\text{-}F}$, 1C), 103.54, 90.50, and 47.44. HPLC-MS (APCI/ESI): purity 97%, t_R = 2.48 min, (*m*/*z*) $[M+H]^+$ = 403.9.

1-(4-Fluoro-2-(trifluoromethyl)benzyl)-3-iodo-1*H*-pyrazolo[3,4-*d*]pyrimidin-4-amine, 32a

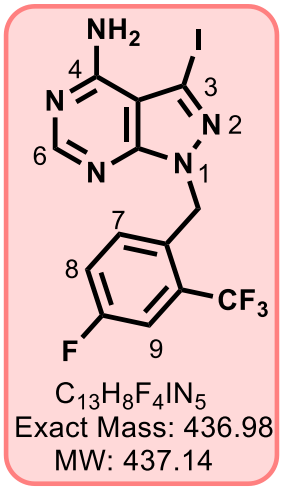

Using the general procedure 2 and a reaction mixture containing **3** (0.47 g, 1.80 mmol), K_2CO_3 (2 eq.) and 4-fluoro-2-trifluorobenzyl bromide (1.2 eq.), the product was obtained as an off-white powder (0.41 g, 52%); R_f (10% MeOH/DCM) 0.67; ^{1}H-NMR (DMSO-d_6, 400 MHz): δ_H 8.25 (s, 1H, H^6), 7.69 (dd, J = 9.2 and 2.8 Hz, 1H, H^9), 7.48 (td, J = 8.4 and 2.8 Hz, 1H, H^8), 7.05 (dd, J = 8.8 and 5.6 Hz, 1H, H^7), and 5.65 (s, 2H, CH_2). ^{13}C-NMR (DMSO-d_6, 101 MHz): δ_C 161.43 (d, J = 247.5 Hz, $^1J_{C\text{-}F}$, 1C), 158.28, 156.95, 154.47, 132.51 (d, J = 8.1 Hz, $^3J_{C\text{-}F}$, 1C), 131.49, 128.70 (dd, J = 31.3 and 8.1 Hz, $^2J_{C\text{-}F}$ and $^3J_{C\text{-}F}$, 1C), 123.72 (d, J = 274.7 Hz, $^1J_{C\text{-}F}$, 1C), 120.33 (d, J = 21.2 Hz, $^2J_{C\text{-}F}$, 1C), 114.30 (dq, J = 25.3 and 6.1 Hz, 1C, $^2J_{C\text{-}F}$ and $^3J_{C\text{-}F}$, 1C), 103.71, 90.81, and 46.45. HPLC-MS (APCI/ESI): purity 97%, t_R = 2.55 min, (*m*/*z*) $[M+H]^+$ = 438.0.

2-((4-Amino-3-iodo-1*H*-pyrazolo[3,4-*d*]pyrimidin-1-yl)methyl)-2-fluorobenzonitrile, 33a

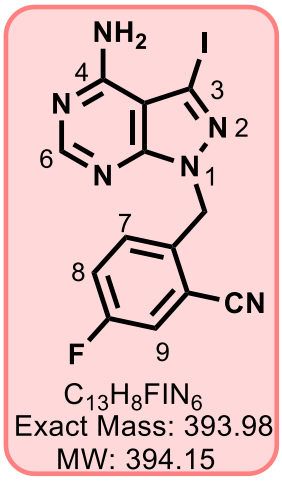

Using the general procedure 2 and a reaction mixture containing **3** (0.42 g, 1.61 mmol), K_2CO_3 (2 eq.) and 3-cyano-4-fluorobenzyl bromide (1.2 eq.), the product was obtained as an off-white powder (0.26 g, 41%); R_f (10% MeOH/DCM) 0.63; ^{1}H-NMR (DMSO-d_6, 600 MHz): δ_H 8.21 (s, 1H, H^6), 7.80 (dd, J = 6.6 and 2.4 Hz, 1H, H^9), 7.58 (ddd, J = 8.8, 5.4 and 2.4 Hz, 1H, H^7), 7.44 (t, J = 9.0 Hz, 1H, H^8), and 5.49 (s, 2H, CH_2). ^{13}C-NMR (DMSO-d_6, 151 MHz): δ_C 162.32 (d, J = 256.7 Hz, $^1J_{C\text{-}F}$, 1C), 158.21, 156.85, 154.08, 135.88 (d, J = 7.6 Hz, $^3J_{C\text{-}F}$, 1C), 134.91 (d, J = 4.5 Hz, $^4J_{C\text{-}F}$, 1C), 133.40, 117.40 (d, J = 19.6 Hz, $^2J_{C\text{-}F}$, 1C), 114.16, 103.70, 100.71 (d, J = 15.1 Hz, $^2J_{C\text{-}F}$, 1C), 90.62, and 48.93. HPLC-MS (APCI/ESI): purity 96%, t_R = 2.28 min, (*m*/*z*) $[M+H]^+$ = 394.9.

1-(4-Fluoro-2-methylbenzyl)-3-iodo-1*H*-pyrazolo[3,4-*d*]pyrimidin-4-amine, 34a

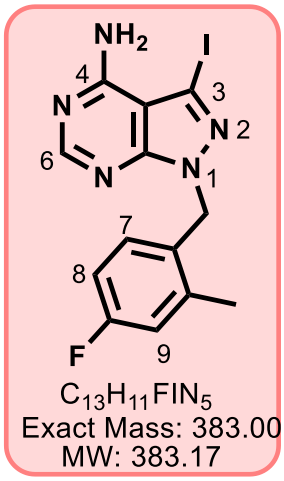

Using the general procedure 2 and a reaction mixture containing **3** (0.75 g, 2.87 mmol), K_2CO_3 (2 eq.) and 4-fluoro-2-methylbenzyl bromide (1.2 eq.), the product was obtained as an off-white powder (0.50 g, 45%); R_f (10% MeOH/DCM) 0.42; ^{1}H-NMR (DMSO-d_6, 400 MHz): δ_H 8.25 (s, 1H, H^6), 7.11–7.02 (m, 2H, $H^{7,9}$), 6.96 (td, J = 8.8 and 2.8 Hz, 1H, H^8), 5.46 (s, 2H, CH_2), and 2.36 (s, 3H, CH_3). ^{13}C-NMR (DMSO-d_6, 101 MHz): δ_C 161.96 (d, J = 244.4 Hz, $^1J_{C\text{-}F,}$ 1C), 158.23, 156.70, 154.01, 139.43 (d, J = 8.1 Hz, $^3J_{C\text{-}F,}$ 1C), 131.54 (d, J = 2.4 Hz, $^4J_{C\text{-}F,}$ 1C), 131.11 (d, J = 8.8 Hz, $^3J_{C\text{-}F,}$ 1C), 117.21 (d, J = 21.2 Hz, $^2J_{C\text{-}F,}$ 1C), 113.02 (d, J = 21.2 Hz, $^2J_{C\text{-}F,}$ 1C), 103.53, 89.87, 47.74, and 19.32. HPLC-MS (APCI/ESI): purity 96%, t_R = 2.43 min, (*m*/*z*) $[M+H]^+$ = 383.9.

1-(3-Chloro-4-fluorobenzyl)-3-iodo-1*H*-pyrazolo[3,4-d]pyrimidin-4-amine, 35a (GS 104)

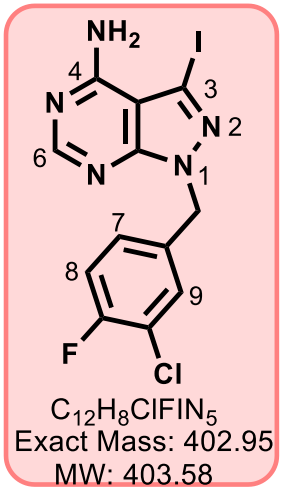

Using the general procedure 2 and a reaction mixture containing **3** (0.65 g, 2.49 mmol), K_2CO_3 (2 eq.) and 3-chloro-4-fluorobenzyl bromide (1.2 eq.), the product was obtained as an off-white powder (0.40 g, 40%); R_f (10% MeOH/DCM) 0.67; ^{1}H-NMR (DMSO-d_6, 600 MHz): δ_H 8.21 (s, 1H, H^6), 7.47 (dd, J = 7.2 and 2.4 Hz, 1H, H^9), 7.32 (dd, J = 9.0 and 8.4 Hz, 1H, H^8), 7.19 (ddd, J = 8.4, 4.8 and 2.4 Hz, 1H, H^7), and 5.45 (s, 2H, CH_2). ^{13}C-NMR (DMSO-d_6, 151 MHz): δ_C 158.21, 157.15 (d, J = 247.6 Hz, $^1J_{C\text{-}F}$, 1C), 156.84, 153.99, 135.13 (d, J = 4.5 Hz, $^3J_{C\text{-}F}$, 1C), 128.93 (d, J = 7.6 Hz, $^3J_{C\text{-}F}$, 1C), 130.31, 119.91 (d, J = 18.1 Hz, $^2J_{C\text{-}F}$, 1C), 117.60 (d, J = 21.1 Hz, $^2J_{C\text{-}F}$, 1C), 103.64, 90.39, and 49.18. HPLC-MS (APCI/ESI): purity 95%, t_R = 2.47 min, (*m*/*z*) $[M+H]^+$ = 403.9.

2-((4-Amino-3-iodo-1*H*-pyrazolo[3,4-*d*]pyrimidin-1-yl)methyl)-5-fluorobenzonitrile, 36a

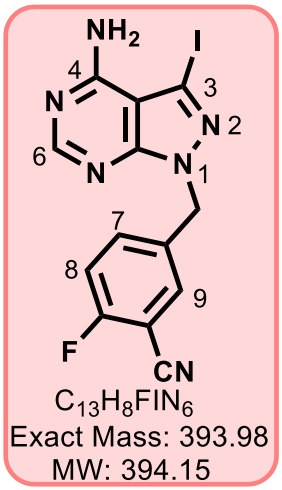

Using the general procedure 2 and a reaction mixture containing **3** (0.48 g, 1.84 mmol), K_2CO_3 (2 eq.) and 2-cyano-4-fluorobenzyl bromide (1.2 eq.), the product was obtained as a pink powder (0.31 g, 43%); R_f (10% MeOH/DCM) 0.53; ^{1}H-NMR (DMSO-d_6, 400 MHz): δ_H 8.26 (s, 1H), 7.83 (dd, J = 8.4 and 2.4 Hz, 1H, H^9), 7.53 (td, J = 8.8 and 2.8 Hz, 1H, H^8), 7.37 (dd, J = 8.8 and 5.6 Hz, 1H, H^7), and 5.66 (s, 2H, CH_2). ^{13}C-NMR (DMSO-d_6, 101 MHz): δ_C 162.68, 158.30, 156.86, 154.51, 136.71 (d, J = 3.0 Hz, $^4J_{C\text{-}F}$, 1C), 132.15 (d, J = 9.1 Hz, $^3J_{C\text{-}F}$, 1C), 121.54 (d, J = 21.2 Hz, $^2J_{C\text{-}F}$, 1C), 120.45 (d, J = 25.3 Hz, $^2J_{C\text{-}F}$, 1C), 116.27, 113.08 (d, J = 11.1 Hz, $^3J_{C\text{-}F}$, 1C), 103.81, 90.35, and 48.15. HPLC-MS (APCI/ESI): purity 96%, t_R = 2.31 min, (*m*/*z*) $[M+H]^+$ = 395.0.

1-(3,4-Difluorobenzyl)-3-iodo-1*H*-pyrazolo[3,4-*d*]pyrimidin-4-amine, 37a (GS 142)

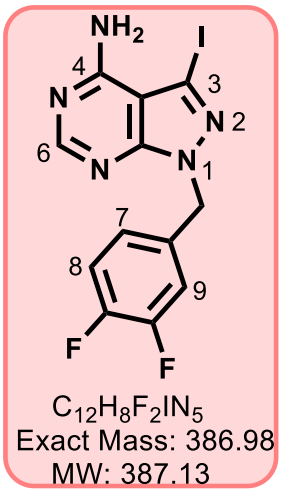

Using the general procedure 2 and a reaction mixture containing **3** (0.65 g, 2.49 mmol), K_2CO_3 (2 eq.) and 3,4-difluorobenzyl bromide (1.2 eq.), the product was obtained as an off-white powder (425 mg, 44%); R_f (10% MeOH/DCM) 0.56; ^{1}H NMR (DMSO-d_6, 600 MHz): δ_H 8.21 (s, 1H, H^6), 7.34 (dt, J = 10.8 and 8.4 Hz, 1H, H^8), 7.29 (ddd, J = 11.4, 7.8 and 2.4 Hz, 1H, H^9), 7.04–7.01 (m, 1H, H^7), and 5.44 (s, 2H, CH_2). ^{13}C-NMR (DMSO-d_6, 151 MHz): δ_C 158.20, 156.83, 154.00, 150.34 (dd, J = 43.8 and 13.6 Hz), 148.71 (dd, J = 42.3 and 12.1 Hz), 134.93 (pseudo t, J = 4.5 Hz), 125.01 (dd, J = 6.0 and 3.0 Hz), 118.18 (d, J = 18.1 Hz), 117.29 (d, J = 16.6 Hz), 103.64, 90.36, and 49.34. HPLC-MS (APCI/ESI): purity 95%, t_R = 2.44 min, (*m*/*z*) $[M+H]^+$ = 388.0.

1-(4-Fluoro-3-(trifluoromethyl)benzyl)-3-iodo-1*H*-pyrazolo[3,4-*d*]pyrimidin-4-amine, 38a (GS 144)

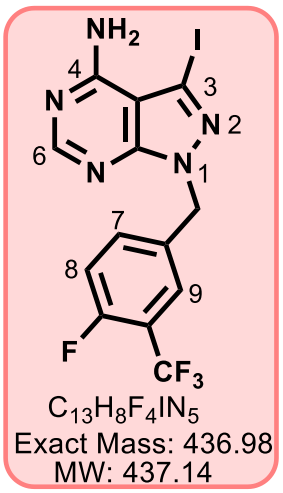

Using the general procedure 2 and a reaction mixture containing **3** (0.61 g, 2.34 mmol), K_2CO_3 (2 eq.) and 4-fluoro-3-trifluorobenzyl bromide (1.2 eq.), the product was obtained as an off-white powder (0.38 g, 37%); R_f (10% MeOH/DCM) 0.50; ^{1}H-NMR (DMSO-d_6, 600 MHz): δ_H 8.21 (s, 1H, H^6), 7.72 (dd, J = 7.2 and 2.4 Hz, 1H, H^9), 7.52 (ddd, J = 7.8, 5.4 and 2.4 Hz, 1H, H^7), 7.43 (dd, J = 10.8 and 8.4 Hz, 1H, H^8), and 5.54 (s, 2H, CH_2). ^{13}C-NMR (DMSO-d_6, 151 MHz): δ_C 158.75 (d, J = 253.7 Hz, $^1J_{C\text{-}F}$, 1C), 158.22, 156.87, 154.05, 135.05 (d, J = 9.1 Hz, $^3J_{C\text{-}F}$, 1C), 134.43 (d, J = 4.5 Hz, $^4J_{C\text{-}F}$, 1C), 127.05 (q, J = 3.0 Hz, $^3J_{C\text{-}F}$, 1C), 122.89 (q, J = 271.8 Hz, $^1J_{C\text{-}F}$, 1C), 118.08 (d, J = 19.6 Hz, $^2J_{C\text{-}F}$, 1C), 117.01 (dq, J = 31.7 and 12.1 Hz, $^2J_{C\text{-}F}$, 1C), 103.66, 90.51, and 49.16. HPLC-MS (APCI/ESI): purity 97%, t_R = 2.49 min, (*m*/*z*) $[M+H]^+$ = 437.9.

3-Iodo-1-((6-(trifluoromethyl)pyridin-3-yl)methyl)-1*H*-pyrazolo[3,4-*d*]pyrimidin-4-amine, 39a (GS 98)

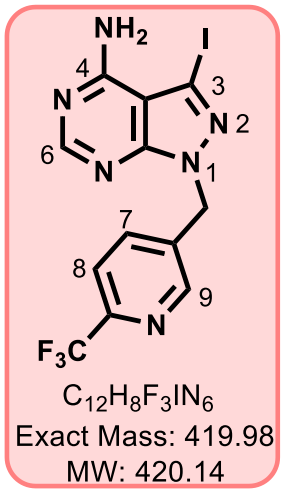

Using the general procedure 2 and a reaction mixture containing **3** (0.50 g, 1.92 mmol), K_2CO_3 (1.2 eq.) and 5-(bromomethyl)-2-(trifluoromethyl)pyridine, (1.2 eq.), the product was obtained as an off-white solid (0.52 g, 65%); MP 215–216°C; R_f (10% MeOH/DCM) 0.4; ^{1}H-NMR (DMSO-d_6, 600 MHz): δ_H 8.70 (broad s, 1H, H^9), 8.23 (s, 1H, H^6), 7.85 (broad s, 1H, H^8), and 7.84 (broad s, 1H, H^7). ^{13}C-NMR (151 MHz, DMSO-d_6): δ_C 158.26, 156.93, 154.21, 149.92, 146.26 (q, J = 34.7 Hz, $^2J_{C\text{-}F}$, 1C), 122.0 (q, J = 274.8 Hz, $^1J_{C\text{-}F}$, 1C), 121.29 (broad q, J = 1.5 Hz, $^3J_{C\text{-}F}$, 1C), 103.75, 90.85, and 47.64. HPLC-MS (APCI/ESI): purity 97%, t_R = 2.35 min, (*m*/*z*) $[M+H]^+$ = 420.9.

1-((6-Chloropyridin-3-yl)methyl)-3-iodo-1*H*-pyrazolo[3,4-*d*]pyrimidin-4-amine, 40a

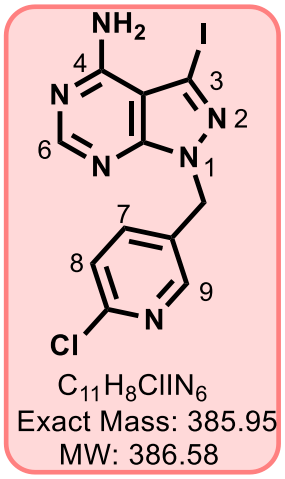

Using the general procedure 2 and a reaction mixture containing **3** (0.40 g, 1.53 mmol), K_2CO_3 (2 eq.) and 2-chloro-5-pyridylmethyl chloride (1.2 eq.), the product was obtained as an off-white powder (0.31 g, 52%); R_f (10% MeOH/DCM) 0.50; ^{1}H-NMR (DMSO-d_6, 400 MHz): δ_H 8.39 (dd, J = 2.4 and 0.8 Hz, 1H, H^9), 8.25 (s, 1H, H^6), 7.70 (dd, J = 8.0 and 2.4 Hz, 1H, H^7), 7.48 (dd, J = 8.4 and 0.7 Hz, 1H, H^8), and 5.55 (s, 2H, CH_2). ^{13}C-NMR (DMSO-d_6, 101 MHz): δ_C 158.25, 156.87, 154.10, 150.17, 149.69, 139.78, 132.45, 124.83, 103.75, 90.50, and 47.32. HPLC-MS (APCI/ESI): purity 95%, t_R = 2.27 min, (m/z) $[M+H]^+$ = 387.0.

1-((6-Fluoropyridin-3-yl)methyl)-3-iodo-1*H*-pyrazolo[3,4-*d*]pyrimidin-4-amine, 41a

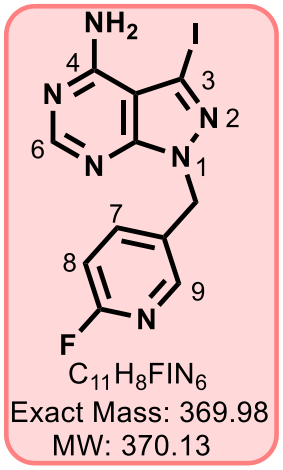

Using the general procedure 2 and a reaction mixture containing **3** (0.53 g, 2.03 mmol), K_2CO_3 (2 eq.) and 2-fluoro-5-pyridylmethyl chloride (1.2 eq.), the product was obtained as an off-white powder (0.35 g, 47%); R_f (10% MeOH/DCM) 0.58; ^{1}H-NMR (DMSO-d_6, 400 MHz): δ_H 8.24 (s, 1H, H^6), 8.21 (broad d, J = 2.4 Hz, 1H, H^9), 7.84 (td, J = 8.4 and 2.4 Hz, 1H, H^8), 7.13 (dd, J = 8.4 and 2.8 Hz, 1H, H^7), and 5.53 (s, 2H, CH_2). ^{13}C-NMR (DMSO-d_6, 101 MHz): δ_C 163.02 (d, J = 237.4 Hz, $^1J_{C\text{-}F}$, 1C), 158.24, 156.86, 154.04, 147.40 (d, J = 16.2 Hz, $^3J_{C\text{-}F}$, 1C), 142.32 (d, J = 8.1 Hz, $^3J_{C\text{-}F}$, 1C), 131.20 (d, J = 5.1 Hz, $^4J_{C\text{-}F}$, 1C), 110.14 (d, J = 38.4 Hz, $^2J_{C\text{-}F}$, 1C), 103.75, 90.38, and 47.21. HPLC-MS (APCI/ESI): purity 95%, t_R = 2.19 min, (m/z) $[M+H]^+$ = 370.9.

3-Iodo-1-((6-methylpyridin-3-yl)methyl)-1*H*-pyrazolo[3,4-*d*]pyrimidin-4-amine, 42a

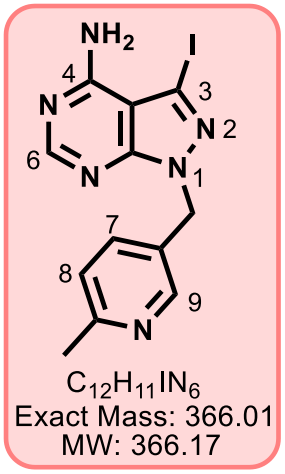

Using the general procedure 2 and a reaction mixture containing **3** (0.60 g, 2.30 mmol), K_2CO_3 (2 eq.) and 2-methyl-5-pyridylmethyl bromide (1.2 eq.), the product was obtained as an off-white powder (395 mg, 47%); R_f (10% MeOH/DCM) 0.40; ^{1}H-NMR (DMSO-d_6, 400 MHz): δ_H 8.41 (d, J = 2.4 Hz, 1H, H^9), 8.25 (s, 1H, H^6), 7.53 (dd, J = 8.0 and 2.4 Hz, 1H, H^7), 7.20 (d, J = 8.0 Hz, 1H, H^8), 5.48 (s, 2H, CH_2), and 2.43 (s, 3H, CH_3). ^{13}C-NMR (DMSO-d_6, 101 MHz): δ_C 158.22, 157.94, 156.79, 153.99, 148.80, 136.37, 129.82, 123.43, 103.69, 90.08, 47.98, and 24.16. HPLC-MS (APCI/ESI): purity 95%, t_R = 2.09 min, (*m*/*z*) $[M+H]^+$ = 367.0.

3-Iodo-1-(pyridin-4-ylmethyl)-1*H*-pyrazolo[3,4-*d*]pyrimidin-4-amine, 43a (GS 78)

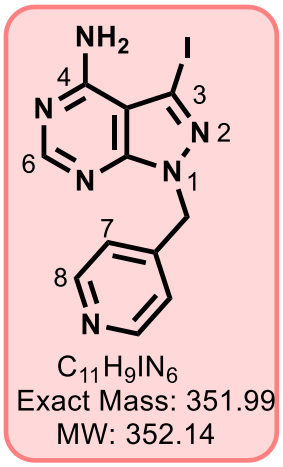

Using the general procedure 2 and a reaction mixture containing **3** (0.50 g, 1.92 mmol), K_2CO_3 (3.2 eq.) and 4-picolyl chloride hydrochloride (1.2 eq.), the product was obtained as a yellow powder (0.38 g, 56%); MP 216–217°C; R_f (15% MeOH/DCM) 0.4; ^{1}H-NMR (DMSO-d_6, 600 MHz): δ_H 8.49 (pseudo dd, J = 6.0 and 1.2 Hz, 2H, H^8), 8.22 (s, 1H, H^6), 7.13 (pseudo dd, J = 6.0 and 1.8 Hz, 2H, H^7), and 5.53 (s, 2H, CH_2). ^{13}C-NMR (DMSO-d_6, 151 MHz): δ_C 158.26, 156.90, 154.30, 150.34 (2C), 146.09, 122.64 (2C), 103.66, 90.64, and 49.33. HPLC-MS (APCI/ESI): purity 97%, t_R = 2.04 min, (*m*/*z*) $[M+H]^+$ = 353.0.

1-((2-Fluoropyridin-4-yl)methyl)-3-iodo-1*H*-pyrazolo[3,4-*d*]pyrimidin-4-amine, 45a

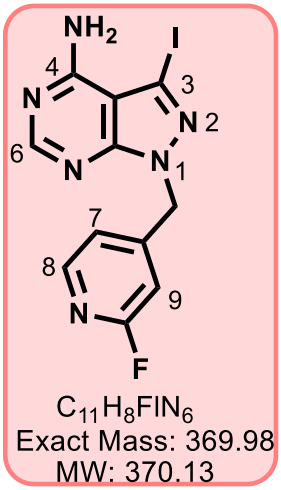

Using the general procedure 2 and a reaction mixture containing **3** (0.60 g, 2.30 mmol), K_2CO_3 (2 eq.) and 4-(bromomethyl)-2-fluoropyridine (1.2 eq.), the product was obtained as an off-white powder (375 mg, 44%); R_f (10% MeOH/DCM) 0.42; ^{1}H-NMR (DMSO-d_6, 400 MHz): δ_H 8.24 (s, 1H, H^6), 8.18 (d, J = 6.8 Hz, 1H, H^8), 7.08 (dt, J = 6.8 and 2.4 Hz, 1H, H^7), 6.98 - 6.95 (m, 1H, H^9), and 5.61 (s, 2H, CH_2).^{13}C-NMR (DMSO-d_6, 101 MHz): δ_C 163.74 (d, J = 236.5 Hz, $^1J_{C\text{-}F}$, 1C), 158.30, 156.95, 154.40, 152.66 (d, J = 8.1 Hz, $^3J_{C\text{-}F}$, 1C), 148.48 (d, J = 15.5 Hz, $^3J_{C\text{-}F}$, 1C), 120.94 (d, J = 4.0 Hz, $^4J_{C\text{-}F}$, 1C), 108.29 (d, J = 38.7 Hz, $^2J_{C\text{-}F}$, 1C), 103.75, 90.87, and 48.99 (d, J = 2.1 Hz, $^4J_{C\text{-}F}$, 1C). HPLC-MS (APCI/ESI): purity 96%, t_R = 2.12 min, (*m*/*z*) $[M+H]^+$ = 371.0.

3-Iodo-1-((2-(trifluoromethyl)pyridin-4-yl)methyl)-1*H*-pyrazolo[3,4-*d*]pyrimidin-4-amine, 46a

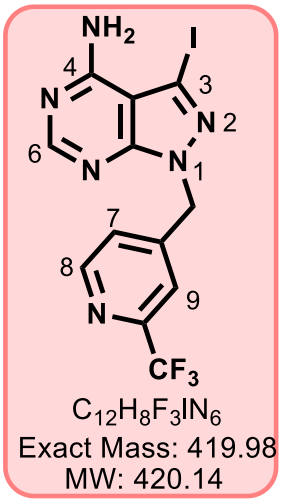

Using the general procedure 2 and a reaction mixture containing **3** (0.55 g, 2.11 mmol), K_2CO_3 (2 eq.) and 4-(chloromethyl)-2-trifluoropyridine (1.2 eq.), the product was obtained as an off-white powder (0.39 g, 44%); R_f (10% MeOH/DCM) 0.63; ^{1}H-NMR (DMSO-d_6, 400 MHz): δ_H 8.70 (broad d, J = 7.2 Hz, 1H, H^8), 8.25 (s, 1H, H^6), 7.79 (broad d, J = 1.6 Hz, 1H, H^9), 7.38 (dd, J = 7.8 and 2.4 Hz, 1H, H^7), and 5.69 (s, 2H, CH_2). ^{13}C-NMR (DMSO-d_6, 101 MHz): δ_C 158.31, 156.99, 154.46, 151.16, 148.83, 147.22 (q, J = 34.2 Hz, $^2J_{C\text{-}F,}$ 1C), 126.06, 121.98 (q, J = 274.7 Hz, $^1J_{C\text{-}F,}$ 1C), 119.75 (broad q, J = 2.3 Hz, $^3J_{C\text{-}F,}$ 1C), 103.77, 91.01, and 49.08. HPLC-MS (APCI/ESI): purity 95%, t_R = 2.33 min, (*m*/*z*) $[M+H]^+$ = 421.0.

3-Iodo-1-((2-methylpyridin-4-yl)methyl)-1*H*-pyrazolo[3,4-*d*]pyrimidin-4-amine, 47a

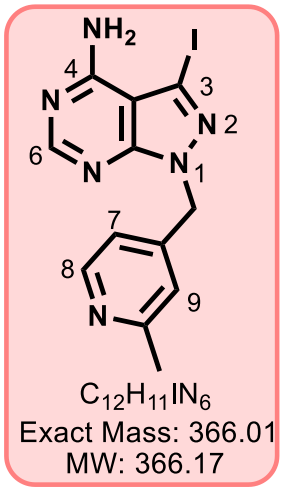

Using the general procedure 2 and a reaction mixture containing **3** (0.45 g, 1.72 mmol), K_2CO_3 (2 eq.) and 4-(chloromethyl)-2-methylpyridine (1.2 eq.), the product was obtained as an off-white powder (0.31 g, 49%); R_f (10% MeOH/DCM) 0.39; ^{1}H-NMR (DMSO-d_6, 600 MHz): δ_H 8.32 (broad d, J = 5.4 Hz, 1H, H^8), 8.20 (s, 1H, H^6), 6.99 (broad d, J = 2.4 Hz, 1H, H^9), 6.88 (dd, J = 4.8 and 2.4 Hz, 1H, H^7), 5.45 (s, 2H, CH_2), and 2.37 (s, 3H, CH_3). ^{13}C-NMR (DMSO-d_6, 151 MHz): δ_C 158.68, 158.23, 156.86, 154.24, 149.69, 146.22, 121.82, 119.82, 103.61, 90.51, 49.34, and 24.43. HPLC-MS (APCI/ESI): purity > 99%, t_R = 2.38 min, (m/z) $[M+H]^+$ = 367.0.

3-Iodo-1-(pyridin-3-ylmethyl)-1*H*-pyrazolo[3,4-*d*]pyrimidin-4-amine, 48a (GS 82)

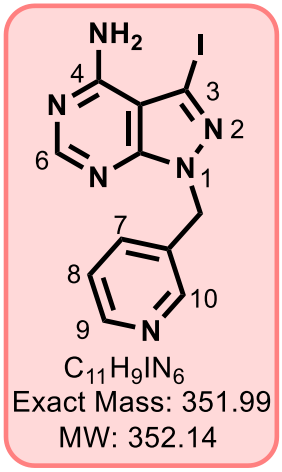

Using the general procedure 2, a reaction mixture containing **3** (0.50 g, 1.92 mmol), K_2CO_3 (3.2 eq.) and 3-picolyl chloride hydrochloride (1.2 eq.), the product was obtained as a yellow powder (0.34 g, 50%); MP 215–216°C; R_f (12% MeOH/DCM) 0.4; ^{1}H-NMR (DMSO-d_6, 600 MHz): δ_H 8.52 (dd, J = 2.4 and 0.6 Hz, 1H, H^{10}), 8.48 (dd, J = 4.8 and 1.2 Hz, 1H, H^9), 8.24 (s, 1H, H^6), 7.62 (ddd, J = 7.8, 2.4 and 1.8 Hz, 1H, H^7), 7.34 (ddd, J = 7.8, 2.4 and 1.8 Hz, 1H, H^8), and 5.62 (s, 2H, CH_2). ^{13}C-NMR (DMSO-d_6, 151 MHz): δ_C 158.22, 156.84, 154.05, 149.48, 149.42, 136.02, 132.88, 124.20, 103.68, 90.35, and 48.11. HPLC-MS (APCI/ESI): purity 97%, t_R = 2.01 min, (m/z) $[M+H]^+$ = 353.0.

3-Iodo-1-((5-methylpyridin-3-yl)methyl)-1*H*-pyrazolo[3,4-*d*]pyrimidin-4-amine, 49a

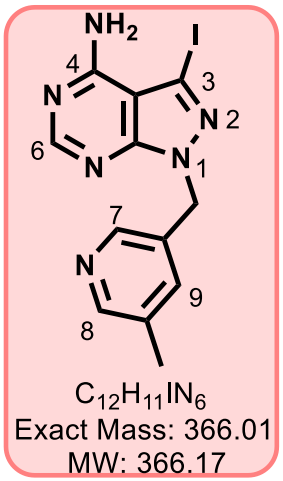

Using the general procedure 2 and a reaction mixture containing **3** (0.50 g, 1.92 mmol), K_2CO_3 (3.2 eq.) and 3-(chloromethyl)-5-methylpyridine HCl (1.2 eq.), the product was obtained as an off-white powder (0.30 g, 43%); R_f (10% MeOH/DCM) 0.45; ^{1}H-NMR (DMSO-d_6, 400 MHz): δ_H 8.34 (d, J = 2.0 Hz, 1H, H^8), 8.33 (d, J = 2.4 Hz, 1H, H^7), 8.26 (s, 1H, H^6), 7.46 (t, J = 2.4 Hz, 1H, H^9), 5.50 (s, 2H, CH_2), and 2.26 (s, 3H, CH_3). ^{13}C-NMR (DMSO-d_6, 101 MHz): δ_C 158.23, 156.84, 154.05, 149.88, 146.66, 136.24, 133.46, 132.32, 103.69, 90.20, 48.05, and 18.21. HPLC-MS (APCI/ESI): purity 95%, t_R = 2.14 min, (m/z) $[M+H]^+$ = 367.0.

1-((5-Chloropyridin-2-yl)methyl)-3-iodo-1*H*-pyrazolo[3,4-*d*]pyrimidin-4-amine, 50a

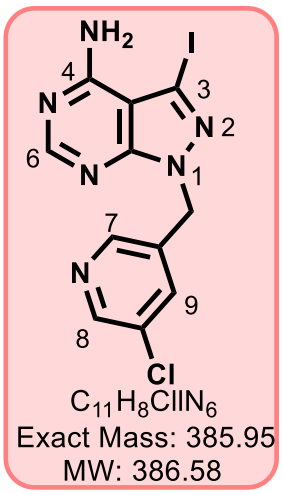

Using the general procedure 2 and a reaction mixture containing **3** (0.52 g, 1.99 mmol), K_2CO_3 (2 eq.) and 3-(chloromethyl)-5-chloropyridine (1.2 eq.), the product was obtained as an off-white powder (0.43 g, 56%); R_f (10% MeOH/DCM) 0.61; ^{1}H-NMR (DMSO-d_6, 600 MHz): δ_H 8.53 (broad d, J = 2.4 Hz, 1H, H^8), 8.42 (broad d, J = 1.8 Hz, 1H, H^7), 8.22 (s, 1H, H^6), 7.77 (dd, J = 2.4 and 1.8 Hz, 1H, H^9), and 5.53 (s, 2H, CH_2). ^{13}C-NMR (DMSO-d_6, 151 MHz): δ_C 158.23, 156.88, 154.11, 148.06, 147.77, 135.74, 134.55, 131.40, 103.73, 90.72, and 47.40. HPLC-MS (APCI/ESI): purity 96%, t_R = 2.30 min, (m/z) $[M+H]^+$ = 386.9.

1-((5-Fluoropyridin-3-yl)methyl)-3-iodo-1*H*-pyrazolo[3,4-*d*]pyrimidin-4-amine, 51a

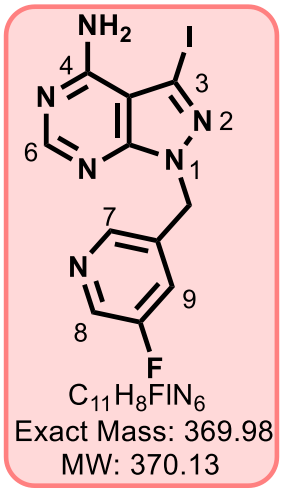

Using the general procedure 2 and a reaction mixture containing **3** (0.65 g, 2.49 mmol), K_2CO_3 (2 eq.) and 3-(chloromethyl)-5-fluoropyridine (1.2 eq.), the product was obtained as an off-white powder (455 mg, 49%); R_f (10% MeOH/DCM) 0.53; ^{1}H-NMR (DMSO-d_6, 600 MHz): δ_H 8.47 (d, J = 3.0 Hz, 1H, H^8), 8.35 (t, J = 1.8 Hz, 1H, H^7), 8.21 (s, 1H, H^6), 7.55 (ddd, J = 9.6, 2.4, and 1.8 Hz, 1H, H^9), and 5.55 (s, 2H, CH_2). ^{13}C-NMR (DMSO-d_6, 151 MHz): δ_C 159.28 (d, J = 255.3 Hz, $^1J_{C\text{-}F}$, 1C), 158.22, 156.86, 154.10, 145.61 (d, J = 4.5 Hz, $^4J_{C\text{-}F}$, 1C), 137.65 (d, J = 22.7 Hz, $^2J_{C\text{-}F}$, 1C), 134.81 (d, J = 4.5 Hz, $^3J_{C\text{-}F}$, 1C), 122.90 (d, J = 18.1 Hz, $^2J_{C\text{-}F}$, 1C), 103.72, 90.66, and 47.40. HPLC-MS (APCI/ESI): purity 95%, t_R = 2.12 min, (*m*/*z*) $[M+H]^+$ = 370.9.

3-Iodo-1-(pyridin-2-ylmethyl)-1*H*-pyrazolo[3,4-*d*]pyrimidin-4-amine, 52a (GS 86)

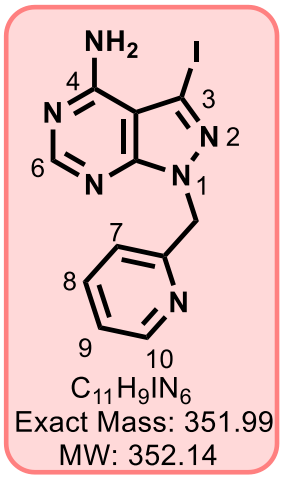

Using the general procedure 2 and a reaction mixture containing **3** (0.50 g, 1.92 mmol), K_2CO_3 (3.2 eq.) and 2-picolyl chloride hydrochloride (1.2 eq.), the product was obtained as a yellow powder (0.35 g, 52%); 217–218°C; R_f (12% MeOH/DCM) 0.3; ^{1}H-NMR (DMSO-d_6, 600 MHz): δ_H 8.46 (ddd, J = 4.8, 1.8 and 0.6 Hz, 1H, H^{10}), 8.20 (s, 1H, H^6), 7.74 (td, J = 7.8 and 1.8 Hz, 1H, H^8), 7.28 (ddd, J = 7.8, 4.8 and 1.2 Hz, 1H, H^9), 7.09 (dt, J = 7.8 and 1.2 Hz, 1H, H^7), and 5.57 (s, 2H, CH_2). ^{13}C-NMR (DMSO-d_6, 151 MHz): δ_C 158.21, 156.74, 156.39, 154.42, 149.68, 137.54, 123.29, 122.09, 103.61, 90.17, and 52.06. HPLC-MS (APCI/ESI): purity 97%, t_R = 2.01 min, (*m*/*z*) $[M+H]^+$ = 353.0.

1-((5-Chloropyridin-2-yl)methyl)-3-iodo-1*H*-pyrazolo[3,4-*d*]pyrimidin-4-amine, 53a

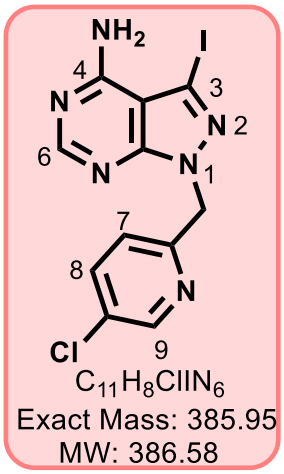

Using the general procedure 2 and a reaction mixture containing **3** (0.50 g, 1.92 mmol), K_2CO_3 (3.2 eq.) and 3-chloro-6-(chloromethyl) pyridine HCl (1.2 eq.), the product was obtained as an off-white powder (365 mg, 49%); R_f (10% MeOH/DCM) 0.59; ^{1}H-NMR (DMSO-d_6, 600 MHz): δ_H 8.35 (d, J = 2.4 Hz, 1H, H^9), 8.21 (s, 1H, H^6), 7.65 (dd, J = 8.4 and 2.4 Hz, 1H, H^8), 7.44 (d, J = 8.4 Hz, 1H, H^7), and 5.51 (s, 2H, CH_2). ^{13}C-NMR (DMSO-d_6, 151 MHz): δ_C 158.21, 156.85, 154.05, 150.13, 149.66, 139.76, 132.45, 124.82, 103.70, 90.57, and 47.27. HPLC-MS (APCI/ESI): purity 96%, t_R = 2.25 min, (m/z) $[M+H]^+$ = 386.9.

1-((5-Fluoropyridin-2-yl)methyl)-3-iodo-1*H*-pyrazolo[3,4-*d*]pyrimidin-4-amine, 54a

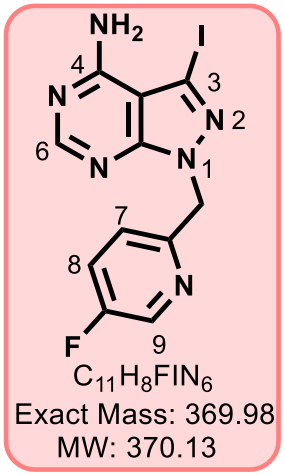

Using the general procedure 2 and a reaction mixture containing **3** (0.63 g, 2.41 mmol), K_2CO_3 (2 eq.) and 2-(chloromethyl)-5-fluoropyridine (1.2 eq.), the product was obtained as an off-white powder (475 mg, 53%); R_f (10% MeOH/DCM) 0.58; ^{1}H-NMR (DMSO-d_6, 600 MHz): δ_H 8.44 (d, J = 3.0 Hz, 1H, H^9), 8.18 (s, 1H, H^6), 7.65 (td, J = 8.4 and 3.0 Hz, 1H, H^8), 7.23 (dd, J = 8.4 and 4.2 Hz, 1H, H^7), and 5.55 (s, 2H, CH_2). ^{13}C-NMR (DMSO-d_6, 151 MHz): δ_C 158.91 (d, J = 253.4 Hz, $^1J_{C\text{-}F}$, 1C), 158.18, 156.74, 154.36, 152.64 (d, J = 3.6 Hz, $^2J_{C\text{-}F}$, 1C), 137.68 (d, J = 23.7 Hz, $^2J_{C\text{-}F}$, 1C), 124.44 (d, J = 18.7 Hz, $^2J_{C\text{-}F}$, 1C), 123.76 (d, J = 4.8 Hz, $^3J_{C\text{-}F}$, 1C), 103.61, 90.27, and 51.34. HPLC-MS (APCI/ESI): purity 96%, t_R = 2.08 min, (m/z) $[M+H]^+$ = 370.9.

3-Iodo-1-((5-(trifluoromethyl)pyridin-2-yl)methyl)-1*H*-pyrazolo[3,4-*d*]pyrimidin-4-amine 55a

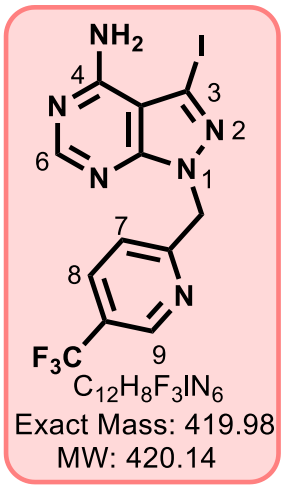

Using the general procedure 2 and a reaction mixture containing **3** (0.51 g, 1.95 mmol), K_2CO_3 (2 eq.) and 3-trifluoro-6-(chloromethyl) pyridine (1.2 eq.), the product was obtained as an off-white powder (0.38 g, 46%); R_f (10% MeOH/DCM) 0.58; ^{1}H-NMR (DMSO-d_6, 600 MHz): δ_H 8.85 (broad d, J = 2.4 Hz, 1H, H^9), 8.18 (s, 1H, H^6), 8.14 (dd, J = 8.4 and 2.4 Hz, 1H, H^8), 7.34 (d, J = 8.4 Hz, 1H, H^7), and 5.68 (s, 2H, CH_2). ^{13}C-NMR (DMSO-d_6, 151 MHz): δ_C 160.89, 158.22, 156.81, 154.53, 146.50 (q, J = 4.1 Hz), 135.04 (q, J = 3.6 Hz), 124.68 (q, J = 33.2 Hz, $^2J_{C\text{-}F}$, 1C), 124.08 (q, J = 273.3 Hz, $^1J_{C\text{-}F}$, 1C), 122.39, 103.66, 90.60, and 51.75. HPLC-MS (APCI/ESI): purity 95%, t_R = 2.34 min, (*m*/*z*) $[M+H]^+$ = 420.9

1-((6-Chloropyridin-2-yl)methyl)-3-iodo-1*H*-pyrazolo[3,4-*d*]pyrimidin-4-amine, 56a

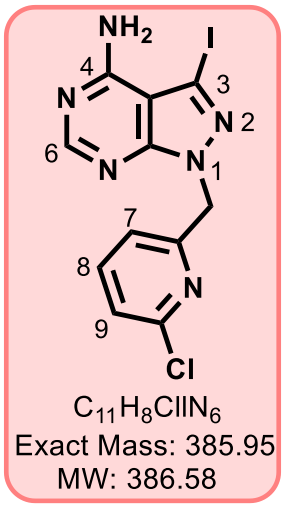

Using the general procedure 2 and a reaction mixture containing **3** (0.80 g, 3.06 mmol), K_2CO_3 (2 eq.) and 2-chloro-6-(chloromethyl) pyridine (1.2 eq.), the product was obtained as an off-white powder (0.51 g, 43%); R_f (10% MeOH/DCM) 0.50; ^{1}H-NMR (DMSO-d_6, 600 MHz): δ_H 8.18 (s, 1H, H^6), 7.78 (t, J = 7.8 Hz, 1H, H^8), 7.39 (d, J = 8.0 Hz, 1H, H^7), 7.05 (d, J = 7.8 Hz, 1H, H^9), and 5.53 (s, 2H, CH_2). ^{13}C-NMR (DMSO-d_6, 151 MHz): δ_C 158.21, 157.46, 156.82, 154.38, 150.22, 141.21, 123.87, 121.41, 103.63, 90.58, and 51.44. HPLC-MS (APCI/ESI): purity 95%, t_R = 2.21 min, (*m*/*z*) $[M+H]^+$ = 386.9**.**

3-Iodo-1-((6-methylpyridin-2-yl)methyl)-1*H*-pyrazolo[3,4-*d*]pyrimidin-4-amine, 57a

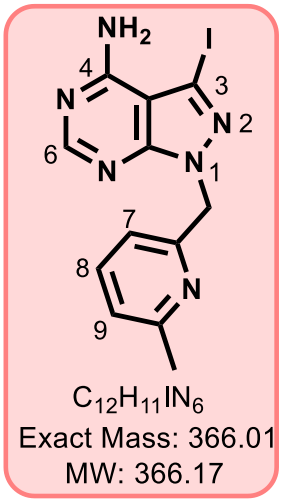

Using the general procedure 2 and a reaction mixture containing **3** (0.60 g, 2.30 mmol), K_2CO_3 (2 eq.) and 2-methyl-6-(bromomethyl) pyridine (1.2 eq.), the product was obtained as an off-white powder (0.38 g, 45%); R_f (10% MeOH/DCM) 0.38; ^{1}H-NMR (DMSO-d_6, 400 MHz): δ_H 8.23 (s, 1H), 7.61 (t, J = 8.0 Hz, 1H, H^8), 7.16 (d, J = 7.6 Hz, 1H, H^7), 6.77 (d, J = 7.6 Hz, 1H, H^9), 5.53 (s, 2H, CH_2), and 2.43 (s, 3H, CH_3). ^{13}C-NMR (DMSO-d_6, 101 MHz): δ_C 158.23, 158.10, 156.77, 155.84, 154.37, 137.78, 122.58, 118.91, 103.65, 90.12, 52.28, and 24.40. HPLC-MS (APCI/ESI): purity 95%, t_R = 2.10 min, (*m*/*z*) $[M+H]^+$ = 366.9.

1-((6-Fluoropyridin-2-yl)methyl)-3-iodo-1*H*-pyrazolo[3,4-*d*]pyrimidin-4-amine, 58a

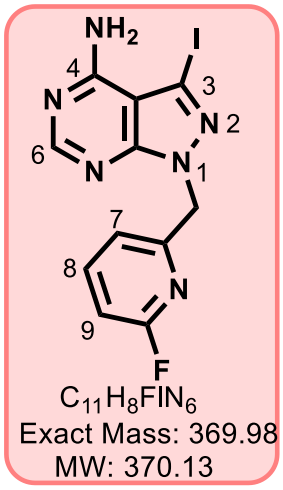

Using the general procedure 2 and a reaction mixture containing **3** (0.50 g, 1.92 mmol), K_2CO_3 (2 eq.) and 2-(chloromethyl)-6-fluoropyridine (1.2 eq.), the product was obtained as an off-white powder (0.41 g, 58%); R_f (10% MeOH/DCM) 0.54; ^{1}H-NMR (DMSO-d_6, 600 MHz): δ_H 8.18 (s, 1H, H^6), 7.91 (q, J = 8.4 Hz, 1H, H^8), 7.05 (dd, J = 7.8 and 2.4 Hz, 1H, H^7), 7.03 (dd, J = 7.8 and 2.4 Hz, 1H, H^9), and 5.51 (s, 2H, CH_2). ^{13}C-NMR (DMSO-d_6, 151 MHz): δ_C 162.91 (d, J = 238.6 Hz, $^1J_{C\text{-}F}$, 1C), 158.20, 156.80, 155.37 (d, J = 13.6 Hz, $^3J_{C\text{-}F}$, 1C), 154.42, 143.52 (d, J = 7.6 Hz, $^3J_{C\text{-}F}$, 1C), 120.06 (d, J = 4.5 Hz, $^4J_{C\text{-}F}$, 1C), 108.99 (d, J = 36.2 Hz, $^2J_{C\text{-}F}$, 1C), 103.60, 90.49, and 51.13. HPLC-MS (APCI/ESI): purity 95%, t_R = 2.17 min, (*m*/*z*) $[M+H]^+$ = 370.9.

3-Iodo-1-((6-(trifluoromethyl)pyridin-2-yl)methyl)-1*H*-pyrazolo[3,4-*d*]pyrimidin-4-amine, 59a

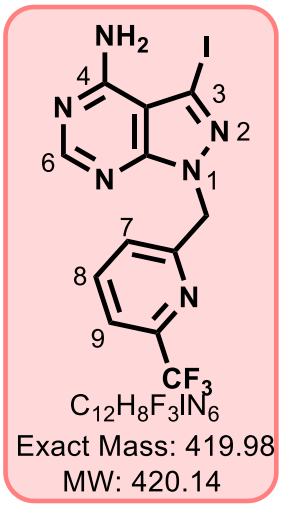

$C_{12}H_8F_3IN_6$
Exact Mass: 419.98
MW: 420.14

Using the general procedure 2 and a reaction mixture containing **3** (0.75 g, 2.87 mmol), K_2CO_3 (2 eq.) and 2-(chloromethyl)-6-(trifluoromethyl) pyridine (1.2 eq.), the product was obtained as an off-white powder (0.58 g, 48%); R_f (10% MeOH/DCM) 0.52; ^{1}H-NMR (DMSO-d_6, 600 MHz): δ_H 8.19 (s, 1H, H^6), 8.01 (t, J = 7.8 Hz, 1H, H^8), 7.79 (d, J = 7.8 Hz, 1H, H^7), 7.28 (d, J = 8.4 Hz, 1H, H^9), and 5.65 (s, 2H, CH_2). ^{13}C-NMR (DMSO-d_6, 151 MHz): δ_C 158.23, 157.63, 156.86, 154.50, 146.46 (q, J = 34.7 Hz), 140.08, 125.67, 121.86 (q, J = 274.8 Hz), 120.26 (q, J = 4.5 Hz), 103.68, 90.77, and 51.79. HPLC-MS (APCI/ESI): purity 95%, t_R = 2.36 min, (*m*/*z*) $[M+H]^+$ = 421.0.

1-(Cyclohexyl methyl)-3-iodo-1*H*-pyrazolo[3,4-*d*]pyrimidin-4-amine, 60a

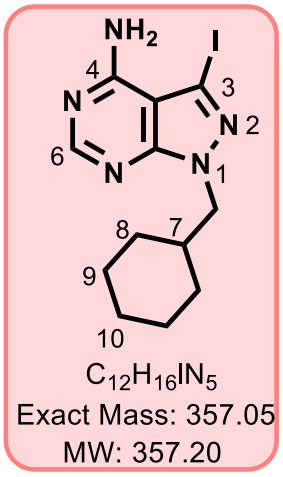

$C_{12}H_{16}IN_5$
Exact Mass: 357.05
MW: 357.20

Using the general procedure 2 and a reaction mixture containing **3** (0.60 g, 2.30 mmol), K_2CO_3 (2 eq.) and cyclohexylmethyl bromide (1.2 eq.), the product was obtained as an off-white powder (485 mg, 59%); R_f (10% MeOH/DCM) 0.48; ^{1}H-NMR (DMSO-d_6, 600 MHz): δ_H 8.15 (s, 1H, H^6), 4.07 (d, J = 7.2 Hz, 2H, CH_2), 1.83 (ttt, J = 10.8, 7.2 and 3.6 Hz, 1H, H^7), 1.61–1.58 (m, 2H, H^{9a}), 1.54–1.52 (m, 1H, H^{10e}), 1.44–1.42 (m, 2H, H^{8e}), 1.14–1.04 (m, 3H, $H^{10a, 9e}$), 0.91 (qd, J = 11.7 and 3.4 Hz, 2H, H^{8a}). ^{13}C-NMR (DMSO-d_6, 151 MHz): δ_C 158.12, 156.40, 154.15, 103.32, 88.89, 52.87, 38.16, 30.43 (2C), 26.23, and 25.50 (2C). HPLC-MS (APCI/ESI): purity 95%, t_R = 2.54 min, (m/z) $[M+H]^+$ = 358.0.

1-((4,4-Difluorocyclohexyl)methyl)-3-iodo-1*H*-pyrazolo[3,4-*d*]pyrimidin-4-amine, 61a

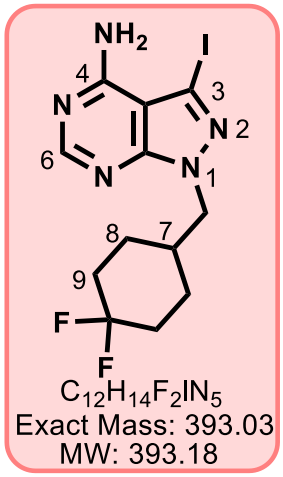

Using the general procedure 2 and a reaction mixture containing **3** (0.75 g, 2.87 mmol), K_2CO_3 (2 eq.) and 4-(bromomethyl)-1,1-difluorocyclohexane (1.2 eq.), the product was obtained as an off-white powder (535 mg, 47%); R_f (10% MeOH/ DCM) 0.55; ^{1}H-NMR (DMSO-d_6, 600 MHz): δ_H 8.16 (s, 1H, H^6), 4.16 (d, J = 7.2 Hz, 2H, CH_2), 2.02 - 1.99 (m, 1H, H^7), 1.95–1.91 (m, 2H, H^{9a}), 1.77 - 1.67 (m, 2H, H^{9e}), 1.57–1.53 (m, 2H, H^{8e}), and 1.24–1.17 (m, 2H, H^{9e}). ^{13}C-NMR (DMSO-d_6, 151 MHz): δ_C 158.15, 156.50, 154.17, 124.56 (t, J = 240.4 Hz, $^1J_{C\text{-}F}$, 1C), 103.37, 89.28, 51.38, 35.90, 32.56 (t, J = 23.7 Hz, $^2J_{C\text{-}F}$, 2C), and 26.56 (broad d, J = 9.4 Hz, $^3J_{C\text{-}F}$, 2C). HPLC-MS (APCI/ESI): purity 96%, t_R = 2.45 min, (m/z) $[M+H]^+$ = 394.0.

3-Iodo-1-(3-nitrobenzyl)-1*H*-pyrazolo[3,4-*d*]pyrimidin-4-amine, (GS 152)

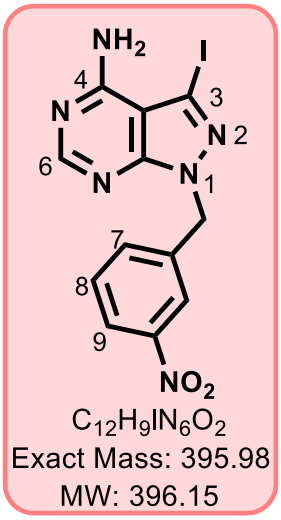

Using the general procedure 2 and a reaction mixture containing **3** (0.70 g, 2.68 mmol), K_2CO_3 (2 eq.) and 3-nitrobenzyl bromide (1.2 eq.), the product was obtained as an off-white powder (0.67 g, 63%); R_f (10% MeOH/DCM) 0.60; ^{1}H-NMR (DMSO-d_6, 400 MHz): δ_H 8.25 (s, 1H, H^6), 8.15 (t, J = 2.0 Hz, 1H, H^{10}), 8.13–8.10 (m, 1H, H^9), 7.67–7.62 (m, 2H, $H^{7,8}$), and 5.64 (s, 2H, CH_2). ^{13}C-NMR (DMSO-d_6, 101 MHz): δ_C 158.27, 156.94, 154.20, 148.35, 139.44, 134.74, 130.76, 123.18, 122.79, 103.72, 90.56, and 49.62. HPLC-MS (APCI/ESI): purity 95%, t_R = 2.36 min, (*m*/*z*) $[M+H]^+$ = 397.0.

3-Iodo-1-(4-nitrobenzyl)-1*H*-pyrazolo[3,4-*d*]pyrimidin-4-amine, (GS 94)

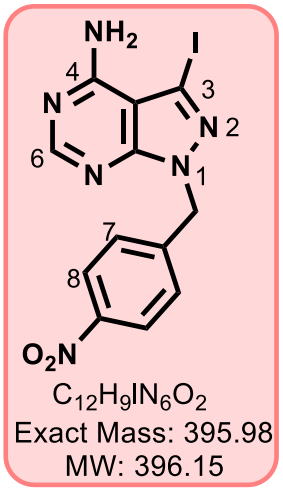

$C_{12}H_9IN_6O_2$
Exact Mass: 395.98
MW: 396.15

Using the general procedure 2 and a reaction mixture containing **3** (0.60 g, 2.30 mmol), K_2CO_3 (2 eq.) and 4-nitrobenzyl bromide (1.2 eq.), the product was obtained as an off-white powder (382 mg, 42%); R_f (10% MeOH/DCM) 0.50; ^{1}H-NMR (DMSO-d_6, 600 MHz): δ_H 8.20 (s, 1H, H^6), 8.15 (d, J = 9.0 Hz, 2H, H^8), 7.41 (d, J = 9.0 Hz, 2H, H^7), and 5.61 (s, 2H, CH_2). ^{13}C-NMR (DMSO-d_6, 151 MHz): δ_C 158.23, 156.90, 154.20, 147.45, 144.79, 129.11 (2C), 124.26 (2C), 103.66, 90.67, and 49.74. HPLC-MS (APCI/ESI): purity 95%, t_R = 2.35 min, (m/z) $[M+H]^+$ = 397.0.

1-(3-Aminobenzyl)-3-iodo-1*H*-pyrazolo[3,4-*d*]pyrimidin-4-amine, 18a

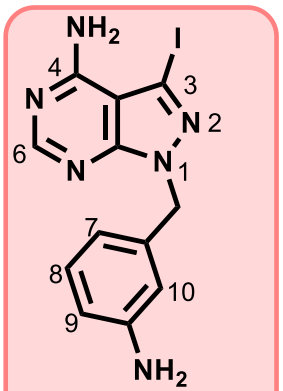

$C_{12}H_{11}IN_6$
Exact Mass: 366.01
MW: 366.17

A reaction mixture containing the nitro precursor synthesized in-house **GS 152** (1.10 g, 2.78 mmol), iron dust (6 eq.), conc. HCl (5 eq.) in dioxane (5 mL) was stirred at 85°C for 48 hours. The mixture was then cooled to 20°C, basified to pH 10 with aqueous NaOH and extracted with EtOAc (50 mL × 3). The combined organic filtrate was washed with distilled water (50 mL × 3), dried over anhydrous Na_2SO_4, concentrated *in vacuo* and purified by column chromatography (0–10 % MeOH/DCM) to obtain the expected product as an off-white powder (0.42 g, 41%); R_f (10% MeOH/DCM) 0.33; ^{1}H-NMR (DMSO-d_6, 400 MHz): δ_H 8.24 (s, 1H, H^6), 6.95 (t, J = 7.6 Hz, 1H, H^8), 6.45 (ddd, J = 8.0, 2.4 and 1.2 Hz, 1H, H^7), 6.40 (t, J = 1.2 Hz, 1H, H^{10}), 6.38–6.37 (m, 1H, H^9), 5.31 (s, 2H, CH_2), and 5.06 (s, 2H, benzyl NH_2). ^{13}C-NMR (DMSO-d_6, 101 MHz): δ_C 158.18, 156.67, 153.95, 149.32, 137.85, 129.48, 115.43, 113.70, 113.18, 103.55, 89.47, and 50.76. HPLC-MS (APCI/ESI): purity < 95%, t_R = 1.40 min, (m/z) $[M+H]^+$ = 367.0.

1-(4-Aminobenzyl)-3-iodo-1*H*-pyrazolo[3,4-*d*]pyrimidin-4-amine, 13a

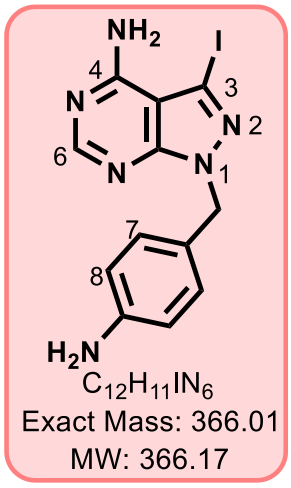

Using similar procedure as **18a** in a reaction mixture containing the appropriate nitro compound **GS 94** (0.4 g, 1.0 mmol), the product was obtained as an off-white powder (0.21 g, 57%); R_f (10% MeOH/DCM) 0.27; ^{1}H-NMR (DMSO-d_6, 600 MHz): δ_H 8.19 (s, 1H, H^6), 6.92 (d, J = 8.4 Hz, 2H, H^7), 6.44 (d, J = 8.4 Hz, 2H, H^8), 5.22 (s, 2H, CH_2), and 5.01 (s, 2H, benzyl NH_2). ^{13}C-NMR (DMSO-d_6, 151 MHz): δ_C 158.10, 156.55, 153.58, 148.79, 129.36 (2C), 124.09, 114.11 (2C), 103.52, 89.17, and 50.45. HPLC-MS (APCI/ESI): purity 95%, t_R = 0.90 min, (*m*/*z*) $[M+H]^+$ = 367.0.

10.2.1.6 General procedure 3: Synthesis of target compounds

A solution of the appropriate *N*-alkylated intermediate (1 eq.) and 5-(4,4,5,5-tetramethyl-1,3,2-dioxaborolan-2-yl-)benzo[*d*]oxazol-2-amine, (**5**) (1.3 eq.) in 7 mL dioxane/water mixture (3:1) was purged with N_2 for 5 min. To the resulting mixture was sequentially added Na_2CO_3 (5 eq.) and $Pd(PPh_3)_4$ (0.08 eq.), tightly sealed and then heated with stirring at 100°C for 12 h. The reaction mixture was then cooled to 20°C, filtered through celite and the cake washed with 50% MeOH/DCM (50 mL). The organic filtrate was concentrated *in vacuo* and purified by column chromatography (0–12 % MeOH/DCM) to obtain the crude product, which was washed with MeOH and dried, to afford the expected product.

5-(4-Amino-1-isopropyl-1*H*-pyrazolo[3,4-*d*] pyrimidin-3-yl) benzo[*d*]oxazol-2-amine, 62 (GS-20b; MLN0128)

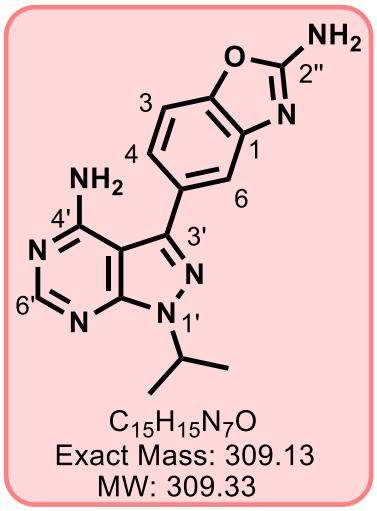

Using the general procedure 3 and a reaction mixture containing **62a** (0.30 g, 0.99 mmol), the product was obtained as an off-white solid (0.16 g, 53%); MP 273–274°C; R_f (10% MeOH/DCM) 0.5; ^{1}H-NMR (DMSO-d_6, 600 MHz): δ_H 8.23 (s, 1H, $H^{6'}$), 7.51 (s, 2H, $NH^{2''}$), 7.46 (d, J = 8.1 Hz, 1H, H^3), 7.41 (d, J = 1.8 Hz, 1H, H^6), 7.25 (dd, J = 8.1 and 1.8 Hz, 1H, H^4), 5.06 (septet, 1H, -CH) and 1.50 (d, J = 6.6 Hz, 6H, CH_3). ^{13}C-NMR (DMSO-d_6, 151 MHz): δ_C 163.88, 158.35, 155.55, 153.55, 148.75, 144.82, 144.27, 129.18, 120.94, 115.48,

109.31, 97.92, 48.57, and 22.26. HPLC-MS (APCI/ESI): purity 98%, t_R = 2.50 min, (*m/z*) $[M+H]^+$ = 310.1.

5-(4-Amino-1-benzyl-1*H*-pyrazolo[3,4-*d*]pyrimidin-3-yl)benzo[*d*]oxazol-2-amine, 6 (GS-77)

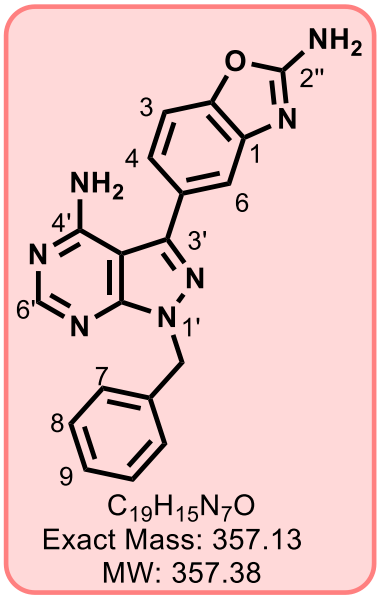

Using the general procedure 3 and a reaction mixture containing **6a** (0.31 g, 0.88 mmol), the product was obtained as a brown solid (0.11 g, 36%); MP 287–289°C; R_f (8% MeOH/DCM) 0.4; ^{1}H-NMR (DMSO-d_6, 400 MHz): δ_H 8.29 (s, 1H, $H^{6'}$), 7.51 (s, 2H, $NH_2^{2''}$), 7.46 (d, *J* = 8.0 Hz, 1H, H^3), 7.42 (d, *J* = 2.0 Hz, 1H, H^6), 7.36–7.27 (m, 5H, $H^{7,8,9}$), 7.25 (dd, *J* = 8.0 and 2.0 Hz, 1H, H^4), and 5.56 (s, 2H, CH_2). ^{13}C-NMR (DMSO-d_6, 101 MHz): δ_H 163.92, 158.68, 156.43, 154.74, 148.86, 145.05, 144.90, 137.71, 129.00 (2C), 128.89, 128.08 (2C), 127.98, 120.93 (1C), 115.48, 109.33, 97.88, and 50.26. HPLC-MS (APCI/ESI): purity 99%, t_R = 2.40 min, (*m/z*) $[M+H]^+$ = 358.1.

5-(4-Amino-1-(4-chlorobenzyl)-1*H*-pyrazolo[3,4-*d*]pyrimidin-3-yl)benzo[*d*]oxazol-2-amine, 7 (GS 55)

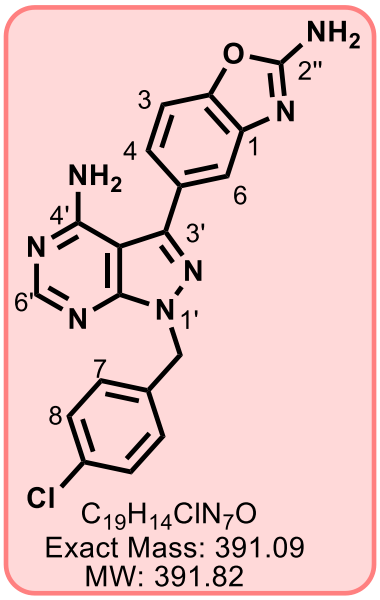

Using the general procedure 3 and a reaction mixture containing **7a** (0.15 g, 0.39 mmol), the product was obtained as an off-white solid (64 mg, 42%); MP 292–294°C; R_f (100% EtOAc) 0.6; ^{1}H-NMR (600 MHz, DMSO-d_6): δ_H 8.27 (s, 1H, $H^{6'}$), 7.52 (s, 2H, $NH_2^{2''}$), 7.46 (d, *J* = 8.1 Hz, 1H, H^3), 7.40 (d, *J* = 1.7 Hz, 1H, H^6), 7.39 (d, *J* = 9.0 Hz, 2H, H^8), 7.32 (d, *J* = 9.0 Hz, 2H, H^7), 7.23 (dd, *J* = 8.1 and 1.7 Hz, 1H, H^4), and 5.55 (s, 2H, CH_2). ^{13}C-NMR (DMSO-d_6, 150 MHz): δ_C 163.90, 158.67, 156.48, 154.72, 148.85, 145.23, 144.87, 136.67, 132.68, 129.98 (2C), 129.02 (2C), 128.77, 120.92, 115.46, 109.34, 97.85, and 49.51. HPLC-MS (APCI/ESI): purity 96%, t_R = 2.49 min, (*m/z*) $[M+H]^+$ = 392.0.

5-(4-Amino-1-(4-flourobenzyl)-1*H*-pyrazolo[3,4-*d*]pyrimidin-3-yl)benzo[*d*]oxazol-2-amine, 8 (GS 65)

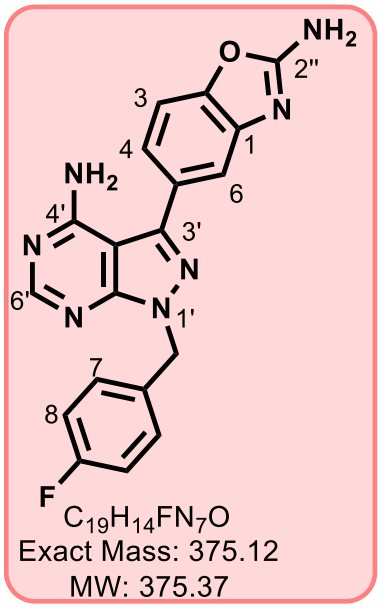

$C_{19}H_{14}FN_7O$
Exact Mass: 375.12
MW: 375.37

Using the general procedure 3 and a reaction mixture containing **8a** (0.20 g, 0.54 mmol), the product was obtained as a brown solid (0.11 g, 54%); MP 298–300°C; R_f (10% MeOH/DCM) 0.4; ^{1}H-NMR (DMSO-d_6, 600 MHz): δ_H 8.26 (s, 1H, $H^{6'}$), 7.49 (s, 2H, $NH_2^{2''}$), 7.43 (d, J = 8.1 Hz, 1H, H^3), 7.38 (d, J = 1.8 Hz, 1H, H^6), 7.34 (dd, J = 8.4 and 5.4 Hz, 2H, H^8), 7.21 (dd, J = 7.8 and 1.8 Hz, 1H, H^4), 7.13 (t, J = 9.0 Hz, 2H, H^7), and 5.52 (s, 2H, CH_2). ^{13}C-NMR (DMSO-d_6, 151 MHz): δ_C 163.90, 162.82 (d, J = 241.6 Hz, $^1J_{C\text{-}F}$, 2C), 158.67, 156.46, 154.65, 148.84, 145.14, 144.87, 133.90, 130.27 (d, J = 9.1 Hz, $^3J_{C\text{-}F}$, 2C), 128.81, 120.92, 115.88 (d, J = 21.1 Hz, $^2J_{C\text{-}F}$, 2C), 115.74, 109.33, 97.86, and 49.48. HPLC-MS (APCI/ESI): purity 98%, t_R = 2.42 min, (*m*/*z*) $[M+H]^+$ = 376.1.

4-(4-Amino-3-(2-aminobenzo[*d*]oxazol-5-yl)-1*H*-pyrazolo[3,4-*d*]pyrimidin-1-yl)methyl) benzonitrile, 9 (GS 63)

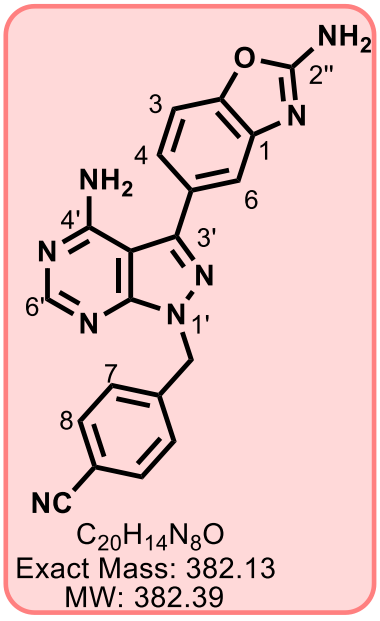

$C_{20}H_{14}N_8O$
Exact Mass: 382.13
MW: 382.39

Using the general procedure 3 and a reaction mixture containing **9a** (0.39 g, 1.0 mmol), the product was obtained as a white solid (0.13 g, 32%); MP 309–310°C; R_f (10% MeOH/DCM) 0.5; ^{1}H-NMR (DMSO-d_6, 600 MHz): δ_H 8.25 (s, 1H, $H^{6'}$), 7.77 (d, J = 8.4 Hz, 2H, H^8), 7.50 (s, 2H, $NH_2^{2''}$), 7.43 (d, J = 8.4 Hz, 1H, H^3), 7.41 (d, J = 8.4 Hz, 2H, H^7), 7.40 (d, J = 1.2 Hz, 1H, H^6), 7.22 (dd, J = 7.8 and 1.8 Hz, 1H, H^4), and 5.64 (s, 2H, CH_2). ^{13}C-NMR (DMSO-d_6, 151 MHz): δ_C 163.91, 158.71, 156.58, 154.93, 148.89, 145.52, 144.88, 143.26, 133.03 (2C), 128.82 (2C), 128.69, 120.94, 119.10, 115.49, 110.84, 109.35, 97.88, and 49.78. HPLC-MS (APCI/ESI): purity 99%, t_R = 2.34 min, (*m*/*z*) $[M+H]^+$ = 383.1.

5-(4-Amino-1-(4-(trifluoromethyl)benzyl)-1*H*-pyrazolo[3,4-*d*]pyrimidin-3-yl) benzo[*d*]oxazol-2-amine, 10 (GS 59)

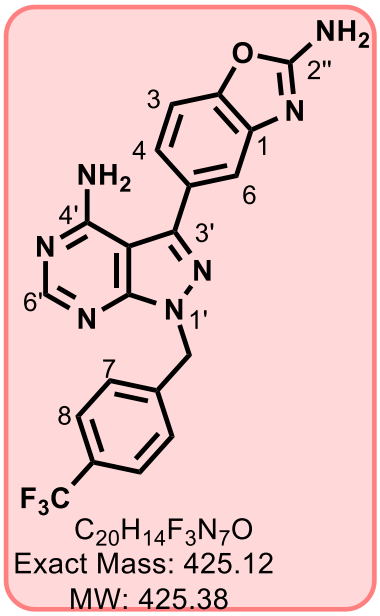

Using the general procedure 3 and a reaction mixture containing **10a** (0.30 g, 0.72 mmol), the product was obtained as a pale yellow solid (0.11 g, 37%); MP 307–308°C; R_f (8% MeOH/DCM) 0.4; ^{1}H-NMR (DMSO-d_6, 600 MHz): δ_H 8.28 (s, 1H, $H^{6'}$), 7.70 (d, J = 8.1 Hz, 2H, H^8), 7.52 (s, 2H, $NH_2^{2''}$), 7.49 (d, J = 8.1 Hz, 2H, H^7), 7.46 (d, J = 8.1 Hz, 1H, H^3), 7.42 (d, J = 1.7 Hz, 1H, H^6), 7.24 (dd, J = 8.1 and 1.7 Hz, 1H, H^4), and 5.67 (s, 2H, CH_2). ^{13}C-NMR (DMSO-d_6, 151 MHz): δ_C 163.91, 158.70, 156.56, 154.88, 148.88, 145.42, 144.89, 142.38, 132.01, 128.74 (2C), 128.53 (q, J = 31.7 Hz, $^2J_{C\text{-}F}$, 1C), 125.97 (2C), 125.53 (q, J = 271.8 Hz, $^1J_{C\text{-}F}$, 1C), 120.93, 115.48, 109.34, 97.87, and 49.70. HPLC-MS (APCI/ESI): purity 98%, t_R = 2.53 min, (*m/z*) $[M+H]^+$ = 426.1.

5-(4-Amino-1-(4-methylbenzyl)-1*H*-pyrazolo[3,4-*d*]pyrimidin-3-yl)benzo[*d*]oxazol-2-amine, 11 (GS 69)

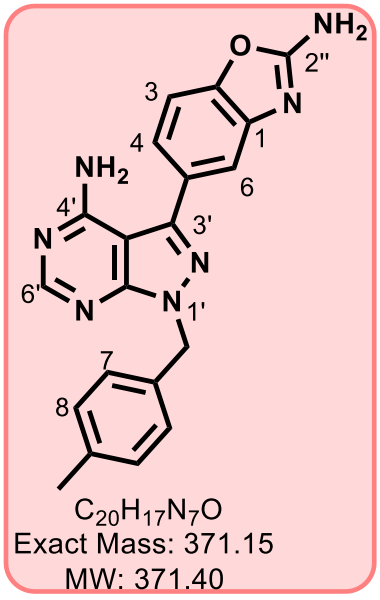

Using the general procedure 3 and a reaction mixture containing **11a** (0.33 g, 0.90 mmol), the product was obtained as a brown solid (0.16 g, 49%); MP 276–278°C; R_f (8% MeOH/DCM) 0.5; ^{1}H-NMR (DMSO-d_6, 300 MHz): δ 8.28 (s, 1H, $H^{6'}$), 7.52 (s, 2H, $NH_2^{2''}$), 7.46 (d, J = 8.4 Hz, 1H, H^3), 7.41 (d, J = 1.8 Hz, 1H, H^6), 7.23 (dd, J = 8.4 and 1.8 Hz, 1H, H^4), 7.20 (d, J = 7.8 Hz, 2H, H^7) 7.12 (d, J = 7.8 Hz, 2H, H^8), 5.50 (s, 2H, CH_2), and 2.25 (s, 3H, CH_3). ^{13}C-NMR (DMSO-d_6, 151 MHz): δ_C 163.90, 158.64, 156.38, 154.62, 148.81, 144.93, 144.86, 137.20, 134.69, 129.52 (2C), 128.89, 128.12 (2C), 120.91, 115.45, 109.32, 97.83, 50.03, and 21.12. HPLC-MS (APCI/ESI): purity 97%, t_R = 2.48 min, (*m/z*) $[M+H]^+$ = 372.1.

5-(4-Amino-1-(4-methoxybenzyl)-1*H*-pyrazolo[3,4-*d*]pyrimidin-3-yl)benzo[*d*]oxazol-2-amine, 12 (GS 42)

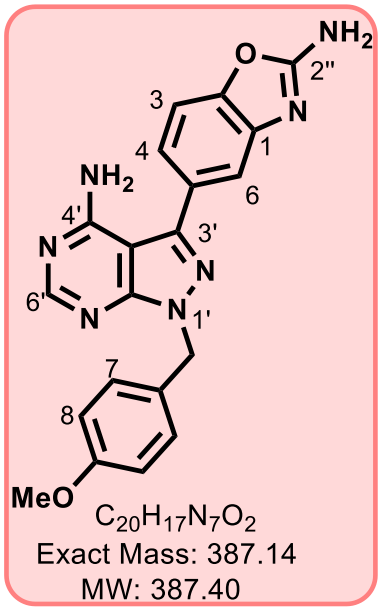

Using the general procedure 3 and a reaction mixture containing **12a** (0.60 g, 1.57 mmol), the product was obtained as a brown solid (0.35 g, 57%); MP 285–287°C; R_f (10% MeOH/DCM) 0.5; ^{1}H-NMR (600 MHz, DMSO-d_6): δ_H 8.28 (s, 1H, $H^{6'}$), 7.51 (s, 2H, $NH_2^{2''}$), 7.45 (d, J = 8.1 Hz, 1H, H^3), 7.39 (d, J = 1.7 Hz, 1H, H^6), 7.27 (d, J = 9.0 Hz, 2H, H^7), 7.22 (dd, J = 8.1 and 1.7 Hz, 1H, H^4), 6.88 (d, J = 9.0 Hz, 2H, H^8), 5.47 (s, 2H, CH_2), and 3.70 (s, 4H, OMe). ^{13}C-NMR (151 MHz, DMSO-d_6): δ_C 163.89, 159.19, 158.53, 156.22, 154.45, 148.81, 144.91, 144.83, 129.63 (2C), 128.87, 120.91, 115.43, 114.40 (2C), 109.33, 97.82, 55.53, and 49.77. HPLC-MS (APCI/ESI): purity 97%, t_R = 2.40 min, (*m*/*z*) $[M+H]^+$ = 388.1.

5-(4-Amino-1-(4-aminobenzyl)-1*H*-pyrazolo[3,4-*d*]pyrimidin-3-yl)benzo[*d*]oxazol-2-amine, 13 (GS 149)

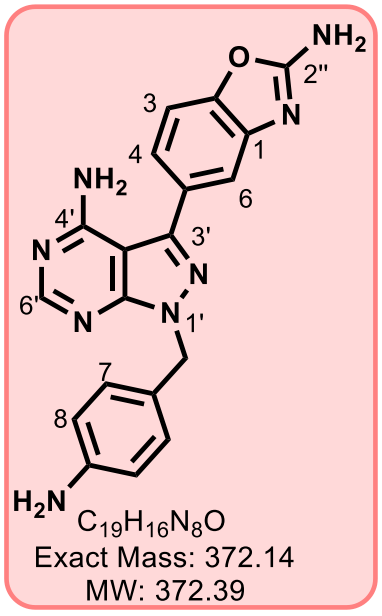

Using the general procedure 3 and a reaction mixture containing **13a** (145 mg, 0.40 mmol), the product was obtained as an off-white solid (25 mg, 17%); MP 282–283°C; R_f (15% MeOH/DCM) 0.45; ^{1}H-NMR (600 MHz, DMSO-d_6) δ_H 8.23 (s, 1H, $H^{6'}$), 7.47 (s, 2H, $NH_2^{2''}$), 7.41 (d, J = 8.4 Hz, 1H, H^3), 7.35 (d, J = 1.8 Hz, 1H, H^6), 7.18 (dd, J = 8.4 and 1.8 Hz, 1H, H^4), 6.99 (d, J = 8.4 Hz, 2H, H^7), 6.45 (d, J = 8.4 Hz, 2H, H^8), 5.30 (s, 2H, CH_2), and 4.98 (s, 2H, benzyl NH_2). ^{13}C-NMR (DMSO-d_6, 151 MHz): δ_C 163.86, 158.56, 156.21, 154.28, 148.74, 148.65, 144.83, 144.52, 129.34 (2C), 129.00, 124.50, 120.88, 115.41, 114.11 (2C), 109.29, 97.79, and 50.15. HPLC-MS (APCI/ESI): purity 95%, t_R = 2.20 min, (*m*/*z*) $[M+H]^+$ = 373.1.

5-(4-Amino-1-(3-flourobenzyl)-1*H*-pyrazolo[3,4-*d*]pyrimidin-3-yl)benzo[*d*]oxazol-2-amine, 14 (GS 73)

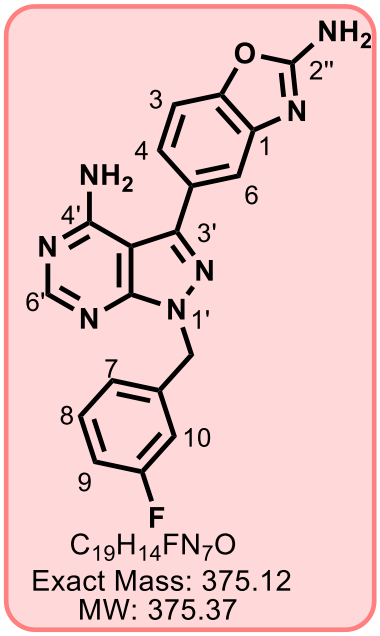

Using the general procedure 3 and a reaction mixture containing **14a** (0.36 g, 0.98 mmol), the product was obtained as an off-white solid (0.12 g, 34%); MP 305–307°C; R_f (10% MeOH/DCM) 0.5; ^{1}H-NMR (DMSO-d_6, 400 MHz): δ_H 8.29 (s, 1H, $H^{6'}$), 7.51 (s, 2H, $NH_2^{2''}$), 7.47 (d, J = 8.4 Hz, 1H, H^3), 7.43 (d, J = 1.6 Hz, 1H, H^6), 7.41–7.35 (m, 1H, H^8), 7.25 (dd, J = 8.4 and 2.0 Hz, 1H, H^4), 7.13–7.09 (m, 3H, $H^{7,9,10}$), and 5.59 (s, 2H, CH_2). ^{13}C-NMR (DMSO-d_6, 101 MHz): δ_C 163.93, 163.80 (d, J = 244.4 Hz, $^1J_{C\text{-}F}$), 158.70, 156.51, 154.82, 148.89, 145.30, 144.90, 140.52 (d, J = 8.1 Hz, $^3J_{C\text{-}F}$, 1C), 131.13 (d, J = 8.1 Hz, $^3J_{C\text{-}F}$, 1C), 128.80, 124.07 (d, J = 2.0 Hz, $^4J_{C\text{-}F}$, 1C), 120.95, 115.49, 114.95 (d, J = 5.1 Hz, $^2J_{C\text{-}F}$, 1C), 114.74 (d, J = 6.1 Hz, $^2J_{C\text{-}F}$, 1C), 109.35, 97.91, and 49.66. HPLC-MS (APCI/ESI): purity 99%, t_R = 2.00 min, (*m*/*z*) $[M+H]^+$ = 376.1.

5-(4-Amino-1-(3-(trifluoromethyl)benzyl)-1*H*-pyrazolo[3,4-*d*]pyrimidin-3-yl)benzo[*d*]oxazol-2-amine, 15 (GS 71)

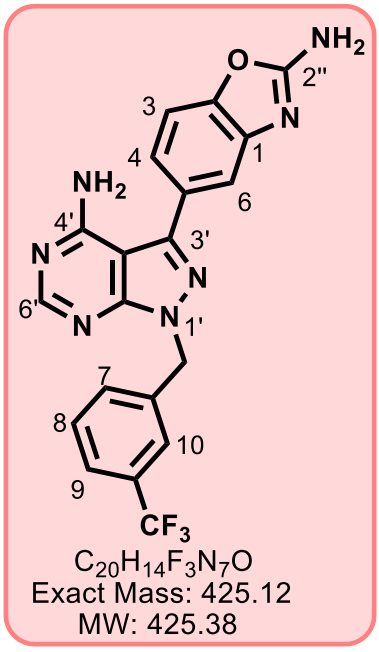

Using the general procedure 3 and a reaction mixture containing **15a** (0.40 g, 0.95 mmol), the product was obtained as an off-white solid (0.14 g, 35%); MP 281–283°C; R_f (10% MeOH/DCM) 0.6; ^{1}H-NMR (DMSO-d_6, 600 MHz): δ_H 9.12 (s, 1H, $H^{6'}$), 8.53–8.52 (m, 1H, H^{10}), 8.48–8.46 (m, 1H, H^9), 8.41–8.36 (m, 2H, $H^{7,8}$), 8.34 (s, 2H, $NH_2^{2''}$), 8.28 (dd, J = 7.8 and 0.6 Hz, 1H, H^3), 8.22 (dd, J = 1.8 and 0.6 Hz, 1H, H^6), 8.05 (dd, J = 8.4 and 1.8 Hz, 1H, H^4), and 6.49 (s, 2H, CH_2). ^{13}C-NMR (DMSO-d_6, 151 MHz): δ_C 164.73, 159.53, 157.38, 155.67, 149.70, 146.24, 145.71, 139.92, 132.99, 131.07, 130.60 (q, J = 31.7 Hz, $^2J_{C\text{-}F}$, 1C), 129.54, 126.25 (q, J = 273.3 Hz, $^1J_{C\text{-}F}$, 1C), 125.64 (broad q, J = 3.17 Hz, $^3J_{C\text{-}F}$, 1C), 125.47 (q, J = 3.47 Hz, $^3J_{C\text{-}F}$, 1C), 121.72, 116.27, 110.18, 98.69, and 50.43. HPLC-MS (APCI/ESI): purity 99%, t_R = 2.51 min, (*m*/*z*) $[M+H]^+$ = 426.1.

5-(4-Amino-1-(3-methylbenzyl)-1*H*-pyrazolo[3,4-*d*]pyrimidin-3-yl)benzo[*d*]oxazol-2-amine, 16 (GS 67)

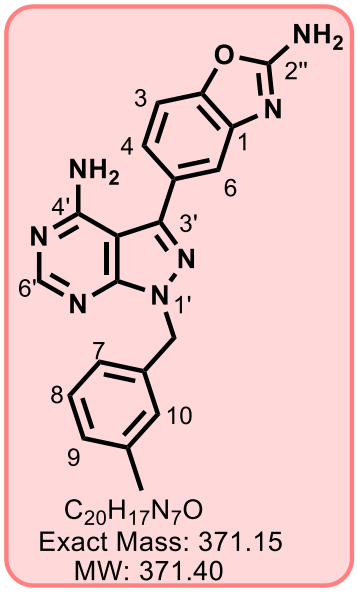

Using the general procedure 3 and a reaction mixture containing **16a** (0.29 g, 0.79 mmol), the product was obtained as an off-white solid (0.16 g, 53%); MP 299–301°C; R_f (8% MeOH/DCM) 0.3; ^{1}H-NMR (DMSO-d_6, 600 MHz): δ_H 8.26 (s, 1H, $H^{6'}$), 7.49 (s, 2H, $NH_2^{2''}$), 7.43 (dd, J = 7.8 and 0.6 Hz, 1H, H^3), 7.38 (dd, J = 1.8 and 0.6 Hz, 1H, H^6), 7.21 (dd, J = 8.4 and 1.8 Hz, 1H, H^4), 7.18 (pseudo t, J = 7.8 Hz, 1H, H^8), 7.12–7.10 (m, 1H, H^9), 7.064–7.058 (m, 1H, H^7), 7.05 (broad d, J = 1.8 Hz, 1H, H^{10}), 5.48 (s, 2H, -CH_2), and 2.24 (s, 3H, CH_3). ^{13}C-NMR (DMSO-d_6, 151 MHz): δ_C 163.90, 158.66, 156.41, 154.67, 148.83, 144.97, 144.87, 138.16, 137.62, 128.93, 128.88, 128.66, 125.24, 120.92, 115.46, 109.33, 97.82, 50.21, and 21.43. HPLC-MS (APCI/ESI): purity 99%, t_R = 2.48 min, (*m*/*z*) $[M+H]^+$ = 372.1.

5-(4-Amino-1-(3-chlorobenzyl)-1*H*-pyrazolo[3,4-*d*]pyrimidin-3-yl)benzo[*d*]oxazol-2-amine, 17 (GS 57)

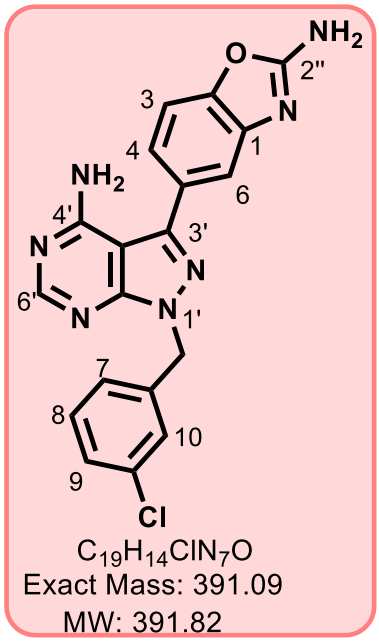

Using the general procedure 3 and a reaction mixture containing **17a** (0.35 g, 0.91 mmol), the product was obtained as an off-white solid (0.13 g, 38%); MP 310–312°C; R_f (10% MeOH/DCM) 0.5; ^{1}H-NMR (DMSO-d_6, 600 MHz): δ_H 7.52 (s, 2H, $NH_2^{2''}$), 7.46 (d, J = 8.4 Hz, 1H, H^3), 7.41 (d, J = 1.8 Hz, 1H, H^6), 7.38 - 7.34 (m, 3H, $H^{8,9,10}$), 7.25–7.23 (m, 2H, $H^{4,7}$), 5.57 (s, 2H, CH_2); ^{13}C-NMR (DMSO-d_6, 151 MHz): δ_C 163.91, 158.70, 156.54, 154.79, 148.87, 145.32, 144.89, 140.13, 135.02, 133.56, 131.01, 128.75, 128.02, 127.89, 126.75, 120.92, 115.46, 109.36, 97.87, and 49.56. HPLC-MS (APCI/ESI): purity 96%, t_R = 2.50 min, (*m*/*z*) $[M+H]^+$ = 392.0.

5-(4-Amino-1-(3-aminobenzyl)-1*H*-pyrazolo[3,4-*d*]pyrimidin-3-yl)benzo[*d*]oxazol-2-amine, 18 (GS 155)

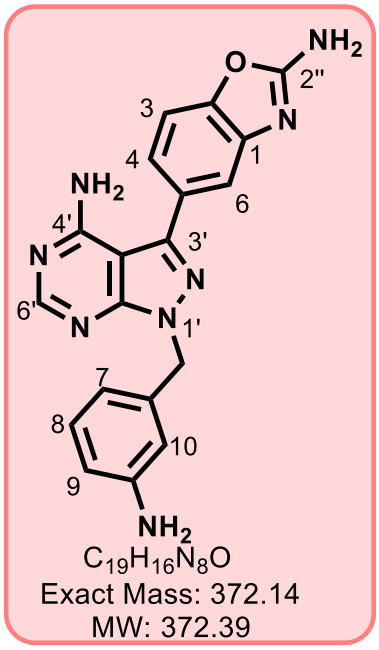

Using the general procedure 3 and a reaction mixture containing **18a** (190 mg, 0.52 mmol), the product was obtained as an off-white solid (53 mg, 28%); MP 286–287°C; R_f (10% MeOH/ DCM) 0.45; ^{1}H-NMR (DMSO-d_6, 400 MHz): δ_H 8.28 (s, 1H, $H^{6'}$), 7.52 (s, 2H, $NH_2^{2''}$), 7.47 (d, J = 8.4 Hz, 1H, H^3), 7.42 (d, J = 1.6 Hz, 1H, H^6), 7.25 (dd, J = 8.0 and 1.6 Hz, 1H, H^4), 6.95 (t, J = 8.0 Hz, 1H, H^8), 6.48–6.43 (m, 3H, $H^{7,9,10}$), 5.38 (s, 2H, CH_2), and 5.06 (s, 2H, benzyl NH_2). ^{13}C-NMR (DMSO-d_6, 101 MHz): δ_H 163.91, 158.63, 156.32, 154.65, 149.28, 148.83, 144.88, 144.77, 138.24, 129.41, 128.99, 120.94, 115.50 (2C), 113.59, 113.28, 109.32, 97.83, and 50.50. HPLC-MS (APCI/ESI): purity 98%, t_R = 2.21 min, (*m*/*z*) $[M+H]^+$ = 373.1.

5-(4-Amino-1-(3-(dimethylamino)benzyl)-1*H*-pyrazolo[3,4-*d*]pyrimidin-3-yl)benzo[*d*] oxazol-2-amine, 19 (GS 175)

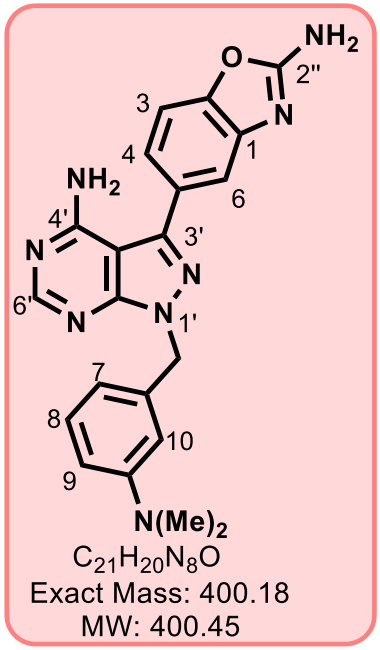

Using the general procedure 3 and a reaction mixture containing **19a** (240 mg, 0.61 mmol), the product was obtained as an off-white solid (58 mg, 24%); MP 269–270°C; R_f (10% MeOH/DCM) 0.43; ^{1}H-NMR (DMSO-d_6, 400 MHz): δ_H 8.28 (s, 1H, $H^{6'}$), 7.49 (s, 2H, $NH_2^{2''}$), 7.46 (d, J = 8.4 Hz, 1H, H^3), 7.41 (d, J = 1.6 Hz, 1H, H^6), 7.24 (dd, J = 8.0 and 1.6 Hz, 1H, H^4), 7.10 (t, J = 8.0 Hz, 1H, H^8), 6.73 (broad t, J = 2.4 Hz, 1H, H^{10}), 6.62 (dd, J = 8.0 and 2.4 Hz, 1H, H^9), 6.53 (broad d, J = 7.6 Hz, 1H, H^7), 5.48 (s, 2H, CH_2), and 2.85 (s, 6H, CH_3). ^{13}C-NMR (DMSO-d_6, 101 MHz): δ_H 163.92, 158.64, 156.34, 154.72, 150.98, 148.83, 144.88, 144.84, 138.33, 129.52, 128.96, 120.90, 115.73, 115.44, 112.06, 112.03, 109.34, 97.86, 50.76 and 40.46 (2C). HPLC-MS (APCI/ESI): purity 99%, t_R = 2.45 min, (*m*/*z*) $[M+H]^+$ = 401.1.

5-(4-Amino-1-(2-methylbenzyl)-1*H*-pyrazolo[3,4-*d*]pyrimidin-3-yl)benzo[*d*]oxazol-2-amine, 20 (GS 97)

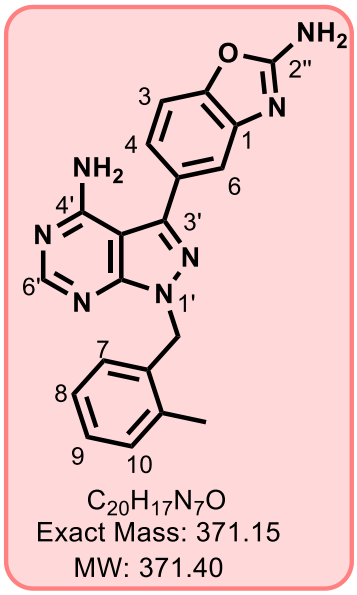

Using the general procedure 3 and a reaction mixture containing **20a** (0.38 g, 1.0 mmol), the product was obtained as an off-white solid (0.13 g, 34%); MP 300–301°C; R_f (10% MeOH/DCM) 0.5; ^{1}H-NMR (DMSO-d_6, 600 MHz): δ_H 8.25 (s, 1H, $H^{6'}$), 7.49 (s, 2H, $NH_2^{2''}$), 7.43 (dd, J = 8.4 and 0.6 Hz, 1H, H^3), 7.37 (dd, J = 1.8 and 0.6 Hz, 1H, H^6), 7.21 (dd, J = 8.4 and 1.8 Hz, 1H, H^4), 7.17 (ddt, J = 7.2, 1.8 and 0.6 Hz, 1H, H^{10}), 7.15 (td, J = 7.2 and 1.2 Hz, 1H, H^8), 7.09 (td, J = 7.2 and 1.8 Hz, 1H, H^9), 6.95 (broad dd, J = 7.6 and 1.2 Hz, 1H, H^7), 5.52 (s, 2H, CH_2), and 2.39 (s, 3H, CH_3). ^{13}C-NMR (DMSO-d_6, 151 MHz): δ_C 163.90, 158.68, 156.34, 154.77, 148.82, 145.00, 144.87, 136.26, 135.77, 130.60, 128.90, 128.62, 128.00, 126.41, 120.89, 115.44, 109.33, 97.72, 48.08, and 19.41. HPLC-MS (APCI/ESI): purity > 99%, t_R = 2.44 min, (*m*/*z*) $[M+H]^+$ = 372.1.

5-(4-Amino-1-(2-flourorobenzyl)-1*H*-pyrazolo[3,4-*d*]pyrimidin-3-yl)benzo[*d*]oxazol-2-amine, 21 (GS 91)

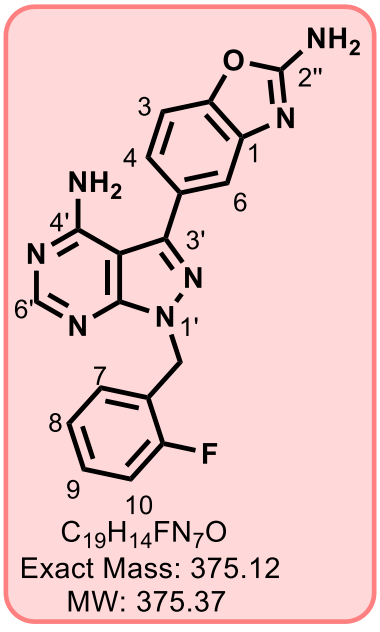

Using the general procedure 3 and a reaction mixture containing **21a** (0.30 g, 0.81 mmol), the product was obtained as an off-white solid (0.13 g, 43%); MP 296–297°C; R_f (10% MeOH/DCM) 0.4; ^{1}H-NMR (DMSO-d_6, 600 MHz): δ_H 8.26 (s, 1H, $H^{6'}$), 7.49 (s, 2H, $NH_2^{2''}$), 7.43 (dd, J = 7.8 and 0.6 Hz, 1H, H^3), 7.37 (dd, J = 1.8 and 0.6 Hz, 1H, H^6), 7.34–7.31 (m, 1H, H^9), 7.20 (dd, J = 7.8 and 1.8 Hz, 1H, H^4), 7.20–7.19 (m, 1H, H^{10}), 7.18–7.17 (m, 1H, H^7), 7.12 (td, J = 7.8 and 1.2 Hz, 1H, H^8), and 5.59 (s, 2H, CH_2). ^{13}C-NMR (DMSO-d_6, 151 MHz): δ_C 163.90, 161.11 (d, J = 244.6 Hz, $^1J_{C\text{-}F}$, 1C) 158.66, 156.46, 154.85, 148.86, 145.27, 144.87, 130.61 (d, J = 3.0 Hz, $^3J_{C\text{-}F}$, 1C), 130.33 (d, J = 7.6 Hz, $^3J_{C\text{-}F}$, 1C), 128.77, 125.08 (d, J = 3.0 Hz, $^4J_{C\text{-}F}$, 1C), 124.43 (d, J = 13.6 Hz, $^2J_{C\text{-}F}$, 1C), 120.92, 115.93 (d, J = 21.1 Hz, $^2J_{C\text{-}F}$, 1C), 115.46, 109.34, 97.80, and 43.89 (d, J = 3.0 Hz, $^3J_{C\text{-}F}$, 1C). HPLC-MS (APCI/ESI): purity > 99%, t_R = 2.38 min, (*m*/*z*) $[M+H]^+$ = 376.1.

5-(4-Amino-1-(2-(chloromethyl)benzyl)-1*H*-pyrazolo[3,4-*d*]pyrimidin-3-yl)benzo[*d*] oxazol-2-amine, 22 (GS 115)

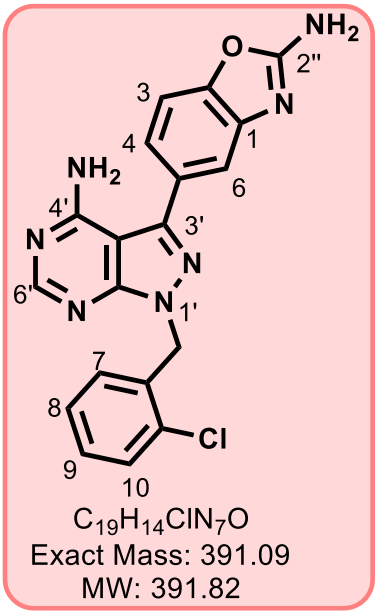

Using the general procedure 3 and a reaction mixture containing **22a** (250 mg, 0.65 mmol), the product was obtained as an off-white solid (46 mg, 18%); MP 293–294°C; R_f (10% MeOH/ DCM) 0.50; ^{1}H-NMR (DMSO-d_6, 600 MHz): δ_H 8.26 (s, 1H, $H^{6'}$), 7.51 (s, 2H, $NH_2^{2''}$), 7.48 (dd, J = 8.4 and 1.2 Hz, 1H, H^{10}), 7.45 (d, J = 8.4 Hz, 1H, H^3), 7.40 (d, J = 1.8 Hz, 1H, H^6), 7.32 (td, J = 7.2 and 1.8 Hz, 1H, H^9), 7.26 (td, J = 7.2 and 1.2 Hz, 1H, H^8), 7.23 (dd, J = 8.4 and 1.8 Hz, 1H, H^4), 6.99 (dd, J = 7.8 and 1.8 Hz, 1H, H^7), and 5.64 (s, 2H, CH_2). ^{13}C-NMR (DMSO-d_6, 151 MHz): δ_C 163.92, 158.71, 156.51, 155.09, 148.88, 145.46, 144.88, 134.95, 132.33, 129.84 (2C), 129.80, 128.77, 127.94, 120.94, 115.49, 109.35, 97.83, and 47.73. HPLC-MS (APCI/ESI): purity 98%, t_R = 2.47 min, (*m/z*) $[M+H]^+$ = 392.0.

5-(4-Amino-1-(2-(trifluoromethyl)benzyl)-1*H*-pyrazolo[3,4-*d*]pyrimidin-3-yl)benzo[*d*] oxazol-2-amine, 23 (GS 113)

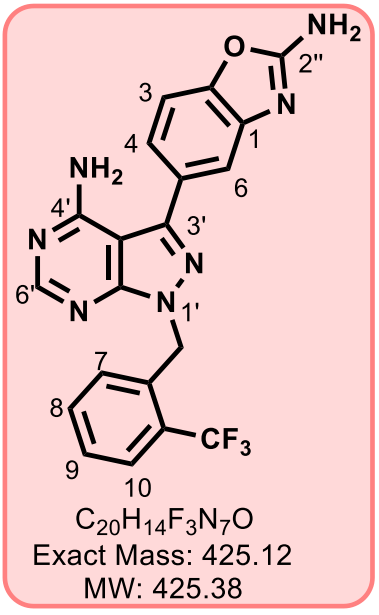

Using the general procedure 3 and a reaction mixture containing **23a** (410 mg, 0.98 mmol), the product was obtained as an off-white solid (88 mg, 21%); MP 279–280°C; R_f (10% MeOH/ DCM) 0.46; ^{1}H-NMR (DMSO-d_6, 600 MHz): δ_H 8.28 (s, 1H, $H^{6'}$), 7.80 (d, J = 7.2 Hz, 1H, H^{10}), 7.59 (t, J = 7.2 Hz, 1H, H^8), 7.53 (s, 2H, $NH_2^{2''}$), 7.52 (overlapping t, J = 7.8 Hz, 1H, H^9), 7.47 (d, J = 7.8 Hz, 1H, H^3), 7.43 (d, J = 1.8 Hz, 1H, H^6), 7.26 (dd, J = 7.8 and 1.8 Hz, 1H, H^4), 6.94 (d, J = 7.8 Hz, 1H, H^7), and 5.76 (s, 2H, CH_2). ^{13}C-NMR (DMSO-d_6, 151 MHz): δ_H 163.92, 158.74, 156.66, 155.29, 148.91, 145.70, 144.89, 135.86, 133.46, 129.10, 128.69, 128.53, 126.58 (q, J = 30.4 Hz, $^2J_{C\text{-}F}$, 1C), 126.49 (q, J = 6.0 Hz, $^3J_{C\text{-}F}$, 1C), 124.81 (q, J = 274.1 Hz, $^1J_{C\text{-}F}$, 1C), 120.96, 115.51, 109.36, 97.89, and 46.67. HPLC-MS (APCI/ESI): purity 98%, t_R = 2.50 min, (*m/z*) $[M+H]^+$ = 426.1.

5-(4-Amino-1-(3,4-dichlorobenzyl)-1*H*-pyrazolo[3,4-*d*]pyrimidin-3-yl) benzo[*d*]oxazol-2-amine, 24 (GS 101)

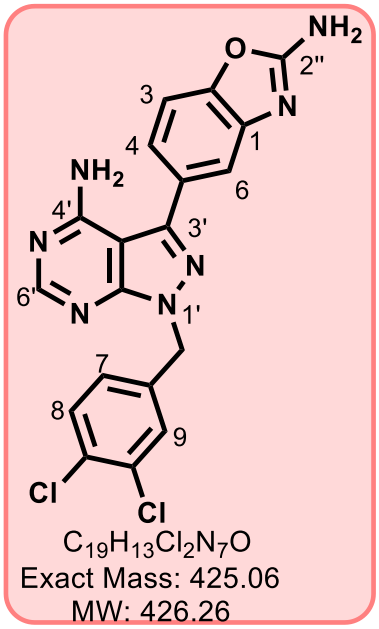

Using the general procedure 3 and a reaction mixture containing **24a** (0.35 g, 0.83 mmol), the product was obtained as an off-white solid (0.13 g, 37%); MP 288–289°C; R_f (10% MeOH/DCM) 0.5; ^{1}H NMR (DMSO-d_6, 600 MHz): δ_H 8.26 (s, 1H, $H^{6'}$), 7.57 (d, J = 1.8 Hz, 1H, H^9), 7.56 (d, J = 8.4 Hz, 1H, H^8), 7.50 (s, 2H, $NH_2^{2''}$), 7.44 (d, J = 8.4 Hz, 1H, H^3), 7.39 (d, J = 1.8 Hz, 1H, H^6), 7.22 (dd, J = 8.4 and 1.8 Hz, 1H, H^7), 7.21 (dd, J = 7.8 and 1.8 Hz, 1H, H^4), and 5.55 (s, 2H, CH_2). ^{13}C-NMR (DMSO-d_6, 151 MHz): δ_C 163.91, 158.69, 156.56, 154.81, 148.89, 145.47, 144.88, 138.74, 131.54, 131.33, 130.75, 130.12, 128.69, 128.43, 120.93, 115.47, 109.36, 97.89, and 48.99. HPLC-MS (APCI/ESI): purity 99%, t_R = 2.56 min, (m/z) $[M+H]^+$ = 426.0.

5-(4-Amino-1-(2,4-dichlorobenzyl)-1*H*-pyrazolo[3,4-*d*]pyrimidin-3-yl) benzo[*d*]oxazol-2-amine, 25 (GS 103)

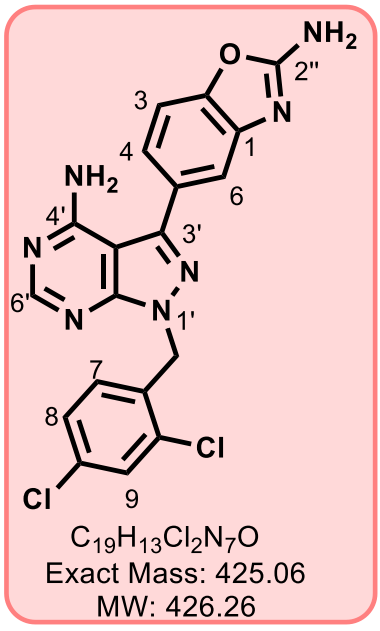

Using general procedure 3 and a reaction mixture containing **25a** (0.27 g, 0.64 mmol), the product was obtained as an off-white solid (0.10 g, 38%); MP 271–272°C; R_f (10% MeOH/DCM) 0.4; ^{1}H-NMR (DMSO-d_6, 600 MHz): δ_H 8.25 (s, 1H, $H^{6'}$), 7.64 (d, J = 2.4 Hz, 1H, H^6), 7.50 (s, 2H, $NH_2^{2''}$), 7.44 (d, J = 7.8 Hz, 1H, H^3), 7.38 (d, J = 1.2 Hz, 1H, H^9), 7.36 (dd, J = 8.4 and 2.4 Hz, 1H, H^8), 7.21 (dd, J = 7.8 and 1.8 Hz, 1H, H^4), 7.04 (d, J = 8.4 Hz, 1H, H^7), and 5.61 (s, 2H, -CH_2). ^{13}C-NMR (DMSO-d_6, 151 MHz): δ_C 164.81, 159.60, 157.44, 155.96, 149.79, 146.48, 145.77, 134.99, 134.46, 134.30, 132.25, 130.24, 129.58, 129.04, 121.83, 116.38, 110.25, 98.73, and 48.18. HPLC-MS (APCI/ESI): purity 99%, t_R = 2.56 min, (m/z) $[M+H]^+$ = 426.0.

5-(4-Amino-1-(4-chloro-2-fluorobenzyl)-1*H*-pyrazolo[3,4-*d*]pyrimidin-3yl)benzo[*d*] oxazol-2-amine, 26 (GS 111)

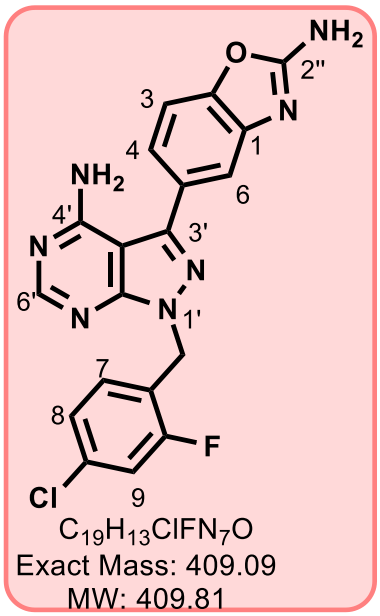

$C_{19}H_{13}ClFN_7O$
Exact Mass: 409.09
MW: 409.81

Using the general procedure 3 and a reaction mixture containing **26a** (450 mg, 1.12 mmol), the product was obtained as an off-white solid (87 mg, 19%); MP 272–273°C; R_f (10% MeOH/ DCM) 0.32; ^{1}H-NMR (DMSO-d_6, 400 MHz): δ_H 8.29 (s, 1H, $H^{6'}$), 7.52 (s, 2H, $NH_2^{2''}$), 7.46 (overlapping d, J = 7.6 Hz, 1H, H^3), 7.45 (overlapping dd, J = 8.8 and 1.2 Hz, 1H, H^9), 7.40 (d, J = 1.6 Hz, 1H, H^6), 7.30–7.25 (m, 2H, $H^{7,8}$), 7.23 (dd, J = 8.4 and 2.0 Hz, 1H, H^4), and 5.60 (s, 2H, CH_2).^{13}C-NMR (DMSO-d_6, 101 MHz): δ_C 163.42, 159.73 (d, J = 249.2 Hz, $^1J_{C\text{-}F}$, 1C), 158.18, 156.02, 154.36, 148.39, 144.93, 144.37, 133.28 (d, J = 10.6 Hz, $^3J_{C\text{-}F}$, 1C), 131.50 (d, J = 4.5 Hz, $^3J_{C\text{-}F}$, 1C), 128.21, 124.89 (d, J = 3.0 Hz, $^4J_{C\text{-}F}$, 1C), 123.11 (d, J = 15.1 Hz, $^2J_{C\text{-}F}$, 1C), 120.44, 116.08 (d, J = 25.7 Hz, $^2J_{C\text{-}F}$, 1C), 114.97, 108.86, 97.33, and 43.04 (d, J = 4.5 Hz, $^4J_{C\text{-}F}$, 1C). HPLC-MS (APCI/ESI): purity 98%, t_R = 2.49 min, (*m/z*) $[M+H]^+$ = 410.0.

2-((4-Amino-3-(2-aminobenzo[*d*]oxazol-5-yl)-1*H*-pyrazolo[3,4-*d*]pyrimidin-1-yl)methyl)-5-chlorobenzonitrile, 27 (GS 107)

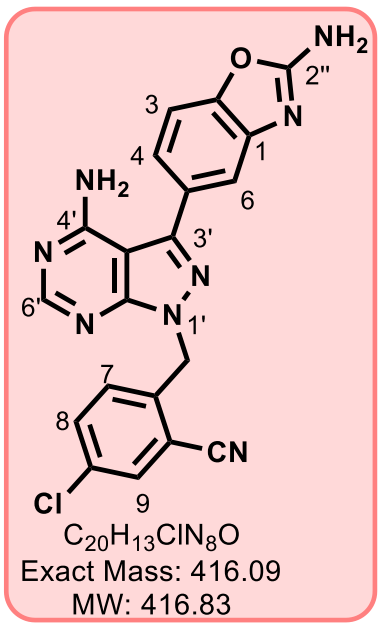

$C_{20}H_{13}ClN_8O$
Exact Mass: 416.09
MW: 416.83

Using the general procedure 3 and a reaction mixture containing **27a** (375 mg, 0.91 mmol), the product was obtained as an off-white solid (65 mg, 18%); MP 280–281°C; R_f (10% MeOH/ DCM) 0.37; ^{1}H-NMR (600 MHz, DMSO-d_6): δ_H 8.29 (s, 1H, $H^{6'}$), 8.08 (d, J = 2.4 Hz, 1H, H^6), 7.74 (dd, J = 8.4 and 2.4 Hz, 1H, H^4), 7.53 (s, 2H, $NH_2^{2''}$), 7.47 (dd, J = 7.8 and 0.6 Hz, 1H, H^3), 7.41 (dd, J = 1.8 and 0.6 Hz, 1H, H^9), 7.34 (d, J = 8.4 Hz, 1H, H^7), 7.24 (dd, J = 7.8 and 1.8 Hz, 1H, H^8), and 5.74 (s, 2H, CH_2). ^{13}C-NMR (151 MHz, DMSO-d_6) δ_C 163.92, 158.70, 156.61, 155.12, 148.92, 145.74, 144.87, 139.74, 134.20, 133.46, 133.04, 131.28, 128.61, 120.94, 116.34, 115.49, 113.12, 109.37, 97.91, and 47.95. HPLC-MS (APCI/ESI): purity 96%, t_R = 2.42 min, (*m/z*) $[M+H]^+$ = 417.0.

5-(4-Amino-1-(4-chloro-3-fluorobenzyl)-1*H*-pyrazolo[3,4-*d*]pyrimidin-3-yl)benzo[*d*] oxazol-2-amine, 28 (GS 105)

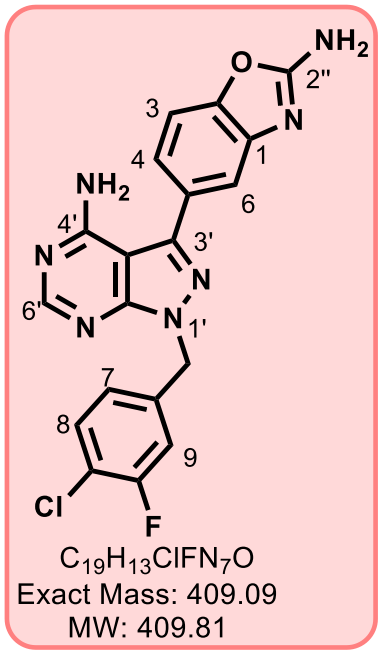

$C_{19}H_{13}ClFN_7O$
Exact Mass: 409.09
MW: 409.81

Using the general procedure 3 and a reaction mixture containing **28a** (250 mg, 0.62 mmol), the product was obtained as a brown solid (42 mg, 17%); MP 318–319°C; R_f (10% MeOH/DCM) 0.45; ^{1}H-NMR (DMSO-d_6, 600 MHz): δ_H 8.29 (s, 1H, $H^{6'}$), 7.54 (pseudo t, J = 8.4 Hz, 1H, H^8), 7.53 (s, 2H, $NH_2^{2''}$), 7.47 (d, J = 8.4 Hz, 1H, H^3), 7.42 (d, J = 1.8 Hz, 1H, H^6), 7.35 (dd, J = 10.1 and 1.8 Hz, 1H, H^9), 7.25 (dd, J = 8.4 and 1.8 Hz, 1H, H^4), 7.12 (dd, J = 8.4 and 1.8 Hz, 1H, H^7) and 5.59 (s, 2H, CH_2). ^{13}C-NMR (DMSO-d_6, 151 MHz): δ_C 163.91, 158.70, 157.50 (d, J = 247.0 Hz, $^1J_{C\text{-}F}$, 1C), 156.56, 154.82, 148.88, 145.46, 144.87, 139.36 (d, J = 7.6 Hz, $^3J_{C\text{-}F}$, 1C), 131.33, 128.71, 125.28 (d, J = 3.0 Hz, $^3J_{C\text{-}F}$, 1C), 120.95, 119.08 (d, J = 16.6 Hz, $^2J_{C\text{-}F}$, 1C), 116.48 (d, J = 21.1 Hz, $^2J_{C\text{-}F}$, 1C), 115.49, 109.36, 97.90 and 49.16. HPLC-MS (APCI/ESI): purity 98%, t_R = 2.50 min, (m/z) $[M+H]^+$ = 410.0.

5-(4-Amino-1-(4-chloro-3-(trifluoromethyl)benzyl)-1*H*-pyrazolo[3,4-*d*]pyrimidin-3-yl)benzo[*d*]oxazol-2-amine, 29 (GS 117)

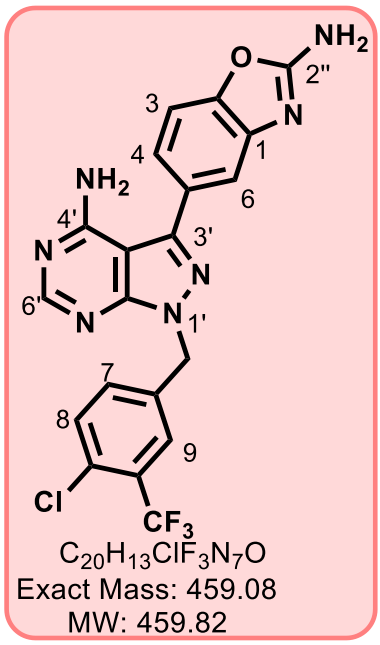

$C_{20}H_{13}ClF_3N_7O$
Exact Mass: 459.08
MW: 459.82

Using the general procedure 3 and a reaction mixture containing **29a** (260 mg, 0.57 mmol), the product was obtained as an off-white solid (60 mg, 23%); MP 285–286°C; R_f (10% MeOH/DCM) 0.40; ^{1}H-NMR (600 MHz, DMSO-d_6) δ_H 8.28 (s, 1H, $H^{6'}$), 7.86 (d, J = 2.4 Hz, 1H, H^9), 7.67 (d, J = 8.4 Hz, 1H, H^8), 7.52 (dd, J = 8.4 and 2.4 Hz, 1H, H^7), 7.51 (s, 2H, $NH_2^{2''}$), 7.45 (dd, J = 8.4 and 0.6 Hz, 1H, H^3), 7.40 (dd, J = 1.8 and 0.6 Hz, 1H, H^6), 7.22 (dd, J = 8.4 and 1.8 Hz, 1H, H^4), and 5.65 (s, 2H, CH_2). ^{13}C-NMR (151 MHz, DMSO-d_6) δ_C 163.43, 158.23, 156.11, 154.38, 148.41, 145.08, 144.41, 137.29, 133.28, 131.98, 129.86, 128.17, 127.02 (broad q, J = 4.5 Hz, $^3J_{C\text{-}F}$, 1C), 126.51 (q, J =30.2 Hz, $^2J_{C\text{-}F}$, 1C), 122.69 (q, J = 273.3 Hz, $^1J_{C\text{-}F}$, 1C), 120.42, 114.98, 108.88, 97.42, and 48.53. HPLC-MS (APCI/ESI): purity 97%, t_R = 2.46 min, (*m*/*z*) $[M+H]^+$ = 460.0.

5-(4-Amino-1-(2,4-difluorobenzyl)-1*H*-pyrazolo[3,4-*d*]pyrimidin-3-yl)benzo[*d*]oxazol-2-amine, 30 (GS 123)

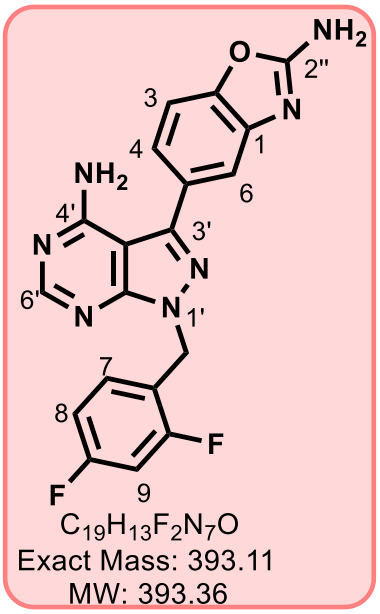

Using the general procedure 3 and a reaction mixture containing **30a** (350 mg, 0.90 mmol), the product was obtained as an off-white solid (84 mg, 23%); MP 294–295°C; R_f (10% MeOH/DCM) 0.48; ^{1}H-NMR (DMSO-d_6, 600 MHz): δ_H 8.29 (s, 1H, $H^{6'}$), 7.51 (s, 2H, $NH_2^{2''}$), 7.46 (d, J = 8.0 Hz, 1H, H^3), 7.40 (d, J = 1.6 Hz, 1H, H^6), 7.34 (td, J = 8.4 and 6.4 Hz, 1H, H^7), 7.26 (overlapping td, J = 9.4 and 1.6 Hz, 1H, H^9), 7.23 (dd, J = 8.0 and 1.6 Hz, 1H, H^4), 7.05 (td, J = 8.8, 7.6 and 2.0 Hz, 1H, H^8), and 5.58 (s, 2H, CH_2). ^{13}C-NMR (DMSO-d_6, 101 MHz): δ_C 163.93, 162.7 (d, J = 247.5 Hz), 160.47 (d, J = 237.4 Hz) 158.68, 156.49, 154.83, 148.90, 145.34, 144.90, 132.10 (dd, J = 5.1 Hz, $^3J_{C\text{-}F}$, 1C), 128.77, 120.93, 120.79 (dd, J = 11.1 and 4.0 Hz, 1C), 115.49, 112.17 (dd, J = 18.2 and 3.0 Hz, 1C), 109.34, 104.44 (t, J = 26.3 Hz, $^2J_{C\text{-}F}$, 1C), 97.86, and 43.48. HPLC-MS (APCI/ESI): purity > 99%, t_R = 2.42 min, (*m/z*) $[M+H]^+$ = 394.1. (confirmed by HSQC and HMBC).

5-(4-Amino-1-(2-chloro-4-fluorobenzyl)-1*H*-pyrazolo[3,4-*d*]pyrimidin-3-yl)benzo[*d*] oxazol-2-amine, 31 (GS 127)

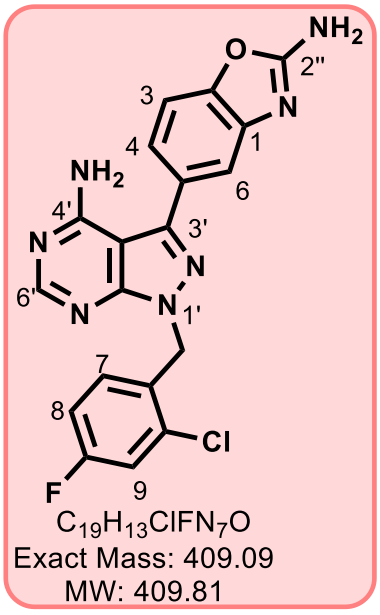

Using the general procedure 3 and a reaction mixture containing **31a** (330 mg, 0.82 mmol), the product was obtained as an off-white solid (67 mg, 20%); MP 277–278°C; R_f (10% MeOH/DCM) 0.44; ^{1}H-NMR (DMSO-d_6, 400 MHz): δ_H 8.28 (s, 1H, $H^{6'}$), 7.50 (s, 2H, $NH_2^{2''}$), 7.48 (dd, J = 8.8 and 2.4 Hz, 1H, H^9), 7.46 (d, J = 8.0 Hz, 1H, H^3), 7.42 (d, J = 1.6 Hz, 1H, H^6), 7.24 (dd, J = 8.4 and 2.0 Hz, 1H, H^4), 7.18 (overlapping ddd, J = 13.6, 8.4 and 2.0 Hz, 1H, H^8), 7.17 (overlapping dd, J = 8.4 and 2.4 Hz, 1H, H^7), and 5.63 (s, 2H, CH_2). ^{13}C-NMR (DMSO-d_6, 101 MHz): δ_C 163.94, 161.81 (d, J = 248.5 Hz, $^1J_{C\text{-}F}$, 1C), 158.71, 156.52, 155.04, 148.91, 145.50, 144.89, 133.33 (d, J = 10.7 Hz, $^3J_{C\text{-}F}$, 1C), 131.68 (d, J = 9.2 Hz, $^3J_{C\text{-}F}$, 1C), 131.34 (d, J = 3.4 Hz, $^4J_{C\text{-}F}$, 1C), 128.75, 120.95, 117.16 (d, J = 25.4 Hz, $^2J_{C\text{-}F}$, 1C), 115.51, 115.11 (d, J = 21.4 Hz, $^2J_{C\text{-}$

$_F$, 1C), 109.35, 97.87, and 47.20. HPLC-MS (APCI/ESI): purity 98%, t_R = 2.49 min, (*m/z*) $[M+H]^+$ = 410.0.

5-(4-Amino-1-(4-fluoro-2-(trifluoromethyl)benzyl)-1*H*-pyrazolo[3,4-*d*]pyrimidin-3-yl)benzo[*d*]oxazol-2-amine, 32 (GS 129)

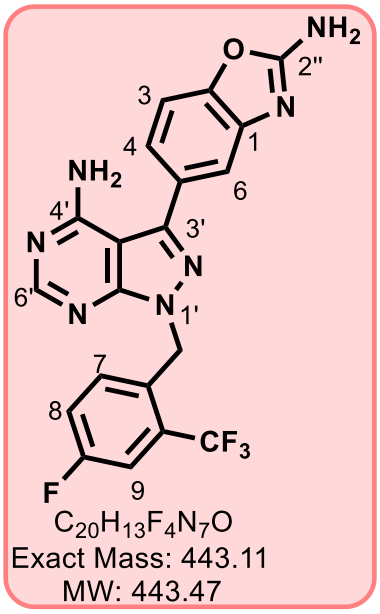

Using the general procedure 3 and a reaction mixture containing **32a** (320 mg, 0.73 mmol), the product was obtained as an off-white solid (78 mg, 24%); MP 289–290°C; R_f (10% MeOH/DCM) 0.45; ^{1}H-NMR (DMSO-d_6, 400 MHz): δ_H 8.28 (s, 1H, $H^{6'}$), 7.69 (dd, *J* = 9.2 and 2.8 Hz, 1H, H^9), 7.51 (s, 2H, $NH_2^{2''}$), 7.48 (overlapping ddd, *J* = 8.8, 6.4 and 2.8 Hz, 1H, H^8), 7.47 (d, *J* = 8.0 Hz, H^3), 7.43 (d, *J* = 1.6 Hz, 1H, H^6), 7.25 (dd, *J* = 8.0 and 1.6 Hz, 1H, H^4), 7.09 (dd, *J* = 8.8 and 5.2 Hz, 1H, H^7), and 5.73 (s, 2H, CH_2). ^{13}C-NMR (DMSO-d_6, 101 MHz): δ_C 163.94, 161.35 (d, *J* = 246.4 Hz, 1C), 158.74, 156.67, 155.24, 148.95, 145.76, 144.91, 132.22 (d, *J* = 8.1 Hz, 1C), 132.00, 128.67, 128.48 (dq, *J* = 31.3 and 7.1 Hz, 1C), 123.82 (q, *J* = 274.3 Hz, 1C), 120.95, 120.31 (d, *J* = 21.2 Hz, 1C), 115.52, 114.23 (dq, *J* = 26.3 and 5.1 Hz, 1C), 109.36, 97.94, and 46.19. HPLC-MS (APCI/ESI): purity > 99%, t_R = 2.53 min, (*m/z*) $[M+H]^+$ = 444.0.

2-((4-Amino-3-(2-aminobenzo[*d*]oxazol-5-yl)-1*H*-pyrazolo[3,4-*d*]pyrimidin-1-yl)methyl)-5-fluorobenzonitrile, 33 (GS 131)

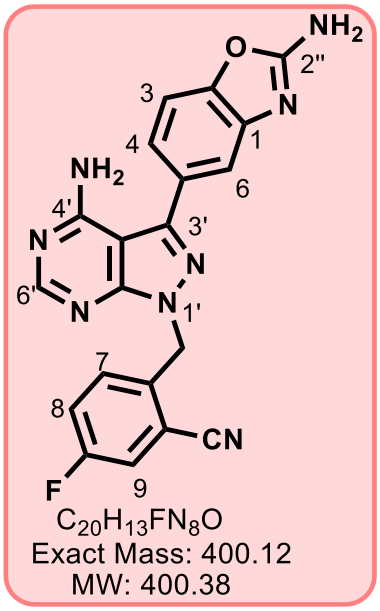

Using the general procedure 3 and a reaction mixture containing **33a** (245 mg, 0.62 mmol), the product was obtained as an off-white solid (42 mg, 16%); MP 287–289°C; R_f (10% MeOH/ DCM) 0.48; ^{1}H-NMR (DMSO-d_6, 400 MHz): δ_H 8.29 (s, 1H, H$^{6'}$), 7.89 (dd, J = 8.4 and 2.8 Hz, 1H, H^9), 7.55 (td, J = 8.8 and 2.8 Hz, 1H, H^8), 7.51 (s, 2H, NH$_2^{2''}$), 7.47 (d, J = 8.0 Hz, 1H, H^3), 7.42 (overlapping t, J = 6.4 Hz, 1H, H^7), 7.41 (overlapping d, J = 2.0 Hz, 1H, H^6), 7.24 (dd, J = 8.4 and 2.0 Hz, 1H, H^4), and 5.73 (s, 2H, CH$_2$). ^{13}C-NMR (DMSO-d_6, 101 MHz): δ_C 163.94, 161.32 (d, J = 248.5 Hz, $^1J_{C\text{-}F}$, 1C), 158.71, 156.59, 155.10, 148.94, 145.67, 144.90, 137.21 (d, J = 3.0 Hz, $^4J_{C\text{-}F}$, 1C), 132.01 (d, J = 9.1 Hz, $^3J_{C\text{-}F}$, 1C), 128.67, 121.60 (d, J = 21.2 Hz, $^2J_{C\text{-}F}$, 1C), 120.94, 120.45 (d, J = 25.3 Hz, $^2J_{C\text{-}F}$, 1C), 116.48, 115.51, 112.95 (d, J = 10.1 Hz, $^3J_{C\text{-}F}$, 1C), 109.35, 97.95, and 47.84. HPLC-MS (APCI/ESI): purity > 99%, t_R = 2.35 min, (*m/z*) [M+H]$^+$ = 401.1.

5-(4-Amino-1-(4-fluoro-2-methylbenzyl)-1*H*-pyrazolo[3,4-*d*]pyrimidin-3-yl)benzo[*d*] oxazol-2-amine, 34 (GS 133)

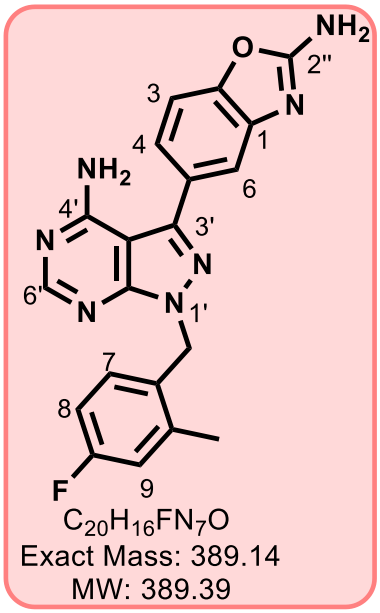

Using the general procedure 3 and a reaction mixture containing **34a** (420 mg, 1.1 mmol), the product was obtained as an off-white solid (115 mg, 27%); MP 282–283°C; R_f (10% MeOH/DCM) 0.47; ^{1}H-NMR (DMSO-d_6, 400 MHz): δ_H 8.28 (s, 1H, H$^{6'}$), 7.50 (s, 2H, NH$_2^{2''}$), 7.46 (d, J = 8.0 Hz, 1H, H^3), 7.40 (d, J = 1.6 Hz, 1H, H^6), 7.23 (dd, J = 8.4 and 2.0 Hz, 1H, H^4), 7.08 (overlapping dd, J = 8.4 and 6.0 Hz, 1H, H^7), 7.06 (overlapping dd, J = 10.0 and 2.8 Hz, 1H, H^9), 6.95 (td, J = 8.8 and 2.8 Hz, 1H, H^8), 5.53 (s, 2H, CH$_2$), and 2.44 (s, 3H, CH$_3$). ^{13}C-NMR (DMSO-d_6, 101 MHz): δ_C 163.93, 161.87 (d, J = 243.4 Hz, $^1J_{C\text{-}F}$, 1C), 158.69, 156.38, 154.72, 148.87, 145.09, 144.89, 139.37 (d, J = 8.1 Hz, $^3J_{C\text{-}F}$, 1C), 131.97 (d, J = 2.0 Hz, $^4J_{C\text{-}F}$, 1C), 130.94 (d, J = 9.1 Hz, $^3J_{C\text{-}F}$, 1C), 128.88, 120.91, 117.13 (d, J = 21.2 Hz, $^2J_{C\text{-}F}$, 1C), 115.46, 112.96 (d, J

= 21.2 Hz, $^{2}J_{C\text{-}F}$, 1C), 109.34, 97.78, 47.47, and 19.42. HPLC-MS (APCI/ESI): purity 98%, t_R = 2.48 min, (*m/z*) $[M+H]^+$ = 390.1.

5-(4-Amino-1-(3-chloro-4-fluorobenzyl)-1*H*-pyrazolo[3,4-*d*]pyrimidin-3-yl)benzo[*d*] oxazol-2-amine, 35 (GS 139)

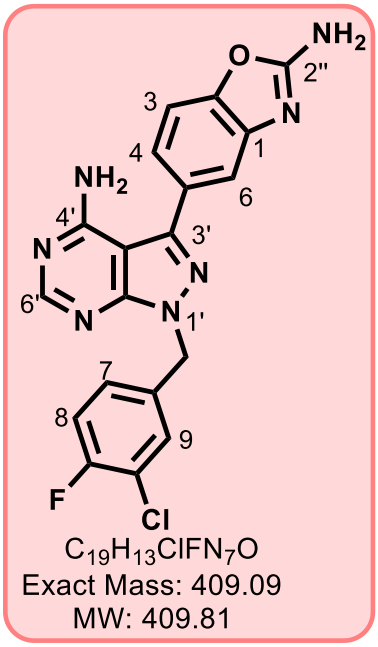

$C_{19}H_{13}ClFN_7O$
Exact Mass: 409.09
MW: 409.81

Using the general procedure 3 and a reaction mixture containing **35a** (250 mg, 0.62 mmol), the product was obtained as an off-white solid (68 mg, 27%); MP 285–286°C; R_f (10% MeOH/DCM) 0.39; ^{1}H-NMR (DMSO-d_6, 600 MHz): δ_H 7.52 (dd, *J* = 7.2 and 2.4 Hz, 1H, H^9), 7.48 (s, 2H, $NH_2^{2''}$), 7.42 (dd, *J* = 7.8 and 0.6 Hz, 1H, H^3), 7.37 (dd, *J* = 1.8 and 0.6 Hz, 1H, H^6), 7.33 (pseudo t, *J* = 8.4 Hz, H^8), 7.26 (ddd, *J* = 8.4, 4.8 and 2.4 Hz, 1H, H^7), 7.20 (dd, *J* = 7.8 and 1.8 Hz, 1H, H^4), and 5.52 (s, 2H, CH_2). ^{13}C-NMR (DMSO-d_6, 151 MHz): δ_C 163.89, 158.67, 157.07 (d, *J* = 246.1 Hz, $^{1}J_{C\text{-}F}$, 1C), 156.53, 154.72, 148.86, 145.37, 144.86, 135.52 (d, *J* = 4.5 Hz, $^{3}J_{C\text{-}F}$, 1C), 130.24, 128.89 (d, *J* = 7.6 Hz, $^{3}J_{C\text{-}F}$, 1C), 128.70, 120.91, 119.86 (d, *J* = 18.1 Hz, $^{2}J_{C\text{-}F}$, 1C), 117.56 (d, *J* = 21.1 Hz, $^{2}J_{C\text{-}F}$, 1C), 115.45, 109.33, 97.87, and 48.96. HPLC-MS (APCI/ESI): purity 98%, t_R = 2.50 min, (*m/z*) $[M+H]^+$ = 410.0.

5-(4-Amino-1-(3-chloro-4-fluorobenzyl)-1*H*-pyrazolo[3,4-*d*]pyrimidin-3-yl)benzo[*d*] oxazol-2-amine, 36 (GS 141)

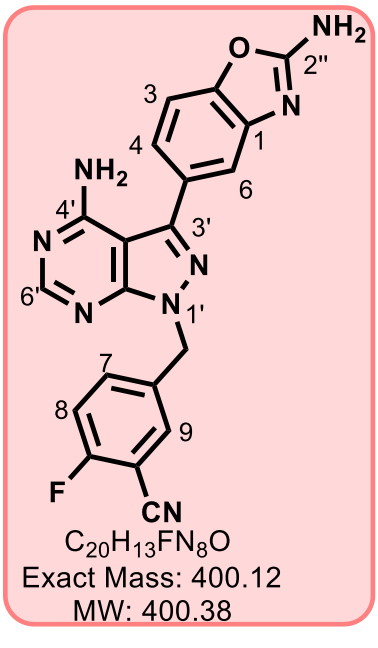

$C_{20}H_{13}FN_8O$
Exact Mass: 400.12
MW: 400.38

Using the general procedure 3 and a reaction mixture containing **36a** (180 mg, 0.46 mmol), the product was obtained as an off-white solid (31 mg, 17%); MP 259–260°C; R_f (10% MeOH/DCM) 0.42; ^{1}H-NMR (DMSO-d_6, 600 MHz): δ_H 8.25 (s, 1H, $H^{6'}$), 7.85 (dd, *J* = 6.0 and 2.4 Hz, 1H, H^9), 7.64 (ddd, *J* = 9.0, 5.4 and 2.4 Hz, 1H, H^7), 7.48 (s, 2H, $NH_2^{2''}$), 7.45 (pseudo t, *J* = 9.0 Hz, 1H, H^8), 7.42 (d, *J* = 7.8 Hz, 1H, H^3), 7.38 (d, *J* = 1.8 Hz, 1H, H^6), 7.20 (dd, *J* = 7.8 and 1.8 Hz, 1H, H^4), and 5.57 (s, 2H, CH_2). ^{13}C-NMR (DMSO-d_6, 151 MHz): δ_C 163.89, 162.27 (d, *J* = 255.2 Hz, $^{1}J_{C\text{-}F}$, 1C), 158.68, 156.55, 154.80, 148.87, 145.52, 144.86,

135.86 (d, J = 7.6 Hz, $^{3}J_{C\text{-}F}$, 1C), 135.30 (d, J = 4.5 Hz, $^{3}J_{C\text{-}F}$, 1C), 133.31, 128.67, 120.92, 117.37 (d, J = 19.6 Hz, $^{2}J_{C\text{-}F}$, 1C), 115.49, 114.23, 109.32, 100.65 (d, J = 15.1 Hz, $^{2}J_{C\text{-}F}$, 1C), 97.93, and 48.71. HPLC-MS (APCI/ESI): purity 95%, t_R = 2.38 min, (*m/z*) $[M+H]^+$ = 401.0.

5-(4-Amino-1-(3,4-difluorobenzyl)-1*H*-pyrazolo[3,4-*d*]pyrimidin-3-yl)benzo[*d*]oxazol-2-amine, 37 (GS 143)

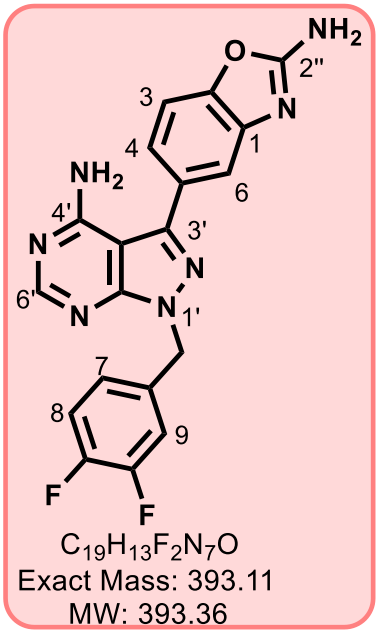

Using the general procedure 3 and a reaction mixture containing **37a** (360 mg, 0.93 mmol), the product was obtained as an off-white solid (58 mg, 16%); MP 289–290°C; R_f (10% MeOH/ DCM) 0.35; ^{1}H-NMR (DMSO-d_6, 600 MHz): δ_H 8.24 (s, 1H, $H^{6'}$), 7.48 (s, 2H, $NH_2^{2''}$), 7.42 (d, J = 8.4 Hz, 1H, H^{3}),7.38 (d, J = 1.8 Hz, 1H, H^{6}), 7.37–7.32 (m, 2H, $H^{7,8}$), 7.20 (dd, J = 7.8 and 1.8 Hz, 1H, H^{4}), 7.11–7.08 (m, 1H, H^{9}), and 5.52 (s, 2H, CH_2). ^{13}C-NMR (DMSO-d_6, 101 MHz): δ_C 163.89, 158.67, 156.51, 154.72, 150.30 (dd, J = 55.9 and 12.1 Hz, 1C), 148.85, 148.67 (dd, J = 54.4 and 12.1 Hz, 1C), 145.35, 144.85, 135.32 (pseudo t, J = 4.5 Hz, 1C), 128.71, 124.96 (dd, J = 7.6 and 3.0 Hz, 1C), 120.92, 118.13 (d, J = 12.1 Hz, 1C), 117.21 (d, J = 12.1 Hz, 1C), 115.46, 109.33, 97.87, and 49.11. HPLC-MS (APCI/ESI): purity > 99%, t_R = 2.43 min, (*m/z*) $[M+H]^+$ = 394.1.

5-(4-Amino-1-(4-fluoro-3-(trifluoromethyl)benzyl)-1*H*-pyrazolo[3,4-*d*]pyrimidin-3-yl) benzo[*d*]oxazol-2-amine, 38 (GS 145)

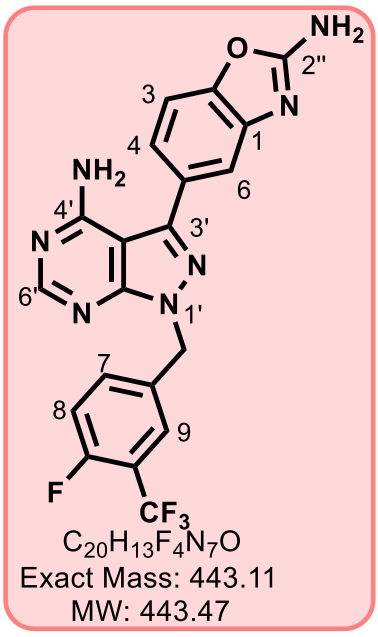

Using the general procedure 3 and a reaction mixture containing **38a** (300 mg, 0.69 mmol), the product was obtained as an off-white solid (58 mg, 19%); MP 289–291°C; R_f (10% MeOH/ DCM) 0.40; ^{1}H-NMR (DMSO-d_6, 600 MHz): δ_H 8.25 (s, 1H, $H^{6'}$), 7.77 (dd, 1H, 7.2 and 2.4 Hz, H^9), 7.61–7.57 (m, 1H, H^7), 7.48 (s, 2H, $NH_2^{2''}$), 7.43 (d, J = 7.8 Hz, 1H, H^3), 7.41 (overlapping dd, J = 8.4 Hz, 1H, H^8), 7.37 (d, J = 1.8 Hz, 1H, H^6), 7.19 (dd, J = 7.8 and 1.8 Hz, 1H, H^4), and 5.61 (s, 2H, CH_2). ^{13}C-NMR (DMSO-d_6, 101 MHz): δ_C 163.89, 158.69, 158.67 (d, J = 253.7 Hz, 1C), 156.56, 154.78, 148.87, 145.47, 144.87, 134.99 (d, J = 9.06 Hz, 1C), 134.82 (d, J = 3.02 Hz, 1C), 128.66, 126.94 (broad q, J = 6.0 Hz, 1C), 122.93 (q, J = 273.3 Hz, 1C), 120.88, 118.03 (d, J = 21.1 Hz, 1C), 116.97 (dq, J = 12.1 Hz, 1C), 115.44, 109.34, 97.88, and 48.92. HPLC-MS (APCI/ESI): purity 98%, t_R = 2.53 min, (*m/z*) $[M+H]^+$ = 444.1.

5-(4-Amino-1-((6-(trifluoromethyl)pyridin-3-yl)methyl)-1*H*-pyrazolo[3,4-*d*]pyrimidin-3-yl)benzo[*d*]oxazol-2-amine, 39 (GS 99)

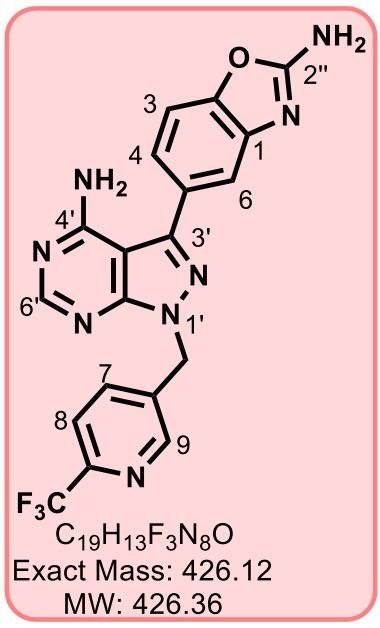

Using the general procedure 3 and a reaction mixture containing **39a** (0.40 g, 0.95 mmol), the product was obtained as an off-white solid (0.15 g, 36%); MP 299–300°C; R_f (12% MeOH/DCM) 0.5; ^{1}H-NMR (DMSO-d_6, 600 MHz): δ_H 8.75 (d, J = 1.8 Hz, 1H, H^9), 8.27 (s, 1H, $H^{6'}$), 7.92 (dd, J = 8.4 and 1.8 Hz, 1H, H^7), 7.85 (dd, J = 8.4 and 1.2 Hz, 1H, H^8), 7.50 (s, 2H, $NH_2^{2''}$), 7.44 (dd, J = 8.4 and 0.6 Hz, 1H, H^3), 7.40 (dd, J = 1.8 and 0.6 Hz, 1H, H^6), 7.22 (dd, J = 8.4 and 1.8 Hz, 1H, H^4), and 5.72 (s, 2H, CH_2). ^{13}C-NMR (DMSO-d_6, 101 MHz): δ_C 163.91, 158.72, 156.63, 154.93, 149.88, 148.91, 146.05 (q, J = 34.7 Hz, $^2J_{C\text{-}F}$, 1C), 145.71, 144.88, 137.98, 137.21, 128.63, 121.26 (broad q, J = 1.5 Hz, $^3J_{C\text{-}F}$, 1C), 121.13 (q, J = 274.8 Hz, $^1J_{C\text{-}F}$, 1C), 120.95, 115.51, 109.35, 97.97, and 47.42. HPLC-MS (APCI/ESI): purity 99%, t_R = 2.38 min, (*m/z*) $[M+H]^+$ = 427.1.

5-(4-Amino-1-((6-chloropyridin-3-yl)methyl)-1*H*-pyrazolo[3,4-*d*]pyrimidin-3-yl) benzo[*d*]oxazol-2-amine, 40 (GS 121)

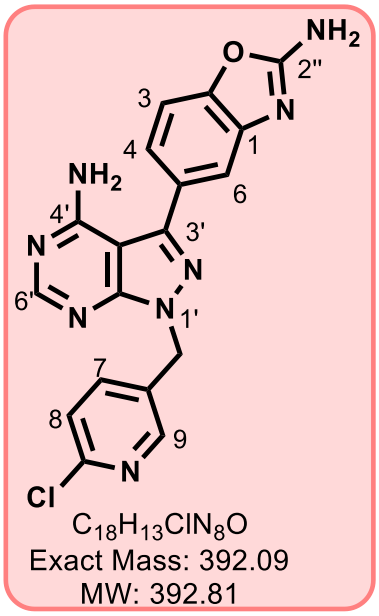

Using general procedure 3 and a reaction mixture containing **40a** (200 mg, 0.52 mmol), the product was obtained as a brown solid (45 mg, 21%); MP 289–291°C; R_f (10% MeOH/DCM) 0.30; ^{1}H-NMR (DMSO-d_6, 600 MHz): δ_H 8.42 (dd, J = 2.4 and 0.6 Hz, 1H, H^9), 8.27 (s, 1H, $H^{6'}$), 7.75 (dd, J = 7.8 and 2.4 Hz, 1H, H^7), 7.51 (s, 2H, $NH_2^{2''}$), 7.47 (dd, J = 8.4 and 0.6 Hz, 1H, H^8), 7.45 (dd, J = 8.4 and 0.6 Hz, 1H, H^3), 7.40 (dd, J = 1.8 and 0.6 Hz, 1H, H^6), 7.22 (dd, J = 7.8 and 1.8 Hz, 1H, H^7), and 5.60 (s, 2H, CH_2). ^{13}C-NMR (DMSO-d_6, 151 MHz): δ_C 163.42, 158.21, 156.08, 154.31, 149.53, 149.15, 148.40, 145.04, 144.39, 139.29, 132.34, 128.18, 124.32, 120.44, 115.00, 108.85, 97.46, and 46.56. HPLC-MS (APCI/ESI): purity > 99%, t_R = 2.56 min, (m/z) $[M+H]^+$ = 392.1.

5-(4-Amino-1-((6-flouropyridin-3-yl)methyl)-1*H*-pyrazolo[3,4-*d*]pyrimidin-3-yl) benzo[*d*]oxazol-2-amine, 41 (GS 135)

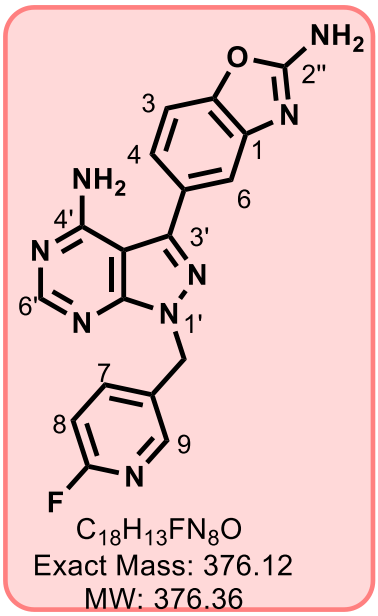

Using the general procedure 3 and a reaction mixture containing **41a** (225 mg, 0.61 mmol), the product was obtained as a brown solid (55 mg, 24%); MP 275–276°C; R_f (10% MeOH/DCM) 0.30; ^{1}H-NMR (DMSO-d_6, 400 MHz): δ_H 8.30 (s, 1H, $H^{6'}$), 8.28–8.27 (broad m, 1H, H^9), 7.93 (td, J = 8.0 and 2.4 Hz, 1H, H^7), 7.50 (s, 2H, $NH_2^{2''}$), 7.46 (d, J = 8.0 Hz, 1H, H^3), 7.42 (d, J = 1.6 Hz, 1H, H^6), 7.24 (dd, J = 8.0 and 1.6 Hz, 1H, H^4), 7.15 (ddd, J = 8.8, 3.2 and 0.8 Hz, 1H, H^8) and 5.62 (s, 2H, CH_2). ^{13}C-NMR (DMSO-d_6, 101 MHz): δ_C 163.93, 162.97 (d, J = 236.3 Hz, $^1J_{C\text{-}F}$, 1C), 158.71, 156.55, 154.76, 148.91, 147.32 (d, J = 16.2 Hz, $^3J_{C\text{-}F}$, 1C), 145.46, 144.90, 142.30 (d, J = 8.1 Hz, $^3J_{C\text{-}F}$, 1C), 131.55 (d, J = 5.1 Hz, $^4J_{C\text{-}F}$, 1C), 128.73, 120.94, 115.51, 110.09 (d, J = 37.4 Hz, $^2J_{C\text{-}F}$, 1C), 109.34, 97.99, and 46.97. HPLC-MS (APCI/ESI): purity 99%, t_R = 2.25 min, (*m*/*z*) $[M+H]^+$ = 377.1.

5-(4-Amino-1-((6-methylpyridin-3-yl)methyl)-1*H*-pyrazolo[3,4-*d*]pyrimidin-3-yl) benzo[*d*]oxazol-2-amine, 42 (GS 137)

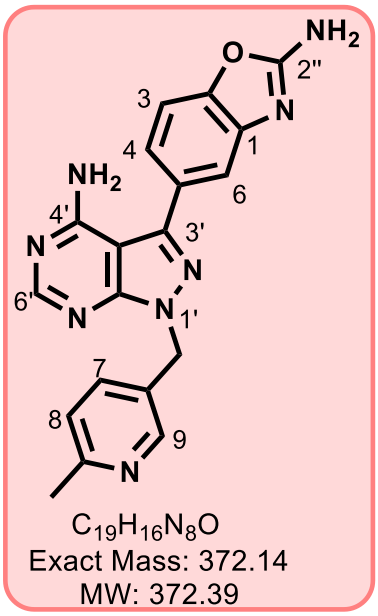

Using the general procedure 3 and a reaction mixture containing **42a** (400 mg, 1.10 mmol), the product was obtained as an off-white solid (164 mg, 40%); MP 279–280°C; R_f (10% MeOH/ DCM) 0.39; ^{1}H-NMR (DMSO-d_6, 600 MHz): δ_H 8.42 (d, J = 2.4 Hz, 1H, H^9), 8.25 (s, 1H, $H^{6'}$), 7.55 (dd, J = 7.8 and 2.4 Hz, 1H, H^4), 7.48 (s, 2H, $NH_2^{2''}$), 7.42 (d, J = 7.8 Hz, 1H, H^3), 7.36 (d, J = 1.8 Hz, 1H, H^6), 7.19 (dd, J = 7.8 and 2.4 Hz, 1H, H^7), 7.16 (d, J = 7.8 Hz, 1H, H^8), 5.51 (s, 2H, CH_2), and 2.38 (s, 3H, CH_3). ^{13}C-NMR (DMSO-d_6, 151 MHz): δ_C 163.88, 158.64, 157.74, 156.45, 154.65, 148.83, 148.74, 145.21, 144.84, 136.36, 130.14, 128.75, 123.40, 120.90, 115.44, 109.31, 97.88, 47.68, and 24.12. HPLC-MS (APCI/ESI): purity 99%, t_R = 2.22 min, (m/z) $[M+H]^+$ = 373.1.

5-(4-Amino-1-(pyridin-4-ylmethyl)-1*H*-pyrazolo[3,4-*d*]pyrimidin-3-yl) benzo[*d*]oxazol-2-amine, 43 (GS 79B)

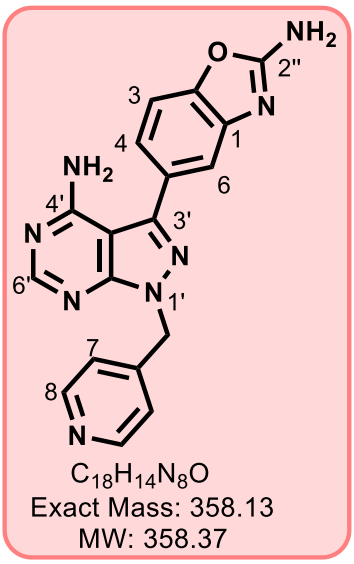

Using the general procedure 3 and a reaction mixture containing **43a** (0.33 g, 0.94 mmol), the product was obtained as a white solid (0.13 g, 39%); MP 299–300°C; R_f (10% MeOH/DCM) 0.4; ^{1}H-NMR (DMSO-d_6, 400 MHz): δ_H 8.52 (pseudo dd, J = 6.0 and 1.6 Hz, 2H, H^8), 8.28 (s, 1H, $H^{6'}$), 7.51 (s, 2H, $NH_2^{2''}$), 7.47 (d, J = 8.4 Hz, 1H, H^3), 7.44 (d, J = 1.6 Hz, 1H, H^6), 7.26 (dd, J = 8.4 and 1.6 Hz, 1H, H^4), 7.21 (pseudo dd, J = 6.0 and 1.6 Hz, 2H, H^7), and 5.62 (s, 2H, CH_2). ^{13}C-NMR (DMSO-d_6, 101 MHz): δ_C 163.93, 158.73, 156.59, 155.06, 150.32 (2C), 148.92, 146.46, 145.55, 144.91, 128.73, 122.69 (2C), 120.96, 115.52, 109.35, 97.92, and 49.13. HPLC-MS (APCI/ESI): purity 99%, t_R = 2.04 min, (m/z) $[M+H]^+$ = 359.1.

5-(4-Amino-1-((2-chloropyridin-4-yl)methyl)-1*H*-pyrazolo[3,4-*d*]pyrimidin-3-yl) benzo[*d*] oxazol-2-amine, 44 (GS 157)

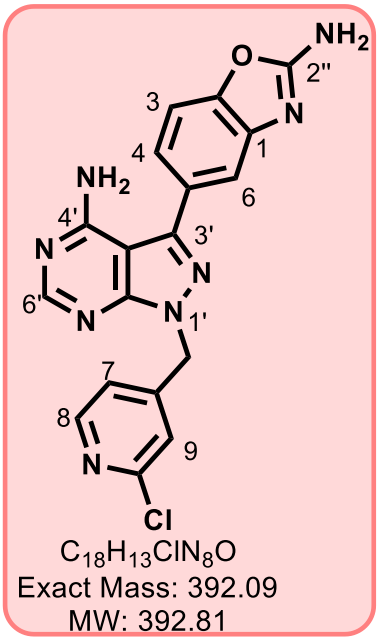

$C_{18}H_{13}ClN_8O$
Exact Mass: 392.09
MW: 392.81

Using the general procedure 3 and a reaction mixture containing crude **44a** (320 mg, 0.83 mmol), the product was obtained as a white solid (55 mg, 17%); MP 292–293°C; R_f (10% MeOH/DCM) 0.41; ^{1}H-NMR (DMSO-d_6, 400 MHz): δ_H 8.34 (d, J = 5.2 Hz, 1H, H^8), 8.27 (s, 1H, $H^{6'}$), 7.51 (s, 2H, $NH_2^{2''}$), 7.46 (d, J = 8.4 Hz, 1H, H^3), 7.43 (d, J = 1.6 Hz, 1H, H^6), 7.36 (d, J = 1.2 Hz, 1H, H^9), 7.25 (dd, J = 8.0 and 1.6 Hz, 1H, H^4), 7.18 (dd, J = 5.2 and 1.2 Hz, 1H, H^7), and 5.63 (s, 2H, CH_2). ^{13}C-NMR (DMSO-d_6, 101 MHz): δ_C 163.94, 158.60, 156.46, 155.05, 151.00, 150.72, 150.54, 148.96, 145.88, 144.86, 128.59, 123.04, 122.13, 120.99, 115.53, 109.40, 97.96, and 48.66. HPLC-MS (APCI/ESI): purity 99%, t_R = 2.30 min, (*m*/*z*) $[M+H]^+$ = 393.1.

5-(4-Amino-1-((2-fluoropyridin-4-yl)methyl)-1*H*-pyrazolo[3,4-*d*]pyrimidin-3-yl) benzo[*d*] oxazol-2-amine, 45 (GS 165)

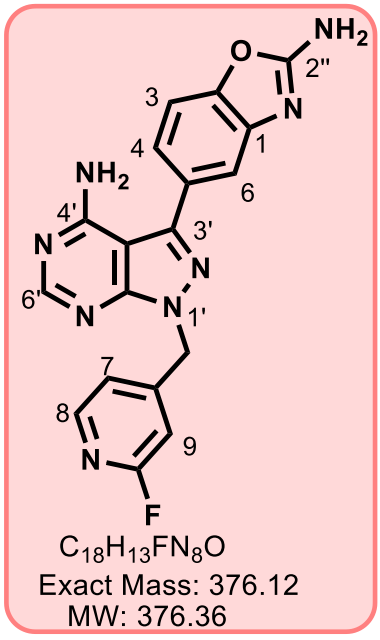

$C_{18}H_{13}FN_8O$
Exact Mass: 376.12
MW: 376.36

Using the general procedure 3 and a reaction mixture containing **45a** (0.33 g, 0.89 mmol), the product was obtained as a white solid (48 mg, 14%); MP 299–300°C; R_f (10% MeOH/DCM) 0.48; ^{1}H-NMR (DMSO-d_6, 600 MHz): δ_H 8.24 (s, 1H, $H^{6'}$), 8.14 (d, J = 4.8 Hz, 1H, H^8), 7.49 (s, 2H, $NH_2^{2''}$), 7.43 (d, J = 8.4 Hz, 1H, H^3), 7.40 (d, J = 1.8 Hz, 1H, H^6), 7.22 (dd, J = 8.4 and 1.8 Hz, 1H, H^4), 7.10 (dd, J = 5.4 and 1.2 Hz, 1H, H^7), 6.96 (broad d, J = 1.2 Hz, 1H, H^9), and 5.64 (s, 2H, CH_2). ^{13}C-NMR (DMSO-d_6, 151 MHz): δ_C 163.90, 163.72 (d, J = 235.5 Hz), 158.71, 156.62, 155.06, 153.11 (d, J = 7.8 Hz, $^3J_{C\text{-}F}$, 1C), 148.90, 148.4 (d, J = 15.1 Hz, $^3J_{C\text{-}F}$, 1C), 145.76, 144.84, 128.60, 120.96, 120.93, 115.50, 109.35, 108.21 (d, J = 38.4 Hz, $^2J_{C\text{-}F}$, 1C), 97.91, and 48.75 (d, J = 3.4 Hz, $^4J_{C\text{-}F}$, 1C). HPLC-MS (APCI/ESI): purity 99%, t_R = 2.17 min, (*m*/*z*) $[M+H]^+$ = 377.1.

5-(4-Amino-1-((2-trifluoromethylpyridin-4-yl)methyl)-1*H*-pyrazolo[3,4-*d*]pyrimidin-3-yl) benzo[*d*] oxazol-2-amine, 46 (GS 187)

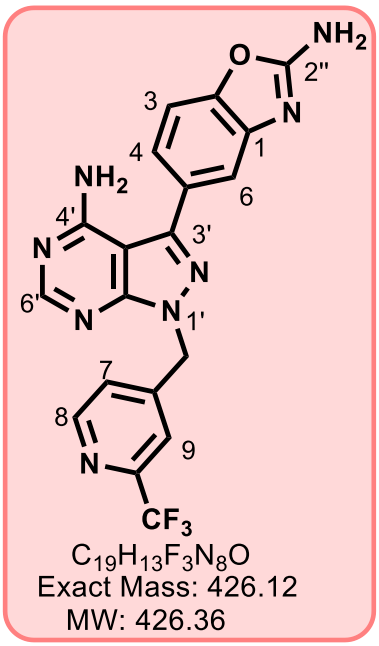

Using the general procedure 3 and a reaction mixture containing **46a** (290 mg, 0.69 mmol), the product was obtained as a white solid (85 mg, 29%); MP 280–281°C; R_f (10% MeOH/ DCM) 0.37; ^{1}H-NMR (DMSO-d_6, 400 MHz): δ_H 8.71 (d, J = 4.8 Hz, 1H, H^8), 8.29 (s, 1H, $H^{6'}$), 7.84 (broad d, J = 1.2 Hz, 1H, H^9), 7.51 (s, 2H, $NH_2^{2''}$), 7.48 (d, J = 8.4 Hz, 1H, H^3), 7.46 (overlapping dd, J = 5.2 and 1.2 Hz, 1H, H^7), 7.44 (d, J = 1.6 Hz, 1H, H^6), 7.26 (dd, J = 8.0 and 1.6 Hz, 1H, H^4), and 5.77 (s, 2H, CH_2). ^{13}C-NMR (DMSO-d_6, 101 MHz): δ_C 163.95, 158.77, 156.69, 155.19, 151.13, 149.26, 148.97, 147.19 (q, J = 34.3 Hz, $^2J_{C\text{-}F}$, 1C), 145.90, 144.93, 128.62, 126.07, 122.02 (q, J = 274.7 Hz, $^2J_{C\text{-}F}$, 1C), 120.94, 119.72 (q, J = 3.0 Hz, $^3J_{C\text{-}F}$, 1C), 115.53, 109.38, 97.98, and 48.86. HPLC-MS (APCI/ESI): purity 99%, t_R = 2.36 min, (m/z) $[M+H]^+$ = 427.1.

5-(4-Amino-1-((2-methylpyridin-4-yl)methyl)-1*H*-pyrazolo[3,4-*d*]pyrimidin-3-yl) benzo[*d*] oxazol-2-amine, 47 (GS 189)

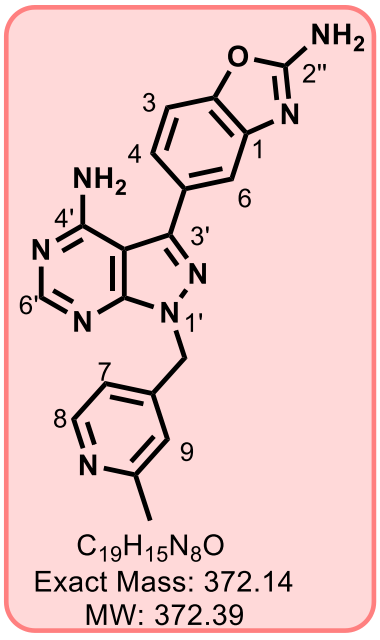

Using the general procedure 3 and a reaction mixture containing **47a** (255 mg, 0.70 mmol), the product was obtained as a white solid (125 mg, 48%); MP 273–274°C; R_f (10% MeOH/ DCM) 0.29; ^{1}H-NMR (DMSO-d_6, 400 MHz): δ_H 8.37 (d, J = 5.2 Hz, 1H, H^8), 8.28 (s, 1H, $H^{6'}$), 7.51 (s, 2H, $NH_2^{2''}$), 7.47 (d, J = 8.4 Hz, 1H, H^3), 7.44 (d, J = 1.6 Hz, 1H, H^6), 7.26 (dd, J = 8.0 and 1.6 Hz, 1H, H^4), 7.10 (broad d, 1H, J = 1.2 Hz, H^9), 6.99 (broad dd, J = 5.2 and 1.2 Hz, 1H, H^7), 5.56 (s, 2H, CH_2) and 2.42 (s, 3H, CH_3). ^{13}C-NMR (DMSO-d_6, 101 MHz): δ_C 163.93, 158.72, 158.63, 156.56, 155.01, 149.65, 148.91, 146.66, 145.48, 144.89, 128.75, 121.91, 120.97, 119.90, 115.52, 109.36, 97.90, 49.16, and 24.45. HPLC-MS (APCI/ESI): purity 99%, t_R = 2.28 min, (m/z) $[M+H]^+$ = 373.1.

5-(4-Amino-1-(pyridin-3-ylmethyl)-1*H*-pyrazolo[3,4-*d*]pyrimidin-3-yl) benzo[*d*]oxazol-2-amine, 48 (GS 83)

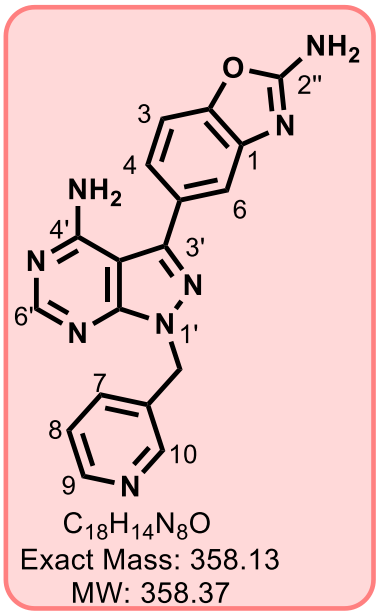

$C_{18}H_{14}N_8O$
Exact Mass: 358.13
MW: 358.37

Using the general procedure 3 and a reaction mixture containing **48a** (0.30 g, 0.85 mmol), the product was obtained as an off-white solid (0.15 g, 50%); MP 286–287°C; R_f (15% MeOH/DCM) 0.6; ^{1}H-NMR (DMSO-d_6, 400 MHz): δ_H 8.59 (dd, J = 2.4 and 1.2 Hz, 1H, H^{10}), 8.50 (dd, J = 4.8 and 1.6 Hz, 1H, H^9), 8.30 (s, 1H, $H^{6'}$), 7.71 (ddd, J = 7.9, 2.3 and 1.7 Hz, 1H, H^7), 7.50 (s, 2H, $NH_2^{2''}$), 7.46 (dd, J = 8.0 and 0.8 Hz, 1H, H^3), 7.42 (dd, J = 1.6 and 0.4 Hz, 1H, H^6), 7.36 (ddd, J = 7.8, 4.8 and 0.9 Hz, 1H, H^8), 7.24 (dd, J = 8.1 and 1.7 Hz, 1H, H^4), and 5.62 (s, 2H, CH_2). ^{13}C-NMR (DMSO-d_6, 101 MHz): δ_C 163.93, 158.70, 156.53, 154.80, 149.42, 149.34, 148.90, 145.37, 144.90, 136.00, 133.22, 128.77, 124.17, 120.94, 115.50, 109.34, 97.96, and 47.91. HPLC-MS (APCI/ESI): purity 99%, t_R = 2.20 min, (*m*/*z*) $[M+H]^+$ = 359.1.

5-(4-Amino-1-((5-methylpyridin-3-yl)methyl)-1*H*-pyrazolo[3,4-*d*]pyrimidin-3-yl) benzo[*d*]oxazol-2-amine, 49 (GS 167)

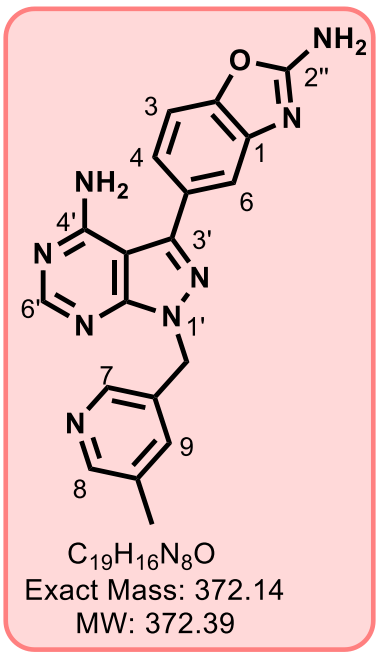

$C_{19}H_{16}N_8O$
Exact Mass: 372.14
MW: 372.39

Using the general procedure 3 and a reaction mixture containing **49a** (260 mg, 0.71 mmol), the product was obtained as a white solid (48 mg, 18%); MP 285–286°C; R_f (10% MeOH/DCM) 0.32; ^{1}H-NMR (DMSO-d_6, 400 MHz): δ_H 8.38 (d, J = 2.0 Hz, 1H, H^7), 8.33 (d, J = 2.0 Hz, 1H, H^8), 8.30 (s, 1H, $H^{6'}$), 7.53 (broad t, J = 2.4 Hz, 1H, H^9), 7.50 (s, 2H, $NH_2^{2''}$), 7.46 (d, J = 8.0 Hz, 1H, H^3), 7.42 (d, J = 1.6 Hz, 1H, H^6), 7.24 (dd, J = 8.4 and 1.6 Hz, 1H, H^4), 5.57 (s, 2H, CH_2), and 2.26 (s, 3H, CH_3). ^{13}C-NMR (101 MHz, DMSO-d_6): δ_C 163.93, 158.68, 156.50, 154.74, 149.71, 148.89, 146.63, 145.32, 144.87, 136.27, 133.42, 132.67, 128.77, 120.97, 115.50, 109.36, 97.94, 47.82, and 18.22. HPLC-MS (APCI/ESI): purity 97%, t_R = 2.21 min, (*m*/*z*) $[M+H]^+$ = 373.1.

5-(4-Amino-1-((5-chloropyridin-3-yl)methyl)-1*H*-pyrazolo[3,4-*d*]pyrimidin-3-yl)benzo[*d*] oxazol-2-amine, 50 (GS 203)

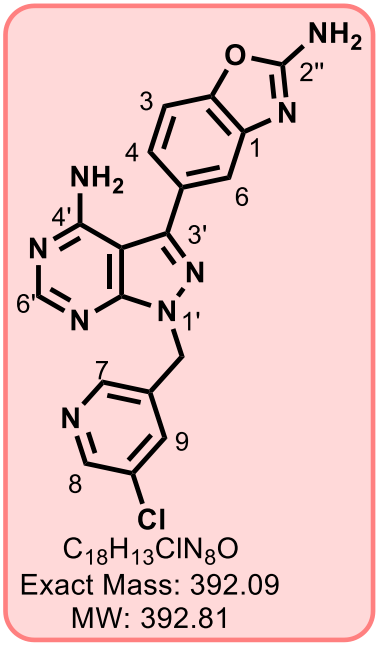

Using the general procedure 3 and a reaction mixture containing **50a** (340 mg, 0.88 mmol), the product was obtained as a white solid (97 mg, 28%); MP 274–275°C; R_f (10% MeOH/DCM) 0.34; ^{1}H-NMR (DMSO-d_6, 600 MHz): δ_H 8.52 (d, J = 2.4 Hz, 1H, H^8), 8.48 (d, J = 2.4 Hz, 1H, H^7), 8.26 (s, 1H, $H^{6'}$), 7.82 (t, J = 2.4 Hz, 1H, H^9), 7.48 (s, 2H, $NH_2^{2''}$), 7.42 (d, J = 7.8 Hz, 1H, H^3), 7.38 (d, J = 1.8 Hz, 1H, H^6), 7.20 (dd, J = 7.8 and 1.8 Hz, 1H, H^4), and 5.60 (s, 2H, CH_2). ^{13}C-NMR (151 MHz, DMSO-d_6): δ_C 163.89, 158.69, 156.59, 154.83, 148.88, 147.93, 147.75, 145.59, 144.86, 135.68, 134.93, 131.38, 128.63, 120.92, 115.47, 109.34, 97.96, and 47.19. HPLC-MS (APCI/ESI): purity 99%, t_R = 2.34 min, (m/z) $[M+H]^+$ = 393.1.

5-(4-Amino-1-((5-fluoropyridin-3-yl)methyl)-1*H*-pyrazolo[3,4-*d*]pyrimidin-3-yl)benzo[*d*] oxazol-2-amine, 51 (GS 199)

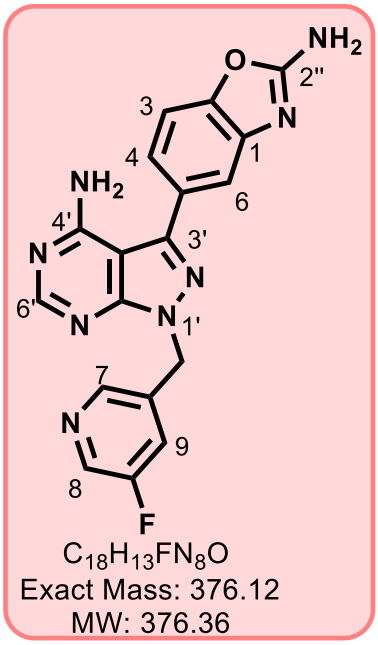

Using the general procedure 3 and a reaction mixture containing **51a** (305 mg, 0.82 mmol), the product was obtained as a white solid (74 mg, 24%); MP 285–286°C; R_f (10% MeOH/ DCM) 0.36; ^{1}H-NMR (DMSO-d_6, 600 MHz): δ_H 8.47 (broad d, J = 2.4 Hz, 1H, H^8), 8.40 (broad t, J = 1.8 Hz, 1H, H^7), 8.25 (s, 1H, $H^{6'}$), 7.60 (dt, J = 9.0 and 2.4 Hz, 1H, H^9), 7.48 (s, 2H, $NH_2^{2''}$), 7.42 (d, J = 7.8 Hz, 1H, H^3), 7.38 (d, J = 1.8 Hz, 1H, H^6), 7.20 (dd, J = 8.4 and 1.8 Hz, 1H, H^4), and 5.62 (s, 2H, CH_2). ^{13}C-NMR (151 MHz, DMSO-d_6): δ_C 163.89, 159.31 (d, J = 253.7 Hz, $^1J_{C\text{-}F}$, 1C), 158.69, 156.57, 154.83, 148.88, 145.61 (overlapping d, J = 4.5 Hz, $^4J_{C\text{-}F}$, 1C), 145.58, 144.85, 137.52 (d, J = 22.7 Hz, $^2J_{C\text{-}F}$, 1C), 135.21 (d, J = 3.0 Hz, $^3J_{C\text{-}F}$, 1C), 128.64, 122.84 (d, J = 19.6 Hz, $^2J_{C\text{-}F}$, 1C), 120.94, 115.48, 109.33, 97.96, and 47.18. HPLC-MS (APCI/ESI): purity 98%, t_R = 2.26 min, (m/z) $[M+H]^+$ = 377.1.

5-(4-Amino-1-(pyridin-2-ylmethyl)-1*H*-pyrazolo[3,4-*d*]pyrimidin-3-yl) benzo[*d*]oxazol-2-amine, 52 (GS 87)

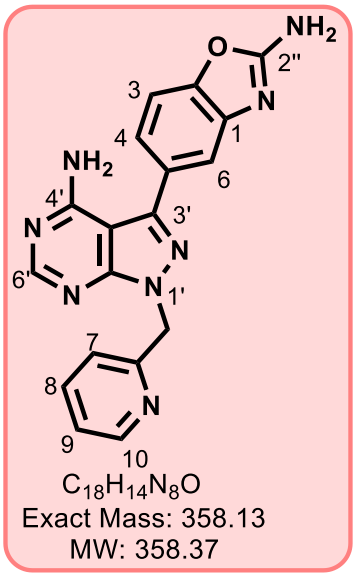

Using the general procedure 3 and a reaction mixture containing **52a** (0.34 g, 0.97 mmol), the product was obtained as an off-white solid (0.11 g, 32%); MP 271–273°C; R_f (12% MeOH/DCM) 0.4; ^{1}H-NMR (DMSO-d_6, 400 MHz): δ_H 8.51 (ddd, J = 4.8, 1.6 and 0.8 Hz, 1H, H^{10}), 8.27 (s, 1H, $H^{6'}$), 7.75 (td, J = 7.6 and 2.0 Hz, 1H, H^8), 7.51 (s, 2H, $NH_2^{2''}$), 7.47 (d, J = 8.4 Hz, 1H, H^3), 7.43 (d, J = 1.6 Hz, 1H, H^6), 7.30 (ddd, J = 7.6, 4.8 and 1.2 Hz, 1H, H^9), 7.25 (dd, J = 8.0 and 1.6 Hz, 1H, H^4), 7.11 (broad dd, J = 8.0 and 1.2 Hz, 1H, H^7), and 5.66 (s, 2H, CH_2). ^{13}C-NMR (DMSO-d_6, 101 MHz): δ_C 163.92, 158.69, 156.90, 156.45, 155.17, 149.62, 148.87, 145.29, 144.89, 137.50, 128.87, 123.16, 121.97, 120.93, 115.48, 109.34, 97.90, and 51.94. HPLC-MS (APCI/ESI): purity 99%, t_R = 2.17 min, (*m/z*) $[M+H]^+$ = 359.1.

5-(4-Amino-1-((5-chloropyridin-2-yl)methyl)-1*H*-pyrazolo[3,4-*d*]pyrimidin-3-yl) benzo[*d*] oxazol-2-amine, 53 (GS 185)

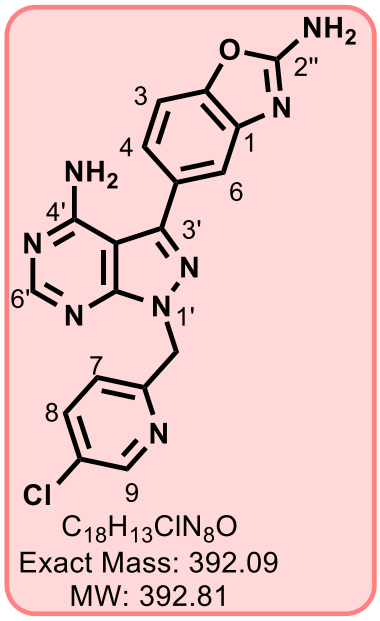

Using the general procedure 3 and a reaction mixture containing **53a** (345 mg, 0.89 mmol), the product was obtained as a white solid (98 mg, 28%); MP 289–290°C; R_f (10% MeOH/DCM) 0.41; ^{1}H-NMR (DMSO-d_6, 600 MHz): δ_H 8.40 (d, J = 2.4 Hz, 1H, H^9), 8.25 (s, 1H, $H^{6'}$), 7.73 (dd, J = 8.4 and 2.4 Hz, 1H, H^8), 8.48 (s, 2H, $NH_2^{2''}$), 7.44 (d, J = 8.4 Hz, 1H, H^7), 7.42 (d, J = 7.8 Hz, 1H, H^3), 7.37 (d, J = 1.8 Hz, 1H, H^6), 7.19 (dd, J = 7.8 and 1.8 Hz, 1H, H^4), and 5.58 (s, 2H, CH_2). ^{13}C-NMR (DMSO-d_6, 151 MHz): δ_C 163.89, 158.68, 156.54, 154.78, 150.00, 149.62, 148.87, 145.51, 144.86, 139.75, 132.80, 128.65, 124.79, 120.91, 115.47, 109.32, 97.93, and 47.03. HPLC-MS (APCI/ESI): purity 99%, t_R = 2.31 min, (*m/z*) $[M+H]^+$ = 393.1.

5-(4-Amino-1-((5-fluoropyridin-2-yl)methyl)-1*H*-pyrazolo[3,4-*d*]pyrimidin-3-yl) benzo[*d*] oxazol-2-amine, 54 (GS 183)

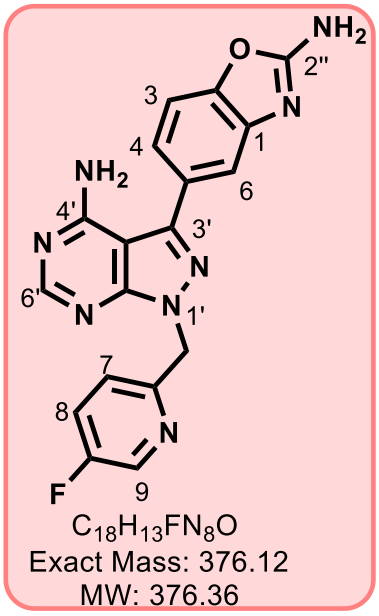

Using the general procedure 3 and a reaction mixture containing **54a** (430 mg, 1.162 mmol), the product was obtained as a white solid (115 mg, 27%); MP 274–275°C; R_f (10% MeOH/DCM) 0.31; ^{1}H-NMR (DMSO-d_6, 600 MHz): δ_H 8.46 (broad d, J = 3.0 Hz, 1H, H^9), 8.22 (s, 1H, H$^{6'}$), 7.64 (td, J = 9.0 and 3.0 Hz, 1H, H^8), 7.48 (s, 2H, NH$_2^{2''}$), 7.42 (d, J = 7.8 Hz, 1H, H^3), 7.37 (d, J = 1.8 Hz, 1H, H^6), 7.22 (dd, J = 8.4 and 4.2 Hz, 1H, H^7), 7.20 (dd, J = 8.4 and 1.8 Hz, 1H, H^4), and 5.62 (s, 2H, CH$_2$). ^{13}C-NMR (DMSO-d_6, 151 MHz): δ_C 163.88, 158.86 (d, J = 252.2 Hz, $^1J_{C\text{-}F}$, 1C), 158.66, 156.45, 155.08, 153.13 (d, J = 4.5 Hz, $^4J_{C\text{-}F}$, 1C), 148.83, 145.33, 144.85, 137.59 (d, J = 24.2 Hz, $^2J_{C\text{-}F}$, 1C), 128.77, 124.42 (d, J = 19.6 Hz, $^2J_{C\text{-}F}$, 1C), 123.65 (d, J = 4.5 Hz, $^3J_{C\text{-}F}$, 1C), 120.89, 115.43, 109.32, 97.85, and 51.20. HPLC-MS (APCI/ESI): purity 99%, t_R = 2.24 min, (m/z) [M+H]$^+$ = 377.1.

5-(4-Amino-1-((5-(trifluoromethyl)pyridin-2-yl)methyl)-1*H*-pyrazolo[3,4-*d*]pyrimidin-3-yl)benzo[*d*]oxazol-2-amine, 55 (GS 191)

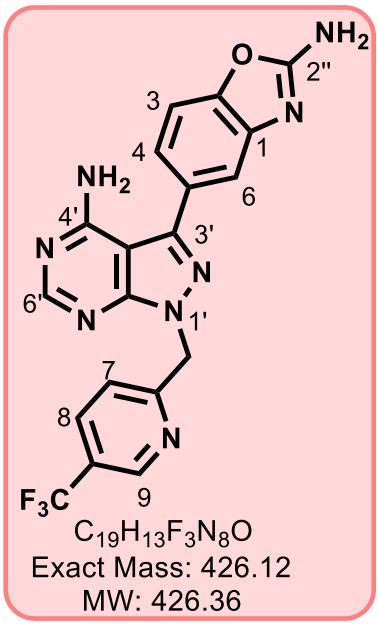

Using the general procedure 3 and a reaction mixture containing **55a** (310 mg, 0.74 mmol), the product was obtained as a white solid (79 mg, 25%); MP 303–305°C; R_f (10% MeOH/DCM) 0.43; ^{1}H-NMR (DMSO-d_6, 400 MHz): δ_H 8.92 (d, J = 2.8 Hz, 1H, H^9), 8.27 (s, 1H, H$^{6'}$), 8.18 (dd, J = 8.4 and 2.4 Hz, 1H, H^8), 7.51 (s, 2H, NH$_2^{2''}$), 7.47 (d, J = 8.4 Hz, 1H, H^3), 7.43 (d, J = 2.0 Hz, 1H, H^6), 7.37 (d, J = 8.4 Hz, 1H, H^7), 7.26 (dd, J = 8.0 and 2.0 Hz, 1H, H^4), and 5.79 (s, 2H, CH$_2$). ^{13}C-NMR (101 MHz, DMSO-d_6): δ_C 163.93, 161.43, 158.73, 156.56, 155.32, 148.92, 146.47 (q, J = 3.0 Hz, $^3J_{C\text{-}F}$, 1C), 145.61, 144.92, 135.05 (broad q, J = 3.0 Hz, $^3J_{C\text{-}F}$, 1C), 128.75, 125.50 (q, J = 272.7 Hz, $^1J_{C\text{-}F}$, 1C), 124.47 (q, J = 32.3 Hz, $^2J_{C\text{-}F}$, 1C), 122.33, 120.93, 115.49, 109.35, 97.95, and 51.69. HPLC-MS (APCI/ESI): purity 99%, t_R = 2.39 min, (m/z) [M+H]$^+$ = 427.1.

5-(4-Amino-1-((6-chloropyridin-2-yl)methyl)-1*H*-pyrazolo[3,4-*d*]pyrimidin-3-yl)benzo[*d*] oxazol-2-amine, 56 (GS 181)

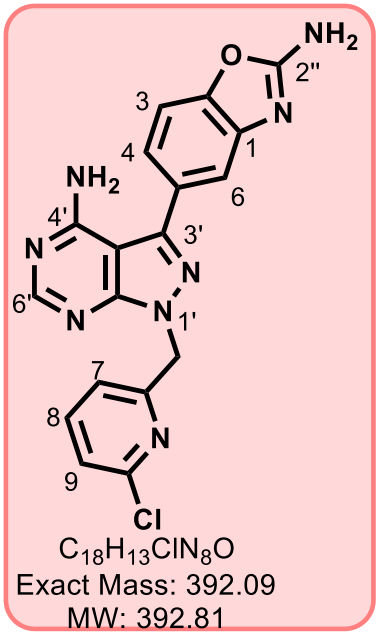

$C_{18}H_{13}ClN_8O$
Exact Mass: 392.09
MW: 392.81

Using the general procedure 3 and a reaction mixture containing **56a** (410 mg, 1.06 mmol), the product was obtained as a white solid (100 mg, 24%); MP 280–281 °C; R_f (10% MeOH/DCM) 0.37; ^{1}H-NMR (DMSO-d_6, 600 MHz): δ_H 8.23 (s, 1H, $H^{6'}$), 7.78 (t, J = 7.8 Hz, 1H, H^8), 7.48 (s, 2H, $NH_2^{2''}$), 7.43 (d, J = 8.4 Hz, 1H, H^3), 7.40 (broad d, J = 7.8 Hz, 1H, H^7), 7.38 (d, J = 1.8 Hz, 1H, H^6), 7.21 (dd, J = 7.8 and 1.8 Hz, 1H, H^4), 7.05 (broad d, J = 7.8 Hz, 1H, H^9), and 5.60 (s, 2H, CH_2). ^{13}C-NMR (151 MHz, DMSO-d_6): δ_C 163.89, 158.68, 157.98, 156.54, 155.13, 150.17, 148.87, 145.55, 144.85, 141.20, 128.69, 123.73, 121.28, 120.92, 115.46, 109.35, 97.87, and 51.29. HPLC-MS (APCI/ESI): purity 99%, t_R = 2.32 min, (*m*/*z*) $[M+H]^+$ = 393.0.

5-(4-Amino-1-((6-methylpyridin-2-yl)methyl)-1*H*-pyrazolo[3,4-*d*]pyrimidin-3-yl) benzo[*d*]oxazol-2-amine, 57 (GS 177)

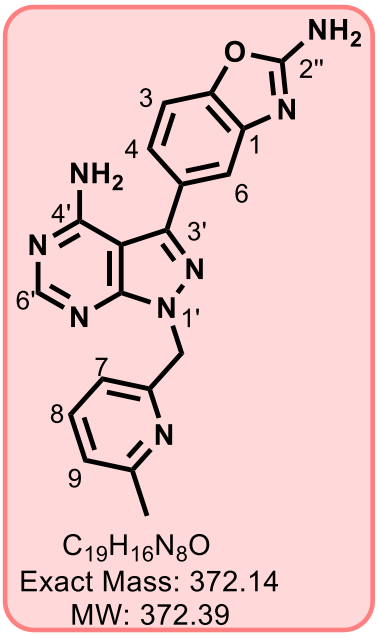

$C_{19}H_{16}N_8O$
Exact Mass: 372.14
MW: 372.39

Using the general procedure 3 and a reaction mixture containing **57a** (280 mg, 0.75 mmol), the product was obtained as a white solid (87 mg, 31%); MP 279–280°C; R_f (10% MeOH/DCM) 0.31; ^{1}H-NMR (DMSO-d_6, 600 MHz): δ_H 8.22 (s, 1H, $H^{6'}$), 7.56 (t, J = 7.8 Hz, 1H, H^8), 7.49 (s, 2H, $NH_2^{2''}$), 7.42 (d, J = 8.4 Hz, 1H, H^3), 7.38 (d, J = 1.8 Hz, 1H, H^6), 7.21 (dd, J = 8.4 and 1.8 Hz, 1H, H^4), 7.10 (broad d, J = 7.8 Hz, 1H, H^9), 6.73 (broad d, J = 7.2 Hz, 1H, H^7), 5.56 (s, 2H, CH_2), and 2.41 (s, 3H, CH_3). ^{13}C-NMR (151 MHz, DMSO-d_6): δ_C 163.89, 158.66, 157.98, 156.45, 156.33, 155.05, 148.83, 145.29, 144.84, 137.74, 128.80, 122.42, 120.92, 118.73, 115.46, 109.33, 97.84, 52.02, and 24.38. HPLC-MS (APCI/ESI): purity 99%, t_R = 2.28 min, (*m*/*z*) $[M+H]^+$ = 373.1.

5-(4-Amino-1-((6-fluoropyridin-2-yl)methyl)-1*H*-pyrazolo[3,4-*d*]pyrimidin-3-yl) benzo[*d*]oxazol-2-amine, 58 (GS 193)

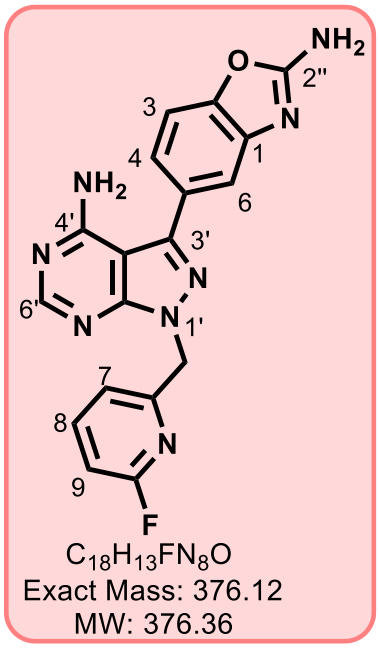

$C_{18}H_{13}FN_8O$
Exact Mass: 376.12
MW: 376.36

Using the general procedure 3 and a reaction mixture containing **58a** (370 mg, 1.0 mmol), the product was obtained as a white solid (88 mg, 23%); MP 293–294°C; R_f (10% MeOH/DCM) 0.38; ^{1}H-NMR (DMSO-d_6, 600 MHz): δ_H 8.23 (s, 1H, $H^{6'}$), 7.91 (q, J = 7.8 Hz, 1H, H^8), 7.48 (s, 2H, $NH_2^{2''}$), 7.43 (d, J = 7.8 Hz, 1H, H^3), 7.38 (d, J = 1.8 Hz, 1H, H^6), 7.21 (dd, J = 7.8 and 1.8 Hz, 1H, H^4), 7.05 (dd, J = 8.4 and 2.4 Hz, 1H, H^9), 7.02 (dd, J = 7.2 and 2.4 Hz, 1H, H^7), and 5.58 (s, 2H, CH_2). ^{13}C-NMR (151 MHz, DMSO-d_6): δ_C 163.89, 162.90 (d, J = 237.1 Hz, $^1J_{C\text{-}F}$, 1C), 158.67, 156.50, 155.90 (d, J = 12.1 Hz, $^3J_{C\text{-}F}$, 1C), 155.17, 148.86, 145.48, 144.86, 143.48 (d, J = 7.6 Hz, $^3J_{C\text{-}F}$, 1C), 128.72, 120.91, 119.91 (d, J = 4.5 Hz, $^4J_{C\text{-}F}$, 1C), 115.45, 109.33, 108.82 (d, J = 36.2 Hz, $^2J_{C\text{-}F}$, 1C), 97.85, and 50.99. HPLC-MS (APCI/ESI): purity 99%, t_R = 2.24 min, (*m*/*z*) $[M+H]^+$ = 377.1.

5-(4-Amino-1-((6-(trifluoromethyl)pyridin-2-yl)methyl)-1*H*-pyrazolo[3,4-*d*]pyrimidin-3-yl) benzo[*d*]oxazol-2-amine, 59 (GS 195)

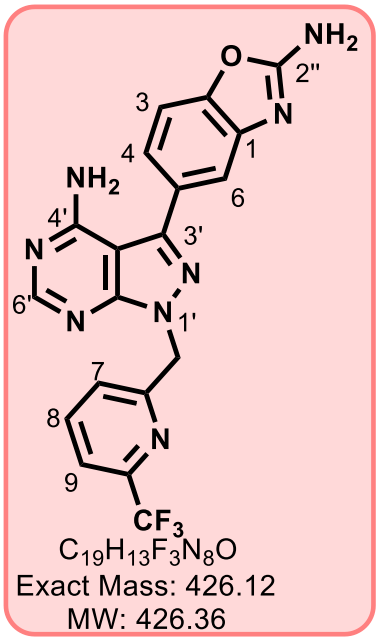

$C_{19}H_{13}F_3N_8O$
Exact Mass: 426.12
MW: 426.36

Using the general procedure 3 and a reaction mixture containing **59a** (400 mg, 0.95 mmol), the product was obtained as a white solid (107 mg, 26%); MP 257–258°C; R_f (10% MeOH/DCM) 0.38; ^{1}H-NMR (DMSO-d_6, 600 MHz): δ_H 8.28 (s, 1H, $H^{6'}$), 8.05 (t, J = 7.6 Hz, 1H, H^8), 7.83 (broad d, J = 7.6 Hz, 1H, H^9), 7.51 (s, 2H, $NH_2^{2''}$), 7.47 (d, J = 8.0 Hz, 1H, H^3), 7.43 (d, J = 1.6 Hz, 1H, H^6), 7.34 (broad d, J = 8.0 Hz, 1H, H^7), 7.26 (dd, J = 8.4 and 2.0 Hz, 1H, H^4), and 5.76 (s, 2H, CH_2). ^{13}C-NMR (151 MHz, DMSO-d_6): δ_C 163.94, 158.73, 158.14, 156.60, 155.29, 148.93, 146.48 (q, J = 34.3 Hz, $^2J_{C\text{-}F}$, 1C), 145.74, 144.91, 140.05, 128.72, 125.60, 121.95 (d, J = 275.7 Hz, $^1J_{C\text{-}F}$, 1C), 120.95, 120.15 (broad q, J = 3.0 Hz, $^3J_{C\text{-}F}$, 1C), 115.52, 109.36, 97.98, and 51.65. HPLC-MS (APCI/ESI): purity 99%, t_R = 2.38 min, (*m*/*z*) $[M+H]^+$ = 427.1.

5-(4-Amino-1-(cyclohexylmethyl)-1*H*-pyrazolo[3,4-*d*]pyrimidin-3-yl)benzo[*d*]oxazol-2-amine, 60 (GS 125)

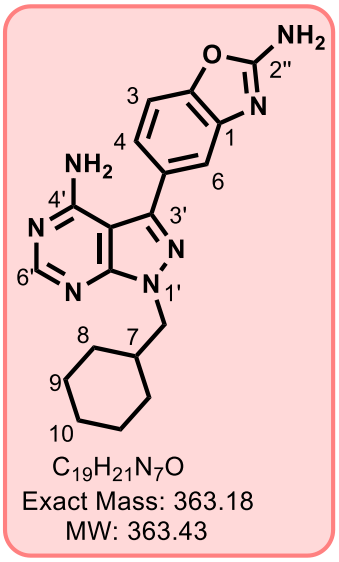

Using the general procedure 3 and a reaction mixture containing **60a** (395 mg, 1.11 mmol), the product was obtained as an off-white solid (97 mg, 24%); MP 285–286°C; R_f (10% MeOH/ DCM) 0.46; ^{1}H-NMR (DMSO-d_6, 400 MHz): δ_H 8.19 (s, 1H, $H^{6'}$), 7.47 (s, 2H, $NH_2^{2''}$), 7.42 (d, J = 7.8 Hz, 1H, H^3), 7.37 (d, J = 1.2 Hz, 1H, H^3), 7.20 (dd, J = 8.4 and 1.8 Hz, 1H, H^4), 4.14 (d, J = 6.6 Hz, 2H, CH_2), 1.92 (ttt, J = 10.8, 7.1 and 3.4 Hz, 1H, H^7), 1.63–1.60 (m, 2H, H^{9a}), 1.55–1.49 (m, 3H, $H^{8e, 10e}$), 1.16–1.08 (m, 3H, $H^{10a, 9e}$) and 1.00–0.94 (m, 2H, H^{8a}). ^{13}C-NMR (DMSO-d_6, 101 MHz): δ_C 163.87, 158.59, 156.06, 154.83, 148.74, 144.84, 144.32, 129.06, 120.88, 115.44, 109.28, 97.54, 52.52, 38.19, 30.58 (2C), 26.30, 25.58 (2C). HPLC-MS (APCI/ESI): purity > 99%, t_R = 2.51 min, (*m/z*) $[M+H]^+$ = 364.1.

5-(4-amino-1-((4,4-difluorocyclohexyl)methyl)-1*H*-pyrazolo[3,4-*d*]pyrimidin-3-yl) benzo[*d*]oxazol-2-amine, 61 (GS 197)

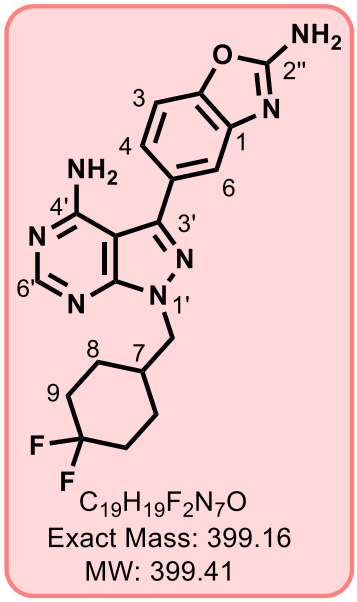

Using the general procedure 3 and a reaction mixture containing **61a** (410 mg, 1.04 mmol), the product was obtained as an off-white solid (186 mg, 45%); MP 288–289°C; R_f (10% MeOH/DCM) 0.37; ^{1}H-NMR (DMSO-d_6, 600 MHz): δ_H 8.21 (s, 1H, $H^{6'}$), 7.48 (s, 2H, $NH_2^{2''}$), 7.43 (d, J = 7.8 Hz, 1H, H^3), 7.38 (d, J = 1.8 Hz, 1H, H^6), 7.21 (dd, J = 8.4 and 1.8 Hz, 1H, H^4), 4.23 (d, J = 7.2 Hz, 1H, CH_2), 2.08 (ddd, J = 10.3, 7.8, and 3.6 Hz, 1H, H^7), 1.98–1.93 (m, 2H, H^{9e}), 1.78–1.69 (m, 2H, H^{9a}), 1.63–1.60 (m, 2H, H^{8e}), 1.26 (qd, J = 13.2 and 3.6 Hz, 2H, H^{8a}). ^{13}C-NMR (DMSO-d_6, 151 MHz): δ_C 163.88, 158.62, 156.17, 154.85, 148.78, 144.84, 144.60, 128.96, 124.63 (t, J = 241.6 Hz, $^1J_{C\text{-}F}$, 1C), 120.89, 115.46, 109.30, 97.57, 51.01, 35.93, 32.63 (t, J = 24.2 Hz, $^2J_{C\text{-}F}$, 2C), and 26.67 (d, J = 9.1 Hz, $^3J_{C\text{-}F}$, 2C). HPLC-MS (APCI/ESI): purity 98%, t_R = 2.41 min, (*m/z*) $[M+H]^+$ = 400.1.

10.2.2 Synthesis and characterization of imidazo[1,2-*a*]pyridines

10.2.2.1 Synthesis of 6-Bromo-3-iodoimidazo[1,2-*a*]pyridine, 75

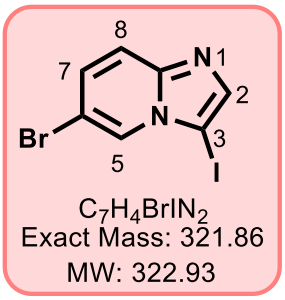

A solution of 6-bromoimidazo[1,2-*a*] pyridine (1.0 g, 5.1 mmol) in anhydrous ACN (20 mL) was charged with *N*-iodosuccinimide (1.05 eq.). The resulting reaction mixture was then stirred at 25°C for 15 hours. After completion of the reaction, the resulting precipitate was filtered off, washed with ACN (50 mL), and allowed to dry affording the product, as an off-white solid. (1.24 g, 76%); R_f (8% MeOH/DCM) 0.60; ^{1}H-NMR (400 MHz, $CDCl_3$): δ_H 8.30 (d, J = 2.2 Hz, 1H, H^5), 7.72 (s, 1H, H^2), 7.54 (d, J = 9.7 Hz, 1H, H^8), and 7.32 (dd, J = 9.5 and 1.9 Hz, 1H, H^7). ^{13}C-NMR (101 MHz, $CDCl_3$): δ_C 146.27, 140.93, 128.56, 126.32, 118.46, 108.37, and 61.21. HPLC-MS (APCI/ESI): purity 95%, t_R = 2.36 min, (*m/z*) $[M+H]^+$ = 322.8.

10.2.2.2 General procedure 4: Synthesis of intermediates 76, 77, 78 and target compounds 79–82

A suspension of appropriate halogenated precursors such as **75** (1 eq.), and appropriate boronic acid (1.1 eq.) in 7 mL dioxane/ water mixture (3:1) was purged with N_2 for 5 min. To the mixture was sequentially added K_2CO_3 (1.05 eq.) and $Pd(PPh_3)_2Cl_2$ (0.05 eq.) and the resulting mixture was heated to 90°C while stirring for 12 h. The mixture was then cooled to 20°C, filtered through celite and the cake washed with 50% MeOH/DCM (50 mL). The organic filtrate was concentrated *in vacuo* and purified by column chromatography (0–8 % MeOH/DCM) or reverse phase column for **78** (0–70% water/ MeOH) to obtain the expected product.

6-Bromo-3-(4-(methylsulfonyl)phenyl)imidazo[1,2-*a*]pyridine, 76

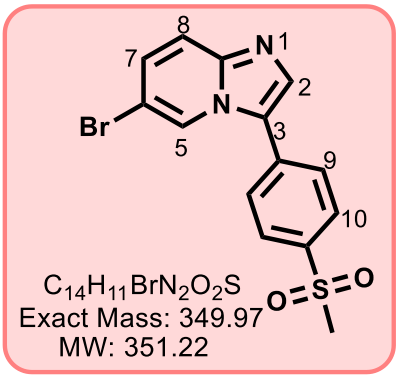

Using the general procedure 4 and a reaction mixture containing **75** (0.850 g, 2.48 mmol) and (4-(methylsulfonyl)phenyl)boronic acid (1.1 eq.), the product was obtained as an off-white solid (740 mg, 80%); R_f (10% MeOH/DCM) 0.32; ^{1}H-NMR (400 MHz, acetone-d_6): δ_H 8.82 (dd, J = 2.0 and 0.8 Hz, 1H, H^5), 8.14 (d, J = 8.8 Hz, 2H, H^9), 8.02 (d, J = 8.4 Hz, 2H, H^{10}), 7.91 (s, 1H, H^2), 7.64 (dd, J = 9.6 and 0.8 Hz, 1H, H^8), 7.46 (dd, J = 9.6 and 2.0 Hz, 1H, H^7), and 3.21 (s, 3H, SO_2Me). ^{13}C-NMR (101 MHz, acetone-d_6): δ_C 145.34, 140.64, 134.80, 133.99, 128.31 (2C), 128.11

(2C), 128.08, 124.75, 124.25, 118.90, 107.39, and 43.46. HPLC-MS (APCI/ESI): purity 95%, t_R = 2.26 min, (*m/z*) $[M+H]^+$ = 351.0.

3-(3-(4-(Methylsulfonyl)phenyl)imidazo[1,2-a]pyridin-6-yl)benzoic acid, 78 (GS1 08)

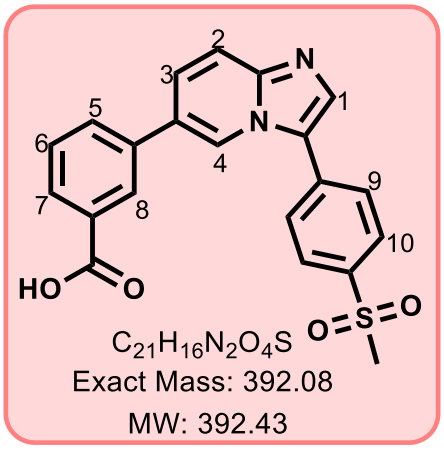

Using the general procedure 4 and a reaction mixture containing **76** (850 mg, 2.42 mmol) and 3-boronobenzoic acid (1.1 eq.) with purification by reverse phase flash chromatography (0–70% H_2O:MeOH), the product was obtained as an off-white solid (500 mg, 52%); MP 297–299°C; R_f (8% MeOH/DCM) tails; ^{1}H-NMR (600 MHz, acetic acid-d_4): δ_H 8.89 (broad s, 1H, H^4), 8.37 (t, *J* = 1.8 Hz, 1H, H^8), 8.28 (d, *J* = 9.0 Hz, 1H, H^2), 8.21 (s, 1H, H^1), 8.19 (d, *J* = 8.4 Hz, 2H, H^9), 8.16 (dt, *J* = 7.8 and 1.8 Hz, 1H, H^7), 8.13 (dd, *J* = 9.0 and 1.8 Hz, 1H, H^3), 8.03 (d, *J* = 8.4 Hz, 2H, H^{10}), 7.96 (dt, *J* = 7.8 and 1.8 Hz, 1H, H^5), 7.64 (t, *J* = 7.8 Hz, 1H, H^6), and 3.20 (s, 3H, SO_2Me). ^{13}C-NMR (151 MHz, acetic acid-d_4): δ_C 170.10, 141.72, 141.49, 136.17, 132.43, 131.69, 131.53, 130.67, 130.14, 129.84, 129.59 (2C), 129.51, 128.69, 128.48 (2C), 125.75, 122.65, 115.09, and 43.17. HPLC-MS (APCI/ESI): purity 98%, t_R = 2.32 min, (*m/z*) $[M+H]^+$ = 393.0.

***N, N*-Dimethyl-3-(3-(4-(methylsulfonyl)phenyl)imidazo[1,2-*a*]pyridin-6-yl) , 79 (GS1 09)**

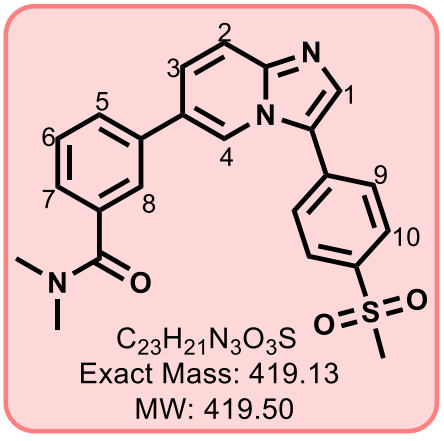

Using the general procedure 4 and a reaction mixture containing **76** (350 mg, 1.0 mmol) and (3-(dimethylcarbamoyl)phenyl) boronic acid (1.1 eq) the product was obtained as an off-white solid (230 mg, 55%); MP 98–100°C; R_f (10% MeOH/DCM) 0.73; ^{1}H-NMR (400 MHz, methanol-d_4): δ_H 8.77 (d, *J* = 1.6 Hz, 1H, H^4), 8.15 (d, *J* = 8.4 Hz, 2H, H^9), 8.12–8.08 (m, 1H, H^7), 8.00 (d, *J* = 8.2 Hz, 2H, H^{10}), 7.89 (s, 1H, H^1), 7.87–7.82 (m, 3H, $H^{2,3,5}$), 7.76 (broad d, *J* = 1.2 Hz, 1H, H^8), 7.58 (t, *J* = 8.0 Hz, 1H, H^6), 3.37 (s, 3H, SO_2Me), 3.21 (s, 3H, CH_3), and 2.96 (s, 3H, CH_3). ^{13}C-NMR (151 MHz, MeOD): δ_C 171.81, 145.93, 139.96, 137.35, 136.89, 134.09, 133.27, 129.02, 128.22, 128.19 (2C), 128.04 (2C), 127.26, 126.44, 126.20, 125.39, 125.04, 121.34, 116.98, 42.95, and 38.63. HPLC-MS (APCI/ESI): purity 98%, t_R = 2.35 min, (*m/z*) $[M+H]^+$ = 420.1.

3-(3-(4-(Methylsulfonyl)phenyl)imidazo[1,2-*a*]pyridin-6-yl)benzamide, 80 (GS1 11)

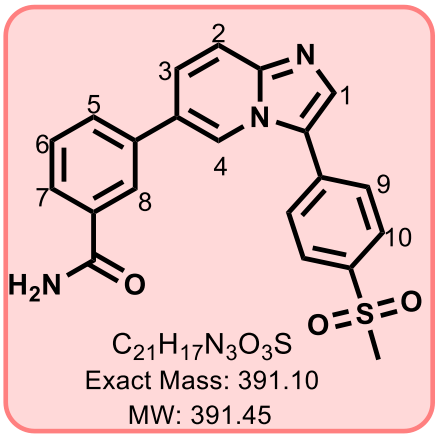

Using the general procedure 4 and a reaction mixture containing **76** (350 mg, 1.0 mmol) and (3-carbamoylphenyl) boronic acid (1.1 eq.), the product was obtained as an off-white solid (245 mg, 54%); MP 139–141°C; R_f (10% MeOH/DCM) 0.58; ^{1}H-NMR (400 MHz, acetone-d_6): δ_H 8.93 (d, J = 1.5 Hz, 1H, H^4), 8.27 (t, J = 1.8 Hz, 1H, H^8), 8.12 (d, J = 8.5 Hz, 2H, H^9), 8.08 (d, J = 8.6 Hz, 2H, H^{10}), 7.99 (broad d, J = 7.8 Hz, 1H, H^3), 7.93 (s, 1H, H^1), 7.91–7.87 (m, 1H, H^5), 7.77 (d, J = 9.3 Hz, 1H, H^2), 7.72 (dt, J = 9.3, and 1.8 Hz, 1H, H^7), 7.59 (t, J = 7.8 Hz, 1H, H^6), 6.75 (broad s, 2H, NH_2), and 3.21 (s, 3H, SO_2Me). ^{13}C-NMR (101 MHz, acetone-d_6): δ_C 167.77, 146.28, 140.26, 137.48, 135.39, 134.95, 134.54, 129.87, 129.08, 128.31, 127.91, 127.01, 126.72, 126.17, 125.45, 124.78, 121.62, 118.05, and 43.47. HPLC-MS (APCI/ESI): purity 99%, t_R = 2.26 min, (m/z) $[M+H]^+$ = 392.0.

3-(3-(4-(Methylsulfinyl)phenyl)imidazo[1,2-*a*]pyridin-6-yl)benzamide, 82 (GS1 22)

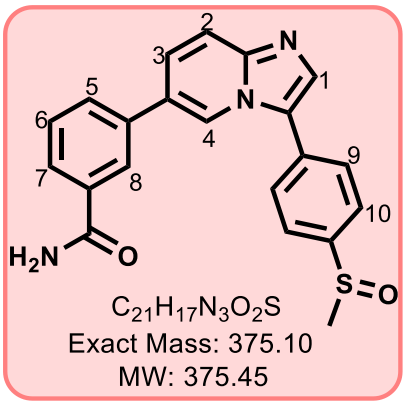

Using the general procedure 4 and a reaction mixture containing **77** (350 mg, 1.0 mmol) and (3-carbamoylphenyl)boronic acid (1.1 eq.) the product was obtained as a white solid (145 mg, 36%); MP 213–215°C; R_f (10% MeOH/DCM) 0.50; ^{1}H-NMR (600 MHz, DMSO-d_4): δ_H 8.76 (broad s, 1H, H^4), 8.17 (dt, J = 15.6 and 1.8 Hz, 1H, H^7), 8.07 (broad s, 1H, H^8), 7.95 (d, J = 8.4 Hz, 2H, H^9), 7.88 (s, 1H, H^1), 7.87–7.86 (m, 1H, H^5), 7.82 (d, J = 8.4 Hz, 2H, H^{10}), 7.78 (d, J = 9.0 Hz, 1H, H^2), 7.69 (dd, J = 9.4 and 1.8 Hz, 1H, H^3), 7.54 (t, J = 7.2 Hz, H^6), 7.41 (broad s, 2H, NH_2), and 2.78 (s, 3H, SOMe). ^{13}C-NMR (151 MHz, DMSO-d_4): δ_C 168.03, 146.06, 145.75, 140.03, 137.26, 135.49, 134.70, 131.56, 130.23, 129.54, 128.48, 127.46, 126.30, 125.76, 125.39, 125.16, 121.93, 118.21, and 43.61. HPLC-MS (APCI/ESI): purity 99%, t_R = 2.15 min, (*m/z*) $[M+H]^+$ = 376.1.

_N,N_-Dimethyl-3-(3-(4-(methylsulfinyl)phenyl)imidazo[1,2-a]pyridin-6-yl)benzamide, 81 (GS1 21)

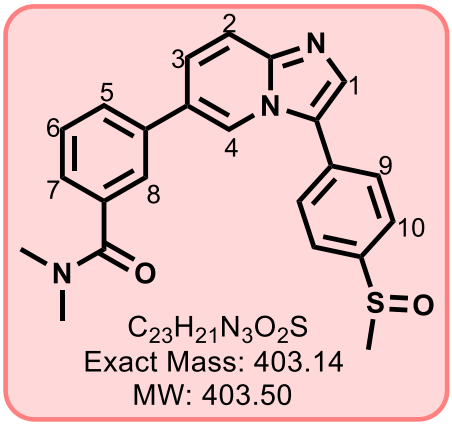

Using the general procedure 4 and a reaction mixture containing **77** (350 mg, 1.0 mmol) and (3-(dimethylcarbamoyl)phenyl)boronic acid (1.1 eq.), the product was obtained as a brown crystalline solid (135 mg, 32%); MP 74–76°C; R_f (10% MeOH/DCM) 0.59; ^{1}H-NMR (400 MHz, acetone-d_4): δ_H 8.83 (broad s, 1H, H^4), 8.01 (d, J = 8.4 Hz, 2H, H^9), 7.86 (d, J = 8.4 Hz, 2H, H^{10}), 7.85 (s, 1H, H^1), 7.79 (overlapping dt, J = 7.8 and 1.8 Hz, 1H, H^7), 7.76–7.73 (m, 2H, $H^{2,8}$), 7.67 (dd, J = 9.3 and 1.6 Hz, 1H, H^3), 7.55 (t, J = 7.6 Hz, 1H, H^6), 7.45 (dt, J = 7.6 and 1.8 Hz, 1H, H^5), 3.04 (s, 6H, CH_3) and 2.79 (s, 3H, SOMe). ^{13}C-NMR (101 MHz, acetone-d_4): δ_C 170.02, 146.74, 145.86, 138.11, 137.56, 134.17, 131.80, 128.94, 128.36, 127.79, 126.42, 126.38, 125.67, 125.31, 125.01, 124.55, 121.46, 118.00, 43.35, 38.61, and 34.28. HPLC-MS (APCI/ESI): purity 98%, t_R = 2.28 min, (*m/z*) $[M+H]^+$ = 404.1.

10.2.2.3 General procedure 5: synthesis of target compounds by HATU-mediated amide coupling

A mixture of the carboxylic acid intermediate **77** or **78**, HATU (3 eq.), and DIPEA (2.5 eq.) in DMF (6 mL) was cooled in ice while magnetically stirring. The appropriate amine (1.3 eq.) was then added, and the reaction mixture heated to 25°C for 12h. The reaction mixture was cooled to 20°C, diluted with DCM (50 mL × 3) and washed with saturated aqueous solution of $NaHCO_3$. The organic layer was dried over Na_2SO_4, concentrated *in vacuo* and subjected to normal-phase column chromatography (0–8% MeOH/DCM) to deliver the title compound.

(3-(3-(4-(Methylsulfonyl)phenyl)imidazo[1,2-*a*]pyridin-6-yl)phenyl)(morpholino) methanone, 85 (GS1 12)

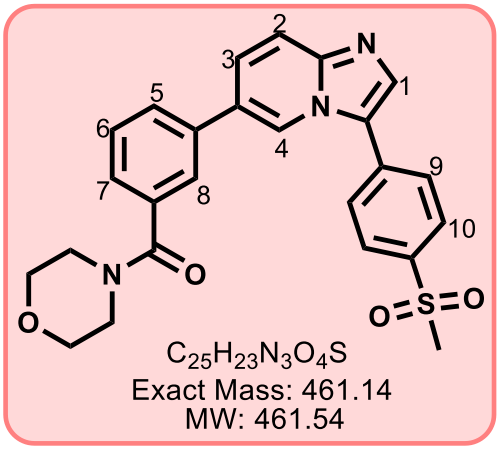

Using the general procedure 5 and a reaction mixture containing **78** (850 mg, 2.48 mmol) and morpholine (1 eq.), the product was obtained as an off-white solid (195 mg, 43%); MP 119–121°C; R_f (10% MeOH/DCM) 0.62; ^{1}H-NMR (400 MHz, methanol-d_4): δ_H 8.78 (broad s, 1H, H^8), 8.16 (d, J = 8.3 Hz, 2H, H^9), 8.02 (d, J = 8.3 Hz, 2H, H^{10}), 7.91 (s, 1H, H^1), 7.82 (broad d, J = 7.8 Hz, 1H, H^3), 7.78–7.74 (m, 3H, $H^{4,5,7}$), 7.61 (t, J = 7.7 Hz, 1H, H^6), 7.49 (d, J = 7.6 Hz, 1H, H^2), 3.87–3.40 (m, 8H, morpholino), and 3.21 (s, 3H, SO_2Me). ^{13}C-NMR (101 MHz, MeOD): δ_C 169.18, 144.56, 138.63, 136.16, 134.66, 132.73, 131.88, 127.79, 127.08, 126.78, 126.71, 125.80, 125.01, 124.89, 124.11, 123.67, 120.02, 115.61, 64.92 (2C), 46.81 (2C), and 41.56. HPLC-MS (APCI/ESI): purity 98%, t_R = 2.32 min, (m/z) $[M+H]^+$ = 462.1.

***N*-Cyclopropyl-3-(3-(4-(methylsulfonyl)phenyl)imidazo[1,2-a]pyridin-6-yl)benzamide, 83 (GS1 29)**

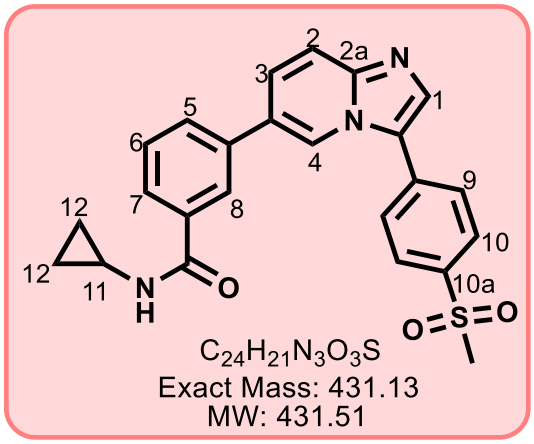

Using the general procedure 5 and a reaction mixture containing **78** (150 mg, 0.38 mmol) and cyclopropanamine (1.0 eq.), the product was obtained as a white solid (80 mg, 49%); MP 151–152°C; R_f (8% MeOH/DCM) 0.45; ^{1}H NMR (600 MHz, acetone-d_6): δ_H 8.85 (broad s, 1H, H^4), 8.13 (t, J = 1.8 Hz, 1H, H^8), 8.08 (d, J = 9.0 Hz, 2H, H^9), 8.03 (d, J = 8.4 Hz, 2H, H^{10}), 7.89 (s, 1H, H^1), 7.85 (dt, J = 7.8 and 1.2 Hz, 1H, H^7), 7.82 (dt, J = 7.8 and 1.2 Hz, 1H, H^5), 7.72 (d, J = 9.0 Hz, 1H, H^2), 7.65 (dd, J = 9.0 and 1.8 Hz, 1H, H^3), 7.51 (t, J = 7.8 Hz, 1H, H^6), 3.17 (s, 3H, SO_2Me), 2.91 (dp, J = 10.0 and 3.3 Hz, 1H, H^{11}), 0.72 (td, J = 7.0 and 4.9 Hz, 2H, H^{12e}), and 0.61–0.52 (m, 2H, H^{12a}). ^{13}C-NMR (151 MHz, acetone-d_6): δ_C 167.25, 146.22, 140.21, 137.40, 135.85, 134.91, 134.49, 129.58, 129.00, 128.31 (2C), 127.89 (2C), 126.68, 126.56, 125.76, 125.42, 124.74, 121.57, 118.01, 43.43, 22.97 (2C), and 22.84. HPLC-MS (APCI/ESI): purity 98%, t_R = 2.37 min, (*m/z*) $[M+H]^+$ = 432.1.

(4-Hydroxypiperidin-1-yl)(3-(3-(4-(methylsulfonyl)phenyl)imidazo[1,2-*a*]pyridin-6-yl)phenyl)methanone, 86 (GS1 16)

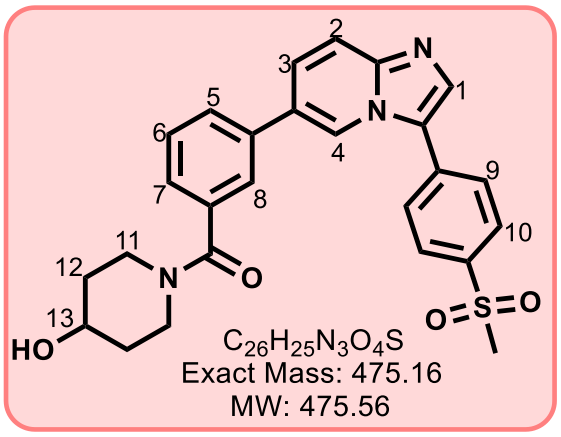

Using the general procedure 5 and a reaction mixture containing **78** (250 mg, 0.71 mmol) and 4-hydroxypiperidine (1.0 eq.), the product was obtained as a white solid (110 mg, 33%); MP 217–218°C; R_f (8% MeOH/DCM) 0.40; ^{1}H-NMR (600 MHz, acetic acid-d_4): δ_H 8.88 (broad s, 1H, H^4), 8.27 (d, J = 7.8 Hz, 1H, H^2), 8.21 (s, 1H, H^1), 8.19 (d, J = 8.4 Hz, 2H, H^9), 8.14 (dd, J = 7.8 and 1.2 Hz, 1H, H^3), 8.04 (d, J = 8.4 Hz, 2H, H^{10}), 7.85 (t, J = 1.8 Hz, 1H, H^8), 7.81 (dt, J = 7.8 and 1.8 Hz, 1H, H^7), 7.59 (t, J = 7.8 Hz, 1H, H^6), 7.53 (dt, J = 7.8 and 1.2 Hz, 1H, H^5), 4.22–4.03 (m, 2H, H^{11e}), 3.72–3.69 (m, 1H, H^{13}), 3.45–3.26 (m, 2H, H^{11a}), 3.21 (s, 3H, SO_2Me), 2.01–1.86 (m, 2H, H^{12e}), and 1.69–1.57 (m, 2H, H^{12a}). ^{13}C-NMR (151 MHz, acetic acid-d_4): δ_C 170.70, 141.63, 141.49, 136.13, 135.98, 131.63, 131.54, 129.95, 129.60, 129.35, 128.83, 128.49, 127.03, 126.03, 125.78, 125.63, 122.61, 114.97, 66.74, 45.12, 43.18, 39.84, and 33.50, and 32.69. HPLC-MS (APCI/ESI): purity 98%, t_R = 2.32 min, (*m/z*) $[M+H]^+$ = 476.1.

***N*-Cyclohexyl-3-(3-(4-(methylsulfonyl)phenyl)imidazo[1,2-*a*]pyridin-6-yl)benzamide, 84 (GS1 31)**

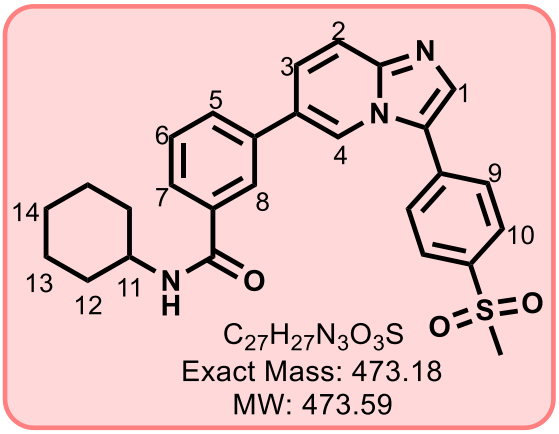

Using the general procedure 5 and a reaction mixture containing **78** (150 mg, 0.38 mmol) and cyclohexanamine (1.0 eq.) the product was obtained as an off-white solid (85 mg, 47%); MP 216–218°C; R_f (8% MeOH/DCM) 0.42; ^{1}H-NMR (600 MHz, acetic acid-d_4): δ_H 8.91 (broad s, 1H, H^4), 8.27 (d, J = 9.6 Hz, 1H, H^6), 8.21 (s, 1H, H^1), 8.19 (d, J = 8.4 Hz, 2H, H^9), 8.16 (dd, J = 9.0 and 1.2 Hz, 1H, H^3), 8.04 (d, J = 8.4 Hz, 2H, H^{10}), 7.90 (dt, J = 7.8 and 1.2 Hz, 1H, H^7), 7.85 (dt, J = 7.8 and 1.2 Hz, 1H, H^5), 7.57 (t, J = 7.8 Hz, 1H, H^6), 3.95 (tt, J = 10.8 and 4.0 Hz, 1H, H^{11}), 3.21 (s, 3H, SO_2Me), 2.01–1.98 (m, 1H, H^{14e}), 1.79–1.75 (m, 3H, H$^{12a, 14a}$), and 1.44–1.12 (m, 6H, H$^{12e, 13a, 13e}$). ^{13}C-NMR (151 MHz, acetic acid-d_4): δ_C 167.62, 141.54, 141.48, 135.85, 135.30, 131.90, 131.55, 130.33, 130.24, 129.56, 129.32, 128.51,

127.45, 126.74, 125.81, 125.33, 122.68, 114.81, 49.59, 43.19, 32.31 (2C), 25.25, and 24.79 (2C). HPLC-MS (APCI/ESI): purity 96%, t_R = 2.32 min, (*m/z*) $[M+H]^+$ = 474.2.

(3-(3-(4-(Methylsulfinyl)phenyl)imidazo[1,2-a]pyridin-6-yl)phenyl)(morpholino) methanone, 87 (GS1 25)

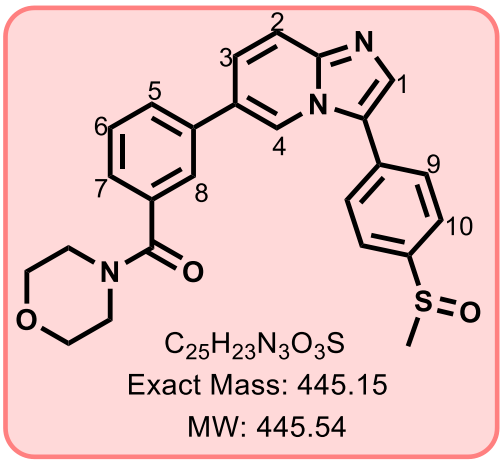

Using the general procedure 5 and a reaction mixture containing crude **77** (300 mg, 0.90 mmol) and morpholine (1.0 eq.) the product was obtained as a brown crystalline solid (130 mg, 33%); MP 107–109°C; R_f (10% MeOH/DCM) 0.67; ^{1}H-NMR (600 MHz, MeOD): δ_H 8.67 (broad s, 1H, H^4), 7.91 (d, *J* = 9.0 Hz, 2H, H^9), 7.87 (d, *J* = 8.4 Hz, 2H, H^{10}), 7.79 (s, 1H, H^1), 7.75 (ddd, *J* = 7.8, 1.8, and 1.2 Hz, 1H, H^7), 7.71 (d, *J* = 9.0 Hz, 1H, H^2), 7.70 (t, *J* = 1.8 Hz, 1H, H^8), 7.68 (dd, *J* = 9.6 and 1.8 Hz, 1H, H^3), 7.55 (t, *J* = 7.8 Hz, 1H, H^6), 7.43 (dt, *J* = 7.8 and 1.8 Hz, 1H, H^5), 3.77–3.40 (m, 8H, morpholino), and 2.85 (s, 3H, SOMe). ^{13}C-NMR (151 MHz, MeOD): δ_C 170.56, 145.63, 144.63, 137.61, 136.04, 132.67, 131.83, 129.20, 128.60, 128.45, 127.00, 126.27, 126.14, 125.49, 124.69, 121.30, 116.95, 66.32 (2C), 42.49 (2C) and 42.16. HPLC-MS (APCI/ESI): purity 99%, t_R = 2.27 min, (*m/z*) $[M+H]^+$ = 446.1.

(3-(3-(4-(Methylsulfinyl)phenyl)imidazo[1,2-a]pyridin-6-yl)phenyl)(pyrrolidin-1-yl)methanone, 88 (GS1 26)

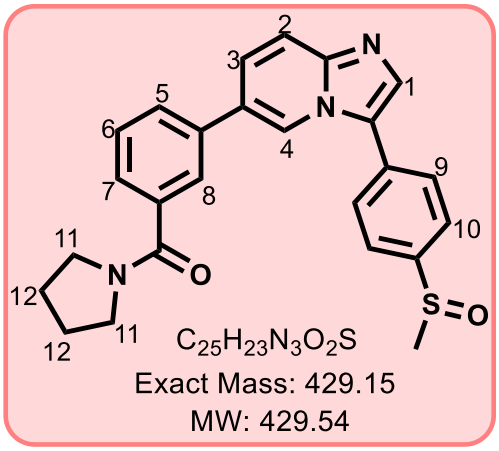

Using the general procedure 5 and a reaction mixture containing crude **77** (350 mg, 1.0 mmol) and pyrrolidine (1.0 eq.) the product was obtained as a brown crystalline solid (145 mg, 32%); MP 81–83°C; R_f (8% MeOH/DCM) 0.46; ^{1}H-NMR (600 MHz, MeOD): δ_H 8.67 (broad s, 1H, H^4), 7.91 (d, *J* = 8.4 Hz, 2H, H^9), 7.87 (d, *J* = 8.4 Hz, 2H, H^{10}), 7.79 (s, 1H, H^1), 7.77 (broad t, *J* = 1.2 Hz, 1H, H^8), 7.74 (dt, *J* = 6.6 and 1.8 Hz, 1H, H^7), 7.72 (dd, *J* = 9.0 and 0.6 Hz, 1H, H^2), 7.68 (dd, *J* = 9.3 and 1.8 Hz, 1H, H^3), 7.53 (overlapping t, *J* = 7.2 Hz, 1H, H^6), 7.53 - 7.51 (m, 1H, H^5), 3.59 (t, *J* = 7.2 Hz, 2H, H^{11a}), 3.47 (t, *J* = 7.2 Hz, 2H, H^{11e}), 2.85 (s, 3H, SOMe), 1.97 (p, *J* = 6.6 Hz, 2H, H^{12a}), and 1.89 (p, *J* = 7.2 Hz, 2H, H^{12e}). ^{13}C-NMR (151 MHz, MeOD): δ_C 169.88, 145.63, 144.62, 137.58, 137.34, 132.64, 131.84, 128.99,

128.59, 128.49, 127.15, 126.22, 126.17, 125.46, 125.42, 124.69, 121.23, 116.93, 49.46, 48.43, 46.09, 42.16, and 25.82 and 23.91. HPLC-MS (APCI/ESI): purity 96%, t_R = 2.39 min, (*m/z*) $[M+H]^+$ = 430.1.

(3-(3-(4-(Methylsulfinyl)phenyl)imidazo[1,2-a]pyridin-6-yl)phenyl)(piperidin-1-yl)methanone, 89 (GS1 27)

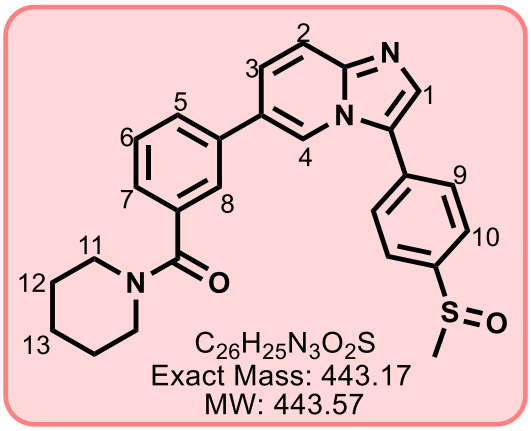

Using the general procedure 5 and a reaction mixture containing crude **77** (350 mg, 1.0 mmol) and piperidine the product was obtained as a brown crystalline solid (160 mg, 34%); MP 97–99°C; R_f (8% MeOH/DCM) 0.44; ^{1}H-NMR (600 MHz, MeOD): δ_H 8.67 (broad s, 1H, H^4), 7.92 (d, *J* = 8.4 Hz, 1H, H^9), 7.88 (d, *J* = 8.4 Hz, 1H, H^{10}), 7.80 (s, 1H, H^1), 7.73 (overlapping dt, *J* = 7.2 and 1.2 Hz, 1H, H^7), 7.72 (overlapping d, *J* = 6.0 Hz, 1H, H^2), 7.69 (dd, *J* = 9.0 and 1.8 Hz, 1H, H^3), 7.66 (t, *J* = 1.8 Hz, 1H, H^8), 7.54 (t, *J* = 7.8 Hz, 1H, H^6), 7.40 (dt, *J* = 7.2 and 1.8 Hz, 1H, H^5), 3.71–3.69 (m, 4H, H^{11}), 2.85 (s, 3H, SOMe), and 1.73–1.53 (m, 6H, $H^{12,13}$). ^{13}C-NMR (151 MHz, MeOD): δ_C 170.38, 145.64, 144.63, 137.52, 136.91, 132.63, 131.85, 129.15, 128.63, 128.14, 127.10, 126.16, 125.92, 125.48, 125.07, 124.69, 121.27, 116.94, 48.68, 42.96, 42.17, 26.14, 25.28, and 24.02. HPLC-MS (APCI/ESI): purity 97%, t_R = 2.45 min, (*m/z*) $[M+H]^+$ = 444.1.

10.3 Biological assays

10.3.1 *In vivo* antimalarial blood stage activity in the *Pf*SCID mouse model

The therapeutic efficacy of MLN0128 was studied in a mouse model of malaria infection based on methods previously described.[1] The compound was formulated in 0.5% hydroxypropyl methylcellulose (HPMC), 0.4% Tween 80, and 0.5% benzoyl alcohol before administration to a cohort of age-matched female non-obese diabetic (NOD)-SCID interleukin (IL)-2Rγc-null mice previously engrafted with human erythrocytes as per literature.[1,2] The mice were intravenously infected with 2 × 10^7 *P. falciparum Pf*3D70087/N9-infected erythrocytes (day 0).

On day 3, mice were randomly administered a daily dose (0, 0.05, 0.1, 0.5, 1.0, or 10 mg.kg^{-1}) for four consecutive days via oral gavage, with each dosing group comprising two mice.

Parasitemia was measured via flow cytometry using the fluorescent nucleic acid dye SYTO-16 and anti-murine erythrocyte TER119 monoclonal antibody (Pharmingen, San Diego, CA, USA) in 2 µL blood samples harvested every 24 h until assay completion.

10.3.2 *In vivo* pharmacokinetic (PK) in the *Pf*SCID mouse model

To rationalize the efficacy observed, mouse snapshot plasma PK investigations were performed on the infected mice.[3] Following the first oral administration, compound concentrations were measured in blood to provide insight into the PK profile.[3] Serial samples of peripheral blood (25 µL) were obtained via tail puncture from mice included in the efficacy experiment at 0.25, 0.5, 1, 3, 6, 8, 18, and 23 h after the drug administration. The samples were immediately lysed by mixing with 25 µL water containing 0.1% saponin, frozen on dry ice, and stored at -80°C until analysis. The compound was extracted from 10 µL lysate via liquid-liquid extraction in the MultiScreen Solvinert 0.45 µm hydrophobic polytetrafluoroethylene (PTFE) 96-well plate system (Millipore) and stored at -80°C until analysis via LC-MS/MS. The compound concentration-versus-time data were analyzed via non-compartmental analysis (NCA) using WinNonlin® Professional Version 5.2 (Pharsight Corporation, Mountain View, CA, USA). Additional statistical analyses were performed using GraphPad Prism® Version 5.01 (GraphPad Software Inc, San Diego, CA, USA).

10.3.3 Metabolomics assay

Metabolomics culturing and experiments were performed at the Department of Chemistry and Molecular Biology, Pennsylvania State University, USA based on methods described by Murithi *et al*.[4] Sorbitol-synchronized trophozoites were purified by MACS columns and either exposed to 10 × the IC_{50} of test compound for 2.5 h. MMV390048, KAI407, MMV030084 and atovaquone were included as controls in the experiments. About 4 mL of the media supernatant was aliquoted while the remaining one was centrifuged (VWR Galaxy 5D microcentrifuge) for 0.5 min at 8,500 rpm, and the pellet quenched with 1 mL ice cold 1 × PBS. The metabolites were then extracted in 1 mL 90% methanol containing 0.5 mM [^{13}C,^{15}N]-labelled aspartate (Isotec Stable Isotopes) as an internal standard. Triplicate blank samples comprising of 1 mL of 90% MeOH spiked with 0.5 µM [^{13}C,^{15}N]-labeled aspartate standard were included in the experiments. The samples were then dried in nitrogen and stored at -80°C before analysis using UHPLC-MS. Data analysis was performed using the el-MAVEN software and the Metaboanalyst package in R. Studio.[4,5]

10.3.4 *In vitro* asexual blood stage anti-plasmodium LDH assay

The CQ-sensitive *Pf*NF54 and multi-drug resistant *Pf*K1 strains were used in the assay. These assays were carried out at the Division of Clinical Pharmacology, Department of Medicine, UCT. Parasites were cultured and maintained according to the approach by Trager and Jensen with slight variations.[1] The anti-plasmodial activity was monitored using the parasite lactate dehydrogenase (pLDH) assay**.** Stock solutions of test compounds were prepared at 10 mM in 100% HPLC-grade DMSO (Sigma Aldrich). Subsequent dilutions of the stock solutions were prepared in medium to give the highest starting concentration of 6 µM.

From these, serial dilutions in complete medium were performed to achieve ten concentrations with the concentration range being between 0.2-100 µg/ml. Using these concentrations, dose response curves were generated to establish the concentration resulting in inhibition of parasite growth by 50%. Chloroquine and artesunate were employed as positive controls. The dilution approach adopted for the samples and controls was similar. Non-linear dose-response curves generated in GraphPad Prism v.6.01 software were used to evaluate the IC_{50} values.

10.3.5 *In vitro* asexual blood stage anti-plasmodium [^{3}H]-hypoxanthine incorporation assay

Compounds were screened at Swiss Tropical and Public Health Institute (STPH) against multidrug resistant (K1) and sensitive (NF54) strains of *P. falciparum* using the modified [^{3}H]-hypoxanthine incorporation *in vitro* assay.[6] The parasites were cultivated in a variation of the medium previously described.[7] In this case, it consisted of RPMI 1640 supplemented with 0.5% ALBUMAX® II, 0.36 mM hypoxanthine, 100 µg/mL neomycin and 25 mM HEPES titrated to pH 7.3 using 25 mM $NaHCO_3$. Human erythrocytes served as host cells. Cultures were maintained at 37°C in an atmosphere of 3% O_2, 4% CO_2 and 93% N_2 in humidified modular chambers. Compounds were dissolved by sonication to a stock solution of 10 mg/mL in HPLC-grade DMSO (Sigma Aldrich) and diluted in hypoxanthine-free culture medium. Infected erythrocytes (100 µL per well with 2.5% hematocrit and 0.3% parasitemia) were added to each drug titrated in 100 µL duplicates over a 64-fold range. A 48-hour incubation was then effected, after which 0.5 µCi of [^{3}H] hypoxanthine in 50 µL medium was added and plates incubated for an additional 24 h. Parasites were then harvested onto glass-fiber filters and radioactivity was counted using a Betaplate liquid scintillation counter (Wallac, Zurich). The results were

recorded as counts per min (cpm) per well at each drug concentration, normalized and expressed as a percentage of the untreated controls. IC_{50} were obtained by linear interpolation.

10.3.6 *In vitro* Luciferase Reporter gametocytocidal assay

Two transgenic parasite lines (NF54-*Pf*S16-GFP-Luc (early stage) and NF54-Mal8p1.16-GFP-Luc (late stage)) were used in the luciferase assays which facilitated stage-specific determination of gametocytocidal activity. This work was undertaken at the Department of Biochemistry and Institute of Sustainable Malaria Control, University of Pretoria (UP). Gametocytes were produced according to Reader *et al*.[8] On days 5 and 10 which respectively represent > 90% of early stage (I – III) and > 90% of late stage (IV and V) gametocytes, drug assays were set up. In both cases, 2 - 3% gametocytaemia and 1.5% haematocrit culture were used with a 48-h drug pressure in a gas chamber (90% N_2, 5% O_2 and 5% CO_2) at 37ºC. To 20 µL parasite lysates, 50 µL of luciferin substrate (Promega Luciferase Assay System) was added at room temperature (22ºC).

Luciferase activity was determined by detection of resulting bioluminescence at an integration constant of 10 seconds using the GloMax®-Multi$^+$ Detection System with Instinct® Software. Methylene blue and dihydroartemisinin were used as controls in the experiment.

10.3.7 *In vitro Pv*PI4K inhibition assay

Full-length *Pv*PI4K (PVX_098050) recombinant protein expressed in a baculovirus-insect cell expression system and purified as previously described was used in the assay.[9] The assay was undertaken at the H3D Biology Labs, Institute of Infectious Disease and Molecular Medicine, UCT. A 3-fold serial dilution of each inhibitor was carried out in DMSO (Sigma-Aldrich) and subsequently diluted into assay buffer (25 mM HEPES pH 7.4, 100 mM NaCl, 3 mM MgCl2, 1 mM DTT, 0.025 mg/ml BSA, 0.2% (v/v) Triton-X-100) to 4 × the final required concentration. 5 µL of each inhibitor dilution was transferred into a white 384-shallow well plate (Nunc #264706). L-alpha-phosphatidylinositol (PI; Avanti Polar Lipid, cat. 840042P) dissolved in 3% n-Octylglucoside to a stock concentration of 20 mg/ml was used as the lipid substrate. The assay components was then manually dispensed [5 µL substrate buffer (ATP and PI), followed by 10 µL of *Pv*PI4K protein] and added to each well. The final 20 µL kinase reaction contained ~6 nM *Pv*PI4K protein (for 10% ATP conversion), 10 µM ATP, 0.1 mg/ml PI, 1% (v/v) DMSO and inhibitor in assay buffer.

10 µM MMV390048 was included in the assays as the positive control for the experiments. The reaction plates were then incubated at 22°C for 40 min then stopped by aliquoting 4 µL of the enzyme reaction and adding equal volume of ADP-Glo reagent prepared as per manufacturers protocol. This was then incubated for a further 30 min at the same temperature. Luciferase-coupled reaction was then effected by adding 8 µL Kinase Detection Reagent (KDR) and incubating at 22°C for 40 min. Luminescence proportional to the remaining ATP at the end of the reaction was measured using an EnSpire® Multimode Plate Reader (PerkinElmer) at λ = 680 nm). Ten-point dose-response curves were obtained from the 3-fold dilutions of the test compound, normalized and the IC_{50} values determined using GraphPad Prism® v6.02 (GraphPad Software Inc, San Diego, CA, USA). The measurements were done in duplicates and the assay independently repeated.

10.3.8 *In vitro Pf*PKG inhibition assay

Full length *Pf*PKG (*Pf*3D7_1436600) expressed in *Escherichia coli* using methods previously described was used in the assay.[10] This assay was also undertaken at the H3D Biology Labs, Institute of Infectious Disease and Molecular Medicine, UCT. *Pf*PKG IC_{50} values were determined using an ADP-Glo Kinase kit from Promega® and conducted as per literature.[11] A 3-fold serial dilution of each inhibitor was carried out in DMSO (Sigma-Aldrich) and subsequently diluted into assay buffer (25 mM HEPES pH 7.4, 0.1 mg/mL BSA, 0.01 % (v/v) Triton-X 100, 20 mM $MgCl_2$, 2 mM DTT, 10 µM cGMP) to 4 × the final required concentration.[11] 5 µL of each inhibitor dilution was transferred into a white 384-shallow well plate (Nunc #264706). The remaining assay components were then manually dispensed [10 µL of *Pf*PKG protein, followed by 5 µL substrate buffer (ATP and peptide substrate GRTGRRNSI-NH2], and added to each well. The final 20 µL kinase reaction contained ˜0.6 nM *Pf*PKG protein, 10 µM ATP, 20 µM GRTGRRNSI-NH2, 1 % (v/v) DMSO and inhibitor in assay buffer.

Control reactions using the peptide mix and 500 nM ML10 (LifeArc), a known *Pf*PKG inhibitor was included as positive control, and another using no protein to ensure that the inhibitor did not interfere with the ADP-Glo detection component of the assay and to account for background signal. Reactions were incubated at 22°C for 40 min.

After the incubation, 4 µL of each kinase reaction mix was transferred into a white, 384-well plate in replicates, and the reaction terminated by adding 4 µL ADP-Glo reagent to quench any remaining ATP by incubating at 22°C for 30 min. Conversion of ADP generated in the kinase

reaction to ATP for luciferase-coupled reaction was then effected by adding 8 µL Kinase Detection Reagent (KDR) and incubating at 22°C for 40 min. Luminescence measurements were then performed using an EnSpire® Multimode Plate Reader (PerkinElmer) at a λ = 680 nm and the IC_{50} values calculated using similar as those employed for *Pv*PI4K. Percentage PKG inhibition was evaluated for some compounds at a maximum concentration of 10 µM using the same protocol,

10.3.9 *In vitro* human mTOR assay

In vitro mTOR profiling was performed at Reaction Biology Corporation® (Biotech) using the "HotSpot" assay platform.[12] Briefly, mTOR/substrate pair along with required cofactors were prepared in reaction buffer; 20 mM HEPES pH 7.5, 10 mM $MgCl_2$, 1 mM ethylene glycol-bis(β-aminoethyl ether)-*N*,*N*,*N*′,*N*′-tetraacetic acid (EGTA), 0.02% Brij35, 0.02 mg/ml BSA, 0.1 mM Na_3VO_4, 2 mM DTT, 1% DMSO. Compounds in DMSO were delivered into the reaction by acoustic technology (Echo550; nanoliter range), followed ~20 min later by addition of ^{33}P-ATP to a final concentration of 10 µM for dose-response curves or 1 µM for single-point inhibition. Reactions were carried out at 25°C for 120 min, followed by spotting of the reactions onto P81 ion exchange filter paper (Whatman). Unbound phosphate was removed by extensive washing of filters in 0.75% phosphoric acid. After subtraction of background derived from control reactions containing inactive enzyme, kinase activity data were expressed as the percent remaining kinase activity in test samples compared to vehicle (DMSO) reactions. Curve fits and IC_{50} values were obtained using GraphPad Prism® v. 6.01 Software.

10.3.10 Cytotoxicity on the CHO cell line

In vitro cytotoxicity was conducted on the CHO cell lines using the 3-(4,5-dimethylthiazol-2-yl)-2,5-diphenyltetrazolium bromide (MTT) assay.[13] Test compounds were dissolved in 100% DMSO to yield a 20 mM stock solution while the reference standard, emetine, was dissolved in distilled water to a 2 mg/mL solution. From an initial test compound and control concentration of 100 µg/mL, serial 10-fold dilutions, in assay medium, were performed to achieve six concentrations with 0.001 µg/mL being the lowest concentration. The highest concentration of DMSO exposed to cells had no effects on cell viability. Plates were incubated for 48 h with 100 µL of drug and 100 µL of cell suspension in each well after which they were developed by the addition of 25 µL of sterile MTT (Thermo Fisher Scientific) to each well and a further incubation in the dark for 4 hours. Thereafter, the plates were centrifuged, the medium

aspirated off and DMSO (100 µL) added to dissolve crystals and absorbance readings taken at 540 nM. Non-linear dose-response curve fitting analysis conducted using GraphPad Prism v.4.0 software (La Jolla, USA), was applied to generate IC_{50} values. The assay was conducted in triplicate and two independent assays (n = 2) were carried out for each compound.

10.3.11 Cytotoxicity on the HepG2 cell line

Human hepatocellular liver carcinoma cells (HepG2) were maintained in Dulbecco's Modified Eagle's Medium (DMEM) supplemented with 10% heat inactivated fetal bovine serum and 1% penicillin/streptomycin at 37°C (5% CO_2, 90% humidity). Cytotoxicity was measured using the lactate dehydrogenase assay (LDH).[14] Cells (100000) were seeded in 96-well plates and grown for 24h at 37°C, after which cells were treated with 2 µM compound. After 48 h exposure, cells were pelleted at 250 g for 10 min and LDH activity was measured in the supernatant (10 µL) by adding 100 µL LDH reaction mix (BioVision) and incubating for 30 min at room temperature. Colorimetric detection of NADH levels using the CytoSelectTM® cytotoxicity Assay Kit (Cell Biolabs Inc., CBA-241) (as a measurement of LDH-mediated oxidation of lactate indicating LDH activity) was measured at 450 nm. Experiments were performed in duplicate for at least two independent biological repeats ($n \geq 2$).

10.3.12 *In vitro* metabolic stability

Metabolic stability was conducted using the one-time point assay as described in literature.[15,16] Experiments were performed in triplicate in a 96-well microtiter plate using test compounds at a concentration of 0.1 µM, incubated individually in a solution containing 0.35 mg/mL mouse (male mouse BALB/c, Xenotech) or human (mixed gender, Xenotech) liver microsomes.

To initiate metabolic reactions, NADPH (1 mM) in phosphate buffer (100 mM, pH 7.4) were added to the wells and the plates incubated for 30 mi. After this period, 300 µL of ice-cold acetonitrile (ACN) containing internal standard (carbamazepine, 0.0236 µg/mL) was added to each well to quench the reactions. The supernatant was filtered after which LCMS/MS (Agilent Rapid Resolution HPLC, AB SCIEX 4000 QTRAP MS) analysis was performed to determine the concentration of test compound. Differences in the amounts of compounds before and after incubation were determined by LC-MS/MS and results recorded as percent compound remaining after 30 min incubation. The relative loss of parent compound over time was monitored and plots of concentration versus time were prepared for each compound to determine the first order rate constant for compound depletion. This was used to calculate the

degradation half-life ($t_{1/2}$) and predict the *in vivo* hepatic extraction ratio (E_H). Metabolite identification was not performed during the microsomal metabolic stability assay.

10.3.13 *In vitro* hERG inhibition assay

The hERG inhibition assay was performed on QPatch 16X or QPatchHTX automated patch-clamp system at B'SYS GmbH, Witterswil, Switzerland.[17] This is a multi-channel chip array system comprising of a series of microfluidic chamber (Q-plates), each containing extra- and intracellular solutions separated by a silicon/glass surface with a miniature hole. Cells fed into each chamber, interact with the glass surface to form a stable giga-ohm seal across the aperture resulting in an electrophysiology pattern that can be evaluated.

Initially, test compounds were dissolved in DMSO (Sigma-Aldrich) to a 10 mM stock solution and thereafter serially diluted to the screening concentrations of 30, 10, 3, and 0 μM in freshly prepared extracellular solution to ensure a final 1 × components of NaCl (137 mM), KCl (4 mM), $CaCl_2$ (1.8 mM), $MgCl_2$ (1 mM), D-glucose (10 mM) in HEPES buffer (10 mM) titrated to a pH of 7.4 in NaOH. The intracellular solution used in the system comprised of KCl (130 mM), $CaCl_2$ (2 mM), $MgCl_2$ (4 mM), Na_2-ATP (4 mM), EGTA (5 mM), in HEPES buffer (10 mM) stabilized to a pH of 7.2 in KOH. The potassium ion hERG channel was stably expressed in a CHO cell line, grown in sterile culture flasks in a mixture of HAM/F-12 (1 × liquid with L-Glutamine) supplemented with 10% foetal bovine serum and 1.0% Penicillin/Streptomycin solution, and harvested in standard laboratory conditions.

Cells were then transferred as suspension in serum-free medium to the QPatch system and kept in the cell storage tank/stirrer during the experiments. All solutions applied to cells including the intracellular solution were maintained at room temperature (19 to 30°C). Voltage ramps were then employed, from a holding potential of -80 mV, depolarization of the cell membrane to +20 mV for 2 s and upon subsequent repolarisation to -40 mV for 3 s, the outward hERG tail currents were measured. A pre-programmed waiting time of 5 s was employed, before the next pulse. This application protocol was undertaken in triplicate for the test solutions, vehicle, and the control standard (E-4031). The normalized currents were then plotted using SigmaPlot 11.0 software, fitted to the Hill equation, upon which IC_{50} and IC_{20} values were deduced.

10.4 Solubility evaluation

10.4.1 Turbidimetric-based kinetic solubility

The target compounds were subjected to turbidimetric based solubility studies[18] performed in polypropylene, flat-bottomed, 96-well microtiter plates (Thermo Fisher Scientific, UK) in freshly prepared phosphate buffered saline (PBS) solution. This comprised of 0.14 M NaCl, 0.003 M KCl and 0.01 M phosphate buffer in distilled water, titrated to pH 7.4 using 1M NaOH or HCl. Precipitates were then removed by filtration through a 0.22 µM nylon filter. The test compounds were serially diluted in plates from the 10 mM DMSO stock solutions to obtain final concentrations between 0 to 200 µM in both PBS and HPLC-grade DMSO (Sigma Aldrich). The PBS wells contained a maximum concentration of 2% DMSO. Hydrocortisone and reserpine were prepared in a similar manner and included as positive controls.

Plates were then equilibrated at 25°C (Memmert, GmbH$^+$ Co.) for 2 h. UV-vis absorbance was then measured at λ = 620 nm using a SpectraMax 340PC^{384} microplate reader (Molecular Devices, Sunnydale, CA). Absorbance readings were then obtained from the DMSO and PBS wells and normalized with the blanks and plotted against concentration using Microsoft® Excel 2018 application software with the point of inflection of PBS plot from that of DMSO, considered as the limit of solubility.

10.4.2 Solubility using HPLC-based DMSO "dry-down" method

This modified kinetic solubility determination method was employed to minimize solvent enhancement of solubility observed in the turbidimetric method.[19] Test compounds were dissolved in DMSO (Sigma-Aldrich) to yield 10 mM stock solutions. HPLC analysis was used with UV detection to construct calibration curves for each compound using low (11 µM), medium (100 µM), and high (220 µM) concentration standards. High and medium standards were prepared by placing 4.4 µL and 2 µL of the 10 mM stock solution into wells A and B of a 96-well microtiter plate and diluted by adding 195.6 µL and 198 µL DMSO, respectively. The low standard was prepared in well C by diluting 10 µL, obtained from well A, with 190 µL DMSO to obtain a 20-fold dilution of the 220 µM solution.

Thereafter, each test sample (4 µL of 10 mM stock) was placed in triplicate in wells D, E, and F and DMSO was removed by freeze-drying under Genevac®. This step reduces DMSO-associated solubility enhancement. PBS (200 µL, pH 7.4) was added to the wells now

containing dry, solid material from test samples. The plates were covered and placed on a shaker at 37°C for 24 h. After this period, the plates were put under centrifugation (Digtor 21R®) at 3500 rpm for 15 min at a temperature of 23°C. The supernatants were then carefully transferred to an analytical 96-well microtiter plate for HPLC analysis fitted with UV detection. The concentrations of dissolved samples were determined by comparing the average peak areas of the samples (wells D, E, and F) against the previously constructed standard curve using samples in wells A, B, and C.

References

1. Jiménez-Díaz, M.; Mulet, T.; Viera, S.; Gomez, V.; Garuti, H.; Ibanez, J.; Alvarez-Doval, A.; Shultz, L.; Martinez, A.; Gargallo-Viola, D.; Angulo-Barturen, I.Improved murine model of malaria using *Plasmodium falciparum* competent strains and non-myelodepleted NOD-scid IL2Rγnull mice engrafted with human erythrocytes. *Antimicrob. Agents Chemother*. **2009**; 53 (10): 4533 - 4536. doi:10.1128/AAC.00519-09.

2. Angulo-Barturen, I.; Jiménez-Díaz, M.; Mulet, T.; Rullas, J.; Herreros, E.; Ferrer, S.; Jimenez, E.; Mendoza, A.; Regadera, J.; Rosenthal, P.; Bathurst, I.; Pompliano, D.; Heras, F.; Gargallo-Viola, D. A murine model of *falciparum*-malaria by *in vivo* selection of competent strains in non-myelodepleted mice engrafted with human erythrocytes. *PLoS One*. **2008**; 3 (5): 1 - 14. doi:10.1371/journal.pone.0002252.

3. Gibhard, L.; Njoroge, M.; Paquet, T.; Brunschwig, C.; Taylor, D.; Lawrence, N.; Abay, E.; Wittlin, S.; Wiesner, L.; Street, L.; Chibale, K.; Basarab, G. Investigating sulfoxide-to-sulfone conversion as a prodrug strategy for a phosphatidylinositol 4-kinase inhibitor in a humanized mouse model of malaria. *Antimicrob. Agents Chemother*. **2018**; 62 (12): 1 - 11. doi:10.1128/AAC.00261-18.

4. Murithi, J.; Owen, E.; Istvan, E.; Lee, M.; Ottilie, S.; Chibale, K,; Goldberg, D.; Winzeler, E.; Llinas, M.; Fidock, D.; Vanaerschot, M. Combining stage specificity and metabolomic profiling to advance antimalarial drug discovery. *Cell Chem. Biol*. **2020**; 27 (2): 158 - 171.e3. doi:10.1016/j.chembiol.2019.11.009.

5. Allman, E.; Painter, H.; Samra, J.; Carrasquilla, M.; Llinás, M. Metabolomic profiling of the Malaria Box reveals antimalarial target pathways. *Antimicrob. Agents Chemother*. **2016**; 60 (11): 6635 - 6643. doi:10.1128/aac.01224-16.

6. Huber, W. and Koella, J. A comparison of three methods of estimating EC_{50} in studies of drug resistance of malaria parasites. *Acta. Trop*. **1993**; 55 (4): 257 - 261. doi:10.1016/0001-706X(93)90083-N.

7. Trager, W. and Jensen, J. Human Malaria parasites in continous culture. *Science*. **1976**; 193 (8): 673 - 675.

8. Reader, J.; Botha, M.; Theron, A.; Lauterbach, S.; Rossouw, C.; Englebrecht, D.;

Wepener, M.; Smit, A.; Leroy, D.; Mancama, D.; Coetzer, T.; Birkholtz, L. Nowhere to hide: Interrogating different metabolic parameters of *Plasmodium falciparum* gametocytes in a transmission blocking drug discovery pipeline towards malaria elimination. *Malar. J.* **2015**; 14 (1):1 - 17. doi:10.1186/s12936-015-0718-z.

9. McNamara, C.; Lee, M.; Lim, C.; Lim, S.; Roland, J.; Nagle, A.; Simon, O.; Yeung, B.; Chatterjee, A.; McCormack, S.; Manary, M.; Zeeman, A.; Dechering, K.; Kumar, T.; Henrich, P.; Gagaring, K.; Ibanez, M.; Kato, N.; Kuhen, K.; Fischli, C.; Rottmann, M.; Plouffe, D.; Bursulaya, B.; Meister, S.; Rameh, L.; Trappe, J.; Haasen, D.; Timmerman, M.; Sauerwein, R.; Suwanarusk, R.; Russell, B.; Renia, L.; Nosten, F.; Tully, D.; Kocken, C.; Glynne, R.; Bodenreider, C.; Fidock, D.; Diagana, T.; Winzeler, E. Targeting *Plasmodium* PI(4)K to eliminate malaria. *Nature*. **2013**; 504 (7479): 248 - 253. doi:10.1038/nature12782.

10. Cheuka, P.; Centani, L.; Arendse, L.; Fienberg, S.; Wambua, L.; Renga, S.; Dziwornu, G.; Kumar, M.; Lawrence, N.; Taylor, D.; Wittlin, S.; Coertzen, D.; Reader, J.; van der Watt, M.; Birkholtz, L.; Chibale, K. New amidated 3,6-diphenylated imidazopyridazines with potent anti-plasmodium activity are dual inhibitors of *Plasmodium* phosphatidylinositol-4-kinase and cGMP-dependent protein kinase. *ACS Infect. Dis.* **2021**; 7 (1): 34 - 46. doi:10.1021/acsinfecdis.0c00481.

11. Vanaerschot, M.; Murithi, J.; Pasaje, C.; Ghidelli-Disse, S.; Dwomoh, L.; Bird, M.; Spottiswoode, N.; Mittal, N.; Arendse, L.; Owen, E.; Wicht, K.; Siciliano, G.; Bosche, M.; Yeo, T.; Kumar, T.; Mok, S.; Carpenter, E.; Giddins, M.; Sanz, O.; Ottilie, S.; Alano, P.; Chibale, K.; Llinas, M.; Uhlemann, A.; Delves, M.; Tobin, A.; Doerig, C.; Winzeler, E.; Lee, M.; Niles, J.; Fidock, D. Inhibition of resistance-refractory *P* . *falciparum* Inhibition of resistance-refractory *P. falciparum* kinase PKG delivers prophylactic, blood stage, and transmission-blocking anti-plasmodial activity. **2020**: 1 - 11. doi:10.1016/j.chembiol.2020.04.001.

12. Anastassiadis, T.; Deacon, S.; Devarajan, K.; Ma, H.; Peterson, J. Comprehensive assay of kinase catalytic activity reveals features of kinase inhibitor selectivity. *Nat. Biotechnol*. **2011**; 29 (11): 1039 - 1045. doi:10.1038/nbt.2017.

13. Liu, Y.; Peterson, D.; Kimura, H.; and Schubert, D. Mechanism of cellular 3-(4,5-Dimethylthiazol-2-yl)-2,5- Diphenyltetrazolium Bromide (MTT) reduction. *J. Neurochem*. **1997**; 69 (2): 581 - 593.

14. Verlinden, B.; Niemand, J.; Snyman, J.; Sharma, S.; Beattie, R.; Woster, P.; Birkholtz, L. Discovery of novel alkylated (bis)urea and (bis)thiourea polyamine analogues with potent antimalarial activities. *J. Med. Chem*. **2011**; 54 (19): 6624 - 6633. doi:10.1021/jm200463z.

15. Kandepedu N.; Cabrera, D.; Eedubilli, S.; Taylor, D.; Brunschwig, C.; Gibhard, L. Njoroge, M.; Lawrence, N.; Paquet, T.; Eyermann, C.; Spangenberg, T.; Basarab, G.; Street, L.; Chibale, K. Identification, characterization, and optimization of 2,8-disubstituted-1,5-naphthyridines as novel *Plasmodium falciparum* phosphatidylinositol-4-kinase inhibitors with *in vivo* efficacy in a humanized mouse model of malaria. *J. Med. Chem.* **2018**; 61 (13): 5692 - 5703. doi:10.1021/acs.jmedchem.8b00648.

16. Gibhard, L.; Pravin, K.; Abay, E.; Wilhelm, A.; Swart, K.; Lawrence, N.; Khoury, R. Westhuizen, J.; Smith, P.; Wiesner, L. *In vitro* and *in vivo* pharmacokinetics of aminoalkylated diarylpropanes NP085 and NP102. *Antimicrob. Agents Chemother*. **2016**; 60 (5): 3065 - 3069. doi:10.1128/AAC.02104-15.

17. Houtmann, S.; Schombert, B.; Sanson, C.; Partiseti, M.; Bohme, G. Automated patch-clamp methods for the hERG cardiac potassium channel. In: *Drug Safety Evaluation: Methods and Protocols, Methods in Molecular Biology*. **2017**; 1641: 187 - 199. doi:10.1007/978-1-4939-7172-5.

18. Pan, L.; Ho, Q.; Tsutsui, K. and Takahashi, L. Comparison of chromatographic and spectroscopic methods used to rank compounds for aqueous solubility. *J. Pharm. Sci*. **2001**; 90 (4): 521 - 529. doi:10.1002/1520-6017(200104)90:4<521:AID-JPS1009>3.0.CO;2-B.

19. Glomme, A.; März, J. and Dressman, J. Comparison of a miniaturized shake-flask solubility method with automated potentiometric acid/base titrations and calculated solubilities. *J. Pharm. Sci*. **2005**; 94 (1): 1 - 16. doi:10.1002/jps.20212.